UNIVERSITÀ
DEGLI STUDI
DI PADOVA

Sede Amministrativa: Università degli Studi di Padova

Dipartimento di Astronomia

SCUOLA DI DOTTORATO DI RICERCA IN ASTRONOMIA
CICLO XXII

Dynamics induced by the central supermassive black holes in galaxies

Direttore della Scuola: Prof. Giampaolo Piotto
Supervisori: Prof. Francesco Bertola
Prof. Enrico Maria Corsini

Dottoranda: Alessandra Beifiori

alla nonna Nora

Riassunto

Questa tesi è dedicata alla misura della massa $M_\bullet$ dei buchi neri supermassicci (SMBH) e allo studio delle relazioni di scala tra le masse dei buchi neri e le proprietà delle galassie ospiti con lo scopo di capire il ruolo dei SMBH nell'evoluzione delle galassie.

La prima parte della tesi è dedicata alla presentazione di un atlante di spettri e immagini di un ampio campione di galassie lungo tutta la sequenza morfologica di Hubble, il quale è stato selezionato per misurare $M_\bullet$ (Capitolo 2). Gli spettri sono stati estratti dall'archivio di *Hubble Space Telescope* (*HST*). Il campione comprende 177 galassie vicine $D < 100$ Mpc con spettro nucleare ottenuto con lo Space Telescope Imaging Spectrograph (STIS) nell'intervallo spettrale che include le righe di emissione di [N II] $\lambda\lambda 6548, 6583$, H$\alpha$ e [S II] $\lambda\lambda 6716, 6731$. Per 65 galassie è stato inoltre possibile misurare i parametri strutturali del sferoide e dello disco ottenuti attraverso la decomposizione fotometrica bidimensionale di immagini 2MASS e UKIDSS in banda K.

Sono stati ottenuti dei robusti limiti superiori della $M_\bullet$ per un sottocampione di 105 galassie (Capitolo 3) di diversi tipi morfologici (E−Sc) e con diverse dispersioni di velocità stellare σ (58−419 km s^{-1}). Questi limiti superiori sono stati misurati dalla larghezza delle righe di emissione, assumendo che il gas ionizzato delle regioni nucleari risieda in un disco sottile di orientazione incognita ma di cui si conosce l'estensione spaziale. I limiti superiori di $M_\bullet$ sono consistenti con le relazioni $M_\bullet - \sigma$ di Ferrarese & Ford (2005) e di Lauer et al. (2007a) e con le determinazioni accurate di $M_\bullet$ dei SMBH di cui è stata risolta la sfera d'influenza. Inoltre, questi limiti superiori di $M_\bullet$ si dispongono parallelamente e in prossimità della relazione $M_\bullet - \sigma$ senza mostrare alcuna dipendenza dalla distanza degli oggetti, dal loro tipo morfologico e dalla presenza o meno di una barra. Questo significa che la larghezza delle righe di emissione rappresenta un buon tracciante del potenziale gravitazionale del buco nero. Inoltre, il grande numero di galassie, che abbiamo a disposizione, permette di escludere che le

larghezze delle righe siano dovute al solo contributo delle forze non gravitazionali. Tuttavia, per valori di σ inferiori ai 90 km s^{-1} metà dei limiti superiori eccedono sistematicamente il valore previsto dalla relazione $M_\bullet - \sigma$. Questa peculiarità è stata imputata al maggior contributo stellare sul potenziale gravitazionale dovuto alla presenza di ammassi stellari nucleari e alla maggiore distanza dell'oggetto. Ad alte dispersioni di velocità ($\sigma > 220$ km s^{-1}) i valori di $M_\bullet$ sembrano concordare con i valori attesi, soprattutto per le galassie ellittiche giganti, suggerendo un appiattimento della relazione $M_\bullet - \sigma$. Questo fenomeno potrebbe essere dovuto al meccanismo di coevoluzione con le galassie ospiti attraverso fenomeni di interazione e fusioni in assenza di gas. Tuttavia misure più precise di σ e luminosità in banda K sono necessarie per escludere definitivamente gli eventuali effetti sistematici.

Con i risultati ottenuti si è visto come i limiti superiori della $M_\bullet$ possano essere utilizzati nel confronto con le relazioni di scala (Capitolo4). Pertanto, sono stati usati per interpretare la demografia dei SMBH, in particolare per capire se $M_\bullet$ risulta più strettamente connessa con il solo sferoide o con l'intera galassia. A questo scopo i limiti superiori della $M_\bullet$ sono stati combinati con le $M_\bullet$ la cui sfera di influenza è nota per essere stata risolta. Sono stati poi raccolti i dati relativi alle dispersioni di velocità e alle velocità circolari e sono stati misurati i parametri fotometrici dall'analisi delle immagini SDSS in banda i. Sono state considerate le correlazioni tra la $M_\bullet$ e la dispersione di velocità stellare, la luminosità in banda i, la massa viriale e l'indice di Sérsic dello sferoide, la luminosità, la massa stellare, la velocità circolare e le masse viriale e dinamica della galassia. È stata confermato che la relazione $M_\bullet - \sigma$ risulta la più stretta tra tutte le correlazioni. La $M_\bullet$ risulta principalmente correlata con σ per tutti i tipi morfologici e, analogamente, il piano fondamentale dei SMBH dipende principalmente da σ con un piccolo contributo dovuto al raggio efficace.

È stata caratterizzata la parte alta della funzione di massa dei SMBH dell'universo locale, dal momento che è proprio alle masse più alte che il legame tra l'evoluzione dei SMBH e la formazione gerarchica delle galassie è più stringente. Questo è stato fatto misurando la $M_\bullet$ in una galassia ellittica molto massiccia, NGC 1265, usando dati della cinematica stellare ottenuti con ottica adattiva (Capitolo 5) e stimando la $M_\bullet$ in tre galassie molto brillanti attraverso la cinematica del gas derivata da dati di *HST* (Capitolo 6). Queste misure sono importanti per capire l'andamento della relazione $M_\bullet - \sigma$ nella regione ad alte σ.

Sono state analizzati dati spettroscopici della regione centrale della radio galassia NGC 1265/3C 83.1B(Capitolo 5). Gli spettri sono stati ottenuti in banda K al telescopio Gemini Nord con lo spettrografo Near InfraRed Imager

and Spectrograph (NIRI) accoppiato con il sistema di ottica adattiva Altair permettendo una risoluzione spaziale di FWHM=0.″11 (39 pc). Per la stima del contributo stellare è stato interpolato il profilo di luce della galassia con una serie di gaussiane usando in combinazione l'immagine NIRI ad alta risoluzione e un'immagine ottenuta al TNG per coprire anche le parti esterne della galassia. La cinematica stellare è stata estratta dalle bande di assorbimento del CO a 2.29 μm. Sono stati adottati modelli di Jeans per interpolare la cinematica stellare e la distribuzione di brillanza superficiale per determinare i valori di anisotropia (β) e $M_\bullet$. La qualità dei dati spettroscopici non ha permesso di misurare una cinematica molto estesa, pertanto sono state fatte delle assunzioni su $(M/L)_K$ e su β. Il limite superiore della $M_\bullet$ risulta nell'intervallo tra 1×10^9 $M_\odot$ e 3.45×10^9 $M_\odot$ a seconda dei valori che vengono assunti per $(M/L)_K$ e β.

Sono state osservate con STIS, la Wide Field and Planetary Camera 2 (WFPC2), e la Advanced Camera for Surveys (ACS) montati su *HST*, tre galassie che per le loro grandi masse, luminosità e dispersioni di velocità sono degli ottimi candidati per ospitare dei SMBH eccezionalmente massivi: Abell 1836-BCG, Abell 2052-BCG, Abell 3565-BCG (Capitolo 6). I dati hanno fornito dettagli sulla struttura e sul profilo di massa della componente stellare, sulla profondità ottica della polvere e sulle distribuzioni spaziale e cinematica del gas ionizzato entro le regioni più centrali delle galassie. Sono stati costruiti modelli dinamici, che tengono conto del profilo di massa osservato e includono il contributo del SMBH, per riprodurre la cinematica ottenuta dallo studio della riga di emissione di [N II] λ6583. La cinematica e la morfologia regolari di Abell 1836-BCG e Abell 3565-BCG, hanno permesso di ottenere rispettivamente $M_\bullet = 3.61^{+0.41}_{-0.50} \times 10^9$ $M_\odot$ e $1.34^{+0.21}_{-0.19} \times 10^9$ $M_\odot$. La mancanza di moti ordinati in Abell 2052-BCG, invece, ha impedito un accurato modello dinamico. È stato così stimato un limite superiore della $M_\bullet < 4.60 \times 10^9$ $M_\odot$. Queste misure rappresentano un importante passo avanti verso la caratterizzazione della funzione di massa dei SMBH, suggerendo un andamento più ripido della $M_\bullet - \sigma$ nella regione ad alte σ a causa o di una più grande dispersione della relazione o perché la legge $M_\bullet - \sigma$ risulta diversa.

Infine, è stata stimata la massa del SMBH di NGC 4278 (Capitolo 7) utilizzando il teorema del viriale e misurando le componenti larghe delle righe di emissione osservate nello spettro STIS. Si è assunto che il gas fosse uniformemente distribuito in una sfera di un certo raggio. A seconda delle dimensioni adottate per la regione in cui si formano le righe larghe, la massa va da 7×10^7 a 2×10^9 $M_\odot$, in accordo con i limiti superiori trovati seguendo altre assunzioni sulla distribuzione del gas. Il nucleo di NGC 4278 è una sorgente ultravioletta molto variabile. L'ampiezza e il tempo scala di questa variazione sono analoghi a quelli trovati per le galassie con una debole attività nucleare. Questa

variabilità in ultravioletto è tipica dei nuclei galattici attivi a bassa luminosità.

Le conclusioni di questa tesi possono essere riassunte in tre punti: 1) con le $M_\bullet$ ottenute attraverso modelli semplici siamo riusciti a mappare la relazione $M_\bullet - \sigma$ per un campione molto ampio e vario di galassie che comprende tutta la popolazione locale dei SMBH. Queste stime risultano consistenti con la relazione $M_\bullet - \sigma$, senza mostrare dipendenze dovute alla distanza delle galassie, al loro tipo morfologico e alla presenza di barre. Queste stime di $M_\bullet$ possono essere usate per studiare l'andamento e la dispersione delle altre relazioni di scala dei SMBH. 2) Usando i risultati di questo lavoro è stato studiato il legame tra la $M_\bullet$, lo sferoide e l'intera galassia (compreso l'alone di materia oscura). È stato confermato che $M_\bullet$ risulta strettamente connesso con σ indipendentemente dal tipo morfologico, e che il piano fondamentale dei buchi neri è principalmente legato da questa proprietà. 3) È stata caratterizzata la parte alta della funzione di massa dei SMBH dell'universo locale per capire il legame tra l'evoluzione dei SMBH e la formazione gerarchica delle galassie. Questo è stato fatto misurando $M_\bullet$ in una galassia ellittica molto massiccia NGC 1265 usando dati della cinematica stellare ottenuti con ottica adattiva e in tre galassie molto brillanti attraverso la cinematica del gas derivata da dati di *HST*. Queste misure suggeriscono un andamento più ripido della $M_\bullet - \sigma$ in nella regione ad alte σ, dovuta o a una più grande dispersione della relazione o a una legge diversa che predice una crescita più veloce dei SMBH rispetto a σ.

Abstract

In this thesis we focused on the determination of the mass $M_\bullet$ of supermassive black hole (SMBHs) and on the interpretation of their demography. We studied their scaling relations with the aim of understanding the rôle of SMBHs in the evolution of galaxies. This was done by increasing the demography of $M_\bullet$ and studying whether $M_\bullet$ results more closely linked to the bulge or to the global galaxy properties, including the dark matter halo.

In the first part of the thesis we focused on the presentation of a spectral and imaging atlas of a large and various sample of galaxies we studied to obtain upper limits on their $M_\bullet$. The data were retrieved from *Hubble Space Telescope* (*HST*) archive (Chapter 2). This atlas comprises of 177 nearby galaxies (D <100 Mpc) with nuclear spectra obtained with the Space Telescope Imaging Spectrograph (STIS) in the region of Hα line and the [N II] $\lambda\lambda$6548, 6583 and [S II] $\lambda\lambda$6716, 6731 emission-line doublets. Structural parameters of bulge and disk derived from the two-dimensional bulge-to-disk decompositions of K-band 2MASS and UKIDSS images for 65 sample galaxies are presented, too.

We derived stringent upper bounds on the mass of the central SMBH for a sub-sample of 105 galaxies spanning a wide range of Hubble types (E−Sc) and values of the central stellar velocity dispersion, σ (58−419 km s^{-1}). These $M_\bullet$ upper limits were derived by modeling the widths of the observed emission lines in terms of gas motions in a thin disk of unknown orientation but known spatial extent. The upper limits that we derived are consistent with both the $M_\bullet - \sigma$ relation of Ferrarese & Ford (2005) and Lauer et al. (2007a) and with secure $M_\bullet$ determinations. Most important, independent of the galaxy distance, morphological type or bar presence, our $M_\bullet$ upper limits run parallel and above the previous two version of $M_\bullet - \sigma$ relations. This suggests that, although strictly speaking we cannot rule out the rôle of non-gravitational forces, our line-width measurements actually trace well the nuclear regions dominated by the central SMBH, which in practice allows us to estimate $M_\bullet$ (Chapter 3). Yet, at

small σ some $M_\bullet$ upper limits systematically exceed the expected $M_\bullet$, as the line-width measurements for such low-σ outliers are most likely affected by the stellar contribution to the gravitational potential either due to the presence of conspicuous nuclear clusters or because of a greater distance compared to the other galaxies at the low-σ end of the $M_\bullet - \sigma$ relation. Conversely, the $M_\bullet$ upper bounds appear to lie closer to the expected $M_\bullet$ in the most massive elliptical galaxies with values σ>220 km s^{-1}. Such a flattening of the $M_\bullet - \sigma$ relation at its high-σ end would appear consistent with a coevolution of SMBHs and galaxies driven by dry mergers, although better and more consistent measurements for σ and K-band luminosity are needed for these kinds of objects before systematic effects can be ruled out.

Following these results we focused on the interpretation of the demography of SMBHs, specifically in trying to understand whether the $M_\bullet$ relates more closely to the bulge or to the total mass of a galaxy (Chapter4). The large sample of upper limits on $M_\bullet$ and the latest compilation of secure $M_\bullet$, coupled with libraries of host galaxy velocity dispersions, rotational velocities and photometric parameters extracted from SDSS i-band images were used to establish correlations between $M_\bullet$ and the properties of the bulge and of the host galaxy. We tested the correlations between $M_\bullet$ and stellar velocity dispersion, i-band bulge luminosity, bulge virial mass, bulge Sérsic index, total i-band luminosity of the galaxy, galaxy stellar mass, maximum circular velocity, and galaxy dynamical and virial masses. The tightness of the $M_\bullet - \sigma$ relation was derived, and it resulted that correlations with other galaxy parameters do not yield tighter trends. $M_\bullet$ is fundamentally driven by σ for all Hubble types. The fundamental plane of the SMBHs is mainly driven by σ too, with a small fraction of the tilt being due to the effective radius.

We explored the high-mass end of the SMBH mass function to understand the link between the evolution of SMBHs and the hierarchical build-up of galaxies, by measuring $M_\bullet$ in the massive elliptical galaxy NGC 1265 with adaptive-optics stellar observations (Chapter 5) and in three brightest cluster galaxies from the gaseous kinematics derived from *HST* data (Chapter 6). These works are important to understand the $M_\bullet$ distribution at high σ, where different works found either a flattening or a steepening of the $M_\bullet - \sigma$ relation.

We presented the K-band adaptive-optics assisted spectroscopic observations of the central region of the archetype head-tail radio galaxy NGC 1265/ 3C 83.1B with the aim of constraining the mass of its SMBH (Chapter 5). The near-infrared data taken with the Altair/NIRI on the Gemini North have a spatial resolution of FWHM = $0\farcs11$ (39 pc). To account for the stellar contribution, we performed a multi-Gaussian expansion by using a combination of our NIRI high-resolution K-band image and a TNG K'-band image to cover

the outer parts of the galaxy. We extracted the stellar kinematics by using the penalized pixel fitting method from the CO absorption bands at 2.29 μm. Jeans anisotropic models were adopted to fit the stellar kinematics and surface distribution to determine the best fitting value for anisotropy and $M_\bullet$. The limited quality of our kinematical data did not allow us to measure very extended kinematics. Hence, we resorted to assuming fixed values for both the $(M/L)_K$ and the anisotropy β. The derived upper limit on $M_\bullet$ ranges between $1{\times}10^9$ $M_\odot$ and $3.45{\times}10^9$ $M_\odot$ depending on the assumed values of β and $(M/L)_K$, respectively. This range of masses is consistent with the $M_\bullet - L_{K,\mathrm{bulge}}$ relation of Marconi & Hunt (2003).

We derived $M_\bullet$ in three brightest cluster galaxies (BCGs), Abell 1836-BCG, Abell 2052-BCG, and Abell 3565-BCG, by using observations with STIS, Wide Field and Planetary Camera 2 (WFPC2), and Advanced Camera for Surveys (ACS) on *HST* (Chapter 6). The data provided detailed information on the structure and mass profile of the stellar component, dust optical depth, and spatial distribution and kinematics of the ionized gas within the innermost region of each galaxy. Dynamical models, which account for the observed stellar mass profile and include the contribution of a central SMBH were constructed to reproduce the kinematics derived from the [N II] λ6583 emission line. Secure SMBH detection with $M_\bullet = 3.61^{+0.41}_{-0.50} \times 10^9$ $M_\odot$ and $1.34^{+0.21}_{-0.19} \times 10^9$ $M_\odot$, respectively, were obtained for Abell 1836-BCG and Abell 3565-BCG, which show regular rotation curves and strong central velocity gradients. In the case of Abell 2052-BCG, the lack of an orderly rotational motion prevented a secure determination, although an upper limit of $M_\bullet < 4.60 \times 10^9$ $M_\odot$ could be placed on the mass of the central black hole. These measurements are an important step forward in characterizing the high-mass end of the SMBH mass function. In fact, the results suggest a steepening of the trend of the $M_\bullet - \sigma$ relation in the high-σ range, that suggest either a higher scatter or the necessity of a different law, which predicts a faster grow of the SMBH with respect to the σ.

Finally, we estimated the mass of the SMBH of NGC 4278 by using the virial theorem and measuring the broad components of the emission lines observed in the STIS spectrum, assuming that the gas is uniformly distributed in a sphere of radius R. The $M_\bullet$ is found to be in the range between 7×10^7 and 2×10^9 $M_\odot$ depending on the radius we obtained from simple estimation of the dimension of the broad line region (Chapter 7). This is in agreement with previous findings based on different assumptions about the gas distribution. The nucleus of NGC 4278 hosts a barely resolved but strongly variable UV source. Its UV luminosity increased by a factor of 1.6 in a period of 6 months. The amplitude and scale time of this UV flare are remarkably similar to those of the brightest UV nuclear transients which were earlier found in other low-

luminosity AGNs. This ultraviolet variability represents the typical signatures of the low-luminosity active galactic nuclei.

The main conclusions of this thesis can be summarized as follows. 1) We could map the $M_\bullet - \sigma$ relation from the lower to the upper end of the local SMBH population by using simple estimates of $M_\bullet$ but for the largest and most various sample of host galaxies. These $M_\bullet$ estimates are consistent with the known $M_\bullet - \sigma$ relation, with no dependence on galaxy distance, morphological type or bar presence. They can be adopted to study the trend and scatter of the other $M_\bullet$ scaling relations. 2) Following the results of this work we focused on the interpretation of the demography of SMBHs, specifically in trying to understand whether the $M_\bullet$ relates more closely to the mass of the bulge or to the total mass of the host galaxy, included dark matter. We confirmed that $M_\bullet$ is fundamentally driven by σ for all Hubble types. The same is true for the fundamental plane of SMBHs. 3) We explored the high-mass end of the SMBH mass function to understand the link between the evolution of SMBHs and the hierarchical build-up of galaxies, by analyzing adaptive-optics stellar observations of the central regions of massive elliptical galaxies such us NGC 1265 and estimating $M_\bullet$ in three brightest cluster galaxies by measuring the gaseous kinematics with *Hubble Space Telescope* (*HST*). The first results indicates a steepening of the trend of the $M_\bullet - \sigma$ relation in the high-σ range, that suggests either a higher scatter or the necessity of a different law, which predicts a faster grow of the SMBH with respect to σ.

Contents

List of Tables

List of Figures

1

Introduction

In the last years the extragalactic research has been focused on the understanding of galaxy formation and evolution, in terms of different mechanisms and galaxy constituents that play a rôle in the processes. One of the key questions is whether the galaxies formed early through a dissipational collapse of large protogalaxies, in a "monolithic" process, or whether they are the result of successive mergers between small structures in a "hierarchical"' merging process.

To pursue these studies an important rôle is the understanding of the physics of the central region of galaxies, where supermassive black holes (SMBH) resides. The name of these compact objects was chosen because they are somewhat similar to the stellar black holes that are the end result of the life of massive stars. The mass accretion of SMBHs is thought to power active galactic nuclei (AGNs) and the quasars (QSOs). SMBHs are found in the center of many galaxies with a mass that ranges from millions and to billions times the mass of the sun. It seems to be connected with several properties of the hosting galaxies (e.g., the luminosity and stellar velocity dispersion of the spheroidal component). The link between these different galaxy components suggests a coevolution between galaxies and SMBHs, that can be seen as variation of the gas reservoir that fuel the accretion onto the SMBHs due to the galaxy, and as effect of the nuclear activity in the quenching of the star formation and consequent SMBH growth.

1.1 Supermassive black holes

Soon after the discovery of quasars (Schmidt 1963), it has been suggested that active galactic nuclei are powered by mass accretion onto SMBHs with masses

between 10^6 and 10^{10} $M_\odot$ (see Rees 1984, for a review). This constitutes now the widely agreed paradigm for the origin of the quasar and AGN energy. The paradigm together with the comparison of the integrated radiation density from quasars to the integrated mass density in local SMBHs (e.g., Yu & Tremaine 2002), the upper bound on SMBH masses, and the high incidence of low-luminosity AGNs in the nucleus of nearby galaxies (see Ho 2008 for a review) implies that a significant fraction of galaxies of the local universe should harbor a SHBH as a relic of the past activity (e.g., Soltan 1982; Cavaliere & Padovani 1989; Chokshi & Turner 1992; Shankar et al. 2004; Shankar 2009). In this framework SMBHs are expected to be ubiquitous in galactic nuclei as a fundamental component of both quiescent and active galaxies (Kormendy 2004). Although less common in low-mass systems, central SMBHs also have been identified in some late-type spirals (Filippenko & Ho 2003; Barth et al. 2004; Shields et al. 2008; Barth et al. 2009).

The discovery that SMBH masses $M_\bullet$ are strongly connected with the properties of the hosting galaxies (see Ferrarese & Ford 2005, for a review) suggested the idea of a common evolution between SMBHs and galaxies.

1.2 Mass estimates of supermassive black hole

Spectrosopic and photometric observations made with the *Hubble Space Telescope* (*HST*) allowed to study the central region of galaxy and derive relatively accurate $M_\bullet$ if the sphere of influence is resolved. This represents the region where the SMBH dominates the gravitational potential before the stars take over; in this region the rotation is Keplerian. With the current facilities such us the *HST* and 8-m class ground-based telescopes, this radius (see Equation 2.2) can be resolved for galaxies at a few Mpc distance for $M_\bullet \leq 10^8 M_\odot$ (Ferrarese & Ford 2005).

Several techniques have been used so far to detect and measure $M_\bullet$, depending on the activity their hosting galaxies. The stellar and gaseous kinematics are adopted for quiescent galaxies, whereas the reverberation mapping and water megamasers are measured in active galaxies. All these techniques offer merits and limitations.

Our own Galactic Center represents a peculiar case, since its vicinity allowed to map the proper motions of stars in the central few arcseconds. This is one of the most evident signature of the existence of SMBHs (Schödel et al. 2002, 2003; Ghez et al. 2003, 2005, 2008). The study of about 40 stars for more than 10 years orbiting around SagA* allowed to constrain the mass of the central massive component to $(4.31 \pm 0.06) \times 10^6$ $M_\odot$ (Gillessen et al. 2009). This study was possible thanks to the extremely high spatial resolution joined with the new

near-infrared (NIR) facilities coupled with adaptive-optics (AO) systems. Due to this, the stellar proper motion technique can be applied only to our Galaxy.

Among the several techniques that have been used so far to detect and measure $M_\bullet$, the most common for quiescent galaxies are stellar (e.g., Verolme et al. 2002; Gebhardt et al. 2003; Houghton et al. 2006; Nowak et al. 2007, 2008, 2009; Cappellari et al. 2009; Krajnović et al. 2009; see also Chapter 5) and gaseous kinematics (e.g., Barth et al. 2001, Coccato et al. 2006, Neumayer et al. 2007, Dalla Bontà et al. 2009; see also Chapters 3 and 6).

Stellar kinematics requires modeling of the stellar motions unveiled by the line-of-sight-velocity distribution (LOSVD) measured from the absorption lines of the galaxy spectra. Stellar dynamical models are powerful because give information not only on the mass of the SMBH but also on the orbital structure of the galaxy. The use of the absorption features requires high S/N spectra to fit the LOSVD. The sophisticated modeling is subject to high degeneracy that can produce a significant range of consistent $M_\bullet$ (Valluri et al. 2004). Moreover, both observational and computational requirements are expensive (Kormendy 2004). So far several absorption lines have been used in these studies from the optical to NIR, although it is still unclear if different absorption lines gives the same mass estimate. It has been noted that measuring the stellar kinematics from optical features gives larger velocity dispersions than NIR bands, suggesting that dust extinction in optical wavebands might affect the results (Silge & Gebhardt 2003; Nowak et al. 2009). In the past, the required high S/N required, restricted the sample of galaxies in which this method was applied to the ones with a relatively high central surface brightness and *HST* data. For example, M 31 represents one of the most stringent $M_\bullet$ estimation (Bender et al. 2005). Only in the last few years, the 8-m class NIR telescopes with AO facilities allowed to resolve the sphere of influence of SMBHs in galaxies that could not have been studied in the same way with *HST*, such us giant elliptical with a low central surface brightness and dusty spirals (Davies et al. 2006; Houghton et al. 2006; Nowak et al. 2007, 2008, 2009; Cappellari et al. 2009; Krajnović et al. 2009). The current dynamical models of stellar kinematics are based on the orbit superposition Schwarzschild's approach (Schwarzschild 1979). These three-integral models were first build to explore the orbital structure of axysimmetric galaxies with a constant mass-to-light ratio, M/L (van der Marel et al. 1998; Gebhardt et al. 2003; Valluri et al. 2005; Cappellari et al. 2006, 2009; Nowak et al. 2009). More recently they have been extended to triaxial galaxies (de Lorenzi et al. 2007; van den Bosch et al. 2008). Moreover, recent results on the $M_\bullet$ for M87 (Gebhardt & Thomas 2009) suggests that the dark matter is a fundamental component that must be taken into account in the modeling of galaxies with steeper light profiles, introducing the variation of M/L.

However, the Jeans modeling used in the past can still be useful helping in an accurate search of the best fitting parameters estimate and to test the reliability of the modeling results from three-integral models, although it suffer from larger systematic uncertainties (Cappellari et al. 2009, 2010). Moreover, the use of integral field spectroscopy is a fundamental ingredient to build accurate dynamical models (Cappellari & McDermid 2005; Krajnović et al. 2005).

The dynamical modeling of gaseous kinematics is based on the analysis of dusty and gaseous disks with morphology regular enough to claim that the gas is rotating onto circular orbits in a thin disk. Optical gaseous studies represent one of the most prolific method carried out using *HST* high-resolution data. Gaseous kinematics is the easiest way to trace the gravitational potential of galaxy nuclei, but the measurements are prone to errors by non-circular or non-gravitational forces (e.g., inflows, outflows, and turbolences). The gas, in fact, is often found in non-equilibrium configurations. Moreover, it is not always possible to obtain a well-constrained disk inclination. The typical optical lines used in this method are the Hα and [N II] $\lambda\lambda 6548, 6583$ (see Chapters 3 and 6). Several lines in the NIR have been used so far, such us Brγ2.165 μm, [Fe II]1.644 μm, [Si VI]1.962 μm and molecular hydrogen H_2 2.12 μm (Neumayer et al. 2007) and [Ne II]12.8 μm (Wold et al. 2006). Another complication is due to the presence of broad line components originated by the AGN. AGNs in fact produces spatially unresolved broad emission lines that must be subtracted in order to construct a clear rotation curve (see Chapter 3). On the other hand, the use of strong emission lines means that high S/N spectra can be obtained in a relative short time. The dynamical model results straightforward with the ionized-gas assumed in a rotating Keplerian disk (Coccato et al. 2006, Dalla Bontà et al. 2009; see also Chapter 6). Once the regularity of the gas kinematics is observationally verified and the inclination is derived by looking at the orientation of dust lanes close to the nucleus (Sarzi et al. 2001; Ho et al. 2002). The analysis of position-velocity diagrams of the emission-line spectra observed with ground-based spectroscopy allows the identification of those galaxies which are good candidates for hosting a circumnuclear Keplerian disk rotating around a central mass concentration (Bertola et al. 1998; Sofue et al. 1998). These objects have been proved to be good candidates for a spectroscopic follow-up with the *HST* (Coccato et al. 2006).

Masses of SMBHs in active galaxies have been obtained by means of the reverberation mapping technique (see Peterson & Bentz 2006, for a review). It is based on the observed time lag between the light curve of the continuum and broad-emission lines. This method is calibrated from the scaling relations based on unknown geometry of the inner broad line region (BLR). Therefore, in principle the high luminosity makes QSOs optimal candidates to study the

SMBHs at high redshift. However, a low understanding of the scaling relations, the unknown geometry of the BLR, and long observational time needed for this technique affects the reverberation mapping calibration. For this reason, $M_\bullet$ in AGNs is most commonly estimated using the "virial" method based on an empirically calibrated photoionization relation between the continuum luminosity of the reverberation mapping sample and size of the BLR (Wandel et al. 1999; Kaspi et al. 2000, 2005; Vestergaard 2002; Greene & Ho 2005b; Vestergaard & Peterson 2006) and the velocity given by the width of the broad emission lines.

Galaxies hosting a disk of water megamasers offered another stringent probe of the existence of the SMBHs (Miyoshi et al. 1995; Herrnstein et al. 2005, for NGC 4258). The use of the VLBI technique allowed to identify systems of nuclear clouds moving in Keplerian rotation. But water masers are not common (Braatz et al. 1994). and can be used only if the plane of the rotating gas is aligned with the line-of-sight and the absorption is relatively low such us in Seyfert 2 galaxies. This limited applicability is therefore the main drawback of the method.

Several authors have tried to compare $M_\bullet$ determinations obtained with different methods finding in some cases a good agreement. For example, the mass of the SMBH of Centaurus A has been measured within a factor ~ 2 by stellar (Silge et al. 2005; Cappellari et al. 2009) and gaseous (Marconi et al. 2006; Neumayer et al. 2007) kinematics. Another case with broad agreement but large uncertainty is NGC 3379. Shapiro et al. (2006) found a mass of $1.4^{+2.6}_{-1.0} \times 10^8$ $M_\odot$ with stars and $(2.0 \pm 0.1) \times 10^8$ $M_\odot$ with gas which are both consistent with the results of Gebhardt et al. (2000b) based on stellar dynamics. On the contrary, the SMBH mass of IC 1459 from gaseous dynamics is a factor of $\sim$5 smaller than that from stellar dynamics (Verdoes Kleijn et al. 2000; Cappellari et al. 2002). Finally, for NGC 4258 $M_\bullet$ from water maser (Herrnstein et al. 2005; $(3.82 \pm 0.01) \times 10^7$ $M_\odot$), stellar kinematics (Siopis et al. 2009; $(3.3 \pm 0.2) \times 10^7$ $M_\odot$) and gaseous kinematics (Pastorini et al. 2007(@; $2.5 \times 10^7 - 2.6 \times 10^8$ $M_\odot$) are in good agreement, although the $M_\bullet$ from gaseous kinematics spans a factor 10 in $M_\bullet$. More determination with different method are needed to test the validity of the measured $M_\bullet$.

1.3 The coevolution between supermassive black holes and their hosting galaxy

The SMBH masses correlate with the luminosity, $L_{\rm bulge}$ (Kormendy & Richstone 1995; Marconi & Hunt 2003; Graham 2007; Gültekin et al. 2009b) and the stellar velocity dispersion, σ (Ferrarese & Merritt 2000, Gebhardt et al.

2000a, Tremaine et al. 2002, Ferrarese & Ford 2005, Gültekin et al. 2009b) of the spheroidal component of the host galaxy (i.e., the galaxy itself in the case of elliptical galaxies or the bulge in the case of disk galaxies). Both correlations indicate that the mass of SMBHs in quiescent and active galaxies is tightly correlated with the stellar mass, $M_{\rm bulge}$, of their host spheroids. The latter can be estimated in low redshift galaxies from the bulge luminosity assuming the mass-to-light ratio (Kormendy & Richstone 1995), from velocity dispersion through the virial theorem (Marconi & Hunt 2003), or by building dynamical models (Magorrian et al. 1998; Häring & Rix 2004). Moreover, it has been noted that $M_\bullet$ correlates well with the central light concentration, C (Graham et al. 2001), the Sérsic index n (Graham & Driver 2007), the virial mass of the galaxy, $M_{\rm vir}$ (Ferrarese et al. 2006), the gravitational binding energy, $E_{\rm g}$ (Aller & Richstone 2007), the kinetic energy of random motions of the bulge (Feoli & Mancini 2009), and the stellar light and mass deficit associated to the core elliptical galaxies (Kormendy & Bender 2009). Most of these relations are compared in Novak et al. (2006). Past studies have shown that $M_\bullet$ only weakly correlates with the total luminosity of the galaxy, $L_{\rm gal}$. This is particularly true for late-type spirals (see Kormendy & Gebhardt 2001; Kormendy 2001) and suggests that the evolution of SMBHs is linked with bulges and not with disks. Given the $M_\bullet - \sigma$ and the $V_{\rm c} - \sigma$ relation between the circular velocity, $V_{\rm c}$, and σ Ferrarese (2002) and Pizzella et al. (2005) suggested a link between $M_\bullet$ and $V_{\rm c}$ (or equivalently with the mass of the dark matter halo). However, more extensive analysis by Courteau et al. (2007) and Ho (2007) showed the $V_{\rm c} - \sigma$ relation depends on the morphological type (or equivalently the light concentration or surface brightness of the galaxy) thus excluding a simple connection between $M_\bullet$, σ, and $V_{\rm c}$ (see Chapter 4).

Several authors have noted that the residuals of the $M_\bullet - \sigma$, and $M_\bullet - L_{\rm bulge}$ scaling relations correlate with the effective radius (e.g., Marconi & Hunt 2003). Hopkins et al. (2007a,b) suggested the possibility of a linear combination between galaxy properties to reduce the scatter of the $M_\bullet$ relations, introducing the idea of a fundamental plane of SMBHs (BHFP). All the SMBH scaling relations could thus be seen as projections of the BHFP (Aller & Richstone 2007; Barway & Kembhavi 2007).

The existence of SMBH-host galaxy scaling relations suggests a connection between the evolution of SMBHs and that of their host galaxies. A better understanding of the relations would significantly improve the theoretical models of the SMBH growth and evolution. The local characterization and cosmic evolution of these scaling relations have already provided valuable constrains on theoretical models for the coevolution of galaxies and SMBHs (Granato et al. 2004; Vittorini et al. 2005; Hopkins et al. 2006; Croton et al. 2006; De Lucia

et al. 2006; Cavaliere & Menci 2007; Monaco et al. 2007; Marulli et al. 2008). The tightness of the relations linking galactic properties to $M_\bullet$ is indicative of a formation and evolution history in which SMBHs and galaxies are causally connected. Indeed, feedback from AGN activity is believed to play an important, perhaps even fundamental rôle in the evolution of galaxies (e.g., Binney & Tabor 1995; Suchkov et al. 1996; Ciotti & Ostriker 2001; Schawinski et al. 2006; Springel et al. 2005; Hopkins et al. 2007b; Di Matteo et al. 2008). Analytical models and numerical simulations have demonstrated that the observed scaling relations could be reproduced in feedback-regulated models of SMBH growth with strong feedback from the AGN (Silk & Rees 1998; Cox et al. 2006; Robertson et al. 2006a,b; Di Matteo et al. 2005; Younger et al. 2008; Hopkins et al. 2009). In particular, these models can predict and explain the existence of a BHFP (Hopkins et al. 2007a,b, 2009). Volonteri & Natarajan (2009) investigated the observational signature of the self-regulated SMBH growth by analyzing the mass assembly history of the black hole seeds through simulations. They found that the existence of the $M_\bullet - \sigma$ relation depends on the merging history of massive dark halos. The slope and scatter of the relation depends on the seed and on the kind of self-regulation process. Therefore, we could discriminate the different theoretical models of formation by having a better asses of the scatter of the relations (e.g., Somerville 2009). However, even if the observed relations can be reproduced, the models still depend on the assumed trend and scatter, which are far to be in agreement in the several works on $M_\bullet$ scaling relations.

The scaling relations were studied for a limited sample of galaxy. Up to now, the sample comprises about 50 dynamically measured masses in quiescent galaxies (Gültekin et al. 2009b) and about 150 masses in active galaxies (Kaspi et al. 2000; Greene & Ho 2005a; Peterson & Bentz 2006; Ho et al. 2008b). A better statistics in term of number of targets, Hubble type of the hosting galaxy, and method of measurement would be helpful in the understanding of the coevolution between SMBHs and their host. Moreover, $M_\bullet$ in the most massive galaxies can be barely predicted. The small number of SMBH masses for this population of galaxies (Houghton et al. 2006; Gebhardt et al. 2007; Dalla Bontà et al. 2009; Gebhardt & Thomas 2009; see also Chapters 5 and 6) do not allow a complete understanding of the $M_\bullet$ distribution at high-σ where a steepening is suggested (Wyithe 2006; Dalla Bontà et al. 2009). At present, the ambiguities on the trend of the scaling relations at high σ are fundamental for determining the parameterization of the scaling relation (e.g., Gültekin et al. 2009b) and for characterizing the SMBH mass function above 10^9 $M_\odot$ (Lauer et al. 2007a).

Low-mass galaxies suffer of the limited number of determinations too (see

Nowak et al. 2007; Barth et al. 2009). The current angular resolution is inadequate to directly detect SMBHs with masses $\leq 10^6$ $M_\odot$ in quiescent galaxies (with the exceptions of the stellar cluster G1, Gebhardt et al. 2002; Ulvestad et al. 2007; and ω Centauri Noyola et al. 2008, Anderson & van der Marel 2009, and dwarfs galaxies Barth et al. 2005). Consequently, the low end of the SMBH mass function is quite unknown. Pure disk galaxies, on the other hand, do not seem to contain SMBHs, with the exception of NGC 4395 (Filippenko & Ho 2003), POX 52 (Barth et al. 2004), and NGC 1042 (Shields et al. 2008). In addition, over the last few years a series of imaging and spectroscopic surveys carried out with the *HST* has revealed that the nuclear regions of late-type spirals and of small early-type galaxies often host a compact stellar cluster (Böker et al. 2002; Côté et al. 2006). Most intriguingly, the mass of such nuclear clusters (NCs) appears to be also correlated with the mass of their host galaxies like SMBHs do (Rossa et al. 2006; Ferrarese et al. 2006). NCs tend to be approximately ten times more massive than SMBHs for a given bulge mass. These findings have led to suggest that SMBHs may find it more difficult or may not even not form at all in the center of the galaxies less massive than 10^{10} $M_\odot$, where NCs may instead replace SMBHs at the principal nuclear component. Although signs of black-hole accretion have been detected in a few objects with NCs (e.g., Barth et al. 2009), the presence and mass of a SMBH in a galaxy with a NC has yet to be directly established. By studying these object we could understand whether SMBHs and NCs can coexist, and the range of masses that can host either one or the other compact object.

The importance of the analysis of the scaling relations for different morphological types is suggested higher scatter of the $M_\bullet - \sigma$ relation introduced by the addition of a larger amount of spirals (Gültekin et al. 2009b). Moreover, barred and unbarred galaxies seems to follow different $M_\bullet - \sigma$ and/or $M_\bullet - L_{\rm bulge}$ relations (Graham 2008; Hu 2008; Graham & Li 2009; Gadotti & Kauffmann 2009; Hu 2009) that can be explained as either due to a undermassive SMBHs in barred galaxies or larger σ and luminosity due to the presence of the bar. These different scaling relations could reflect structural differences between bulges formed via mergers and secular evolution processes (see Kormendy & Kennicutt 2004, for a review). Greene et al. (2008) investigated the relationship between $M_\bullet$ and host galaxy properties for a sample of active galaxies with no classical bulge. $M_\bullet$ was estimated with virial technique and a deviation in the relation $M_\bullet - M_{\rm bulge}$ was found. On the other hand, Beifiori et al. (2009, see Chapter 3) did not find this difference in the $M_\bullet - \sigma$ relation, while using upper limits on $M_\bullet$ in a large and various sample of hosting galaxies. This issue could be understood with a larger sample of pseudobulges or barred galaxies for which a careful decomposition of the central components must be

done, such us in Nowak et al. (2009).

To constrain the evolutionary models it must be determined whether the scaling relations evolve. Consequently, an accurate and complete census of $M_\bullet$ must be done for a wide range of Hubble types and reshifts. If the relation linking the central SMBH mass with the mass of the host galaxy still holds at high redshifts (e.g., McLure & Dunlop 2002; Corbett et al. 2003; Shields et al. 2003), one can obtain further physical insight on the evolution of spheroidal galaxies and SMBHs with cosmic epoch by studying high-redshift quasar hosts. The evolution of scaling relations is still unclear with some observational studies finding evolution in the $M_\bullet - \sigma$ (Woo et al. 2006, 2008) and $M_\bullet - M_{\rm bulge}$ relations (Treu et al. 2004; Shields et al. 2006; Treu et al. 2007; Decarli et al. 2010) with the high redshift SMBHs being overmassive for a fixed σ (and $M_{\rm bulge}$) compared to the local population, whereas other studies are consistent with no redshift evolution (Gaskell 2009; Jahnke et al. 2009). One possible explanation for this discrepancy lies in the uncertainties of the selection biases and in the evolution of the intrinsic scatter (Lauer et al. 2007b). From simulations of the evolution of galaxy mergers on the $M_\bullet - \sigma$ and $M_\bullet - M_{\rm bulge}$ relations Johansson et al. (2009) found that SMBHs starting below the relation evolve onto the relation, instead the ones above do not. Therefore, overmassive black holes do not evolve onto the relation through gas-rich merger.

The spatial resolution of the present instrumentation is still a problem for the local universe. Despite the recent progress, the SMBH demography is far to be complete. Most of the $M_\bullet$ determination were obtained in early-type systems and it is still not clear if the scaling relations hold also in the disk-dominated systems. A poorly determined $M_\bullet - \sigma$ relation introduces large uncertainties in the extrapolated values of $M_\bullet$ and influence our understanding of both SMBH and galaxy formation and evolution.

1.4 Future development on supermassive black hole research

The understanding of SMBHs scaling relations will be improved in the next future with high-quality direct $M_\bullet$ estimates in a wide range of redshift combined with the refinements of galaxy evolution models.

The launch of the *HST* opened a new era in the study of SMBHs research. The first instruments, the Faint Object Spectrograph (FOS) and Faint Object Camera (FOC) were used to obtain $M_\bullet$ from both gaseous (e.g., Harms et al. 1994; Macchetto et al. 1997; Ferrarese et al. 1996; van der Marel & van den Bosch 1998; Ferrarese & Ford 1999; Verdoes Kleijn et al. 2000) and stellar kinematics (e.g., Cretton & van den Bosch 1999; Gebhardt et al. 2000b). The true innovation came when the Space Telescope Imaging Spectrograph (STIS)

was installed on the *HST* allowing to resolve the sphere of influence of the SMBHs for many nearby galaxies. With the failure of the STIS in 2004 we lost the capability to get diffraction-limited spectra from space, but the recent refurbishment after the Servicing Mission 4 (SM4) will allow us to obtain the data to perform new $M_\bullet$ measurements. Even though STIS stopped operating in 2004 its data continued to produce new scientific results (e.g., Beifiori et al. 2009, see also Chapter 3). Only a small fraction of galaxies targeted with *HST* showed a regular gaseous kinematics (Sarzi et al. 2001), this is particularly true for radio galaxies where the non-gravitational motions are dominant (Verdoes Kleijn et al. 2006). A way to circumvent this problem is to pre-select the galaxy sample from those that show regular nuclear gas kinematics suggested from an analysis of ordered dust morphology (Ho et al. 2002). Since *HST* is a 2.5 m telescope it will not be able to observe faint objects, and an optical spectrograph like STIS it will not deliver useful data for dusty galaxies and late-type spirals. The use of ground-based telescopes in the NIR wavelengths coupled with AO systems will give a spatial resolution comparable to *HST* combined with a much larger light collecting power.

Further perspective of $M_\bullet$ measurements will be the use of extremely large ground-based telescopes and new space telescopes, such as the 30 m class telescopes equipped with integral-field spectrographs and the James Webb Space Telescope (JWST). JWST with a primary mirror of 6.6 m will be the best telescope in the spectral region between 1.7 and 28 μm. During my M. Sc. thesis we have worked on the assessment of the capabilities of JWST in the search of SMBHs, investigating two main aspects of the problem. We analyzed whether the sharper core of the JWST PSF allows to find black holes to larger distances or down to smaller masses than *HST* has done so far. Moreover, we determined the maximum distance at which we can detect a SMBH with JWST in a galaxy such us M 87, by using gaseous dynamical models. The combination of the Near Infrared Spectrograph (NIRSpec) with a pixel scale of $0\farcs1$ and the 6.6 m aperture will provide diffraction limited integral-field and long-slit spectra in the wavelength range between 0.6 and 5μm. The study of the Paα 1.87μm did not improve the capabilities of *HST*. STIS resulted more efficient in the SMBH search in nearby galaxies and slightly more powerful for furthest galaxies, because of the larger JWST pixel scale. Similarly, Batcheldor & Koekemoer (2009) found that the larger aperture of JWST will allow more efficient observations for absorption-line spectroscopy devoted to stellar dynamical measurements.

New insights on $M_\bullet$ determination will be done with the 30-m class ground-based telescopes such us the Thirty Meter Telescope (TMT), the 24.5-Giant Magellan Telescope (GMT), and the 42-m European Extremely Large Telescope

(E-ELT) that will allow to solve the sphere of influence at higher redshifts (Batcheldor & Koekemoer 2009). 30-m ground-based and 16-m space-based telescopes will be able to sample $M_\bullet \sim 10^9$ $M_\odot$ across the cosmic history. The SMBHs as small as $M_\bullet \sim 10^6$ $M_\odot$ will be sampled at distance of the Coma cluster and intermediate black holes ($M_\bullet \sim 10^{3-4}$ $M_\odot$) at distance of the Local Group (Batcheldor & Koekemoer 2009).

Finally, the study of the SMBHs will be improved with different facilities. The Laser interferometer Space antenna (LISA, Hughes et al. 2003), will be able to study coalescing binary SMBHs through the gravitational wave signature. On the other hand, the Atacama Large Millimeter/Sub-millimeter Array (ALMA) will be able to map the CO kinematics with a high resolution ($0\farcs036$ Batcheldor & Koekemoer 2009). The increase of the computational power will lead an improvement of the theoretical simulations of galaxy formation, but also of the modeling of the SMBHs.

1.5 Aim and outline of this thesis

In this thesis, we focused on the $M_\bullet$ determinations and analysis of the scaling relations with the aim of understanding the rôle of SMBHs in the evolution of galaxies. This was done by increasing the demography of $M_\bullet$ and studying whether $M_\bullet$ results more closely linked to the bulge or to the global galaxy properties (including the dark matter halo). As we have shown above, a lot of progress have been done in the last years in the measurements of $M_\bullet$, but still the existing sample comprises mainly of early-type galaxies. There are with few $M_\bullet$ determinations in galaxies with high and small σ, or in spiral galaxies. The uncertainties in the actual slope and scatter of all the scaling relations are still under debate.

In order to progress in the understanding of the coevolution of SMBHs and host galaxies we planned to increase the number of $M_\bullet$ determination. We mapped the $M_\bullet - \sigma$ relation from the lower to the upper end of the local SMBH population by using different methods to estimate $M_\bullet$. The detailed structure of this thesis is as follows.

Chapter 2. We present a spectral and imaging atlas of a large and various sample of galaxies we studied to obtain upper limits on their $M_\bullet$. The data were retrieved from *Hubble space Telescope* (*HST*) archive. This atlas comprises of 177 nearby galaxies (D <100 Mpc) with nuclear spectra obtained with the Space Telescope Imaging Spectrograph (STIS) in the region of Hα line and the [N II] $\lambda\lambda 6548, 6583$ and [S II] $\lambda\lambda 6716, 6731$ emission-line doublets. Structural parameters of bulge and disk derived from the two-dimensional bulge-to-disk decompositions of K-band 2MASS and UKIDSS images are presented, too.

Chapter 3. We derived stringent upper bounds on the mass of the central SMBH for a sub-sample of 105 galaxies spanning a wide range of Hubble types (E−Sc) and values of the central stellar velocity dispersion, σ (58−419 km s^{-1}). These $M_\bullet$ upper limits were derived by modeling the widths of the observed emission lines in terms of gas motions in a thin disk of unknown orientation but known spatial extent. The upper limits that we derived are consistent with both the $M_\bullet - \sigma$ relation of Ferrarese & Ford (2005) and Lauer et al. (2007a) and with secure $M_\bullet$ determinations. Most important, independent of the galaxy distance, morphological type or bar presence, our $M_\bullet$ upper limits run parallel and above the previous two version of $M_\bullet - \sigma$ relations. This suggests that, although strictly speaking we cannot rule out the rôle of non-gravitational forces, our line-width measurements actually trace well the nuclear regions dominated by the central SMBH, which in practice allows us to estimate $M_\bullet$.

Chapter 4. In this chapter we study whether the $M_\bullet$ relates more closely to the bulge formation or to the total mass of a galaxy, including the dark matter. We coupled the large sample of upper limits from Chapter 3 and the most up to date compilation of secure $M_\bullet$ from Gültekin et al. (2009b) with libraries of galaxy velocity dispersions, maximum rotational velocities, and galaxy photometric parameters extracted from SDSS i-band images. While we confirmed the tightness of the $M_\bullet - \sigma$ relation, we found that galaxies do not follow a $M_\bullet - V_c$ relation. Moreover, the total galaxy potential plays less role in setting $M_\bullet$. We confirmed that $M_\bullet$ is fundamentally driven by σ for all Hubble types, and the fundamental plane of the SMBH is mainly driven by σ, with a small fraction of the tilt due to the effective radius.

Chapter 5. We present the K-band adaptive optics spectroscopic observations of the nucleus of NGC 1265-3C 83.1 with the aim of measuring the mass of the SMBH by modeling the stellar kinematics from the CO absorption bands at 2.3 μm. The spectroscopic data were taken with the NIRI instrument at the Gemini North with a spatial resolution of FWHM = $0\farcs11$. Jeans anisotropic models were adopted to fit the stellar kinematics and surface distribution to determine the orbital anisotropy and $M_\bullet$. The $M_\bullet$ upper limit ranges between 1×10^9 M$_\odot$ and 3.45×10^9 M$_\odot$ depending on the adopted values of anisotropy (0−0.2) and K-band mass-to-light ratio (0.5−2.5), respectively. This range of SMBH masses is consistent with the prediction based on the K-band luminosity of the galaxy.

Chapter 6. We present three $M_\bullet$ estimates in brightest cluster galaxies, Abell 1836-BCG, Abell 2052-BCG, and Abell 3565-BCG, by using observations made with STIS, the Wide Field and Planetary Camera 2 (WFPC2) the Advanced Camera for Surveys (ACS) on *HST*. Secure SMBH detections with

$M_\bullet = 3.61^{+0.41}_{-0.50} \times 10^9$ $M_\odot$ and $1.34^{+0.21}_{-0.19} \times 10^9$ $M_\odot$, respectively, are obtained for Abell 1836-BCG and Abell 3565-BCG, which show regular rotation curves and strong central velocity gradients. In the case of Abell 2052-BCG, the lack of an orderly rotational motion prevents a secure determination, although an upper limit of $M_\bullet < 4.60 \times 10^9$ $M_\odot$ can be placed on the mass of the central black hole. These measurements are an important step forward in characterizing the high-mass end of the SMBH mass function. The results suggest a steepening of the trend of the $M_\bullet - \sigma$ relation in the high-σ range, that suggest either a higher scatter or the necessity of a different law, which predicts a faster grow of the SMBH with respect to the σ.

Chapter 7. We estimated the mass of the SMBH of NGC 4278, by using the virial theorem and measuring the broad components of the emission lines observed in the STIS spectrum, assuming that the gas is uniformly distributed in a sphere of radius R. The $M_\bullet$ is found to be in the range between 7×10^7 and 2×10^9 $M_\odot$ depending on the radius we obtained from estimations of the dimensions of the broad line region. This is in agreement with previous findings based on different assumptions about the gas distribution. The nucleus of NGC 4278 hosts a barely resolved but strongly variable UV source. Its UV luminosity increased by a factor of 1.6 in a period of 6 months. The amplitude and scale time of this UV flare are remarkably similar to those of the brightest UV nuclear transients which were earlier found in other low-luminosity AGNs. This ultraviolet variability represents the typical signatures of the low-luminosity active galactic nuclei.

Chapter 8. The conclusions of the thesis as well as few lines of future research are reviewed in this Chapter.

2

Atlas of *HST*/STIS Spectra and Images of 177 nearby galaxies [1]

We present the data compilation of all nearby galaxies ($D < 100$ Mpc) with long-slit spectra available in the *Hubble Space Telescope* archive and taken with the Space Telescope Imaging Spectrograph mounting the G750M grating. These spectra cover the region of Hα line and of [N II] $\lambda\lambda$6548, 6583 and [S II] $\lambda\lambda$6716, 6731 emission line doublets. This atlas comprises 177 galaxies observed in their central $0\farcs1 - 0\farcs3$. We measured the ionized-gas velocity dispersion from the width of the [N II] emission line. The gaseous kinematics could be measured in 122 galaxies. This represents the most comprehensive spectral atlas of low-luminosity active galactic nuclei. We performed also the two-dimensional bulge-to-disk decomposition of the 2MASS and UKIDSS images of 65 sample galaxies in order to derive the K-band luminosity and effective radius of the spheroid. In most cases deeper images are needed to constrain spheroid parameters.

2.1 Introduction

Over the last years, the mass $M_\bullet$ of supermassive black hole (SMBH) has been measured for about 50 quiescent galaxies (see Gültekin et al. 2009b) allowing to investigate possible scaling relations between $M_\bullet$ and properties of the hosting galaxies. Among the tightest relations, SMBH masses correlate well with the bulge luminosity, $L_{\rm bulge}$ (Kormendy & Richstone 1995; Marconi & Hunt 2003; Gültekin et al. 2009b), bulge mass, $M_{\rm bulge}$ (Magorrian et al. 1998;

[1] Based on observations with the NASA/ESA *Hubble Space Telescope* obtained at STScI, which is operated by the Association of Universities for Research in Astronomy, Incorporated, under NASA contract NAS5-26555.

Häring & Rix 2004), and stellar velocity dispersion, σ (Ferrarese & Merritt 2000, Gebhardt et al. 2000a, Tremaine et al. 2002, Ferrarese & Ford 2005, Gültekin et al. 2009b). Pure disk galaxies, on the other hand, do not in general, seem to contain SMBHs. Special cases in this respect are NGC 4395 (Filippenko & Ho 2003), POX 52 (Barth et al. 2004) and NGC 1042 (Shields et al. 2008). The main aim of these studies is to understand the rôle of SMBHs in the coevolution with their hosts. The scaling relations are an important challenge for the models of galaxy formation. But, with the uncertainties in their actual slope and scatter it is difficult to discriminate the very large number of theoretical models that better reproduce the observations. In fact, the existing sample still comprises mainly of early-type galaxies, with few $M_\bullet$ determinations in galaxies with high and small stellar velocity dispersion, or in spiral galaxies, where instead nuclear clusters often appear as a prominent nuclear component. A better statistics in term of number of targets, morphological type subdivision, and method of measurements would be helpful in addressing this issue.

SMBHs in quiescent galaxies can be detected by observationally resolving their influence in the motion of stars and gas. The radius of influence $r_{\rm infl}$ of a SMBH of mass $M_\bullet$ can be defines as:

$$r_{\rm infl} = \frac{GM_\bullet}{\sigma^2}, \tag{2.1}$$

where σ is the rotational velocity or velocity dispersion characteristic of the inner part of the galaxy, and G is the gravitational constant. At the distance D of the object, this translates into and angular radius of influence $r_{\rm infl}$ of

$$r_{\rm infl}('') = 11'' \left(\frac{M_\bullet}{10^8 {\rm M}_\odot}\right) \left(\frac{\sigma}{200 \text{ km s}^{-1}}\right)^{-2} \left(\frac{D}{0.206265}\right)^{-1}. \tag{2.2}$$

SMBHs at a few Mpc distance with masses below $10^8 {\rm M}_\odot$ require *Hubble Space Telescope* (*HST*) resolution or adaptive-optics on the ground-based telescopes for resolving the sphere of influence (Ferrarese & Ford 2005).

Among the several techniques that have been used so far to detect and measure $M_\bullet$, the most common for quiescent galaxies rely on stellar kinematics (e.g., Verolme et al. 2002; Gebhardt et al. 2003; Houghton et al. 2006; Nowak et al. 2007, 2008, 2009; Cappellari et al. 2009; Krajnović et al. 2009, see also Chapter 5) and gaseous kinematics (e.g., Sarzi et al. 2001; Barth et al. 2001; de Francesco et al. 2006; Coccato et al. 2006; Pastorini et al. 2007(@; Neumayer et al. 2007; Dalla Bontà et al. 2009, see also Chapter 6).

Gaseous kinematics is simpler to be obtained and analyzed if compared to the stellar kinematics, but the measurements are prone to errors due to non-circular or non-gravitational forces. It requires that the gas is rotating in a

thin disk with simple circular motion and the spatial resolution is high enough to probe the sphere of influence of the SMBH. Yet, only a handful of objects targeted by *HST* turned out to have sufficiently regular gas velocity fields for the purpose of modeling (Sarzi et al. 2001; Ho et al. 2002). The *HST* Science Archive contains an untapped resource that can be used to better constrain the black-hole mass budget across the different morphological types of galaxies, which consists of the vast number of the STIS spectra from which a central emission-line width can be measured. The modeling of this kind of data can indeed lead to tight upper limits on $M_\bullet$, as first shown by Sarzi et al. (2002).

With the idea of increasing the demography of $M_\bullet$ determinations for a large and various sample of host galaxies, we started a project aimed at measuring upper limits on $M_\bullet$ of SMBHs that can be present in the center of nearby galaxies ($D < 100$ Mpc) by studying the gaseous kinematics in the available archival STIS/G750M spectra. These spectra have been obtained for the nuclei of 177 galaxies. For only a fraction of our data sample we could model a regular velocity field and we resolve the sphere of influence of the SMBH to obtain precise $M_\bullet$ estimation.

In this chapter we present the spectral and imaging atlas of the 177 sample galaxies. The spectral atlas is a useful dataset to characterize the galaxies that have been studied in the past with STIS and can be used for planning new STIS observations after the recent refurbishment of *HST*. We show also the two-dimensional bulge-to-disk decomposition of the sample galaxies we obtained by analyzing the K-band Two Micron All Sky Survey (2MASS) and in the United Kingdom InfraRed Deep Sky Surveys (UKIDSS) images.

The chapter is organized as follows. In Section 2.2, we describe our sample, in Section 2.3 we analyze the STIS spectra and measure the central emission-line width. In Section 2.4 we present the two-dimensional bulge-to-disk decomposition we have performed on the 2MASS and UKIDSS images in order to determine the K-band bulge luminosity of the sample galaxies. In Section 2.5 we summarize the main results and discuss the future work.

2.2 Sample selection

In order to assemble the largest possible sample of homogeneous measurements of the central emission-line width, we searched in the *HST* Science Archive for objects with STIS spectra obtained with the G750M grating through either the $0\farcs1 \times 52''$ or the $0\farcs2 \times 52''$ slit placed across the galaxy nucleus, most often at random position angles. This is indeed by far the most common configuration in the archive, which always gives us access to the [N II] $\lambda\lambda 6548, 6583$, H$\alpha$, and [S II] $\lambda\lambda 6716, 6731$ emission lines. Limiting ourselves to galaxies within 100 Mpc

to minimize the impact of the stellar potential on our following estimation of $M_\bullet$, we retrieved data for 177 galaxies spanning the whole range of morphological types. Table 2.1 lists the sample of galaxies analyzed in this chapter, which comprises 177 galaxies of which 22 (12%) are classified as ellipticals, 41 (23%) are lenticulars, and 114 (64%) are spirals. The large amount of these galaxies are classified as LINERS but the sample contains also a fraction of Seyferts and transition objects (31 LINERS, 18%; 36 H II nuclei, 20%; 37 Seyferts, 21%; 25 transition objects, 14%; 48 objects have an unknown classification, 27%).

When available, galactic distances were adopted from measurements based on either surface-brightness fluctuations (Tonry et al. 2000, 2001), Cepheid variables (Freedman et al. 2001) or from Tully (1988). Otherwise we used the weighted mean recessional velocity corrected to the reference frame defined by the microwave background radiation from de Vaucouleurs et al. (1991, RC3 hereafter) to derive the distance to our sample galaxies by assuming $H_0 = 75$ km s^{-1} Mpc^{-1}, $\Omega_{\rm m} = 0.3$, and $\Omega_\Lambda = 0.7$. The median distance of the sample galaxies is 20.2 Mpc. The distance of each galaxy is shown in Table 2.1 where we have indicated also the reference and main properties of the sample galaxies, either from RC3 and Hyperleda[1].

Since the aim of our work was to estimate $M_\bullet$ from the emission line widths and compare them with the scaling relations we sought for the published values of the stellar velocity dispersion for our galaxy sample. With the idea to have the most homogeneous sample of σ, we searched for measurements part of the same dataset, derived from the same author and with the same instrument, comprehensive of both photometric and spectroscopic data, focusing on the newest measurements. When several σ from the same author were available, we adopted a weighted average of the values. In Table 2.2 we show all published spectroscopic and photometric data we found for 147 galaxies. To homogenize all our σ, we rescaled our data to the values we would have had within a circular aperture of radius equal to 1/8 of the effective radius, $r_{\rm e}$, following Jørgensen et al. (1995). We first obtain the σ we would have had into a circular aperture

$$2r_{\rm ap} \sim 1.025 \times 2(xy/\pi)^{1/2} \tag{2.3}$$

then we applied the correction

$$\sigma_{r_{\rm e}/8} = \sigma_{\rm ap} \left(\frac{r_{\rm ap}}{r_{\rm e}/8} \right)^{0.04} \tag{2.4}$$

In Table 2.2 we show the dimensions of the rectangular aperture in arcsec within which the σ was measured. For some galaxies σ was already measured in

[1] http://leda.univ-lyon1.fr

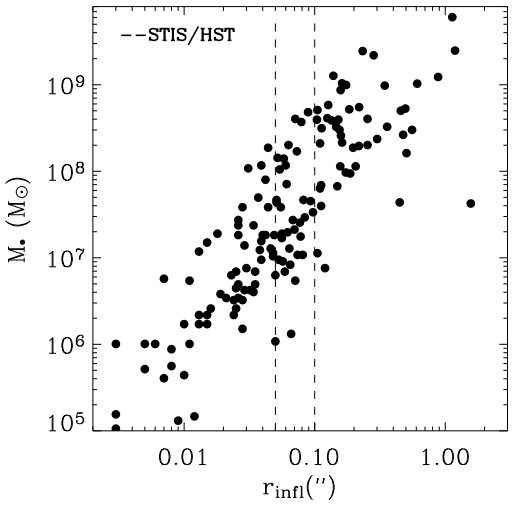

Figure 2.1 Predicted $M_\bullet$ from the $M_\bullet - \sigma$ relation by Ferrarese & Ford (2005) against the $r_{\rm infl}$ for our data sample. The sphere of influence is resolved for galaxies with $r_{\rm infl} \geq 0\farcs05$ for the slit width $0\farcs1$, and $0\farcs1$ for the slit width $0\farcs2$ (dashed line).

a circular aperture and we indicated the radius in the second column. Among the published data we derived also $r_{\rm e}$ for the spheroidal component. For all the elliptical galaxies we retrieved $r_{\rm e}$ from RC3. For the lenticulars and spirals we searched mainly in the large sample of photometric decompositions by Baggett et al. (1998) who extracted the surface-brightness profiles in V-band. For some galaxies we adopted our own values from the two-dimensional decomposition of 2MASS images (see Section 2.4.1 for details and Tables 2.2 and 3.1).

In Table 2.1 we show also the predicted values of $M_\bullet$ from the $M_\bullet - \sigma$ relation by Ferrarese & Ford (2005) to show the large range of $M_\bullet$ we cover with our sample populating the $M_\bullet - \sigma$ relation from small to high σ. For 48 (33%) out of 147 galaxies with published σ, we found that the radius of the sphere of influence is resolved by our data (Figure 2.1).

2.3 Space Telescope Imaging Spectrograph spectroscopy and imaging

The instrumental setup of the STIS spectra retrieved for the sample galaxies is given in Table 2.3

The detector was the SITe CCD with 1024 × 1024 pixels of 21 × 21 μm^2

with a spatial scale of $0\farcs0507$ pixel^{-1} and a spectral scale of 0.554 Å pixel^{-1}.

The wavelength range was either 6482−7054 Å or 6295 − 6867 Å, depending on whether the G750M grating was used at the primary or secondary tilt, respectively. This spectral range includes the Hα, [N II] $\lambda\lambda$6548, 6583, and [S II] $\lambda\lambda$6716, 6731 emission lines. The galaxies were observed with either the $0\farcs1 \times 52''$ or the $0\farcs2 \times 52''$ slit. In most cases the CCD was read out with no on-chip binning. Alternatively, it was read binning along both the spatial and dispersion axis. The spatial scale ranged from $0\farcs0507$ pixel^{-1} to $0\farcs1$ pixel^{-1}, and the reciprocal dispersion ranged from 0.554 Å pixel^{-1} to 1.108 Å pixel^{-1}. The spectra were obtained with the slit placed across the galaxy nucleus with random position angle. The instrumental FWHM was 0.87 Å (corresponding to $\sigma_{\rm inst} = 17$ km s^{-1} at [N II] λ6583) and 1.6 Å ($\sigma_{\rm inst} = 32$ km s^{-1}) for the $0\farcs1$ and the $0\farcs2$-wide slit, respectively. These values were obtained as an average of the instrumental broadening we derived by using observations of the STIS wavelength calibration map for all our data sample. Gaussian models were fitted to the emission line profiles of the extracted calibration-lamp spectra.

2.3.1 Data Reduction

The archival spectra were reduced using IRAF[1] and the STIS reduction pipeline maintained by the Space Telescope Science Institute (Dressel et al. 2007). The basic reduction steps included overscan subtraction, bias subtraction, dark subtraction, and flatfield correction. Different spectra obtained for the same slit position were aligned using IMSHIFT and knowledge of the adopted shifts along the slit position. Cosmic ray events and hot pixels were removed using the task LACOS_SPEC by van Dokkum (2001). Residual bad pixels were corrected by means of a linear one-dimensional interpolation using the data quality files and stacking individual spectra with IMCOMBINE. This allowed us to increase the signal-to-noise ratio of the resulting spectra. We performed wavelength and flux calibration as well as geometrical correction for two-dimensional distortion following the standard reduction pipeline and applying the X2D task. This task corrected the wavelength scale to the heliocentric frame as well.

To measure the nuclear emission-line width we generally extracted aperture spectra one ($0\farcs1$), three ($0\farcs15$), and five pixels wide ($0\farcs25$) centered on the continuum peak, for the $0\farcs1$ and $0\farcs2$-wide slit cases, respectively. When the spectra were obtained with a 2-pixel binning read-out mode along the spatial direction, we extracted aperture spectra three pixels wide ($0\farcs3$) for the $0\farcs2$-wide slit. The extracted spectra thus consist of the central emission convolved with

[1]IRAF is distributed by NOAO, which is operated by AURA Inc., under contract with the National Science Foundation

the STIS spatial point-spread function (PSF) and sampled over nearly square apertures of $0\farcs1 \times 0\farcs1$, $0\farcs15 \times 0\farcs1$, $0\farcs25 \times 0\farcs2$ or $0\farcs3 \times 0\farcs2$, roughly corresponding to a circular aperture with radius of $0\farcs06$, $0\farcs07$, $0\farcs13$, and $0\farcs14$, respectively. Details for each sample galaxy are given in Table 2.3.

During each observation, acquisition images were taken to acquire the nucleus with a field of view of $5'' \times 5''$ (0.5 kpc $\times$ 0.5 kpc at the median galaxy distance) and the optical long-pass filter F28X50LP. The pixel scale of the images is $0\farcs05073$ pixel^{-1} (see Kim Quijano et al. 2007, for details). The images are optically centered. The central wavelength (7230 Å) and band pass are roughly equivalent to the *R*-band. Integration times of each image vary between 20 and 60 s. The STIS images were originally taken to acquire the nucleus of each galaxy so that spectroscopic apertures could be accurately placed. Two images were taken for each galaxy. The first was based on previous estimates of the nucleus location. A 7×7 pixels boxcar averaging was then used to find the peak intensity, which was assumed to be the location of the nucleus. Although their original purpose was to locate the nucleus of the galaxy, these images also were used to detect the possible presence of a nuclear cluster component in the galaxies (see Section 3.3.2 for details).

The images were reduced by the flight software, which performed the subtraction of a single bias number and removal of the hot pixels.

In Figure 2.2 we show the STIS acquisition image of each galaxy. It is associated to the nuclear two-dimensional and one-dimensional spectra obtained by extracting a squared aperture centered on the continuum peak. In the acquisition image we also show the location and the size of the slit placed on the galaxy center and the orientation of the galaxy. Offset spectra are not considered because we needed only the nuclear one. All the nuclear spectra obtained at different position angles for the same galaxy are shown.

The acquisition images show different nuclear morphologies: regular dust lanes (NGC 1300, NGC 4258, NGC 4435), patchy dust absorption with very bright nucleus in the center of the image(NGC 2179, NGC 4051, NGC 4552), brightest knots not at the center of the image (see NGC 255, NGC 3067, NGC 3705), and nucleus not well defined (NGC 2748, NGC 3003, NGC 4374). In the case of NGC 134, NGC 3521, NGC 3917 for instance the first estimate of the galaxy nucleus was significantly in error such that *HST* was unable to image the nucleus.

Upon a closer inspection ten objects revealed an unrelaxed morphology. Since we are searching for reliable emission-line estimate we dropped these objects, with a possibly disturbed gaseous kinematics. They are identified with an "i" in Table 2.3. Those objects were observed by program GO-8669, which

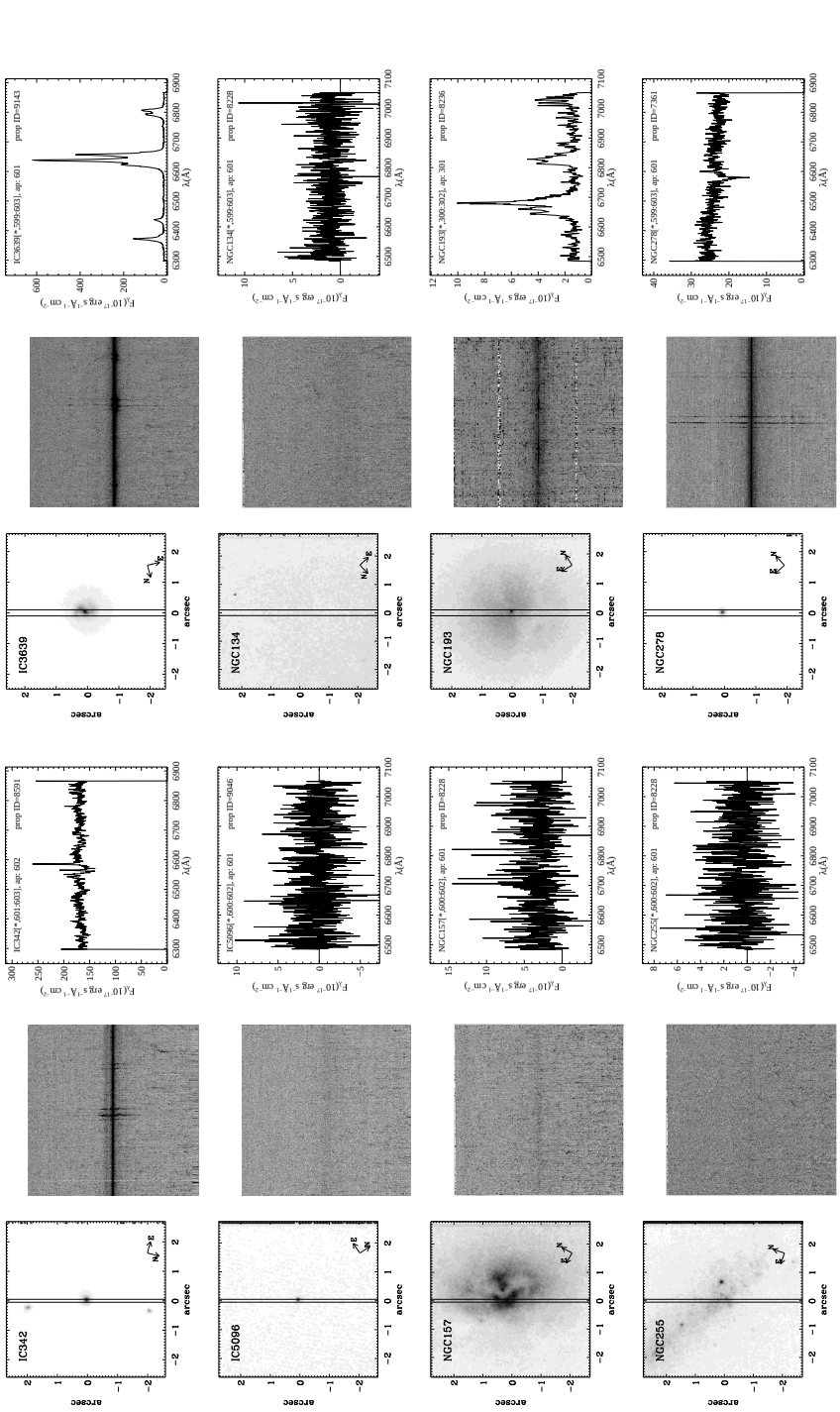

Figure 2.2 STIS acquisition image (*left panel*), nuclear two-dimensional spectrum (*central panel*), and central one-dimensional spectrum (*right panel*) for the sample galaxies. The location and size of the slit as well as the orientation and size of the field of view are given for each acquisition image.

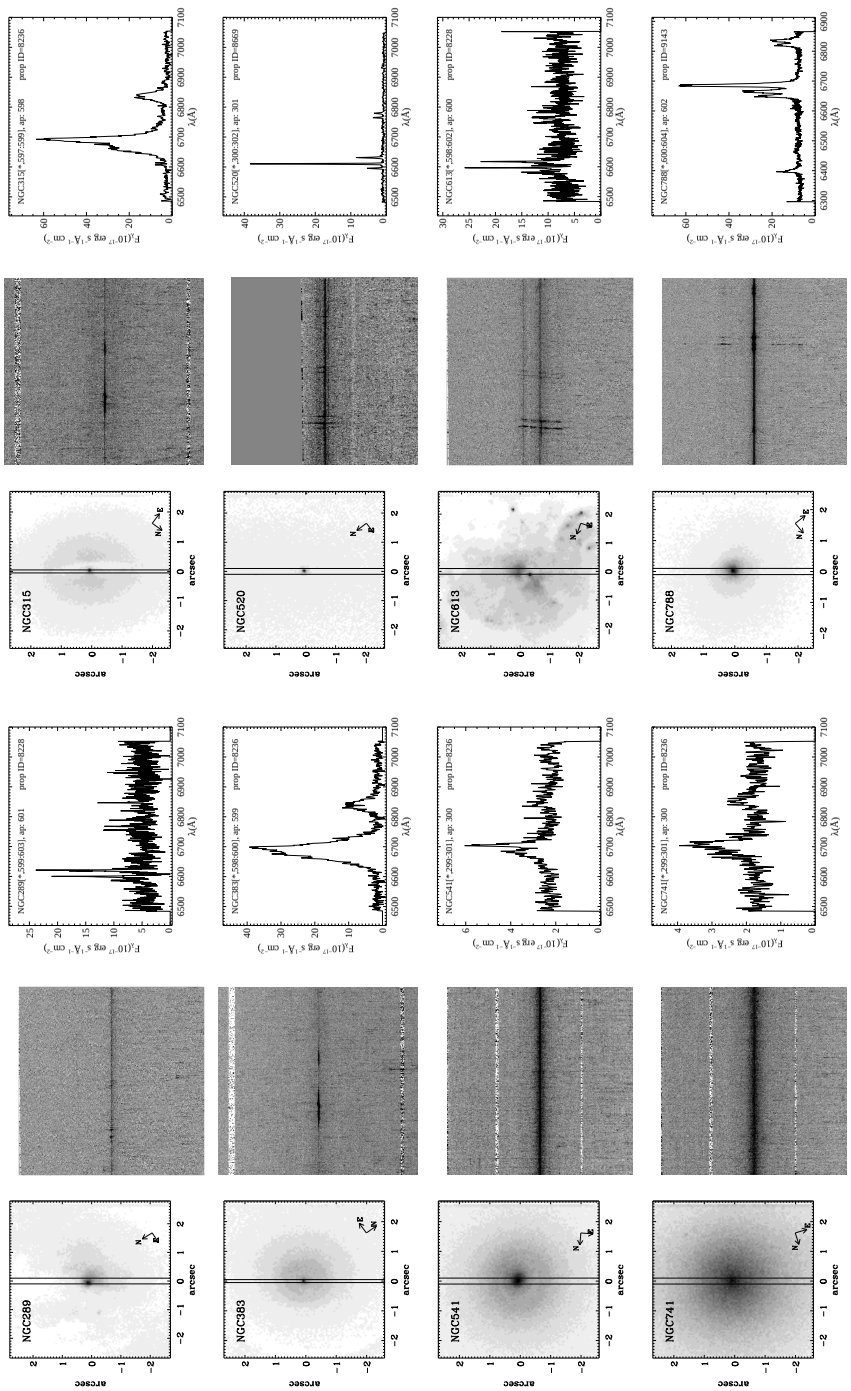

Figure 2.2 – Continued

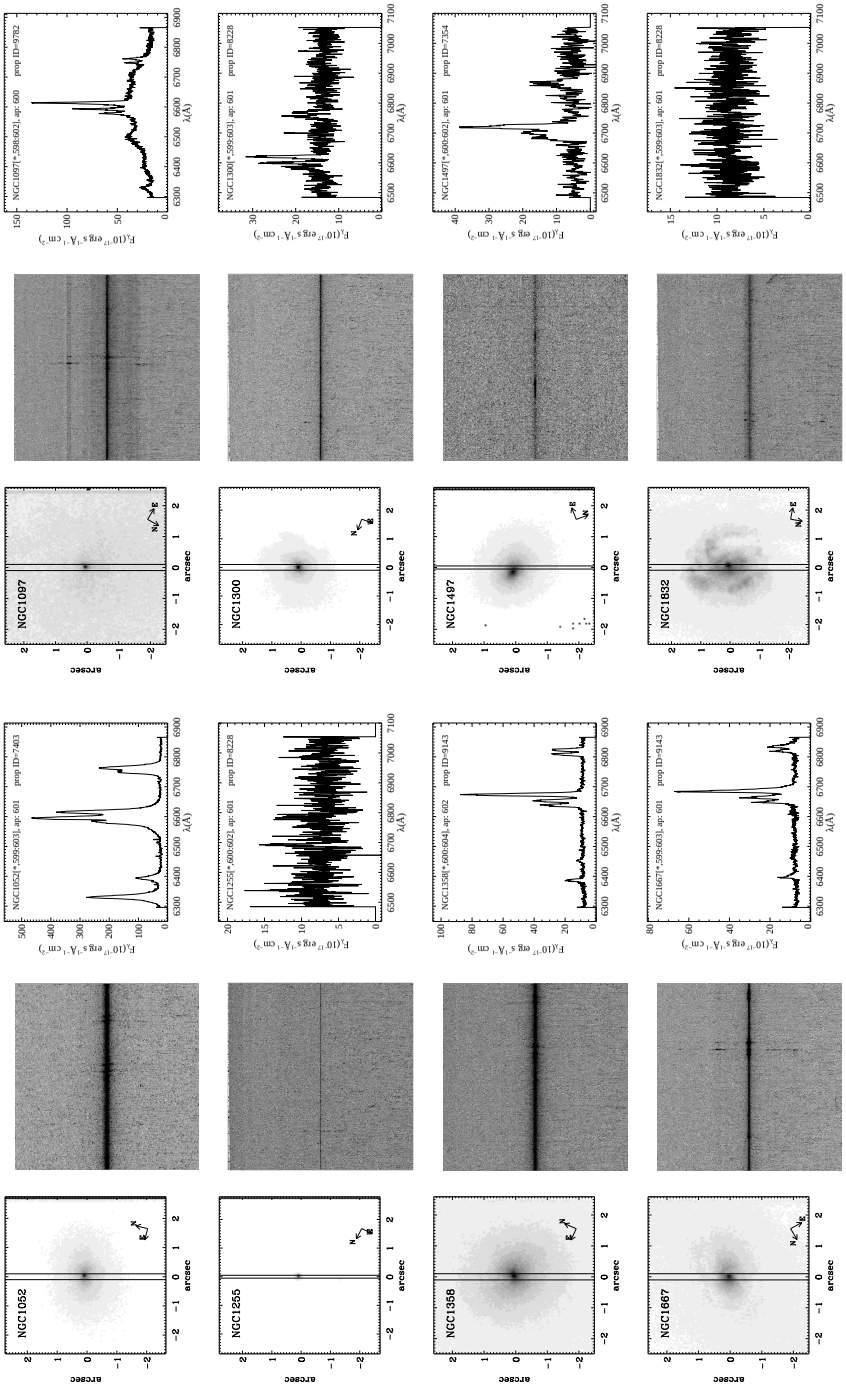

Figure 2.2 – Continued

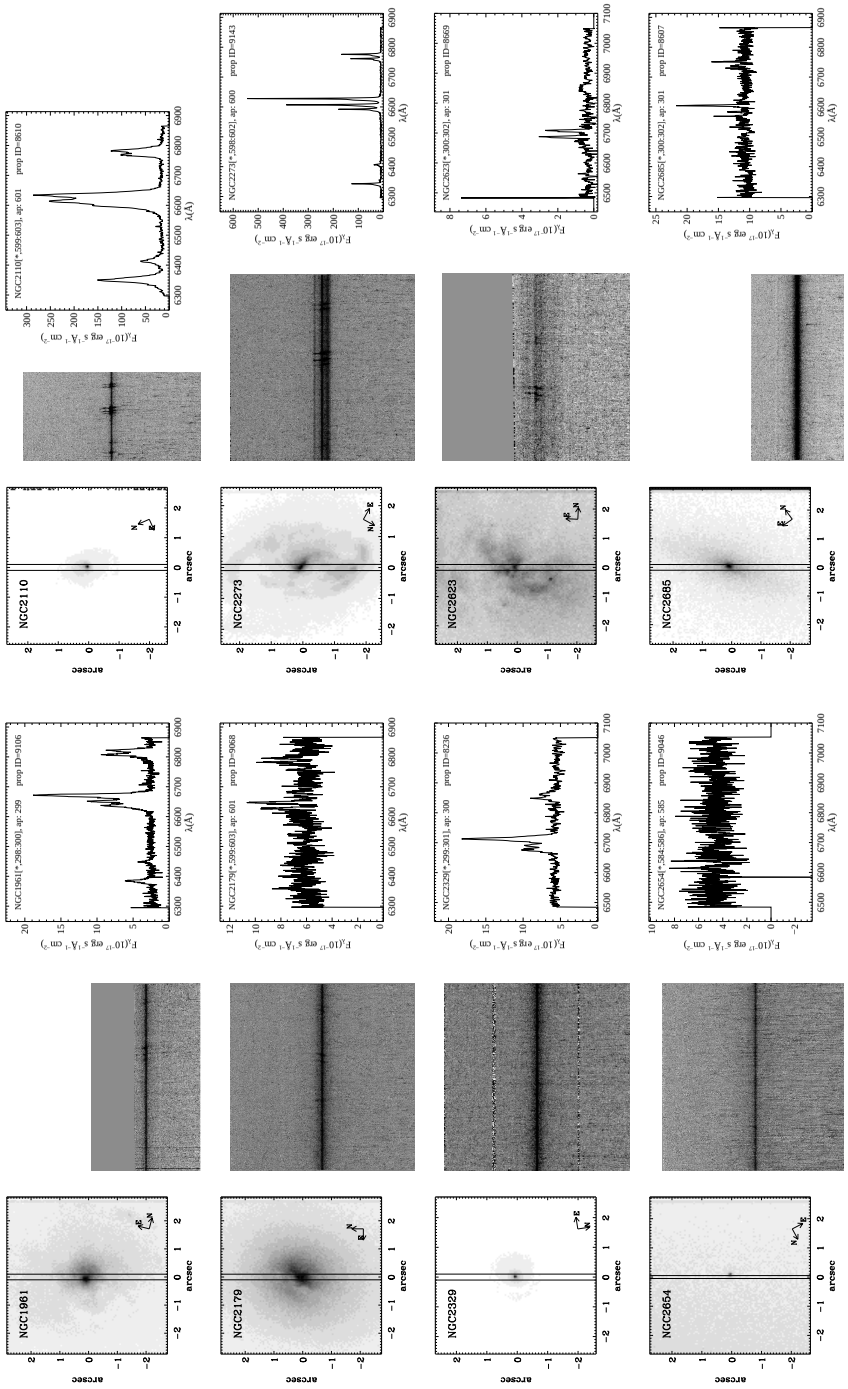

Figure 2.2 – Continued

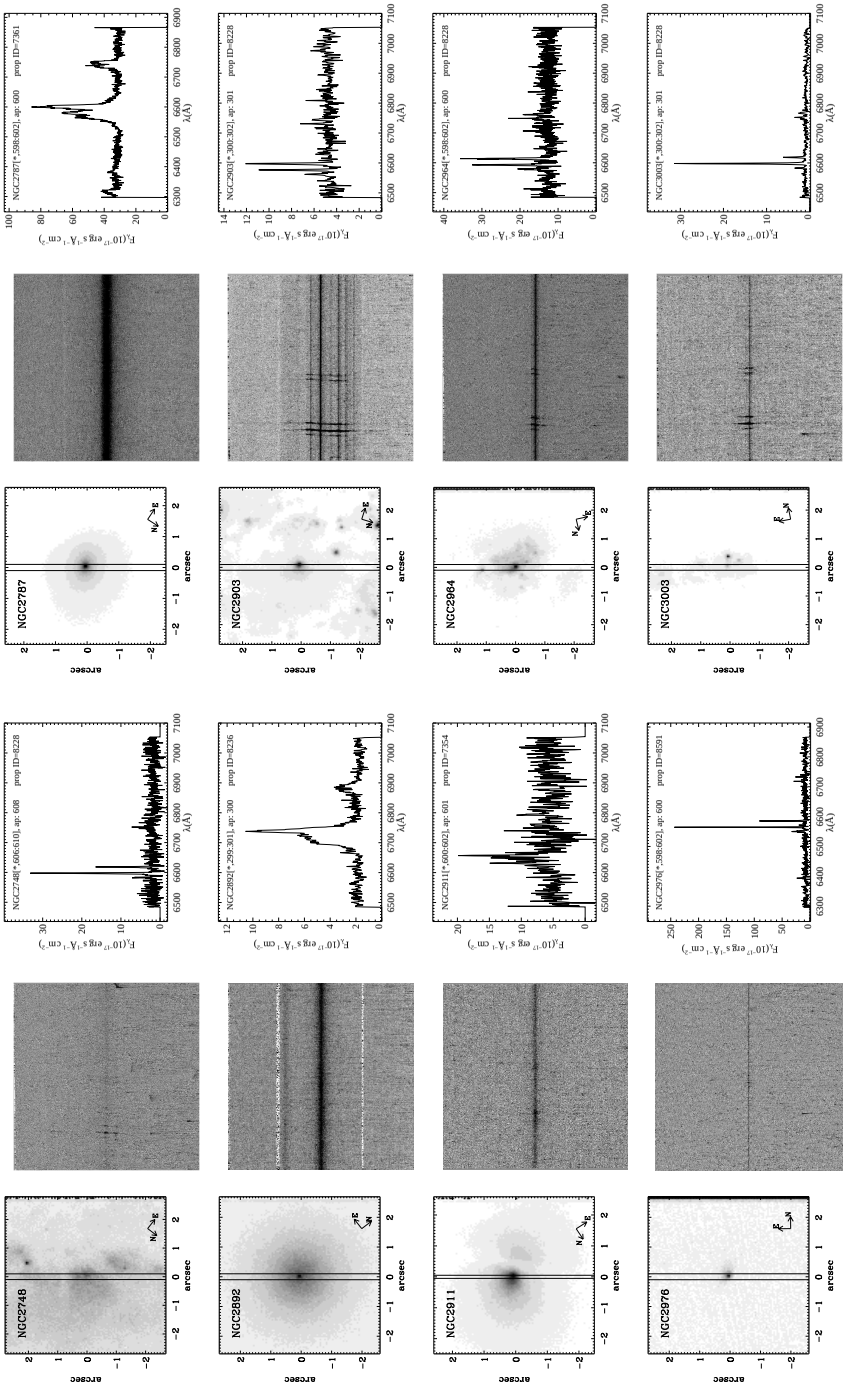

Figure 2.2 – Continued

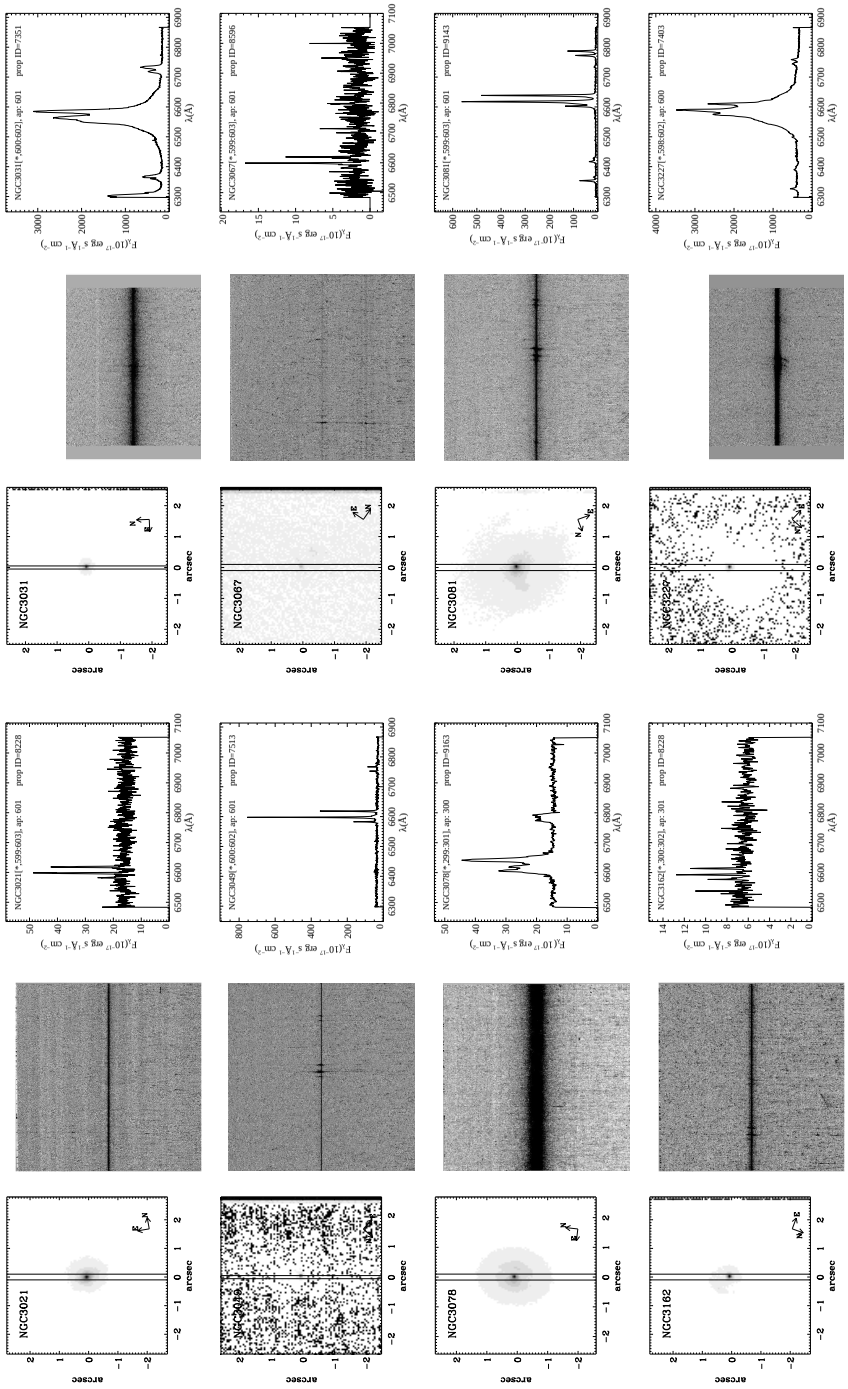

Figure 2.2 – Continued

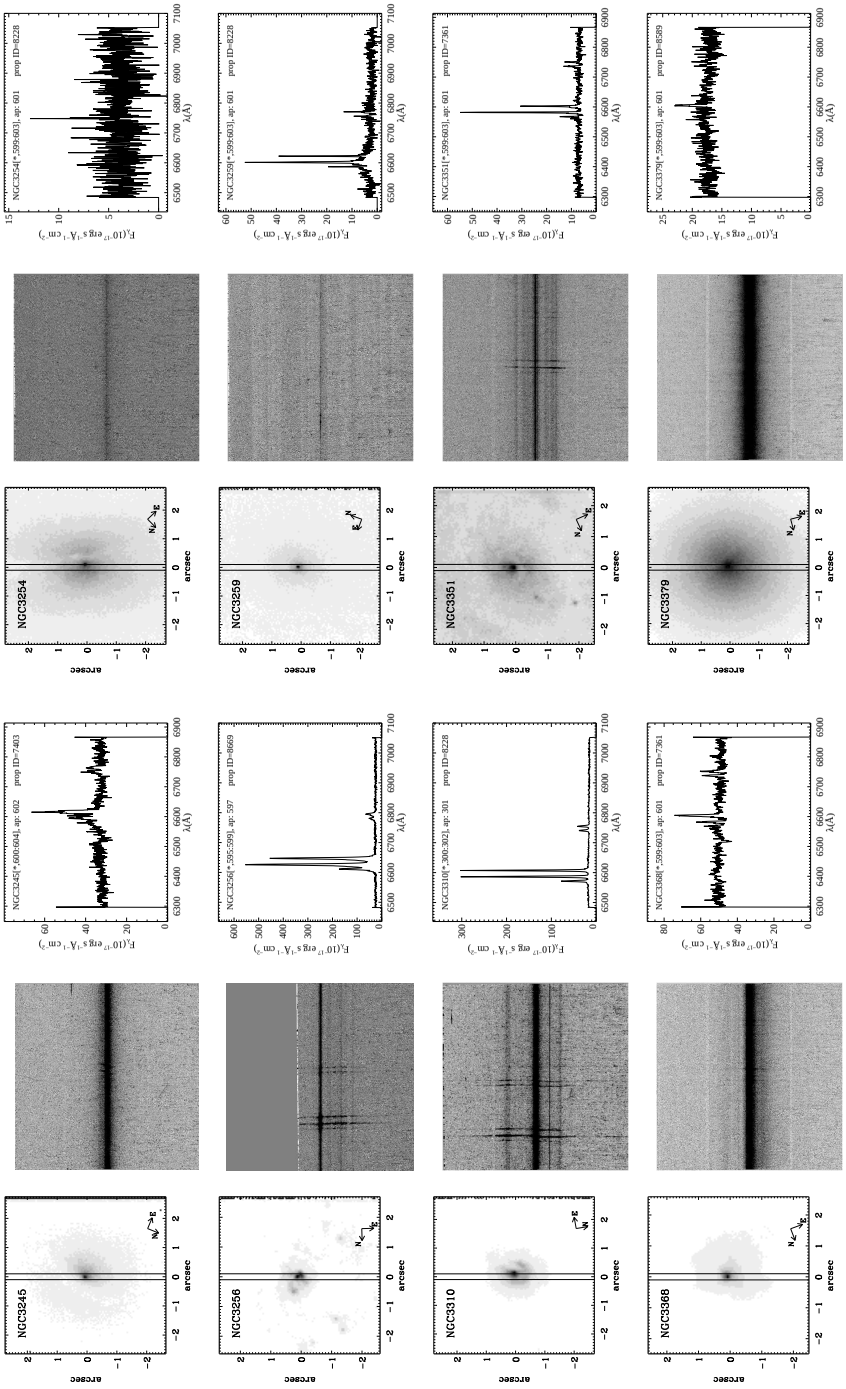

Figure 2.2 – Continued

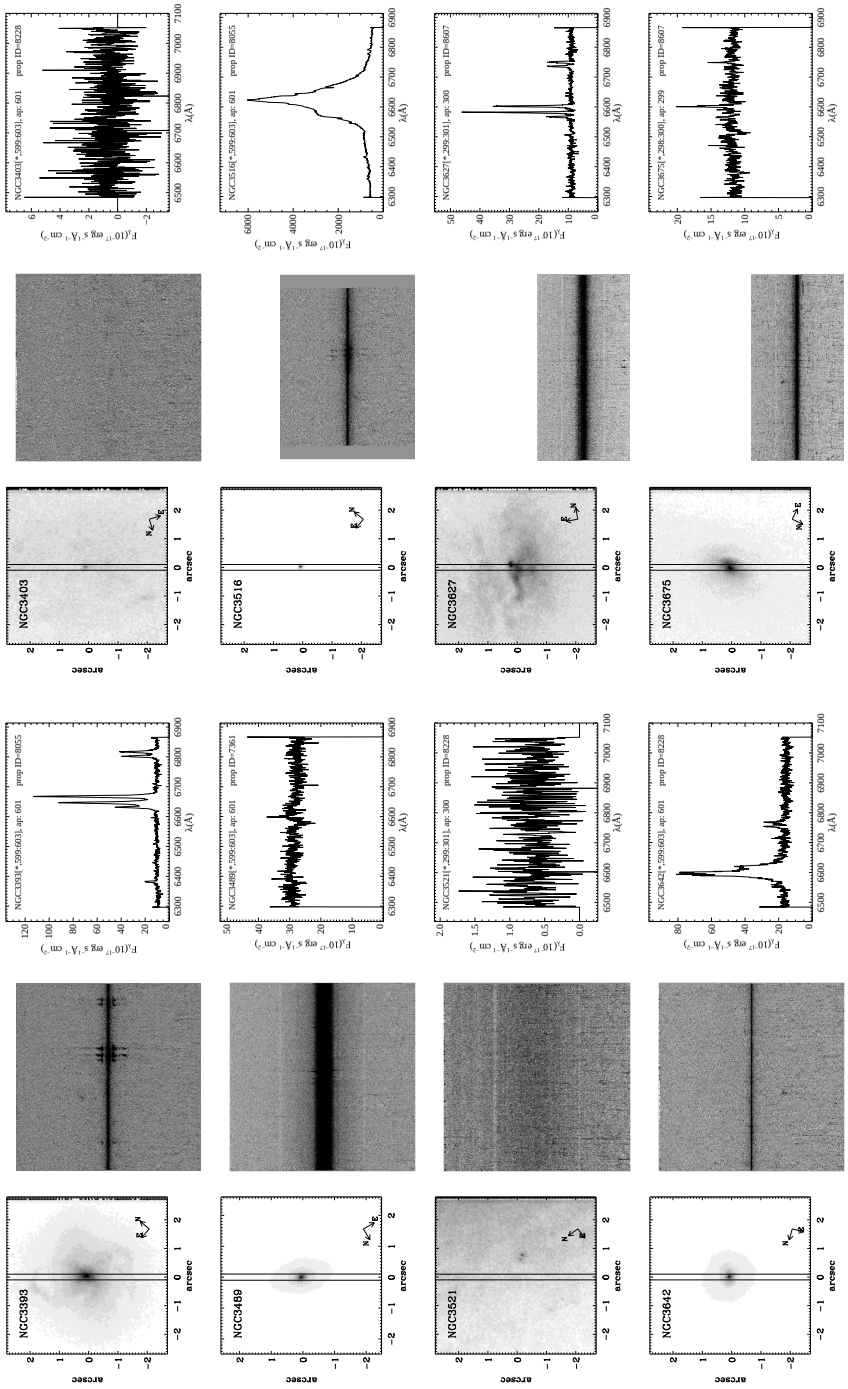

Figure 2.2 – Continued

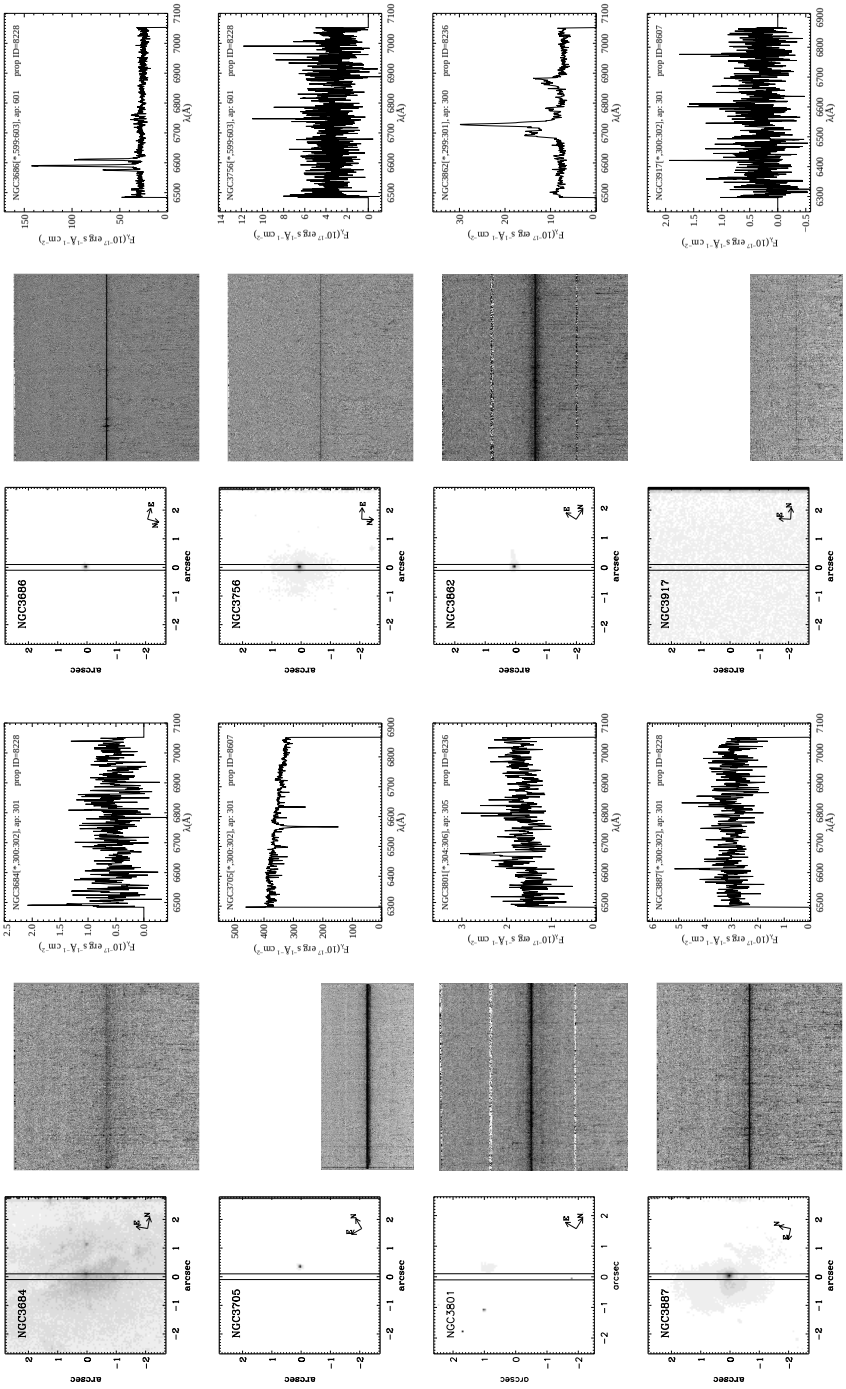

Figure 2.2 – Continued

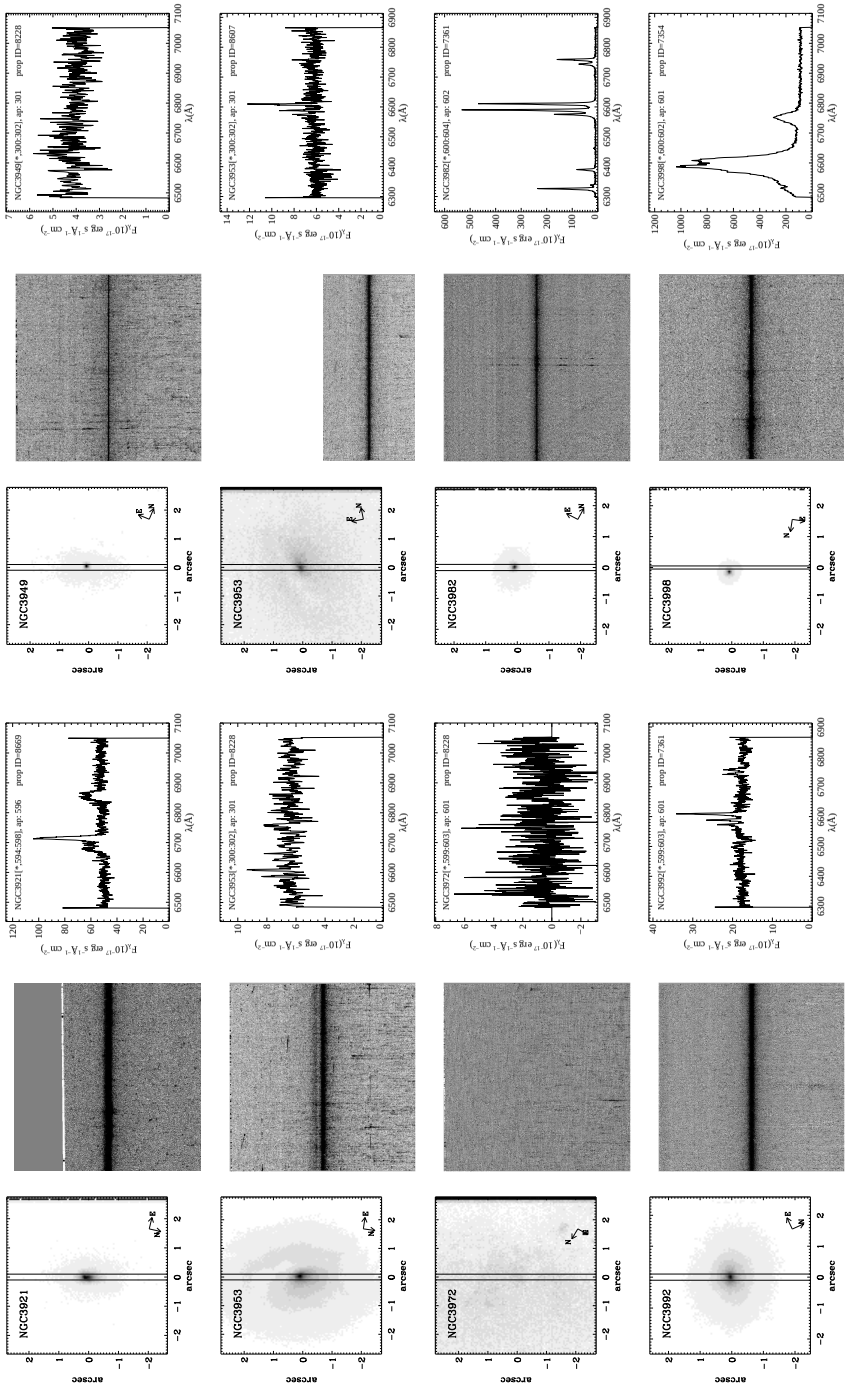

Figure 2.2 – Continued

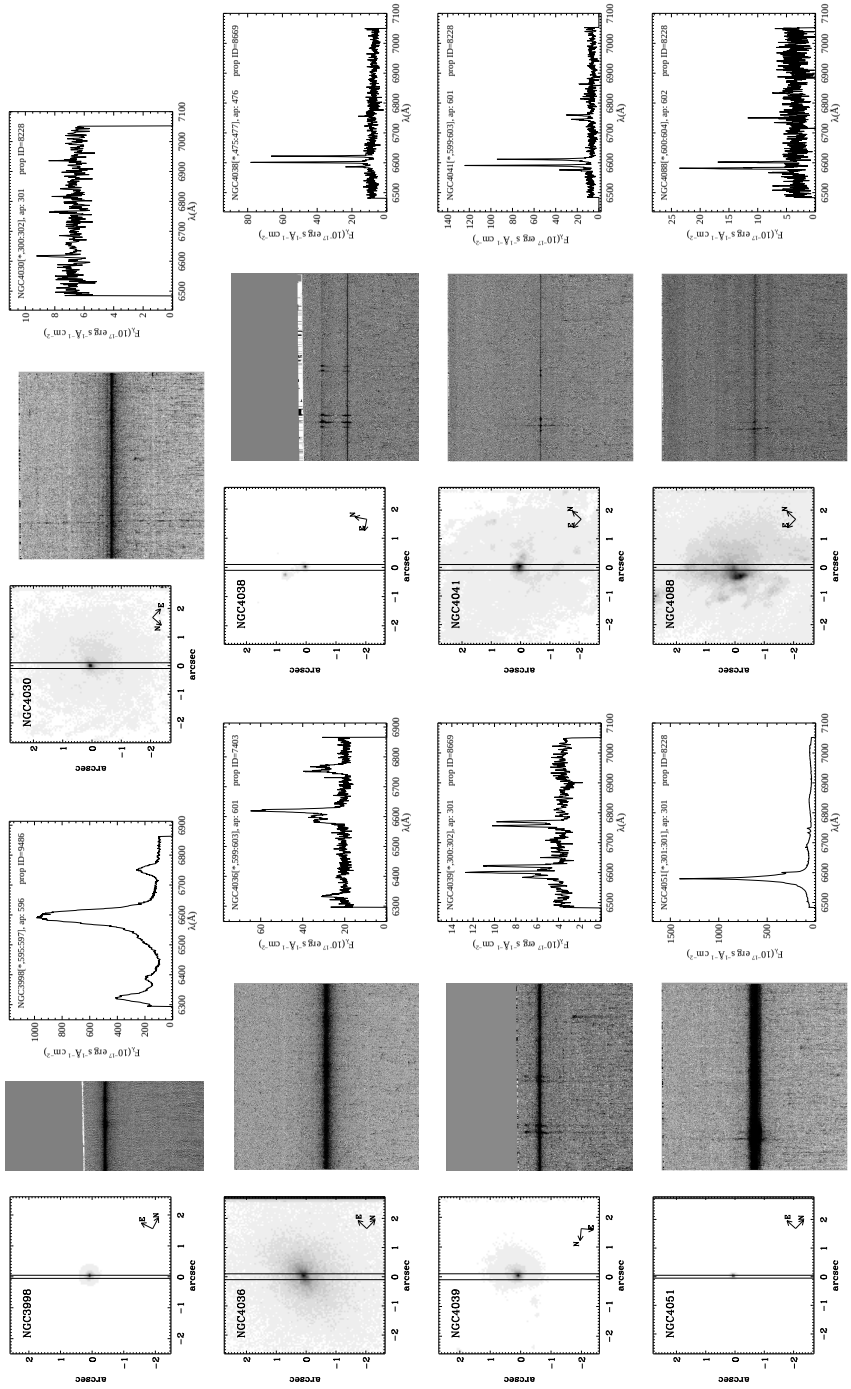

Figure 2.2 – Continued

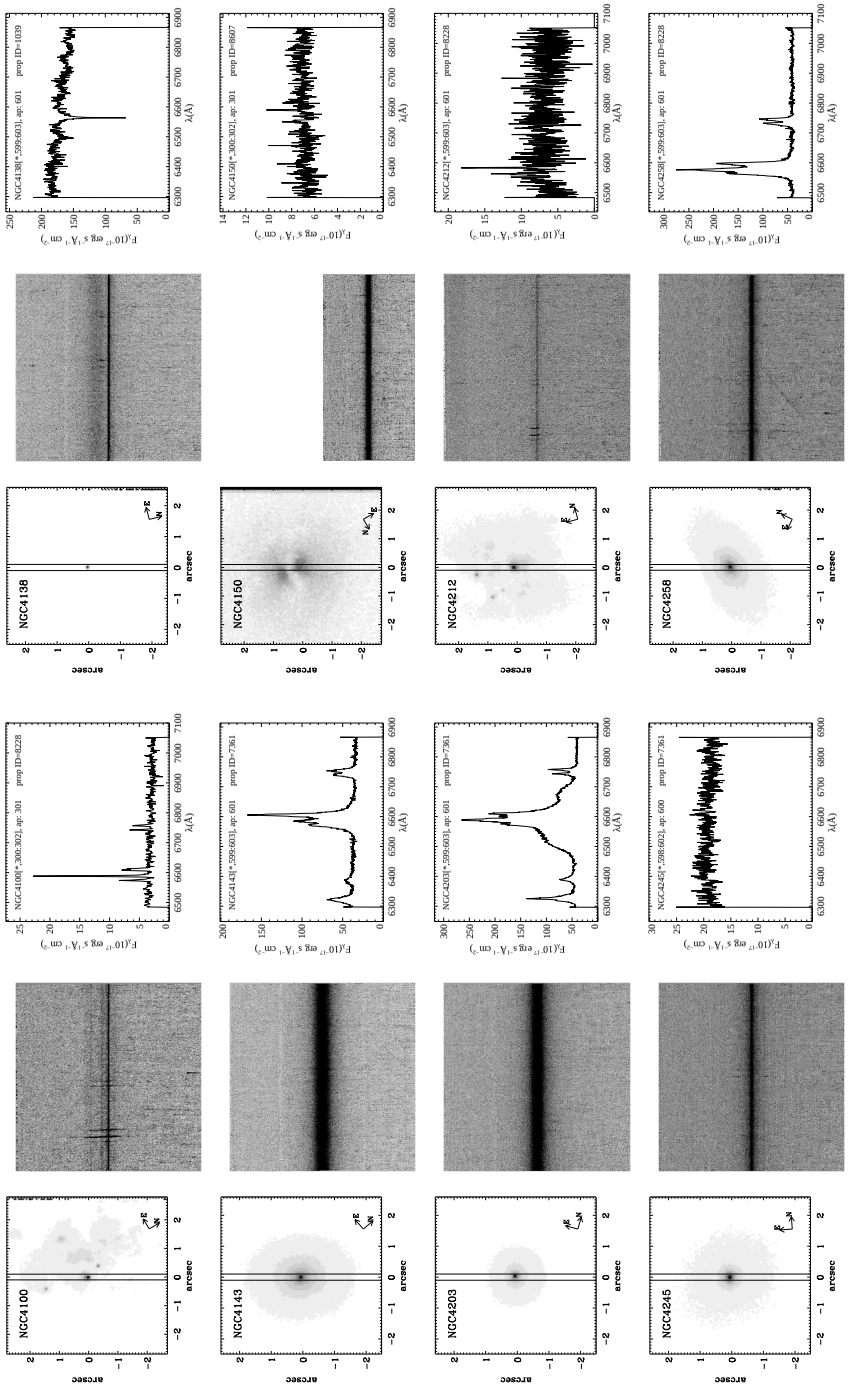

Figure 2.2 – Continued

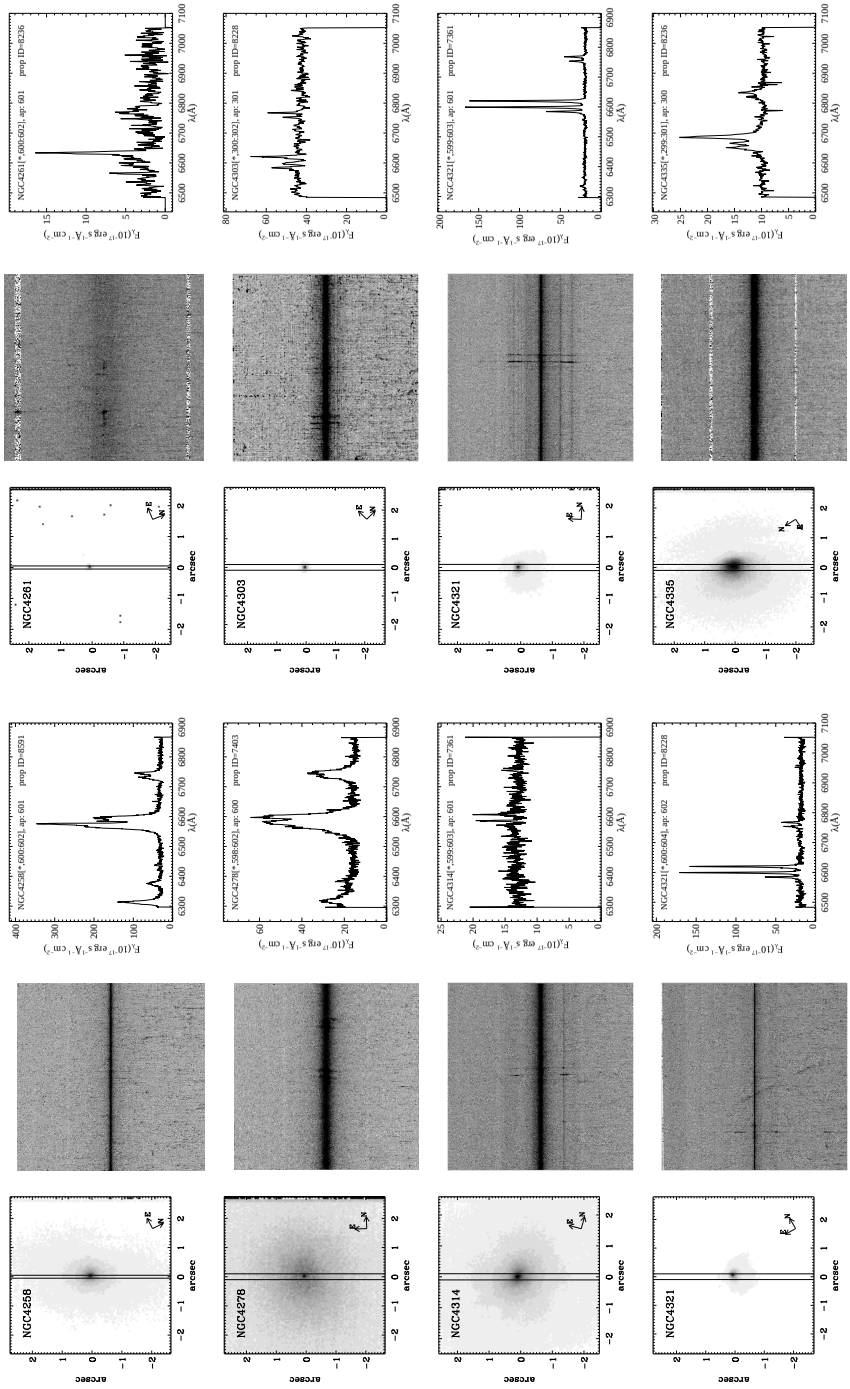

Figure 2.2 – Continued

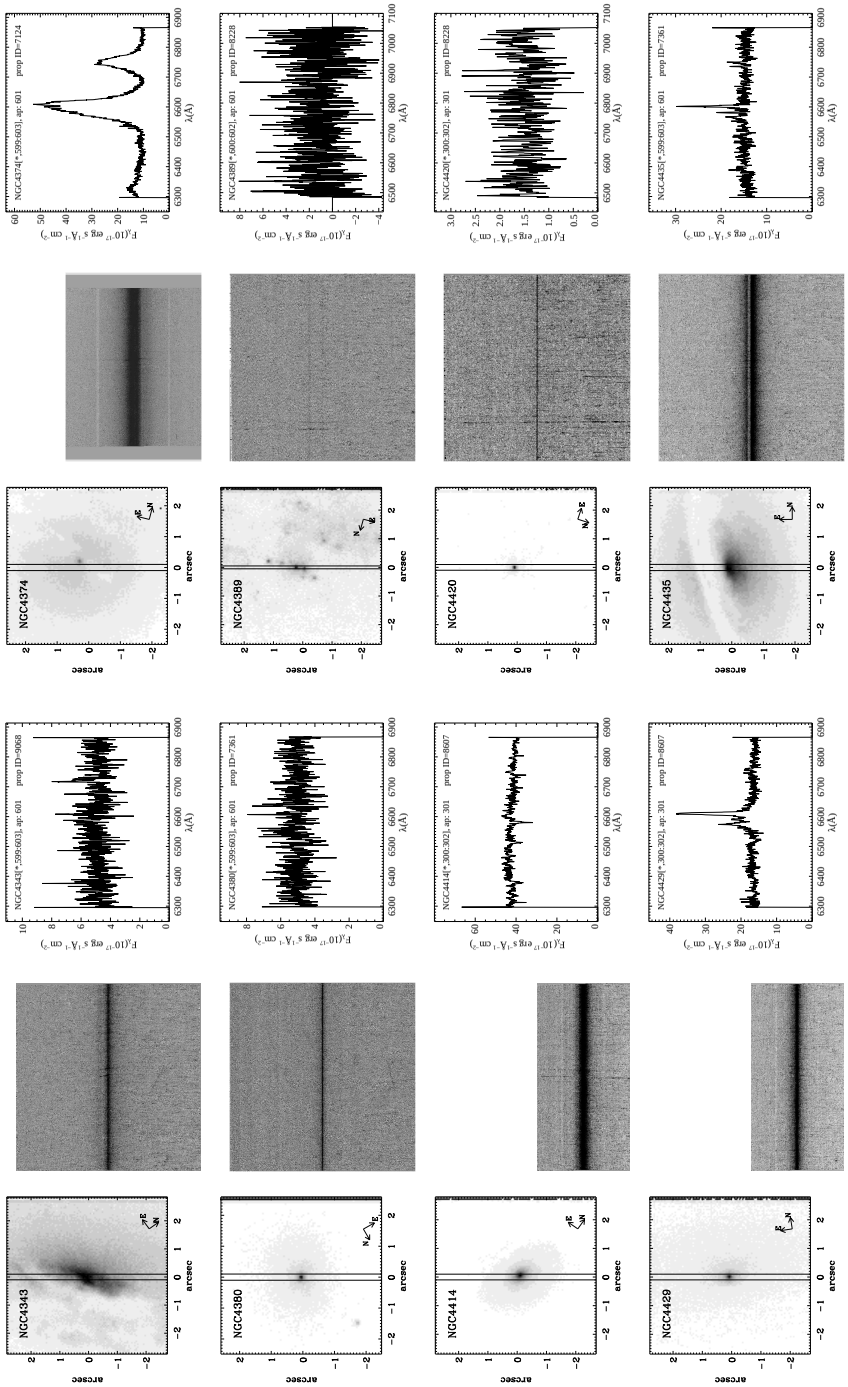

Figure 2.2 – Continued

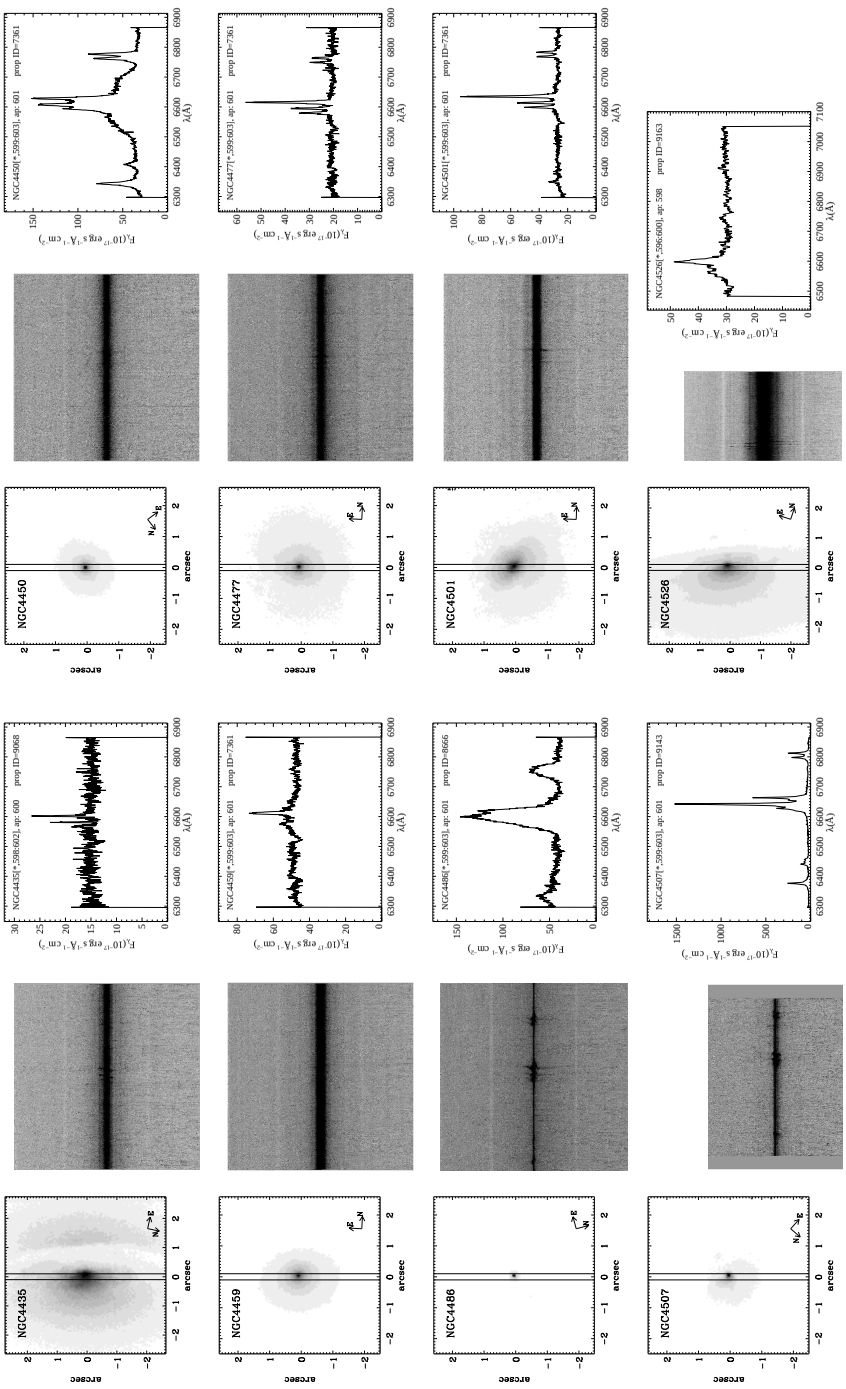

Figure 2.2 – Continued

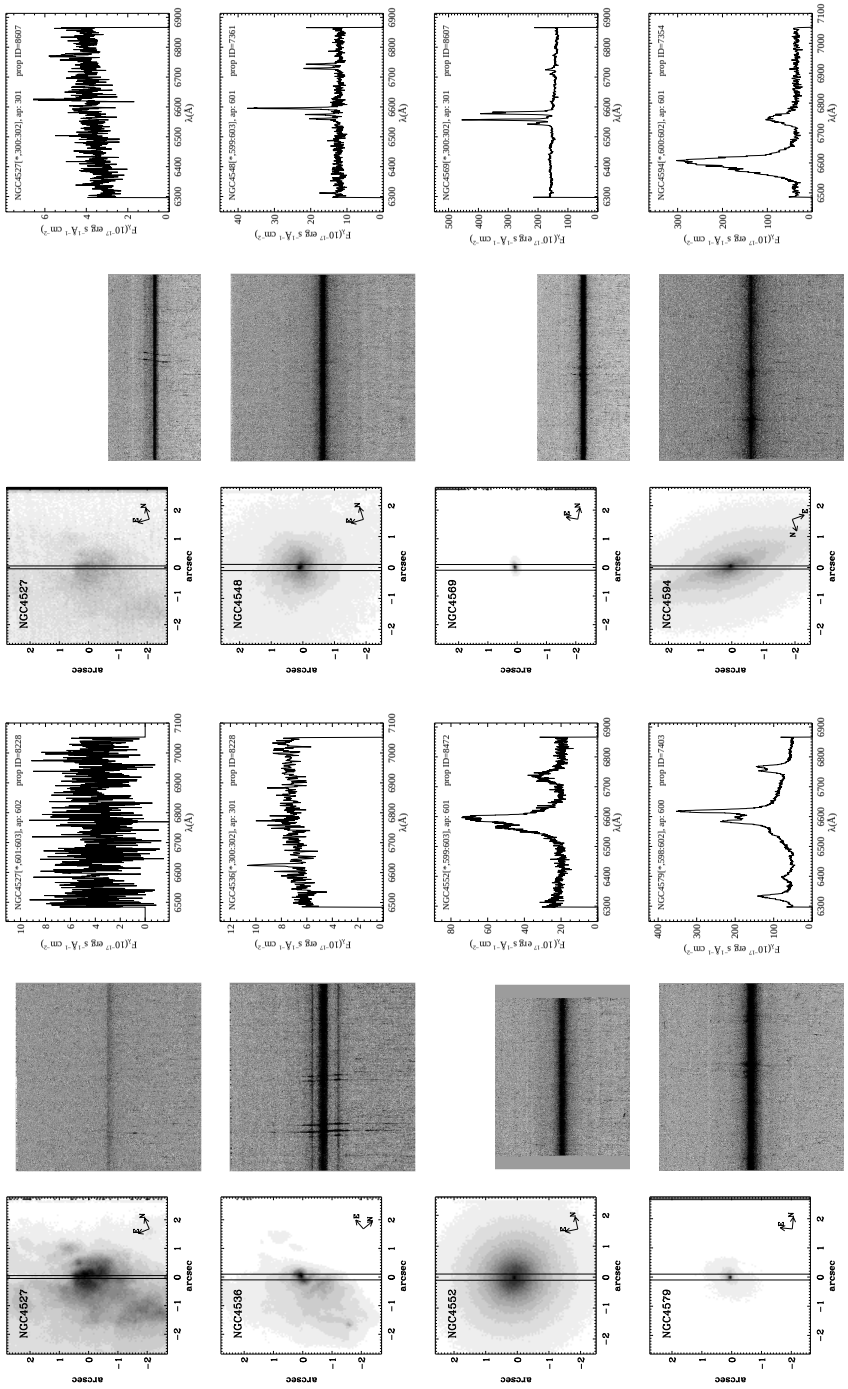

Figure 2.2 – Continued

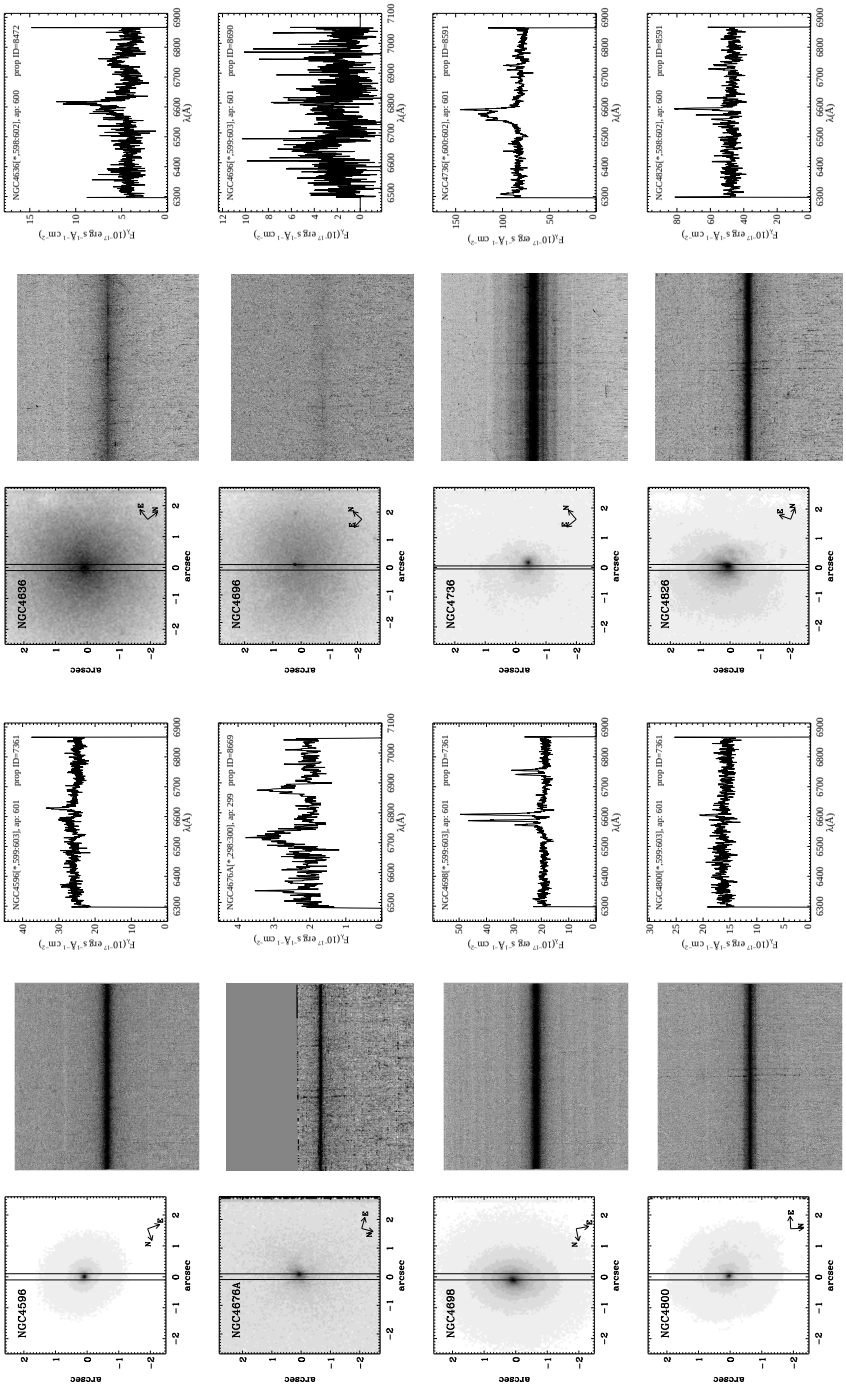

Figure 2.2 – Continued

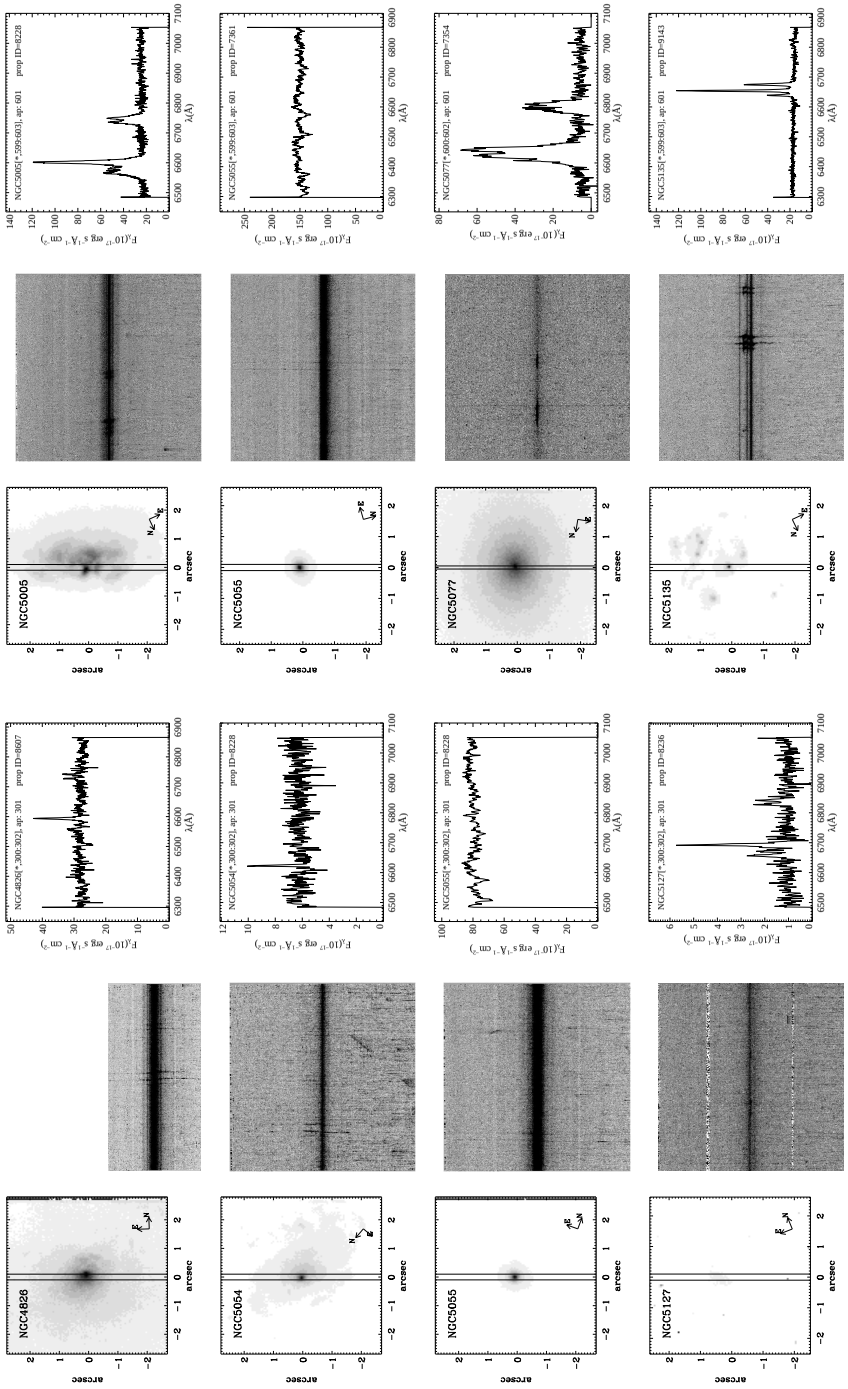

Figure 2.2 – Continued

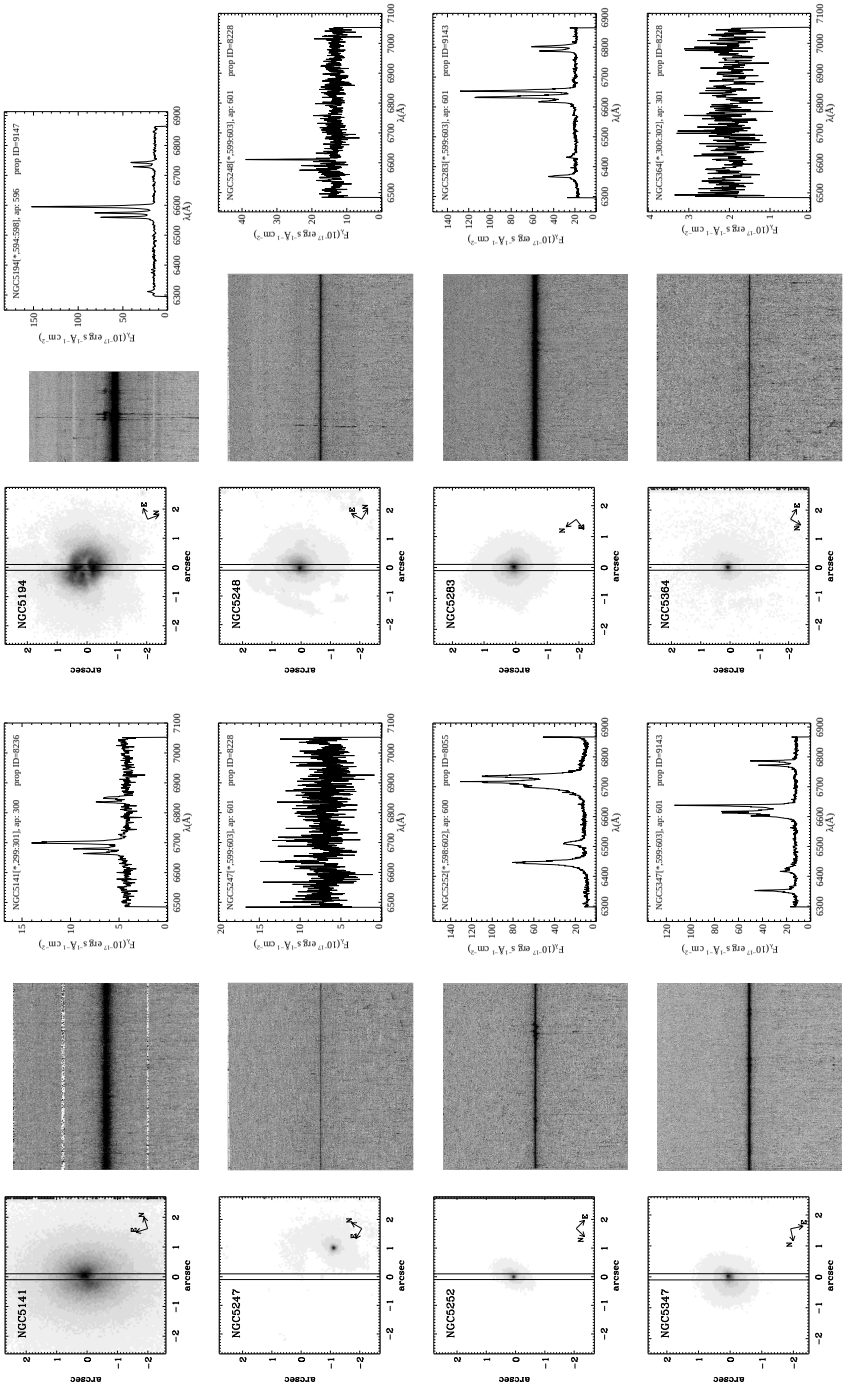

Figure 2.2 – Continued

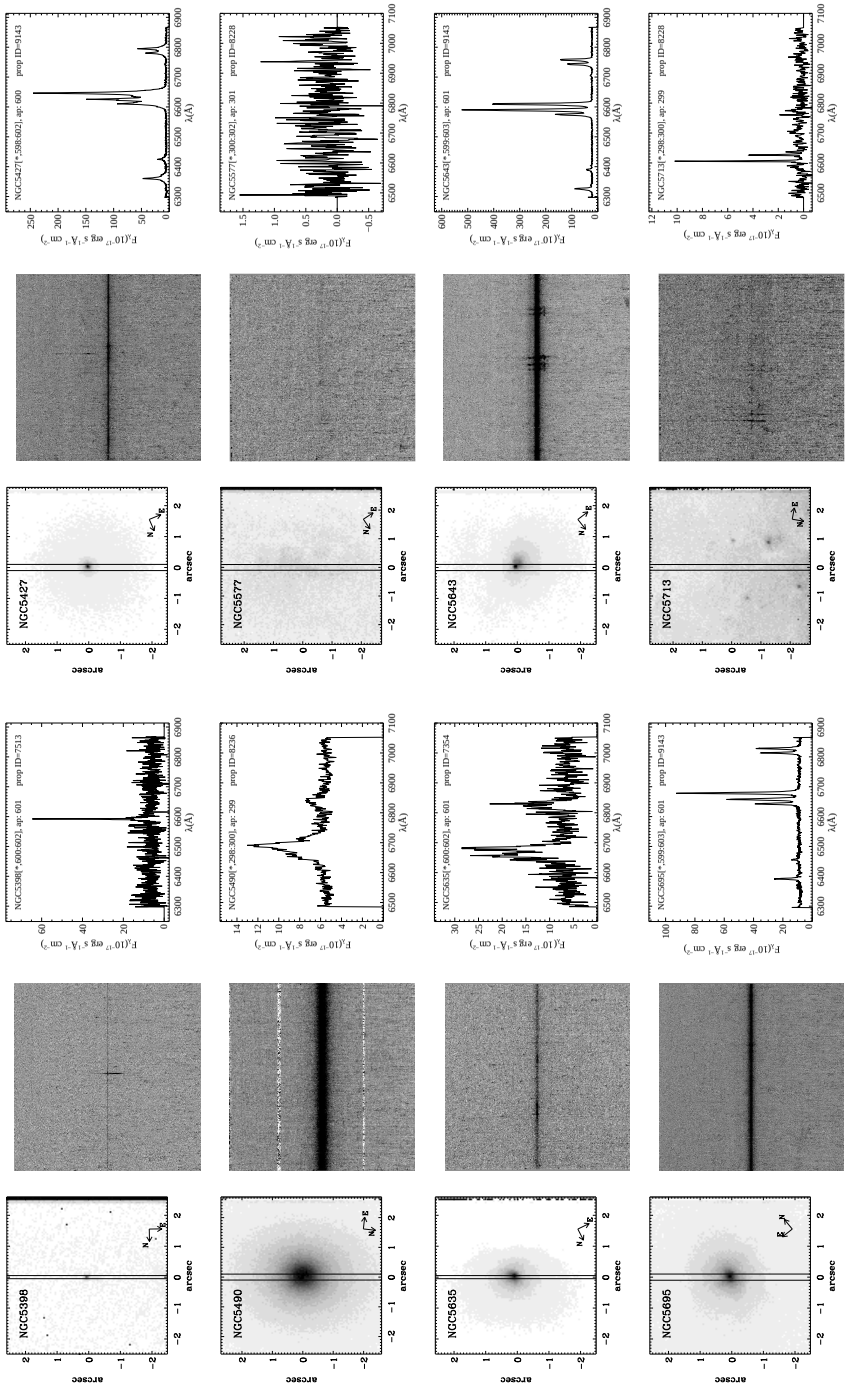

Figure 2.2 – Continued

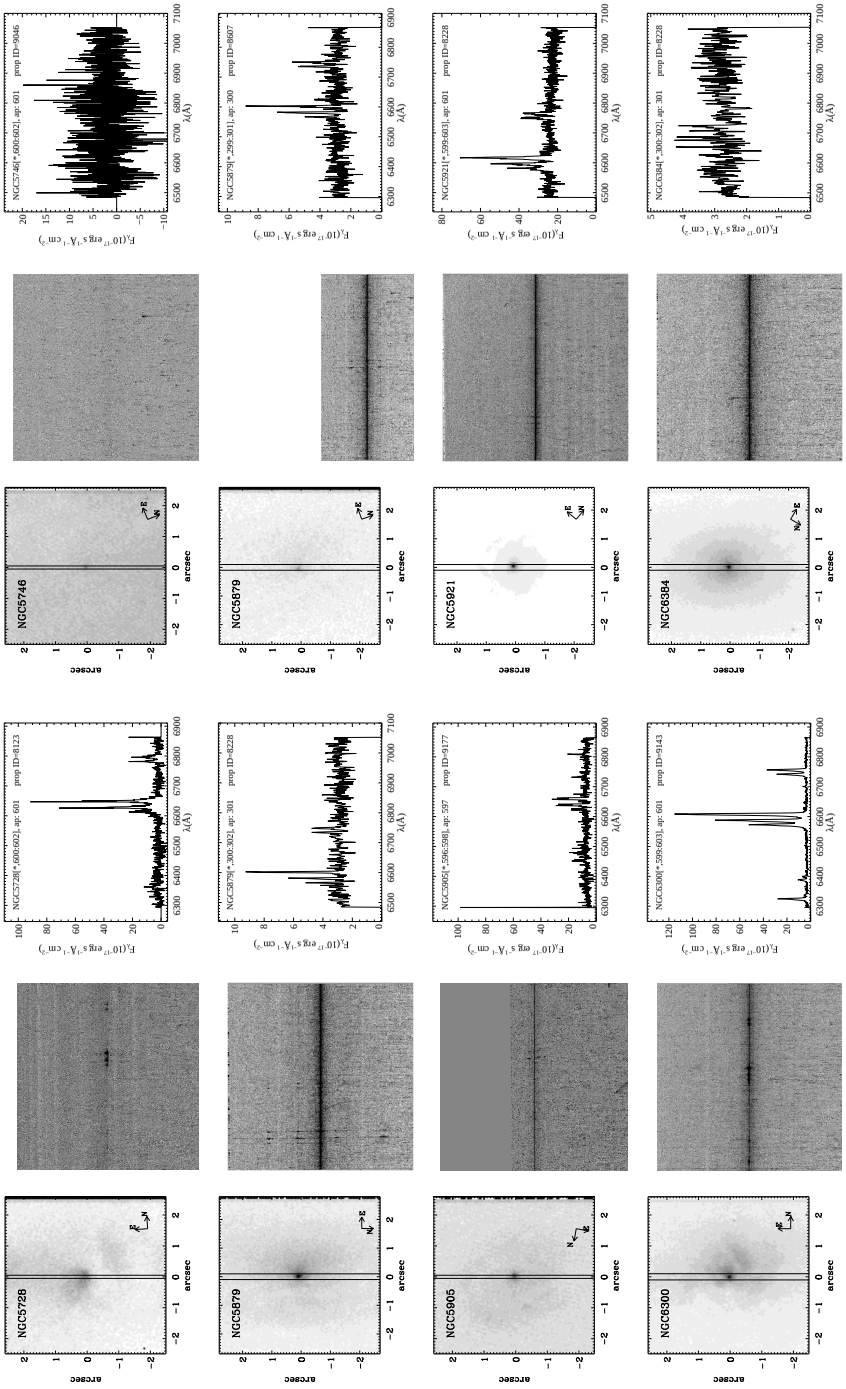

Figure 2.2 – Continued

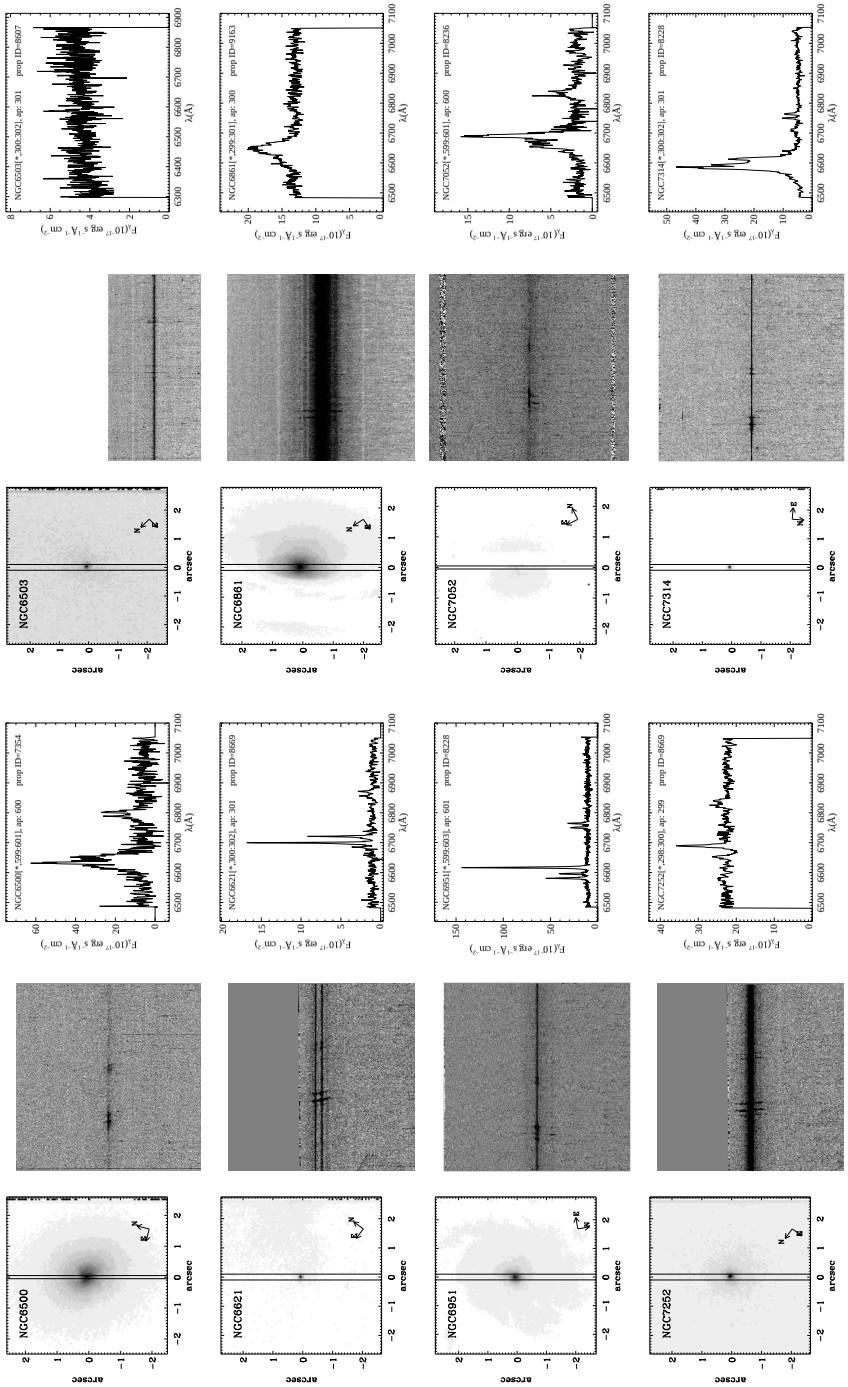

Figure 2.2 – Continued

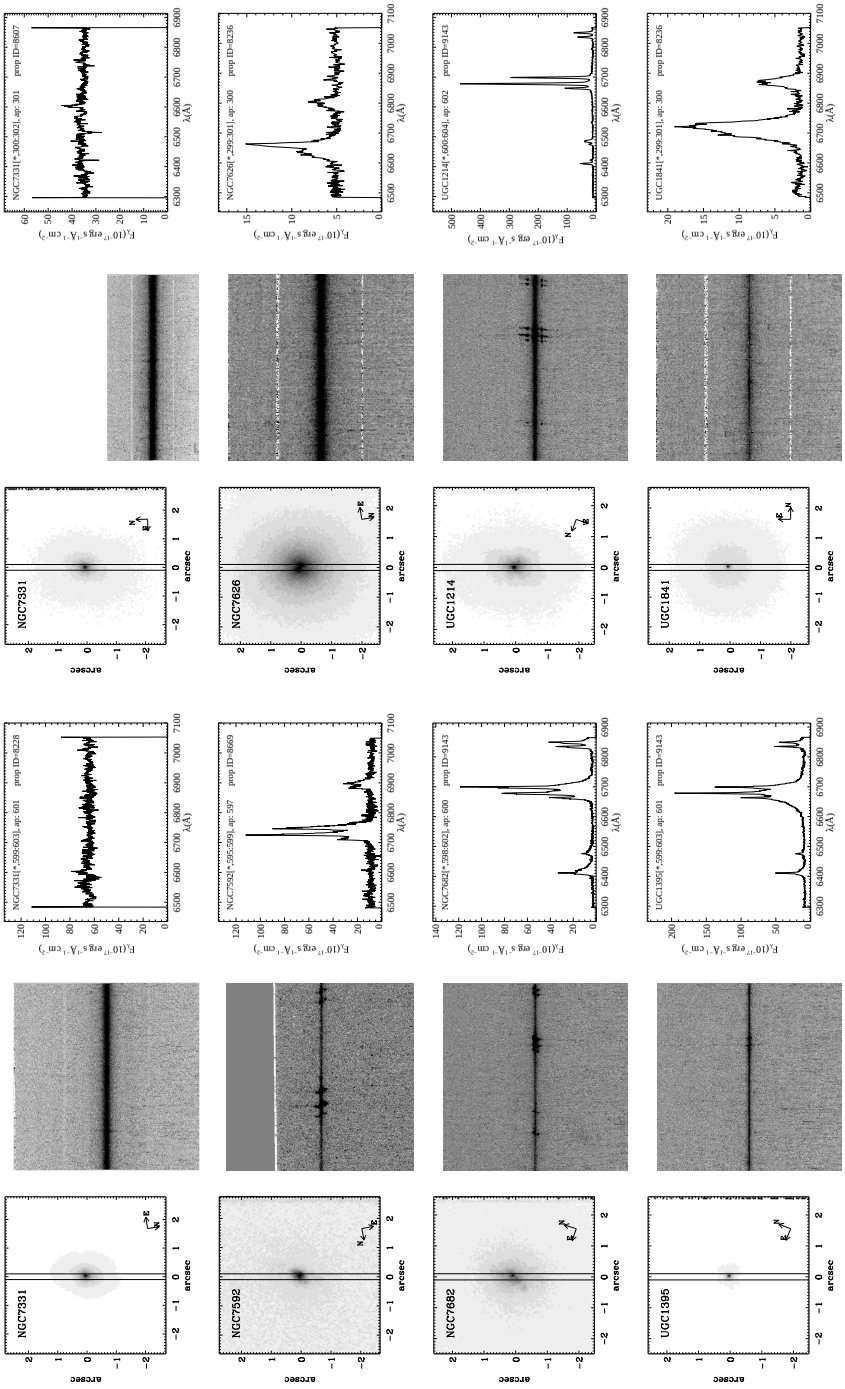

Figure 2.2 – Continued

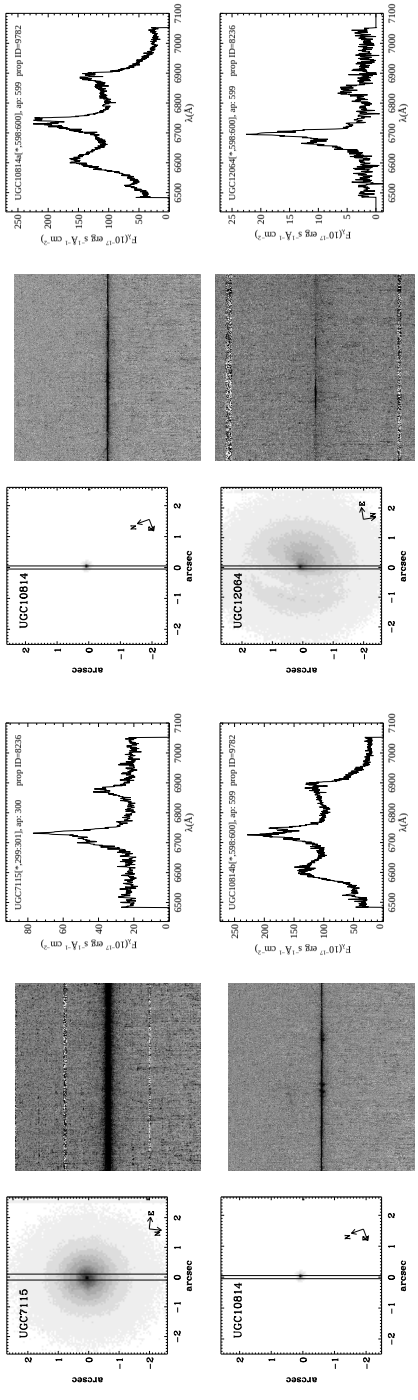

Figure 2.2 – Continued

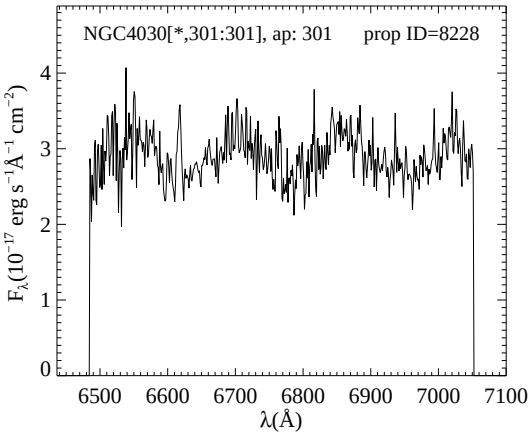

Figure 2.3 An example of the rectification problem as it appears in the central one-dimensional spectrum of NGC 4030.

was specifically focused on the study the structural, star-forming, and kinematic properties of merging galaxies.

2.3.2 Rectification problems

For 13 objects with a strongly peaked surface-brightness profile, the two-dimensional rectification of the spectrum produced anomalous flux variations in the continuum of the very central rows. This is due to the under-sampling of the spectra, when different spectra taken with sub-pixel offsets are combined to produce a single spectrum with higher spatial resolution than that of the original spectra (see Kim Quijano et al. 2007, for details). This spatial sub-sampling becomes apparent after the spectra rectification. The rectification interpolation spreads flux in adjacent rows of the spectrum, if the flux is strongly peaked in the central row. This introduces artificial fluctuations in the flux profiles of the continuum and emission lines (Figure 2.3). Since the correct estimate of the concentration of the nebular emission is key to our modeling, this problem forced us to reject these objects. The galaxies with a spectrum presenting this effect are indicated with "r" in Table 2.3.

2.3.3 Measurement of the emission lines in STIS spectra

The general behavior of the spectra in Figure 2.2 is heterogeneous: some have strong narrow emission lines of [N II] Hα and [S II], other present also broad components in either Hα and forbidden lines. Some AGN show also

[O I] $\lambda\lambda 6300, 6364$, and other do not have obvious [S II] emission. They in general show a low continuum while in other cases it is strong. The 31% of the galaxy sample do not show emission lines.

In order to derive upper limits on $M_\bullet$ following the method of Sarzi et al. (2002) (see Section 3.2.3) we need to measure the width of the central nebular emission lines so that we can gauge the depth of the potential well. The ionized-gas velocity dispersion was measured in the continuum-subtracted spectra by simultaneously fitting Gaussians to the broad and narrow components of the observed lines. To side-step the impact of broad and/or asymmetric emission arising from regions much smaller than our resolution limit, we focus on the width of the narrow component of the emission from forbidden transitions and disregard the broad-line emission in our spectra.

In the wavelength range of our spectra, this means measuring the central width and flux profile of the [N II] $\lambda\lambda 6548, 6583$ lines since these are usually brighter than the [S II] $\lambda\lambda 6716, 6731$ lines. The [N II] doublet also traces the nuclear kinematics better than Hα, given that this line could be significantly affected by emission from circumnuclear star-forming regions (e.g., Verdoes Kleijn et al. 2000; Coccato et al. 2006).

To measure the central width and flux profile of the narrow component of the [N II] lines, we fit our spectra with multiple Gaussians to match both the broad and narrow components of all the observed lines, while describing the stellar continuum with a low-order polynomial. The [N II] were constrained to have equal velocity widths. The widths of the [S II] lines were also required to be the same, when present, which was necessary due to the lower S/N of these lines in some spectra. Although the widths of the two [S II] can differ, the effect is small (Filippenko & Halpern 1984; Filippenko & Sargent 1988). The Hα line was let free to follow a different kinematics. A flux ratio of 1:3 was assumed for the [N II] doublet, as dictated by atomic physics (e.g., Osterbrock 1989).

The instrumental resolution was 17 km s^{-1} and 32 km s^{-1} for the $0\farcs1$ and $0\farcs2$ slit widths, respectively. It was subtracted in quadrature from the observed line-width values to obtain the intrinsic gas velocity dispersion. The intrinsic line widths were resolved for all of the objects, and for the vast majority the line widths correction for the instrumental width were negligible. Only for few galaxies the instrumental width contributed significantly to the observed line width. For NGC 2976 the [N II] $\lambda 6583$ width was too close to the STIS resolution limit, small errors on the estimation of the instrumental broadening would led a large difference in the intrinsic line width, therefore we did not account for such measurement in the following analysis.

In most cases, only one additional Gaussian component was needed in our fits to describe the Hα emission from the broad-line region, although in many

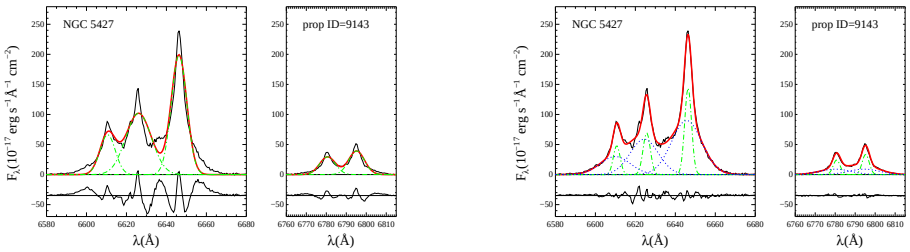

Figure 2.4 Example of fit with and without additional broad components for NGC 5427.

objects also the forbidden [N II] and [S II] lines required double-Gaussian profiles (see Sections 3.2.2, 6.4.1 and 7.3.2). We judged the effectiveness of additional broad components both by eye and by comparing the reduced χ^2 of the fit. The broad components could originate either as an artifact of attempting to fit Gaussians to non-Gaussian line profiles, or from a physical source such as a broad-line region or a change in the characteristics of the gas as the inner regions of the disk are approached. We detect broad components only in the central few pixels; this could be a consequence of either the fall in signal-to-noise or the fact that the component is an unresolved source. In Figure 2.4 we show a comparison between the fit with and without broad components. The contribution of the broad blue wings in NGC 5427 for example, has been properly isolated by means of a fit including double-Gaussian profiles and by following only the narrow-component. Sticking blindly to a single Gaussian to describe the line profiles of this object would have led to much larger estimates for the line width, from the actual 84 ± 2 km s^{-1}, to 177 ± 4 km s^{-1}, and the larger residual are shown.

This procedure allowed us to describe also lines with Voigt profiles we found in part of our galaxy sample. A Voigt profile is produced when the spectral line is broadened by two types of mechanisms: the Doppler or terminal broadening and the Lorentzian collisional broadening. The first one is due to the moving atoms that absorb and emit radiations, while the second one by the interactions between the particles. The Voigt profile is then a convolution of the Lorentzian profile and a Gaussian profile:

$$G(x;\sigma) = \frac{\exp^{-x^2/(2\sigma^2)}}{\sigma\sqrt{2\pi}} \tag{2.5}$$

where x is the frequency for line center

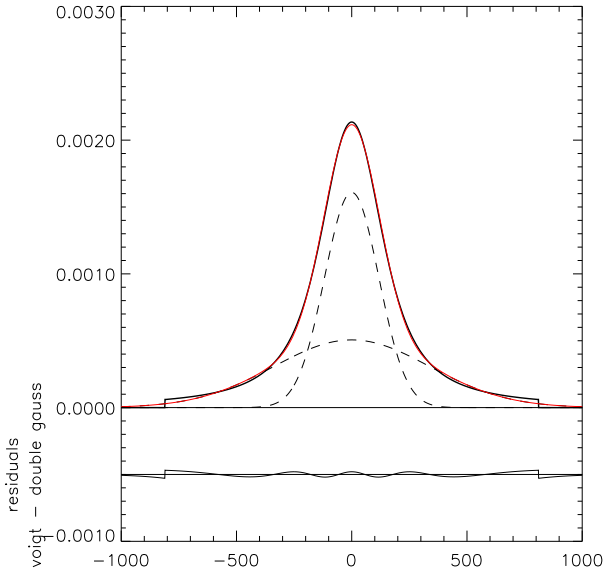

Figure 2.5 Voigt profile fitted with a double Gaussian.

$$L(x;\gamma) = \frac{\gamma}{\pi(x^2+\gamma^2)} \tag{2.6}$$

$$V(x;\sigma,\gamma) = \int_{-\infty}^{+\infty} G(x';\sigma)L(x-x';\gamma)dx' \tag{2.7}$$

Voigt and double-Gaussian profiles provide essentially the same level of agreement for those objects with clearly triangular emission lines, at the present quality of our central spectra and for the observed strength of the emission lines. Yet, the widths of thermal component of the Voigt profile and of the narrowest of the Gaussians components differ systematically, and to estimate by how much we have used 18 objects in our sample with triangular lines to compare the results of fits with Voigts and double-Gaussian profiles. The results of these tests showed that, if the true profile is indeed a Voigt one, the narrow Gaussian component of our double-Gaussian fit would underestimate the width of the thermal component of the Voigt profile by only 20% (see the comparison between the double-Gaussian fit and the Voigt function in Figure 2.5). The

presence of such a Voigt profile indicates that collisions in this gas are the main mechanism of the ionization. It is large and therefore wee see the Lorentzian part of the profile.

The extra Gaussian in the [N II] and [S II] lines was also used to isolate the contribution of blue- or redshifted wings (see in Figure 2.7 some example of such a kind of profiles). Similar results were found by Rice et al. (2006) in their sample of Seyfert 2 galaxies.

For some of our sample galaxies the deblending of the Hα+[N II] was complex, because of narrow lines heavily blended together and peculiar profiles. For galaxies with double-peaked profiles we followed the method by Ho et al. (1997b) to assign to both the [N II] lines and the narrow Hα emission the line profile that was predetermined by fitting the [S II] lines. In fact they are less entangled than the Hα + [N II] complex. We fitted the [S II] doublets with narrow or narrow plus broad components, and we used the minimum χ^2 resulted from one of these fits with one or two Gaussian per line. We extended the Gaussian model of these lines to fit the entire profile of the five emission lines. By then testing various sets of additional Gaussian to reproduce the double-peak we were able to discover the optimal set. For three galaxies (NGC 1097, NGC 3516, UGC 10814) this method did not gave a reliable deblending of the narrow and broad emission lines and we decided to discard these galaxies, otherwise the fitted profile would be unrealistic. these galaxies are identified with "d" in Table 2.3.

The fit of emission lines was done using a non-linear least-squares minimization method. It was based on the robust Levenberg-Marquardt method (e.g. Press et al. 1996) implemented by Moré et al. (1980). The actual computation was done using the MPFIT[2] algorithm implemented by C. B. Markwardt under the IDL[3] environment. MPFIT allows the user to keep constant or impose boundary constraints on any parameter during the fitting process. We estimated the errors in the fit by using the formal error of MPFIT rescaled according to the reduced χ^2.

In general, a low-order polynomial is not a very good continuum model near Hα, but given the low S/N in the continuum with respect to the emission lines, the small wavelength range, and the AGN dominance in the nuclei of some objects a proper starlight subtraction would not change our results and in some cases it would be not possible. However, in objects with conspicuous stellar absorption features that cannot be accounted for by our minimization routine we checked our results against the line-width and flux measurements obtained

[2]The code is available at http://cow.physics.wisc.edu/ craigm/idl/idl.html
[3]Interactive Data Language

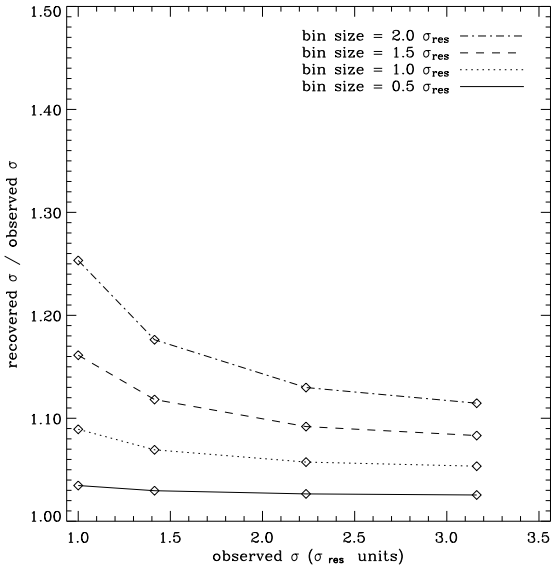

Figure 2.6 Correction to be applied to the instrumental width as a function of the on-chip pixel binning and slit width.

with the GANDALF software[4] by Sarzi et al. (2006), adopting either very young (300 Myr) or old (10 Gyr) stellar population templates. In most cases the measurements agreed within the errors, except for IC 342 and NGC 7331 where the Hα absorption line is particularly prominent. For these galaxies we adopted the GANDALF values.

The emission line width we measured in the case of 2-pixel binning by were then corrected to the ones we would have obtained from no on-chip binning. We tested the deviation between the recovered and observed emission-line width (defined as the square root of the sum in quadrature of the intrinsic width and instrumental width) due to the resolution of the measurement for different slit widths (i.e., different resolutions) and for different bin size in terms of resolution. The bias in the recovered width increases with the bin size and for higher resolution (Figure 2.6). We found that in the case of 2-pixel binning the recovered width should be rescaled of a factor 9% and 16% in the case of $0\farcs2$ and $0\farcs1$ slit width, respectively (see Figure 2.6).

We discarded two galaxies (NGC 1300 and NGC 5905) because their line profile could not be well represented as a simple sum of Gaussian components.

[4]The code is available at http://www.strw.leidenuniv.nl/sauron/software.html.

In this case the gas could be distributed in a ring therefore they are not suitable for our modeling assuming the gas in a thin disk configuration. Wang et al. (2009) by studying a sample of type 2 AGNs from the Sloan Digital Sky Survey seventh data release (SDSS, York et al. 2000; Abazajian et al. 2009, DR7) suggested an alternative explanation for such a kind of double-peaked emission lines, as an evidence of dual AGNs, one redshifted and the other blue-shifted relative to their host galaxy. Wang et al. (2009) found that the ratios of the shifts correlate with the double-peak fluxes. In this case the double-peaked narrow lines are caused by the two orbiting narrow-line regions of the dual AGNs during an ongoing merger of their host galaxies (Bogdanović et al. 2008). This suggests that the models of co-rotating AGNs can be a better explanation instead of the generally employed disk or bi-polar outflows (e.g., Eracleous & Halpern 2003; Heckman et al. 1981, 1984; Whittle 1985a,b).

In the case we had different spectra from different proposals for the same galaxy, we selected the emission-line width from fit to the highest S/N spectrum. It gave us the lower rms of the residuals. These spectra listed in Table 2.3 with a "*".

Finally, in defining our detection thresholds we compared the amplitude (A) of the best-fitting line profile to the noise level (N) in the residuals of the continuum fit. We defined as detected only those emission lines for which the $A/N > 3$. In 28 galaxies the nebular emission was too faint to be detected given the quality of the spectra. They were consequently dropped from our sample. In Table 2.3 we have indicated them with a "n".

Figure 2.7 shows the galaxy spectra illustrating the various fitting strategies explained above. Other examples of fit obtained with the same routine can be found in Figures 3.1, 6.17, 6.18, 6.19, and 7.3. The central velocity dispersion of the ionized-gas component and the size of the aperture we used for the 122 galaxies with good measurements of the emission-line widths are given in Table 2.3. It also lists the 55 rejected galaxies with the specific comment on it. Among the measurable spectra that will be used to calculate the $M_\bullet$ in Section 3.2.3, we found 111 galaxies with published σ (Table 2.2). The comparison between the $M_\bullet$ and the galaxy properties will be shown in Section 3.3 and 4.3.

Part of the sample galaxies were already presented and discussed in previous studies (Bower et al. 1998; Verdoes Kleijn et al. 2000; Barth et al. 2001; Sarzi et al. 2001, 2002; Verdoes Kleijn et al. 2002; Marconi et al. 2003; Noel-Storr et al. 2003; Atkinson et al. 2005; Coccato et al. 2006; Rice et al. 2006; Noel-Storr et al. 2007; de Francesco et al. 2006, 2008; Verdoes Kleijn et al. 2006; Pastorini et al. 2007(@; Shields et al. 2007; Walsh et al. 2008). Our measurements are consistent within the errors with those of these authors. For some galaxies the spectra allowed to obtain an accurate $M_\bullet$ determination or at least a tight

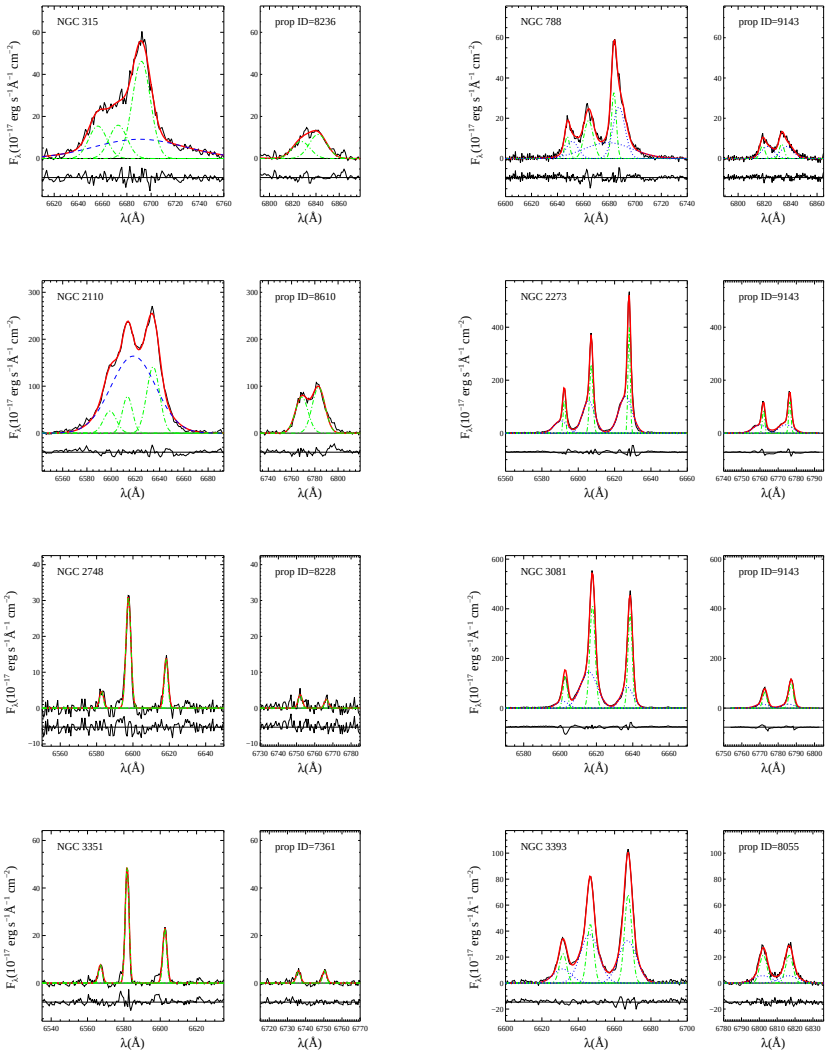

Figure 2.7 Continuum-subtracted central G750M spectra from our spectral atlas illustrating the various fitting strategies adopted to match the Hα, [N II] $\lambda\lambda$6548, 6583, and [S II] $\lambda\lambda$6716, 6731 emission lines. In each panel, the red solid line shows the overall line blend, whereas the green dashed-dotted lines and blue dotted or dashed lines show the adopted narrow and broad Gaussian components, respectively. Shown are also the fit residuals, which are offset for better visibility.

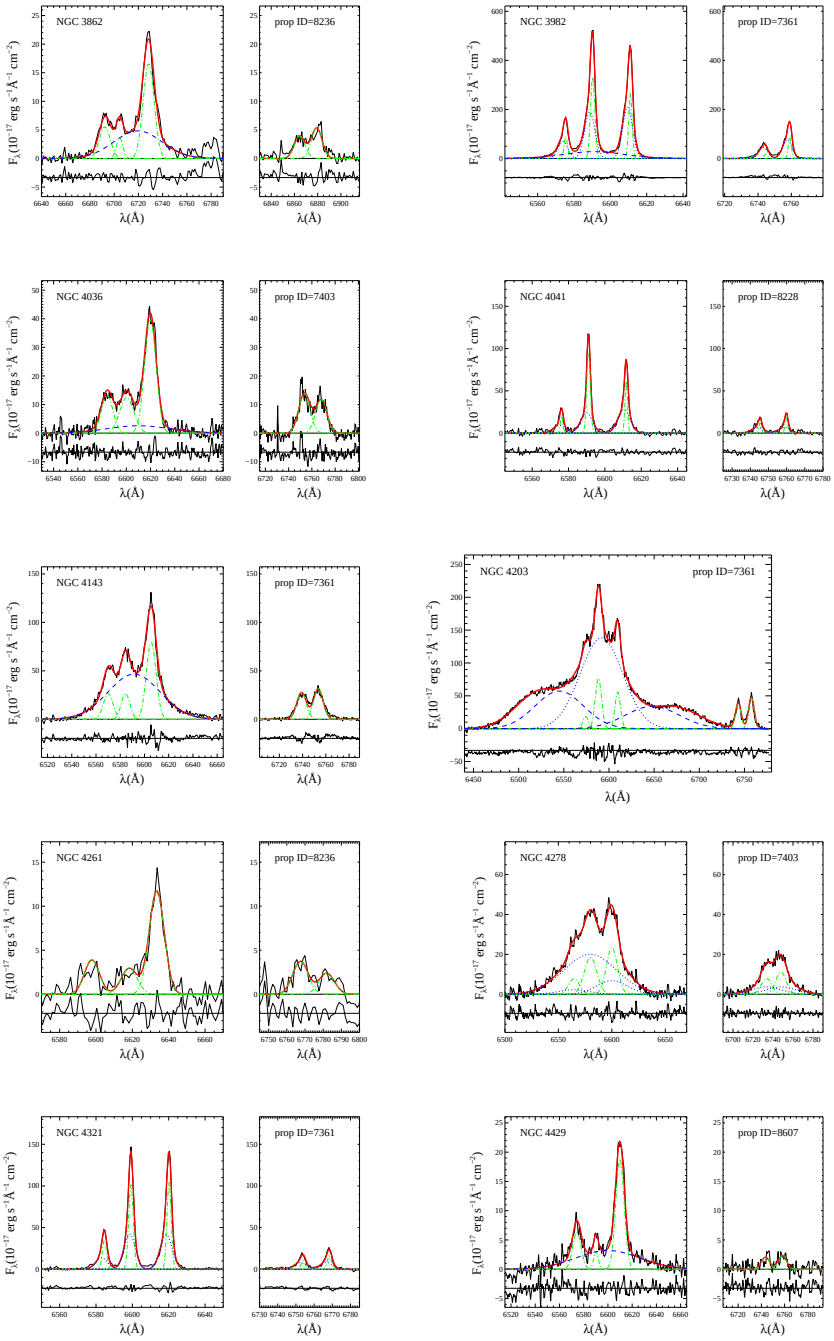

Figure 2.7 – Continued

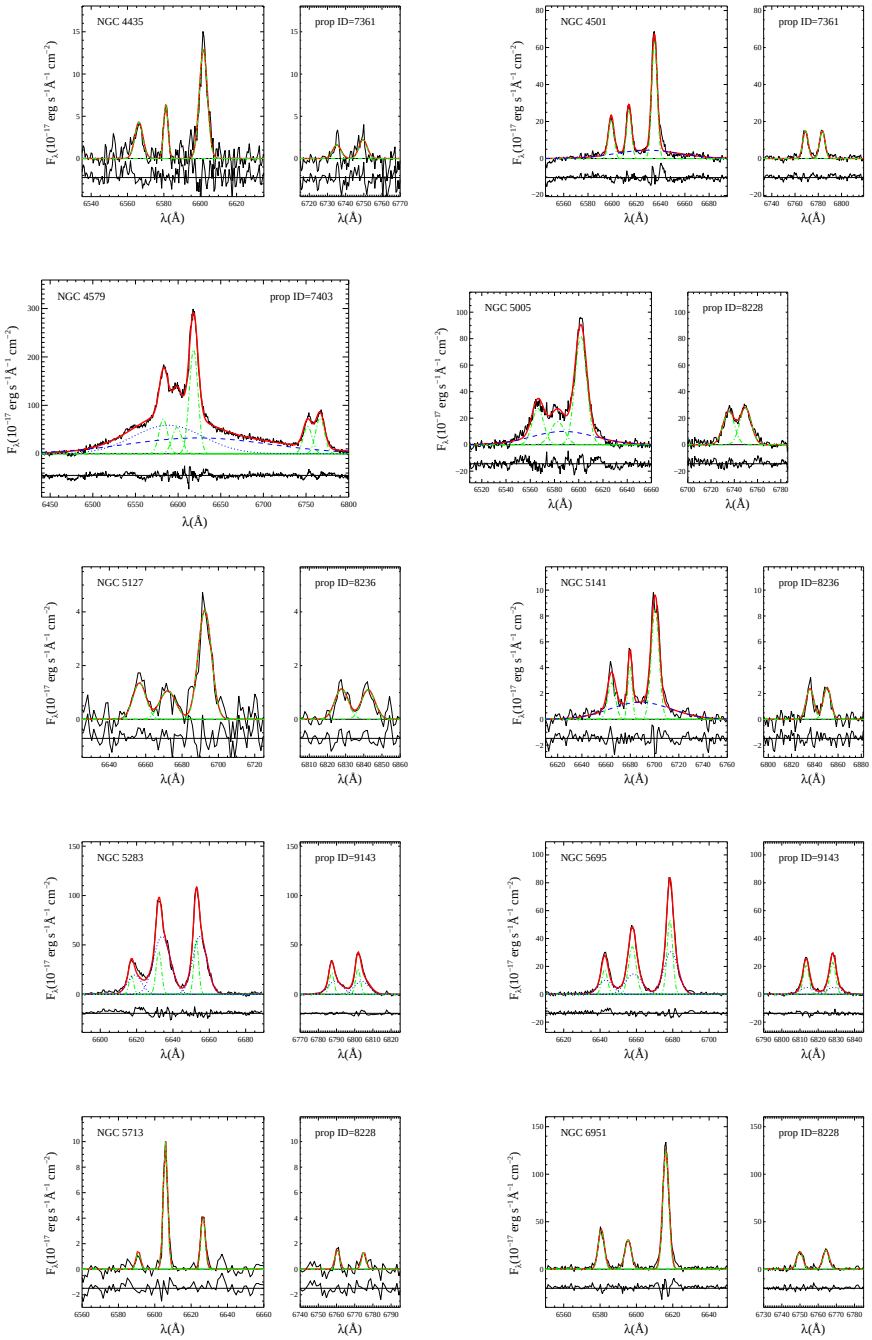

Figure 2.7 – Continued

estimate of its upper limit (i.e., Coccato et al. 2006) displaying symmetric gas velocity curves that could be consistently modelled as a rotating disk in the join potential of a stellar bulge and putative central SMBH. In other cases, the spectra were used to study the behavior of the gas in the central region of the galaxies. A wide variety of kinematics was found: in a few galaxies the gas is in a disk-like rotation, in the others the gas is moving in a chaotic way or dominated by outflows. By looking to our study and comparing it with the previous studies the typical percentage of regular kinematics in our sample is about ∼30%, close to the value found by the Sarzi et al. (2001); Ho et al. (2002).

2.4 2MASS and UKIDSS K-band imaging

Among the connection between SMBHs and the properties of their host galaxies, the relation between the $M_\bullet$ and the total K-band bulge luminosity ($L_{K,\mathrm{bulge}}$) is one of the tightest (Marconi & Hunt 2003; Graham 2007). The $L_{K,\mathrm{bulge}}$ was found to correlate with the $M_\bullet$ by (Marconi & Hunt 2003) although on the basis of a limited sample of galaxies. $L_{K,\mathrm{bulge}}$ traces well the stellar mass of evolved stars and avoid the contamination due to dust and bright young stars and can be disentangled from the disk luminosity. In order to compare our $M_\bullet$ mass estimates with the relation of (Marconi & Hunt 2003) we need to derive $L_{K,\mathrm{bulge}}$.

2.4.1 K-band bulge luminosity from 2MASS images

We searched the K-band images in the Extended Source Catalogue (XCS, Jarrett et al. 2000) of the Two Micron All Sky Survey (2MASS, Skrutskie et al. 2006). We retrieved the 2MASS K-band images from the NASA/IPAC Infrared Science Archive (2MASS/XCS). We came out with a sample of 121 out of 122 galaxies with measurable STIS spectra. The galaxy images were reduced and flux calibrated with the standard 2MASS extended source processor (GALWORKS Jarrett et al. 2000). We found either a single or a mosaic image for each galaxy with a spatial scale of $1''$ pixel^{-1} and total exposure time of 1 s. The average seeing was FWHM $\sim 3\farcs11$ as measured by fitting a two dimensional Gaussian to a field star close to the galaxy.

We performed the two-dimensional bulge-to-disk decomposition by using the GAlaxy Surface Photometry 2Dimensional Decomposition (GASP2D, Méndez-Abreu et al. 2008a), which allows to obtain the photometric parameters of the bulge and disk without the systematic errors associated to one-dimensional decompositions (see Byun & Freeman 1995, for a discussion).

Similar analysis will be presented in Section 4.2.2 in which we will extract structural properties of the galaxies from the i-band images from the SDSS,

DR7.

For the spiral and lenticular galaxies of our sample we assumed that the surface-brightness distribution was the sum of the contributions of a bulge and a disk component. We adopted only the bulge component for the ellipticals. To test the morphological classification of our galaxies we then repeated the same procedure by fitting only a bulge component to the spirals and lenticulars and a bulge with a disk to the ellipticals.

Bulge and disk components are characterized by elliptical and concentric isophotes with constant, but possibly different, ellipticity and position angles. Let (x, y, z) be Cartesian coordinates with the origin corresponding to the position of the galaxy surface-brightness peak, the $x-$axis parallel to direction of right ascension and pointing westward, the $y-$axis parallel to direction of declination and pointing northward, and the $z-$axis along the line-of-sight and pointing toward the observer. The plane of the sky is confined to the (x, y) plane. Bulge isophotes are ellipses centered on (x_0, y_0), with constant position angle $\mathrm{PA_b}$ and constant axial ratio q_b. Disk isophotes are ellipses centered on (x_0, y_0), with constant position angle $\mathrm{PA_d}$ and constant axial ratio q_d, implying that the galaxy inclination is $i = \arccos q_\mathrm{d}$.

We adopted the Sérsic law (Sersic 1968) to describe the surface brightness of the bulge component, and ellipticals

$$I_\mathrm{b}(x, y) = I_\mathrm{e} 10^{-b_n\left[(r_\mathrm{b}/r_\mathrm{e})^{1/n}-1\right]}, \tag{2.8}$$

where r_e, I_e and n are respectively the effective radius, surface brightness at r_e, and the shape parameter describing the curvature of the profile. The value of b_n is coupled to n so that half of the total flux is always within r_e and can be approximated as $b_n = 0.868n - 0.142$ (Caon et al. 1993).

For the surface brightness distribution of the disk component we assumed the exponential law (Freeman 1970)

$$I_\mathrm{d}(x, y) = I_0\, e^{-r_\mathrm{d}/h}, \tag{2.9}$$

where h and I_0 are the scale length and central surface brightness of the disk, respectively.

To derive the photometric parameters of the bulge (I_e, r_e, n, $\mathrm{PA_b}$, q_b) and disk (I_0, h, $\mathrm{PA_d}$, q_d) and the position of the galaxy center (x_0, y_0) we fitted iteratively a model of the surface brightness $I_\mathrm{m}(x, y) = I_\mathrm{b}(x, y) + I_\mathrm{d}(x, y)$ to the pixels of the galaxy image using a non-linear least-squares minimization based on the robust Levenberg-Marquardt method by Moré et al. (1980). The actual computation has been done using the MPFIT algorithm under the IDL environment. Each image pixel has been weighted according to the variance of

its total observed photon counts due to the contribution of both the galaxy and sky, and determined assuming photon noise limitation and taking into account for the detector read-out noise. The seeing effects were taken into account by convolving the model image with a circular Gaussian PSF with the FWHM measured from the stars in the galaxy image. The convolution was performed as a product in Fourier domain before the least-squares minimization.

We first assess all the galaxy parameters from the analysis of our image and with the calibration constant present as a keyword in the header of the image.

The guesses for the free parameters were derived by parametric fit of the ellipticaly-averaged SB radial profile, ellipticity and position angle of the galaxy ($I_{\rm e}$, $r_{\rm e}$, n, I_0, h), and by the analysis of the ellipticity, by using the ELLIPSE task in IRAF that fits elliptical isophote on the image of the galaxy. The image was measured with an iterative method (Jedrzejewski 1987) along a fixed semi-major axis, that produces a one dimensional intensity distribution as a function of the ellipticity and PA, with the errors that are obtained from the rms scatter of intensity data along the fitted ellipse. The final data table comprises the semi-major axis length in pixels the mean isophotal intensity, the errors in the isophotal intensity given as rms scatter around isophotal intensity, ellipticity, and PA divided by the squared root of number of fitted point.

The fit is done in intensity units, and all the pixels, can be masked automatically to reject the foreground stars, dust lanes, spiral arms, and all the features that can spoil the fit.

To derive the free parameters of the model surface-brightness distribution, we adopted as initial trial for least-squares minimization the values obtained by performing a standard photometric decomposition with a parametric technique similar to that adopted by Kormendy (1977).

The ellipse-averaged surface-brightness profile of the galaxy has been fitted in two steps by considering first separately and then simultaneously the light contributions of the bulge and disk.

We began by fitting an exponential law to the galaxy surface-brightness profile at large radii, where it is dominated by the light contribution of the disk. In this way we derived the values of I_0 and h. Then we extrapolated the exponential profile to small radii and subtracted it from the galaxy surface-brightness profile. This gave us a first estimate of the light distribution of the bulge. We fitted to this a Sersíc profile by assuming the bulge shape parameter in the range of $n = 0.5 - 8$ and deriving the corresponding values of $I_{\rm e}$ and $r_{\rm e}$. Finally, for each set of $I_{\rm e}$, $r_{\rm e}$, n, I_0, and h we fitted simultaneously both bulge and disk to the galaxy surface-brightness profile and we assumed those giving the best fit as the trial values for the two-dimensional fit, where all the parameters are allowed to vary.

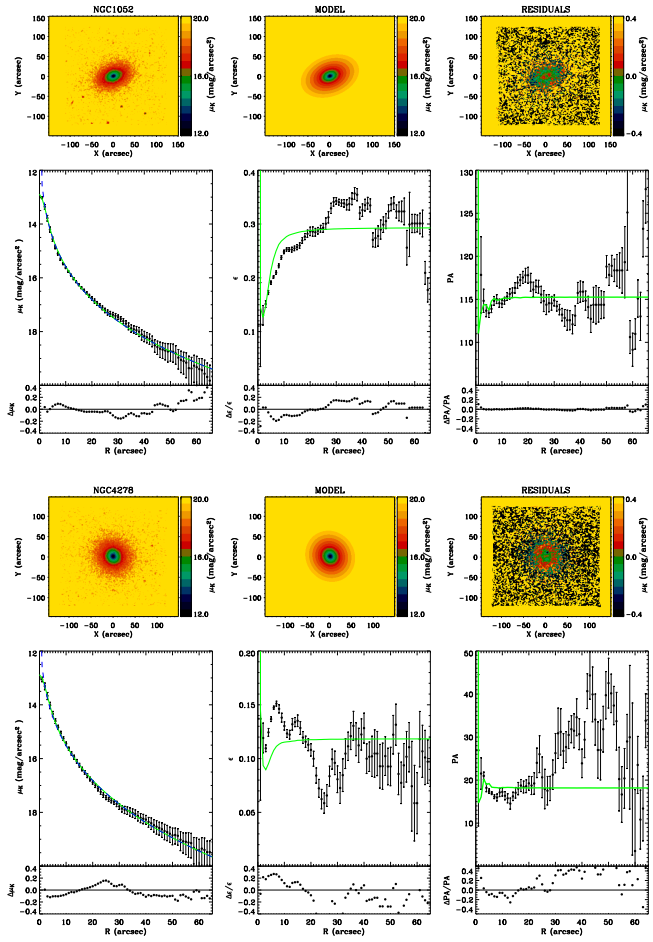

Figure 2.8 Example of two-dimensional photometric decomposition of some elliptical galaxies of the sample. *Upper panels* (from *left* to *right*): Map of the observed, modeled, and residual (observed-modeled) surface-brightness distribution of the galaxy. The surface-brightness range of each image is indicated at the right of the panel. In each panel the spatial coordinates with respect to the galaxy center are given in arcsec. *Lower panels* (from *left* to *right*): Ellipse-averaged radial profile of surface-brightness, position angle, and ellipticity measured in the observed (dots with error-bars) and modeled image (solid line). The blue dashed line represents the intrinsic surface-brightness profile. The difference between the ellipse-averaged radial profiles extracted from the observed and modeled images is also shown.

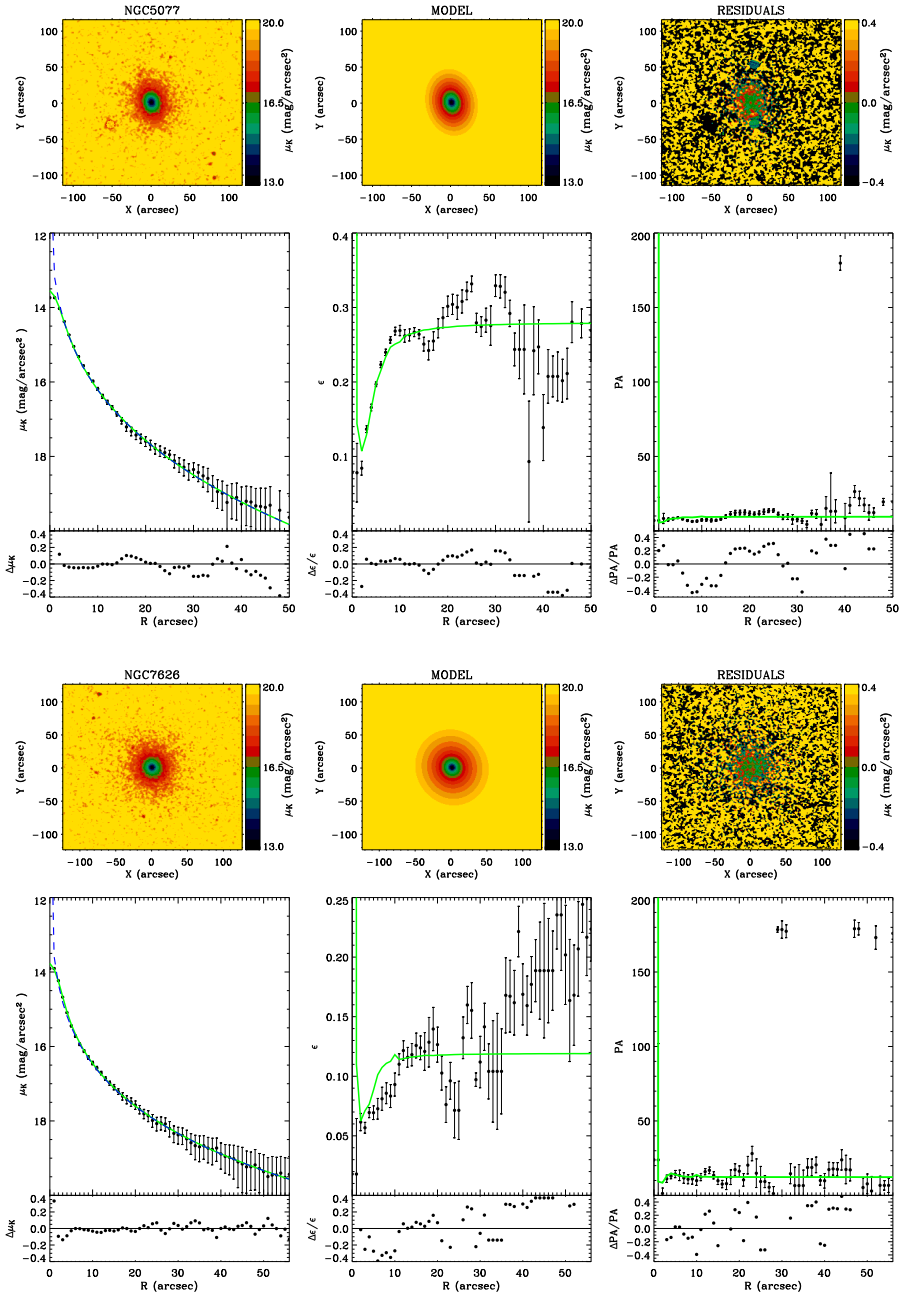

Figure 2.8 – Continued

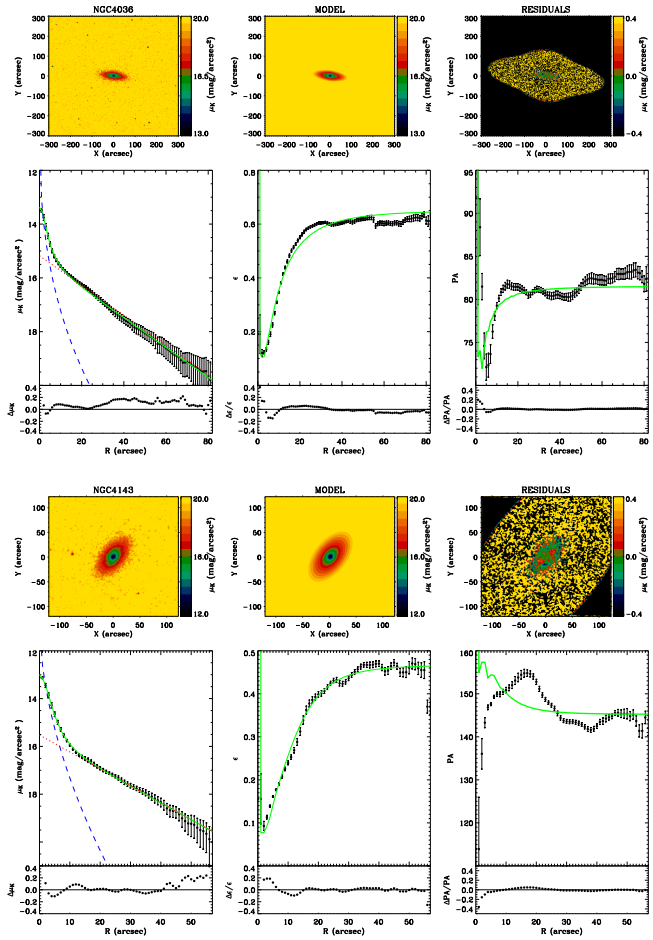

Figure 2.9 Example of two-dimensional photometric decomposition of some lenticulars and spiral galaxies of the sample. *Upper panels* (from *left* to *right*): Map of the observed, modeled, and residual (observed-modeled) surface-brightness distribution of the galaxy. The surface-brightness range of each image is indicated at the right of the panel. In each panel the spatial coordinates with respect to the galaxy center are given in arcsec. *Lower panels* (from *left* to *right*): Ellipse-averaged radial profile of surface-brightness, position angle, and ellipticity measured in the observed (dots with error-bars) and modeled image (red solid line). The blue dashed and the red dotted lines represent the intrinsic surface-brightness contribution of the bulge and disk, respectively. The difference between the ellipse-averaged radial profiles extracted from the observed and modeled images is also shown.

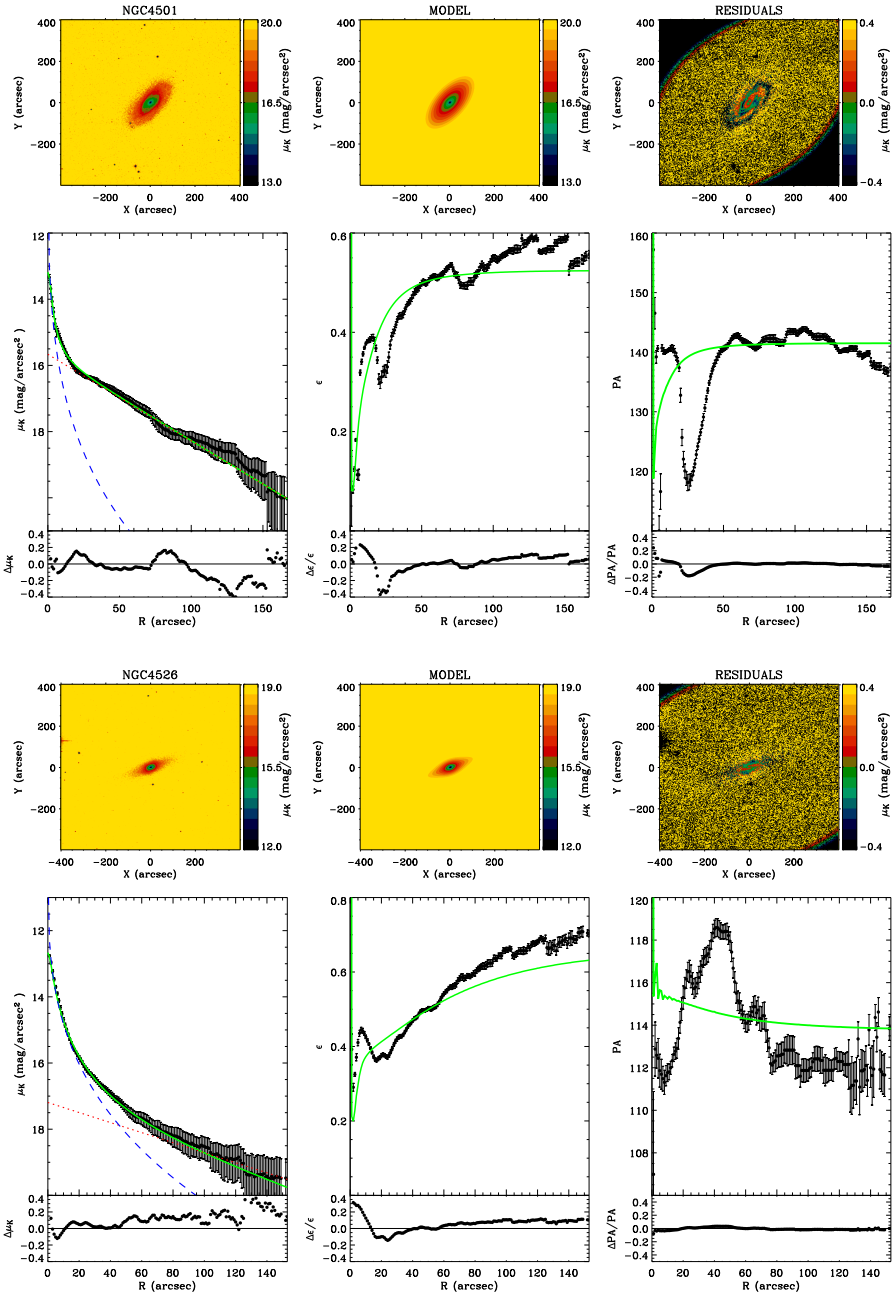

Figure 2.9 – Continued

The trial values of $\mathrm{PA_b}$ and q_b were obtained by interpolating at r_e the ellipse-averaged position-angle and ellipticity profiles, respectively. We assumed the coordinates of the image pixel where the maximum galaxy surface brightness is measured as the trial values of the coordinates (x_0, y_0) of the galaxy center.

The parameters derived for the structural components of the sample galaxies are collected in Table 2.4. The results of the photometric decomposition of the sample galaxies are shown in Figure 2.8 for the elliptical galaxies and in Figure 2.9 for lenticulars and spirals.

The errors given in Table 2.4 were obtained through a series of Monte Carlo simulations. The formal errors obtained from the χ^2 minimization method are usually not representative of the real errors in the structural parameters because they are coupled together. We have carried out extensive simulations on artificial galaxies in order to give a reliable estimation of these errors. We generated a set of 2000 images of galaxies with a Sérsic bulge for the elliptical galaxies and a set of 2000 images of galaxies with a Sérsic bulge and an exponential disk to associate the errors to the decompositions of lenticulars and spirals. The structural parameters of the artificial elliptical galaxies were randomly chosen among the following typical parameters in K-band (Möllenhoff & Heidt 2001)

$$0.5 \leq r_\mathrm{e} \leq 8 \text{ kpc} \qquad 0.3 \leq q_\mathrm{b} \leq 0.9 \qquad 0.5 \leq n \leq 7 \tag{2.10}$$

and

$$7 \leq K_\mathrm{T} \leq 12 \text{ mag} \tag{2.11}$$

while for lenticulars and spirals

$$0.5 \leq r_\mathrm{e} \leq 8 \text{ kpc} \qquad 0.4 \leq q_\mathrm{b} \leq 0.9 \qquad 0.5 \leq n \leq 7 \tag{2.12}$$

for the bulge parameters, and

$$1 \leq h \leq 21 \text{ kpc} \qquad 0.4 \leq q_\mathrm{d} \leq 0.9 \tag{2.13}$$

for the disk parameters, and

$$q_\mathrm{d} \leq q_\mathrm{b} \qquad 6 \leq K_\mathrm{T} \leq 12 \text{ mag} \tag{2.14}$$

where K_T is the galaxy total observed K-band magnitude from the 2MASS all-sky extended source catalogue.

The simulated galaxies were assumed to be at the median distance of our sample (20.2 Mpc). The pixel scale used was $1''$ pixel^{-1} and the CCD gain and RON were 7 e$^-$ ADU^{-1} and 40 e$^-$ to mimic the instrumental setup of the

2MASS data. Finally, a background level and a photon noise were added to the resulting images to yield a signal-to-noise ratio similar to that of the 2MASS images.

To estimate the errors associated to the decomposition, the code GASP2D was applied to the artificial images as if they were real. Then, the relative errors (1- v_i/v_o) were estimated by comparing the input (v_i) and output (v_o) values. To assign to every single galaxy the corresponding error for every structural parameter, we divided our catalogue of artificial galaxies in bins of 0.5 magnitudes, we assumed that the errors were normally distributed, with mean and standard deviation corresponding to the systematic and typical error, respectively. Then we placed our observed galaxy in its magnitude bin and assigned to every parameter the corresponding error.

We could perform a "correct" decomposition for 17 elliptical galaxies fitted with a Sérsic profile, and 47 lenticulars and spirals fitted with a Sérsic bulge plus an exponential disk. The decomposition, in general, gave us appropriate structural parameters for all the galaxies with a total observed K-band magnitude from the 2MASS all-sky extended source catalogue < 9 mag. All the galaxies we discarded and the reason for that are summarized in Table 2.6.

The 2MASS decomposition were useful also to derive the effective radii we needed to apply the Jørgensen et al. (1995) correction to the published σ (see Sections 2.2 and 3.3).

Archival K-band images such as those from the 2MASS survey do not always fulfill the requirements to perform an appropriate two-dimensional decomposition for such a large sample of galaxies with different total K-band magnitude we had (see Table 2.6). Measuring $L_{K,\mathrm{bulge}}$ from such shallow images is further complicated by the presence in the disk galaxies of additional structures such as bars and active nuclei. Deeper images are indeed necessary to constrain the disk properties and properly isolate the contribution of the bulge light to the total luminosity of the galaxy, in particular in galaxies with $K_\mathrm{T} > 9$ mag.

2.4.2 K-band bulge luminosity from UKIDSS images

We searched for deeper images in the United Kingdom Infrared Telescope (UKIRT) InfraRed Deep Sky Surveys (UKIDSS) archive. UKIDSS is a large survey of the Northern sky, extending over both high and low Galactic latitudes, in J, H, K-band, three magnitudes deeper than 2MASS (Lawrence et al. 2007). Therefore it is suitable for our aims. The survey instrument is the Wide Field Camera (WFCAM, Casali et al. 2007) mounted on the 3.8m UK Infrared Telescope in Hawaii. WFCAM has four 2048 $\times$ 2048 Rockwell devices, with a scale of $0\farcs4$ pixel^{-1}. The K-band images of the first data release (DR1, Warren et al.

2007) of the Large Area Survey (LAS) were available for 20 out of 122 galaxies. WFCAM data are processed by an automated pipeline that flat-fields data, subtracts counts from the background sky, detects and parameterizes objects, and performs photometric and astrometric calibrations. The reduced frames and catalogues are ingested into the WFCAM Science Archive, described by Hambly et al. (2008). All the data were taken between May 2006 and April 2007. The total integration time was of 80 s splitted in one or more exposures that are averaged by the data acquisition system, resulting in a single final image. Only the exposure time of a single complete cycle of the detector readout mode is needed to calibrate any frame; for our images it corresponds to 10 s. The UKIDSS photometric system and conversion to the 2MASS magnitudes are discussed by Hewett et al. (2006). The zero-point for the calibration that relates counts per seconds to magnitudes is given in the header of the image.

The two-dimensional bulge to disk decomposition was performed with the same method described on Section 2.4.1. In Table 2.5 we show the parameters derived for this subsample and in Figures 2.10 and 2.11 we show some examples of the results. The errors were estimated through a series of Monte Carlo simulations as described above, but using the typical UKIDSS pixel scale. The CCD gain and RON were assumed 4.5 e^- ADU^{-1} and 25 e^-, respectively, to mimic the instrumental setup of the UKIDSS data and the typical FWHM of the PSF was $0\farcs7$. Finally, a background level and a photon noise were added to the resulting images to yield a signal-to-noise ratio similar to that of the UKIDSS images.

The UKIDSS images were deep enough to perform an accurate two-dimensional decomposition for the images in which we could not find trustable structural parameters from 2MASS images. For NGC 2911, for instance, we could not fit the exponential disk form the 2MASS images, while a Sérsic profile plus exponential is well reproduced by the UKIDSS images. For the 2MASS galaxies well decomposed the UKIDSS structural parameters were consistent. From this comparison we saw also that the higher resolution and the the best FWHM of the PSF were fundamental to obtain accurate structural parameters for the part of our sample galaxies in which the structural parameters were not constrained with 2MASS. Such a kind of images for the remaining part of the sample still without an estimation of the $L_{K,\mathrm{bulge}}$, will be useful.

2.5 Summary

In this chapter we present the atlas of all nearby galaxies ($D < 100$ Mpc), with long-slit spectra available in the *HST*/STIS archive and taken with the G750M grating in the Hα spectral region. This atlas comprises of 177 galaxies which

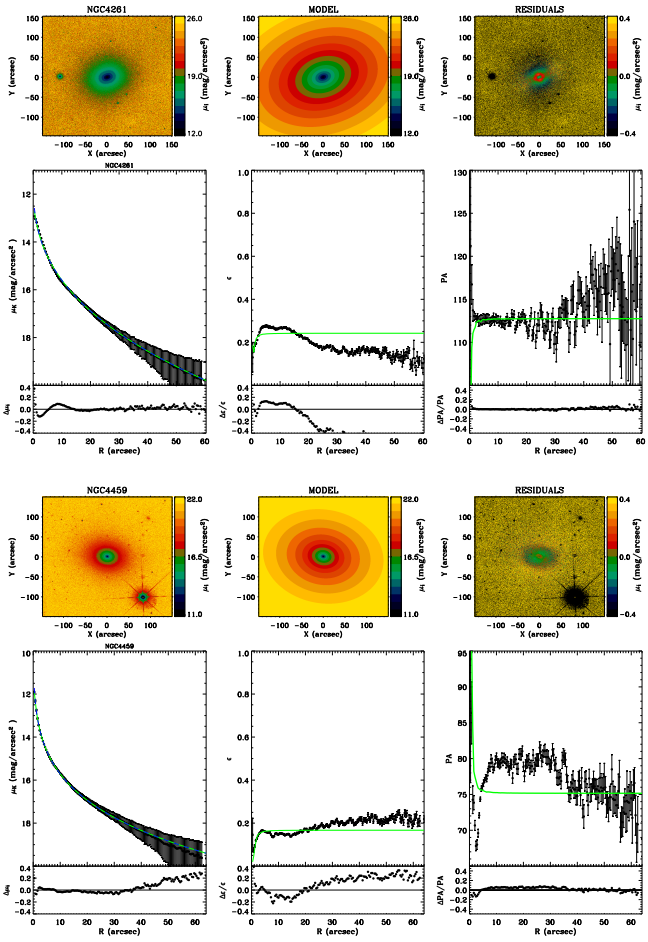

Figure 2.10 Two-dimensional photometric decomposition of two of the sample the elliptical galaxies with images in the UKIDSS archive. *Upper panels* (from *left* to *right*): Map of the observed, modeled, and residual (observed-modeled) surface-brightness distribution of the galaxy. The surface-brightness range of each image is indicated at the right of the panel. In each panel the spatial coordinates with respect to the galaxy center are given in arcsec. *Lower panels* (from *left* to *right*): Ellipse-averaged radial profile of surface-brightness, position angle, and ellipticity measured in the observed (dots with error-bars) and modeled image (solid line). The blue dashed line represents the intrinsic surface-brightness profile. The difference between the ellipse-averaged radial profiles extracted from the observed and modeled images is also shown in green.

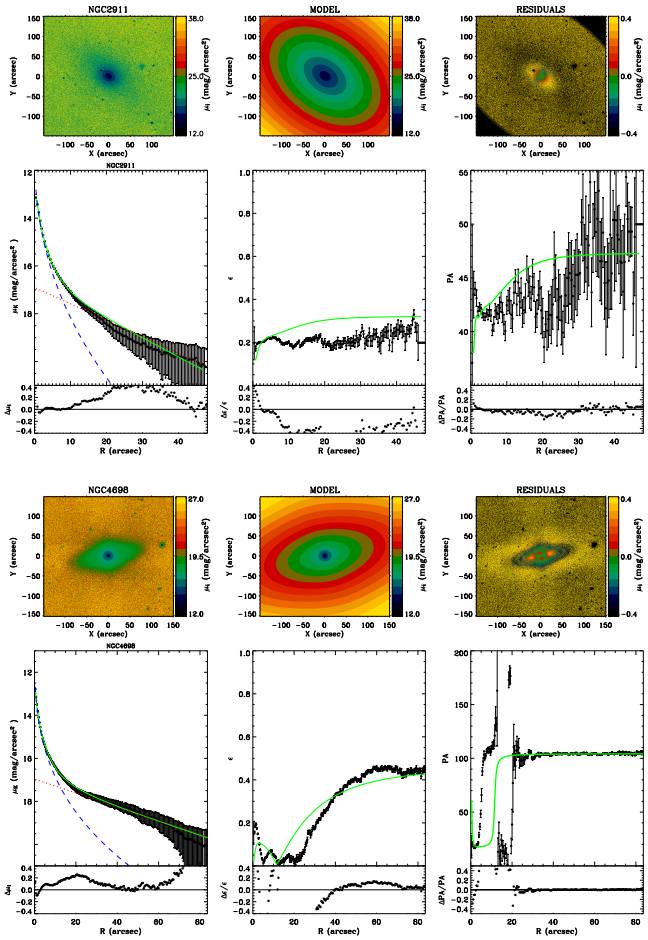

Figure 2.11 Two-dimensional photometric decomposition of a lenticular and a spiral galaxy of the sample with images in the UKIDSS archive. *Upper panels* (from *left* to *right*): Map of the observed, modeled, and residual (observed-modeled) surface-brightness distribution of the galaxy. The surface-brightness range of each image is indicated at the right of the panel. In each panel the spatial coordinates with respect to the galaxy center are given in arcsec. *Lower panels* (from *left* to *right*): Ellipse-averaged radial profile of surface-brightness, position angle, and ellipticity measured in the observed (dots with error-bars) and modeled image (red solid line). The blue dashed and the red dotted lines represent the intrinsic surface-brightness contribution of the bulge and disk, respectively. The difference between the ellipse-averaged radial profiles extracted from the observed and modeled images is also shown in green.

were observed in their central $0\farcs1 - 0\farcs3$. We measured the width of the [N II] λ6583 emission line in the nucleus of 122 galaxies.

These measurements allowed us to derive upper limits on $M_\bullet$ for the most comprehensive spectral atlas of low-luminosity active galactic nuclei (see Chapter 3). The STIS acquisition images were used to detect the possible presence of a nuclear cluster component in the galaxies (see Section 3.3.2 for details), although they did not allow us to perform a detailed study of the central components of our sample galaxies. Moreover, because of their small extension they were not useful to obtain the stellar surface density for our galaxy sample.

The bulge-to-disk decomposition from the 2MASS images allowed us to derive the structural parameters and $L_{K,\mathrm{bulge}}$ for 64 sample galaxies. The remaining part of the images was not suitable for the decomposition because too shallow, or with too low resolution to disentangle the contribution of the bulge with respect to the disk light. Measuring $L_{K,\mathrm{bulge}}$ from such shallow images is further complicated by the presence in the disk galaxies of additional structures such as bars. The use of images such as the UKIDSS ones was useful to obtain reliable structural parameters for 5 galaxies, one, NGC 2911, without a successful fit of the 2MASS images, and obtain an accurate estimation of $L_{K,\mathrm{bulge}}$ to derive $M_\bullet$ from the $M_\bullet - L_{K,\mathrm{bulge}}$ relationship to be compared with upper limits on $M_\bullet$ we will present in Chapter 3.

This dataset will allow us to extend the previous analysis as follows.

- The reduced spectra will allow us to measure the velocity and velocity dispersion as a function of the radius for all our sample galaxies.

- For a large fraction of the sample galaxies there are offset spectra too and we can model the velocity fields of these galaxies to obtain secure $M_\bullet$ estimates (e.g., Verdoes Kleijn et al. 2000; Barth et al. 2001; Pastorini et al. 2007(@; de Francesco et al. 2008; Dalla Bontà et al. 2009, see also Chapter 6). By identifying the galaxies with regular dust lanes following the method of Ho et al. (2002), we will be able to preselect other cases to be observed with STIS to complete the data set needed for modeling.

- With the addition of the Advanced Camera for Surveys (ACS) and Wide-Field Planetary Camera 2 (WFPC2) archival images we will be able to study the structural components (e.g., nuclear disks, nuclear bars, and nuclear spirals) of the inner regions. This is not always possible with the acquisition images that are too small to properly perform a decomposition of the central components. The ACS and WFPC2 images will be also useful to obtain the parameterization of the stellar surface density for our sample galaxies by applying multi-Gaussian expansion (MGE, Cappellari

2002). This will allow us to account properly of the stellar component in the estimation of $M_\bullet$.

- The addition of Near-Infrared Camera and Multi Object Spectrometer (NICMOS) archival images will allow to produce color maps of the dust features. The study of the morphologies of these features in a such a large sample of galaxies will allow us to have a complete knowledge of the interplay of dust and gas in the nearby nuclei. This will extend the previous works by Carollo et al. (1998), Martini & Pogge (1999), Laine et al. (2001), and Hughes et al. (2003),

- For 11 galaxies of our sample with measurable spectra we did not find published σ. they are indicated with "yes s" in Table 2.3. We are planning long-slit observations of the stellar component of this subsample of galaxies. The σ will be derived by simultaneously fitting the emission and absorption lines in the spectra by using the GANDALF software Sarzi et al. (2006), coupled with a stellar library developed for stellar population synthesis modeling (e.g., Sánchez-Blázquez et al. 2006).

- All the data collected from the STIS spectra will allow us to map the narrow-line region structure within the central $\sim$100 pc from the galaxy nucleus and study the emission-line ratios to analyze the ionization mechanisms at work in the nuclear regions of this large and various sample of galaxies. Previous studies (e.g., Noel-Storr et al. 2003) found line ratios compatible with typical values due to the photo-ionization and shock models (see Dopita et al. 1997) but for a smaller sample of radio galaxies. Recently, Sarzi et al. (2009) found that the diffuse and old stellar sources are the the main contributors of the ionizing photons by studying a sample of early-type galaxies. This study will be done by comparing the trend of the [N II] flux as a function of the flux of the narrow component of Hα. We will also derive the ratio [S II] λ6716/[S II] λ6731 as a function of the radial distance to estimate the electron density (see Osterbrock 1989).

- We will search in the latest UKIDSS data release for new images of the sample galaxies and seeking the Visible and Infrared Survey Telescope for Astronomy (VISTA, Dalton et al. 2004) archive for images of the sample galaxies in the Southern hemisphere.

- The remaining galaxies will be observed with the infrared spectrograph and imaging camera (Sofi) on the New Technology Telescope (NTT) at La Silla Observatory in Chile, and with the Near Infrared Camera Spectrometer (NICS) at the Telescopio Nazionale Galileo, La Palma.

- The new version of the GASP2D code (Méndez-Abreu et al., in preparation; see also Méndez-Abreu 2008) will allow us to correctly decompose barred galaxies. The fit in this case will be performed with 3 components: a Sérsic bulge and exponential disk, and a bar surface brightness distribution described by either a flat (Prieto et al. 2001; Aguerri et al. 2005), elliptical (Freeman 1966; Aguerri et al. 2005) or Ferrers profiles (Laurikainen et al. 2005).

Table 2.1: Properties of the sample galaxies

Galaxy (1)	RA (h:m:s) (2)	DEC (d:m:s) (3)	Morph. T. (4)	Spec. Cl. (5)	D (Mpc) (6)	Ref. (7)	M_B^0 (mag) (8)	PA (°) (9)	R_{25} ($''$) (10)	i (°) (11)	$M_\bullet$ from $M_\bullet - \sigma$ ($M_\odot$) (12)	$r_{\rm infl}$ ($''$) (13)
IC 342	03:46:48.5	+68 : 05 : 46	SABcd(rs)	H	4.0	1	−21.97		641.39	12	1.08E6	0.050
IC 3639	12:40:52.8	−36 : 45 : 21	SBbc(rs):	S2*	48.0	2	−20.70		36.91	18	5.44E6	0.011
IC 5096	21:18:21.5	−63 : 45 : 38	Sbc sp	...	39.8	2	−20.94	148	94.87	90	...	...
NGC 134	00:30:22.0	−33 : 14 : 39	SABbc(s)	...	17.5	2	−21.00	50	255.34	86	...	...
NGC 157	00:34:46.7	−08 : 23 : 47	SABbc(rs)	...	17.9	2	−20.67	30	125.06	52	...	...
NGC 193	00:39:18.6	+03 : 19 : 52	SAB0$^-$(s):	...	53.2	2	−20.22	55	43.36	40	1.70E8	0.073
NGC 255	00:47:47.3	−11 : 28 : 07	SABbc(rs)	...	17.2	2	−19.04	175*	90.60	35	...	
NGC 278	00:52:04.3	+47 : 33 : 02	SABb(rs)	H	5.2	2	−17.92		62.68	18	1.47E5	0.012
NGC 289	00:52:42.3	−31 : 12 : 21	SBbc(rs)	...	18.3	2	−19.91	130	153.86	47	1.28E7	0.046
NGC 315	00:57:48.9	+30 : 21 : 09	E$^+$:	L1.9	61.8	2	−22.09	40	97.08	77	2.19E9	0.283
NGC 383	01:07:24.9	+32 : 24 : 45	SA0$^-$:	...	63.4	2	−21.33	30	47.55	32	5.83E8	0.127
NGC 520	01:24:35.1	+03 : 47 : 33	pec	H*	25.5	2	−20.29	130	134.01	66	4.03E8	0.254
NGC 541	01:25:44.3	−01 : 22 : 46	S0$^-$:	...	68.2	2	−21.19	69*	53.35	15	2.01E8	0.063
NGC 613	01:34:18.2	−29 : 25 : 06	SBbc(rs)	H*	16.5	2	−20.56	120	164.86	42	2.55E7	0.077
NGC 741	01:56:21.0	+05 : 37 : 44	E0:	...	70.4	2	−22.17	93*	88.54	17	5.10E8	0.105
NGC 788	02:01:06.4	−06 : 48 : 56	SA0/a(s)	S1/S2*	51.3	2	−20.75	105*	57.16	45	2.73E7	0.026
NGC 1052	02:41:04.8	−08 : 15 : 21	E4	L1.9	19.4	3	−20.09	120	90.60	82	1.96E8	0.218
NGC 1097	02:46:19.0	−30 : 16 : 30	SBb(s)	S1*	14.7	2	−20.92	130	279.98	50	...	...
NGC 1255	03:13:32.0	−25 : 43 : 31	SAB(rs)bc	...	20.6	2	−20.31	117	125.06	53	8.77E5	0.008
NGC 1300	03:19:41.1	−19 : 24 : 41	SBbc(rs)	...	18.9	2	−20.61	106	184.98	50	3.43E6	0.021
NGC 1358	03:33:39.7	−05 : 05 : 22	SAB0/a(r)	S2	51.6	2	−20.86		77.11	41	1.17E8	0.060
NGC 1497	04:02:06.8	+23 : 07 : 59	S0	...	80.6	2	−21.24	60	54.59	57	4.82E8	0.089
NGC 1667	04:48:37.1	−06 : 19 : 12	SAB(r)c	S2	60.1	2	−21.49	20*	53.35	40	1.40E8	0.058
NGC 1832	05:12:03.3	−15 : 41 : 16	SBbc(r)	...	25.9	2	−20.47	9*	77.11	50	...	...
NGC 1961	05:42:04.6	+69 : 22 : 42	SABc(rs)	L2	52.1	2	−22.58	85	137.13	51	4.11E8	0.125
NGC 2110	05:52:11.4	−07 : 27 : 22	SAB0$^-$	S2*	31.2	2	−20.62	175*	50.95	53	2.58E8	0.159
NGC 2179	06:08:02.2	−21 : 44 : 48	SA0/a(s)	...	38.4	2	−20.09	170	50.95	51	7.11E7	0.061
NGC 2273	06:50:08.6	+60 : 50 : 45	SBa(r):	S2	25.0	2	−19.97	50	97.08	44	1.83E7	0.042
NGC 2329	07:09:08.0	+48 : 36 : 56	S0$^-$:	...	77.5	2	−21.36	175	38.65	38	3.71E8	0.079
NGC 2623	08:38:24.1	+25 : 45 : 17	pec	S2	76.8	2	−21.28		71.96	73	5.72E6	0.007
NGC 2654	08:49:11.9	+60 : 13 : 16	SBab:sp	...	19.3	2	−19.76	63	127.97	90	...	...
NGC 2685	08:55:34.7	+58 : 44 : 04	(R)SB0$^+$ pec	S2/T2:	13.4	2	−18.81	38	134.01	70	3.24E6	0.028
NGC 2748	09:13:43.0	+76 : 28 : 31	SAbc	H	19.9	2	−19.90	38	90.60	72	1.71E6	0.013
NGC 2787	09:19:18.5	+69 : 12 : 12	SB0(r)$^+$	L1.9	7.5	3	−17.76	117	94.87	57	1.62E8	0.505
NGC 2892	09:32:52.9	+67 : 37 : 03	E$^+$ pec:	...	91.5	2	−21.15		42.38	0	1.27E9	0.139
NGC 2903	09:32:10.1	+21 : 30 : 03	SABbc(rs)	H	11.2	2	−21.14	17	377.68	64	6.29E6	0.050
NGC 2911	09:33:46.1	+10 : 09 : 09	SA0(s): pec	L2	46.6	2	−21.09	140	122.21	46	3.87E8	0.135
NGC 2964	09:42:54.2	+31 : 50 : 50	SABbc(r):	H	21.1	2	−20.03	97	86.52	59	7.59E6	0.030
NGC 2976	09:47:15.4	+67 : 54 : 59	SAc pec	H*	1.2	2	−15.17	143	176.65	65	...	...
NGC 3003	09:48:36.0	+33 : 25 : 17	Sbc?	H	23.1	2	−20.55	79	172.63	87	...	...
NGC 3021	09:50:57.1	+33 : 33 : 13	SAbc(rs)	...	23.9	2	−19.37	110	47.55	58	5.17E5	0.005
NGC 3031	09:55:33.2	+69 : 03 : 55	SABab(s)	S1.5	3.9	3	−20.57	157	807.46	63	4.37E7	0.448
NGC 3049	09:54:49.5	+09 : 16 : 16	SBab(rs)	H*	24.2	2	−19.15	25	65.63	52	...	...
NGC 3067	09:58:21.1	+32 : 22 : 12	SABab(s)	H*	23.2	2	−19.61	105	73.64	75	2.18E6	0.013
NGC 3078	09:58:24.6	−26 : 55 : 37	E2-3	...	35.2	3	−20.79	177	75.36	50	3.01E8	0.155

Table 2.1 – Continued

Galaxy (1)	RA (h:m:s) (2)	DEC (d:m:s) (3)	Morph. T. (4)	Spec. Cl. (5)	D (Mpc) (6)	Ref. (7)	M_B^0 (mag) (8)	PA (°) (9)	R_{25} ($''$) (10)	i (°) (11)	$M_\bullet$ from $M_\bullet - \sigma$ ($M_\odot$) (12)	$r_{\rm infl}$ ($''$) (13)
NGC 3081	09:59:29.5	−22 : 49 : 35	(R)SAB0/a(r)	S2*	35.9	2	−20.19	158	62.68	43	2.37E7	0.034
NGC 3162	10:13:31.6	+22 : 44 : 15	SABbc(rs)	...	21.4	2	−19.72	25*	90.60	35	2.59E6	0.016
NGC 3227	10:23:30.6	+19 : 51 : 54	SABa(s) pec	S1.5	19.6	2	−20.28	155	161.11	51	2.73E7	0.068
NGC 3245	10:27:18.4	+28 : 30 : 27	$SA0^0$(r):?	T2:	20.9	3	−19.53	120	97.08	72	1.87E8	0.197
NGC 3254	10:29:19.9	+29 : 29 : 31	SAbc(s)	S2	21.5	2	−20.15	46	150.36	77	1.83E7	0.049
NGC 3256	10:27:51.3	−43 : 54 : 14	pec	H*	40.8	2	−21.75	100	114.06	56	1.83E7	0.026
NGC 3259	10:32:34.8	+65 : 02 : 28	SABbc(rs)	...	24.2	2	−19.42	20	65.63	59	...	...
NGC 3310	10:38:45.9	+53 : 30 : 12	SABbc(r) pec	H	15.6	2	−20.01		92.71	40	1.04E7	0.048
NGC 3351	10:43:57.7	+11 : 42 : 14	SBb(r)	H	10.0	4	−19.74	13	222.39	50	6.92E6	0.059
NGC 3368	10:46:45.7	+11 : 49 : 12	SABab(rs)	L2	10.4	3	−20.28	5	227.57	49	1.08E7	0.074
NGC 3379	10:47:49.6	+12 : 34 : 54	E1	L2/T2::	10.6	3	−19.94		161.11	38	2.64E8	0.476
NGC 3393	10:48:23.4	−25 : 09 : 43	(R′)SBa(rs):	S2*	54.2	2	−21.03	13*	65.63	26	1.05E8	0.054
NGC 3403	10:53:54.8	+73 : 41 : 25	SAbc:	...	17.7	2	−19.01	73	90.60	71	...	...
NGC 3489	11:00:18.6	+13 : 54 : 04	$SAB0^+$(rs)	T2/S2	12.1	3	−19.26	70	106.44	64	9.08E6	0.057
NGC 3516	11:06:47.5	+72 : 34 : 07	(R)SB0(s)	S1.2	35.9	2	−20.64		52.13	46	4.66E7	0.051
NGC 3521	11:05:48.6	−00 : 02 : 09	SABbc(rs)	H/L2	15.5	2	−21.66	163	328.94	65	3.36E7	0.097
NGC 3627	11:20:15.0	+12 : 59 : 30	SABb(s)	T2/S2	10.1	4	−20.88	173	273.60	67	8.31E6	0.065
NGC 3642	11:22:17.8	+59 : 04 : 28	SAbc(r):	L1.9	23.2	2	−20.37	105	161.11	35	6.92E6	0.025
NGC 3675	11:26:08.6	+43 : 35 : 09	SAb(s)	T2	13.3	2	−20.10	178	176.65	62	1.28E7	0.064
NGC 3684	11:27:11.2	+17 : 01 : 49	SAbc(rs)	H	19.9	2	−19.68	130	92.71	48	1.06E5	0.003
NGC 3686	11:27:44.0	+17 : 13 : 27	SBbc(s)	H	19.8	2	−19.86	15	97.08	40	6.33E7	0.110
NGC 3705	11:30:07.4	+09 : 16 : 36	SABab(r)	T2	18.2	2	−20.05	122	146.93	72	9.49E6	0.039
NGC 3756	11:36:48.0	+54 : 17 : 37	SABbc(rs)	H	19.5	2	−19.82	177	125.06	63	1.55E5	0.003
NGC 3801	11:40:16.9	+17 : 43 : 41	S0?	...	49.6	2	−20.69	120	104.02	65	3.14E8	0.113
NGC 3862	11:45:05.0	+19 : 36 : 23	E	...	90.6	2	−21.27		44.37	0	4.03E8	0.071
NGC 3887	11:47:04.6	−16 : 51 : 17	SBbc(r)	H	20.8	2	−20.40	20	99.34	42	...	...
NGC 3917	11:50:45.4	+51 : 49 : 29	SAcd:	T2:	15.5	2	−19.39	77	153.86	80	3.02E4	0.002
NGC 3921	11:51:06.9	+55 : 04 : 43	(R′)SA0/a(rs)pec	...	80.3	2	−21.63	20	64.14	58	1.17E8	0.039
NGC 3949	11:53:41.7	+47 : 51 : 31	SAbc(s):	H	13.4	2	−19.50	120	86.52	57	2.59E6	0.025
NGC 3953	11:53:48.9	+52 : 19 : 36	SBbc(r)	T2	16.5	2	−20.71	13	207.55	63	2.93E7	0.084
NGC 3972	11:55:45.1	+55 : 19 : 15	SAbc(s)	...	13.5	2	−18.58	120	116.71	81	...	...
NGC 3982	11:56:28.1	+55 : 07 : 31	SABb(r):	S1.9	17.0	2	−19.47		70.33	31	1.71E6	0.015
NGC 3992	11:57:36.0	+53 : 22 : 28	SBbc(rs)	T2:	16.4	2	−20.81	68	227.57	54	2.12E7	0.070
NGC 3998	11:57:56.1	+55 : 27 : 13	$SA0^0$(r)?	L1.9	14.1	3	−19.26	140	80.75	39	1.23E9	0.882
NGC 4030	12:00:23.6	−01 : 06 : 00	SAbc(s)	...	24.2	2	−20.75	27	125.06	45	6.29E6	0.023
NGC 4036	12:01:26.7	+61 : 53 : 45	$S0^-$	L1.9	20.4	2	−20.06	85	127.97	90	6.91E7	0.112
NGC 4038	12:01:53.0	−18 : 52 : 03	SBm(s) pec	...	26.3	2	−21.48	80	157.44	55	...	...
NGC 4039	12:01:53.5	−18 : 53 : 10	SBm(s) pec	L	26.7	2	−21.41	130	92.71	60	...	...
NGC 4041	12:02:12.2	+62 : 08 : 14	SAbc(rs):	H	18.2	2	−19.54		80.75	22	4.45E6	0.025
NGC 4051	12:03:09.6	+44 : 31 : 53	SABbc(rs)	S1.2	12.6	2	−19.76	135	157.44	44	2.18E6	0.024
NGC 4088	12:05:34.2	+50 : 32 : 21	SABbc(rs)	H	12.7	2	−20.00	43	172.63	71	4.02E6	0.034
NGC 4100	12:06:08.4	+49 : 34 : 58	(R′)SAbc(rs)	H	17.0	2	−20.10	167	161.11	76	1.01E6	0.011
NGC 4138	12:09:29.8	+43 : 41 : 07	$SA0^+$(r)	S1.9	13.8	3	−18.60	150	77.11	56	4.23E6	0.032
NGC 4143	12:09:36.1	+42 : 32 : 03	$SAB0^0$(s)	L1.9	15.9	3	−19.11	144	68.73	62	3.27E8	0.359
NGC 4150	12:10:33.6	+30 : 24 : 06	$SA0^0$(r)?	T2	13.7	3	−18.29	147	70.33	55	4.93E6	0.035
NGC 4203	12:15:05.0	+33 : 11 : 50	$SAB0^-$:	L1.9	15.1	3	−19.29	10	101.65	25	6.71E7	0.149

Table 2.1 – Continued

Galaxy	RA	DEC	Morph. T.	Spec. Cl.	D	Ref.	M_B^0	PA	R_{25}	i	$M_\bullet$	$r_{\rm infl}$
	(h:m:s)	(d:m:s)			(Mpc)		(mag)	(°)	($''$)	(°)	from $M_\bullet - \sigma$ ($M_\odot$)	($''$)
(1)	(2)	(3)	(4)	(5)	(6)	(7)	(8)	(9)	(10)	(11)	(12)	(13)
NGC 4212	12:15:39.3	+13 : 54 : 05	SAc:	H	3.4	2	−16.31	75	94.87	54	1.32E6	0.066
NGC 4245	12:17:36.8	+29 : 36 : 29	SB0/a(r):	H	15.6	2	−18.96	153*	86.52	45	3.24E6	0.024
NGC 4258	12:18:57.5	+47 : 18 : 14	SABbc(s)	S1.9	7.3	3	−20.78	150	558.63	71	5.44E6	0.071
NGC 4261	12:19:23.2	+05 : 49 : 31	E2-3	L2	31.6	3	−21.14	160	122.21	38	9.77E8	0.344
NGC 4278	12:20:06.8	+29 : 16 : 51	E1-2	L1.9	16.1	3	−20.06		122.21	29	5.01E8	0.457
NGC 4303	12:21:54.9	+04 : 28 : 25	SABbc(rs)	H	25.5	2	−21.91	162*	193.70	28	1.71E6	0.010
NGC 4314	12:22:32.0	+29 : 53 : 43	SBa(rs)	L2	16.6	2	−19.93		125.06	29	1.13E7	0.048
NGC 4321	12:22:54.9	+15 : 49 : 21	SABbc(s)	T2	15.2	4	−20.93	30	222.39	33	3.43E6	0.026
NGC 4335	12:23:01.9	+58 : 26 : 40	E	...	63.3	2	−20.67	145	57.16	56	9.93E8	0.174
NGC 4343	12:23:38.7	+06 : 57 : 15	SAb(rs):	...	18.0	2	−18.91	133	75.36	82	...	...
NGC 4374	12:25:03.7	+12 : 53 : 13	E1	L2	18.4	3	−21.31	135	193.70	42	1.03E9	0.610
NGC 4380	12:25:22.2	+10 : 01 : 01	SAb(rs):?	H	17.3	2	−19.13	153	104.02	60	5.60E5	0.008
NGC 4389	12:25:35.1	+45 : 41 : 05	SBbc(rs) pec	...	12.4	2	−18.28	105	78.91	62	...	...
NGC 4414	12:26:27.1	+31 : 13 : 25	SAc(rs)?	T2:	17.7	4	−20.62	155	108.92	58	1.69E7	0.056
NGC 4420	12:26:58.5	+02 : 29 : 40	SBbc(r):	...	27.0	2	−19.88	8	61.25	64	...	...
NGC 4429	12:27:26.5	+11 : 06 : 27	$SA0^+$(r)	T2	19.5	2	−20.48	99	168.70	79	1.14E8	0.157
NGC 4435	12:27:40.5	+13 : 04 : 44	$SB0^0$(s)	T2/H:	14.8	2	−19.23	13	82.63	52	3.97E7	0.112
NGC 4450	12:28:29.6	+17 : 05 : 06	SAab(s)	L1.9	30.3	2	−21.66	175	157.44	45	1.39E7	0.029
NGC 4459	12:29:00.0	+13 : 58 : 43	$SA0^+$(r)	T2:	16.1	3	−19.83	110	106.44	46	9.68E7	0.173
NGC 4477	12:30:02.2	+13 : 38 : 11	SB0(s):?	S2	22.3	2	−20.44	15	114.06	28	4.66E7	0.082
NGC 4486	12:30:49.4	+12 : 23 : 28	E^+0-1 pec	L2	15.9	3	−21.51	160*	249.53	50	2.48E9	1.189
NGC 4501	12:31:59.2	+14 : 25 : 14	SAb(rs)	S2	34.6	2	−22.84	140	207.55	61	4.37E7	0.051
NGC 4507	12:35:36.6	−39 : 54 : 33	(R′)SABb(rs)	S2*	50.4	2	−21.23	50*	49.79	39	4.96E7	0.037
NGC 4526	12:34:03.0	+07 : 41 : 57	SAB0(s):	H	16.9	3	−20.61	113	217.33	90	2.01E8	0.254
NGC 4527	12:34:08.5	+02 : 39 : 14	SABbc(s)	T2	27.6	2	−21.54	67	184.98	75	2.15E8	0.162
NGC 4536	12:34:27.0	+02 : 11 : 17	SABbc(rs)	H	14.9	4	−20.29	130	227.57	68	1.14E8	0.206
NGC 4548	12:35:26.4	+14 : 29 : 47	SBb(rs)	L2	19.2	3	−20.63	150	161.11	39	4.52E7	0.093
NGC 4552	12:35:39.8	+12 : 33 : 23	E0-1	T2:	15.4	3	−20.36		153.86	34	5.30E8	0.495
NGC 4569	12:36:49.8	+13 : 09 : 46	SABab(rs)	T2	1.1	2	−15.40	23	286.50	68	4.24E7	1.570
NGC 4579	12:37:43.5	+11 : 49 : 05	SABb(rs)	S1.9/L1.9	24.6	2	−21.66	95	176.65	39	1.56E7	0.039
NGC 4594	12:39:59.4	−11 : 37 : 23	SAa(s) sp	L2	9.8	3	−21.57	90	261.29	75	3.01E8	0.557
NGC 4596	12:39:55.9	+10 : 10 : 34	$SB0^+$(r)	L2::	29.3	2	−20.83	135	119.43	48	3.84E7	0.055
NGC 4636	12:42:49.9	+02 : 41 : 16	E0-1	L1.9	14.7	3	−20.40	150	180.77	60	9.42E7	0.187
NGC 4676A	12:46:10.1	+30 : 43 : 55	S0 pec ?	...	91.8	2	−20.58	180*	68.73	90	...	...
NGC 4696	12:48:49.3	−41 : 18 : 40	E^+1 pec	L	35.5	3	−21.90	95	134.01	60	5.51E8	0.219
NGC 4698	12:48:22.9	+08 : 29 : 14	SAab(s)	S2	17.6	2	−19.99	170	119.43	55	1.97E7	0.062
NGC 4736	12:50:53.0	+41 : 07 : 14	(R)SAab(r)	L2	5.2	3	−19.83	105	336.61	38	7.59E6	0.120
NGC 4800	12:54:37.8	+46 : 31 : 52	SAb(rs)	H	13.4	2	−18.51	25	47.55	44	9.49E6	0.053
NGC 4826	12:56:43.7	+21 : 40 : 58	(R)SAab(rs)	T2	7.5	3	−20.55	115	300.00	62	1.13E7	0.105
NGC 5005	13:10:56.2	+37 : 03 : 33	SABbc(rs)	L1.9	15.7	2	−20.79	65	172.63	64	2.36E8	0.301
NGC 5054	13:16:58.5	−16 : 38 : 05	SAbc(s)	...	27.3	2	−21.05	160	153.86	57	...	...
NGC 5055	13:15:49.3	+42 : 01 : 45	SAbc(rs)	T2	9.5	2	−20.85	105	377.68	57	1.08E7	0.081
NGC 5077	13:19:31.7	−12 : 39 : 25	E3-4	L1.9	41.9	2	−20.90	4*	58.50	60	3.95E8	0.152
NGC 5127	13:23:45.0	+31 : 33 : 57	E pec	...	67.0	2	−21.32	75	84.55	60	1.43E8	0.052
NGC 5135	13:25:44.0	−29 : 50 : 01	SBab(s)	S2*	58.4	2	−21.46	119*	77.11	48	1.90E7	0.018
NGC 5141	13:24:51.4	+36 : 22 : 42	S0	...	72.5	2	−20.59	80	39.55	46	...	...
NGC 5194	13:29:52.7	+47 : 11 : 43	SAbc(s) pec	S2	8.5	2	−20.99	163	336.61	54	1.51E6	0.028

Table 2.1 – Continued

Galaxy (1)	RA (h:m:s) (2)	DEC (d:m:s) (3)	Morph. T. (4)	Spec. Cl. (5)	D (Mpc) (6)	Ref. (7)	M_B^0 (mag) (8)	PA (°) (9)	R_{25} ($''$) (10)	i (°) (11)	$M_\bullet$ from $M_\bullet - \sigma$ ($M_\odot$) (12)	$r_{\rm infl}$ ($''$) (13)
NGC 5247	13:38:03.0	−17 : 53 : 03	SAbc(s)	...	22.0	2	−21.43	20	168.70	30	...	...
NGC 5248	13:37:32.1	+08 : 53 : 06	SABbc(rs)	H	19.2	2	−20.78	110	184.98	45	1.90E7	0.056
NGC 5252	13:38:15.9	+04 : 32 : 33	S0	S1.9*	95.7	2	−20.98	10	41.41	63	1.08E8	0.031
NGC 5283	13:41:05.7	+67 : 40 : 20	S0?	S2*	37.0	2	−18.72	131*	32.15	28	3.84E7	0.044
NGC 5347	13:53:17.8	+33 : 29 : 27	(R′)SBab(rs)	S2*	34.6	2	−19.60	130	50.95	39	1.01E6	0.006
NGC 5364	13:56:12.0	+05 : 00 : 52	SAbc(rs) pec	H	20.2	2	−20.73	30	202.82	52	2.18E6	0.015
NGC 5398	14:01:21.5	−33 : 03 : 50	SB(rs)dm	...	19.6	2	−19.21	172	84.55	54	...	...
NGC 5427	14:03:26.0	−06 : 01 : 51	SAc(s)pec	S2*	38.9	2	−21.22		84.55	32	1.01E6	0.005
NGC 5490	14:09:57.3	+17 : 32 : 44	E	...	69.9	2	−21.34	5	71.96	50	1.04E9	0.162
NGC 5577	14:21:13.1	+03 : 26 : 09	SAbc(rs):	...	23.1	2	−19.61	56	101.65	79	...	...
NGC 5635	14:28:31.7	+27 : 24 : 32	S pec	L*	60.2	2	−20.97	65	70.33	64	...	...
NGC 5643	14:32:40.8	−44 : 10 : 29	SABc(rs)	S2*	18.6	2	−21.11	88*	137.13	30	4.93E6	0.026
NGC 5695	14:37:22.1	+36 : 34 : 04	S?	S2*	58.5	2	−20.47	150	46.46	47	3.84E7	0.028
NGC 5713	14:40:11.5	−00 : 17 : 20	SABbc(rs) pec	H	28.1	2	−20.66	10	82.63	28	...	...
NGC 5728	14:42:23.9	−17 : 15 : 11	SABa(r):	S2*	40.3	2	−21.37	30	92.71	60	2.10E8	0.110
NGC 5746	14:44:55.9	+01 : 57 : 18	SABb(rs)?sp	...	25.9	2	−21.92	170	222.39	90	1.83E7	0.040
NGC 5879	15:09:46.8	+57 : 00 : 01	SAbc(rs):?	T2/L2	11.4	2	−18.88	0	125.06	76	4.40E5	0.010
NGC 5905	15:15:23.3	+55 : 31 : 02	SBb(r)	H/S1*	46.1	2	−21.13	135	119.43	51	2.37E7	0.026
NGC 5921	15:21:56.5	+05 : 04 : 14	SBbc(r)	T2	22.0	2	−20.37	130	146.93	37	3.81E6	0.019
NGC 6300	17:16:59.5	−62 : 49 : 14	SBb(rs)	S2*	15.2	2	−20.71	118	134.01	51	4.23E6	0.029
NGC 6384	17:32:24.3	+07 : 03 : 37	SABbc(r)	T2	21.9	2	−21.10	30	184.98	50	1.23E7	0.038
NGC 6500	17:55:59.8	+18 : 20 : 18	SAab:	L2	39.1	2	−20.50	50	65.63	45	3.27E8	0.146
NGC 6503	17:49:26.5	+70 : 08 : 40	SAcd(s)	T2/S2:	6.5	5	−18.95	123	212.38	73	1.31E5	0.009
NGC 6621	18:12:55.3	+68 : 21 : 48	Sb: pec	H	82.6	2	−22.24	145	62.68	72	...	...
NGC 6861	20:07:19.5	−48 : 22 : 13	$SA0^-$(s):	...	28.1	3	−20.32	140	84.55	65	6.04E9	1.133
NGC 6951	20:37:14.1	+66 : 06 : 20	SABbc(rs)	S2	17.1	2	−20.45	170	116.71	35	6.92E6	0.035
NGC 7052	21:18:33.0	+26 : 26 : 49	E	...	61.7	2	−21.26	64	75.36	90	3.95E8	0.104
NGC 7252	22:20:44.8	−24 : 40 : 42	(R)$SA0^0(r)$	...	59.5	2	−21.40	125*	58.50	39	7.98E7	0.042
NGC 7314	22:35:46.2	−26 : 03 : 01	SABbc(rs)	S1.9*	15.0	2	−19.79	3	137.13	66	4.05E5	0.007
NGC 7331	22:37:04.1	+34 : 24 : 56	SAb(s)	T2	13.1	3	−21.21	171	314.14	75	1.76E7	0.078
NGC 7592	23:18:22.2	−04 : 25 : 01	$S0^+$ pec:	S2	92.8	2	−20.67	85	35.25	42	...	...
NGC 7626	23:20:42.5	+08 : 13 : 01	E pec:	L2::	40.8	2	−21.00	20*	78.91	38	5.20E8	0.184
NGC 7682	23:29:03.9	+03 : 32 : 00	SBab(r)	S2*	63.5	2	−20.34	147*	36.91	28	1.50E7	0.015
UGC 1214	01:43:57.8	+02 : 21 : 00	(R)$SAB0^+$(rs):	S2*	64.2	2	−20.47		40.47	14	1.18E7	0.013
UGC 1395	01:55:22.0	+06 : 36 : 43	SAb(rs)	S1.9*	65.2	2	−20.21	159*	37.77	39	1.01E6	0.003
UGC 1841	02:23:11.4	+42 : 59 : 31	E	...	80.3	2	−21.28	144*	90.60	0	2.45E9	0.233
UGC 7115	12:08:05.5	+25 : 14 : 14	E	...	94.5	2	−20.70		26.13	24	1.87E8	0.044
UGC 10814	17:19:21.3	+49 : 02 : 25	Sb	...	95.3	2	−20.42	17	26.13	52	...	...
UGC 12064	22:31:20.6	+39 : 21 : 30	$S0^-$:	...	64.4	2	−20.19	39*	2.89	0	8.67E8	0.158

NOTES. — Col.(1): Galaxy name. Col.(2): RA from NASA/IPAC Extragalactic Database (NED). Col.(3): DEC from NED. Col.(4): Morphological type from de Vaucouleurs et al. (1991, RC3). Col.(5): Nuclear spectral class from Ho et al. (1997a), where H = H II nucleus, L = LINER (Heckman 1980), S = Seyfert , T = transition object whose [O I] strengths are intermediate between those of H II nuclei and LINERS, 1 = type 1, 2 = type 2, and a fractional number between 1 and 2 denotes various intermediate types; uncertain and highly uncertain classifications are followed by a single and double colon, respectively. The nuclear spectral class of galaxies marked with * is from NED. Col.(6): Distance. Col.(7): Reference for Col.(6). All the distances were taken from literature (see attached list), except those we obtained from V_{3K}, the weighted mean recessional velocity corrected to the reference frame of the microwave background radiation given in RC3. These were derived as $D = V_{3K}/H_0$ with $H_0 = 75$ km s^{-1} Mpc^{-1}. Col.(8): Absolute corrected B magnitude derived from B_T^0 (RC3) with the adopted distance. Col.(9): Position angle of the galaxy major axis. The values marked with * are from Hyperleda. Col.(10): Radius of the isophote with surface brightness of $\mu_B = 25$ mag arcsec^{-2}, derived from the diameter D_{25} listed in RC3. Col.(11): Inclination derived from the logarithm of the ratio between the major and minor diameters of the isophote with surface brightness of $\mu_B = 25$ mag arcsec^{-2} in RC3, accounting for the intrinsic disk thickness as in Paturel et al. (1997). Col.(12): $M_\bullet$ predicted from the $M_\bullet - \sigma$ relation by Ferrarese & Ford (2005) for the galaxies with published σ (see Table 2.2). Col.(13): Radius of the sphere of influence estimated by the Eq. 2.2. REFERENCES. — (1) Tully (1988); (2) de Vaucouleurs et al. (1991); (3) Tonry et al. (2001); (4) Freedman et al. (2001); (5) Ho (2007).

Table 2.2: Spectroscopic and photometric properties of the sample galaxies

Galaxy	x ($''$)	y ($''$)	$\sigma \pm \delta\sigma$ (km s^{-1})	$\sigma_c \pm \delta\sigma_c$ (km s^{-1})	Ref.	r_e ($''$)	Band	Ref.
(1)	(2)	(3)	(4)	(5)	(6)	(7)	(8)	(9)
IC 342	2.8	1.0	77 ± 28	71 ± 26	1	64.1	*K*	53
IC 3639	2	2.46	95 ± 5	99 ± 5	2	3.5	*K*	53
IC 5096	...	...	...	...	...	...	...	...
NGC 134	...	...	...	...	...	...	...	...
NGC 157	...	...	...	...	...	7.0	*V*	54
NGC 193	3.39	...	203 ± 13	201 ± 13	3	3.5	*K*	53
NGC 255	...	...	...	...	...	11.6	*V*	54
NGC 278	2	4	48 ± 9	47.1 ± 8.8	4	16.9	*V*	54
NGC 289	1.35	...	114 ± 12	118 ± 13	5	4.0	*K*	55
NGC 315	4.0	1.5	357 ± 31	340 ± 30	6	36.9	*B*	56
NGC 383	1.2	2.2	258 ± 18	259 ± 18	7	6.5	*K*	53
NGC 520	2.34	2.0	240 ± 25	...	8	...	...	...
NGC 541	2.4	...	213 ± 4	208 ± 4	9	35.8	*R*	57
NGC 613	12.5	3.2	126 ± 19	136 ± 20	10	4.2	*H*	58
NGC 741	2.9	1.5	270 ± 13	252 ± 12	11	52.1	*B*	56
NGC 788	3.6	2.2	140 ± 20	138 ± 20	12	17.5	*I*	59
NGC 1052	2.0	3.74	215 ± 7	207 ± 7	13	33.7	*B*	56
NGC 1097	...	...	...	...	...	58.5	*B*	56
NGC 1255	1.35	...	68 ± 3	68 ± 3	5	9.7	*K*	53
NGC 1300	1.35	...	90 ± 6	90 ± 6	5	23.9	*V*	54
NGC 1358	3.6	2.2	185 ± 20	186 ± 20	12	10.8	*V*	59
NGC 1497	3.39	...	245 ± 21	249 ± 21	3	19.5	*K*	53
NGC 1667	1.6	0.9	173 ± 28	193 ± 31	1	0.3	*V*	59
NGC 1832	...	...	...	...	...	5.0	*V*	54
NGC 1961	12.5	3.2	257 ± 44	241 ± 41	10	139.1	*V*	54
NGC 2110	3.6	2.2	220 ± 25	219 ± 25	12	14.9	*V*	59
NGC 2179	2.43	2.5	166 ± 12	168 ± 12	14	8.9	*V*	54
NGC 2273	2.3	1.5	121 ± 11	127 ± 11	12	2.6	*K*	60
NGC 2329	1.2	2.2	246 ± 15	236 ± 14	15	20.3	*B*	61
NGC 2623	4.8	2.4	95 ± 13	100 ± 14	16	4.1	*H*	62
NGC 2654	...	...	...	...	...	9.3	*V*	54
NGC 2685	1.2	2.2	92 ± 8	89 ± 8	17	15.2	*V*	54
NGC 2748	1.35	...	78 ± 5	78 ± 5	5	...	...	...
NGC 2787	2.0	3.74	202 ± 5	199 ± 5	13	17.3	*V*	54
NGC 2892	3.39	...	297 ± 19	304 ± 19	3	...	...	...
NGC 2903	1.2	2.2	101 ± 13	102 ± 13	18	5.7	*V*	54
NGC 2911	1.2	2.4	237 ± 17	238 ± 17	19	7.0	*K*	60
NGC 2964	1.2	2.2	97 ± 19	106 ± 21	18	0.8	*V*	54
NGC 2976	...	...	...	...	...	...	...	...
NGC 3003	...	...	...	...	...	...	...	...
NGC 3021	1.2	2.2	59 ± 26	61 ± 27	20	2.9	*B*	63
NGC 3031	0.30	1.25	173 ± 5	152 ± 4	21	66.2	*V*	54
NGC 3049	...	...	...	...	...	...	...	...
NGC 3067	1.2	2.2	82 ± 28	...	20	...	...	...
NGC 3078	1.1	1.6	238 ± 14	226 ± 13	22	22.8	*B*	56
NGC 3081	2.	2.46	129 ± 8	134 ± 8	2	4.2	*K*	53
NGC 3162	1.35	...	85 ± 1	85 ± 1	5	...	...	...
NGC 3227	2.1	1.5	128 ± 13	138 ± 14	12	1.3	*V*	54
NGC 3245	1.2	2.2	211 ± 19	205 ± 18	23	15.6	*V*	54
NGC 3254	3.6	1.25	123 ± 2	127 ± 2	24	4.3	*V*	54
NGC 3256	2.2	4.4	127 ± 20	...	25	...	...	...
NGC 3259	...	...	...	...	...	1.6	*R*	64
NGC 3310	4.2	1.0	111 ± 28	113 ± 29	1	5.4	*V*	54
NGC 3351	10.0	3.0	101 ± 16	104 ± 16	26	13.1	*V*	54
NGC 3368	0.30	1.25	129 ± 5	114 ± 4	21	56.4	*V*	54
NGC 3379	0.56	1.4	240 ± 5	220 ± 5	27	35.2	*B*	56
NGC 3393	2.1	1.0	184 ± 28	182 ± 28	1	8.7	*K*	53
NGC 3403	...	...	...	...	...	...	...	...
NGC 3489	2.0	3.74	112 ± 3	110 ± 3	13	21.7	*V*	54
NGC 3516	3.0	...	144 ± 35	154 ± 37	28	4.4	*R*	65
NGC 3521	1.25	1.25	145 ± 10	144 ± 10	29	7.0	*K*	55
NGC 3627	1.2	2.2	117 ± 9	108 ± 8	18	51.9	*V*	54
NGC 3642	5.6	0.8	109 ± 28	104 ± 27	1	28.4	*V*	54
NGC 3675	1.2	2.2	121 ± 5	118 ± 5	18	13.4	*H*	58
NGC 3684	2	4	43 ± 9	44 ± 9	4	8.5	*V*	54
NGC 3686	2	4	151 ± 10	164 ± 10	4	1.7	*H*	58
NGC 3705	0.30	1.25	110 ± 9	111 ± 9	21	2.3	*V*	54
NGC 3756	2	4	48 ± 9	...	4	...	...	...
NGC 3801	1.2	2.4	225 ± 19	228 ± 19	19	5.5	*K*	53
NGC 3862	3.4	3.0	242 ± 15	240 ± 15	30	17.7	*B*	56

Table 2.2 – Continued

Galaxy	x ($''$)	y ($''$)	$\sigma \pm \delta\sigma$ (km s^{-1})	$\sigma_c \pm \delta\sigma_c$ (km s^{-1})	Ref.	r_e ($''$)	Band	Ref.
(1)	(2)	(3)	(4)	(5)	(6)	(7)	(8)	(9)
NGC 3887	...	...	...	...	...	1.4	V	54
NGC 3917	2	4	38 ± 9	34 ± 8	4	104.0	V	54
NGC 3921	1.2	2.2	186 ± 18	...	15	...	...	...
NGC 3949	...	...	82 ± 2	85 ± 2	5	5.7	V	54
NGC 3953	1.35	...	146 ± 1	140 ± 1	5	32.0	V	54
NGC 3972	...	...	...	...	...	...	...	...
NGC 3982	2.0	3.7	78 ± 2	78 ± 2	31	...	...	...
NGC 3992	2.5	3.3	140 ± 20	131 ± 19	31	64.4	V	54
NGC 3998	0.8	2.0	316 ± 9	302 ± 8	32	17.6	V	54
NGC 4030	2.4	2.4	100 ± 10	102 ± 10	33	7.5	V	54
NGC 4036	0.8	2.0	175 ± 6	167 ± 5	32	19.9	V	54
NGC 4038	...	...	...	...	...	1.5	V	54
NGC 4039	...	...	...	...	...	...	...	...
NGC 4041	1.35	...	95 ± 5	95 ± 5	5	9.1	K	53
NGC 4051	2.1	1.5	88 ± 13	82 ± 12	12	48.1	V	54
NGC 4088	1.35	...	88 ± 4	93 ± 4	5	2.4	V	54
NGC 4100	2	4	76 ± 9	70 ± 9	4	90.7	V	54
NGC 4138	0.58	2.0	100 ± 10	94 ± 9	34	21.6	V	54
NGC 4143	1.2	2.2	211 ± 6	230 ± 6	35	0.9	V	54
NGC 4150	2.0	3.74	87 ± 3	97 ± 3	12	0.9	V	54
NGC 4203	2.0	3.74	167 ± 3	166 ± 3	13	14.7	V	54
NGC 4212	1.35	...	76 ± 3	74 ± 3	5	22.4	V	54
NGC 4245	...	...	86 ± 3	89 ± 10	36	5.7	V	54
NGC 4258	1.2	2.2	115 ± 10	99 ± 9	18	332.4	V	54
NGC 4261	3.4	3.0	299 ± 15	288 ± 14	30	36.1	B	56
NGC 4278	2.0	3.74	261 ± 8	251 ± 8	13	34.4	B	56
NGC 4303	1.2	2.2	74 ± 9	78 ± 10	18	1.7	V	54
NGC 4314	2.0	3.74	117 ± 4	115 ± 4	13	21.0	V	54
NGC 4321	2.0	3.74	92 ± 4	90 ± 4	13	20.7	V	54
NGC 4335	0.38	1.0	308 ± 6	289 ± 6	37	15.0	K	53
NGC 4343	...	...	...	...	...	...	...	...
NGC 4374	2.0	3.74	308 ± 7	291 ± 7	13	50.9	B	56
NGC 4380	1.2	2.2	65 ± 19	62 ± 18	20	24.5	V	54
NGC 4389	...	...	...	...	...	...	...	...
NGC 4414	2.0	3.74	117 ± 4	125 ± 4	13	2.5	V	54
NGC 4420	...	...	...	...	...	...	...	...
NGC 4429	1.2	2.2	195 ± 8	185 ± 8	15	28.0	V	54
NGC 4435	1.2	2.2	156 ± 7	149 ± 7	15	24.0	V	54
NGC 4450	10.0	3.0	116 ± 16	120 ± 16	38	10.8	V	54
NGC 4459	8.04	...	170 ± 12	179 ± 13	9	16.7	V	54
NGC 4477	1.17	2.0	162 ± 10	154 ± 9	39	24.4	V	54
NGC 4486	7.64	...	355 ± 8	349 ± 8	9	94.9	B	56
NGC 4501	1.2	2.2	151 ± 17	152 ± 17	18	6.0	V	54
NGC 4507	2.	2.46	146 ± 7	156 ± 7	2	3.9	K	53
NGC 4526	3.6	1.25	214 ± 3	208 ± 3	24	19.7	V	54
NGC 4527	...	...	211 ± 10	...	40	5.9	V	54
NGC 4536	1.35	...	185 ± 11	185 ± 11	5	86.5	V	54
NGC 4548	10.0	3.0	155 ± 14	153 ± 14	38	35.2	V	54
NGC 4552	1.2	2.2	268 ± 12	254 ± 11	15	29.3	B	56
NGC 4569	2.0	3.74	136 ± 3	151 ± 3	13	0.9	V	54
NGC 4579	1.2	2.2	127 ± 17	123 ± 16	18	17.0	V	54
NGC 4594	3.8	3.0	237 ± 6	226 ± 6	30	50.9	V	54
NGC 4596	0.9	1.5	155 ± 15	148 ± 14	41	17.4	V	54
NGC 4636	0.56	2.1	200 ± 10	178 ± 9	27	88.5	B	56
NGC 4676A	...	...	...	...	...	...	...	...
NGC 4696	1.1	1.3	256 ± 11	...	22	...	...	...
NGC 4698	2.43	2.5	134 ± 9	129 ± 9	14	29.4	V	54
NGC 4736	2.0	3.74	112 ± 3	106 ± 3	13	45.2	V	54
NGC 4800	2.0	3.7	112 ± 2	111 ± 2	31	15.4	R	66
NGC 4826	1.2	2.2	113 ± 13	115 ± 13	18	5.0	V	54
NGC 5005	1.35	...	210 ± 7	215 ± 8	5	5.8	V	54
NGC 5054	...	...	...	...	...	30.5	R	64
NGC 5055	1.2	2.2	117 ± 7	114 ± 7	18	15.8	V	54
NGC 5077	1.1	1.6	252 ± 12	239 ± 11	22	22.8	B	56
NGC 5127	3.39	...	198 ± 29	194 ± 5	42	40.5	K	53
NGC 5135	2	2.46	128 ± 8	...	2	...	...	...
NGC 5141	...	...	...	...	...	...	...	...
NGC 5194	2.1	1.5	82 ± 11	76 ± 10	12	47.7	V	54
NGC 5247	...	...	...	...	...	8.3	H	58
NGC 5248	...	...	122 ± 10	128 ± 12	43	0.6	R	64
NGC 5252	2.3	1.5	190 ± 27	183 ± 26	12	20.7	J	67

Table 2.2 – Continued

Galaxy	x ($''$)	y ($''$)	$\sigma \pm \delta\sigma$ (km s^{-1})	$\sigma_c \pm \delta\sigma_c$ (km s^{-1})	Ref.	r_e ($''$)	Band	Ref.
(1)	(2)	(3)	(4)	(5)	(6)	(7)	(8)	(9)
NGC 5283	2.3	1.5	148 ± 14	148 ± 14	12	5.4	K	53
NGC 5347	2.3	1.5	73 ± 14	70 ± 13	12	20.5	V	54
NGC 5364	1.2	2.2	95 ± 54	82 ± 46	20	291.7	V	54
NGC 5398	...	...	...	...	...	...	...	...
NGC 5427	2.3	1.5	74 ± 13	70 ± 12	12	29.7	V	54
NGC 5490	1.2	2.2	303 ± 29	292 ± 28	15	18.5	B	56
NGC 5577	...	...	...	...	...	...	...	...
NGC 5635	...	...	...	...	...	...	...	...
NGC 5643	2.	1.5	93 ± 1	97 ± 1	44	2.6	H	58
NGC 5695	2.1	1.5	147 ± 2	148 ± 2	12	7.1	K	53
NGC 5713	...	...	...	...	...	181.3	V	54
NGC 5728	2.24	...	220 ± 46	210 ± 44	45	56.0	V	54
NGC 5746	1.1	1.2	133 ± 8	127 ± 8	46	17.4	B	46
NGC 5879	1.1	1.2	57 ± 8	59 ± 9	46	3.0	B	46
NGC 5905	1.	1.	153 ± 7	134 ± 6	47	127.0	V	54
NGC 5921	2	4	84 ± 9	92 ± 10	4	1.2	V	54
NGC 6300	2.	2.46	92 ± 5	94 ± 5	2	6.0	K	55
NGC 6384	3.5	1.0	122 ± 28	117 ± 27	1	25.9	V	54
NGC 6500	2.0	3.74	214 ± 6	230 ± 6	13	2.1	K	55
NGC 6503	2.0	3.74	46 ± 3	...	13	...	...	...
NGC 6621	...	...	...	...	...	...	...	...
NGC 6861	3.39	...	433 ± 17	419 ± 15	48	9.8	K	53
NGC 6951	12.5	3.2	97 ± 10	104 ± 11	10	5.4	V	54
NGC 7052	0.33	0.8	266 ± 26	239 ± 23	49	34.7	J	67
NGC 7252	2.0	2.0	177 ± 18	172 ± 17	50	19.7	R	57
NGC 7314	2.	1.5	60 ± 1	58 ± 1	44	22.3	R	64
NGC 7331	0.30	1.25	141 ± 5	126 ± 4	21	48.6	V	54
NGC 7592	...	...	...	...	...	...	...	...
NGC 7626	3.8	3.0	262 ± 12	253 ± 11	30	38.7	B	56
NGC 7682	2.3	1.5	123 ± 17	122 ± 17	12	9.3	K	53
UGC 1214	2.3	1.5	123 ± 16	116 ± 15	12	37.0	I	59
UGC 1395	2	2.34	66 ± 6	70 ± 6	2	3.4	K	53
UGC 1841	0.335	1.5	348 ± 29	348 ± 29	51	...	...	...
UGC 7115	12.0	3.0	198 ± 37	205 ± 38	52	10.9	B	56
UGC10814	...	...	...	...	...	...	...	...
UGC12064	0.335	1.5	279 ± 19	281 ± 19	51	3.7	K	53

NOTES. — Col.(1): Galaxy name. Col.(2): x dimension of the rectangular aperture, or radius of the circular aperture if no value is given in Col.(3). Col.(3): y dimension of the rectangular aperture. Col.(4): Central velocity dispersion of the stellar component within the rectangular (or circular) aperture indicated in Col.(2) and Col.(3). Col.(5): Central velocity dispersion of the stellar component within $r_e/8$. Col.(6): Reference for the measured stellar velocity dispersion and for the corresponding size of the central aperture from which we calculated the value given in Col.(5) by following Jørgensen et al. (1995). We did not apply any aperture correction to the measured stellar velocity dispersions of NGC 520, NGC 2748, NGC 3067, NGC 3162, NGC 3256, NGC 3756, NGC 3921, NGC 3982, NGC 4696, NGC 5135, NGC 6503, and UGC 1841, because no information about the effective radius was available. Col.(7): Effective radius of the spheroidal component. Col.(8): Band in which the effective radius was measured. Col.(9): Reference for Col.(7).

REFERENCES. — (1) Terlevich et al. (1990); (2) Garcia-Rissmann et al. (2005); (3) Wegner et al. (2003); (4) Ho et al. (2009); (5) Batcheldor et al. (2005); (6) Davies et al. (1987); (7) Simien & Prugniel (1997a); (8) Standord & Balcells (1990); (9) Bernardi et al. (2002); (10) Schechter (1983); (11) Bonfanti et al. (1995); (12) Nelson & Whittle (1995); (13) Barth et al. (2002); (14) Corsini et al. (1999); (15) Simien & Prugniel (1997b); (16) Shier et al. (1996); (17) Simien & Prugniel (1997c); (18) Héraudeau & Simien (1998); (19) di Nella et al. (1995); (20) Héraudeau et al. (1999); (21) Vega Beltrán et al. (2001); (22) Carollo et al. (1993); (23) Simien & Prugniel (1998); (24) Proctor & Sansom (2002); (25) Oliva et al. (1995); (26) Whitmore et al. (1979); (27) Bender et al. (1994); (28) Arribas et al. (1997); (29) Zeilinger et al. (2001); (30) Smith et al. (2000); (31) Sarzi et al. (2002); (32) Fisher (1997); (33) Ganda et al. (2006); (34) Jore et al. (1996); (35) Simien & Prugniel (2002); (36) Falcón-Barroso et al. (2006); (37) Verdoes Kleijn et al. (2002); (38) Whitmore & Kirshner (1981); (39) Jarvis et al. (1988); (40) Ho (2007); (41) Bettoni & Galletta (1997); (42) Noel-Storr et al. (2007); (43) Dumas et al. (2007); (44) Gu et al. (2006); (45) Wagner & Appenzeller (1988); (46) Falcón-Barroso et al. (2002); (47) Moiseev et al. (2004); (48) Koprolin & Zeilinger (2000); (49) van den Bosch & van der Marel (1995); (50) Lake & Dressler (1986); (51) Balcells et al. (1995); (52) Tonry & Davis (1981); (53) r_e from our photometric decomposition of 2MASS images (see Section 2.4.1); (54) Baggett et al. (1998); (55) Kassin et al. (2006); (56) de Vaucouleurs et al. (1991); (57) de Souza et al. (2004); (58) Laurikainen et al. (2004); (59) Xanthopoulos (1996); (60) Laurikainen et al. (2005); (61) Fisher et al. (1995); (62) Hinz & Rieke (2006); (63) Kodaira et al. (1990); (64) Scarlata et al. (2004); (6565) Kent (1985)65; (66) Andredakis & Sanders (1994); (67) Marconi & Hunt (2003).

Table 2.3: Summary of STIS Observations

Galaxy	Program GO ID	UT Date	Slit Or.	Aperture		Binning	n	Exp. Time	Quality	Brightest Row	σ_g
			(° E of N)	(″)	(pc)			(s)			(km s^{-1})
(1)	(2)	(3)	(4)	(5)	(6)	(7)	(8)	(9)	(10)	(11)	(12)
IC 0342	8591	2001-09-22	−166.1	0.15 × 0.1	3 × 2	1 × 1	2	2880	yes	602	60 ± 4
IC 3639	9143	2002-01-23	−104.0	0.25 × 0.2	58 × 47	1 × 1	3	3138	yes	601	96 ± 3
IC 5096	9046	2002-02-18	146.1	0.15 × 0.1	29 × 19	1 × 1	1	1027	ns	601	...
NGC 0134	8228	2000-07-07	−132.9	0.25 × 0.2	21 × 17	1 × 1	2	786	ns	601	...
NGC 0157	8228	1999-11-03	29.1	0.15 × 0.1	13 × 9	1 × 1	2	840	ns	601	...
NGC 0193	8236	1999-10-03	58.0	0.30 × 0.2	77 × 52	2 × 2	2	1300	yes	301	183 ± 14
NGC 0255	8228	1999-10-26	18.1	0.15 × 0.1	12 × 8	1 × 1	2	840	ns	601	...
NGC 0278	7361	1998-12-10	47.6	0.25 × 0.2	6 × 5	1 × 1	3	2914	r	601	...
NGC 0289	8228	2000-10-25	−31.9	0.25 × 0.2	22 × 18	1 × 1	2	786	yes	601	79 ± 6
NGC 0315	8236	2000-06-18	−143.7	0.15 × 0.1	45 × 30	2 × 1	2	1000	yes	598	335 ± 11
NGC 0383	8236	2000-10-15	144.5	0.15 × 0.1	46 × 31	2 × 1	2	1000	yes	599	248 ± 19
NGC 0520	8669	2001-10-15	−37.7	0.30 × 0.2	37 × 25	2 × 2	2	1530	ir	301	...
NGC 0541	8236	1999-10-05	−85.5	0.30 × 0.2	99 × 66	2 × 2	2	1300	yes	300	206 ± 17
NGC 0613	8228	2000-09-22	−70.7	0.25 × 0.2	20 × 16	1 × 1	2	720	yes	600	151 ± 9
NGC 0741	8236	1999-10-08	−107.3	0.30 × 0.2	102 × 68	2 × 2	2	1145	yes	300	496 ± 44
NGC 0788	9143	2001-10-14	−119.8	0.25 × 0.2	62 × 50	1 × 1	3	3000	yes	602	159 ± 5
NGC 1052	7403	1999-01-02	13.8	0.25 × 0.2	24 × 19	1 × 1	1	1973.9	yes	601	226 ± 5
NGC 1097	9782	2004-07-25	−149.9	0.25 × 0.2	18 × 14	1 × 1	4	4740	ds	600	...
NGC 1255	8228	1999-10-17	−62.9	0.15 × 0.1	15 × 10	1 × 1	2	840	n	601	...
NGC 1300	8228	2000-10-29	−69.9	0.25 × 0.2	23 × 18	1 × 1	2	740	p	601	...
NGC 1358	9143	2002-01-25	24.3	0.25 × 0.2	63 × 50	1 × 1	3	3000	yes	602	176 ± 1
NGC 1497	7354	1997-11-23	159.3	0.15 × 0.1	59 × 39	2 × 1	1	442	yes	601	276 ± 18
NGC 1667	9143	2001-10-14	−119.8	0.25 × 0.2	73 × 58	1 × 1	3	3000	yes	601	97 ± 1
NGC 1832	8228	2000-07-22	−169.9	0.25 × 0.2	31 × 25	1 × 1	2	738	ns	601	...
NGC 1961	9106	2001-12-27	104.1	0.30 × 0.2	76 × 51	1 × 2	2	4963	yes	299	167 ± 4
NGC 2110	8610	2000-12-30	−23.9	0.25 × 0.2	38 × 30	2 × 1	1	1440	yes	601	242 ± 4
NGC 2179	9068	2002-01-28	0.1	0.25 × 0.2	47 × 37	1 × 1	3	3007	yes	601	137 ± 8
NGC 2273	9143	2001-11-04	−151.2	0.25 × 0.2	30 × 24	1 × 1	2	2366	yes	600	27 ± 1
NGC 2329	8236	2000-12-15	171.2	0.30 × 0.2	113 × 75	2 × 2	2	1245	yes	300	201 ± 8
NGC 2623	8669	2002-02-05	92.7	0.30 × 0.2	112 × 74	2 × 2	2	1600	i	301	...
NGC 2654	9046	2003-10-22	−118.0	0.15 × 0.1	14 × 9	1 × 1	9	4500	yes s	585	67 ± 15
NGC 2685	8607	2001-05-06	54.4	0.30 × 0.2	19 × 13	1 × 2	1	3097	yes	301	69 ± 4
NGC 2748	8228	2000-11-09	−141.9	0.25 × 0.2	24 × 19	1 × 1	2	864	yes	608	43 ± 4
NGC 2787	7361	1998-12-05	−146.8	0.25 × 0.2	9 × 7	1 × 1	3	3012	yes	600	209 ± 6
NGC 2892	8236	2000-02-06	142.1	0.30 × 0.2	133 × 89	2 × 2	2	1300	yes	300	270 ± 13
NGC 2903	8228	2000-02-03	−162.9	0.30 × 0.2	16 × 11	2 × 2	2	720	yes	301	74 ± 4
NGC 2911	7354	1998-12-03	−122.9	0.15 × 0.1	34 × 23	2 × 1	1	486	yes	601	400 ± 38
NGC 2964	8228	2000-10-04	−102.9	0.25 × 0.2	26 × 20	1 × 1	2	864	yes	600	80 ± 4
NGC 2976	8591	2001-03-12	89.7	0.25 × 0.2	2 × 1	1 × 1	1	1176	res	600	15 ± 3
NGC 3003	8228	2000-03-20	79.1	0.30 × 0.2	34 × 22	2 × 2	2	822	yes s	301	46 ± 7
NGC 3021	8228	2000-04-24	80.1	0.25 × 0.2	29 × 23	1 × 1	2	786	yes	601	69 ± 4
NGC 3031	7351	1999-07-14	−2.0	0.15 × 0.1	3 × 2	1 × 1	1	1000	yes	601	192 ± 1
NGC 3049	7513	1999-01-18	−137.9	0.15 × 0.1	18 × 12	1 × 1	1	972	yes s	601	41 ± 2
NGC 3067	8596	2001-03-02	124.3	0.25 × 0.2	28 × 23	1 × 1	1	2244	yes	601	45 ± 8
NGC 3078	9163	2002-03-25	6.5	0.30 × 0.2	51 × 34	2 × 2	2	1600	yes	300	192 ± 6
NGC 3081	9143	2001-12-04	−110.1	0.25 × 0.2	44 × 35	1 × 1	3	3000	yes	601	52 ± 1

Table 2.3 – Continued

Galaxy	Program ID	UT Date	Slit Or.	Aperture		Binning	n	Exp. Time	Quality	Brightest	σ_g
			(° E of N)	($''$)	(pc)			(s)		Row	(km s^{-1})
(1)	(2)	(3)	(4)	(5)	(6)	(7)	(8)	(9)	(10)	(11)	(12)
NGC 3162	8228	2000-01-27	−159.9	0.30 × 0.2	31 × 21	2 × 2	2	720	r	301	...
NGC 3227	7403	1999-01-31	−137.5	0.25 × 0.2	24 × 19	1 × 1	1	1890	yes	600	117 ± 3
NGC 3245	7403	1999-02-02	−157.6	0.25 × 0.2	25 × 20	1 × 1	1	2714.9	yes	602	138 ± 8
NGC 3254	8228	2000-12-05	−133.9	0.25 × 0.2	26 × 21	1 × 1	2	764	n	601	...
NGC 3256	8669	2002-01-05	−91.0	0.25 × 0.2	49 × 40	1 × 1	2	680	i	597	...
NGC 3259	8228	2000-07-09	20.1	0.25 × 0.2	29 × 23	1 × 1	2	864	yes s	601	41 ± 2
NGC 3310	8228	2000-02-11	170.1	0.30 × 0.2	23 × 15	2 × 2	2	864	yes	301	46 ± 1
NGC 3351	7361	1998-12-25	−114.4	0.25 × 0.2	12 × 10	1 × 1	3	2699	yes	601	45 ± 2
NGC 3368	7361	1998-10-31	−110.5	0.25 × 0.2	13 × 10	1 × 1	3	2703	yes	601	97 ± 4
NGC 3379	8589	2001-12-28	−104.7	0.25 × 0.2	13 × 10	1 × 1	3	6418	yes	601	107 ± 9
NGC 3393	8055	1999-04-22	40.1	0.25 × 0.2	66 × 53	1 × 1	2	1465	yes	601	91 ± 3
NGC 3403	8228	2000-10-30	−106.9	0.25 × 0.2	21 × 17	1 × 1	2	864	ns	601	...
NGC 3489	7361	1999-01-23	−120.9	0.25 × 0.2	15 × 12	1 × 1	3	2569	yes	601	100 ± 6
NGC 3516	8055	2000-06-18	39.1	0.25 × 0.2	44 × 35	1 × 1	2	684	d	601	...
NGC 3521	8228	2000-03-03	−36.9	0.30 × 0.2	23 × 15	2 × 2	2	720	n	300	...
NGC 3627	8607	2001-05-02	80.1	0.30 × 0.2	15 × 10	1 × 2	1	2861	yes	300	79 ± 2
NGC 3642	8228	2000-10-13	−74.9	0.25 × 0.2	28 × 23	1 × 1	2	864	yes	601	147 ± 11
NGC 3675	8607	2001-01-24	−154.1	0.30 × 0.2	19 × 13	1 × 2	1	2984	yes	299	80 ± 4
NGC 3684	8228	2000-03-25	100.1	0.30 × 0.2	29 × 19	2 × 2	2	864	n	301	...
NGC 3686	8228	2001-02-17	−164.9	0.25 × 0.2	24 × 19	1 × 1	2	738	r	601	...
NGC 3705	8607	2000-07-16	59.7	0.30 × 0.2	26 × 18	1 × 2	1	2861	star	301	...
NGC 3756	8228	2001-01-24	−177.9	0.25 × 0.2	24 × 19	1 × 1	2	864	n	601	...
NGC 3801	8236	2000-03-27	121.2	0.30 × 0.2	72 × 48	2 × 2	2	1292.8	yes	305	166 ± 10
NGC 3862	8236	2001-03-26	122.7	0.30 × 0.2	132 × 88	2 × 2	2	731	yes	300	188 ± 7
NGC 3887	8228	2000-04-02	12.1	0.30 × 0.2	30 × 20	2 × 2	2	720	yes s	301	58 ± 10
NGC 3917	8607	2001-05-03	93.0	0.30 × 0.2	22 × 15	1 × 2	1	3073	ns	301	...
NGC 3921	8669	2002-07-28	20.1	0.25 × 0.2	97 × 78	1 × 1	2	720	i	596	...
NGC 3949	8228	2000-04-04	112.5	0.30 × 0.2	20 × 13	2 × 2	2	864	n	301	...
NGC 3953	8228	2000-02-11	−171.9	0.30 × 0.2	24 × 16	2 × 2	2	792	yes*	301	103 ± 6
	8607	2001-05-05	79.1	0.30 × 0.2	24 × 16	1 × 2	1	3073	yes	301	84 ± 7
NGC 3972	8228	2000-10-02	−59.9	0.25 × 0.2	16 × 13	1 × 1	2	864	ns	601	...
NGC 3982	7361	1998-04-11	117.9	0.25 × 0.2	21 × 17	1 × 1	3	2997	yes	602	49 ± 2
NGC 3992	7361	1999-02-19	155.3	0.25 × 0.2	20 × 16	1 × 1	3	2945	yes	601	103 ± 3
NGC 3998	7354	1997-11-01	−81.7	0.15 × 0.1	10 × 7	2 × 1	1	328	yes*	601	426 ± 11
	9486	2002-04-07	117.1	0.15 × 0.1	10 × 7	2 × 1	4	520	yes	596	455 ± 10
NGC 4030	8228	2000-02-20	−137.9	0.30 × 0.2	35 × 23	2 × 2	2	860	r	301	...
NGC 4036	7403	1999-03-25	133.5	0.25 × 0.2	25 × 20	1 × 1	1	2896	yes	601	205 ± 5
NGC 4038	8669	2002-04-21	11.0	0.30 × 0.2	38 × 25	2 × 2	2	620	is	476	...
NGC 4039	8669	2002-01-24	−84.9	0.30 × 0.2	39 × 26	2 × 2	2	660	is	301	...
NGC 4041	8228	1999-07-02	43.1	0.25 × 0.2	22 × 18	1 × 1	2	957	yes	601	36 ± 2
NGC 4051	8228	2000-03-12	132.9	0.10 × 0.1	6 × 6	2 × 2	2	864	r	301	...
NGC 4088	8228	2000-07-09	43.1	0.25 × 0.2	15 × 12	1 × 1	2	838	yes	602	50 ± 5
NGC 4100	8228	2000-02-26	149.1	0.30 × 0.2	25 × 16	2 × 2	2	864	r	301	...
NGC 4138	1039	1999-03-03	165.7	0.25 × 0.2	17 × 13	1 × 1	3	2856	star	601	...
NGC 4143	7361	1999-03-20	139.0	0.25 × 0.2	19 × 15	1 × 1	3	2856	yes	601	211 ± 3
NGC 4150	8607	2001-01-28	−119.9	0.30 × 0.2	20 × 13	1 × 2	1	2907	yes	301	69 ± 9
NGC 4203	7361	1999-04-18	105.6	0.25 × 0.2	18 × 15	1 × 1	3	2779	yes	601	139 ± 3
NGC 4212	8228	2000-05-12	74.8	0.25 × 0.2	4 × 3	1 × 1	2	740	yes	601	59 ± 5

Table 2.3 – Continued

Galaxy	Program ID	UT Date	Slit Or. (° E of N)	Aperture ($''$)	Aperture (pc)	Binning	n	Exp. Time (s)	Quality	Brightest Row	σ_g (km s^{-1})
(1)	(2)	(3)	(4)	(5)	(6)	(7)	(8)	(9)	(10)	(11)	(12)
NGC 4245	7361	1999-04-18	85.7	0.25 × 0.2	19 × 15	1 × 1	3	2697	yes	600	117 ± 24
NGC 4258	8228	2000-08-01	25.1	0.25 × 0.2	9 × 7	1 × 1	2	864	yes*	601	175 ± 3
	8591	2001-03-16	146.4	0.15 × 0.1	5 × 4	1 × 1	1	1440	yes	601	200 ± 5
NGC 4261	8236	2000-03-26	158.0	0.15 × 0.1	23 × 15	2 × 1	2	1000	yes	601	188 ± 8
NGC 4278	7403	2000-05-11	88.0	0.25 × 0.2	19 × 16	1 × 1	1	3127.9	yes	600	333 ± 8
NGC 4303	8228	2000-03-31	135.1	0.30 × 0.2	37 × 25	2 × 2	2	720	r	301	...
NGC 4314	7361	1999-04-19	105.3	0.25 × 0.2	20 × 16	1 × 1	3	2697	yes	601	56 ± 5
NGC 4321	7361	1999-04-23	92.9	0.25 × 0.2	18 × 15	1 × 1	3	2671	yes*	601	65 ± 1
	8228	2000-05-22	60.1	0.25 × 0.2	18 × 15	1 × 1	2	738	yes	602	52 ± 2
NGC 4335	8236	1999-09-22	−32.4	0.30 × 0.2	92 × 61	2 × 2	2	1300	yes	300	171 ± 8
NGC 4343	9068	2002-03-25	144.1	0.25 × 0.2	22 × 17	1 × 1	3	2925	yes s	601	82 ± 13
NGC 4374	7124	1997-04-14	104.1	0.25 × 0.2	22 × 18	1 × 1	2	5181	yes	601	396 ± 14
NGC 4380	7361	1998-12-24	−119.8	0.25 × 0.2	21 × 17	1 × 1	3	2699	n	601	...
NGC 4389	8228	1999-10-26	−74.9	0.15 × 0.1	9 × 6	1 × 1	2	846	ns	601	...
NGC 4414	8607	2001-04-18	125.1	0.30 × 0.2	26 × 17	1 × 2	1	2907	n	301	...
NGC 4420	8228	2000-03-18	−161.9	0.30 × 0.2	39 × 26	2 × 2	2	720	yes s	301	54 ± 30
NGC 4429	8607	2001-04-16	81.1	0.30 × 0.2	28 × 19	1 × 2	1	2861	yes	301	134 ± 5
NGC 4435	7361	1999-04-26	89.6	0.25 × 0.2	18 × 14	1 × 1	3	2673	yes*	601	98 ± 4
	9068	2003-03-09	−167.5	0.25 × 0.2	18 × 14	1 × 1	3	3012	yes	600	82 ± 5
NGC 4450	7361	1999-01-31	−127.0	0.25 × 0.2	37 × 29	1 × 1	3	2697	yes	601	138 ± 3
NGC 4459	7361	1999-04-23	92.9	0.25 × 0.2	20 × 16	1 × 1	3	2673	yes	601	216 ± 9
NGC 4477	7361	1999-04-23	92.8	0.25 × 0.2	27 × 22	1 × 1	3	2612	yes	601	110 ± 2
NGC 4486	8666	2001-03-25	165.1	0.25 × 0.2	19 × 15	1 × 1	3	3420	yes	601	630 ± 14
NGC 4501	7361	1999-04-26	91.9	0.25 × 0.2	42 × 34	1 × 1	3	2673	yes	601	99 ± 1
NGC 4507	9143	2001-11-29	−138.5	0.25 × 0.2	61 × 49	1 × 1	2	2195	yes	601	54 ± 3
NGC 4526	9163	2002-04-23	108.4	0.25 × 0.2	20 × 16	2 × 1	5	4050	yes	598	320 ± 11
NGC 4527	8228	1999-07-13	67.1	0.15 × 0.1	20 × 13	1 × 1	2	840	n	602	...
	8607	2001-04-16	73.1	0.15 × 0.1	20 × 13	1 × 2	1	2861	yes	301	116 ± 9
NGC 4536	8228	2000-03-26	140.1	0.30 × 0.2	22 × 14	2 × 2	2	720	r	301	...
NGC 4548	7361	1999-04-26	73.2	0.25 × 0.2	23 × 19	1 × 1	3	2673	yes	601	77 ± 2
NGC 4552	8472	2000-06-19	78.1	0.25 × 0.2	19 × 15	1 × 1	2	4100	yes	601	476 ± 18
NGC 4569	8607	2001-04-17	100.0	0.30 × 0.2	2 × 1	1 × 2	1	2861	r	301	...
NGC 4579	7403	1999-04-21	95.4	0.25 × 0.2	30 × 24	1 × 1	1	2692	yes	600	231 ± 2
NGC 4594	7354	1999-02-05	−110.4	0.15 × 0.1	7 × 5	2 × 1	1	280	yes	601	489 ± 20
NGC 4596	7361	1998-12-20	−109.7	0.25 × 0.2	36 × 28	1 × 1	3	2699	yes	601	162 ± 11
NGC 4636	8472	2001-04-02	142.1	0.25 × 0.2	18 × 14	1 × 1	2	3590	yes	600	254 ± 13
NGC 4676A	8669	2002-02-20	−164.9	0.30 × 0.2	134 × 89	2 × 2	2	1660	is	299	...
NGC 4696	8690	2001-02-27	−64.9	0.25 × 0.2	43 × 34	1 × 1	1	2100	n	601	...
NGC 4698	7361	1997-11-24	−101.0	0.25 × 0.2	21 × 17	1 × 1	3	2673	yes	601	92 ± 2
NGC 4736	8591	2002-07-15	50.1	0.15 × 0.1	4 × 3	1 × 1	2	3922	yes	601	90 ± 5
NGC 4800	7361	1999-03-03	177.5	0.25 × 0.2	16 × 13	1 × 1	3	2888	yes	601	95 ± 10
NGC 4826	8591	2001-04-21	110.7	0.25 × 0.2	16 × 13	1 × 1	1	2842	yes	600	100 ± 6
	8607	2000-06-14	88.1	0.30 × 0.2	11 × 7	1 × 2	1	2868	yes*	301	99 ± 4
NGC 5005	8228	2000-12-24	−114.9	0.25 × 0.2	19 × 15	1 × 1	2	734	yes	601	204 ± 3
NGC 5054	8228	2000-04-08	−49.9	0.30 × 0.2	40 × 26	2 × 2	2	720	rs	301	...
NGC 5055	7361	1999-03-21	164.5	0.25 × 0.2	11 × 9	1 × 1	3	2856	n	601	...
	8228	2000-04-16	110.1	0.30 × 0.2	14 × 9	2 × 2	2	864	r	301	...
NGC 5077	7354	1998-03-12	−80.9	0.15 × 0.1	30 × 20	1 × 1	1	418	yes	601	397 ± 13

Table 2.3 – Continued

Galaxy	Program ID	UT Date	Slit Or.	Aperture		Binning	n	Exp. Time	Quality	Brightest	σ_g
			(° E of N)	(″)	(pc)			(s)		Row	(km s^{-1})
(1)	(2)	(3)	(4)	(5)	(6)	(7)	(8)	(9)	(10)	(11)	(12)
NGC 5127	8236	2000-07-08	68.4	0.30 × 0.2	97 × 65	2 × 2	2	1000	yes	301	153 ± 7
NGC 5135	9143	2002-01-11	−115.4	0.25 × 0.2	71 × 57	1 × 1	3	3016	r	601	...
NGC 5141	8236	2000-07-02	72.3	0.30 × 0.2	105 × 70	2 × 2	2	1300	yes s	300	160 ± 5
NGC 5194	9147	2002-04-03	159.1	0.25 × 0.2	10 × 8	2 × 1	2	4990	yes	596	36 ± 2
NGC 5247	8228	2000-05-04	30.1	0.25 × 0.2	27 × 21	1 × 1	2	738	ns	601	...
NGC 5248	8228	2000-04-18	120.1	0.25 × 0.2	23 × 19	1 × 1	2	720	yes	601	45 ± 4
NGC 5252	8055	1999-01-28	−135.4	0.25 × 0.2	116 × 93	1 × 1	2	1441	yes	600	197 ± 6
NGC 5283	9143	2001-10-11	−36.7	0.25 × 0.2	45 × 36	1 × 1	3	3313	yes	601	61 ± 3
NGC 5347	9143	2001-12-24	−101.8	0.25 × 0.2	42 × 34	1 × 1	3	3046	yes	601	53 ± 3
NGC 5364	8228	2000-03-05	−149.9	0.30 × 0.2	29 × 20	2 × 2	2	720	n	301	...
NGC 5398	7513	2000-03-20	−90.9	0.15 × 0.1	14 × 10	1 × 1	1	972	yes s	601	76 ± 7
NGC 5427	9143	2002-01-04	−113.0	0.25 × 0.2	47 × 38	1 × 1	3	3000	yes	600	78 ± 1
NGC 5490	8236	2000-03-19	−173.8	0.30 × 0.2	102 × 68	2 × 2	2	1300	yes	299	278 ± 21
NGC 5577	8228	2000-03-06	−123.9	0.30 × 0.2	34 × 22	2 × 2	2	776	ns	301	...
NGC 5635	7354	1999-02-02	−116.4	0.15 × 0.1	44 × 29	2 × 1	1	484	yes s	601	334 ± 25
NGC 5643	9143	2002-01-13	−127.6	0.25 × 0.2	22 × 18	1 × 1	3	3263	yes	601	95 ± 3
NGC 5695	9143	2001-08-11	51.1	0.25 × 0.2	71 × 57	1 × 1	3	3138	yes	601	67 ± 2
NGC 5713	8228	2000-04-01	−169.9	0.30 × 0.2	41 × 27	2 × 2	2	720	yes s	299	57 ± 6
NGC 5728	8123	1999-07-30	86.2	0.15 × 0.1	29 × 20	1 × 1	3	1530	yes	601	121 ± 7
NGC 5746	9046	2002-05-01	158.1	0.15 × 0.1	19 × 13	1 × 1	1	894	n	601	...
NGC 5879	8228	2000-03-12	−179.9	0.30 × 0.2	16 × 11	2 × 2	2	864	yes	301	64 ± 4
	8607	2001-04-28	160.1	0.30 × 0.2	16 × 11	1 × 2	1	3097	yes*	300	73 ± 4
NGC 5905	9177	2001-12-20	−80.5	0.15 × 0.1	34 × 22	1 × 1	1	2980	p	597	...
NGC 5921	8228	2000-05-20	130.1	0.25 × 0.2	27 × 21	1 × 1	2	720	yes	601	122 ± 5
NGC 6300	9143	2001-11-08	90.7	0.25 × 0.2	18 × 15	1 × 1	3	3206	yes	601	75 ± 5
NGC 6384	8228	2000-03-24	−149.9	0.30 × 0.2	32 × 21	2 × 2	2	776	n	301	...
NGC 6500	7354	1998-11-03	14.8	0.15 × 0.1	28 × 19	2 × 1	1	236	yes	600	168 ± 19
NGC 6503	8607	2001-12-13	−44.9	0.30 × 0.2	0 × 0	1 × 2	1	3197	n	301	...
NGC 6621	8669	2001-12-06	−40.4	0.30 × 0.2	120 × 80	2 × 2	2	740	is	301	...
NGC 6861	9163	2002-08-02	−33.3	0.30 × 0.2	41 × 27	2 × 2	7	5070	yes	300	623 ± 61
NGC 6951	8228	2000-06-17	170.1	0.25 × 0.2	21 × 17	1 × 1	2	864	yes	601	72 ± 1
NGC 7052	8236	1999-09-13	63.7	0.15 × 0.1	45 × 30	2 × 1	2	1300	yes	600	235 ± 14
NGC 7252	8669	2001-09-02	−53.9	0.30 × 0.2	86 × 58	2 × 2	2	680	i	299	...
NGC 7314	8228	2000-04-09	−175.8	0.30 × 0.2	22 × 15	2 × 2	2	792	pr	301	...
NGC 7331	8228	2000-07-03	171.1	0.25 × 0.2	16 × 13	1 × 1	2	786	yes*	601	204 ± 26
	8607	2001-01-13	−1.1	0.30 × 0.2	19 × 13	1 × 2	1	2907	yes	301	132 ± 16
NGC 7592	8669	2001-09-10	−100.9	0.25 × 0.2	113 × 90	1 × 1	2	580	is	597	...
NGC 7626	8236	2000-07-31	171.2	0.30 × 0.2	59 × 40	2 × 2	2	1263	yes	300	279 ± 16
NGC 7682	9143	2001-10-23	18.3	0.25 × 0.2	77 × 62	1 × 1	3	3000	yes	600	112 ± 3
UGC 01214	9143	2001-10-17	−70.8	0.25 × 0.2	78 × 62	1 × 1	3	3000	yes	602	76 ± 1
UGC 01395	9143	2001-12-20	21.7	0.25 × 0.2	79 × 63	1 × 1	3	3000	yes	601	24 ± 3
UGC 01841	8236	1999-11-11	90.1	0.30 × 0.2	117 × 78	2 × 2	2	1300	yes	300	330 ± 26
UGC 07115	8236	2001-02-17	−174.0	0.30 × 0.2	137 × 92	2 × 2	3	2058	yes	300	318 ± 14
UGC 10814	9782	2003-11-20	−19.9	0.15 × 0.1	69 × 46	1 × 1	4	4488	ds	599	...
	9782	2004-01-30	−94.3	0.15 × 0.1	69 × 46	1 × 1	4	4450	ds	599	...
UGC 12064	8236	2000-07-19	171.0	0.15 × 0.1	47 × 31	2 × 1	2	1000	yes	599	426 ± 21

NOTES. — Col.(1): Galaxy name. Col.(2): *HST* proposal number under which the STIS/G750M spectrum was obtained. Col.(3): Observation date. Col.(4): Position angle of the STIS slit. Col.(5): Size of the central aperture where we measured the velocity dispersion of the ionized gas. Col.(6): Physical size of the central aperture where we measured the velocity dispersion of the ionized gas. Col.(7): Pixel binning. Col.(8): Number of coadded spectra. Col.(9): Exposure time of the combined spectrum. Col.(10): Quality of the fit. yes= successful spectrum fit with stellar velocity dispersion available in literature (in the case of two different proposals for the same object we have marked with * the emission line width we used), d = problem in deblending the emission lines, i = interacting galaxy, n = faint or absent emission lines, p = double-peaked emission lines, r = unsuccessful two-dimensional rectification of the spectrum, yes s = successful spectrum fit with no stellar velocity dispersion available in literature, res = the observed velocity dispersion too close to the resolution limit of *HST*, star= stellar spectrum accidentally acquired instead of the galaxy. Col.(11): Location of the brightest row of the spectrum. Col.(12): Central velocity dispersion of the ionized-gas component within the aperture in Col.(5). This is the intrinsic velocity dispersion obtained from the observed one by subtracting the instrumental velocity dispersion.

Table 2.4 Structural parameters derived from the 2MASS images with GASP2D

Name	μ_e (mag arcsec^{-2})	r_e ($''$)	n	q_b	PA_b ($^\circ$)	μ_0 (mag arcsec^{-2})	h ($''$)	q_d	PA_d ($^\circ$)	B/T	$m_{K,tot}$ (mag)
(1)	(2)	(3)	(4)	(5)	(6)	(7)	(8)	(9)	(10)	(11)	(12)
IC 342	19.23 ± 0.05	64.07 ± 0.46	7.10 ± 0.15	0.92 ± 0.01	173.63 ± 1.06	17.85 ± 0.04	202.64 ± 0.91	0.79 ± 0.01	0.81 ± 0.01	0.13	6.59 ± 0.13
IC 3639	15.66 ± 0.21	3.47 ± 0.46	2.78 ± 0.24	0.55 ± 0.05	143.00 ± 5.67	16.78 ± 0.21	9.47 ± 1.21	0.76 ± 0.04	40.34 ± 8.86	0.44	10.45 ± 0.21
NGC 193	15.92 ± 0.09	3.46 ± 0.47	1.39 ± 0.03	0.92 ± 0.02	66.63 ± 2.41	16.78 ± 0.09	12.17 ± 0.15	0.80 ± 0.02	54.90 ± 1.12	0.31	10.47 ± 0.10
NGC 315	18.59 ± 0.04	39.36 ± 0.26	3.90 ± 0.04	0.73 ± 0.01	45.15 ± 0.09	...	...	...	...	1	7.58 ± 0.46
NGC 383	16.19 ± 0.05	6.50 ± 0.49	2.09 ± 0.07	0.88 ± 0.01	144.16 ± 0.31	17.86 ± 0.05	25.08 ± 0.31	0.90 ± 0.02	143.37 ± 0.06	0.45	9.22 ± 0.07
NGC 741	19.16 ± 0.02	39.50 ± 0.49	4.62 ± 0.03	0.79 ± 0.01	88.93 ± 0.05	...	...	...	...	1	7.97 ± 0.37
NGC 788	17.00 ± 0.09	3.86 ± 0.52	5.73 ± 0.19	0.82 ± 0.02	122.17 ± 4.41	15.91 ± 0.09	9.08 ± 0.12	0.79 ± 0.02	109.84 ± 2.41	0.23	10.71 ± 0.39
NGC 1052	17.70 ± 0.02	31.28 ± 0.39	4.78 ± 0.03	0.71 ± 0.01	115.26 ± 0.06	...	...	...	...	1	7.12 ± 0.42
NGC 1358	16.52 ± 0.05	6.10 ± 0.46	3.13 ± 0.08	0.72 ± 0.01	131.66 ± 0.28	18.79 ± 0.05	41.51 ± 0.52	0.93 ± 0.02	46.13 ± 0.02	0.30	9.68 ± 0.10
NGC 1497	19.54 ± 0.21	19.51 ± 2.63	6.65 ± 0.57	0.90 ± 0.07	44.40 ± 6.04	17.13 ± 0.21	13.22 ± 1.69	0.39 ± 0.02	55.37 ± 9.16	0.71	9.55 ± 0.53
NGC 2892	20.01 ± 0.03	35.45 ± 0.45	6.12 ± 0.03	0.94 ± 0.01	3.55 ± 0.18	...	...	...	–	1	8.72 ± 0.33
NGC 3031	18.27 ± 0.05	156.42 ± 1.13	5.80 ± 0.11	0.73 ± 0.01	147.41 ± 0.90	16.53 ± 0.05	131.16 ± 0.89	0.39 ± 0.01	153.04 ± 0.01	0.70	4.05 ± 0.36
NGC 3078	17.49 ± 0.02	21.41 ± 0.26	4.81 ± 0.04	0.75 ± 0.01	177.30 ± 0.09	...	...	...	...	1	7.66 ± 0.46
NGC 3081	15.56 ± 0.08	4.18 ± 0.32	1.18 ± 0.04	0.71 ± 0.00	113.56 ± 0.24	17.57 ± 0.12	36.77 ± 4.58	0.42 ± 0.01	66.61 ± 0.03	0.22	10.05 ± 0.08
NGC 3245	14.79 ± 0.07	4.47 ± 0.45	2.74 ± 0.13	0.63 ± 0.01	175.76 ± 5.57	16.30 ± 0.04	21.97 ± 0.16	0.49 ± 0.01	177.83 ± 2.42	0.39	8.86 ± 0.10
NGC 3351	15.26 ± 0.05	7.39 ± 0.53	0.98 ± 0.04	0.83 ± 0.01	6.90 ± 0.04	16.77 ± 0.05	37.53 ± 0.40	1.00 ± 0.01	180.01 ± 0.01	0.20	8.44 ± 0.07
NGC 3368	14.70 ± 0.05	6.99 ± 0.50	1.67 ± 0.06	0.74 ± 0.01	165.42 ± 1.01	15.58 ± 0.05	29.49 ± 0.31	0.65 ± 0.01	130.25 ± 0.01	0.25	7.87 ± 0.07
NGC 3379	17.72 ± 0.02	47.02 ± 0.33	5.01 ± 0.05	0.88 ± 0.01	70.31 ± 0.01	...	...	...	...	1	5.99 ± 0.29
NGC 3393	17.22 ± 0.08	8.74 ± 0.32	3.84 ± 0.04	0.72 ± 0.00	159.32 ± 0.24	19.28 ± 0.12	104.05 ± 4.58	0.22 ± 0.01	115.00 ± 0.03	0.35	9.50 ± 0.08
NGC 3489	15.54 ± 0.05	8.38 ± 0.84	3.36 ± 0.16	0.78 ± 0.01	61.90 ± 5.63	16.47 ± 0.12	26.02 ± 0.93	0.43 ± 0.01	71.36 ± 9.72	0.60	7.89 ± 0.18
NGC 3642	18.07 ± 0.09	6.26 ± 0.85	7.82 ± 0.17	0.94 ± 0.02	134.97 ± 4.88	16.94 ± 0.09	12.39 ± 0.16	0.95 ± 0.03	161.04 ± 3.54	0.31	10.41 ± 0.78
NGC 3801	16.65 ± 0.05	5.47 ± 0.41	2.61 ± 0.09	0.85 ± 0.01	118.84 ± 0.26	16.73 ± 0.04	15.65 ± 0.19	0.55 ± 0.01	120.63 ± 0.05	0.38	9.96 ± 0.09
NGC 3953	17.73 ± 0.05	20.19 ± 0.15	3.78 ± 0.04	0.61 ± 0.01	45.16 ± 0.27	17.06 ± 0.05	54.27 ± 0.58	0.44 ± 0.01	11.45 ± 0.01	0.27	8.38 ± 0.10
NGC 3998	14.44 ± 0.07	4.98 ± 0.50	2.20 ± 0.03	0.82 ± 0.01	132.77 ± 4.21	16.67 ± 0.04	25.29 ± 0.19	0.78 ± 0.02	138.40 ± 1.88	0.46	8.09 ± 0.09
NGC 4036	15.48 ± 0.07	4.78 ± 0.48	2.60 ± 0.02	0.85 ± 0.01	68.50 ± 2.17	15.18 ± 0.04	19.63 ± 0.14	0.33 ± 0.01	81.64 ± 1.11	0.25	9.10 ± 0.07
NGC 4041	16.26 ± 0.08	9.05 ± 0.68	1.17 ± 0.04	0.78 ± 0.00	95.93 ± 0.21	17.63 ± 0.12	23.17 ± 2.89	0.67 ± 0.01	22.01 ± 0.01	0.56	8.98 ± 0.06
NGC 4143	14.36 ± 0.07	3.35 ± 0.34	1.82 ± 0.09	0.80 ± 0.01	156.42 ± 4.96	15.53 ± 0.04	15.35 ± 0.11	0.53 ± 0.01	145.23 ± 1.98	0.34	8.99 ± 0.07
NGC 4150	15.05 ± 0.06	3.85 ± 0.14	2.62 ± 0.04	0.80 ± 0.01	142.54 ± 0.79	16.45 ± 0.02	13.35 ± 0.44	0.57 ± 0.01	144.93 ± 0.02	0.41	9.85 ± 0.07
NGC 4203	15.75 ± 0.07	8.10 ± 0.81	3.13 ± 0.05	0.83 ± 0.01	6.73 ± 2.13	17.57 ± 0.04	35.11 ± 0.26	0.94 ± 0.02	176.88 ± 2.41	0.44	8.16 ± 0.14
NGC 4245	15.66 ± 0.05	4.38 ± 0.33	1.41 ± 0.05	0.83 ± 0.01	160.12 ± 0.35	16.72 ± 0.04	22.41 ± 0.28	0.59 ± 0.01	139.32 ± 0.06	0.24	9.78 ± 0.08
NGC 4261	17.81 ± 0.02	32.90 ± 0.41	4.06 ± 0.03	0.79 ± 0.01	159.62 ± 0.08	...	...	...	...	1	7.09 ± 0.32
NGC 4278	16.90 ± 0.02	20.86 ± 0.26	3.71 ± 0.03	0.88 ± 0.01	18.17 ± 0.01	...	...	...	...	1	7.10 ± 0.27
NGC 4258	20.29 ± 0.05	141.62 ± 0.92	7.74 ± 0.28	0.59 ± 0.01	135.23 ± 0.82	16.36 ± 0.05	75.18 ± 0.80	0.47 ± 0.01	169.31 ± 0.01	0.37	6.38 ± 0.31
NGC 4335	18.01 ± 0.03	14.98 ± 0.19	5.05 ± 0.02	0.81 ± 0.01	150.97 ± 7.52	...	...	...	...	1	8.85 ± 0.25
NGC 4343	19.65 ± 0.05	32.14 ± 0.24	7.90 ± 0.27	0.62 ± 0.01	135.63 ± 0.29	15.88 ± 0.04	13.46 ± 0.17	0.20 ± 0.01	129.81 ± 0.05	0.73	8.88 ± 0.55

Table 2.4 – Continued

Name	μ_e	r_e	n	q_b	PA_b	μ_0	h	q_d	PA_d	B/T	$m_{K,tot}$
	(mag arcsec^{-2})	($''$)			($^\circ$)	(mag arcsec^{-2})	($''$)		($^\circ$)		(mag)
(1)	(2)	(3)	(4)	(5)	(6)	(7)	(8)	(9)	(10)	(11)	(12)
NGC 4374	17.87 ± 0.01	52.01 ± 0.37	4.56 ± 0.02	0.87 ± 0.01	126.53 ± 0.01	...	...	...	...	1	5.99 ± 0.25
NGC 4435	16.34 ± 0.05	15.23 ± 0.11	3.23 ± 0.02	0.57 ± 0.01	9.34 ± 0.06	18.93 ± 0.05	97.96 ± 0.94	0.67 ± 0.01	18.26 ± 0.01	0.42	7.76 ± 0.11
NGC 4450	17.24 ± 0.07	13.36 ± 0.13	4.39 ± 0.05	0.75 ± 0.01	172.67 ± 5.48	16.53 ± 0.04	37.33 ± 0.28	0.49 ± 0.01	5.74 ± 0.78	0.28	8.48 ± 0.15
NGC 4459	18.22 ± 0.02	41.19 ± 0.37	5.19 ± 0.02	0.83 ± 0.01	103.09 ± 2.90	...	...	...	...	1	6.83 ± 0.20
NGC 4477	16.84 ± 0.07	16.62 ± 0.17	3.98 ± 0.09	0.63 ± 0.01	14.36 ± 4.56	17.72 ± 0.04	43.85 ± 0.32	0.72 ± 0.02	88.79 ± 1.21	0.50	7.86 ± 0.20
NGC 4501	16.60 ± 0.05	10.48 ± 0.76	3.94 ± 0.04	0.72 ± 0.01	130.17 ± 0.79	15.66 ± 0.05	41.53 ± 0.44	0.47 ± 0.01	141.63 ± 0.01	0.13	8.47 ± 0.09
NGC 4507	14.30 ± 0.05	3.85 ± 0.14	4.47 ± 0.05	0.73 ± 0.01	65.64 ± 0.14	16.94 ± 0.04	15.68 ± 0.20	0.76 ± 0.01	57.05 ± 0.02	0.37	9.85 ± 0.14
NGC 4526	16.32 ± 0.05	23.11 ± 0.17	3.05 ± 0.01	0.61 ± 0.01	115.33 ± 0.70	17.19 ± 0.05	71.53 ± 0.76	0.21 ± 0.01	113.28 ± 0.01	0.68	6.79 ± 0.14
NGC 4548	18.95 ± 0.07	35.27 ± 0.35	5.23 ± 0.15	0.81 ± 0.01	73.67 ± 2.34	17.92 ± 0.04	57.37 ± 0.42	0.61 ± 0.01	69.08 ± 9.40	0.44	7.91 ± 0.27
NGC 4552	17.34 ± 0.02	29.75 ± 0.36	4.81 ± 0.02	0.93 ± 0.01	123.62 ± 0.02	...	...	...	...	1	6.57 ± 0.20
NGC 4579	17.16 ± 0.05	24.67 ± 0.18	3.97 ± 0.14	0.66 ± 0.01	66.90 ± 0.41	17.54 ± 0.05	68.98 ± 0.73	0.64 ± 0.01	68.19 ± 0.01	0.40	7.26 ± 0.13
NGC 4636	16.29 ± 0.05	13.37 ± 0.32	1.83 ± 0.02	0.95 ± 0.01	154.26 ± 0.81	17.13 ± 0.04	55.04 ± 0.39	0.75 ± 0.01	143.69 ± 0.03	0.29	7.73 ± 0.13
NGC 4698	17.05 ± 0.07	10.58 ± 0.11	3.41 ± 0.06	0.95 ± 0.01	17.23 ± 0.01	16.94 ± 0.05	32.92 ± 0.24	0.56 ± 0.01	166.75 ± 2.27	0.35	8.63 ± 0.12
NGC 4800	16.21 ± 0.05	4.52 ± 0.34	2.62 ± 0.09	0.95 ± 0.01	88.38 ± 0.19	15.60 ± 0.04	12.13 ± 0.15	0.64 ± 0.01	22.97 ± 0.01	0.27	9.77 ± 0.08
NGC 4826	17.57 ± 0.05	44.63 ± 0.32	5.48 ± 0.20	0.70 ± 0.01	110.99 ± 0.67	15.90 ± 0.04	54.86 ± 0.58	0.54 ± 0.01	109.75 ± 0.01	0.43	6.16 ± 0.22
NGC 5077	17.26 ± 0.03	17.21 ± 0.22	3.57 ± 0.02	0.72 ± 0.01	9.47 ± 0.47	...	...	...	...	1	8.11 ± 0.16
NGC 5127	19.99 ± 0.03	40.53 ± 0.52	5.08 ± 0.02	0.74 ± 0.01	63.87 ± 3.18	...	...	...	...	1	8.76 ± 0.25
NGC 5283	17.70 ± 0.21	5.41 ± 0.36	8.00 ± 0.15	0.74 ± 0.07	169.42 ± 9.29	16.25 ± 0.21	5.21 ± 0.90	0.77 ± 0.03	74.47 ± 0.86	0.58	10.61 ± 0.12
NGC 5427	16.86 ± 0.05	4.51 ± 0.34	1.30 ± 0.02	0.85 ± 0.01	48.21 ± 0.10	17.31 ± 0.04	24.10 ± 0.30	0.94 ± 0.02	73.92 ± 0.03	0.09	10.95 ± 0.09
NGC 5490	18.05 ± 0.03	16.66 ± 0.21	5.15 ± 0.02	0.79 ± 0.01	0.18 ± 0.01	...	...	...	...	1	8.67 ± 0.27
NGC 5635	16.48 ± 0.05	5.49 ± 0.42	2.36 ± 0.08	0.75 ± 0.01	62.94 ± 0.14	16.82 ± 0.04	20.25 ± 0.25	0.36 ± 0.01	64.87 ± 0.03	0.37	9.98 ± 0.08
NGC 5695	17.88 ± 0.06	7.11 ± 0.96	6.10 ± 0.12	0.30 ± 0.02	120.83 ± 4.37	16.57 ± 0.09	10.36 ± 0.13	0.65 ± 0.02	137.80 ± 3.02	0.22	11.32 ± 0.42
NGC 5921	15.27 ± 0.05	3.78 ± 0.21	2.43 ± 0.08	0.81 ± 0.01	170.31 ± 0.37	17.13 ± 0.04	32.65 ± 0.41	0.51 ± 0.01	15.68 ± 0.01	0.15	10.15 ± 0.08
NGC 6861	15.40 ± 0.04	9.79 ± 0.76	2.49 ± 0.02	0.54 ± 0.01	142.19 ± 0.19	17.95 ± 0.08	33.00 ± 0.16	0.66 ± 0.01	132.00 ± 9.85	0.68	7.98 ± 0.12
NGC 7052	18.66 ± 0.03	33.88 ± 0.43	4.45 ± 0.02	0.55 ± 0.01	64.07 ± 3.19	...	...	...	...	1	8.21 ± 0.21
NGC 7626	19.72 ± 0.02	60.28 ± 0.75	5.66 ± 0.04	0.88 ± 0.01	12.27 ± 0.01	...	...	...	...	1	7.39 ± 0.52
NGC 7682	18.84 ± 0.20	9.35 ± 0.54	4.32 ± 0.12	0.94 ± 0.01	4.75 ± 0.04	16.85 ± 0.13	10.69 ± 0.96	0.28 ± 0.00	158.67 ± 0.05	0.61	10.62 ± 0.17
UGC 1395	16.73 ± 0.21	3.46 ± 0.33	5.15 ± 0.44	0.61 ± 0.05	136.07 ± 9.17	18.02 ± 0.21	18.76 ± 0.90	0.60 ± 0.03	147.03 ± 2.28	0.19	11.79 ± 0.29
UGC 12064	15.71 ± 0.21	3.70 ± 0.36	1.77 ± 0.15	0.83 ± 0.07	166.85 ± 8.29	16.71 ± 0.21	8.64 ± 0.90	0.65 ± 0.03	13.05 ± 2.86	0.43	10.79 ± 0.12

Notes. — Col.(1): Galaxy name. Col.(2): Effective surface brightness of the bulge. Col.(3): Effective radius of the bulge. Col.(4): Shape parameter of the bulge. Col.(5): Axial ratio of the bulge isophotes. Col.(6): Position angle of the bulge major-axis. Col.(7): Central surface brightness of the disk. Col.(8): Scale length of the disk. Col.(9): Axial ratio of the disk isophotes. Col.(10): Position angle of the disk major-axis. Col.(11): Bulge-to-total luminosity ratio. Col.(12): K-band total magnitude of the bulge.

Table 2.5 Structural parameters derived from the UKIDSS images with GASP2D

Galaxy name	μ_e (mag arcsec^{-2})	r_e ($''$)	n	q_b	PA_b ($^\circ$)	μ_0 (mag arcsec^{-2})	h ($''$)	q_d	PA_d ($^\circ$)	B/T	m_K (mag)
(1)	(2)	(3)	(4)	(5)	(6)	(7)	(8)	(9)	(10)	(11)	(12)
NGC 2911	15.67 ± 0.06	3.73 ± 0.06	2.28 ± 0.04	0.77 ± 0.03	42.07 ± 0.02	16.90 ± 0.05	15.78 ± 0.03	0.67 ± 0.03	47.49 ± 0.02	0.35	10.00 ± 0.02
NGC 4261	16.67 ± 0.02	18.01 ± 0.02	2.63 ± 0.02	0.76 ± 0.01	112.75 ± 0.01	...	...	...	...	1.00	7.53 ± 0.01
NGC 4435	14.82 ± 0.02	4.69 ± 0.02	1.70 ± 0.02	0.74 ± 0.01	84.11 ± 0.01	15.44 ± 0.03	14.50 ± 0.02	0.43 ± 0.01	79.57 ± 0.02	0.43	8.84 ± 0.01
NGC 4459	18.06 ± 0.02	35.10 ± 0.02	5.28 ± 0.02	0.83 ± 0.01	75.16 ± 0.01	...	...	...	...	1.00	7.00 ± 0.01
NGC 4501	16.50 ± 0.01	9.94 ± 0.02	3.70 ± 0.01	0.71 ± 0.01	130.73 ± 0.01	15.70 ± 0.02	41.40 ± 0.01	0.47 ± 0.01	129.55 ± 0.01	0.13	8.54 ± 0.01
NGC 4548	16.83 ± 0.02	8.53 ± 0.02	3.52 ± 0.02	0.87 ± 0.01	151.50 ± 0.01	16.76 ± 0.03	35.14 ± 0.02	0.48 ± 0.02	25.10 ± 0.02	0.25	9.01 ± 0.01
NGC 4552	16.12 ± 0.02	15.24 ± 0.02	3.21 ± 0.02	0.95 ± 0.01	60.20 ± 0.01	...	...	...	...	1.00	7.00 ± 0.01
NGC 4698	16.71 ± 0.02	9.34 ± 0.02	3.06 ± 0.02	0.88 ± 0.01	17.23 ± 0.01	16.96 ± 0.03	33.80 ± 0.02	0.52 ± 0.02	104.24 ± 0.02	0.34	8.75 ± 0.01

NOTES. — Col.(1): Galaxy name. Col.(2): Effective surface brightness of the bulge. Col.(3): Effective radius of the bulge. Col.(4): Shape parameter of the bulge. Col.(5): Axial ratio of the bulge isophotes. Col.(6): Position angle of the bulge major-axis. Col.(7): Central surface brightness of the disk. Col.(8): Scale lenght of the disk. Col.(9): Axial ratio of the disk isophotes. Col.(10): Position angle of the disk major-axis. Col.(11): Bulge-to-total luminosity ratio. Col.(12): K-band total magnitude of the bulge.

Table 2.6: Quality of the fit for the 2MASS and UKIDSS decompositions

	2MASS fit		UKIDSS fit	
Galaxy	Type	Quality	Type	Quality
(1)	(2)	(3)	(4)	(5)
IC 342	BD	ok	...	...
IC 3639	BD	ok	...	...
NGC 193	BD	ok	...	...
NGC 289	BD	three	...	...
NGC 315	S	ok	...	...
NGC 383	BD	ok	...	...
NGC 541	BD	shallow	...	...
NGC 613	BD	three	...	...
NGC 741	S	ok	...	...
NGC 788	BD	ok	...	...
NGC 1052	S	ok	...	...
NGC 1358	BD	ok	...	...
NGC 1497	BD	ok	...	...
NGC 1667	BD	three	...	...
NGC 1961	BD	embedded	...	...
NGC 2110	S/BD	shallow	...	...
NGC 2179	BD	shallow	...	...
NGC 2273	BD	three	...	...
NGC 2329	BD	embedded	...	...
NGC 2654	BD	embedded	...	...
NGC 2685	BD	embedded	...	...
NGC 2748	BD	shallow	...	...
NGC 2787	BD	three	...	...
NGC 2892	S	ok but noisy	...	...
NGC 2903	BD	three	...	...
NGC 2911	S/BD	shallow	BD	ok
NGC 2964	BD	three	...	...
NGC 3003	BD	shallow	...	...
NGC 3021	BD	F2	...	...
NGC 3031	BD	ok	...	...
NGC 3049	BD	shallow	BD	bad
NGC 3067	BD	three	...	...
NGC 3078	S	ok	...	...
NGC 3081	BD	ok	...	...
NGC 3227	BD	three	...	...
NGC 3245	BD	ok	...	...
NGC 3259	BD	shallow	...	...
NGC 3310	BD	three	...	...
NGC 3351	BD	ok	...	...
NGC 3368	BD	ok	...	...
NGC 3379	S	ok	...	...
NGC 3393	BD	ok	...	...
NGC 3489	BD	ok	...	...
NGC 3627	BD	three	...	...
NGC 3642	BD	ok	...	...
NGC 3675	BD	F2	...	...
NGC 3801	BD	ok	...	...
NGC 3862	S	shallow	...	...
NGC 3887	BD	F2	...	...
NGC 3953	BD	ok	...	...

Table 2.6 – Continued

Galaxy	2MASS fit		UKIDSS fit	
	Type	Quality	Type	Quality
(1)	(2)	(3)	(4)	(5)
NGC 3982	BD	three+seeing	...	...
NGC 3992	BD	three	...	...
NGC 3998	BD	ok	...	...
NGC 4036	BD	ok	...	...
NGC 4041	BD	ok	...	...
NGC 4088	BD	three	...	...
NGC 4143	BD	ok	...	...
NGC 4150	BD	ok	...	...
NGC 4203	BD	ok	...	...
NGC 4212	BD	F2	BD	F2
NGC 4245	BD	ok	...	...
NGC 4258	BD	ok	...	...
NGC 4261	S	ok	S	ok
NGC 4278	S	ok	...	...
NGC 4314	BD	three	...	...
NGC 4321	BD	bad	BD	three
NGC 4335	S	ok	...	...
NGC 4343	BD	ok	BD	three
NGC 4374	S	ok	...	...
NGC 4420	BD	shallow	...	...
NGC 4429	BD	F2	BD	F2
NGC 4435	BD	ok	BD	ok
NGC 4450	BD	ok	...	...
NGC 4459	BD/S	ok	S	ok
NGC 4477	BD	ok	BD	three
NGC 4486	S	extra light	S	extra light
NGC 4501	BD	ok	BD	ok
NGC 4507	BD	ok	...	...
NGC 4526	BD	ok	BD	three
NGC 4527	BD	three	...	...
NGC 4548	BD	ok	BD	ok
NGC 4552	S	ok	S	ok
NGC 4579	BD	ok	BD	embedded
NGC 4594	BD	three	...	...
NGC 4596	BD	three	BD	F2
NGC 4636	S/BD	ok	...	...
NGC 4698	BD	ok	BD	ok
NGC 4736	BD	F2	...	...
NGC 4800	BD	ok	...	...
NGC 4826	BD	ok	...	...
NGC 5005	BD	embedded	...	...
NGC 5077	S	ok	...	...
NGC 5127	S	ok	...	...
NGC 5141	BD/S	shallow	...	...
NGC 5194	BD	F2	...	...
NGC 5248	BD	three	BD	F2
NGC 5252	BD	embedded	...	...
NGC 5283	BD	shallow	...	...
NGC 5347	BD	shallow	...	...
NGC 5398	BD	shallow	...	...
NGC 5427	BD	ok	...	...

Table 2.6 – Continued

Galaxy	2MASS fit Type	2MASS fit Quality	UKIDSS fit Type	UKIDSS fit Quality
(1)	(2)	(3)	(4)	(5)
NGC 5490	S	ok	...	...
NGC 5635	BD	ok	...	...
NGC 5643	BD	three	...	...
NGC 5695	BD	ok	...	...
NGC 5713	BD	embedded	BD	F2
NGC 5728	BD	three	...	...
NGC 5879	BD	bad	...	...
NGC 5921	BD	ok	...	...
NGC 6300	BD	three	...	...
NGC 6500	BD	shallow	...	...
NGC 6861	BD	ok	...	...
NGC 6951	BD	three	...	...
NGC 7052	S	ok	...	...
NGC 7331	BD	embedded	...	...
NGC 7626	S	ok	...	...
NGC 7682	BD	ok	...	...
UGC 1214	BD	shallow	...	...
UGC 1395	BD	ok	...	...
UGC 7115	S	shallow	...	...
UGC 12064	BD	ok	...	...

NOTES. — Col.(1): Galaxy name. Col.(2): Type of fit: S = spheroidal component fitted with a Sérsic function, BD= bulge component fitted with a Sérsic function and disk component fitted with an exponential law. Col.(3): Quality of the fit: ok = successful fit; embedded = disk is embedded in the bulge; three = strongly barred galaxy, we would need 3 components; F2 = Freeman 2 profile (Freeman 1970); bad = neither S nor BD can reproduce the profile or the galaxy is edge-on; extra light = this is the case of NGC 4486. The light excess cannot be parameterized with an exponential function and we would need a cut-off profile (Oemler 1976); shallow = the image is too shallow to obtain reliable structural parameters or the resolution is not good enough; seeing = the FWHM of the seeing PSF is larger than the bulge effective radius.

3

Upper limits on the masses of 105 supermassive black holes from *HST*/STIS archival data [1]

Based on Beifiori A., Sarzi M., Corsini E. M., Dalla Bontà E., Pizzella A., Coccato L., & Bertola F., 2009, ApJ, 692, 856

Based on the modeling of the central emission-line width measured over subarcsecond apertures with the *Hubble Space Telescope*, we present stringent upper bounds on the mass of the central supermassive black hole, $M_\bullet$, for a sample of 105 nearby galaxies ($D < 100\,\mathrm{Mpc}$) spanning a wide range of Hubble types (E − Sc) and values of the central stellar velocity dispersion, σ_c ($58 - 419\ \mathrm{km\ s^{-1}}$). For the vast majority of the objects the derived $M_\bullet$ upper limits run parallel and above the well-known $M_\bullet - \sigma_\mathrm{c}$ relation independently of the galaxy distance, suggesting that our nebular line-width measurements trace rather well the nuclear gravitational potential. For values of σ_c between 90 and 220 $\mathrm{km\ s^{-1}}$ 68% of our upper limits falls immediately above the $M_\bullet - \sigma_\mathrm{c}$ relation without exceeding the expected $M_\bullet$ values by more than a factor 4.1. No systematic trends or offsets are observed in this σ_c range as a function of the galaxy Hubble type or with respect to the presence of a bar. For 6 of our 12 $M_\bullet$ upper limits with $\sigma_\mathrm{c} < 90\ \mathrm{km\ s^{-1}}$ our line-width measurements are more sensitive to the stellar contribution to the gravitational potential, either due to the presence of a

[1] Based on observations with the NASA/ESA *Hubble Space Telescope* obtained at STScI, which is operated by the Association of Universities for Research in Astronomy, Incorporated, under NASA contract NAS5-26555.

nuclear stellar cluster or because of a greater distance compared to the other galaxies at the low-σ_c end of the $M_\bullet - \sigma_c$ relation. Conversely, our $M_\bullet$ upper bounds appear to lie closer to the expected $M_\bullet$ in the most massive elliptical galaxies with values of σ_c above 220 km s^{-1}. Such a flattening of the $M_\bullet - \sigma_c$ relation at its high-σ_c end would appear consistent with a coevolution of supermassive black holes and galaxies driven by dry mergers, although better and more consistent measurements for σ_c and K-band luminosity are needed for these kinds of objects before systematic effects can be ruled out.

3.1 Introduction

Supermassive black holes (SMBHs) have now been discovered in the center of a sufficiently large number of nearby galaxies to probe possible links between the masses of SMBHs ($M_\bullet$) and the global properties of their host galaxies. In fact, it has emerged that $M_\bullet$ correlates with the luminosity (Kormendy & Richstone 1995; Marconi & Hunt 2003), mass (Magorrian et al. 1998; Häring & Rix 2004), stellar velocity dispersion (Ferrarese & Merritt 2000; Gebhardt et al. 2000a; Tremaine et al. 2002; Ferrarese & Ford 2005), light concentration (Graham et al. 2001), and gravitational binding energy (Aller & Richstone 2007) of the host galaxy spheroidal component, i.e., the entire galaxy in the case of elliptical galaxies or the bulge of disk galaxies. In light of these findings it is now widely accepted that the mass-accretion history of a SMBH is tightly related through feedback to the formation and evolution of the host spheroid (e.g., Silk & Rees 1998; Haehnelt & Kauffmann 2000; Di Matteo et al. 2005) with some studies having suggested a link with the mass of the dark-matter halo (Ferrarese 2002; Pizzella et al. 2005).

The slope and scatter of all these correlations remain quite uncertain (Novak et al. 2006), however, particularly since they are still based on a limited sample of galaxies with reliable $M_\bullet$ that is biased toward early-type systems and that is clustered around a rather limited range of stellar velocity dispersion (σ), approximately between 150 and 250 km s^{-1}. Given the great theoretical interest spurred by these findings, there is a pressing need to acquire better $M_\bullet$ statistics, both in terms of the number of targets and in terms of broadening the range of parent galaxies, in particular toward spiral galaxies.

Secure $M_\bullet$ measurements in external galaxies are traditionally obtained through the modeling of the stellar and/or gaseous kinematics, most often as derived using *Hubble Space Telescope* (*HST*) observations in the optical domain. The advent of adaptive-optics systems working at near-infrared wavelengths has led to more stellar-dynamical measurements of $M_\bullet$ from the ground (Houghton et al. 2006; Nowak et al. 2007, see also Chapter 5). Yet, such measurements are still quite expensive, not only because good-quality measurements of the stellar kinematics in the near-infrared require relatively long observations, but also

because proper modeling of the stellar kinematics in the immediate vicinity of SMBHs needs robust constraints on the importance of radial orbits and thus additional large-scale observations, possibly with integral-field spectroscopy (Valluri et al. 2004; Cappellari & McDermid 2005). Water masers have provided the most accurate extragalactic $M_\bullet$ measurements to date, but such gaseous systems are exceedingly rare (Braatz et al. 1994; Greenhill et al. 2003). The modeling of the nuclear ionized-gas kinematics has also led to accurate $M_\bullet$ measurements (e.g., Barth et al. 2001; Dalla Bontà et al. 2009, see also Chapter 6), and at a relatively cheap cost in terms of observation time compared to stellar-dynamical $M_\bullet$ determinations (e.g., Verolme et al. 2002; Gebhardt et al. 2003). Yet, only a handful of the objects targeted by *HST* turned out to have sufficiently regular gas velocity fields for the purpose of modeling (Sarzi et al. 2001). Thus, unless a large number of galaxies preselected to have regular nuclear gas kinematics (for instance following Ho et al. 2002) is observed with *HST* if and when the Space Telescope Imaging Spectrograph (STIS) is successfully refurbished, it is unlikely that the number of galaxies with secure $M_\bullet$ measurements will increase dramatically in the near future.

The *HST* Science Archive already contains an untapped resource that can be used to better constrain the black-hole mass budget across the different morphological types of galaxies, which consists of the vast number of the STIS spectra from which a central emission-line width can be measured. The modeling of this kind of data can indeed lead to tight upper limits on $M_\bullet$, as first shown by Sarzi et al. (2002). For this reason we started a program aimed at deriving $M_\bullet$ upper limits based on *HST* spectra for the largest possible number of galaxies and a wide range of morphological types. In this chapter we present the results based on a sample of 105 nearby galaxies for which STIS/G750M spectra in the Hα region and measurements of the stellar velocity dispersion were available from the *HST* archive and in the literature, respectively. Although we will be able only to set an upper limit on the $M_\bullet$ of our galaxies, the lack of exact measurements will be compensated for by the large number of upper limits when studying SMBH mass−host galaxy relationships (see also Section 4.3).

The chapter is organized as follows. In Section 3.2, we describe our sample selection and the measurement of central emission-line width, before briefly describing our modeling. We will then present our results and discuss our findings in the context of the $M_\bullet - \sigma$ relation between the SBHM mass and central stellar velocity dispersion of the host spheroid in Section 3.3.

3.2 Data compilation and analysis

3.2.1 Sample selection and data reduction

In order to assemble the largest possible sample of homogeneous measurements of the central emission-line width, we queried the *HST* Science Archive for objects with STIS spectra obtained with the G750M grating through either the $0\farcs1 \times 52''$ or the $0\farcs2 \times 52''$ slit placed across the galaxy nucleus, most often at random position angles. This is indeed by far the most common configuration in the archive, which always gives us access to the [N II] $\lambda\lambda 6548, 6583$, H$\alpha$ and [S II] $\lambda\lambda 6716, 6731$ emission lines. Limiting ourselves to galaxies within 100 Mpc to minimize the impact of the stellar potential on our results, we retrieved data for 177 galaxies spanning the whole range of morphological types (see also Section 2.2). When available, galactic distances were adopted from measurements based either on surface-brightness fluctuations (Tonry et al. 2000, 2001), Cepheid variables (Freedman et al. 2001) or from Tully (1988). Otherwise we used the weighted mean recessional velocity corrected to the reference frame defined by the microwave background radiation from de Vaucouleurs et al. (1991, RC3 hereafter) to derive the distance to our sample galaxies by assuming $H_0 = 75$ km s^{-1} Mpc^{-1}, $\Omega_{\rm m} = 0.3$, and $\Omega_\Lambda = 0.7$. The median distance of the sample galaxies is 21.4 Mpc.

The archival spectra were reduced using IRAF[1] and the STIS reduction pipeline maintained by the Space Telescope Science Institute (Dressel et al. 2007). The basic reduction steps included overscan subtraction, bias subtraction, dark subtraction, and flatfield correction. Different spectra obtained for the same slit position were aligned using IMSHIFT and knowledge of the adopted shifts along the slit position. Cosmic ray events and hot pixels were removed using the task LACOS_SPEC by van Dokkum (2001). Residual bad pixels were corrected by means of a linear one-dimensional interpolation using the data quality files and stacking individual spectra with IMCOMBINE. This allowed us to increase the signal-to-noise ratio of the resulting spectra. We performed wavelength and flux calibration as well as geometrical correction for two-dimensional distortion following the standard reduction pipeline and applying the X2D task. This task corrected the wavelength scale to the heliocentric frame as well (see also Sections 2.3, 6.4, and 7.3.2).

To measure the nuclear emission-line width we generally extracted aperture spectra three ($0\farcs15$) and five pixels wide ($0\farcs25$) centered on the continuum peak, for the $0\farcs1$ and $0\farcs2$-wide slit cases, respectively. When the spectra were obtained with a 2-pixel binning read-out mode along the spatial direction, we extracted

[1]IRAF is distributed by NOAO, which is operated by AURA Inc., under contract with the National Science Foundation

aperture spectra three pixels wide (0.″3) for the 0.″2-wide slit (Table 3.1). The extracted spectra thus consist of the central emission convolved with the STIS spatial point-spread function (PSF) and sampled over nearly square apertures of $0.''15 \times 0.''1$, $0.''25 \times 0.''2$ or $0.''3 \times 0.''2$, roughly corresponding to a circular aperture with **a** radius of 0.″07, 0.″13, and 0.″14, respectively. The wavelength range of our spectra is either 6482−7054 Å or 6295 − 6867 Å, depending on whether the G750M grating was used at the primary or secondary tilt. The instrumental FWHM was 0.87 Å ($\sigma_{\rm inst}$ = 17 km s^{-1}) and 1.6 Å ($\sigma_{\rm inst}$ = 32 km s^{-1}) for the 0.″1 and the 0.″2-wide slit, respectively. The atlas of all the extracted spectra is be presented in Figure 2.2.

To place our $M_\bullet$ upper limits with the $M_\bullet - \sigma$ relation, here we consider only galaxies with velocity dispersion measurements in the literature, which were available for 137 objects. We also dropped a further five objects, since upon closer inspection they revealed unrelaxed morphologies. For a number of objects with a sharp central surface-brightness profile, the two-dimensional rectification of the spectrum performed during the data reduction produced anomalous undulations in the flux level of continuum of the very central rows (see Kim Quijano et al. 2007, for details). This introduced also artificial fluctuations in the emission-line flux profiles across the nucleus. As constraining the concentration of the nebular emission is key to our modeling (see Section 3.2.3), this problem forced us to remove a further eight galaxies from our sample (see also Section 2.3.2).

3.2.2 Measurement of the emission lines

In order to derive upper limits on $M_\bullet$ following the method of Sarzi et al. (2002, see also Section 3.2.3) we need to measure both the width of the central nebular emission and the radial profile of the emission-line flux, so that we can gauge both the depth of the potential well and the concentration of its gaseous tracer. To side-step the impact of broad and/or asymmetric emission arising from regions much smaller than our resolution limit, we focus on the width of the narrow component of the emission from forbidden transitions and disregard the broad-line emission in our spectra. In the wavelength range of our spectra, this means measuring the central width and flux profile of the [N II] $\lambda\lambda 6548, 6583$ lines since these are usually brighter than the [S II] $\lambda\lambda 6716, 6731$ lines. The [N II] doublet also traces the nuclear kinematics better than Hα, given that this line could be significantly affected by emission from circumnuclear star-forming regions (e.g., Verdoes Kleijn et al. 2000; Coccato et al. 2006).

To measure the central width and flux profile of the narrow component of the [N II] lines, we fit our spectra with multiple Gaussians to match both the

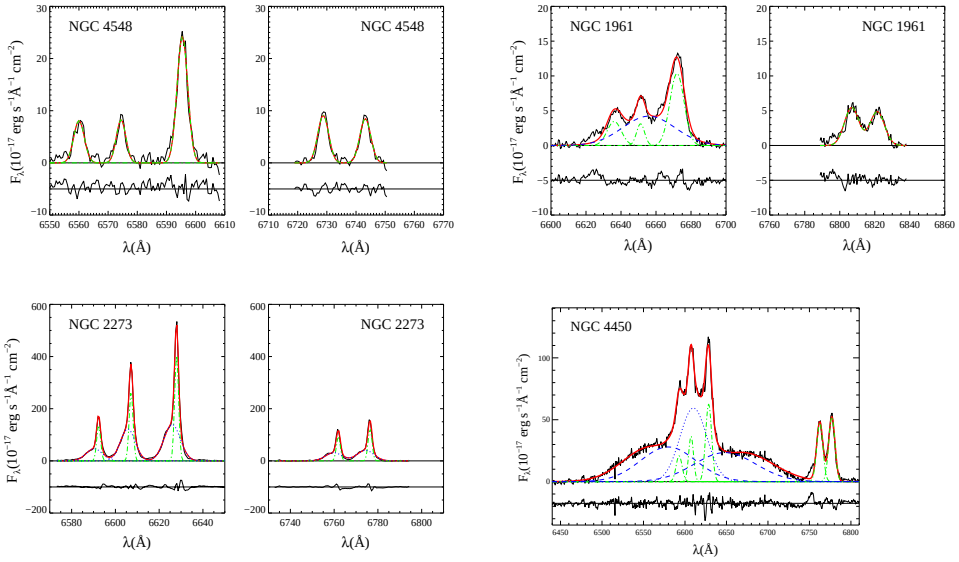

Figure 3.1 Few examples of continuum-subtracted central G750M spectra from our spectral atlas illustrating the various fitting strategies adopted to match Hα, [N II] $\lambda\lambda 6548, 6583$ and [S II] $\lambda\lambda 6716, 6731$ emission lines. In each panel, the red solid line show the overall line blend, whereas the green dashed-dotted lines and blue dotted or dashed lines show the adopted narrow and broad Gaussian components, respectively. Shown are also the fit residuals, offset for better visibility. For NGC 4548, the nebular emission could be matched with single Gaussian profiles. For NGC 1961, we needed to add a broad Hα component, whereas for NGC 2273 an additional broad and blue-shifted component was needed to match the profile of all lines. For NGC 4450, we added two extremely broad Gaussian shoulders to offset from the center by several thousands kilometers per second, in addition to a more typical broad Hα component (see also Ho et al. 2000, for a match to the double-peaked profile of this LINER 1.9 nucleus).

broad and narrow components of all the observed lines, while describing the stellar continuum with a low-order polynomial. A flux ratio of 1:3 was assumed for the [N II] doublet, as dictated by atomic physics (e.g., Osterbrock 1989), and in the presence also of [S II] emission, both the [N II] and [S II] doublets were assumed to share a common line centroid and width. In most cases, only one additional Gaussian component was needed in our fits, to describe the Hα

emission from the broad-line region, although in many objects also the forbidden [N II] and [S II] lines required double-Gaussian profiles. This allowed us to describe also lines with Voigt profiles, where tests on 18 galaxies showed that our narrowest Gaussian component tends to be only slightly broader than the thermal component in the Voigt profiles, generally by less than 20% (see also Section 2.3.3). The extra Gaussian in the [N II] and [S II] lines was also used to isolate the contribution of blue- or redshifted wings. To help deblend the Hα+[N II] region in some cases, we followed Ho et al. (1997b) and assigned to both the [N II] lines and the narrow Hα emission the line profile that was predetermined by fitting the [S II] lines (see also Sections 2.3.3, 6.4.1, and 7.3.2). The best-fitting Gaussian parameters were derived using a nonlinear least-squares minimization based on the robust Levenberg−Marquardt method (e.g., Press et al. 1996) implemented by Moré et al. (1980). The actual computation was done using the MPFIT algorithm[2] implemented by C. B. Markwardt under the IDL[3] environment. In objects with conspicuous stellar absorption features that cannot be accounted for by our minimization routine we checked our results against the line-width and flux measurements obtained with the GANDALF software[4] of Sarzi et al. (2006), adopting either very young (300 Myr) or old (10 Gyr) stellar population templates. In most cases, the measurements agreed within the errors, except for IC 342 and NGC 7331 where the Hα absorption line is particularly prominent. For these galaxies, we adopted the GANDALF values. Finally, in defining our detection thresholds we compared the amplitude (A) of the best-fitting line profile to the noise level (N) in the residuals of the continuum fit, adopting as detected only those emission lines for which the A/N ratio was larger than 3. Figure 3.1 shows a few sample spectra illustrating the various fitting strategies explained above. Other examples are shown in Figures 2.7, 6.17, 6.18, 6.19, and 7.3.A more detailed description of our emission-line measurements for each of our sample galaxy is presented in Section 2.3.3.

In 14 galaxies the nebular emission was too faint for it to be detected given the quality of the corresponding spectra, and were consequently dropped from our sample. Three further galaxies had also to be discarded because their line profile could not be well represented as a simple sum of Gaussian components. Finally, two galaxies were rejected because the radial profile of the flux of the [N II] lines was strongly asymmetric and not suitable for modeling. Table 3.1 lists the final sample of galaxies analyzed in this chapter, which comprises 105

[2]The code is available at http://cow.physics.wisc.edu/∼craigm/idl/idl.html.
[3]Interactive Data Language is distributed by Research System Inc.
[4]The code is available at http://www.strw.leidenuniv.nl/sauron/software.html.

galaxies of which 28 (27%) are classified as ellipticals, 20 (19%) are lenticulars, and 57 (54%) are spirals. The central velocity dispersion of the ionized-gas component and the size of the aperture we measured are given in Table 3.2. Prior to modeling, the instrumental resolution corresponding to the adopted apertures (17 km s^{-1} and 32 km s^{-1} for the 0.″1 and 0.″2 slit widths, respectively) was subtracted in quadrature from the observed line-width values to obtain the intrinsic gas velocity dispersion. Table 3.3 lists the 74 rejected galaxies.

3.2.3 Modeling the central line width

Assuming that the width of the nuclear emission traces the depth of the gravitational well, we can derive stringent upper bounds on the mass of the SMBHs in our sample galaxies thanks to the exquisite spatial resolution of *HST*. Although the stellar contribution to the gravitational potential could affect such estimates, the fundamental reason for which a lower limit on $M_\bullet$ cannot be set from such a simple measurement is that the observed line-broadening may, in principle, be entirely due to additional contributions such as non-gravitational forces (e.g., gas pressure or magnetic forces).

In this study, we follow the procedure described in Sarzi et al. (2002), where a detailed description of the method can be found (see also Section 6.6.3). In short, we assume that the observed line-broadening arises from the motion of ionized gas in a coplanar thin inner disk of unknown inclination, where the gas moves in circular and Keplerian orbits around the putative SMBHs. For a given radial profile of the nebular emission, perfectly edge-on disks lead to the broadest lines and therefore to a lower estimate of $M_\bullet$. Conversely, the $M_\bullet$ value needed to explain the observed line width diverges to infinity as we approach perfectly face-on configurations. Fortunately, such extreme orientations are statistically rare. Since randomly oriented disks have uniformly distributed $\cos i$, it is possible to derive 1σ upper and lower limits on $M_\bullet$ by simply considering models with nearly edge-on ($i = 81°$, $\cos i = 0.16$) and face-on ($i = 33°$, $\cos i = 0.84$) orientations, respectively, comprising 68% of the distribution of $M_\bullet$ values that can explain a given line width (e.g., Sarzi et al. 2002).

In our models, we could disregard the effect on the unknown position angle of the disk since we extracted our spectra in nearly square apertures, and thus assumed that the STIS slit was placed along the disk major axis.

Clearly, for a given disk orientation, the concentration of the gas tracer impacts heavily on the $M_\bullet$ value needed to explain a given line width, to the point that no lower limit on $M_\bullet$ can be set when the gas profile is unresolved. This is why the intrinsic emissivity distribution of the gaseous disk has to be

constrained from the data. As in Sarzi et al. (2002), we assumed an intrinsically Gaussian flux profile centered on the stellar nucleus, which makes it easier to match the observed flux profile while accounting for instrumental effects. The choice of a Gaussian parameterization is also conservative, since cuspier functions would have led us to estimate smaller $M_\bullet$. For instance, adopting an exponential profile for the subsample of objects studied also by Sarzi et al. (2002) leads on average to a 10% decrease for the $M_\bullet$ estimates.

In this work, we disregarded the contribution of the stellar potential, which would lead to tighter upper limits on $M_\bullet$. In principle, it is possible to estimate the stellar mass contribution by deprojecting the stellar surface brightness observed in the STIS acquisition images while assuming spherical symmetry and a constant mass-to-light ratio (Sarzi et al. 2002). In practice, however, this would only be feasible for a limited number of objects in our sample, given the limited quality of the acquisition images for most of our sample galaxies, and the pervasive presence of dust absorption features, particularly in spiral host galaxies (see Figure 2.2). Still, the impact of the stellar potential is unlikely to change dramatically our $M_\bullet$ estimates, particularly for the upper limits derived for nearly face-on configurations. For their sample of nearby galaxies (at $8-17$ Mpc), Sarzi et al. (2002) found that including the stellar mass contribution reduced the median value of the $M_\bullet$ upper limits by just $\sim 12\%$. For the median distance our sample (21.4 Mpc) the stellar mass contribution to our 33° upper limits would be $\sim 15\%$. Similar considerations would apply to the $M_\bullet$ sensitivity limit of our experiment. In the case of the Sarzi et al. (2002) sample, this value was found to be on average 3.9×10^6 $M_\odot$, which is well below most of the $M_\bullet$ limits derived here and comparable to the smallest $M_\bullet$ limits obtained for the closest objects in our sample.

To conclude, we note that the range spanned by the two $M_\bullet$ values delivered by our Keplerian-disk model includes also $M_\bullet$ that would be estimated under radically different assumptions. For instance, the gaseous disk model at $i = 60°$ is equivalent to that of an isotropic gas sphere in hydrostatic equilibrium (see Sarzi et al. 2002, for details). The $M_\bullet$ estimates we derived for $i = 33°$ and 81° are listed in Table 3.2 for the sample galaxies. Although strictly speaking both values should be regarded as upper-limits, we will refer only to the 33° estimates as $M_\bullet$ upper limits, hereafter.

3.3 Results and discussion

We have determined the 1σ upper and lower confidence limits for the $M_\bullet$ for randomly orientated disks for 105 galaxies with measurable spectra and stellar velocity dispersions available in the literature. For 20 galaxies of the sample,

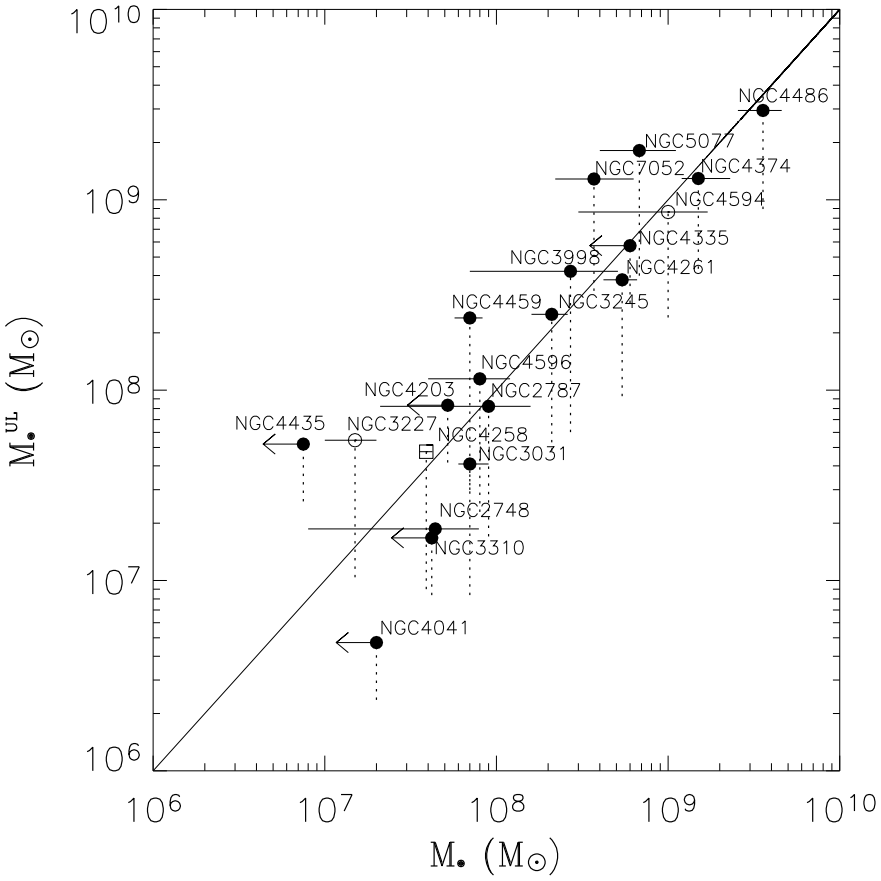

Figure 3.2 Comparison between our $M_\bullet$ upper limits and accurate measurements of $M_\bullet$ based on the resolved kinematics of gas (filled circles), stars (open circles), and water masers (open square) available in the literature. Leftward arrows indicate an upper constrain rather than a definite value for $M_\bullet$. The upper and lower edges of the dotted lines correspond to the $M_\bullet$ values that we estimated assuming an inclination of $i = 33°$ and $81°$ for the unresolved Keplerian disk, respectively.

either $M_\bullet$ measurements or upper limits based on resolved kinematics were available (Table 3.2). Figure 3.2 shows how such measurements compare with our $M_\bullet$ limits, once our values are rescaled accordingly to the distances adopted in these studies. Our $M_\bullet$ upper limits are consistent within 1σ with such estimates, except for NGC 3031 and NGC 4261. Furthermore, no systematic offset appears when our upper limits are compared with similar upper bounds in the literature, rather than definite measurements. A particularly complex blend of narrow Hα+[N II] and broad Hα lines may have biased our $M_\bullet$ estimates in NGC 3031.

To place our $M_\bullet$ limits on the various versions of the $M_\bullet - \sigma$ relation, we applied the aperture correction of Jørgensen et al. (1995) to the literature values of stellar velocity dispersion in order to obtain the values σ_c and σ_e and that would have been measured within a circular aperture of radius $r_e/8$ and r_e, respectively. The effective radii r_e of the spheroidal components of our sample galaxies were taken from various sources in the literature (Table 3.1) except for few disk galaxies for which r_e was obtained from our own photometric decomposition (following Méndez-Abreu et al. 2008a) of the K-band images retrieved from the archive of the Two Micron All Sky Survey (Skrutskie et al. 2006, hereafter 2MASS, see Section 2.4.1 for details)

In Figures 3.3 and 3.4, we compare our $M_\bullet$ upper limits to the $M_\bullet - \sigma$ relation, as given by both Ferrarese & Ford (2005) and Lauer et al. (2007a), initially to establish the validity of our method over a wide range of velocity dispersions. Our upper bounds show a well-defined trend with both σ_c and σ_e, running closely above the $M_\bullet - \sigma_c$ and $M_\bullet - \sigma_e$ relations. In the $M_\bullet - \sigma_c$ plane, a Spearman's rank coefficient of 0.9 suggests the presence of a correlation at 9σ confidence level whereas a Pearson correlation coefficient of 0.8 supports a linear fit to the logaritmic data, which returns a slope of 3.43 ± 0.21. At first glance, such a value would imply a shallower trend than found by Ferrarese & Ford (2005) and a slope closer to that of the Lauer et al. (2007a) relation, but we need to keep in mind that the derived slope could be significantly affected by just a few outliers. In particular, for a small value of σ, our $M_\bullet$ upper-limits could be biased owning to a larger stellar contribution to the gravitational potential in small and distant galaxies. On the other hand, we found that our limits appear to parallel particularly well both versions of the $M_\bullet - \sigma$ relation for $90 \leq \sigma_c, \sigma_e \leq 220$ km s^{-1}, whereas at lower and higher σ a substantial fraction of our $M_\bullet$ limits lie either considerably above or almost on top of the $M_\bullet - \sigma$ relation, respectively (see also Section 4.3.1).

In the following sections, we better quantify and interpret these first considerations.

3.3.1 Main trend in the sample

In the σ_c interval between 90 and 220 km s^{-1}, our $M_\bullet$ upper limits appear to correlate particularly well with σ_c paralleling the $M_\bullet - \sigma_c$ relation. In this σ_c region, a value of 0.8 for the Spearman's rank correlation coefficient suggests the presence of a correlation at a 7-σ confidence level, whereas a Pearson coefficient of 0.8 indicates that the logarithm values of our $M_\bullet$ upper limits and σ_c are very likely to be linearly correlated. A linear fit in the $\log \sigma_c - \log M_\bullet$ plane delivers a best-fitting slope of 4.52 ± 0.41 for our $M_\bullet$ upper limits, compared to the 4.86 ± 0.43 slope of the Ferrarese & Ford (2005) relation, with a scatter of 0.39 dex (Figures. 3.5a). In the $90 \leq \sigma_c \leq 220$ km s^{-1} interval, we have 66 $M_\bullet$ upper limits, which have a median 2.7 times higher than the expected $M_\bullet$ value (Figure 3.5c). These upper limits can range from falling short of the expected $M_\bullet$ values by a factor 3.7 to exceeding them by a factor 17.3, although 68% of them actually do not top the expected $M_\bullet$ values by more than a factor 4.1 and fall immediately above the $M_\bullet - \sigma_c$ relation. For comparison, by fitting our upper limits in the $M_\bullet - \sigma_e$ plane we obtain a slope of 4.12 ± 0.38, very close to the value of 4.13 ± 0.32 found by Lauer et al. (2007a). In fact, the parallel trend of our upper limits holds as far as $\sigma_e \sim 300$ km s^{-1}, with a Spearman's rank coefficient of 0.8, a Pearson linear correlation coefficient of 0.8, and a linear slope of 3.84 ± 0.28.

Figure 3.3a shows that such a trend holds independent of galactic distance −− objects as far away as 60 Mpc appear to run parallel to the $M_\bullet - \sigma_c$ relation. In particular, the objects at and below 20 Mpc are well distributed. In fact, if in this range of σ_c we perform separate linear regression for the three different populations of upper limits with $D < 30$ Mpc, $30 < D < 60$ Mpc, and $60 < D < 100$ Mpc, we find slope values that are consistent within the errors, namely of 4.05 ± 0.51, 3.51 ± 1.01, and 4.52 ± 1.14, respectively. This finding shows that the observed nuclear line widths do not simply trace an increasingly larger subtended stellar mass, as galaxies with progressively larger stellar velocity dispersions are found preferentially at larger distances. Instead, the fact that our upper limits scale in the same way with σ_c as precisely measured $M_\bullet$ determinations indicates that the nuclear emission we measured arises predominantly in regions of the gravitational potential that are dominated by the influence of the central SMBHs.

This is not completely unexpected given that a number of *HST* observations revealed that the narrow-line regions of active nuclei appear to be quite concentrated with scales less than 50 pc, much more so than the underlying stellar density profile (e.g., Ho 2008). Most recently, Walsh et al. (2008) have mapped the behavior of the narrow-line region for galaxies observed with multiple-slit STIS

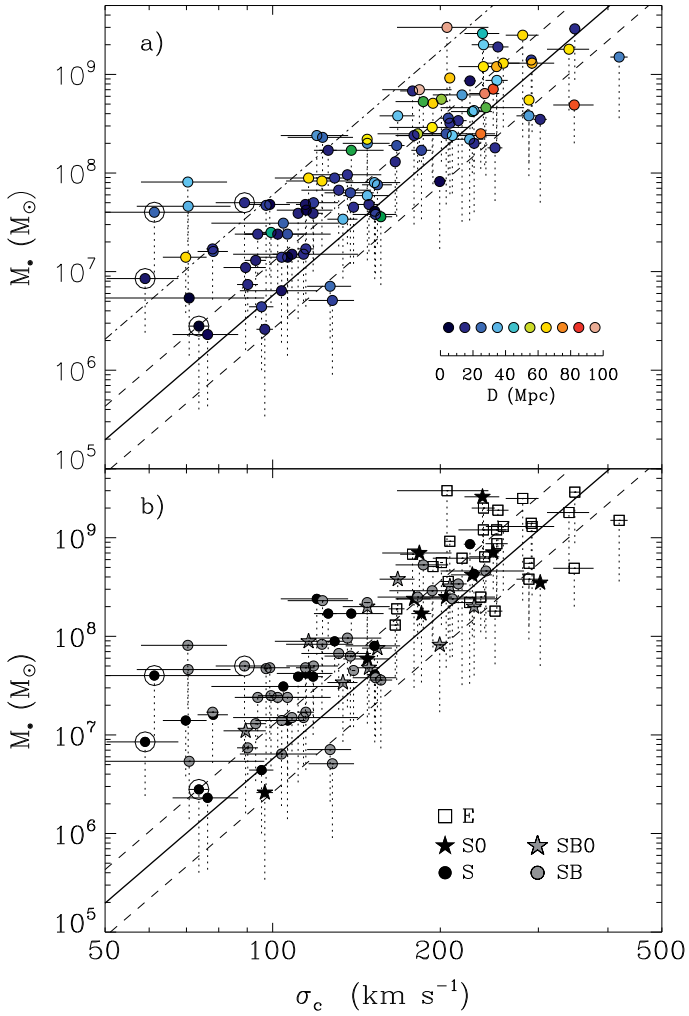

Figure 3.3 Comparison between our $M_\bullet$ upper limits and $M_\bullet - \sigma_c$ relation by Ferrarese & Ford (2005) (thick line) as a function of galaxy distance *(a)* and morphological type *(b)*. The upper and lower edges of the dotted lines correspond to $M_\bullet$ values estimated assuming an inclination of $i = 33°$ and 81° for the unresolved Keplerian disk, respectively. Large circles mark galaxies with $\sigma_c < 90$ km s^{-1} that host a nuclear star cluster. The dashed lines show the 1σ (0.34 dex) scatter in $M_\bullet$. Additionally, to follow the discussion in Sections 3.3.1 and 3.3.2, the dot-dashed line shows the 3σ (1.02 dex) scatter above the $M_\bullet - \sigma$ relation whereas the open circles point to objects where a nuclear cluster is present.

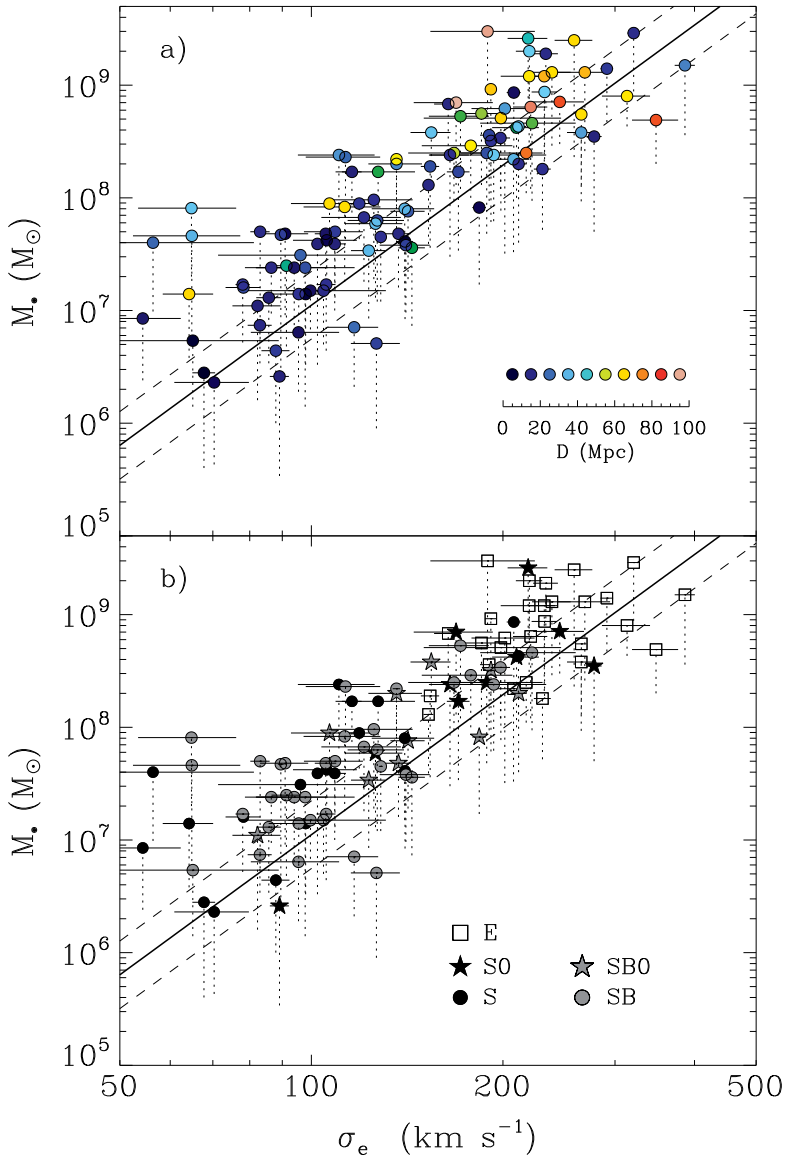

Figure 3.4 Same as Figure 3.3 but now showing the comparison between our $M_\bullet$ upper limits and the $M_\bullet - \sigma_e$ relation of Lauer et al. (2007a).

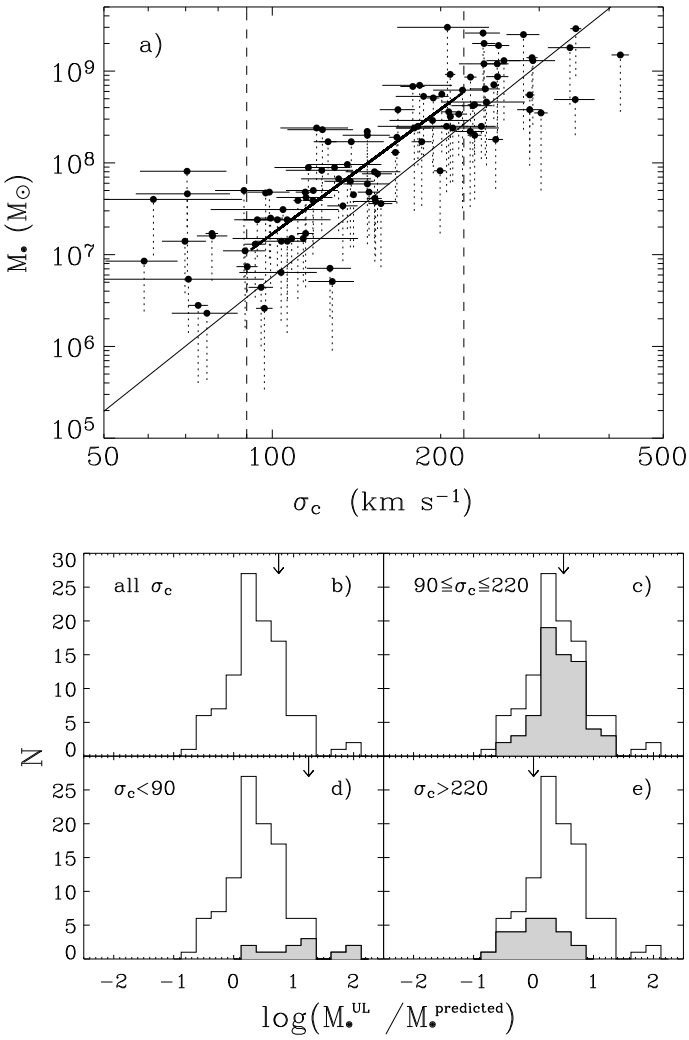

Figure 3.5 *Upper panel (a):* comparison between the linear fit to the $M_\bullet$ upper limits in the range $90 \leq \sigma_c \leq 220$ km s^{-1} (thick line) and the $M_\bullet - \sigma_c$ relation by Ferrarese & Ford (2005, thin line). Our linear fit to the $M_\bullet$ upper limits in the $90 \leq \sigma_c \leq 220$ km s^{-1} range (shown by the vertical dashed lines) delivers a best-fitting slope of 4.52 ± 0.41. *Lower panels:* distribution of the ratios between the measured upper limits and the values of $M_\bullet$ expected from the $M_\bullet - \sigma_c$ relation by Ferrarese & Ford (2005) for *(b)* all the sample galaxies, *(c)* the galaxies with $90 \leq \sigma_c \leq 220$ km s^{-1}, *(d)* with $\sigma_c < 90$ km s^{-1}, and *(e)* with $\sigma_c > 220$ km s^{-1}. The median of each distribution is marked by an arrow.

observations. They found that all galaxies of their sample exhibit a centrally peaked surface brightness profile, with the majority of them further showing a marked gradient of the emission-line widths within the sphere of influence of the central SMBH. The high degree of concentration of the gaseous tracer of the gravitational potential is what allows us to closely trace the presence of the SMBH even in objects where formally its sphere of influence is not resolved. This is similar to the case of the stellar dynamical estimates of $M_\bullet$ for M32, which have not significantly changed when moving from ground- to space-based observations (e.g., Kormendy 2004, and references therein) due to the exceptional concentration of its stellar light profile. Actually, that fact that our upper limits run so closely to the $M_\bullet - \sigma_c$ relations also suggests that non gravitational forces do not generally contribute much to the observed line widths (unless for some reason their importance scales with σ_c), although their rôle cannot be firmly excluded on a single-case basis.

Figure 3.3b also shows that in the $\sigma_c = 90 - 220$ km s^{-1} range, the upper limits derived in galaxies of different Hubble types lie neither closer nor further away from the $M_\bullet - \sigma_c$ relation, although only a relatively small number of elliptical galaxies fall in this σ_c interval. Similarly, even though only 38% of the spiral and lenticular galaxies in this σ_c region are unbarred, we do not notice any systematic trend with the presence of a bar, unlike what was found by Graham (2008).

Since our upper limits appear to trace quite closely the expected values for $M_\bullet$, we can take advantage of the significant number of galaxies in our sample to understand whether the objects that within the present σ_c range appear to show remarkably large or small upper bounds are in fact exceptional. Assuming that our 1σ limits bracket symmetrically the expected values of $M_\bullet$ and that our upper bounds lie 2.7 times above the $M_\bullet - \sigma_c$ relation, with the aid of a Monte Carlo simulation we found that 16% of our $M_\bullet$ upper limits should lie above the $M_\bullet - \sigma_c$ relation by more than three times its scatter (adopting 0.34 dex by Ferrarese & Ford 2005), while 8% of them should lie below it by more than its scatter. As Figure 3.3 shows, only four out of 66 objects in the $\sigma_c = 90 - 220$ km s^{-1} range fall that far above the $M_\bullet - \sigma_c$ relation, with an equal number falling below it by more than its scatter. Both sets of objects correspond to 6% of the galaxies in the considered σ_c range.

The previous considerations strongly argue against the presence of exceedingly large $M_\bullet$ (i.e., above the $M_\bullet - \sigma_c$ relation by more than three times its scatter) in nearby galactic nuclei, and further suggest that galaxies with considerably smaller $M_\bullet-$budgets (i.e., below the $M_\bullet - \sigma_c$ relation by more than its scatter) may be particularly rare. The presence of undermassive SMBHs in field galaxies has been suggested for instance by Vittorini et al. (2005), who

argued that in a low galactic-density environment the $M_\bullet$ growth may be hampered by the lack of gaseous fuel. A population of undermassive SMBH was also discovered by Volonteri (2007) in her simulations of the last stages of black hole mergers, when the binary experiences a recoil due to asymmetric emission of gravitational radiation. According to Figure 4 of Volonteri (2007), up to 25% of the galaxies with $90 \leq \sigma_c \leq 220$ km s^{-1} could contain undermassive SMBHs, with less than 10% with the expected $M_\bullet$. Unfortunately, only a handful of objects in our sample are massive and close enough (e.g., for $\sigma_c > 150$ km s^{-1} and $D < 20$ Mpc) to allow us to probe such a low $M_\bullet$ regime, where our simulations indicate that we should expect only $\sim 1\%$ of our upper limits. Furthermore, although the wide range of Hubble types and of values for σ_c spanned by our sample galaxies suggest these are fairly representative of the general properties of the nearby population, our sample is almost certainly incomplete, particularly as we probe the low-end of the luminosity function where most galaxies are found. Our constraints should therefore be regarded with caution.

3.3.2 The lower end of the $M_\bullet - \sigma_c$ relation

At small σ_c (< 90 km s^{-1}), half of our upper limits systematically exceed the expected $M_\bullet$ values by three times the scatter of the $M_\bullet - \sigma_c$ relation. They are on average larger by more than a factor 40 (Figure 3.5d), consistent with previous works on much more smaller samples (Sarzi et al. 2002; Sarzi 2004; Verdoes Kleijn et al. 2006). They are hosted by NGC 3021, NGC 4245, NGC 5347, NGC 5427, NGC 5879, and UGC 1395, which are late-type spirals with different degrees of nuclear activity, as measured by Ho et al. (1997a, see Table 3.1).

We have considered different possibilities related to the measurement and modeling of the [N II] λ6583 emission line to explain the high values of $M_\bullet$ found in these six objects. For instance, the presence of broad or asymmetric components in our spectra could affect the width of the narrow component of the [N II] lines that we measured and consequently the $M_\bullet$ upper limits giving larger masses. A similar bias would be introduced if the extent of the flux profile were to be systematically overestimated. Blue asymmetries are observed in the top outliers NGC 5347 and NGC 5427, which are also part of the sample of active galactic nuclei studied by Rice et al. (2006), who investigated the resolved kinematics of their narrow-line region with STIS spectra and first reported the presence of blue wings in the [S II] $\lambda\lambda$6716, 6731 lines. In our fits, however, the contribution of such additional features was isolated using double Gaussian profiles (see Figure 2.4). As regards the flux profile of the [N II] doublet of the small-σ_c outliers, these are not systematically shallower than the other galaxies following the $M_\bullet - \sigma_c$ relation in the same σ_c range. Therefore, the $M_\bullet$ upper

limits that we have calculated are not biased by either of these effects.

To explain the largest $M_\bullet$ upper limits found at low σ_c values, we also considered the impact of the presence of a nuclear star cluster (NC), and in general that of a larger stellar contribution due to a greater distance. NCs are massive stellar clusters coincident with the galaxy photocenter (Côté et al. 2006) that are found in about 75% of late-type spiral galaxies (Böker et al. 2002). Their mean effective radius is ~ 3.5 pc (Böker et al. 2004), small enough for them to be completely enclosed within the central aperture of our spectra. Ferrarese et al. (2006) found a different $M_\bullet - \sigma_c$ relation for NCs, with similar slope but a normalization that is larger by roughly an order of magnitude than the one found for SMBHs. The presence of NCs in our low-σ_c outliers could therefore explain why they show such high central mass concentrations as indicated by their high $M_\bullet$ values. To assess the incidence of NCs in the sample galaxies with $\sigma_c < 90$ km s^{-1}, we analyzed their surface brightness radial profile obtained with the IRAF task ELLIPSE on the STIS acquisition images. For half of the low-σ_c outliers, we could recognize the presence of a NC (NGC 3021, NGC 4245, and NGC 5879). On the other hand, we could identify a NC only in one (NGC 4212) of the six galaxies (17%) which run close to the $M_\bullet - \sigma_c$ relation (IC 342, NGC 2685, NGC 2748, NGC 3982, NGC 4212, and NGC 5194). The presence of a NC in the galaxies at the low-σ_c end of our sample is shown in Figure 3.3, and in the case of NGC 3021 and and NGC 5879 it was already known (see Scarlata et al. 2004; Seth et al. 2008, respectively). If our limits indeed trace the dynamical signature of a NC in these nuclei, better data and more detailed modeling (e.g., Barth et al. 2009) would be required to disentangle the contribution of the NC and SMBH to the total mass budget. As regards the distance of the low-σ_c outliers, although we can only rely on distances inferred from their recessional velocities, it is significant that half of them (NGC 5347, NGC 5427, and UGC 1395) are found beyond 30 Mpc, whereas all the other low-σ_c galaxies are significantly closer, including those for which our $M_\bullet$ upper limits lie well within three times the scatter of $M_\bullet - \sigma_c$ relation.

These findings suggest that part, if not all, of the exceedingly large $M_\bullet$ values that we found at the low-σ_c end of the $M_\bullet - \sigma_c$ relation could be ascribed to a more significant stellar contribution to the gravitational potential. This is either because of the presence of a nuclear stellar cluster (in NGC 3021, NGC 4245, and NGC 5879) or due to a larger galactic distance (for NGC 5347, NGC 5427, and UGC 1395) than otherwise required to trace the $M_\bullet - \sigma_c$ relation at these σ_c regimes. Therefore, we presently do not need to invoke either non-gravitational forces (see Sarzi et al. 2002) or a population of more massive SMBHs (see Greene & Ho 2006) to explain the observed flattening of the $M_\bullet - \sigma_c$ relation

at low $M_\bullet$ values.

3.3.3 The upper end of the $M_\bullet - \sigma_c$ relation

At high σ_c (> 220 km s^{-1}), our $M_\bullet$ upper limits nicely bracket the $M_\bullet - \sigma_c$ relation (Figure 3.5e) and most of them are consistent with its scatter (Figure 3.3). In fact, only four objects (15%; NGC 2911, NGC 4552, NGC 4594, and NGC 5077) fall above the $M_\bullet - \sigma_c$ relation by more than its scatter, with the same number of galaxies falling as far below the $M_\bullet - \sigma_c$ relation (NGC 3998, NGC 4278, NGC 6861, and UGC 1841). These outliers do not stand out from the rest of the objects with $\sigma_c > 220$ km s^{-1} for any obvious property such as morphology, nuclear activity, or distance. This behavior is suggestive of an actual flattening of the high-mass end of the $M_\bullet - \sigma_c$ relation, particularly considering that in the most massive and radio-loud galaxies the ionized-gas velocity dispersion can show a significant excess over a purely gravitational model (e.g., Verdoes Kleijn et al. 2006)[5].

The flattening at high-σ values is less evident when our upper limits are compared to the shallower $M_\bullet - \sigma_e$ relation of Lauer et al. (2007a), but is nonetheless present upon closer inspection. In particular, excluding objects with $\sigma_e < 90$ km s^{-1} where the impact of the stellar potential on our $M_\bullet$ estimates could be more important, we found a systematic flattening in the main trend of our upper limits as the high-σ_e end of the $M_\bullet - \sigma_e$ plane is progressively populated. Specifically, whereas a linear fit to objects with $\sigma_e = 90 - 220$ km s^{-1} yields a slope of 4.12 ± 0.38 (Section 3.3), extending this range to 280 km s^{-1}, 340 km s^{-1} and up to the maximum σ_e value in our sample of 386 km s^{-1} results in best-fitting values of 3.86 ± 0.29, 3.78 ± 0.27 and 3.56 ± 0.26, respectively.

This finding would be in agreement with the predictions of semianalytic models for the coevolution of SMBHs and galaxies at the highest end of the mass spectrum, whereby galaxies and SMBHs grow mainly via gas-poor, dry mergers (Schawinski et al. 2006). Yet, the behavior of $M_\bullet - \sigma_c$ relation in this regime is still under debate. In particular, the limited number of galaxies with reliable $M_\bullet$ measurement in the range $M_\bullet > 10^9$ M$_\odot$ are actually consistent with a steepening of the $M_\bullet - \sigma_c$ relation (e.g., Wyithe 2006; Dalla Bontà et al. 2009, see also Section 6.7). Furthermore, the cutoff at $\sigma_c \sim 400$ km s^{-1} of the local velocity dispersion function (Sheth et al. 2003) implies either that SMBHs with $M_\bullet > 3 \times 10^9$ M$_\odot$ are extremely rare or that if they exist their host galaxies

[5] In fact, for the two radio-loud galaxies in our sample that were also studied by Verdoes Kleijn et al. (NGC 383 and UGC 7115) the derived $M_\bullet$ upper limits lie above the $M_\bullet - \sigma_c$ relation.

should lie considerably above the present $M_\bullet - \sigma_c$ relation. In fact, at these regimes, Lauer et al. (2007a) argue that the stellar luminosity L is better suited than σ_c to trace $M_\bullet$. The $M_\bullet - \sigma_c$ relation should steepen at its high-σ_c end if Lauer et al. arguments are correct, since the observed σ_c saturates for the most massive of ellipticals while considering increasingly large values of L.

Although our results suggest a flattening of the $M_\bullet - \sigma_c$ relation, we need to keep in mind that systematic effects related to the measurement of the bulge properties may be significant at the high-σ_c end of the $M_\bullet - \sigma_c$ plane. In particular, the aperture correction for the stellar velocity dispersion may be both more important and more uncertain for the most massive of ellipticals than for smaller elliptical and lenticular galaxies. Indeed, giant ellipticals tend to have shallower central surface brightness profiles than their less massive counterparts, which makes the aperture correction more sensitive to the quality and spatial coverage of the stellar kinematics and to uncertainties on the value of the galaxy effective radius, r_e. Incidentally, measurements on r_e are also generally less accurate for giant ellipticals, due the presence of extended stellar halos. Ideally, rather than σ_c one would like to have a quantity that is more closely connected to the stellar mass, such as the total K-band luminosity, which is also known to relate to $M_\bullet$ (Marconi & Hunt 2003), or a *direct* measurement of σ_e. Obtaining the K-band luminosity of our sample galaxies would require much deeper images than the available 2MASS data (see Section 2.4), whereas properly measuring σ_e requires integral-field observations, such as those derived in the case of the SAURON survey (Emsellem et al. 2007).

3.3.4 Summary

Owing to the exquisite spatial resolution of *HST* and to the concentrated character of the ionized-gas emission in low-luminosity AGNs, we have been able to set tight upper limits on $M_\bullet$ for a sample of 105 nearby galaxies ($D < 100\,\mathrm{Mpc}$) using STIS/G750M spectra. This sample spans a wide range of Hubble types (with 54% of spirals) and includes objects with published values for their central stellar velocity dispersion σ_c. Our main findings are:

- Independent of the galaxy distance, our $M_\bullet$ upper limits run parallel and above the $M_\bullet - \sigma_c$ relation, particularly for values of σ_c between 90 and 220 $\mathrm{km\,s^{-1}}$. The median of the 66 $M_\bullet$ upper limits in this σ_c regime exceeds the expected $M_\bullet$ value by a factor 2.7, with 68% of our upper limits falling immediately above the $M_\bullet - \sigma_c$ relation and without exceeding the expected $M_\bullet$ values by more than a factor 4.1.

- That our nebular line-width measurements trace rather well the nuclear

gravitational potential, makes large samples of $M_\bullet$ upper-limit measurements useful in constraining the frequency of objects with exceedingly low or high values of $M_\bullet$ and in probing the black hole mass budget across the entire Hubble sequence.

- No systematic trends or offsets are observed in this σ_c range as a function of the galaxy Hubble type, or with respect to the presence of a bar. Furthermore, no evidence was found to suggest that the largest or smallest $M_\bullet$ upper limit in the σ_c range between 90 and 220 km s^{-1} was actually bracketing exceptionally high or low values of $M_\bullet$. Thus, galaxies with exceedingly high $M_\bullet$ budgets must be very rare.

- For σ_c values below 90 km s^{-1} half of our $M_\bullet$ upper limits systematically exceed the expected $M_\bullet$ values by more than a factor 40, consistent with previous work on much smaller samples.

  The line-width measurements for such low-σ_c outliers are most likely affected by the stellar contribution to the gravitational potential, either due to the presence of a nuclear stellar cluster or because of a greater distance compared to the other galaxies at the low-σ_c end of the $M_\bullet - \sigma_c$ relation, for which our $M_\bullet$ upper limits are closer to the expected $M_\bullet$ values.

- At the opposite σ_c end of the $M_\bullet - \sigma_c$ relation, for values of σ_c above 220 km s^{-1}, our $M_\bullet$ upper bounds appear to lie much closer the expected $M_\bullet$ in the most massive elliptical galaxies, even falling below the $M_\bullet - \sigma_c$ relation. This flattening is less evident when our upper limits are compared with the shallower $M_\bullet - \sigma_e$ relation by Lauer et al. (2007a), but is nonetheless present upon closer inspection. In particular, excluding objects with $\sigma_e <$ 90 km s^{-1}, we found a systematic flattening in the main trend of our upper limits as the high-σ_e end of the $M_\bullet - \sigma_e$ plane is progressively populated.

  Although such a flattening of the $M_\bullet - \sigma_c$ relations at its high-σ_c end would appear consistent with models for the coevolution of supermassive black holes and galaxies driven by dry mergers, we caution that better and more consistent measurements for either the K-band luminosity or the integrated value of the stellar velocity dispersion σ_e within the bulge effective radius r_e (both better tracers of the bulge mass than σ_c) are needed before systematic effects can be ruled out.

Table 3.1: Properties of the galaxies sample

Galaxy	Morph. T.	Spec. Cl.	D (Mpc)	Ref.	M_B^0 (mag)	r_e ($''$)	Band	Ref.	σ_c (km s^{-1})	Ref.	Prop.	Apert. ($''$)	Apert. (pc)
(1)	(2)	(3)	(4)	(5)	(6)	(7)	(8)	(9)	(10)	(11)	(12)	(13)	(14)
IC 342	SABcd(rs)	H	4.0	1	−21.97	64.1	K	5	71 ± 26	17	8591	0.15×0.1	3×2
IC 3639	SBbc(rs):	S2*	48.0	2	−20.70	3.4	K	5	99 ± 5	18	9143	0.25×0.2	58×46
NGC 193	SAB0$^-$(s):	...	53.2	2	−20.22	3.5	K	5	201 ± 13	19	8236	0.30×0.2	77×52
NGC 289	SBbc(rs)	...	18.3	2	−19.91	4.0	K	6	118 ± 13	20	8228	0.25×0.2	22×18
NGC 315	E$^+$:	L1.9	61.8	2	−22.09	36.9	B	2	340 ± 30	21	8236	0.15×0.1	45×30
NGC 383	SA0$^-$:	...	63.4	2	−21.33	6.5	K	5	259 ± 18	22	8236	0.15×0.1	46×31
NGC 541	S0$^-$:	...	68.2	2	−21.19	35.8	R	7	208 ± 4	23	8236	0.30×0.2	99×66
NGC 613	SBbc(rs)	H*	16.5	2	−20.56	4.2	H	8	136 ± 20	24	8228	0.25×0.2	20×16
NGC 741	E0:	...	70.4	2	−22.17	52.1	B	2	252 ± 12	25	8236	0.30×0.2	102×68
NGC 788	SA0/a(s)	S1/S2*	51.3	2	−20.75	17.5	I	9	138 ± 20	26	9143	0.25×0.2	62×50
NGC 1052	E4	L1.9	19.4	3	−20.09	33.7	B	2	207 ± 7	27	7403	0.25×0.2	23×19
NGC 1358	SAB0/a(r)	S2	51.6	2	−20.86	10.8	V	9	186 ± 20	26	9143	0.25×0.2	62×50
NGC 1497	S0	...	80.6	2	−21.24	19.5	K	5	245 ± 21	19	7354	0.15×0.1	59×39
NGC 1667	SAB(r)c	S2	60.1	2	−21.49	0.3	V	9	193 ± 31	17	9143	0.25×0.2	73×58
NGC 1961	SABc(rs)	L2	52.1	2	−22.58	139.1	V	10	241 ± 41	24	9106	0.30×0.2	76×50
NGC 2110	SAB0$^-$	S2*	31.2	2	−20.62	14.9	V	9	219 ± 25	26	8610	0.25×0.2	38×30
NGC 2179	SA0/a(s)	...	38.4	2	−20.09	8.9	V	10	168 ± 12	28	9068	0.25×0.2	46×37
NGC 2273	SBa(r):	S2	25.0	2	−19.97	2.6	K	11	127 ± 11	26	9143	0.25×0.2	30×24
NGC 2329	S0$^-$:	...	77.5	2	−21.36	20.3	B	12	236 ± 14	29	8236	0.30×0.2	113×75
NGC 2685	(R)SB0$^+$ pec	S2/T2:	13.4	2	−18.81	15.2	V	10	89 ± 8	30	8607	0.30×0.2	19×13
NGC 2748	SAbc	H	19.9	2	−19.90	...	...	...	78 ± 5	20	8228	0.25×0.2	24×19
NGC 2787	SB0(r)$^+$	L1.9	7.5	3	−17.76	17.3	V	10	199 ± 5	27	7361	0.25×0.2	9×7
NGC 2903	SABbc(rs)	H	11.2	2	−21.14	5.7	V	10	102 ± 13	31	8228	0.30×0.2	16×11
NGC 2911	SA0(s): pec	L2	46.6	2	−21.09	7.0	K	11	238 ± 17	32	7354	0.15×0.1	34×23
NGC 2964	SABbc(r):	H	21.1	2	−20.03	0.8	V	10	106 ± 21	31	8228	0.25×0.2	26×20
NGC 3021	SAbc(rs)	...	23.9	2	−19.37	2.9	B	13	61 ± 27	33	8228	0.25×0.2	29×23
NGC 3031	SABab(s)	S1.5	3.9	3	−20.57	66.2	V	10	152 ± 4	34	7351	0.15×0.1	3×2
NGC 3078	E2-3	...	35.2	3	−20.79	22.8	B	2	226 ± 13	35	9163	0.30×0.2	51×34
NGC 3081	(R)SAB0/a(r)	S2*	35.9	2	−20.19	4.2	K	9	134 ± 8	18	9143	0.25×0.2	43×35
NGC 3227	SABa(s) pec	S1.5	19.6	2	−20.28	1.3	V	10	138 ± 14	26	7403	0.25×0.2	24×19
NGC 3245	SA0^0(r):?	T2:	20.9	3	−19.53	15.6	V	10	205 ± 18	36	7403	0.25×0.2	25×20
NGC 3310	SABbc(r) pec	H	15.6	2	−20.01	5.4	V	10	113 ± 29	17	8228	0.30×0.2	23×15
NGC 3351	SBb(r)	H	10.0	4	−19.74	13.1	V	10	104 ± 16	37	7361	0.25×0.2	12×10
NGC 3368	SABab(rs)	L2	10.4	3	−20.28	56.4	V	10	114 ± 4	34	7361	0.25×0.2	13×10
NGC 3393	(R$'$)SBa(rs):	S2*	54.2	2	−21.03	8.7	K	5	182 ± 28	17	8055	0.25×0.2	66×52
NGC 3627	SABb(s)	T2/S2	10.1	4	−20.88	51.9	V	10	108 ± 8	31	8607	0.30×0.2	15×10
NGC 3642	SAbc(r):	L1.9	23.2	2	−20.37	28.4	V	10	104 ± 27	17	8228	0.25×0.2	28×22
NGC 3675	SAb(s)	T2	13.3	2	−20.10	13.4	H	8	118 ± 5	31	8607	0.30×0.2	19×13
NGC 3801	S0?	...	49.6	2	−20.69	5.5	K	5	228 ± 19	32	8236	0.30×0.2	72×48
NGC 3862	E	...	90.6	2	−21.27	17.7	B	2	240 ± 15	38	8236	0.30×0.2	132×88
NGC 3953	SBbc(r)	T2	16.5	2	−20.71	32.0	V	10	140 ± 1	20	8228	0.30×0.2	24×16
NGC 3982	SABb(r):	S1.9	17.0	2	−19.47	...	...	...	78 ± 2	39	7361	0.25×0.2	21×16
NGC 3992	SBbc(rs)	T2:	16.4	2	−20.81	64.4	V	10	131 ± 19	39	7361	0.25×0.2	20×16
NGC 3998	SA0^0(r)?	L1.9	14.1	3	−19.26	17.6	V	10	302 ± 8	40	7354	0.15×0.1	10×7
NGC 4036	S0$^-$	L1.9	20.4	2	−20.06	19.9	V	10	167 ± 5	40	7403	0.25×0.2	25×20

Table 3.1 – Continued

Galaxy	Morph. T.	Spec. Cl.	D (Mpc)	Ref.	M_B^0 (mag)	r_e ($''$)	Band	Ref.	σ_c (km s^{-1})	Ref.	Prop.	Apert. ($''$)	Apert. (pc)
(1)	(2)	(3)	(4)	(5)	(6)	(7)	(8)	(9)	(10)	(11)	(12)	(13)	(14)
NGC 4041	SAbc(rs):	H	18.2	2	−19.54	9.1	K	5	95 ± 5	20	8228	0.25×0.2	22×18
NGC 4088	SABbc(rs)	H	12.7	2	−20.00	2.4	V	10	93 ± 4	20	8228	0.25×0.2	15×12
NGC 4143	SAB0^0(s)	L1.9	15.9	3	−19.11	0.9	V	10	230 ± 6	41	7361	0.25×0.2	19×15
NGC 4150	SA0^0(r)?	T2	13.7	3	−18.29	0.9	V	10	97 ± 3	26	8607	0.30×0.2	20×13
NGC 4203	SAB0$^-$:	L1.9	15.1	3	−19.29	14.7	V	10	166 ± 3	27	7361	0.25×0.2	18×15
NGC 4212	SAc:	H	3.4	2	−16.31	22.4	V	10	74 ± 3	20	8228	0.25×0.2	4×3
NGC 4245	SB0/a(r):	H	15.6	2	−18.96	5.7	V	10	89 ± 10	42	7361	0.25×0.2	19×15
NGC 4258	SABbc(s)	S1.9	7.3	3	−20.78	332.4	V	10	99 ± 9	31	8228	0.25×0.2	9×7
NGC 4261	E2-3	L2	31.6	3	−21.14	36.1	B	2	288 ± 14	38	8236	0.15×0.1	23×15
NGC 4278	E1-2	L1.9	16.1	3	−20.06	34.4	B	2	251 ± 8	27	7403	0.25×0.2	19×16
NGC 4314	SBa(rs)	L2	16.6	2	−19.93	21.0	V	10	115 ± 4	27	7361	0.25×0.2	20×16
NGC 4321	SABbc(s)	T2	15.2	4	−20.93	20.7	V	10	90 ± 4	27	7361	0.25×0.2	18×15
NGC 4335	E	...	63.3	2	−20.67	15.0	K	2	289 ± 6	43	8236	0.30×0.2	92×61
NGC 4374	E1	L2	18.4	3	−21.31	50.9	B	2	291 ± 7	27	7124	0.25×0.2	22×18
NGC 4429	SA0$^+$(r)	T2	19.5	2	−20.48	28.0	V	10	185 ± 8	29	8607	0.30×0.2	28×19
NGC 4435	SB0^0(s)	T2/H:	14.8	2	−19.23	24.0	V	10	149 ± 7	29	7361	0.25×0.2	18×14
NGC 4450	SAab(s)	L1.9	30.3	2	−21.66	10.8	V	10	120 ± 16	44	7361	0.25×0.2	37×29
NGC 4459	SA0$^+$(r)	T2:	16.1	3	−19.83	16.7	V	10	179 ± 13	23	7361	0.25×0.2	19×16
NGC 4477	SB0(s):?	S2	22.3	2	−20.44	24.4	V	10	154 ± 9	45	7361	0.25×0.2	27×22
NGC 4486	E$^+$0-1 pec	L2	15.9	3	−21.51	94.9	B	2	349 ± 8	23	8666	0.25×0.2	19×15
NGC 4501	SAb(rs)	S2	34.6	2	−22.84	6.0	V	10	152 ± 17	31	7361	0.25×0.2	42×33
NGC 4507	(R$'$)SABb(rs)	S2*	50.4	2	−21.23	3.9	K	5	156 ± 7	18	9143	0.25×0.2	61×49
NGC 4526	SAB0(s):	H	16.9	3	−20.61	19.7	V	10	208 ± 3	46	9163	0.25×0.2	20×16
NGC 4548	SBb(rs)	L2	19.2	3	−20.63	35.2	V	10	153 ± 14	44	7361	0.25×0.2	23×19
NGC 4552	E0-1	T2:	15.4	3	−20.36	29.3	B	2	254 ± 11	29	8472	0.25×0.2	19×15
NGC 4579	SABb(rs)	S1.9/L1.9	24.6	2	−21.66	17.0	V	10	123 ± 16	31	7403	0.25×0.2	30×24
NGC 4594	SAa(s) sp	L2	9.8	3	−21.57	50.9	V	10	226 ± 6	38	7354	0.15×0.1	7×5
NGC 4596	SB0$^+$(r)	L2::	29.3	2	−20.83	17.4	V	10	148 ± 14	47	7361	0.25×0.2	35×28
NGC 4636	E0-1	L1.9	14.7	3	−20.40	88.5	B	2	178 ± 9	48	8472	0.25×0.2	18×14
NGC 4698	SAab(s)	S2	17.6	2	−19.99	29.4	V	10	129 ± 9	28	7361	0.25×0.2	21×17
NGC 4736	(R)SAab(r)	L2	5.2	3	−19.83	45.2	V	10	106 ± 3	27	8591	0.15×0.1	4×2
NGC 4800	SAb(rs)	H	13.4	2	−18.51	15.4	R	14	111 ± 2	39	7361	0.25×0.2	16×13
NGC 4826	(R)SAab(rs)	T2	7.5	3	−20.55	5.0	V	10	115 ± 13	31	8607	0.30×0.2	11×7
NGC 5005	SABbc(rs)	L1.9	15.7	2	−20.79	5.8	V	10	215 ± 8	20	8228	0.25×0.2	19×15
NGC 5077	E3-4	L1.9	41.9	2	−20.90	22.8	B	2	239 ± 11	35	7354	0.15×0.1	30×20
NGC 5127	E pec	...	67.0	2	−21.32	40.5	K	5	194 ± 5	49	8236	0.30×0.2	97×65
NGC 5194	SAbc(s) pec	S2	8.5	2	−20.99	47.7	V	10	76 ± 10	26	9147	0.25×0.2	10×8
NGC 5248	SABbc(rs)	H	19.2	2	−20.78	0.6	R	64	128 ± 12	50	8228	0.25×0.2	23×19
NGC 5252	S0	S1.9*	95.7	2	−20.97	20.7	J	15	183 ± 26	26	8055	0.25×0.2	116×93
NGC 5283	S0?	S2*	37.0	2	−18.72	5.4	K	5	148 ± 14	26	9143	0.25×0.2	45×36
NGC 5347	(R$'$)SBab(rs)	S2*	34.6	2	−19.59	20.5	V	10	70 ± 13	26	9143	0.25×0.2	42×33
NGC 5427	SAc(s)pec	S2*	38.9	2	−21.22	29.7	V	10	70 ± 12	26	9143	0.25×0.2	47×38
NGC 5490	E	...	70.0	2	−21.34	18.5	B	2	292 ± 28	29	8236	0.30×0.2	102×68
NGC 5643	SABc(rs)	S2*	18.6	2	−21.11	2.6	H	8	97 ± 1	51	9143	0.25×0.2	22×18
NGC 5695	S?	S2*	58.5	2	−20.46	7.1	K	5	148 ± 2	26	9143	0.25×0.2	71×57
NGC 5728	SABa(r):	S2*	40.3	2	−21.37	56.0	V	10	210 ± 44	52	8123	0.15×0.1	29×19

Table 3.1 – Continued

Galaxy	Morph. T.	Spec. Cl.	D (Mpc)	Ref.	M_B^0 (mag)	r_e ($''$)	Band	Ref.	σ_c (km s^{-1})	Ref.	Prop.	Apert. ($''$)	Apert. (pc)
(1)	(2)	(3)	(4)	(5)	(6)	(7)	(8)	(9)	(10)	(11)	(12)	(13)	(14)
NGC 5879	SAbc(rs):?	T2/L2	11.4	2	−18.88	3.0	B	16	59 ± 9	16	8607	0.30×0.2	17×11
NGC 6300	SBb(rs)	S2*	15.2	2	−20.71	6.0	K	6	94 ± 5	18	9143	0.25×0.2	18×15
NGC 6500	SAab:	L2	39.1	2	−20.50	2.1	K	6	230 ± 6	27	7354	0.15×0.1	28×19
NGC 6861	SA0$^-$(s):	...	28.1	3	−20.32	9.8	K	5	419 ± 15	53	9163	0.30×0.2	41×27
NGC 6951	SABbc(rs)	S2	17.1	2	−20.45	5.4	V	10	104 ± 11	24	8228	0.25×0.2	21×17
NGC 7052	E	...	61.7	2	−21.26	34.7	J	15	239 ± 23	54	8236	0.15×0.1	45×30
NGC 7331	SAb(s)	T2	13.1	3	−21.21	48.6	V	10	126 ± 4	34	8228	0.25×0.2	16×13
NGC 7626	E pec:	L2::	40.8	2	−20.99	38.7	B	2	253 ± 11	38	8236	0.30×0.2	59×40
NGC 7682	SBab(r)	S2*	63.5	2	−20.34	9.4	K	5	122 ± 17	26	9143	0.25×0.2	77×62
UGC 1214	(R)SAB0$^+$(rs):	S2*	64.2	2	−20.47	37.0	I	9	116 ± 15	26	9143	0.25×0.2	78×62
UGC 1395	SAb(rs)	S1.9*	65.2	2	−20.21	3.4	K	5	70 ± 6	18	9143	0.25×0.2	79×63
UGC 1841	E	...	80.3	2	−21.28	...	...	...	348 ± 29	55	8236	0.30×0.2	117×78
UGC 7115	E	...	94.5	2	−20.70	10.9	B	2	205 ± 38	56	8236	0.30×0.2	137×92
UGC 12064	S0$^-$:	...	64.4	2	−20.19	3.7	K	5	281 ± 19	55	8236	0.15×0.1	47×31

NOTES. — Col.(1): Galaxy name. Col.(2): Morphological type from RC3. Col.(3): Nuclear spectral class from Ho et al. (1997a), where H = H II nucleus, L = LINER, S = Seyfert , T = transition object (LINER/H II), 1 = type 1, 2 = type 2, and a fractional number between 1 and 2 denotes various intermediate types; uncertain and highly uncertain classifications are followed by a single and double colon, respectively. The nuclear spectral class of galaxies marked with * is from NASA/IPAC Extragalactic Database (NED). Col.(4): Distance. Col.(5): Reference for Col. (4). All the distances were taken from literature (see attached list), except those we obtained from V_{3K}, the weighted mean recessional velocity corrected to the reference frame of the microwave background radiation given in RC3. These were derived as V_{3K}/H_0 with $H_0 = 75$ km s^{-1} Mpc^{-1}. Col.(6): Absolute corrected B magnitude derived from B_T^0 (RC3) with the adopted distance. Col.(7): Effective radius of the spheroidal component.
Col.(8): Band in which the effective radius were measured. Col.(9): Reference for Col.(7). Col.(10): Central velocity dispersion of the stellar component within $r_e/8$. Col.(11): Reference for the measured stellar velocity dispersion and corresponding size of the central aperture from which we calculated the value given in Col.(10) by following Jørgensen et al. (1995). We did not apply any aperture correction to the measured stellar velocity dispersions of NGC 2748, NGC 3982, and UGC 1841, because no information about the size of the aperture was available. Col.(12): *HST* proposal number under which was obtained the STIS/G750M spectrum from which we measured the central velocity dispersion of the ionized gas. Col.(13): Size of the central aperture where we measured the velocity dispersion of the ionized gas. Col.(14): Physical size of the central aperture where we measured the velocity dispersion of the ionized gas. Col.(15): Central velocity dispersion of the ionized-gas component within the aperture in Col. (13). This is the intrinsic velocity dispersion obtained from the observed one by subtracting the instrumental velocity dispersion. REFERENCES. — (1) Tully (1988); (2) de Vaucouleurs et al. (1991); (3) Tonry et al. (2001); (4) Freedman et al. (2001); (5) r_e from our photometric decomposition of 2MASS images (see Section 2.4.1); (6) Kassin et al. (2006); (7) de Souza et al. (2004); (8) Laurikainen et al. (2004); (9) Xanthopoulos (1996); (10) Baggett et al. (1998); (11) Laurikainen et al. (2005); (12) Fisher et al. (1995); (13) Kodaira et al. (1990); (14) Andredakis & Sanders (1994); (15) Marconi & Hunt (2003); (16 Falcón-Barroso et al. (2002); (17) Terlevich et al. (1990); (18) Garcia-Rissmann et al. (2005); (19) Wegner et al. (2003); (20) Batcheldor et al. (2005); (21) Davies et al. (1987); (22) Simien & Prugniel (1997a); (23) Bernardi et al. (2002); (24) Schechter (1983); (25) Bonfanti et al. (1995); (26) Nelson & Whittle (1995); (27) Barth et al. (2002); (28) Corsini et al. (1999); (29) Simien & Prugniel (1997b); (30) Simien & Prugniel (1997c); (31) Héraudeau & Simien (1998); (32) di Nella et al. (1995); (33) Héraudeau et al. (1999); (34) Vega Beltrán et al. (2001); (35) Carollo et al. (1993); (36) Simien & Prugniel (1998); (37) Whitmore et al. (1979); (38) Smith et al. (2000); (39) Sarzi et al. (2002); (40) Fisher (1997); (41) Simien & Prugniel (2002); (42) Falcón-Barroso et al. (2006); (43) Verdoes Kleijn et al. (2002); (44) Whitmore & Kirshner (1981); (45) Jarvis et al. (1988); (46) Proctor & Sansom (2002); (47) Bettoni & Galletta (1997); (48) Bender et al. (1994); (49) Noel-Storr et al. (2007); (50) Dumas et al. (2007); (51) Gu et al. (2006); (52) Wagner & Appenzeller (1988); (53) Koprolin & Zeilinger (2000); (54) van den Bosch & van der Marel (1995); (55) Balcells et al. (1995); (56) Tonry & Davis (1981).

Table 3.2: Measured properties of the galaxies sample

Galaxy	σ_g (km s^{-1})	$M_\bullet$ ($i = 33°$) ($M_\odot$)	$M_\bullet$ ($i = 81°$) ($M_\odot$)	$M_\bullet$ (low,high) ($M_\odot$)	Ref.
(1)	(2)	(3)	(4)	(5)	(6)
IC 342	60 ± 4	5.4E6	1.4E6		
IC 3639	96 ± 3	2.5E7	4.8E6		
NGC 193	183 ± 14	5.6E8	1.3E8		
NGC 289	79 ± 6	5.0E7	1.3E7		
NGC 315	335 ± 11	1.8E9	4.3E8		
NGC 383	248 ± 19	1.3E9	2.9E8		
NGC 541	206 ± 17	9.2E8	1.9E8		
NGC 613	151 ± 9	9.6E7	1.9E7		
NGC 741	496 ± 44	1.2E9	2.1E8		
NGC 788	159 ± 5	5.4E8	1.4E8		
NGC 1052	226 ± 5	3.6E8	9.4E7		
NGC 1358	176 ± 1	5.3E8	1.2E8		
NGC 1497	276 ± 18	7.1E8	3.0E8		
NGC 1667	97 ± 1	2.9E8	1.0E8		
NGC 1961	167 ± 4	4.6E8	9.4E7		
NGC 2110	242 ± 4	6.2E8	3.2E7		
NGC 2179	137 ± 8	3.8E8	1.3E8		
NGC 2273	27 ± 1	7.1E6	2.1E6		
NGC 2329	201 ± 8	2.5E8	1.1E8		
NGC 2685	69 ± 4	1.1E7	1.6E6		
NGC 2748	43 ± 4	1.6E7	1.6E7	4.4E7(0.8,7.9)	1
NGC 2787	209 ± 6	8.2E7	1.7E7	9.0E7(2.1,15.8)	2
NGC 2903	74 ± 4	2.4E7	6.4E6		
NGC 2911	400 ± 38	2.6E9	6.6E8		
NGC 2964	80 ± 4	2.4E7	1.4E6		
NGC 3021	69 ± 4	4.0E7	9.8E6		
NGC 3031	192 ± 1	4.1E7	8.4E6	9.0E7(2.1,15.8)	3
NGC 3078	192 ± 6	2.2E8	3.3E7		
NGC 3081	52 ± 1	3.4E7	8.5E6		
NGC 3227	117 ± 3	6.3E7	1.2E7	1.5E7(1.0,2.0)	4
NGC 3245	138 ± 8	2.5E8	4.8E7	2.1E8(1.6,2.6)	5
NGC 3310	46 ± 1	1.5E7	5.0E6	$<$ 4.7E7	6
NGC 3351	45 ± 2	6.4E6	1.9E6		
NGC 3368	97 ± 4	4.8E7	1.5E7		
NGC 3393	91 ± 3	2.5E8	9.4E7		
NGC 3627	79 ± 2	1.5E7	6.8E6		
NGC 3642	147 ± 11	3.1E7	2.6E7		
NGC 3675	80 ± 4	3.9E7	1.0E7		
NGC 3801	166 ± 10	4.2E8	1.0E8		
NGC 3862	188 ± 7	6.4E8	1.2E8		
NGC 3953	103 ± 6	4.5E7	1.2E7		
NGC 3982	49 ± 2	1.7E7	5.2E6		
NGC 3992	103 ± 3	6.7E7	1.8E7		
NGC 3998	426 ± 11	3.5E8	5.0E7	2.7E8(0.3,4.7)	7
NGC 4036	205 ± 5	1.9E8	3.6E7		
NGC 4041	36 ± 2	4.4E6	1.0E6	$<$ 2.0E7	8
NGC 4088	50 ± 5	1.3E7	3.4E6		
NGC 4143	211 ± 3	2.0E8	4.0E7		
NGC 4150	69 ± 9	2.6E6	3.4E5		
NGC 4203	139 ± 3	1.3E8	3.9E7	$<$ 5.2E7	2

Table 3.2 – Continued

Galaxy	σ_g (km s^{-1})	$M_\bullet$ ($i = 33°$) ($M_\odot$)	$M_\bullet$ ($i = 81°$) ($M_\odot$)	$M_\bullet$ (low,high) ($M_\odot$)	Ref.
(1)	(2)	(3)	(4)	(5)	(6)
NGC 4212	59 ± 5	2.8E6	4.0E5		
NGC 4245	117 ± 24	5.0E7	5.6E6		
NGC 4258	175 ± 3	4.8E7	9.1E6	3.9E7(3.6,4.2)	9
NGC 4261	188 ± 8	3.8E8	9.3E7	5.4E8(4.2,6.6)	10
NGC 4278	333 ± 8	1.8E8	5.2E7		
NGC 4314	56 ± 5	1.7E7	4.4E6		
NGC 4321	65 ± 1	7.4E6	3.4E6		
NGC 4335	171 ± 8	5.5E8	1.3E8	$<$ 6.0E8	11
NGC 4374	396 ± 14	1.4E9	4.7E8	$1.5E9(0.7, 1.8)$	12
NGC 4429	134 ± 5	1.7E8	3.4E7		
NGC 4435	98 ± 4	4.8E7	1.6E7	$<$ 7.5E6	13
NGC 4450	138 ± 3	2.4E8	6.5E7		
NGC 4459	216 ± 9	2.4E8	3.0E7	7.0E7(5.7,8.3)	2
NGC 4477	110 ± 2	7.6E7	1.9E7		
NGC 4486	630 ± 14	2.9E9	8.8E8	3.8E9(2.8,4.8)	14
NGC 4501	99 ± 1	8.0E7	1.5E7		
NGC 4507	54 ± 3	3.6E7	7.3E6		
NGC 4526	320 ± 11	3.2E8	6.1E7		
NGC 4548	77 ± 2	3.8E7	9.6E6		
NGC 4552	476 ± 18	1.9E9	6.9E8		
NGC 4579	231 ± 2	2.3E8	4.3E7		
NGC 4594	489 ± 20	8.6E8	2.4E8	1.0E9(0.3,1.7)	15
NGC 4596	162 ± 11	2.0E8	4.0E7	8.0E7(4.0,12.0)	2
NGC 4636	254 ± 13	6.8E8	2.5E8		
NGC 4698	92 ± 2	8.9E7	4.3E7		
NGC 4736	90 ± 5	1.4E7	3.3E6		
NGC 4800	95 ± 10	3.9E7	3.3E6		
NGC 4826	99 ± 4	4.2E7	1.8E7		
NGC 5005	204 ± 3	3.4E8	1.2E8		
NGC 5077	397 ± 13	2.0E9	4.4E8	6.8E8(4.0,11.6)	16
NGC 5127	153 ± 7	5.1E8	7.7E7		
NGC 5194	36 ± 2	2.3E6	4.3E5		
NGC 5248	45 ± 4	5.1E6	9.0E5		
NGC 5252	197 ± 6	7.0E8	1.3E8		
NGC 5283	61 ± 3	5.9E7	1.3E7		
NGC 5347	53 ± 3	4.6E7	6.5E6		
NGC 5427	78 ± 1	8.1E7	2.0E7		
NGC 5490	278 ± 21	1.3E9	2.6E8		
NGC 5643	95 ± 3	4.7E7	3.1E6		
NGC 5695	67 ± 2	2.2E8	5.1E7		
NGC 5728	121 ± 7	2.4E8	6.2E7		
NGC 5879	73 ± 4	8.5E6	2.4E6		
NGC 6300	75 ± 5	2.4E7	9.4E6		
NGC 6500	168 ± 19	4.3E8	1.3E8		
NGC 6861	623 ± 61	1.5E9	3.6E8		
NGC 6951	72 ± 1	1.4E7	5.9E6		
NGC 7052	235 ± 14	1.2E9	3.1E8	3.7E8(2.2,6.3)	17
NGC 7331	204 ± 26	1.7E8	7.4E7		
NGC 7626	279 ± 16	8.7E8	1.9E8		
NGC 7682	112 ± 3	4.8E8	1.9E8		
UGC 1214	76 ± 1	8.9E7	3.9E7		

Table 3.2 – Continued

Galaxy	σ_g (km s^{-1})	$M_\bullet$ ($i = 33°$) ($M_\odot$)	$M_\bullet$ ($i = 81°$) ($M_\odot$)	$M_\bullet$ (low,high) ($M_\odot$)	Ref.
(1)	(2)	(3)	(4)	(5)	(6)
UGC 1395	24 ± 3	1.4E7	3.8E6		
UGC 1841	330 ± 26	4.9E8	2.0E8		
UGC 7115	318 ± 14	3.0E9	3.9E8		
UGC 12064	426 ± 21	2.5E9	2.3E8		

NOTES. — Col.(1): Galaxy name. Col.(2): Central velocity dispersion of the ionized-gas component within the aperture in Col. (13). This is the intrinsic velocity dispersion obtained from the observed one by subtracting the instrumental velocity dispersion. Col.(3): $M_\bullet$ upper limit for a Keplerian disk model assuming $i = 33°$. Col.(4): $M_\bullet$ upper limit for $i = 81°$. Col.(5): Mass (and confidence interval) of the SMBH derived from modeling based on the resolved kinematics. The $M_\bullet$ of NGC 3227 and NGC 4258 were obtained by studying the dynamics of stars and water masers, respectively. The ionized-gas dynamics was used for all the remaining galaxies. Col.(6): Reference for Col.(5). REFERENCES. — (1) Atkinson et al. (2005); (2) Sarzi et al. (2001); (3) Devereux et al. (2003); (4) Davies et al. (2006); (5) Barth et al. (2001); (6) Pastorini et al. (2007(@); (7) de Francesco et al. (2006); (8) Marconi et al. (2003); (9) Miyoshi et al. (1995); (10) Ferrarese et al. (1996); (11) Verdoes Kleijn et al. (2002); (12) Bower et al. (1998); (13) Coccato et al. (2006); (14) Macchetto et al. (1997); (15) Kormendy (1988); (16) de Francesco et al. (2008); (17) van der Marel & van den Bosch (1998).

Table 3.3: Properties of the galaxies rejected from the main sample

Galaxy (1)	Morp. T. (RC3) (2)	Prop. (3)	Rej. (4)
IC 5096	Sbc sp	9046	ns
NGC 0134	SABbc(s)	8228	ns
NGC 0157	SABbc(rs)	8228	ns
NGC 0255	SABbc(rs)	8228	ns
NGC 0278	SABb(rs)	7361	r
NGC 0520	pec	8669	ir
NGC 1097	SBb(s)	9782	ds
NGC 1255	SABbc(rs)	8228	n
NGC 1300	SBbc(rs)	8228	p
NGC 1832	SBbc(r)	8228	ns
NGC 2623	pec	8669	i
NGC 2654	SBab sp:	9046	s
NGC 2892	E^+ pec:	8236	s
NGC 2976	SAc pec	8591	ns
NGC 3003	Sbc?	8228	s
NGC 3049	SBab(rs)	7513	s
NGC 3067	SABab(s)	8596	f
NGC 3162	SABbc(rs)	8228	r
NGC 3254	SAbc(s)	8228	n
NGC 3256	pec	8669	i
NGC 3259	SABbc(rs)	8228	s
NGC 3379	E1	8589	f
NGC 3403	SAbc:	8228	ns
NGC 3489	$SAB0^+$(rs)	7361	f
NGC 3516	(R)SB0(s)	8055	d
NGC 3521	SABbc(rs)	8228	ns
NGC 3684	SAbc(rs)	8228	ns
NGC 3686	SBbc(s)	8228	r
NGC 3705	SABab(r)	8607	n
NGC 3756	SABbc(rs)	8228	ns
NGC 3887	SBbc(r)	8228	s
NGC 3917	SAcd:	8607	ns
NGC 3921	(R′)SA0/a(rs) pec	8669	i
NGC 3949	SAbc(s)	8228	ns
NGC 3972	SAbc(s)	8228	ns
NGC 4030	SAbc(s)	8228	r
NGC 4038	SBm(s) pec	8669	is
NGC 4039	SBm(s) pec	8669	is
NGC 4051	SABbc(rs)	8228	r
NGC 4100	(R′)SAbc(rs)	8228	rs
NGC 4138	$SA0^+$(rs)	1039	n
NGC 4303	SABbc(rs)	8228	r
NGC 4343	SAb(rs)	9068	s
NGC 4380	SAb(rs):?	7361	n
NGC 4389	SBbc(rs)	8228	ns
NGC 4414	SAc(rc)?	8607	n
NGC 4420	SBbc(r):	8228	s
NGC 4527	SABbc(s)	8228/8607	nf
NGC 4536	SABbc(rs)	8228	r
NGC 4569	SABab(rs)	8607	r

Table 3.3 – Continued

Galaxy	Morp. T. (RC3)	Prop.	Rej.
(1)	(2)	(3)	(4)
NGC 4676A	S0 pec ? (Irr)	8669	is
NGC 4696	E^+1 pec	8690	n
NGC 5054	SAbc(s)	8228	rs
NGC 5055	SAbc(rs)	7361/8228	nr
NGC 5135	SBab(s)	9143	r
NGC 5141	S0	8236	s
NGC 5247	SAbc(s)	8228	ns
NGC 5364	SAbc(rs) pec	8228	n
NGC 5398	(R′)SBdm(s): pec	7513	s
NGC 5577	SAbc(rs)	8228	ns
NGC 5635	S pec	7354	s
NGC 5713	SABbc(rs)	8228	s
NGC 5746	SABb(rs) sp:	9046	n
NGC 5905	SBb(r)	9177	p
NGC 5921	SBbc(r)	8228	s
NGC 6384	SABbc(r)	8228	n
NGC 6503	SAcd(s)	8607	n
NGC 6621	Sb: pec	8669	is
NGC 7252	$(R)SA0^0$:	8669	i
NGC 7314	SABbc(rs)	8228	pr
NGC 7592	$S0^+$ pec:	8669	is
UGC 10814	Scd:	9782	d

Notes. — Col.(1): Galaxy name. Col.(2): Morphological type from RC3. Col.(3): *HST* proposal number under which was obtained the STIS/G750M spectrum. Col.(4): Reason of rejection, where d = problem in deblending the emission lines, i = interacting galaxy, f = irregular or strongly asymmetric radial profile of the flux of the [N II] emission lines, n = faint or absent emission lines, p = double-peaked emission lines, r = unsuccessful two-dimensional rectification of the spectrum, s = no stellar velocity dispersion available in literature.

4

On the relationships between supermassive black holes, spheroids, and dark matter halos

Based on Beifiori A., Courteau S., Zhu Y., & Corsini E. M., ApJ, to be submitted

We use the largest sample of upper limits on supermassive black hole (SMBH) masses, $M_\bullet$, and the latest compilation of $M_\bullet$, coupled with libraries of host galaxy velocity dispersions, rotational velocities and photometric parameters extracted from SDSS i-band images to establish correlations between the SMBH and host galaxy bulge and total mass. We wish to test if $M_\bullet$ is fundamentally driven by the galaxy bulge or halo. We explore for fundamental correlations between $M_\bullet$ and stellar velocity dispersion, σ, i-band bulge luminosity, $L_{i,\rm bulge}$, bulge virial mass, $M_{\rm vir,bulge}$, bulge Sérsic index, n, i-band luminosity of the galaxy, $L_{i,\rm gal}$, galaxy stellar mass, $M_{\star,\rm gal}$, maximum circular velocity, $V_{\rm c}$, galaxy dynamical and virial masses, $M_{\rm dyn,gal}$ and $M_{\rm vir,gal}$. We verify the tightness of the $M_\bullet - \sigma$ relation, and find that correlations with other galaxy parameters do not yield tighter trends. We confirm that $M_\bullet$ is fundamentally driven by σ for all Hubble types. The fundamental plane of the SMBH is indeed mainly driven by σ, with a small fraction of the tilt being due to the effective radius, $r_{\rm e}$.
We provide a compendium of galaxy structural properties for most SMBH hosts known to date.

4.1 Introduction

It is well known that the mass $M_\bullet$ of the supermassive black holes (SMBHs) is closely tied with the properties of galaxy spheroids such as the bulge lu-

minosity, $L_{\rm bulge}$ (Kormendy & Richstone 1995; Marconi & Hunt 2003; Graham 2007; Gültekin et al. 2009b, hereafter G09), the stellar velocity dispersion, σ (Ferrarese & Merritt 2000, Gebhardt et al. 2000a, Tremaine et al. 2002, Ferrarese & Ford 2005, G09), the mass of the bulge, $M_{\rm bulge}$ (Magorrian et al. 1998; Häring & Rix 2004), the central light concentration, C (Graham et al. 2001), the Sérsic index n (Graham & Driver 2007), the virial mass of the galaxy, $M_{\rm vir,gal}$ (Ferrarese et al. 2006), the gravitational binding energy, $E_{\rm g}$ (Aller & Richstone 2007), the kinetic energy of random motions of the bulge (Feoli & Mancini 2009), and the stellar light and mass deficit associated to the core ellipticals (Kormendy & Bender 2009). Most of these relations are compared in Novak et al. (2006).

Given the $M_\bullet - \sigma$ and the relation between the circular velocity, $V_{\rm c}$, and σ (i.e., the $V_{\rm c}-\sigma$ relation), Ferrarese (2002) and Pizzella et al. (2005) suggested a link between $M_\bullet$ and $V_{\rm c}$ (or equivalently with the mass of the dark-matter halo). However, more extensive analyses by Courteau et al. (2007) and Ho (2007) showed the $V_{\rm c}-\sigma$ relation depends on the morphological type (or equivalently the light concentration or surface brightness of the galaxy) thus excluding a simple connection between $M_\bullet$ and $V_{\rm c}$.

Several authors noted that the residuals of the $M_\bullet - \sigma$, and $M_\bullet - L_{\rm bulge}$ scaling relations correlate with the effective radius of the galaxies (e.g., Marconi & Hunt 2003). Hopkins et al. (2007a,b) suggested the possibility of a linear combination between different galaxy properties to reduce the scatter of the $M_\bullet$ relations, introducing the idea of a fundamental plane of SMBHs (BHFP). All the SMBH scaling relations could thus be seen as projections of the BHFP (Aller & Richstone 2007; Barway & Kembhavi 2007).

The existence of SMBH-host galaxy scaling relations suggests a connection between SMBHs and their host galaxies. A better understanding of these relations would significantly improve the theoretical models of the SMBH growth and evolution. $M_\bullet$ could be not simply related with only one galaxy parameter (such as the stellar mass) but with a combination of them. This would suggest a SMBH growth sensitive to the overall structure of the galaxy. The local characterization and cosmic evolution of scaling relations have already provided valuable constrains on theoretical models for the coevolution of galaxies and SMBHs (Granato et al. 2004; Vittorini et al. 2005; Hopkins et al. 2006; Croton et al. 2006; De Lucia et al. 2006; Cavaliere & Menci 2007; Monaco et al. 2007; Marulli et al. 2008). Analytical models and numerical simulations have demonstrated that the observed scaling relations could be reproduced in feedback-regulated models of SMBH growth with strong feedback from the active galactic nucleus (AGN, Silk & Rees 1998; Cox et al. 2006; Robertson et al. 2006a,b; Di Matteo et al. 2005). In particular, these models predict and explain

the existence of a BHFP (Hopkins et al. 2007a,b, 2009). However, even if the observed relations can be reproduced, the models still depend on their assumed trend and scatter (Somerville 2009). These are far to be in agreement in the several works on $M_\bullet$ scaling relations. A better constrain for the slope and scatter of the scaling relations could be obtained with a larger number of $M_\bullet$ determinations, in particular at the high and small trend of σ and for different morphological types.

With the large sample of galaxies we are using in this work we can improve the understanding of all these connections over a large range of $M_\bullet$, morphological type and nuclear activity and test the possible linear combinations of various galaxy parameters.

The chapter is organized as follows. In Section 4.2 we describe our galaxy sample and investigate its properties. We present our analysis in Section 4.3 and discuss our findings in Section 4.4. In Section 4.5 we discuss our conclusions.

4.2 Sample selection

4.2.1 Supermassive black hole masses data sample

The $M_\bullet$ values were retrieved from two different samples: the compilation of upper limits on SMBH masses from Beifiori et al. (2009, hereafter B09, see Chapter 3) and the compilation of secure $M_\bullet$ by G09.

The $M_\bullet$ estimates of B09 were obtained by modeling the emission-line width of *Hubble Space Telescope* (*HST*)/ Space Telescope Imaging Spectrograph (STIS) archival spectra in terms of gas motions in a thin disk of unknown orientation but known spatial extent following the method of Sarzi et al. (2002) as shown in Section 3.2.3. The sample comprises 105 nearby galaxies (<100 Mpc) for which nuclear spectra were obtained with grating STIS/G750M including the region of the Hα line and the [N II] $\lambda\lambda 6548, 6583$ and [S II] $\lambda\lambda 6716, 6731$ doublets, and with published values for their central σ. This sample of 105 galaxies spans a wide range of Hubble types with 27 % of ellipticals, 19% of lenticulars, and 54% of spirals. In addition, we were able to include 2 upper limits unpublished in B09 (NGC 2892, NGC 5921), thanks to two newly published values of σ (Ho et al. 2009). This will represent our sample 1. Our $M_\bullet$ values are upper limits because the sphere of influence (i.e., the region within which the SMBH dominates the gravitational potential) and the velocity gradient are not resolved. Following Sarzi et al. (2002), we adopted two different inclinations for the gaseous disk corresponding to the 68% upper and lower confidence limits for randomly orientated disks, with a nearly face-on disk ($i = 33°$) hosting a larger $M_\bullet$, and a nearly edge-on disk (81°) corresponding to a smaller $M_\bullet$ (see B09 and Section 3.2.3 for more details). Therefore, mass estimate corresponds

to a range of upper limits on $M_\bullet$ at different inclinations. The case $i = 33°$ maximizes the upper limits on $M_\bullet$, therefore we use it for the computations. The stellar velocity dispersion was retrieved from the literature and then was rescaled to the velocity dispersion within $r_e/8$ and within r_e according to the prescription of Jørgensen et al. (1995). In B09 we used the $M_\bullet - \sigma$ relation of Ferrarese & Ford (2005) and Lauer et al. (2007a) to assess the validity of the $M_\bullet$ upper limits over a wide range of σ and to compare those upper limits against the set of secure $M_\bullet$ values. Independent of the galaxy distance, morphological type or bar presence, our $M_\bullet$ upper limits run parallel the above-mentioned versions of $M_\bullet - \sigma$ relations. Thus, while we could not rule out the presence of non-gravitational forces, our line width measurements broadly trace the nuclear regions dominated by the central SMBH, which allowing us to estimate $M_\bullet$. Ultimately though, we can treat our upper limits estimates as legitimate determinations, albeit with large error bars, and use them to test for correlations of $M_\bullet$ against various galaxy parameters.

The second part of the sample comprises all the precise $M_\bullet$ values compiled by G09 and the upper limits on $M_\bullet$ presented in the same paper. This compilation includes all the direct dynamical measurements published up to November 2008, for 49 galaxies and 19 upper limits on $M_\bullet$. We selected all the secure $M_\bullet$ and five of these upper limits on $M_\bullet$, two of them were not in common with our sample and three were measured with more sophisticated modeling than our. We decided to use our $M_\bullet$ values for the remaining 13 upper limits presented in G09, because they are part of the Sarzi et al. (2002) sample and therefore were measured with our own method. This compilation of $M_\bullet$ and upper limits will represent our sample 2. In general, the agreement between all these values is good as is shown in Figure 3.2.

All the data relative to the sample 1 and 2 are showed in Table 4.1 and 4.2, respectively. We rescaled the upper limits on $M_\bullet$ from B09 to the adopted distances of this chapter obtained assuming $H_0 = 70$ km s^{-1} Mpc^{-1}, $\Omega_m = 0.3$, and $\Omega_\Lambda = 0.7$, to be consistent with the G09 sample. The combination of the samples 1 and 2 of $M_\bullet$ yields to a total sample of 143 $M_\bullet$ determinations, 49 precise $M_\bullet$ values from G09, 5 upper limits from G09, and 89 upper limits from B09. According to the morphological type, 29% of the galaxies are ellipticals, 27% lenticulars, and 44% spirals (RC3). Some of the objects display some amount of nuclear activity: 23% are LINERS, 11% H II nuclei, 25% Seyfert, 8% "transition" objects, and the remaining 33% do not show emission (Ho et al. 1997a).

4.2.2 Galaxy properties

The aim of this chapter is to compare the $M_\bullet$ determinations with the local and global galaxy properties including the stellar velocity dispersion σ, the i-band bulge luminosity $L_{i,\mathrm{bulge}}$, the bulge virial mass $M_{\mathrm{vir,bulge}}$, the Sérsic index of the bulge n, the bulge effective radius $r_{\mathrm{e,bulge}}$, the i-band total luminosity of the galaxy $L_{i,\mathrm{gal}}$, the stellar mass of the galaxy $M_{\star,\mathrm{gal}}$, the circular velocity V_{c}, the virial mass $M_{\mathrm{vir,gal}}$, the dynamical mass $M_{\mathrm{dyn,gal}}$ and the effective radius $r_{\mathrm{e,gal}}$ of the galaxy.

We used the central velocity dispersion of the stellar component obtained within the effective radius of the bulge, $r_{\mathrm{e,bulge}}$, following the prescription of Jørgensen et al. (1995). We did not apply any aperture correction to the measured stellar velocity dispersions of NGC 2748, NGC 3982, and UGC 1841, since no information about the size of the aperture was available. G09 derived the effective velocity dispersion as luminosity-weighted mean of the second moment of the line-of-sight velocity distribution within the effective radius.

We extracted the structural properties of the galaxies from the analysis of g, r, and i-band images retrieved from the seventh release (DR7, Abazajian et al. 2009) of the Sloan Digital Sky Survey (SDSS, York et al. 2000). We found SDSS-DR7 images for 46 galaxies of the sample 1 and for 28 galaxies of the sample 2 yielding a total of 74 sample galaxies. Deep surface-brightness profiles were extracted for these images following the procedures of McDonald et al. (2009, , see Figure 4.1 for some examples).

We performed a two-dimensional bulge-to-disk decomposition to extract the structural parameters of the bulge by using the GASP2D code (GAlaxy Surface Photometry 2Dimensional Decomposition, Méndez-Abreu et al. 2008a, see also Section 2.4). The two-dimensional decomposition is important to obtain the structural parameters of the bulge and the disk without the systematic errors due to the different intrinsic shapes of disk and bulge, combined with the effect of viewed inclination (e.g., Byun & Freeman 1995). The structural parameters in a sample mostly dominated of spiral galaxies are strongly dependent on color (e.g., Möllenhoff et al. 1999; MacArthur et al. 2004; Gadotti et al. 2010). This is a consequence of the dominating stellar population in the corresponding filter and of the effect of dust absorption. Therefore, we focused our analysis on the i-band images to better disentangle the bulge parameters from those of disk. This redder wavelength allowed us to be less affect by the dust or bright young stars and to be able detect better the evolved stars that more contribute to the total mass of the galaxy (e.g., Möllenhoff & Heidt 2001).

We assumed the galaxy surface-brightness distribution to be the sum of the contributions of a bulge and a disk component for lenticulars and spirals, and

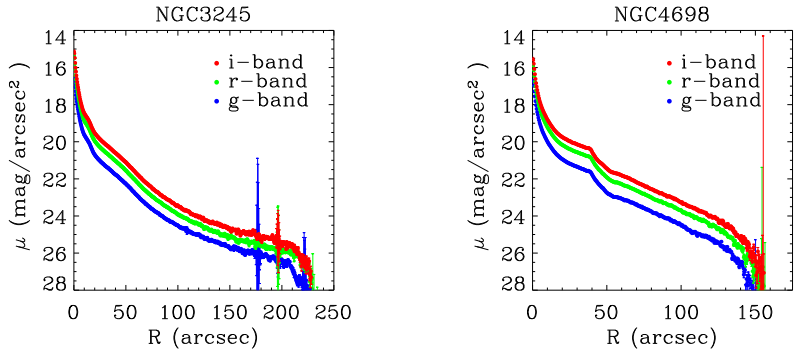

Figure 4.1 Example of surface-brightness profiles in NGC 3245 (*left panel*) and NGC 4698 (*right panel*) extracted following the procedures of McDonald et al. (2009).

due to a spheroidal component for ellipticals. Spheroid isophotes are ellipses centered on the image, with constant position angle, $\mathrm{PA_b}$, and constant axial ratio, q_b. Disk isophotes are ellipses centered on the image, with constant position angle, $\mathrm{PA_d}$, and constant axial ratio, q_d, implying that the galaxy inclination is $i = \arccos q_\mathrm{d}$. We adopted the Sérsic law (Sersic 1968) to describe the surface-brightness of the spheroidal component

$$I_\mathrm{b} = I_\mathrm{e} 10^{-b_n\left[(r_\mathrm{b}/r_\mathrm{e})^{1/n}-1\right]}, \tag{4.1}$$

where r_e, I_e, and n are the effective radius, surface brightness at r_e, and a shape parameter describing the curvature of the profile, respectively . The value of b_n is coupled to n so that half of the total flux is always within r_e and can be approximated as $b_n = 0.868n - 0.142$ (Caon et al. 1993). For the surface-brightness distribution of the disk component we assumed the exponential law (Freeman 1970)

$$I_\mathrm{d} = I_0\, e^{-r_\mathrm{d}/h}, \tag{4.2}$$

where h and I_0 are the scale length and central surface brightness of the disk, respectively. We generally fitted a Sérsic function to all the ellipticals and a Sérsic plus exponential law for lenticulars and spirals. We fitted also a Sérsic with exponential law to galaxies with uncertain classification and we selected the best representation of the galaxy by looking at the residual of the two-dimensional fit.

To derive the photometric parameters of the bulge (I_e, r_e, n, PA_b, and q_b) and disk (I_0, h, PA_d, and q_d) and the position of the galaxy center of the image we fitted iteratively a model of the surface brightness $I_m = I_b + I_d$ to the pixels of the galaxy image using a non-linear least-squares minimization based on the robust Levenberg-Marquardt method by Moré et al. (1980). The actual computation has been done using the `MPFIT`[1] algorithm implemented by C. B. Markwardt under the `IDL`[2] environment. Each image pixel has been weighted according to the variance of its total observed photon counts due to the contribution of both the galaxy and sky, and determined assuming photon noise limitation and taking into account for the detector read-out noise. The seeing effects were taken into account by convolving the model image with a circular Moffat function (Trujillo et al. 2001) with the FWHM measured from the stars in the galaxy image. The convolution was performed as a product in Fourier domain before the least-squares minimization. The fit is done in intensity units, and all the pixels, mask automatic to reject the foreground stars, dust lanes, spiral arms, and all the features that can spoil the fit. We first assess all the galaxy parameters from the analysis of our images and with the calibration derived from the table of parameters relative to the image from SDSS archive. The final sample of galaxies for which we could perform an accurate two-dimensional decomposition comprises 49 galaxies (31 from sample 1 and 18 from sample 2) a couple of examples are shown in Figure 4.2.
We discarded galaxies with Freeman II profiles, with unrealistic or unphysical decompositions, and galaxies that would need a strong bar component to model the light distribution. The photometric parameters and comments on the discarded galaxies are presented in Tables 4.3 and 4.4, respectively.

We assessed our decompositions through a series of Monte Carlo simulations on artificial galaxies. We used these artificial galaxies to have a reliable estimation of the errors, because the formal errors obtained from the χ^2 minimization method are usually not representative of the real errors in the structural parameters (see Table 4.3). Similar analysis was performed in Sections 2.4.1 and 2.4.2. This is the safest way to take into account for the degeneration between the structural parameters.

We generated a set of 400 images of galaxies with a Sérsic bulge and an exponential disk and 400 images with a Sérsic spheroids. The structural parameters of the artificial galaxies with a bulge and a disk were chosen among the values presented in Gadotti (2009) for a representative sample of nearby 1000 galaxies from g, r and i- band SDSS images in which the photometric de-

[1]The code is available at http://cow.physics.wisc.edu/ craigm/idl/idl.html
[2]Interactive Data Language

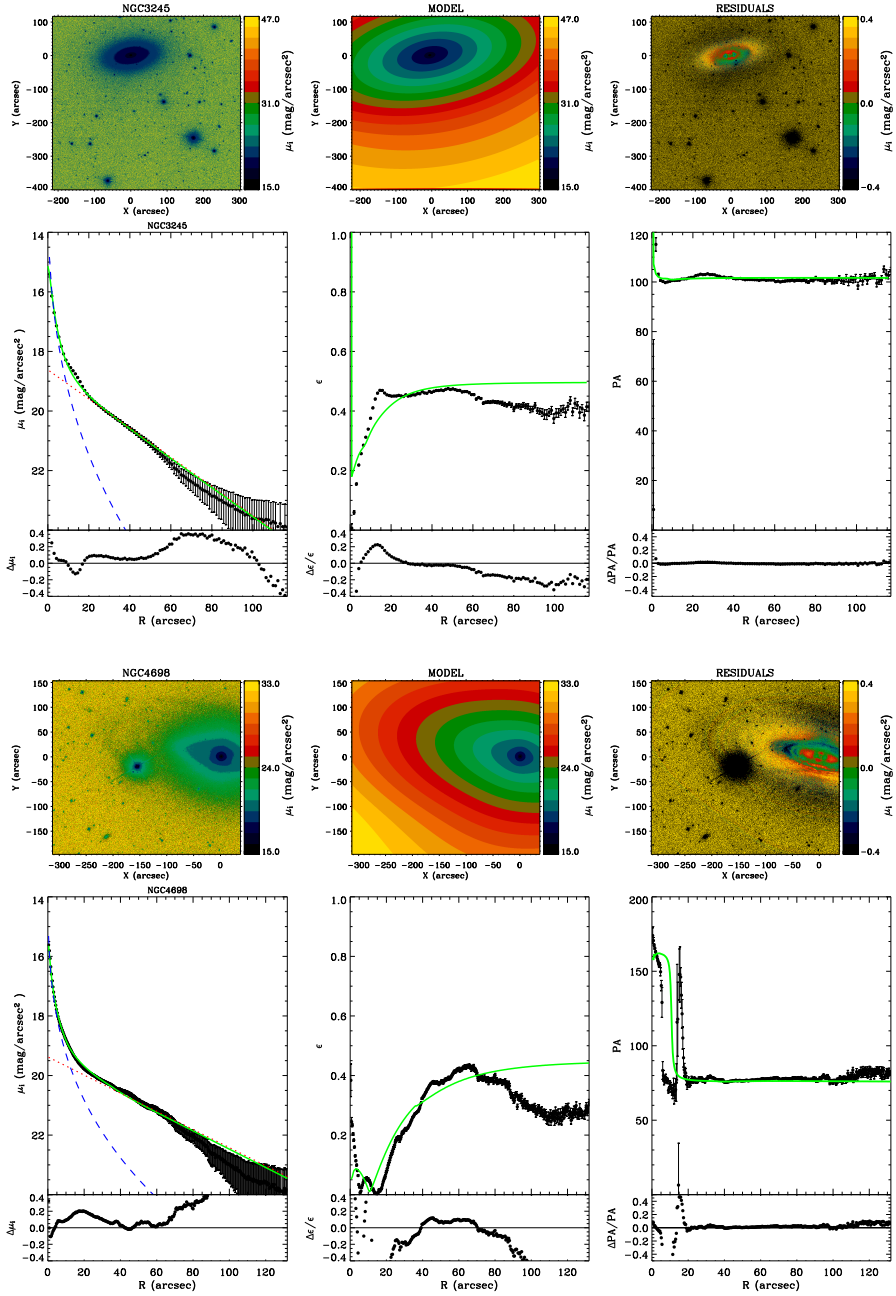

Figure 4.2 Example of two-dimensional photometric decompositions of NGC 3245 (*upper panel*) and NGC 4698 (*lower panel*) with GASP2D.

composition was carefully derived with a two-dimensional code. We extended the range of possible axial ratios to the one of our sample, since Gadotti (2009) analyzed only galaxies with $b/a \geq 0.9$, where a and b are the semi-major and semi-minor axes of the galaxy, respectively. For elliptical galaxies we used the typical values of the large photometric analysis of nearby early-type galaxies by Kormendy et al. (2009). Moreover, we generated galaxies in our range of magnitudes. The simulated galaxies were assumed to be at the median distance of the sub-sample for which we could perform the two-dimensional decomposition of 17.9 Mpc, which corresponds to a scale of ~ 87 pc arcsec^{-1}. We assumed SDSS pixel scale ($0\farcs3946$ pixel^{-1}) and an average value for the CCD gain 4.961 and RON 6.101, to mimic the instrumental setup of the observed galaxies. Finally, a background level and a photon noise were added to the resulting images to yield a signal-to-noise ratio similar to that of the observed images. To estimate the errors associated to the decomposition, the code GASP2D was applied to the artificial images. Then, the relative errors (1- v_i/v_o) were estimated by comparing the input (v_i) and output (v_o) values. To assign to every single galaxy the corresponding error for every structural parameter, we divided our catalogue of artificial galaxies in bins of 0.5 magnitudes, we assumed that the errors were normally distributed, with mean and standard deviation corresponding to the systematic and typical error, respectively. Then we placed our observed galaxy in its magnitude bin and assigned to every parameter the corresponding error.

To account for the global properties of the galaxy we followed the procedure described by McDonald et al. (2009). It yields the total galaxy luminosity by summing the flux at each isophote and extrapolating the surface-brightness profile to infinity. This allowed us to have a complete estimate of the total luminosity of the galaxy and all the global parameters that we needed in our analysis. The inclination of the galaxy was determined from the typical ellipticity of the disk. We extracted the isophotal radius and luminosity at the surface brightness of 24.5 mag arcsec^{-2} (i.e, corresponding to the typical radius at which we could measure the last data point in the surface-brightness profiles). We also derived structural parameters like the effective radius of the galaxy, $r_{\rm e,gal}$, effective surface brightness of the galaxy, $I_{\rm e,gal}$, and concentration $C_{28} = 5\log(r_{80}/r_{20})$, where r_{80} and r_{20} are the radii which enclose at the 80 and 20 percent of total light, respectively. Our structural parameters are based on the i-band photometry, which is less affected by the dust than the g- and r bands. Color gradients made use of all g, r, and i bands. The photometric parameters are given in Tables 4.5 and 4.6. All the photometric parameters we have estimated are zero-pointed to the SDSS system and corrected for Galactic extinction, K correction, and internal extinction (assuming transparent disks) following Shao et al. (2007).

As far as the circular velocities concerned, we retrieved 21-cm line widths from the compilation of Ho (2007) for 46 galaxies (34 of the sample 1 and 12 of the sample 2). The 21-cm rotational velocities of IC 342 and Milky Way were obtained from Pizzella et al. (2005), and Baes et al. (2003), respectively. Maximum circular velocities of 4 elliptical galaxies in sample 1 and 5 in sample 2 were taken from Kronawitter et al. (2000). We found the maximum circular velocity of NGC 1023 from the asymmetric drift solution of Debattista et al. (2002). Finally, for the remaining 35 galaxies of the sample (25 from the sample 1 and 10 from sample 2) we retrieved the 21-cm line widths from the Hyperleda catalog[1] (Paturel et al. 2003a). The data in Hyperleda were corrected following the prescriptions of Ho (2007). The rotational velocities from H I profiles and spatially resolved optical rotation curves in Hyperleda were homogenized in the manner of Paturel et al. (2003b). The line widths in Hyperleda are already corrected for instrumental resolution. Therefore we applied only the correction for cosmological stretching and broadening for interstellar turbulence following Bottinelli et al. (1983) and Verheijen & Sancisi (2001). The H I line widths are then deprojected along the line-of-sight by using RC3 inclinations (de Vaucouleurs et al. 1991) and accounting for the intrinsic disk thickness as in Paturel et al. (1997). Finally, deprojected H I line widths were converted to in circular velocities according to the formula in Ho (2007). Thirty-two of these galaxies presented multiple measurements of the line width at different noise level. The typical rms deviations for multiple measurements rarely exceeds 5%; only in few cases do we find a larger deviation, never greater than 11%. For the uncertaintities associated to V_c we used the values given in Hyperleda.

We have checked the RC3 inclinations. Thanks to our own photometry, we could derive inclinations from the ellipticity of the i-band SDSS images. For the 39 galaxies (lenticulars and spirals) of the sample that had both the circular velocity and SDSS photometric parameters, we compared the distribution of the point in the $V_c - \sigma_e$ relation for the maximum rotational velocities deprojected using both the inclinations from RC3, and the inclination derived from our own photometry (Figure 4.3). The elliptical galaxies with V_c from the stellar models are excluded in this comparison. We obtained the apparent flattening q from the measured SDSS ellipticity, and the inclination from $\cos^2 i = (q^2 - q_0^2)/(1 - q_0^2)$, by assuming the intrinsic thickness q_0 be a function of the morphological type as is given by Haynes & Giovanelli (1984). The V_c obtained from RC3 inclination and from SDSS inclination have the similar trend, although the latter result less consistent with the $V_c - \sigma_e$ relation by Ho (2007). We compared also the distribution of the $\log(V_c/\sigma_e) - C_{28}$ for our joint sample, with the relation found

[1] http://leda.univ-lyon1.fr

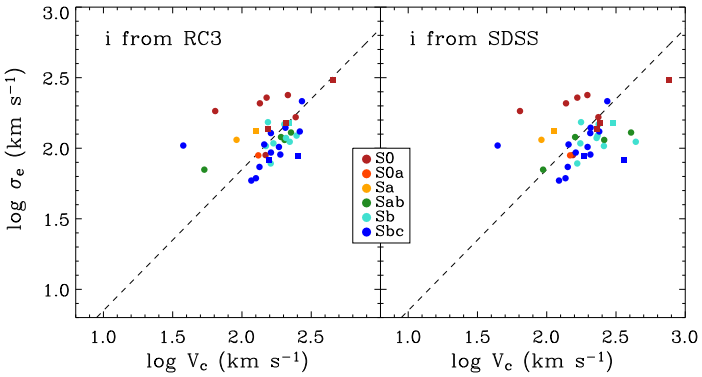

Figure 4.3 Comparison between the maximum rotation velocity, deprojected by using the inclination from RC3 (*left panel*) and from our own SDSS photometry (*right panel*), and σ_e. The sample comprises 39 galaxies with SDSS data and maximum rotational velocities (32 galaxies part of sample 1, dots, and 7 galaxies part of sample 2, squares). The dashed line is the relation by Ho (2007). Galaxies are separated by morphological type.

by Courteau et al. (2007) finding a general agreement (Figure 4.4).

The final collection of circular velocities includes 64 galaxies from sample 1 and 29 galaxies from sample 2 for a total of 93 data point. All the values for the maximum rotational velocity, their references, the circular velocities, and the used inclination are presented in Tables 4.1 and 4.2.

4.3 Analysis

4.3.1 Correlations with $M_\bullet$

In B09 we showed that the upper limits on $M_\bullet$ are a valuable proxy for more secure determinations of $M_\bullet$ (see also Chapter 3). We can thus use this large and homogeneous sample of $M_\bullet$ to estimate the existence of other relations between $M_\bullet$ and galaxy properties. In all the following analysis, we will merge sample 1 and sample 2 as a unique dataset. We will refer to this as the joint dataset. We tested the possibility to combine the two samples with a Kolmogorov-Smirnov (K-S) test on the distributions of $M_\bullet$ and σ. the result indicates that the two samples came from the same parent distribution at better than 80% confidence. In the following subsections, we compare $M_\bullet$ against various bulge and galaxy

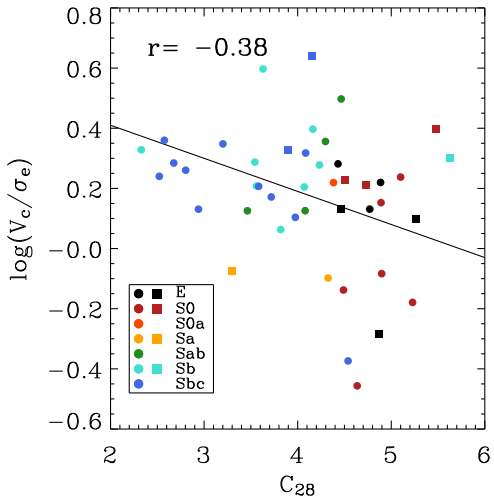

Figure 4.4 V_c/σ_e as a function of C_{28} for 39 galaxies with SDSS data and maximum rotational velocities (32 galaxies part of sample 1, dots, and 7 galaxies part of sample 2, squares). The dashed line is the relation by Courteau et al. (2007). Galaxies are separated by morphological type.

parameters in search for tight correlations. In the cases where we consider structural parameters obtained from the analysis of SDSS images, the i-band data are always used.

$M_\bullet$ *versus* σ_e

We compared the distribution of the $M_\bullet$ determinations against the stellar velocity dispersion within the effective radius, σ_e, in Figure 4.5. For comparison we show the last version of the $M_\bullet - \sigma_e$ relation from G09 as solid line. The joint sample is consistent with the relation (part is by default). In B09 that we already shown the consistency of the upper limits sample with Lauer et al. (2007a) and Ferrarese & Ford (2005), the relation of G09 gives a better agreement. In Figure 4.5 the upper and lower edges of the upper limits represented with dotted lines correspond to $M_\bullet$ values estimated assuming an inclination of $i = 33°$ and $81°$ for the unresolved Keplerian disk, respectively. The Pearson correlation coefficient for the joint distribution is r=0.82.

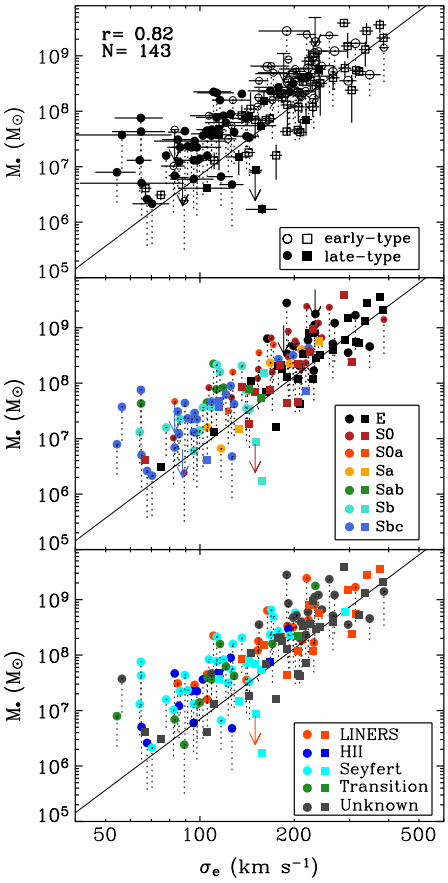

Figure 4.5 $M_\bullet$ as a function of σ_e for sample 1 (89 galaxies, dots) and sample 2 (49 secure $M_\bullet$, squares; 5 upper limits, arrows), comprising together 143 galaxies. The continuous line is the last version of the $M_\bullet - \sigma_e$ relation from G09. The upper and the lower edges of the dotted lines correspond to $M_\bullet$ values are estimated assuming an inclination of $i = 33°$ and $81°$ for the unresolved Keplerian disk, respectively. Galaxies are separated by early-type and late-type (*upper panel*), morphological type (*middle panel*), nuclear activity (*lower panel*). The error bars of σ_e are indicated only in the *upper panel* for sake of clarity.

We applied the linear fit $\log(M_\bullet/\mathrm{M}_\odot) = \alpha + \beta \log(\sigma_\mathrm{e}/200 \text{ km s}^{-1})$ to our joint sample. We calculated the scatter ($\sigma = 0.45$) of the relation as the the root-mean square deviation in log ($M_\bullet/\mathrm{M}_\odot$) from the relation we fitted, assuming zero measurement errors. The scatter of the $M_\bullet - \sigma_\mathrm{e}$ relation that we obtained and the parameters of our fit are reported in Table 4.7. The scatter we derived is consistent with the one found by G09 and larger than in previous works (Ferrarese & Ford 2005; Lauer et al. 2007a). This can be due to either the addition of upper limits to the joint sample, or to the addition of a larger sample of spirals that was found as a reason of the increased scatter in G09. As stated by G09, the upper limits can actually give a valuable constrain on the fit, although our upper limits at lower σ_e can introduce bias on the estimates of the intrinsic scatter and slopes of the relation. In fact, B09 already showed that our sample could well reproduce the scaling relations and is fully consistent with the secure $M_\bullet$ determinations, but still, departures from the expected trends do exist for a few systems. At small σ_e, some $M_\bullet$ upper limits exceed the expected $M_\bullet$, as the line width measurements for such low-σ_e outliers are most likely affected by the conspicuous nuclear clusters (NC, see B09 and Section 3.3.2 for details). By excluding this region from the fit the scatter of the $M_\bullet - \sigma_\mathrm{e}$ is reduced at 0.36. At high σ_e values, the joint sample does not show the flattening of the $M_\bullet$ that B09 found in the comparison with Ferrarese & Ford (2005) (see Section 3.3.3), while a steepening of the $M_\bullet - \sigma_\mathrm{e}$ relation seems to be more reliable (Wyithe 2006; Dalla Bontà et al. 2009, see Section 6.7). This steepening could be even clear by having the larger $M_\bullet$ modelled allowing for different mass-to-light ratios as was done by Gebhardt & Thomas (2009) for M87. They found that the dark matter contribution in the modeling of $M_\bullet$ is a fundamental ingredient that must be taken into account for the most massive galaxies. Therefore, the $M_\bullet$ measured in the high-σ_e range may be affected by the fact that up to now all the dynamical models did not take into account for such a contribution.

In all the figures we will present a subdivision of the $M_\bullet$ in morphological types and nuclear activity to identify their possible effect on the relations. It is crucial to understand which relation is more fundamental (or general) for all the Hubble types. The $M_\bullet - \sigma_\mathrm{e}$ will be used in the following analysis as comparison since it is well known to be a strong (if not the strongest) scaling relation.

$M_\bullet$ *versus* $L_{i,\mathrm{bulge}}$

There is a well-known correlation between $M_\bullet$ and the luminosity of the spheroidal component of a galaxy (Kormendy & Richstone 1995; McLure & Dunlop 2002;

Marconi & Hunt 2003; McLure & Dunlop 2004; Lauer et al. 2007a; Graham 2007). G09 derived an updated value of the intrinsic scatter of the $M_\bullet - L_{\rm bulge}$ relation, which is comparable to that of the $M_\bullet - \sigma_{\rm e}$ relation in early-type galaxies, confirming the results of Marconi & Hunt (2003). Graham (2007) compared the different version of the $M_\bullet - L_{\rm bulge}$ investigating the possible bias against the samples, for example due to a rough estimate of the spheroidal luminosity. He provided a comparison between the different versions of $M_\bullet - L_{\rm bulge}$. The slopes and scatters found in different works, in fact, trend to predict slightly different values of $M_\bullet$. Moreover Graham (2007), suggested the presence of the disk in some galaxies was missed due to the shallow nature of the analyzed 2MASS images. A correct decomposition of the galaxy properties is fundamental to obtain reliable a bulge luminosity.

With our large sample of masses and the deep SDSS photometry in i-band, we searched for the correlation between $M_\bullet$, and $L_{i,\rm bulge}$ (Figure 4.6), finding a good agreement with the coefficient found by Graham (2007) (Table 4.7). We applied a linear fit to our joint sample finding a scatter equal to 0.58 and a Pearson correlation coefficient $r = 0.68$. Our $M_\bullet - L_{i,\rm bulge}$ relation does not show different trends accounting to morphological types and nuclear activity. In the last years, several authors noticed that barred galaxies or pseudobulges follow different relations (Graham 2008; Graham & Li 2009; Gadotti & Kauffmann 2009; Hu 2009). In this analysis we do not see this difference, because we excluded a large number of barred galaxies during the photometric decomposition process. In B09 we did not find offsets in the $M_\bullet - \sigma_{\rm e}$ as a function of the bar presence, in the contrary of Graham (2008) and Graham & Li (2009). An offset in the $M_\bullet - L_{\rm bulge}$ could be explained in the sense that the bar does not affect $M_\bullet$ but the light of the spheroid more than to the fact that the SMBHs in barred galaxies are undermassive. However, addressing this issue requires a larger sample of pseudobulges or barred galaxies with a careful photometric decomposition (e.g., see Nowak et al. 2009). This is not in the aims of this work.

$M_\bullet$ *versus* $M_{\rm vir,bulge}$

The relation between the $M_\bullet$ and $L_{\rm bulge}$ suggested the connection with mass of the spheroidal component of the galaxy. Previous studies showed that $M_\bullet$ correlates linearly with the bulge mass. Marconi & Hunt (2003) combined the bulge K-band effective radii $r_{\rm e,bulge}$ with $\sigma_{\rm e}$ to find a tight correlation between $M_\bullet$ and the virial mass of the bulge $M_{\rm vir,bulge} \propto r_{\rm e,bulge}\sigma_{\rm e}^2$. Similarly, such a relation was found for a sample of active and inactive galaxies by McLure & Dunlop (2002). From both dynamical models available in the literature and

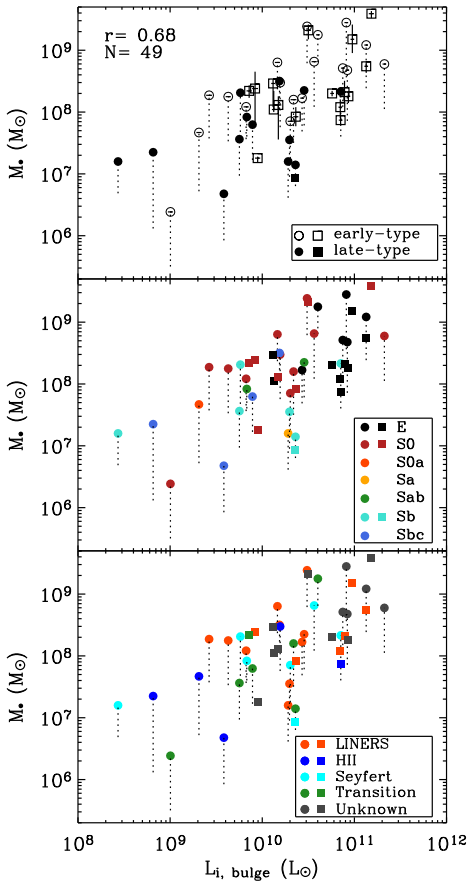

Figure 4.6 $M_\bullet$ as a function of $L_{i,\mathrm{bulge}}$ for 31 galaxies of sample 1 (dots) and 22 of sample 2 (17 secure $M_\bullet$, squares; 5 upper limits, arrows) for which we performed the two-dimensional bulge-to-disk decomposition of the SDSS i-band images using GASP2D (Méndez-Abreu et al. 2008a). Symbols are as in Figure 4.5. The total number of galaxies is N=49 and the Pearson correlation coefficient is r=0.68.

based on Jeans equations, Häring & Rix (2004) found a tight relation between $M_\bullet$ and $M_{\rm vir,bulge}$ for 30 early-type systems. The small scatter of $M_\bullet - M_{\rm vir,bulge}$, suggests that the bulge mass, rather than luminosity, is the main agent of the correlation (McLure & Dunlop 2002; Marconi & Hunt 2003; Erwin et al. 2004).

We estimated the bulge virial mass following Marconi & Hunt (2003) as $M_{\rm vir,bulge} = \alpha\ r_{\rm e,bulge}\sigma_{\rm e}^2/G$, where α is a model dependent dimensionless constant and G is the gravitational constant. We adopted $\alpha = 3$, following the results of dynamical modeling of Magorrian et al. (1998), Gebhardt et al. (2003), Marconi & Hunt (2003), and Hu (2009). We applied a linear fit to our joint sample finding a scatter equal to 0.55 and a Pearson correlation coefficient $r = 0.74$.

This fit is not a strong improvement with respect to the $M_\bullet - \sigma_{\rm e}$ relation, as it would be expected by adding the $r_{\rm e,bulge}$ parameter in the mass measurement. Instead the $M_\bullet - M_{\rm vir,bulge}$ correlation is weaker than the $M_\bullet - \sigma_{\rm e}$ one. However, $M_{\rm vir,bulge}$ is still a better tracer than $L_{i,\rm bulge}$ of $M_\bullet$ as seen from the smaller scatter and the tighter correlation between $M_\bullet$ and $M_{\rm vir,bulge}$. The slope (Table 4.7) we found is consistent within the errors with McLure & Dunlop (2002), Marconi & Hunt (2003), and Aller & Richstone (2007) and slightly lower than Häring & Rix (2004). Different Hubble types follow the same distribution, although a larger sample of galaxies could be useful to address this issue.

$M_\bullet$ versus n and $\langle\mu_{\rm e,bulge}\rangle$

The two-dimensional photometric decompositions yield a panoply of galaxy structural parameters, including the bulge Sérsic shape index n and the mean effective surface brightness $\langle\mu_{\rm e,bulge}\rangle$, both used as measure of the concentration of the light within the bulge.

We compared our $M_\bullet - n$ relation with that of Graham & Driver (2007). The distributions differ significantly for a given $M_\bullet$ (Figure 4.8). The Sérsic index for galaxies with high $M_\bullet$ is not as large as that by Graham & Driver (2007). Hopkins et al. (2007b) found as well no correlation between $M_\bullet$ and n from both observations and hydrodynamical simulations. They argued that that the correlation between $M_\bullet$ and concentration (or Sérsic index) is less strong relative to that in Graham & Driver (2007) by adopting the Sérsic index measured by Kormendy et al. (2009). Reliable estimate of n is therefore crucial to address this issue. Figure 4.8 does not show any dependence on morphological type and nuclear activity.

$\langle\mu_{\rm e,bulge}\rangle$ is another parameter that allows to estimate the degree of concentration of the bulge light. It was estimated from surface brightness at $r_{\rm e,bulge}$ by following the prescription of Graham & Driver (2005) for a Sérsic profile.

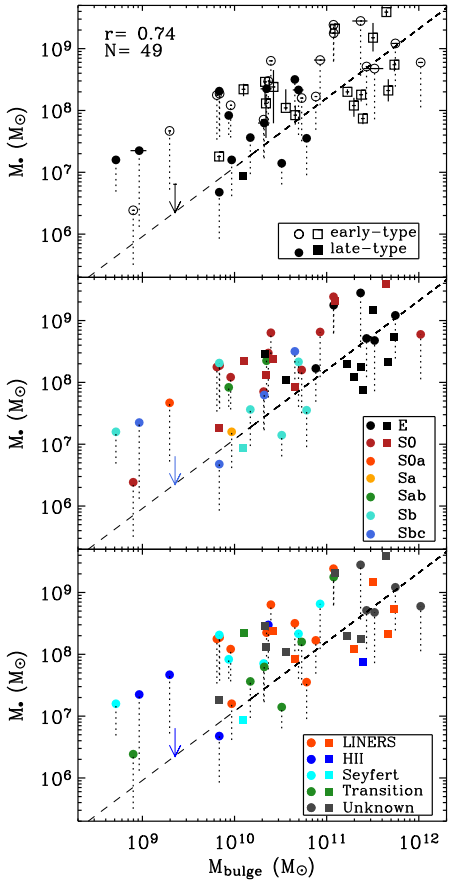

Figure 4.7 $M_\bullet$ as a function of $M_{\rm vir,bulge}$ for 31 galaxies of sample 1 (dots) and 22 of sample 2 (17 secure $M_\bullet$, squares; 5 upper limits, arrows). Symbols are as in Figure 4.5. The total number of galaxies is N=49 and the Pearson correlation coefficient is r=0.74. The dashed line is the $M_\bullet - M_{\rm bulge}$ relation from Häring & Rix (2004).

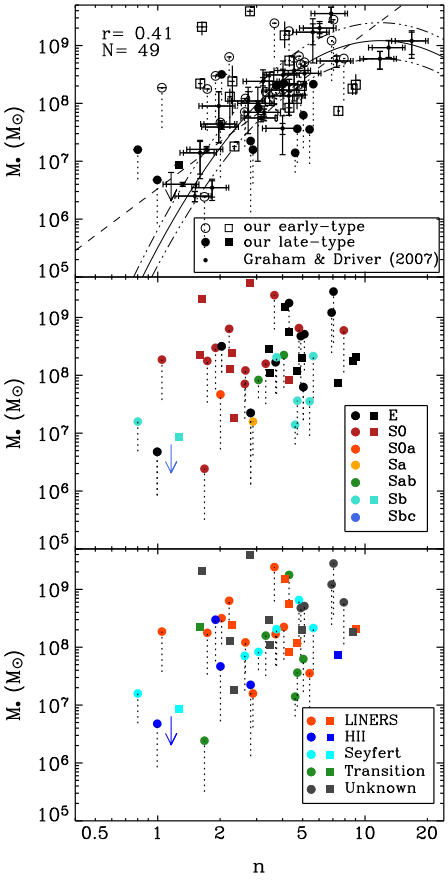

Figure 4.8 $M_\bullet$ as a function of n for 31 galaxies of sample 1 (dots) and 22 of sample 2 (17 secure $M_\bullet$, squares; 5 upper limits, arrows) for which we performed the two-dimensional bulge-to-disk decomposition of the SDSS i-band images using GASP2D (Méndez-Abreu et al. 2008a). Symbols are as in Figure 4.5. The total number of galaxies is N=49 and the Pearson correlation coefficient is r=0.41. In the *upper panel* we overplotted the sample (small dots) and the log-quadratic relation (continuous line) from Graham & Driver (2007). The intrinsic scatter is identified by the dotted-dashed line. The dashed line represent the linear relation suggested by Graham et al. (2001, 2003).

In Figure 4.9 we compare the distribution of our $M_\bullet$ as a function of $\langle\mu_{\rm e,bulge}\rangle$, dividing the galaxies by morphological type and nuclear activity. We did not find any correlation.

$M_\bullet$ versus $L_{i,\rm gal}$

Past studies have shown that $M_\bullet$ only weakly correlate with the global luminosity of the galaxy, $L_{i,\rm gal}$, in particular for late-type spirals (see Kormendy 2001; Kormendy & Gebhardt 2001). Kormendy (2001) compared the B-band total magnitude with dynamically secure $M_\bullet$ estimations in spheroids and few bulgeless disk galaxies to conclude that the SMBHs evolution is linked with bulges and not with disks.

We tested this idea by comparing our own $L_{i,\rm gal}$ with $M_\bullet$ as a function of the morphological type (Figure 4.10). The inclusion of the spirals/lenticulars disk increased the galaxy luminosity and mass resulting in an offset between the elliptical and spiral/lenticulars population, but this is still smaller that what was found in the past. The Pearson correlation coefficient of $r = 0.63$ suggesting that there is a correlation. This relation is not as tight as the relation for $M_\bullet - L_{i,\rm bulge}$, clearly due to the presence of disk light. We fitted a relation to the distribution of our data to compare it with $M_\bullet - L_{i,\rm bulge}$, finding a steeper slope due to the contribution of the disk light, and a larger rms scatter. The fit parameters are given in Table 4.7. Similar correlations were found in g and r-band but with a smaller Pearson r.

We measured the luminosity for 74 galaxies: 32% ellipticals, 28% lenticulars, and 40% spirals (mainly barred galaxies). 78 % of the spirals are late-type objects (Sb−Sbc). Our sample missed bulgeless galaxies which may explain the better trend for our $M_\bullet$ and $L_{i,\rm gal}$ in respect to Kormendy (2001).

Our findings on $M_\bullet - L_{i,\rm gal}$ are consistent with Figure 6 of Hu (2009) that found a loose relation confirming the previous results that bulge luminosity is a better tracer of SMBHs than the galaxy total light.

$M_\bullet$ versus $M_{\star,\rm gal}$

To test a possible relation between the total mass of the galaxy, $M_{\star,\rm gal}$, and the $M_\bullet$, we adopted the derived $L_{i,\rm gal}$ under the assumption of constant mass-to-light-ratio. We inferred $(M/L)_i$ from the $(g-i)$ color from our own SDSS photometry following Bell et al. (2003). They derived the (M/L) in different bands from spectrophotometric galaxy evolution models, which use the stellar population models of Bruzual & Charlot (2003) and are tuned to reproduce local spiral galaxy ages and metallicities. By using the near-infrared light it is possible to trace better the stellar mass, with a smaller effect due to dust

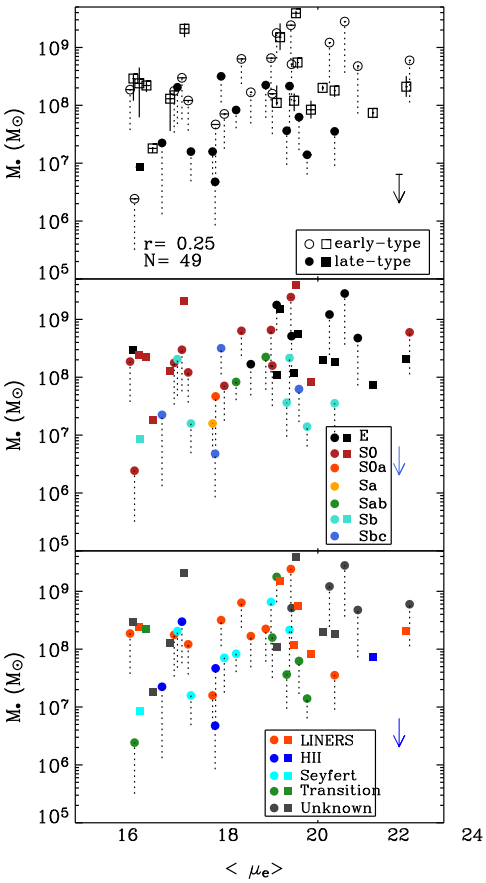

Figure 4.9 $M_\bullet$ as a function of $\langle\mu_{\rm e,bulge}\rangle$ for 31 galaxies of sample 1 (dots) and 22 of sample 2 (17 secure $M_\bullet$, squares; 5 upper limits, arrows) for which we performed the two-dimensional bulge-to-disk decomposition of the SDSS i-band images using GASP2D (Méndez-Abreu et al. 2008a). Symbols are as in Figure 4.5. The total number of galaxies is N=49 and the Pearson correlation coefficient is r=0.25.

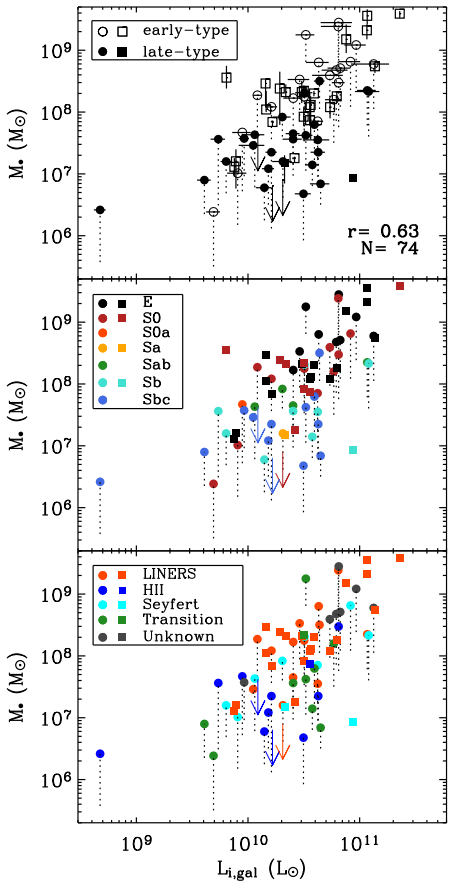

Figure 4.10 $M_\bullet$ as a function of $L_{i,\mathrm{gal}}$ for 46 galaxies of sample 1 (dots) and 28 of sample 2 (25 secure $M_\bullet$, squares; 3 upper limits, arrows) for which we performed the one-dimensional decomposition of the SDSS i-band images using the procedure described in McDonald et al. (2009). Symbols are as in Figure 4.5. The total number of galaxies is N=74 and the Pearson correlation coefficient is r=0.63.

extinction than in B-band. The $M_\bullet - M_{\star,\mathrm{gal}}$ relation has a Pearson $r = 0.68$ with a smaller scatter of the late-type galaxies with respect to $M_\bullet - L_{i,\mathrm{gal}}$, as shown in Figure 4.11. We fitted a linear relation to the distribution of our data to see if the scatter due to the disk light can be reduced by considering the stellar mass. The slope is similar to the one found for $M_\bullet - L_{i,\mathrm{gal}}$, but with a smaller scatter of 0.59. The fit parameters are reported in Table 4.7. The distribution of ellipticals and lenticulars follow a tight a relation as expected from our previous findings on $M_\bullet - L_{\mathrm{bulge}}$, with respect to the late-type galaxies which look like a separated population.

$M_\bullet - V_\mathrm{c}$ and $V_\mathrm{c} - \sigma_\mathrm{e}$ relations

The Jeans equation evokes a relation between the circular velocity of galaxy and its velocity dispersion. This relation has been first observationally mapped by Whitmore et al. (1979) and more recently by Ferrarese (2002) and Pizzella et al. (2005). However, Courteau et al. (2007) and Ho (2007) demonstrated that the $V_\mathrm{c} - \sigma_\mathrm{e}$ relation must depend on a third parameter which they identified as the concentration of the galaxy. This was already considered by Whitmore et al. (1979), who pointed out that the velocity dispersion of bulges are smaller than those of ellipticals at the same magnitude, mainly due to differences in the central surface brightness and bulge-to-disk ratio. In this sense, the density distribution appears to be the dominant factor that determines the $V_\mathrm{c}/\sigma_\mathrm{e}$ ratio. The light concentration is just a way to estimate the degree of dominance of the bulge, since it is roughly related to the bulge-to-disk ratio (Doi et al. 1993).

The rotational velocity V_c in spirals (considered as a tracer of the circular velocity) can be measured with the H I gas disks at very large radii where the dark matter begins to dominate. For elliptical galaxies V_c is obtained instead with dynamical models of absorption-line features and surface-brightness profiles, in the region within about $1-2r_{\mathrm{e,gal}}$, where the dark matter contributes in some cases $\sim$10$-$40% of the total mass (Saglia et al. 1993, 2000; Kronawitter et al. 2000; Gerhard et al. 2001; Magorrian & Ballantyne 2001; Thomas et al. 2007). In the last years several technique allowed to extend kinematical studies to larger radii, with planetary nebulae (Douglas et al. 2007; Coccato et al. 2009; Napolitano et al. 2009) and globular clusters (Pierce et al. 2006).

While assuming that the collected V_c for 93 galaxies trace the dark matter halo, we studied the possible link between SMBHs and dark matter halos by comparing $M_\bullet$ with V_c as well as the dynamical mass of the galaxy $M_{\mathrm{dyn,gal}}$ derived from our V_c for the subsample of spiral and lenticular galaxies. We should keep in mind that a possible relation between $M_\bullet$ and the dark matter depends on the radius were we measure V_c that depends on the method used

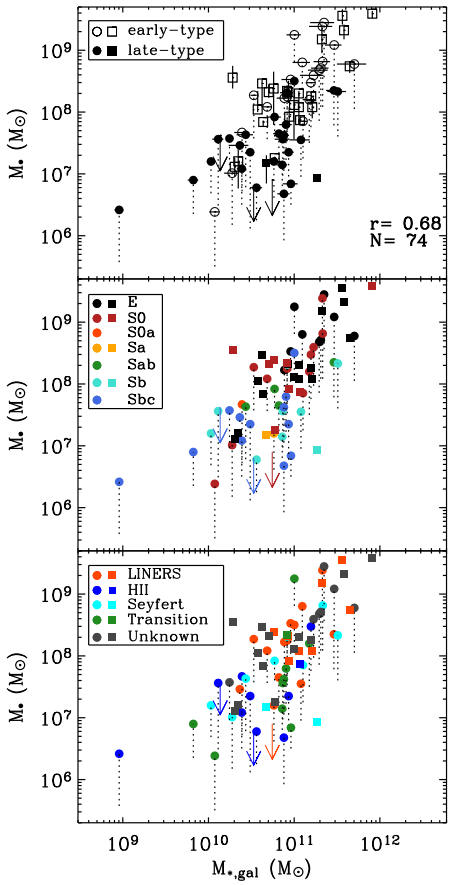

Figure 4.11 $M_\bullet$ as a function of $M_{\star,\mathrm{gal}}$ for 46 galaxies of sample 1 (dots) and 28 of sample 2 (25 secure $M_\bullet$, squares; 3 upper limits, arrows) for which we performed the one-dimensional decomposition of the SDSS g and i-band images using the procedure described in McDonald et al. (2009). Symbols are as in Figure 4.5. The total number of galaxies is N=74 and the Pearson correlation coefficient is r=0.68.

for measuring this quantity. Theoretical models that reproduce the observed luminosity function of quasars (Cattaneo 2001; Adams et al. 2003; Volonteri et al. 2003; Hopkins et al. 2005b; Springel et al. 2005) predict that $M_\bullet$ scales as a power law of the circular velocity of the galactic halo in which the SMBH resides. However, the conversion between the circular velocity and virial velocity, (i.e., the velocity of the galactic halo at the virial radius), depends on the assumed model.

We tested the $M_\bullet$ against V_c in Figure 4.12. There is weak connection between these quantities, with a Pearson coefficient of $r = 0.35$. The early and late-type populations follow two different distributions, one flat and one roughly similar to the one found by (Ho et al. 2008b, dashed line), respectively. Considering only the late-type systems we obtained a Pearson $r = 0.51$. The flat distribution for early-type galaxies may be explained taking into account that V_c for lenticulars is ill-defined. Disk stars display both significant random and ordered motions and some modeling is required to recover V_c. Figure 4.12 also shows the $M_\bullet - V_\mathrm{c}$ relation tagged by morphological type and nuclear activity. Some of the elliptical galaxies for which we obtained the V_c from stellar models follow the same trend as the late-types.

Similar results were obtained by Zasov et al. (2005). They used a collection of 41 galaxies with $M_\bullet$, σ_e, and rotational velocities from optical rotation curves, to conclude that a coarse relation exists with V_c but not as strong as the $M_\bullet - \sigma_\mathrm{e}$. For a given V_c, early-type galaxies tend to have larger $M_\bullet$ that late-type galaxies.

The existence of the $M_\bullet - \sigma_\mathrm{e}$ relation and the absence of a single universal $V_\mathrm{c} - \sigma_\mathrm{e}$ for all morphological types is in contrast with the hypothesis that $M_\bullet$ is more fundamentally connected to the halo mass than the bulge mass. Thus, with few exceptions of bulgeless galaxies (NGC 4395, Filippenko & Ho 2003, POX 52 Barth et al. 2004, and NGC 1042, Shields et al. 2008) $M_\bullet$ seems to be associated with bulges, not halos (see also the case of M33 that does not show an evidence of a SMBH but obviously present an halo, Gebhardt et al. 2001). The same V/σ over a full range of Hubble type does not directly imply that $M_\bullet$ is driven by the mass of the dark matter, since the mass we would measured is strictly connected to the radius at which the V_c is measured and also the radius $R_{24.5}$ at which the dynamical mass is measured.

Ho et al. (2008b) studied the $M_\bullet - V_\mathrm{c}$ relation for a sample of 154 nearby galaxies ($z < 0.1$) comprising both early and late-type systems for which $M_\bullet$ values were estimated from the mass-luminosity-line width relation (Kaspi et al. 2000; Greene & Ho 2005a; Peterson & Bentz 2006) and V_c from H I and optical data (Ho et al. 2008a). They found a coarse relation between $M_\bullet$ and V_c. It improves by using only galaxies with well defined H I profile and more reliable

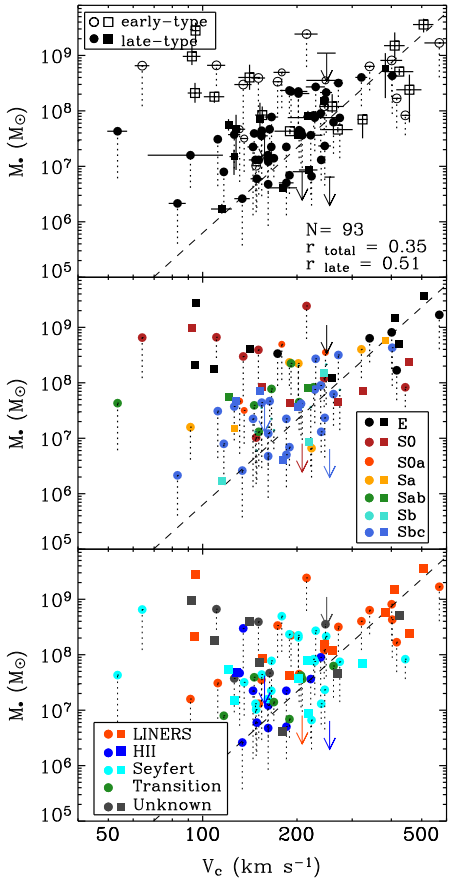

Figure 4.12 $M_\bullet$ as a function of V_c for 64 galaxies of sample 1 (dots) and 29 of sample 2 (25 secure $M_\bullet$, squares; 4 upper limits, arrows). Symbols are as in Figure 4.5. The total number of galaxies is N=94 and the Pearson correlation coefficient is r=0.35. The dashed line is the fit derived by Ho (2007).

measurements. They analyzed the $M_\bullet - V_c$ relation as a function of Hubble type, AGN type, shape of the H I profile, and inclination correction. The objects with the most reliable V_c, from double-dish H I data, have a distribution comparable to our late-type systems. Indeed, Ho et al. (2008b) found that the larger scatter of the $M_\bullet - V_c$ relation could be due to galaxies with uncertain rotational velocities, although they suggested that the main source of scatter ($\sigma(\log M_\bullet)\sim 0.3-0.5$ dex) is related to the dependence on the bulge-to-disk ratio of V_c/σ_e(Courteau et al. 2007; Ho 2007). The fit by Ho et al. (2008b) is consistent with the distribution of our spiral galaxies for which the circular velocity is a more clearly defined.

Even if the the $V_c - \sigma_e$ relation depends on a third parameter, a statistically significant correlation between these two quantity does exists. A Spearman's rank coefficient of 0.6 suggests the presence of a correlation at 4σ confidence level. We compared V_c and σ_e for our sample of galaxies to understand whether their distribution indicates a connection with $M_\bullet$. Figure 4.13 shows the $V_c - \sigma_e$ relation as a function of $M_\bullet$, for $10^6 < M_\bullet < 10^7$ $M_\odot$, $10^7 < M_\bullet < 10^8$ $M_\odot$, $10^8 < M_\bullet < 10^9$ $M_\odot$, and $M_\bullet > 10^9$ $M_\odot$. The dashed line is the fit by Ho (2007). To a given $M_\bullet$ corresponds a small range of possible σ_e and a wide range of V_c demonstrating that the connection between $M_\bullet$ and σ_e is stronger than that with V_c. We found outliers with low- V_c/σ_e ratios at all Hubble types although they appear to be more numerous among early-type galaxies, in particular lenticulars. Similar outliers were found by Ho (2007). Since most of the objects cover a limited dynamical range, the sample does not define a good $V_c - \sigma_e$ relation. We adopted inclinations derived from axial ratios of stellar isophotes, while assuming that gas and stars are coplanar, to deproject the H I rotational velocity. If gas and the stars are misaligned, the inclinations may be over or underestimated increasing the scatter.

$M_\bullet$ versus and galaxy mass

Ferrarese et al. (2006) suggested a tight connection between $M_\bullet$ and the virial mass of the early-type galaxies, computed as $M_{\rm vir,gal} = \alpha r_{\rm e,gal}\sigma_e^2/G$ where $\alpha = 5$ (Cappellari et al. 2006), $r_e = a_e(1-\epsilon)^{1/2}$ is the geometric effective radius, a_e the effective radius measured along the isophotal semi-major axis, and σ_e is the luminosity-weighted second moment of the line-of-sight velocity distribution within the effective radius derived from the central velocity dispersion by using the correction by Cappellari et al. (2006).

With our large data sample we can test the validity of this relation and whether its scatter is comparable to that of the $M_\bullet - \sigma_e$ relation. We used $r_{\rm e,gal}$ from our i-band SDSS global photometry to compute the $M_{\rm vir,gal}$.

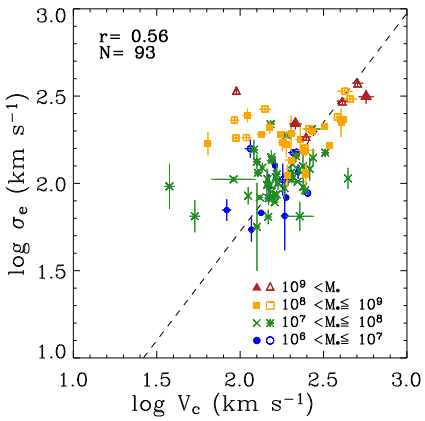

Figure 4.13 $V_c - \sigma_e$ relation for 64 galaxies of sample 1 (filled symbols) and 29 galaxies of sample 2 (empty symbols) as a function of $M_\bullet$. The dashed line is the relation by Ho (2007). Pearson correlation r is given.

Here, we adopted $\alpha = 5$ for comparison with existing literature. Wolf et al. (2009) by studying the mass estimator for dispersion-supported stellar system found a similar formula but with a different coefficient ($\alpha = 4$). By using their relation the resulting $M_{\rm vir,gal}$ is just shifted of a constant in respect to the one we used. The appropriate value of α is actually a function of the Sérsic shape index n (Trujillo et al. 2004). The exact application of the $\alpha(n)$ relation does not affect our conclusions. The most important parameter in the determination of the total virial mass of the galaxy is $r_{\rm e,gal}$. It must be the one of the galaxy, meaning that in our estimation of the $M_{\rm vir,gal}$ we are including the contribution of the galaxy. We show in Figure 4.14 the distribution of $M_\bullet$ as a function of $M_{\rm vir,gal}$ dividing the sample galaxies according to early and late types, morphological types and nuclear activity. The early-type systems follow the relation of Ferrarese et al. (2006), whereas the late types deviate progressively from that trend and show greater scatter. Although the high value of the Pearson coefficient (r=0.78) suggest a linear relations, the different distribution shown as a function of the Hubble types, suggest that this relation is less fundamental than the $M_\bullet - \sigma_e$. Introducing a new parameter $r_{\rm e,gal}$ and a specific exponent for σ_e ought to reduce the scatter of the $M_\bullet - \sigma_e$ relation but, in fact, it does not.

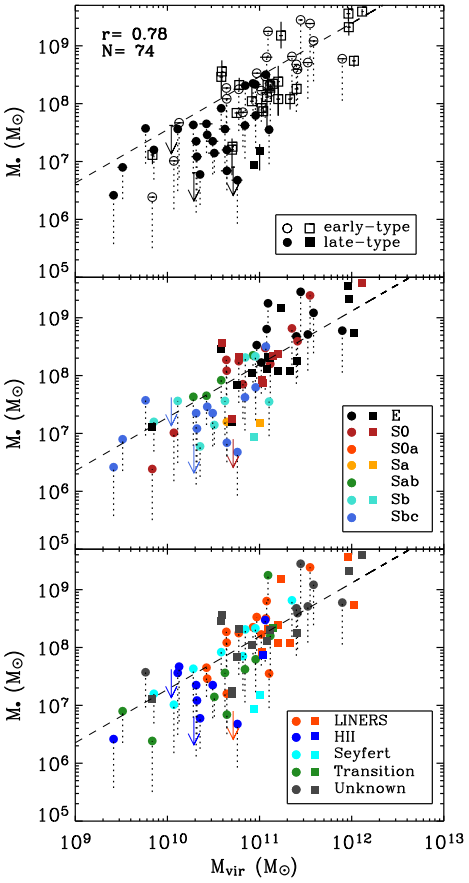

Figure 4.14 $M_\bullet$ as a function of $M_{\rm vir,gal}$ for 46 galaxies of sample 1 (dots) and 29 of sample 2 (25 secure $M_\bullet$, squares; 4 upper limits, arrows). Symbols are as in Figure 4.5. The total number of galaxies is N=74 and the Pearson correlation coefficient is r=0.78. The dashed line is the fit derived by Ferrarese et al. (2006).

We estimated the mass of late-type systems as dynamical mass, $M_{\rm dyn,gal}= RV_c^2/G$, where R is taken as the radius $R_{24.5}$ at which the surface-brightness level is 24.5 mag arcsec^{-2}. Although the H I rotational velocities we derived from literature yield no information on the spatial distribution of the gas, we obtained a rough estimate of the dynamical mass of the galaxies by adopting the optical measurement of the radius based on SDSS photometry. In fact, spatially resolved observations revealed that the size of H I disks of spiral galaxies scale well with their optical sizes as it is suggested in Ho et al. (2008a). Such a dynamical mass is strongly dependent on the adopted radius since we do not have an actual measurement of the extension of the H I disks.

We compared $M_{\rm vir,gal}$ and $M_{\rm dyn,gal}$ for both spirals and lenticulars of our sample, to understand how much the two mass estimators deviate for these populations of galaxies. For lenticulars galaxies the two mass estimators seem to be consistent (Figure 4.15). Major deviation are found for intermediate-to-late spirals where the disk makes $M_{\rm vir,gal}$ less reliable then $M_{\rm dyn,gal}$.

In Figure 4.16 we show $M_\bullet$ versus $M_{\rm dyn,gal}$ for 39 lenticular and spiral galaxies of our sample. $M_{\rm dyn,gal}$ does not correlate with $M_\bullet$ (Pearson coefficient is $r = 0.23$), although the late-type galaxies are distributed close to the relation found by Ho et al. (2008b). Ho et al. (2008b) found a $M_\bullet - M_{\rm dyn,gal}$ relation with an rms scatter of 0.61 dex, in spite of their narrow range of $M_{\rm dyn,gal}$. In fact by excluding the lower $M_{\rm dyn,gal}$ they had the relation looses the tightness they argued. Our lenticulars do not follow this relation. We exclude that this can be due to the $V_{\rm c}$ measurements, since also the late-type galaxies show significant scatter around the relation by Ho et al. (2008b). Ho et al. (2008b) suggested the different properties of the AGN such as line width of the broad line region or the Eddington ratio as possible sources of the scatter. AGNs with an higher accretion rate have systematically less massive SMBHs, since they are still growing with the maximum rate. However, our $M_\bullet$ are mainly measured in quiescent galaxies (or in galaxies with weak activity) and we saw no bias in the distribution of nuclear activity for our galaxies (Figure 4.16).

4.3.2 Linear combination between $M_\bullet$ and galaxy parameters

Marconi & Hunt (2003) considered a correlation between the $M_\bullet$ and the virial mass of the bulge following $M_{\rm vir,bulge} \propto r_{\rm e,bulge}\sigma_{\rm e}^2$. This relation suggests that a possible combination of the spheroidal properties can result in a tighter correlation with $M_\bullet$. A SMBH that satisfies the $M_\bullet - \sigma_{\rm e}$ relation may look discrepant in the $M_\bullet - M_{\rm vir,bulge}$ relation if $r_{\rm e,bulge}$ is smaller or larger than normal. Conversely, the additional fitting parameter and potentially true nature of the process of bulge formation may yield a tighter scatter from $M_\bullet - \sigma_{\rm e}$ to

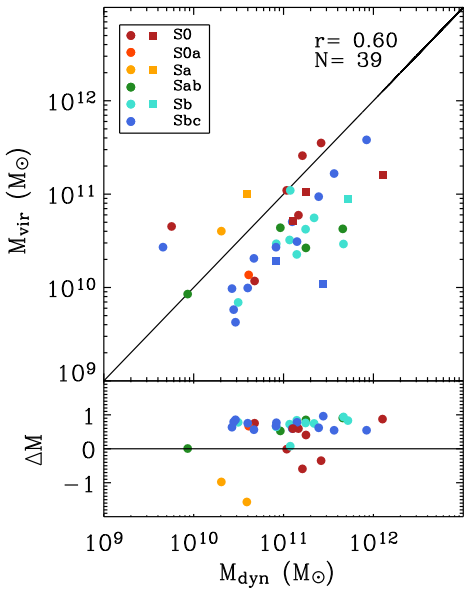

Figure 4.15 Comparison between the $M_{\rm vir,gal}$ and $M_{\rm dyn,gal}$ for the 39 lenticulars and spirals with SDSS data and $V_{\rm c}$ (32 from sample 1, dots, and 7 from sample 2 squares). The solid line indicated the one-to-one correlation. The residuals are shown in the bottom panel.

$M_\bullet - M_{\rm vir,bulge}$.

In Section 4.3.1, we showed that $M_\bullet$ is strongly related with $\sigma_{\rm e}$, as well as with $L_{i,\rm bulge}$ and $M_{\rm vir,bulge}$. To test whether these relations are a sufficient description of our data or there is a evidence for an additional dependence on more parameter, we looked at the residuals of $M_\bullet - \sigma_{\rm e}$, $M_\bullet - L_{\rm bulge}$, $M_\bullet - M_{\rm vir,bulge}$ relations. Residuals were obtained as difference between the data distribution and the relations with coefficients in Table 4.7. Then we compared the residuals $\log(M_\bullet/M_\bullet[\sigma_e])$, $\log(M_\bullet/M_\bullet[L_{i,\rm bulge}])$, and $\log(M_\bullet/M_\bullet[\rm M_{bulge}])$ with bulge photometric and kinematical properties (.i.e., $\langle\mu_{\rm e,bulge}\rangle$, $r_{\rm e,bulge}$, n, and $\sigma_{\rm e}$ (Figure 4.17).

For $\log(M_\bullet/M_\bullet[\sigma_e])$, we do not find any trend with other galaxy properties, whereas $\log(M_\bullet/M_\bullet[L_{i,\rm bulge}])$ and $\log(M_\bullet/M_\bullet[\rm M_{bulge}])$ show a shallow dependence on $r_{\rm e,bulge}$. Hopkins et al. (2007a,b) also studied the residuals of the $M_\bullet - M_{\rm vir,bulge}$ and $M_\bullet - \sigma_{\rm e}$ relations with bulge properties, finding tighter

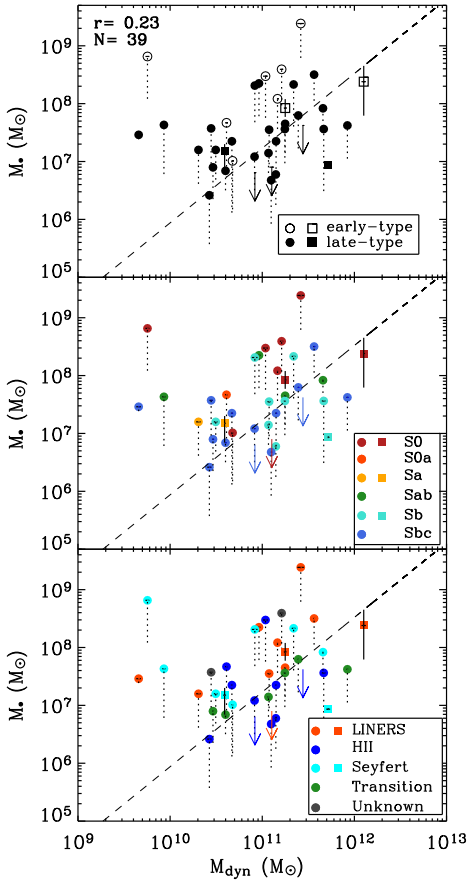

Figure 4.16 $M_\bullet$ as a function of $M_{\rm dyn,gal}$ for 32 galaxies of sample 1 (dots) and 7 of sample 2 (4 secure $M_\bullet$, squares; 3 upper limits, arrows). Symbols are as in Figure 4.5. The total number of galaxies is N=39 and the Pearson correlation coefficient is r=0.23. The dashed line is the fit derived by Ho et al. (2008b).

correlations between the combination of the galaxy parameters and $M_\bullet$, thus bolstering the notion of a fundamental plane of the SMBHs (BHFP). In fact, the bulge parameters described before $M_{\rm vir,bulge}$, $L_{i,\rm bulge}$, and $\sigma_{\rm e}$ are physically related to each other through the fundamental plane of spheroids (FP) and the virial theorem. Each of them is a physical probe of the mass distribution of the bulge. The BHFP exists thanks to the FP that connects the bulge properties $r_{\rm e,bulge}$, $\sigma_{\rm e}$, $\langle\mu_{\rm e,bulge}\rangle$ (Dressler et al. 1987; Djorgovski & Davis 1987; Jørgensen et al. 1996; Pahre et al. 1998; Bernardi et al. 2003; Jørgensen et al. 2007). The existence of such BHFP has important implications for the masses of very largest black holes, and resolves apparent conflict between expected and measured values of $M_\bullet$ for outliers in both $M_\bullet - \sigma$ and $M_\bullet - M_{\rm vir,bulge}$. Similar results were obtained by Barway & Kembhavi (2007) analyzing the connection between $M_\bullet$, $r_{\rm e}$, and $\langle\mu_{\rm e,bulge}\rangle$. They found a correlation between these quantities for nearby ellipticals with measured $M_\bullet$, with a smaller scatter with respect to $M_\bullet - \sigma$ or $M_\bullet - L_{\rm bulge}$ relations.

With our large sample of galaxies we can probe bulge parameter is more fundamental predictor of $M_\bullet$. In Figure 4.18 we show the different linear combinations of the bulge parameters with $M_\bullet$. We assumed correlations of the form $\log(M_\bullet) = \gamma + \alpha\log(x) + \beta\log(y)$ for the different variables (x, y) we tested, where γ is the normalization, and α and β are the logarithmic slopes, respectively. We normalized the expressions for $\sigma_{\rm e} = 200$ km s^{-1}, $L_{i,\rm bulge} = 10^{11}$ L$_\odot$, $M_{\rm vir,bulge} = 10^{11}$ M$_\odot$ and $r_{\rm e,bulge}$= 5 kpc. We applied a linear fit to the variables by measuring the scatter from the root-mean square of the residual between the best-fit and the data points. The fit parameters are given in Table 4.8.

We notice a tight connection between $M_\bullet$, $\sigma_{\rm e}$, and $r_{\rm e,bulge}$ (Pearson coefficient $r = 0.81$) as tight as the $M_\bullet - \sigma_{\rm e}$ (Pearson coefficient $r = 0.82$), with a scatter (0.46) slightly lower than $M_\bullet - \sigma_{\rm e}$ (Figure 4.18). The introduction of $r_{\rm e,bulge}$ changes the fit and the correlation very slightly, although the point distribution is better defined than in the $M_\bullet - \sigma_{\rm e}$ in particular for small $\sigma_{\rm e}$. This first correlation is well expected because, since a combination of $\sigma_{\rm e}$ and $r_{\rm e,bulge}$ is given by $M_{\rm vir,bulge}$ that clearly correlate with $M_\bullet$ (see Section 4.3.1). The actual correlation found in this fit shows an higher power for $\sigma_{\rm e}$, than that used for $M_{\rm vir,bulge}$. $M_\bullet$ is proportional to $M_{\rm vir,bulge}$ and the bulge size. Larger SMBHs are associated to more massive and larger bulges, as explained in the framework of coevolution of spheroids and SMBHs.

This is clear from when the combination of $M_{\rm vir,bulge}$ with $r_{\rm e,bulge}$ or $\sigma_{\rm e}$, respectively gives the same point distribution. The two distributions in fact represent the same relation, since $M_{\rm vir,bulge}$ is already a combination of $r_{\rm e,bulge}$ and $\sigma_{\rm e}$. The relation between $M_\bullet$, $L_{i,\rm bulge}$, and $r_{\rm e,bulge}$ is not as strong as that between $M_\bullet$, $\sigma_{\rm e}$, and $r_{\rm e,bulge}$ but it is slightly better than $M_\bullet - L_{i,\rm bulge}$, with a

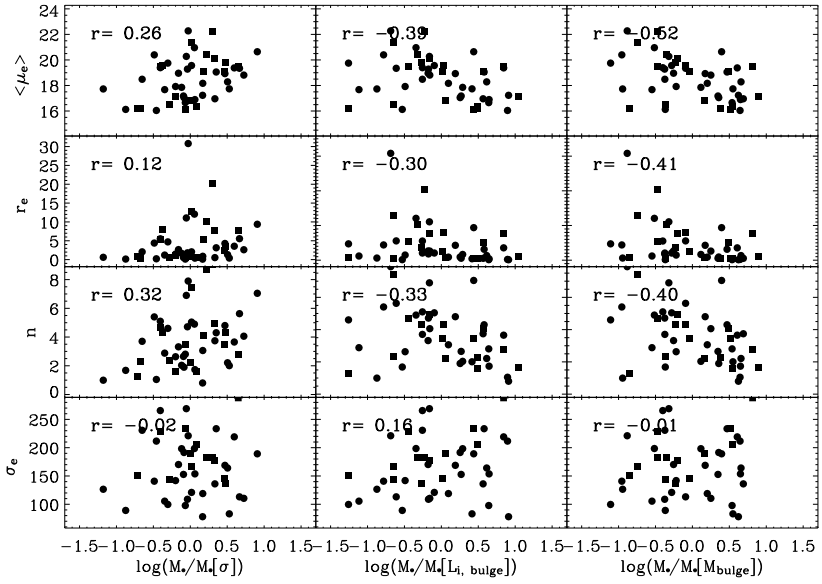

Figure 4.17 Residual of the $M_\bullet - \sigma_{\rm e}$, $M_\bullet - L_{\rm bulge}$, $M_\bullet - M_{\rm vir,bulge}$ relations against $\langle\mu_{\rm e,bulge}\rangle$, $r_{\rm e,bulge}$, n, $\sigma_{\rm e}$ for 31 galaxies from sample 1, dots, and 18 from sample 2, squares. The total number of galaxies is N=49 and Pearson coefficient r of the correlation is given in each panel.

Pearson coefficient r=0.70. The relation between $M_\bullet$, $\sigma_{\rm e}$ and $L_{\rm bulge}$ is as tight as that between $M_\bullet$, $\sigma_{\rm e}$, and $r_{\rm e}$.

Our fit coefficients (Table 4.8) are consistent within the error with the values of Hopkins et al. (2007a,b), (i.e. with $M_\bullet \propto \sigma_{\rm e}^{\alpha} r_{\rm e,bulge}^{\beta}$ where $\alpha = 3.00 \pm 0.30$ and $\beta = 0.43 \pm 0.19$, $M_\bullet \propto {\rm M}_{\rm bulge}^{\alpha} \sigma_{\rm e}^{\beta}$ where $\alpha = 0.54 \pm 0.17$, $\beta = 2.18 \pm 0.58$, and $M_\bullet \propto {\rm M}_{\rm bulge}^{\alpha} {\rm r}_{\rm e,bulge}^{\beta}$ where $\alpha = 1.78 \pm 0.40$, $\beta = -1.05 \pm 0.37$. From this comparison we can argue that the $\sigma_{\rm e}$ is the parameter that drives the connection with $M_\bullet$ in the BHFP, with a small contribution due to $r_{\rm e,bulge}$, or $L_{i,\rm bulge}$.

Moreover, we wanted to understand whether the shallow relations between $M_\bullet$ and global galaxy properties ($M_\bullet - L_{i,\rm gal}$, $M_\bullet - M_{\star,\rm gal}$) can be influenced by the addition of a bulge property. Therefore, we looked at the residuals of $M_\bullet - \sigma_{\rm e}$, $M_\bullet - L_{i,\rm gal}$, and $M_\bullet - M_{\star,\rm gal}$ relations, to see if there is a evidence for additional dependence on more parameters. Residuals were obtained as differ-

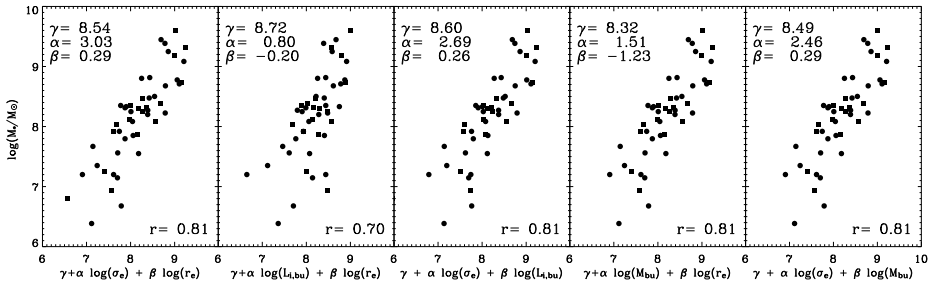

Figure 4.18 $M_\bullet$ as a function of $\sigma_{\rm e}$ and $r_{\rm e,bulge}$ (*first panel*), $L_{i,\rm bulge}$ and $r_{\rm e,bulge}$ (*second panel*), $\sigma_{\rm e}$ and $L_{i,\rm bulge}$ (*third panel*), $M_{\rm vir,bulge}$ and $r_{\rm e,bulge}$ (*fourth panel*), and $\sigma_{\rm e}$ and $M_{\rm vir,bulge}$ (*fifth panel*). The sample comprises 49 galaxies (31 from sample 1, dots; 18 from sample 2, squares). The normalization γ, slopes α and β, and Pearson coefficient r of the correlation are given in each panel.

ence between the the data point distribution and the relations with coefficients in Table 4.7. We also examined the residuals of the $M_\bullet - (g-i)$ relation to confirm that the propagation errors in the determination of $M_{\star,\rm gal}$ do not affect our results. Then we compared the residuals $\log(M_\bullet/M_\bullet[\sigma_e])$, $\log(M_\bullet/M_\bullet[L_{i,\rm gal}])$ and $\log(M_\bullet/M_\bullet[M_{\star,\rm gal}])$ with galaxy C_{28}, $I_{\rm e,gal}$, $r_{\rm e,gal}$, and $\sigma_{\rm e}$ (see Figure 4.19).

For $\log(M_\bullet/M_\bullet[\sigma_e])$, we do not find any trends with other galaxy properties, whereas the $\log(M_\bullet/M_\bullet[L_{i,\rm gal}])$ and $\log(M_\bullet/M_\bullet[M_{\star,\rm gal}])$ show a low dependence on $r_{\rm e}$.

In Figure 4.20 we show the different linear combinations of the galaxy parameters with $M_\bullet$. We assumed correlations of the form $\log(M_\bullet) = \gamma + \alpha\log(x) + \beta\log(y)$ for the different variables (x, y) we tested, where γ is the normalization, and α and β are the logarithmic slopes, respectively. We normalized the expressions for $\sigma_{\rm e} = 200$ km s^{-1}, $L_{i,\rm gal} = 10^{11}$ L$_\odot$, $M_{\star,\rm gal} = 10^{11}$ M$_\odot$ and $r_{\rm e,gal} = 5$ kpc.

We found tight correlations although we are using global galaxy parameters rather than bulge related (the Pearson coefficient $r = 0.83$). The first, third and fifth panels show the same tight result suggesting that $\sigma_{\rm e}$ strengthens the relation when present.

Our fit coefficients (Table 4.8) are consistent within the errors with the values of Hopkins et al. (2007a,b). The main difference between us and and Hopkins et al. (2007a,b) is that we use the global galaxy properties, not the bulge properties. The combination of the $M_{\star,\rm gal}$ with $r_{\rm e,gal}$, gives a better

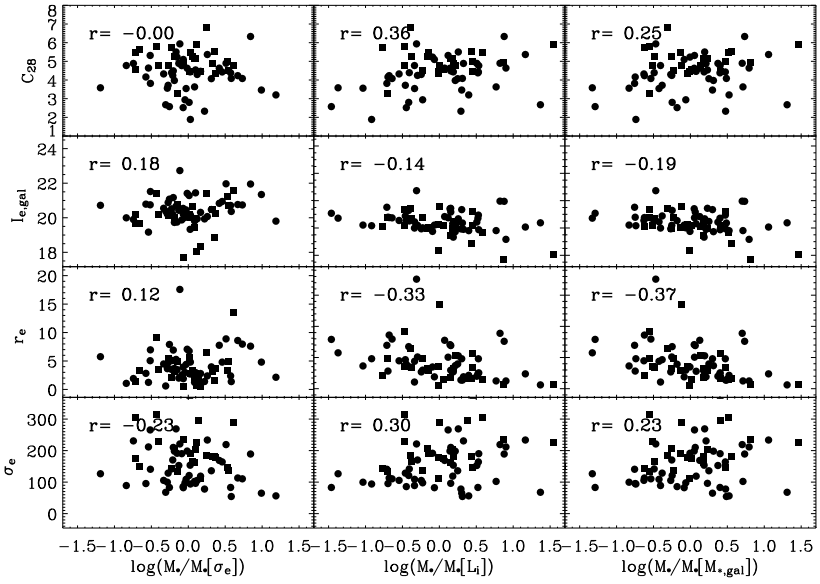

Figure 4.19 Residual of the $M_\bullet - \sigma_{\rm e}$, $M_\bullet - L_{i,\rm gal}$, $M_\bullet - M_{\star,\rm gal}$ relations against C_{28}, $I_{\rm e,gal}$, $r_{\rm e,gal}$, $\sigma_{\rm e}$ for 46 galaxies from sample 1, dots, and 29 galaxies from sample 2, squares. The total number of galaxies is N=74 and Pearson coefficient r of the correlation is given in each panel.

relation than using only the photometric parameter $L_{i,\rm gal}$. The correlation is as tight as the correlation between $\sigma_{\rm e}$ and $r_{\rm e,gal}$, suggesting that $M_{\star,\rm gal}$ plays a more important rôle on $M_\bullet$ than $L_{i,\rm gal}$. All of our tests so far thus confirm that $\sigma_{\rm e}$ is the fundamental driver to $M_\bullet$.

The tightness of SMBH scaling relations depends on the presence of $\sigma_{\rm e}$ as a fit parameter, i.e., the relation has a wish Pearson coefficient only when the $\sigma_{\rm e}$ is taken into account. The constancy of the Pearson coefficient despite the addition of more fit parameters (e.g., $r_{\rm e,bulge}$, $L_{i,\rm bulge}$ or $r_{\rm e,gal}$, $L_{i,\rm gal}$), argues that the main acting parameter is $\sigma_{\rm e}$. The addition of local or global parameters does not appreciably modify the $M_\bullet - \sigma_{\rm e}$ relation . We also verified that there is no correlation between $\sigma_{\rm e}$ and $r_{\rm e,bulge}$ (Figure 4.21). Similar is true for $\sigma_{\rm e}$ and $r_{\rm e,gal}$. Similar is true for $\sigma_{\rm e}$ and $r_{\rm e,gal}$. An anti-correlation between these two variables could explain a scatter conspiracy to remain constant for $M_\bullet - \sigma_{\rm e}$ and $M_\bullet - \sigma_{\rm e} - r_{\rm e}$.

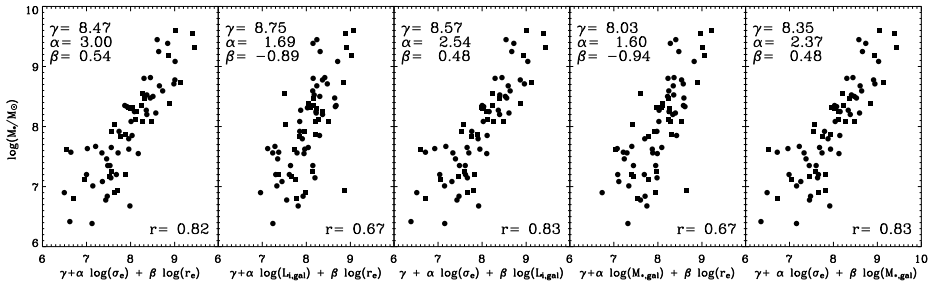

Figure 4.20 $M_\bullet$ as a function of $\sigma_{\rm e}$ and $r_{\rm e,gal}$ (*first panel*), $L_{i,\rm gal}$and $r_{\rm e,gal}$ (*second panel*), $\sigma_{\rm e}$ and $L_{i,\rm gal}$ (*third panel*), $M_{\star,\rm gal}$ and $r_{\rm e,gal}$ (*fourth panel*), and $\sigma_{\rm e}$ and $M_{\star,\rm gal}$ (*fifth panel*). The sample comprises 74 galaxies (46 from sample 1, dots; 25 from sample 3, squares). The normalization γ, slopes α and β, and Pearson coefficient r of the correlation are given in each panel.

Similar results were obtained by Aller & Richstone (2007) that compared $M_\bullet$ with $\sigma_{\rm e}$, $I_{\rm e}$ and $r_{\rm e,bulge}$, finding that the addition of a second parameter in the relation does not improve the quality of the fit, with $\sigma_{\rm e}$ appearing always to be the dominant parameter. However, by applying a combination of three parameters (in terms of $I_{\rm e}$, $r_{\rm e,bulge}$ and $\sigma_{\rm e}$) the energy per $(M/L)^2$ at $r_{\rm e,bulge}$ gives a fit at least statistically good as $M_\bullet - \sigma$. But, this is mainly true for ellipticals.

4.4 Discussion

In this work we wished to test whether the $M_\bullet$ is more fundamentally driven by one of the several bulge parameters known to correlate with the $M_\bullet$, or if the addition of a second parameter can improve the relations. The large sample of galaxies we used allowed to address such a classical problem of the SMBH demography.

Our analysis provided a clear confirmation that $M_\bullet$ is fundamentally driven by $\sigma_{\rm e}$ for all Hubble types, since the $M_\bullet - \sigma_{\rm e}$ relation appears to be the tightest one among all the scaling relations we tested so far. In our joint sample we did not find the difference in the scatter between elliptical/lenticulars and spirals found by G09. We found a larger scatter than previous studies. This can be explained because our joint sample comprises more spirals and because we are combining secure determinations and upper limits. However, B09 already showed that there is no bias in the distribution of the masses against the secure

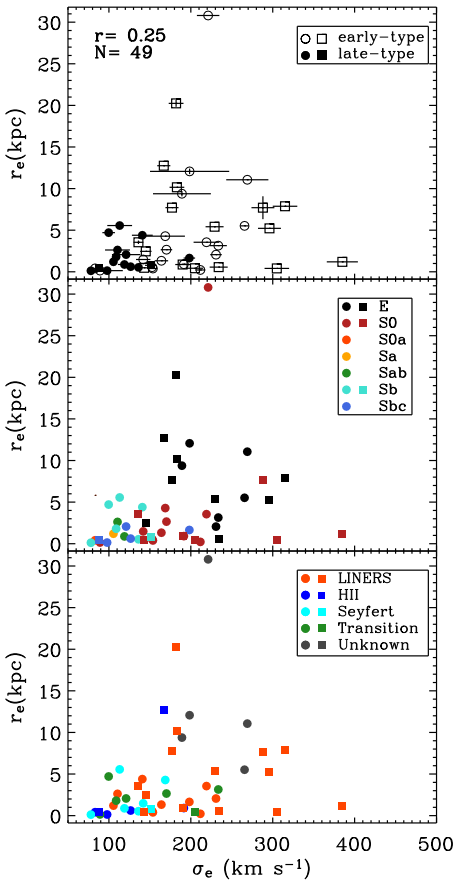

Figure 4.21 $r_{\rm e,bulge}$ as a function of $\sigma_{\rm e}$ f or 31 galaxies of sample 1 (dots) and 22 of sample 2 (17 secure $M_\bullet$, squares; 5 upper limits, arrows). Symbols are as in Figure 4.5. The total number of galaxies is N=49 and the Pearson correlation coefficient is r=0.25.

$M_\bullet$ population. Therefore we think that the various population of hosting galaxies is the fundamental reason of the scatter, although we did not find different relations for early-types and late-types. G09 suggested that they may be a systematic effect in $M_\bullet$ measurements of spirals or because the scatter is actually larger. In this context, Hu (2008) noted that pseudobulges appear to host relatively smaller $M_\bullet$ that classical bulges. In our analysis we have treated at the same way both classical and pseudobulges, maybe the difference between the two populations can increase the scatter but this is not obvious. Our results suggest that the $M_\bullet - L_{K,\rm bulge}$ is not as tight as the $M_\bullet - \sigma_{\rm e}$, contrary to the findings of G09. They obtained a scatter on the $L_{\rm bulge}$ relation for only ellipticals and lenticulars smaller than the previous studies (Lauer et al. 2007a; Aller & Richstone 2007) consistent with the one of the $M_\bullet - \sigma$ relation. The $M_{\rm vir,bulge}$ is a better tracer of $M_\bullet$ then $L_{i,\rm bulge}$ confirming the results of McLure & Dunlop (2002), Marconi & Hunt (2003), Häring & Rix (2004), and Aller & Richstone (2007). But, $M_\bullet - M_{\rm vir,bulge}$ does not seem to be as good as the $M_\bullet - \sigma_{\rm e}$. The use of global parameters, such us the total galaxy light or the total stellar mass unveiled an offset between ellipticals and spirals/lenticulars confirming that the disk is not connect with $M_\bullet$ (Kormendy 2001).

To assess the necessity of additional parameters in our fits, we performed both a residual analysis and a second-parameter fit finding that the so-called fundamental plane of SMBH (BHFP Hopkins et al. 2007a,b; Barway & Kembhavi 2007; Aller & Richstone 2007), is mainly driven by $\sigma_{\rm e}$. A small fraction of the tilt is due to $r_{\rm e}$ (18%). There is no effective increase of the Pearson coefficient and only a slightly better scatter when $r_{\rm e,bulge}$ is included. This is a further confirmation that $\sigma_{\rm e}$ is the fundamental parameter. Our findings are generally consistent with the theoretical predictions of BHFP by Hopkins et al. (2007b), who probed the possible predictors of $M_\bullet$ as well as BHFP using major merger simulations. Aller & Richstone (2007) from a multivariate study of bulge parameters against $M_\bullet$ found that the binding energy of the bulge, obtained by combining $M_\bullet$ with $I_e, bulge$, $r_{\rm e}$, $\sigma_{\rm e}$, is strongly connected with $M_\bullet$, with a scatter as good as the $M_\bullet - \sigma$ for ellipticals.

The existence of the scaling relations imply that SMBH and galaxy formation processes are closely linked. Some of the challenges of the current models of SMBH formation and evolution include reproducing and maintaining the scaling relations regardless of the events that take place during galaxy evolution driven by the process of hierarchical mass assembly (Croton 2009; Wyithe & Loeb 2002, 2003; McLure et al. 2006; Robertson et al. 2006a). The BHFP can be interpreted in terms of a feedback self-regulated SMBH growth, until the feedback is sufficient to unbind the local gas supply and blow it away in momentum or pressure driven winds (Hopkins et al. 2007b, 2009). This terminates the ac-

cretion inflow and cuts off further growth. In this sense, σ_e is the bulge property that is most closely linked to the SMBH because it determines the depth of the potential well from which the gas has to be expelled, and thus the minimum $M_\bullet$ for feedback. Younger et al. (2008) studied the self-regulated models of SMBHs growth in different scenarios of major mergers, minor mergers, and disk instabilities, finding that they depend on the scale in which the self-regulation occur. They compared the bulge binding energy and total binding energy with $M_\bullet$, finding that the total binding energy is not a good predictor for the $M_\bullet$, for disk-dominated systems. This suggests that the bulge properties, rather than the galaxy as whole are more significant, consistently our results. Our study of the BHFP shows also that the galaxies deviating much significantly from the main relation are disk-dominated systems. Hopkins et al. (2009) used simulations of gas inflows in galaxy interactions and mergers to constrain the origin the scaling relations. They found that the SMBH regulates its mass depending on the host global parameters, such as the mass, stellar velocity dispersion, and binding energy of the spheroid. The scatter of the SMBH scaling relations can be explained by the fact that SMBH may self regulate at a critical mass determined by the global properties of the host galaxy as predicted by the feedback models. Volonteri & Natarajan (2009) investigated the observational signature of the self-regulated SMBH growth by analyzing the mass assembly history of the black hole seeds through simulations. They found that the existence of the $M_\bullet - \sigma$ relation depends on the merging history of massive dark halos. The slope and the scatter of the relation depends on the seed and on the kind of self-regulation process. Therefore by having a better asses of the scatter of the relations we could discriminate the different theoretical models of formation.

In our work we compared $M_\bullet$ with V_c as a proxy of the circular velocity of the dark matter halo, finding no relation between the two quantities. Several theoretical models of SMBH formation predict in fact a connection between $M_\bullet$ and the total mass of the galaxy (Haehnelt et al. 1998; Silk & Rees 1998; Adams et al. 2001), in the sense that if the dark and baryonic matter act to form the bulge and SMBH, the halo determines the bulge and SMBH properties. Therefore, and $M_\bullet$ and the dark matter halo should be connected (Cattaneo 2001; Hopkins et al. 2005b,a). To understand this issue Bandara et al. (2009) investigated the correlation between $M_\bullet$ and total mass of the galaxy. Studied a sample of galaxies for which the mass of the galaxy was estimated with gravitational lensing. They derived the $M_\bullet$ from both the $M_\bullet - \sigma$ relation and $M_\bullet - n$ finding a correlation between $M_\bullet$ and the total mass M_{tot} (including the dark matter) of the host galaxy. The relation they found indicates that massive halos are more efficient in forming SMBHs than the less massive and the slope of the relation is representative of merger-driven, feedback regulated processes

of SMBH growth. Consistently, Booth & Schaye (2009) by using self-consistent simulations of the coevolution of SMBHs and galaxies confirmed the previous relation by Bandara et al. (2009). They pointed out that SMBHs regulate their growth and couple their properties to their host galaxies. They also analyzed if this self-regulation occurs on the scale of bulges, galaxy, or dark matter halo, finding that it seems to be connected with the mass of the dark matter halo. Although $M_\bullet$ shows a trend with $M_{\star,\mathrm{gal}}$ we did not find a relation between $M_\bullet$ and V_c, or $M_{\mathrm{dyn,gal}}$. This suggests that or the dark matter is not as strongly correlated with $M_\bullet$ as σ_e does or that V_c measurements we have do not trace the dark matter as good as gravitational lensing. However, we should keep in mind that the conversion used between the circular velocity and the virial velocity depends on the assumed model and mass estimations depend on the assumptions and scatter of the known scaling relations. An improvement of the V_c measurements will be important to trace the region where the dark matter is dominant, in particular in galaxies with a secure estimate of $M_\bullet$.

4.5 Conclusions

We used the largest sample of upper limits on $M_\bullet$ from B09 and the latest compilation of precise estimates of $M_\bullet$ from G09 to compare $M_\bullet$ with several bulge and galaxy properties. The photometric parameters were obtained from the decomposition of SDSS g, r, and i-band images, whereas the σ_e and the maximum circular velocity were extracted from the literature and retrieved from the Hyperleda catalogue. We wished to test if $M_\bullet$ is fundamentally driven by the galaxy bulge or halo. We explored for fundamental correlations between $M_\bullet$ and stellar velocity dispersion, σ_e, the i-band bulge luminosity, L_{bulge}, the bulge virial mass, $M_{\mathrm{vir,bulge}}$, the bulge Sérsic index n, the total i-band luminosity of the galaxy, $L_{i,\mathrm{gal}}$, the galaxy stellar mass, $M_{\star,\mathrm{gal}}$, the maximum circular velocity, V_c, and the galaxy dynamical and virial masses, $M_{\mathrm{dyn,gal}}$ and $M_{\mathrm{vir,gal}}$. We verified the tightness of the $M_\bullet - \sigma_\mathrm{e}$ relation, and found that correlations with other bulge parameters do not yield tighter trends. We confirmed that $M_\bullet$ is fundamentally driven by σ_e for all Hubble types. We searched for linear combinations of the galaxy parameters following the idea of a fundamental plane of SMBH. The BHFP is mainly driven by σ_e, with a small fraction of the tilt being due to r_e. By applying this linear combination to the galaxy parameters and σ_e we resulted with similar good relations suggesting the tightness of SMBH scaling relations depends on the presence of σ_e as a fit parameter, i.e., the relation has a wish Pearson coefficient only when the σ_e is taken into account.

Table 4.1 Properties of the galaxies of the sample 1

Galaxy	Morph. T.	Spec. Cl.	D (Mpc)	M_B^0 (mag)	σ_e (km s^{-1})	V_{max} (km s^{-1})	Ref	i_{RC3}	V_{rot} (km s^{-1})	i_{SDSS}	V_{dep} (km s^{-1})	$M_\bullet$ (33°) ($M_\odot$)	$M_\bullet$ (81°) ($M_\odot$)
(1)	(2)	(3)	(4)	(5)	(6)	(7)	(8)	(9)	(10)	(11)	(12)	(13)	(14)
IC 342	SABcd(rs)	H	3.73 a	−21.97	65.1 ± 23.8	72.9 ± 1.9	1	12	185 ± 10	...	...	5.0E6	1.3E6
IC 3639	SBbc(rs):	S2*	44.80 b	−20.70	91.4 ± 4.8	74.7 ± 3.5	2	18	245.2 ± 11.4	...	...	2.3E7	4.5E6
NGC 193	SAB0$^-$(s):	...	49.65 b	−20.22	203.2 ± 12.9	...	...	41	...	...	...	5.2E8	1.2E8
NGC 289	SBbc(rs)	...	17.08 b	−19.91	108.9 ± 11.6	118.7 ± 1.3	2	46	163.6 ± 2.2	...	...	4.7E7	1.2E7
NGC 315	E$^+$:	L1.9	57.68 b	−22.09	313.3 ± 27.2	569 ± 59	3	77	$569. \pm 59$	...	...	1.7E9	4.0E8
NGC 383	SA0$^-$:	...	59.17 b	−21.33	238.8 ± 16.7	...	...	32	...	...	...	1.2E9	2.7E8
NGC 541	S0$^-$:	...	63.65 b	−21.19	191.4 ± 4.0	...	...	15	...	...	...	8.6E8	1.8E8
NGC 613	SBbc(rs)	H*	15.40 b	−20.56	125.3 ± 18.9	160.0 ± 3.8	4	42	238.0 ± 3.8	...	...	9.0E7	1.8E7
NGC 741	E0:	...	65.71 b	−22.17	232.2 ± 11.2	...	...	16	...	...	...	1.1E9	2.0E8
NGC 788	SA0/a(s)	S1/S2*	47.88 b	−20.75	127.3 ± 18.2	...	...	44	...	...	...	1.6E8	4.4E7
NGC 1052	E4	L1.9	18.11 c	−20.09	190.2 ± 6.2	167.3 ± 6.0	4	74	173.4 ± 6.0	...	...	3.4E8	8.8E7
NGC 1358	SAB0/a(r)	S2	48.16 b	−20.86	171.5 ± 18.5	116.5 ± 9.3	2	41	178.8 ± 10.6	...	...	4.9E8	1.1E8
NGC 1497	S0	...	75.32 b	−21.24	245.1 ± 20.9	92.6 ± 7.0	2	57	110.6 ± 7.3	...	...	6.6E8	2.8E8
NGC 1667	SAB(r)c	S2	56.09 b	−21.49	178.0 ± 28.9	150.0 ± 16.1	4	40	229.4 ± 16.1	...	...	2.7E8	9.3E7
NGC 1961	SABc(rs)	L2	48.63 b	−22.58	222.2 ± 38.0	319.7 ± 15.2	4	52	402.7 ± 15.2	...	...	4.3E8	8.8E7
NGC 2110	SAB0$^-$	S2*	29.12 b	−20.62	201.4 ± 22.8	...	...	53	...	...	...	5.8E8	3.0E7
NGC 2179	SA0/a(s)	...	35.84 b	−20.09	154.3 ± 11.1	193.9 ± 32.4	4	51	246.5 ± 32.4	...	...	3.5E8	1.2E8
NGC 2273	SBa(r):	S2	23.33 b	−19.97	116.7 ± 10.6	154.3 ± 5.6	4	44	222.5 ± 5.6	...	...	6.6E6	2.0E6
NGC 2329	S0$^-$:	...	72.33 b	−21.36	217.6 ± 13.3	...	...	38	...	...	...	2.3E8	1.0E8
NGC 2685	(R)SB0$^+$ pec	S2/T2:	12.51 b	−18.81	82.3 ± 7.1	139.3 ± 4.0	2	70	148.1 ± 4.4	64	154.5 ± 4.4	1.0E7	1.5E6
NGC 2892	E+ pec:	...	86.24	−20.78	297.1 ± 18.8	...	...	16	...	...	...	3.5E8	2.1E8
NGC 2903	SABbc(rs)	H	10.45 b	−21.14	93.9 ± 12.1	167.1 ± 4.3	4	64	184.9 ± 4.3	58	197.1 ± 4.3	2.2E7	6.0E6
NGC 2911	SA0(s): pec	L2	43.49 b	−21.09	219.1 ± 15.7	154.1 ± 16.2	2	46	214.5 ± 18.2	52	196.5 ± 18.2	2.4E9	6.2E8
NGC 2964	SABbc(r):	H	19.69 b	−20.03	97.8 ± 19.1	124.1 ± 3.4	2	59	144.8 ± 5.8	60	143.7 ± 5.8	2.2E7	1.3E6
NGC 3021	SAbc(rs)	...	22.40 b	−19.37	56.4 ± 24.8	107.6 ± 5.6	4	58	126.1 ± 5.6	52	136.6 ± 5.6	3.7E7	9.1E6
NGC 3078	E2-3	...	32.85 c	−20.79	207.8 ± 12.2	...	...	48	...	...	...	2.1E8	3.1E7
NGC 3081	(R)SAB0/a(r)	S2*	33.51 b	−20.19	123.0 ± 7.6	92.1 ± 3.4	2	43	135.6 ± 4.0	...	...	3.2E7	7.9E6
NGC 3351	SBb(r)	H	9.33 d	−19.74	95.4 ± 15.1	113.8 ± 6.6	4	50	148.8 ± 6.6	26	258.7 ± 6.6	6.0E6	1.8E6
NGC 3368	SABab(rs)	L2	9.71 c	−20.28	105.3 ± 4.1	154.2 ± 6.0	4	49	203.1 ± 6.0	37	258.2 ± 6.0	4.5E7	1.4E7
NGC 3393	(R′)SBa(rs):	S2*	50.59 b	−21.03	167.5 ± 25.6	82.0 ± 6.2	2	26	189.1 ± 12.6	...	...	2.3E8	8.8E7
NGC 3627	SABb(s)	T2/S2	9.43 d	−20.88	99.6 ± 7.7	155.6 ± 4.5	4	67	168.7 ± 4.5	63	174.8 ± 4.5	1.4E7	6.3E6
NGC 3642	SAbc(r):	L1.9	21.65 b	−20.37	96.1 ± 24.8	21.7 ± 2.6	4	35	37.7 ± 2.6	29	44.2 ± 2.6	2.9E7	2.4E7
NGC 3675	SAb(s)	T2	12.41 b	−20.10	108.8 ± 4.5	183.7 ± 6.1	4	62	207.9 ± 6.1	53	229.0 ± 6.1	3.6E7	9.3E6
NGC 3801	S0?	...	46.29 b	−20.69	210.1 ± 17.7	135.7 ± 7.0	2	64	150.6 ± 7.6	54	166.2 ± 7.6	3.9E8	9.3E7

Table 4.1 – Continued

Galaxy	Morph. T.	Spec. Cl.	D (Mpc)	M_B^0 (mag)	σ_e (km s^{-1})	V_{max} (km s^{-1})	Ref	i_{RC3}	V_{rot} (km s^{-1})	i_{SDSS}	V_{dep} (km s^{-1})	$M_\bullet$ (33°) ($M_\odot$)	$M_\bullet$ (81°) ($M_\odot$)
(1)	(2)	(3)	(4)	(5)	(6)	(7)	(8)	(9)	(10)	(11)	(12)	(13)	(14)
NGC 3862	E	...	84.56 b	−21.27	221.1 ± 13.7	...	...	5	...	...	...	6.0E8	1.1E8
NGC 3953	SBbc(r)	T2	15.40 b	−20.71	128.5 ± 0.9	183.7 ± 4.7	4	63	206.0 ± 4.7	62	207.3 ± 4.7	4.2E7	1.1E7
NGC 3982	SABb(r):	S1.9	15.87 b	−19.47	78.0 ± 2.0	82.2 ± 7.6	4	30	161.3 ± 7.6	30	166.1 ± 7.6	1.6E7	4.9E6
NGC 3992	SBbc(rs)	T2:	15.31 b	−20.81	120.9 ± 17.3	211.4 ± 3.6	2	54	261.5 ± 5.3	62	239.4 ± 5.3	6.3E7	1.7E7
NGC 4036	$S0^-$	L1.9	19.04 b	−20.06	153.7 ± 5.1	...	...	80	...	...	...	1.8E8	3.4E7
NGC 4088	SABbc(rs)	H	11.85 b	−20.00	85.7 ± 3.8	152.8 ± 2.8	4	70	161.9 ± 3.1	71	162.0 ± 3.1	1.2E7	3.2E6
NGC 4143	$SAB0^0$(s)	L1.9	14.84 c	−19.11	211.6 ± 6.0	...	...	61	...	...	...	1.9E8	3.7E7
NGC 4150	$SA0^0$(r)?	T2	12.79 c	−18.29	89.1 ± 3.1	...	...	55	...	...	...	2.4E6	3.2E5
NGC 4203	$SAB0^-$:	L1.9	14.09 c	−19.29	152.8 ± 2.7	102.4 ± 3.4	2	25	244.2 ± 3.4	...	...	1.2E8	3.6E7
NGC 4212	SAc:	H	3.17 b	−16.31	67.8 ± 2.8	107.6 ± 7.6	2	53	133.8 ± 7.6	49	141.8 ± 7.6	2.6E6	3.7E5
NGC 4245	SB0/a(r):	H	14.56 b	−18.96	83.1 ± 2.9	91.9 ± 5.4	2	44	131.2 ± 5.4	38	147.5 ± 5.4	4.7E7	5.2E6
NGC 4278	E1-2	L1.9	15.03 c	−20.06	230.7 ± 7.1	416 ± 13.0	3	29	416 ± 13	...	...	1.7E8	4.9E7
NGC 4314	SBa(rs)	L2	15.49 b	−19.93	105.5 ± 3.6	43.9 ± 5.2	2	29	91.4 ± 24.6	29	91.6 ± 24.6	1.6E7	4.1E6
NGC 4321	SABbc(s)	T2	14.19 d	−20.93	83.0 ± 3.6	113.4 ± 4.7	4	33	189.2 ± 4.7	33	206.6 ± 4.7	6.9E6	3.2E6
NGC 4335	E	...	59.08 b	−20.67	265.6 ± 5.1	...	...	51	...	...	...	5.1E8	1.2E8
NGC 4429	$SA0^+$(r)	T2	18.20 b	−20.48	170.2 ± 7.0	56.0 ± 4.5	4	79	56.6 ± 4.5	...	...	1.6E8	3.2E7
NGC 4435	$SB0^0$(s)	T2/H:	13.72 b	−19.23	137.0 ± 6.1	163.2 ± 14.0	4	52	207.7 ± 14.0	43	237.2 ± 14.0	4.5E7	1.5E7
NGC 4450	SAab(s)	L1.9	28.28 b	−21.66	110.5 ± 15.2	134.8 ± 6.7	4	44	191.4 ± 6.7	57	160.3 ± 6.7	2.2E8	6.1E7
NGC 4477	SB0(s):?	S2	20.81 b	−20.44	141.9 ± 8.8	...	...	28	...	...	...	7.1E7	1.8E7
NGC 4501	SAb(rs)	S2	32.29 b	−22.84	140.2 ± 15.8	240.1 ± 5.3	4	60	273.8 ± 5.3	...	...	7.5E7	1.4E7
NGC 4507	(R′)SABb(rs)	S2*	47.04 b	−21.23	143.9 ± 6.9	...	...	39	...	...	...	3.4E7	6.8E6
NGC 4526	SAB0(s):	H	15.77 c	−20.61	191.5 ± 2.7	134.9 ± 8.5	4	81	134.7 ± 8.5	78	137.8 ± 8.5	3.0E8	5.7E7
NGC 4548	SBb(rs)	L2	17.92 c	−20.63	140.8 ± 12.7	107.7 ± 7.3	4	39	154.0 ± 7.3	37	176.9 ± 7.3	3.5E7	9.0E6
NGC 4552	E0-1	T2:	14.37 c	−20.36	233.5 ± 10.4	...	...	33	...	...	...	1.8E9	6.4E8
NGC 4579	SABb(rs)	S1.9/L1.9	22.96 b	−21.66	113.1 ± 15.1	156.7 ± 10.9	4	39	247.8 ± 10.9	42	231.9 ± 10.9	2.1E8	4.0E7
NGC 4636	E0-1	L1.9	13.72 c	−20.40	164.1 ± 8.2	341 ± 13.	3	58	341. ± 13.	...	...	6.3E8	2.3E8
NGC 4698	SAab(s)	S2	16.43 b	−19.99	118.9 ± 8.0	188.0 ± 4.6	4	56	226.0 ± 4.6	28	403.4 ± 4.6	8.3E7	4.0E7
NGC 4736	(R)SAab(r)	L2	4.85 c	−19.83	97.9 ± 2.6	91.6 ± 5.3	4	37	151.0 ± 5.3	...	...	1.3E7	3.1E6
NGC 4800	SAb(rs)	H	12.51 b	−18.51	102.2 ± 1.8	165.1 ± 19.8	4	44	221.2 ± 19.8	22	439.3 ± 19.8	3.6E7	3.1E6
NGC 4826	(R)SAab(rs)	T2	7.00 c	−20.55	105.7 ± 12.2	128.3 ± 4.6	4	61	146.0 ± 4.6	...	...	3.9E7	1.7E7
NGC 5005	SABbc(rs)	L1.9	14.65 b	−20.79	198.2 ± 7.0	244.4 ± 6.9	2	64	271.0 ± 9.5	63	273.6 ± 9.5	3.2E8	1.1E8
NGC 5127	E pec	...	62.53 b	−21.32	198.5 ± 48.3	...	...	57	...	...	...	4.8E8	7.2E7
NGC 5194	SAbc(s) pec	S2	7.93 b	−20.99	70.3 ± 9.4	67.3 ± 5.2	4	54	83.1 ± 5.2	...	...	2.1E6	4.0E5
NGC 5248	SABbc(rs)	H	17.92 b	−20.78	126.5 ± 11.2	114.5 ± 1.87	2	45	161.8 ± 2.4	34	206.1 ± 2.4	4.8E6	8.4E5

Table 4.1 – Continued

Galaxy	Morph. T.	Spec. Cl.	D (Mpc)	M_B^0 (mag)	σ_e (km s^{-1})	$V_{\rm max}$ (km s^{-1})	Ref	$i_{\rm RC3}$	$V_{\rm rot}$ (km s^{-1})	$i_{\rm SDSS}$	$V_{\rm dep}$ (km s^{-1})	$M_\bullet$ (33°) ($M_\odot$)	$M_\bullet$ (81°) ($M_\odot$)
(1)	(2)	(3)	(4)	(5)	(6)	(7)	(8)	(9)	(10)	(11)	(12)	(13)	(14)
NGC 5252	S0	S1.9*	89.32 b	−20.97	168.8 ± 24.0	57.3 ± 3.15	2	63	64.1 ± 3.4	59	64.1 ± 3.4	6.5E8	1.2E8
NGC 5283	S0?	S2*	34.53 b	−18.72	126.1 ± 12.9	...	...	28	...	...	...	5.5E7	1.2E7
NGC 5347	(R′)SBab(rs)	S2*	32.29 b	−19.59	64.9 ± 12.4	34.2 ± 3.9	4	39	53.5 ± 3.9	21	94.1 ± 3.9	4.3E7	6.1E6
NGC 5427	SAc(s)pec	S2*	36.31 b	−21.22	64.8 ± 11.4	122.1 ± 16.5	2	32	227.8 ± 41.0	...	...	7.6E7	1.9E7
NGC 5490	E	...	65.24 b	−21.34	268.9 ± 25.7	...	...	48	...	...	...	1.2E9	2.4E8
NGC 5643	SABc(rs)	S2*	17.36 b	−21.11	89.5 ± 2.0	77.4 ± 1.9	2	30	154.3 ± 4.5	...	...	4.4E7	2.9E6
NGC 5695	S?	S2*	54.60 b	−20.46	136.0 ± 1.9	162.9 ± 16.8	4	48	202.1 ± 16.8	44	234.1 ± 16.8	2.1E8	4.8E7
NGC 5728	SABa(r):	S2*	37.61 b	−21.37	193.4 ± 40.4	176.0 ± 13.8	4	60	202.0 ± 13.8	...	...	2.2E8	5.8E7
NGC 5879	SAbc(rs):?	T2/L2	10.55 b	−18.88	54.3 ± 8.0	114.2 ± 2.8	4	77	116.8 ± 2.8	69	121.9 ± 2.8	7.9E6	2.2E6
NGC 5921	SB(r)bc	L	20.49 5	−20.22	84.9 ± 9.3	66.8 ± 1.7	2	37	111.7 ± 2.4	...	...	3.1E7	4.4E6
NGC 6300	SBb(rs)	S2*	14.19 b	−20.71	86.5 ± 4.7	128.4 ± 1.5	2	51	165.5 ± 2.0	...	...	2.2E7	8.8E6
NGC 6500	SAab:	L2	36.49 b	−20.50	211.5 ± 5.9	238.2 ± 14.0	4	45	321.0 ± 14.0	...	...	4.0E8	1.2E8
NGC 6861	SA0$^-$(s):	...	26.13 c	−20.32	386.4 ± 14.1	...	...	63	...	...	...	1.4E9	3.4E8
NGC 6951	SABbc(rs)	S2	15.96 b	−20.45	95.5 ± 9.8	137.0 ± 5.0	4	35	238.9 ± 5.0	...	...	1.3E7	5.5E6
NGC 7331	SAb(s)	T2	12.23 c	−21.21	115.8 ± 4.1	236.3 ± 4.2	4	74	245.3 ± 4.2	...	...	1.6E8	6.9E7
NGC 7626	E pec:	L2::	38.08 b	−20.99	232.5 ± 10.6	$401 \pm 32.$	3	37	$401. \pm 32.$	...	...	8.1E8	1.8E8
NGC 7682	SBab(r)	S2*	59.27 b	−20.34	112.8 ± 15.6	79.0 ± 2.6	2	28	165.8 ± 8.3	...	...	7.7E7	1.7E7
UGC 1214	(R)SAB0$^+$(rs):	S2*	59.92 b	−20.47	106.8 ± 13.9	103.9 ± 5.5	2	13	443.2 ± 12.7	...	...	8.3E7	3.6E7
UGC 1395	SAb(rs)	S1.9*	60.85 b	−20.21	64.2 ± 5.8	92.6 ± 5.7	2	39	147.4 ± 7.1	...	...	1.3E7	3.5E6
UGC 1841	E	...	74.95 b	−21.28	348.0 ± 29.0	...	...	5	...	...	...	4.6E8	1.9E8
UGC 7115	E	...	88.20 b	−20.70	189.1 ± 35.3	...	...	24	...	...	...	2.8E9	3.6E8
UGC 12064	S0$^-$:	...	60.11 b	−20.19	258.7 ± 17.6	...	...	5	...	...	...	2.3E9	2.1E8

Notes. — Col.(1): Galaxy name. Col.(2): Morphological type from RC3. Col.(3): Nuclear spectral class from Ho et al. (1997a), where H = H II nucleus, L = LINER, S = Seyfert , T = transition object (LINER/H II), 1 = Seyfert 1, 2 = Seyfert 2, and a fractional number between 1 and 2 denotes various intermediate types; uncertain and highly uncertain classifications are followed by a single and double colon, respectively. The nuclear spectral class of galaxies marked with * is from the NASA/IPAC Extragalactic Database (NED). Col.(4): Distance. All the distances were taken from the literature. a= Tully (1988); b=$D = V_{3\rm K}/H_0$ where $V_{3\rm K}$ is the weighted mean recessional velocity corrected to the reference frame of the microwave background radiation given in RC3, and $H_0 = 70$ km s^{-1} Mpc^{-1}. d= Freedman et al. (2001); c = Tonry et al. (2001). Col.(5): Absolute corrected B magnitude derived from B_T^0 (RC3) with the adopted distance. Col.(6): Central σ of the stellar component within r_e derived from the measured values following Jørgensen et al. (1995). We did not apply any aperture correction to the measured σ of NGC 2748, NGC 3982, and UGC 1841, because no information about the size of the aperture was available. Col.(7): Apparent maximum gas rotation velocity or circular velocity from stellar models from the literature and Hyperleda. The V_c of NGC 4429 was discarded for uncertain measurement. Col.(8): References for Col.(7). References. — Apparent maximum rotation velocity of gas: (1) Pizzella et al. (2005); (2) Hyperleda, Paturel et al. (2003a); (4) Ho (2007); Maximum circular velocity from the stellar models: (3) Kronawitter et al. (2000). Col.(9): Inclination derived from the apparent flattening of the galaxy as measured from the ratio of the minor and major isophotal diameters at the surface brightness of $\mu_B = 25$ mag arcsec^{-2} from RC3. Col.(10): Deprojected maximum rotation velocity corrected for inclination from RC3. Col.(11): Inclination obtained from the ellipticity of the SDSS photometry. Col.(12): Deprojected maximum rotation velocity obtained with the inclinations from our SDSS photometry. Col.(13): $M_\bullet$ upper limit for a Keplerian disk model assuming $i = 33°$. Col.(14): $M_\bullet$ upper limit for $i = 81°$.

Table 4.2 Properties of the galaxies of sample 2

Galaxy	Morph. T.	Spec. Cl.	D (Mpc)	$M^0_{V,T}$ (mag)	$M^0_{V,bulge}$ (mag)	σ_e (km s^{-1})	V_{max} (km s^{-1})	Ref	i_{RC3}	V_{rot} (km s^{-1})	i_{SDSS}	V_{dep} (km s^{-1})	$M_\bullet$ ($M_\odot$)	$M_{\bullet low}$ ($M_\odot$)	$M_{\bullet high}$ ($M_\odot$)
(1)	(2)	(3)	(4)	(5)	(6)	(7)	(8)	(9)	(10)	(11)	(12)	(13)	(14)	(15)	(16)
					$M_\bullet$ from sample 2										
Abell 1836	E	...	157.5	-23.31	-23.31 ± 0.15	288 ± 14	...	...	...	...	...	...	3.9E9	3.3E9	4.3E9
Abell 3565	E	...	54.4	-23.27	-23.27 ± 0.15	322 ± 16	...	...	...	...	...	...	5.2E8	4.4E8	6.0E8
Circinus	Sb	Sy2 *	4.0	-17.36	...	158 ± 18	107.0 ± 5.5	1	68	115.1 ± 8.8	...	...	1.7E6	1.4E6	2.1E6
IC 1459	E4	L*	30.9	-22.57	-22.57 ± 0.15	340 ± 17	79.5 ± 3	2	68	94.9 ± 3	...	...	2.8E9	1.6E9	3.9E9
MW	Sbc	...	0.008	...	...	105 ± 20	180 ± 20	3	...	180 ± 20	...	...	4.1E6	3.5E6	4.7E6
NGC 221	E2	...	0.86	-16.83	-16.83 ± 0.05	75 ± 3	...	...	...	...	...	...	3.1E6	2.5E6	3.7E6
NGC 224	Sb	L	0.80	-21.84	...	160 ± 8	239.1 ± 6.2	1	78	244.4 ± 6.2	...	...	1.5E8	1.2E8	2.4E8
NGC 821	E4	...	25.5	-21.24	-21.24 ± 0.13	209 ± 10	...	...	...	...	...	...	4.2E7	3.4E7	7.0E7
NGC 1023	SB0	...	12.1	-21.26	-20.61 ± 0.28	205 ± 10	$270. \pm 31$	4	77	$270 \pm 31.$	...	...	4.6E7	4.1E7	5.1E7
NGC 1068	Sb	S1.8	15.4	-22.17	...	151 ± 7	118.6 ± 14.8	1	33	217.6 ± 14.8	46	301.5 ± 14.8	8.6E6	8.3E6	8.9E6
NGC 1300	SBbc	...	20.1	-21.34	...	218 ± 10	117.9 ± 2.5	1	50	152.3 ± 2.5	...	...	7.1E7	3.6E7	1.4E8
NGC 1399	E1	...	21.1	-22.13	-22.13 ± 0.10	337 ± 16	424 ± 46	5	29	424 ± 46	...	...	5.1E8	4.4E8	5.8E8
NGC 1399*	E1	...	21.1	-22.13	-22.13 ± 0.10	337 ± 16	424 ± 46	5	29	424 ± 46	...	...	1.3E9	6.4E8	1.8E9
NGC 2748	Sc	H	24.9	-20.97	...	115 ± 5	121.4 ± 3.7	2	72	127.8 ± 3.72	...	...	4.7E7	8.6E6	8.5E7
NGC 2778	E2	...	24.2	-19.62	-19.62 ± 0.13	175 ± 8	...	...	...	...	...	...	1.6E7	5.8E6	2.5E7
NGC 2787	SB0	L1.9	7.9	-18.90	...	189 ± 9	160.5 ± 20.3	1	57	189.8 ± 20.3	...	...	4.3E7	3.8E7	4.7E7
NGC 3031	Sb	S1.5	4.1	-21.51	...	143 ± 7	192.0 ± 7.5	1	62	216.7 ± 7.5	...	...	8.0E7	6.9E7	1.0E8
NGC 3115	S0	...	10.2	-21.25	-21.18 ± 0.05	230 ± 11	103.4 ± 6.0	1	80	92.4 ± 6.0	...	...	9.6E8	6.7E8	1.5E9
NGC 3227	SBa	S1.5	17.0	-20.73	...	133 ± 12	97.7 ± 4.1	2	51	125.9 ± 4.1	61	112.0 ± 4.1	1.5E7	7.0E6	2.0E7
NGC 3245	S0	T2:	22.1	-20.96	...	205 ± 10	...	...	...	...	...	...	2.2E8	1.7E8	2.7E8
NGC 3377	E6	...	11.7	-20.11	-20.11 ± 0.10	145 ± 7	...	...	...	...	...	...	1.1E8	1.0E8	2.2E8
NGC 3379	E0	L2/T2::	11.7	-21.10	-21.10 ± 0.03	206 ± 10	259 ± 23	5	38	259 ± 23	27	259.0 ± 23	1.2E8	6.2E7	2.0E8
NGC 3384	SB0	...	11.7	-20.50	-19.93 ± 0.22	143 ± 7	18.4 ± 1.0	2	80	18.4 ± 1.01	...	...	1.8E7	1.5E7	1.9E7
NGC 3585	S0	...	21.2	-21.88	-21.80 ± 0.20	213 ± 10	...	...	...	...	...	...	3.4E8	2.8E8	4.9E8
NGC 3607	E1	L2	19.9	-21.62	-21.62 ± 0.10	229 ± 11	...	...	...	...	...	...	1.2E8	7.9E7	1.6E8
NGC 3608	E1	L2/S2:	23.0	-21.05	-21.05 ± 0.10	182 ± 9	59.4 ± 4.9	2	51	94.5 ± 4.93	31	94.5 ± 4.9	2.1E8	1.4E8	3.2E8
NGC 3998	S0	L1.9	14.9	-20.32	...	305 ± 15	290.3 ± 42.2	1	39	456.8 ± 42.2	37	764.1 ± 42.2	2.4E8	6.2E7	4.5E8
NGC 4026	S0	...	15.6	-20.28	-19.83 ± 0.20	180 ± 9	...	...	...	...	...	...	2.1E8	1.7E8	2.8E8
NGC 4258	SABbc	S1.9	7.2	-21.31	...	115 ± 10	191.1 ± 5.2	1	71	201.7 ± 5.2	...	...	3.78E7	3.77E7	3.79E7
NGC 4261	E2	L2	33.4	-22.72	-22.72 ± 0.06	315 ± 15	...	...	...	...	...	...	5.5E8	4.3E8	6.6E8
NGC 4291	E2	...	25.0	-20.67	-20.67 ± 0.13	242 ± 12	...	...	...	...	...	...	3.2E8	8.3E7	4.1E8
NGC 4342	S0	...	18.0	-18.84	...	225 ± 11	...	...	...	...	...	...	3.6E8	2.4E8	5.6E8
NGC 4374	E1	L2	17.0	-22.45	-22.45 ± 0.05	296 ± 14	410 ± 31	5	39	410 ± 31	38	410 ± 31	1.5E9	9.0E8	2.6E9
NGC 4459	E2	H/L	17.0	-21.06	-21.06 ± 0.04	167 ± 8	...	...	...	...	...	...	7.4E7	6.0E7	8.8E7
NGC 4473	E4	...	17.0	-21.14	-21.14 ± 0.04	190 ± 9	...	...	...	...	...	...	1.3E8	3.6E7	1.8E8

Table 4.2 – Continued

Galaxy	Morph. T.	Spec. Cl.	D	$M^0_{V,T}$	$M^0_{V,bulge}$	σ_e	V_{max}	Ref	i_{RC3}	V_{rot}	i_{SDSS}	V_{dep}	$M_\bullet$	$M_{\bullet low}$	$M_{\bullet high}$
			(Mpc)	(mag)	(mag)	(km s^{-1})	(km s^{-1})			(km s^{-1})		(km s^{-1})	($M_\odot$)	($M_\odot$)	($M_\odot$)
(1)	(2)	(3)	(4)	(5)	(6)	(7)	(8)	(9)	(10)	(11)	(12)	(13)	(14)	(15)	(16)
NGC 4486	E1	L2	17.0	-22.92	-22.92 ± 0.04	375 ± 18	507 ± 38	5	55	$507 \pm 38.$	33	507 ± 38	3.6E9	2.6E9	4.6E9
NGC 4486A	E2	...	17.0	-18.70	-18.70 ± 0.05	111 ± 5	...	...	...	...	...	...	1.3E7	9.0E6	1.8E7
NGC 4564	S0	...	17.0	-20.10	-19.60 ± 0.32	162 ± 8	...	...	...	...	...	...	6.9E7	5.9E7	7.3E7
NGC 4594	Sa	L2	10.3	-22.52	-22.44 ± 0.15	240 ± 12	375.1 ± 9.3	1	75	382.7 ± 9.3	...	...	5.7E8	1.7E8	1.1E9
NGC 4596	SB0	L2::	18.0	-20.70	...	136 ± 6	154.9 ± 7.9	2	47	154.9 ± 7.9	42	230.4 ± 7.9	8.4E7	5.9E7	1.2E8
NGC 4649	E2	...	16.5	-22.65	-22.65 ± 0.05	385 ± 19	...	...	...	...	...	...	2.1E9	1.5E9	2.6E9
NGC 4697	E6	...	12.4	-21.29	-21.29 ± 0.11	177 ± 8	...	...	...	...	...	...	2.0E8	1.8E8	2.2E8
NGC 5077	E3	L1.9	44.9	-22.04	-22.04 ± 0.13	222 ± 11	...	...	...	...	...	...	8.0E8	4.7E8	1.3E9
NGC 5128	S0/E	Sy2	4.4	-21.82	-21.82 ± 0.08	150 ± 7	232.7 ± 12.0	2	46	323.8 ± 11.98	...	...	3.0E8	2.8E8	3.4E8
NGC 5128*	S0/E	Sy2	4.4	-21.82	-21.82 ± 0.08	150 ± 7	232.7 ± 12.0	2	46	323.8 ± 11.98	...	...	7.0E7	3.2E7	8.3E7
NGC 5576	E3		27.1	-21.26	-21.26 ± 0.13	183 ± 9	100.9 ± 8.2	2	76	109.0 ± 8.16	59	109.0 ± 8.2	1.8E8	1.4E8	2.1E8
NGC 5845	E3	...	28.7	-19.77	-19.77 ± 0.13	234 ± 11	...	...	...	...	...	...	2.9E8	1.2E8	3.4E8
NGC 6251	E1	Sy2	106.0	...	...	290 ± 14	...	...	...	...	...	...	6.0E8	4.0E8	8.0E8
NGC 7052	E3	...	70.9	...	...	266 ± 13	143.4 ± 11.2	1	78	141.1 ± 11.2	...	...	4.0E8	2.4E8	6.8E8
NGC 7457	S0	...	14.0	-19.80	-18.72 ± 0.11	67 ± 3	...	...	...	..	...	...	4.1E6	2.4E6	5.3E6
NGC 7582	SBab	Sy2	22.3	-21.51	...	156 ± 19	114.7 ± 3.0	2	72	120.9 ± 3.01	...	...	5.5E7	4.4E7	7.1E7
Upper limits on $M_\bullet$ from sample 2															
Abell 2052	E	...	151.1	-24.21	-24.21 ± 0.15	233 ± 11	...	...	...	...	...	...	4.9E9		
NGC 3310**	SB(r)bc	H	17.4	-20.56	...	83 ± 4	102.0 ± 2.5	2	40	157.6 ± 9.2	16	361.7 ± 9.2	4.2E7		
NGC 4041**	S(rs)bc	H	20.9	-20.40	...	88 ± 4	93.8 ± 2.3	2	22	254.1 ± 9.5	30	185.5 ± 9.5	6.4E6		
NGC 4435**	SB0	T2/H:	17.0	-20.45	...	150 ± 7	163.2 ± 14.0	1	52	207.7 ± 14.0	43	237.2 ± 14.0	8.0E6		
NGC 4486B	E1	...	17.0	-17.80	-17.80 ± 0.04	185 ± 9	248.7 ± 17	5	...	$248.7 \pm 17.$	...	$248.7 \pm 17.$	1.1E9		

NOTES. — Col.(1): Galaxy name. In the case of 2 different $M_\bullet$ we used the ones indicated as (*). Col.(2): Morphological type from RC3. Col.(3): Nuclear spectral class from Ho et al. (1997a), where H = H II nucleus, L = LINER, S = Seyfert , T = transition object (LINER/H II), 1 = Seyfert 1, 2 = Seyfert 2, and a fractional number between 1 and 2 denotes various intermediate types; uncertain and highly uncertain classifications are followed by a single and double colon, respectively. The nuclear spectral class of galaxies marked with * is from NED. Col.(4): Distance from G09. Col.(5): Absolute corrected total V magnitude. Col.(6): Absolute corrected bulge V magnitude. Col.(7): Central velocity dispersion of the stellar component within r_e. Col.(8): Col.(7): Apparent maximum gas rotation velocity or circular velocity from stellar models from the literature and Hyperleda. The V_c of NGC 3384 was discarded for uncertain measurement. Col.(9): References for Col.(8). REFERENCES. — Apparent maximum rotation velocity of gas: (2) Hyperleda, Paturel et al. (2003a); (3) Baes et al. (2003); (1) Ho (2007); Maximum circular velocity from the stellar models: (5) Kronawitter et al. (2000); (4) Debattista et al. (2002). Col.(10): Inclination derived from the apparent flattening of the galaxy as measured from the ratio of the minor and major isophotal diameters at the surface brightness of $\mu_B = 25$ mag arcsec^{-2} from RC3. Col.(11): Deprojected maximum rotation velocity corrected for inclination from RC3. Col.(12): Inclination obtained from the ellipticity of the SDSS photometry. Col.(13): Deprojected maximum rotation velocity obtained with the inclinations from our own photometry. Col.(14): $M_\bullet$ or upper limits on $M_\bullet$. Col.(15): $M_\bullet$ low. Col.(16): $M_\bullet$ high.

Table 4.3 Structural properties from two-dimensional decomposition

Galaxy	μ_e (mag arcsec^{-2})	r_e ($''$)	n	q_b	PA$_b$ ($^\circ$)	μ_0 (mag arcsec^{-2})	h ($''$)	q_d	PA$_d$ ($^\circ$)	B/T	$m_{i,tot}$ (mag)
(1)	(2)	(3)	(4)	(5)	(6)	(7)	(8)	(9)	(10)	(11)	(12)
Upper limits on $M_\bullet$ from sample 1											
NGC 2911	20.83 ± 0.10	16.84 ± 1.87	3.65 ± 0.10	0.75 ± 0.01	56.58 ± 1.87	21.70 ± 0.08	70.99 ± 7.43	0.64 ± 0.01	48.11 ± 0.07	0.34 ± 0.01	11.67 ± 0.07
NGC 2964	18.00 ± 0.07	1.45 ± 0.04	2.81 ± 0.09	0.86 ± 0.01	178.97 ± 5.60	18.85 ± 0.05	18.84 ± 0.31	0.73 ± 0.01	30.87 ± 0.02	0.04 ± 0.01	14.15 ± 0.07
NGC 3627	21.37 ± 0.11	102.98 ± 3.22	4.60 ± 0.02	0.45 ± 0.03	69.37 ± 1.18	19.65 ± 0.08	80.38 ± 1.88	0.44 ± 0.01	101.75 ± 0.08	0.57 ± 0.03	7.40 ± 0.08
NGC 3675	20.95 ± 0.09	29.93 ± 1.03	4.71 ± 0.12	0.50 ± 0.01	100.92 ± 9.77	19.37 ± 0.06	49.14 ± 1.52	0.47 ± 0.01	98.91 ± 0.09	0.26 ± 0.01	10.86 ± 0.08
NGC 3862	24.12 ± 0.02	75.14 ± 0.24	7.90 ± 0.04	1.00 ± 0.01	78.66 ± 0.01	...	...	...	...	1.00	10.99 ± 0.01
NGC 3982	17.87 ± 0.08	1.59 ± 0.17	0.80 ± 0.04	0.79 ± 0.01	106.78 ± 2.84	18.39 ± 0.06	12.09 ± 0.83	0.87 ± 0.01	109.01 ± 0.15	0.04 ± 0.01	14.54 ± 0.07
NGC 3992	21.21 ± 0.10	27.81 ± 0.87	5.04 ± 0.16	0.68 ± 0.01	149.86 ± 7.96	20.16 ± 0.07	83.41 ± 2.29	0.53 ± 0.01	155.41 ± 0.12	0.18 ± 0.01	10.90 ± 0.08
NGC 4036	18.03 ± 0.07	4.24 ± 0.11	1.73 ± 0.06	0.88 ± 0.01	154.51 ± 3.64	17.86 ± 0.05	20.18 ± 0.32	0.37 ± 0.01	175.36 ± 0.33	0.18 ± 0.01	12.07 ± 0.07
NGC 4143	16.79 ± 0.08	3.07 ± 0.32	1.05 ± 0.05	0.78 ± 0.01	59.34 ± 2.39	17.84 ± 0.06	14.28 ± 0.93	0.58 ± 0.01	58.71 ± 0.04	0.24 ± 0.01	11.91 ± 0.08
NGC 4150	17.27 ± 0.08	2.32 ± 0.41	1.68 ± 0.06	0.76 ± 0.01	53.91 ± 1.47	18.83 ± 0.07	14.60 ± 1.96	0.65 ± 0.01	57.02 ± 0.42	0.23 ± 0.01	12.80 ± 0.07
NGC 4203	18.52 ± 0.10	8.18 ± 1.22	2.65 ± 0.11	0.87 ± 0.01	99.37 ± 1.59	19.98 ± 0.07	35.38 ± 2.64	0.91 ± 0.01	102.09 ± 0.14	0.37 ± 0.02	10.93 ± 0.07
NGC 4245	18.93 ± 0.08	5.82 ± 0.18	2.01 ± 0.07	0.83 ± 0.01	60.59 ± 3.27	19.49 ± 0.06	24.65 ± 0.48	0.64 ± 0.01	52.25 ± 0.06	0.24 ± 0.01	12.27 ± 0.07
NGC 4278	20.11 ± 0.02	28.24 ± 0.56	3.70 ± 0.05	0.87 ± 0.01	107.34 ± 0.01	...	...	...	...	1.00	9.65 ± 0.01
NGC 4314	19.07 ± 0.09	16.01 ± 0.50	2.88 ± 0.07	0.85 ± 0.01	103.98 ± 6.59	20.78 ± 0.07	45.27 ± 1.24	0.77 ± 0.02	168.40 ± 0.12	0.67 ± 0.03	10.01 ± 0.07
NGC 4335	21.06 ± 0.02	19.27 ± 0.05	5.10 ± 0.02	0.77 ± 0.01	64.27 ± 0.02	...	...	...	...	1.00	11.40 ± 0.01
NGC 4429	20.38 ± 0.09	30.10 ± 0.85	3.32 ± 0.09	0.65 ± 0.01	2.22 ± 0.19	19.33 ± 0.07	52.98 ± 1.46	0.34 ± 0.01	8.23 ± 0.01	0.44 ± 0.02	10.16 ± 0.08
NGC 4450	20.36 ± 0.09	19.11 ± 0.49	4.06 ± 0.15	0.77 ± 0.01	92.92 ± 7.93	19.38 ± 0.06	41.87 ± 0.73	0.53 ± 0.01	90.89 ± 0.12	0.31 ± 0.01	10.85 ± 0.07
NGC 4477	19.23 ± 0.08	14.64 ± 0.37	2.63 ± 0.08	0.75 ± 0.01	105.68 ± 5.59	20.24 ± 0.06	43.17 ± 0.81	0.85 ± 0.01	164.92 ± 0.12	0.43 ± 0.02	10.55 ± 0.07
NGC 4526	18.14 ± 0.09	11.92 ± 0.70	1.90 ± 0.07	0.68 ± 0.01	23.35 ± 0.73	19.00 ± 0.07	53.19 ± 1.68	0.33 ± 0.01	22.59 ± 0.13	0.37 ± 0.03	10.17 ± 0.07
NGC 4548	22.14 ± 0.10	50.57 ± 1.42	5.40 ± 0.23	0.81 ± 0.01	169.09 ± 2.73	20.46 ± 0.07	56.71 ± 1.00	0.89 ± 0.01	10.60 ± 0.13	0.39 ± 0.02	10.30 ± 0.07
NGC 4552	20.60 ± 0.02	45.08 ± 0.49	4.30 ± 0.06	0.94 ± 0.01	33.69 ± 0.01	...	...	...	...	1.00	8.98 ± 0.01
NGC 4579	21.16 ± 0.10	49.95 ± 1.64	5.63 ± 0.25	0.69 ± 0.01	157.18 ± 5.63	19.89 ± 0.07	54.73 ± 0.93	0.70 ± 0.01	153.33 ± 0.53	0.52 ± 0.02	9.50 ± 0.07
NGC 4636	19.52 ± 0.09	19.91 ± 0.61	2.21 ± 0.06	0.94 ± 0.01	148.46 ± 6.22	20.25 ± 0.07	85.91 ± 1.74	0.68 ± 0.01	142.80 ± 0.10	0.28 ± 0.01	10.01 ± 0.07
NGC 4698	19.55 ± 0.08	11.04 ± 0.29	3.06 ± 0.06	0.90 ± 0.01	162.49 ± 2.66	19.44 ± 0.07	35.52 ± 1.27	0.52 ± 0.01	75.79 ± 0.21	0.33 ± 0.01	11.21 ± 0.08
NGC 5005	18.95 ± 0.09	23.24 ± 1.00	2.03 ± 0.13	0.43 ± 0.01	153.26 ± 3.82	19.32 ± 0.06	59.50 ± 1.32	0.37 ± 0.01	147.94 ± 0.14	0.39 ± 0.02	9.99 ± 0.07
NGC 5127	22.55 ± 0.02	39.81 ± 1.10	4.90 ± 0.05	0.77 ± 0.01	151.27 ± 0.01	...	...	...	...	1.00	11.34 ± 0.01
NGC 5248	18.62 ± 0.09	7.06 ± 1.78	0.99 ± 0.05	0.69 ± 0.01	19.22 ± 3.64	19.53 ± 0.07	45.71 ± 5.67	0.58 ± 0.01	33.65 ± 2.10	0.11 ± 0.01	12.09 ± 0.07
NGC 5252	20.55 ± 0.09	9.89 ± 0.76	4.80 ± 0.13	0.41 ± 0.01	102.65 ± 2.93	19.62 ± 0.06	11.63 ± 0.88	0.48 ± 0.01	100.95 ± 0.48	0.51 ± 0.02	13.06 ± 0.07
NGC 5490	22.12 ± 0.02	34.96 ± 0.11	6.90 ± 0.04	0.78 ± 0.01	82.69 ± 0.03	...	–	...	...	1.00	11.00 ± 0.01
NGC 5695	18.49 ± 0.07	2.00 ± 0.12	3.74 ± 0.07	0.69 ± 0.01	14.86 ± 0.45	19.11 ± 0.06	10.81 ± 0.69	0.63 ± 0.01	27.12 ± 0.02	0.19 ± 0.01	14.04 ± 0.07
UGC 7115	22.43 ± 0.02	21.93 ± 0.74	7.05 ± 0.17	0.92 ± 0.01	89.26 ± 0.02	...	...	...	...	1.00	12.12 ± 0.01

Table 4.3 – Continued

Galaxy	μ_e (mag arcsec^{-2})	r_e ($''$)	n	q_b	PA_b ($^\circ$)	μ_0 (mag arcsec^{-2})	h ($''$)	q_d	PA_d ($^\circ$)	B/T	$m_{i,tot}$ (mag)
(1)	(2)	(3)	(4)	(5)	(6)	(7)	(8)	(9)	(10)	(11)	(12)
$M_\bullet$ from sample 2											
Abell 1836	21.08 ± 0.10	10.09 ± 1.80	2.79 ± 0.10	0.89 ± 0.01	78.76 ± 2.14	22.21 ± 0.08	37.11 ± 5.00	0.56 ± 0.01	68.90 ± 0.51	0.50 ± 0.02	12.99 ± 0.07
NGC 1068	17.14 ± 0.08	10.47 ± 0.34	1.26 ± 0.06	0.63 ± 0.01	141.72 ± 5.08	18.30 ± 0.06	32.28 ± 0.55	0.85 ± 0.02	93.28 ± 0.32	0.33 ± 0.01	9.73 ± 0.08
NGC 3245	17.45 ± 0.08	4.00 ± 0.44	1.60 ± 0.04	0.75 ± 0.01	100.77 ± 3.34	18.59 ± 0.07	20.68 ± 2.16	0.51 ± 0.01	101.61 ± 0.15	0.27 ± 0.01	11.83 ± 0.07
NGC 3377	20.40 ± 0.02	43.36 ± 0.25	3.47 ± 0.02	0.51 ± 0.01	137.05 ± 0.01	...	...	...	...	1.00	9.63 ± 0.01
NGC 3384	17.70 ± 0.08	8.43 ± 0.26	2.35 ± 0.06	0.83 ± 0.01	144.46 ± 9.15	19.62 ± 0.07	55.86 ± 1.53	0.46 ± 0.01	148.10 ± 0.10	0.40 ± 0.02	10.16 ± 0.07
NGC 3607	21.13 ± 0.02	56.14 ± 0.72	4.70 ± 0.03	0.80 ± 0.01	38.34 ± 0.01	...	...	...	...	1.00	9.16 ± 0.01
NGC 3608	24.19 ± 0.02	181.54 ± 3.73	9.03 ± 0.07	0.79 ± 0.01	175.16 ± 0.15	...	...	...	...	1.00	9.33 ± 0.01
NGC 3998	17.48 ± 0.08	5.66 ± 0.20	2.29 ± 0.06	0.84 ± 0.01	45.51 ± 8.92	19.33 ± 0.06	25.57 ± 0.79	0.78 ± 0.01	54.96 ± 0.05	0.45 ± 0.02	10.80 ± 0.08
NGC 4261	21.06 ± 0.02	48.65 ± 0.33	4.31 ± 0.05	0.77 ± 0.01	67.96 ± 0.01	...	...	...	...	1.00	9.47 ± 0.01
NGC 4374	20.63 ± 0.02	63.39 ± 0.33	4.10 ± 0.07	0.86 ± 0.01	37.32 ± 0.01	...	...	...	...	1.00	8.38 ± 0.01
NGC 4459	23.22 ± 0.02	154.66 ± 0.69	7.44 ± 0.09	0.82 ± 0.01	13.91 ± 0.01	...	...	...	...	1.00	8.78 ± 0.01
NGC 4473	18.05 ± 0.08	10.60 ± 0.30	2.23 ± 0.06	0.57 ± 0.01	3.27 ± 0.28	19.64 ± 0.07	38.16 ± 1.05	0.56 ± 0.01	1.67 ± 0.01	0.48 ± 0.02	10.44 ± 0.08
NGC 4596	21.35 ± 0.10	40.64 ± 2.37	4.32 ± 0.15	0.87 ± 0.01	16.06 ± 0.50	19.44 ± 0.07	33.16 ± 1.04	0.28 ± 0.01	162.83 ± 0.95	0.75 ± 0.07	10.02 ± 0.07
NGC 4649	18.18 ± 0.09	14.91 ± 0.64	1.63 ± 0.10	0.85 ± 0.01	7.98 ± 0.20	19.03 ± 0.06	54.28 ± 1.20	0.78 ± 0.01	13.83 ± 0.01	0.30 ± 0.02	9.56 ± 0.07
NGC 4697	21.81 ± 0.02	128.22 ± 0.44	4.96 ± 0.03	0.59 ± 0.01	63.86 ± 0.03	...	...	...	...	1.00	8.34 ± 0.01
NGC 5576	22.41 ± 0.02	77.30 ± 0.19	8.71 ± 0.04	0.66 ± 0.01	177.21 ± 0.19	...	...	...	...	1.00	9.62 ± 0.01
NGC 5845	17.62 ± 0.02	4.04 ± 0.08	3.45 ± 0.07	0.63 ± 0.01	50.79 ± 0.01	...	...	...	...	1.00	11.78 ± 0.01
Upper limits on $M_\bullet$ from sample 2											
NGC 4041	19.10 ± 0.09	10.50 ± 1.16	1.16 ± 0.04	0.79 ± 0.00	5.81 ± 0.14	20.31 ± 0.07	30.13 ± 1.34	0.88 ± 0.02	120.97 ± 2.44	0.40 ± 0.03	11.48 ± 0.07

NOTES. — Col.(1): Galaxy name. Col.(2): Effective surface-brightness of the bulge. Col.(3): Effective radius of the bulge. Col.(4): Shape parameter of the bulge. Col.(5): Axial ratio of the bulge isophotes. Col.(6): Position angle of the bulge major-axis. Col.(7): Central surface-brightness of the disk. Col.(8): Scale length of the disk. Col.(9): Axial ratio of the disk isophotes. Col.(10): Position angle of the disk major-axis. Col.(11): Bulge-to-total luminosity ratio. Col.(12): i-band total magnitude of the bulge.

Table 4.4: Quality of the fit for the SDSS decompositions

Galaxy (1)	Kind Fit (2)	Quality Fit (3)
NGC 741	S	ok
NGC 1052	S	bad
NGC 1667	BD	bad
NGC 2685	BD	bad
NGC 2892	BD	ok
NGC 2903	BD	bad
NGC 2911	BD	ok
NGC 2964	BD	ok
NGC 3021	BD	three
NGC 3351	BD	three
NGC 3368	BD	three
NGC 3627	BD	ok
NGC 3642	BD	embedded
NGC 3675	BD	ok
NGC 3801	BD	bad
NGC 3862	BD	ok
NGC 3953	BD	three
NGC 3982	BD	ok
NGC 3992	BD	ok
NGC 4036	BD	ok
NGC 4088	BD	FR2
NGC 4143	BD	ok
NGC 4150	BD	ok
NGC 4203	BD	ok
NGC 4212	BD	FR2
NGC 4245	BD	ok
NGC 4278	S	ok
NGC 4314	BD	ok
NGC 4321	BD	three
NGC 4335	S	ok
NGC 4429	BD	ok
NGC 4450	BD	ok
NGC 4477	BD	ok
NGC 4501	BD	FR2
NGC 4526	BD	ok
NGC 4548	BD	ok
NGC 4552	S	ok
NGC 4579	BD	ok
NGC 4636	BD	ok
NGC 4698	BD	ok
NGC 4736	BD	three
NGC 4800	BD	FR2
NGC 4826	BD	ok
NGC 5005	BD	ok
NGC 5127	S	ok
NGC 5194	BD	bad
NGC 5248	BD	ok
NGC 5252	BD	ok
NGC 5347	BD	FR2
NGC 5490	S	ok

Table 4.4 – Continued

Galaxy (1)	Kind Fit (2)	Quality Fit (3)
NGC 5695	BD	ok
NGC 5879	BD	bad
NGC 5921	BD	three
NGC 7331	BD	bad
NGC 7626	S	ok
UGC 1395	BD	bad
UGC 7115	S	ok
Abell 1836	BD	ok
NGC 221	S	ok
NGC 224	BD	i
NGC 821	S	ok
NGC 1068	BD	ok
NGC 2778	S/BD	embedded
NGC 3031	BD	ok
NGC 3227	BD	three
NGC 3245	BD	ok
NGC 3377	S	ok
NGC 3379	S	bad
NGC 3384	BD	ok
NGC 3607	S	ok
NGC 3608	S	ok
NGC 3998	BD	ok
NGC 4026	BD	bad
NGC 4258	BD	bad
NGC 4261	S	ok
NGC 4342	BD	embedded
NGC 4374	S	ok
NGC 4459	S	ok
NGC 4473	BD	ok
NGC 4486	S	extra
NGC 4486A	S	ok
NGC 4564	S/BD	embedded
NGC 4594	BD	i
NGC 4596	BD	ok
NGC 4649	BD	ok
NGC 4697	S	ok
NGC 5576	S	ok
NGC 5845	S	ok
Abell 2052	S	embedded
NGC 3310	BD	three
NGC 4041	BD	ok
NGC 4435	BD	three
NGC 4486B	S	ok

Notes. — Col.(1): Galaxy name. Col.(2): Kind of fit: S= fitted with a Sérsic function, BD= fitted with a Sérsic plus exponential. Col.(3): Quality of the fit: ok = successful fit; embedded = disk is embedded in the bulge; three = strongly barred galaxy, we would need 3 components; F2 = Freeman 2 profile (Freeman 1970); bad = neither S nor BD can reproduce the profile or the galaxy is edge-on. extra light = this is the case of NGC 4486. The light excess cannot be parameterized with an exponential function and we would need a cut-off profile (Oemler 1976); i=impossible because image too big this does not allow to evaluate the sky.

Table 4.5 Structural parameters of the galaxies from SDSS i-band images

Galaxy	PA (°)	ϵ	$m_{24.5}$ (mag)	$R_{24.5}$ ($''$)	$m_{\rm tot}$ (mag)	$m_{\rm disk}$ (mag)	D/T	μ_0 (mag arcsec^{-2})	h ($''$)	C_{28}	$\mu_{\rm e}$ (mag arcsec^{-2})	$r_{\rm e}$ ($''$)
Upper limits on $M_\bullet$ from sample 1												
NGC 1052	141.62	0.19	9.71	151.82	9.64	10.85	0.37	20.96	46.50	4.77	19.87	28.98
NGC 2685	3.71	0.52	10.30	141.32	10.22	11.32	0.52	20.51	39.62	5.10	20.21	31.26
NGC 2903	54.50	0.46	8.10	308.12	8.08	8.41	0.95	18.44	54.88	1.89	20.17	94.84
NGC 2911	129.46	0.35	10.75	138.18	10.63	11.19	0.74	20.72	39.94	4.90	21.96	42.13
NGC 2964	162.05	0.48	10.53	102.10	10.50	10.77	1.00	18.37	18.30	2.94	20.01	31.16
NGC 3021	142.43	0.37	11.42	59.09	11.40	11.65	0.95	18.13	10.01	3.20	19.80	19.69
NGC 3351	64.60	0.10	9.06	199.27	9.03	8.88	1.25	18.58	36.52	4.16	20.79	62.43
NGC 3368	104.57	0.19	8.51	239.62	8.47	8.70	0.91	18.80	46.51	4.30	19.94	57.12
NGC 3627	93.08	0.52	8.01	359.49	7.98	8.82	0.62	19.36	73.56	3.56	20.21	79.79
NGC 3642	107.72	0.13	11.14	95.44	10.96	11.91	0.45	21.89	42.22	4.54	21.44	28.22
NGC 3675	79.91	0.39	9.04	239.51	8.97	10.01	0.47	20.65	68.51	3.54	20.45	73.02
NGC 3801	144.11	0.39	11.07	112.49	10.97	11.79	0.59	20.89	33.70	4.49	21.17	30.81
NGC 3862	121.80	0.34	11.40	116.84	11.14	11.93	0.59	22.16	54.38	5.94	22.73	42.87
NGC 3953	69.23	0.52	9.22	204.72	9.20	9.08	1.50	17.96	34.35	3.72	20.88	62.31
NGC 3982	89.38	0.13	11.07	65.24	11.05	11.38	0.79	18.59	11.84	2.33	19.93	18.09
NGC 3992	17.60	0.51	9.02	239.99	8.98	8.93	1.40	18.26	42.07	2.80	21.29	90.88
NGC 4036	4.46	0.51	9.72	140.08	9.69	10.71	0.52	19.23	28.87	4.43	19.33	29.33
NGC 4088	34.26	0.64	9.49	182.01	9.47	8.00	5.46	15.70	23.07	2.52	20.54	68.32
NGC 4143	121.10	0.32	10.23	88.69	10.21	10.87	0.63	18.44	15.77	4.64	19.17	17.19
NGC 4150	123.60	0.33	10.89	78.23	10.86	11.52	0.64	19.04	15.62	4.78	20.00	17.19
NGC 4203	82.54	0.09	9.80	122.53	9.77	9.79	1.04	18.37	21.73	4.89	20.43	29.20
NGC 4212	13.46	0.34	10.40	99.19	10.38	9.88	1.91	17.36	15.35	2.68	20.38	39.46
NGC 4245	97.00	0.20	10.52	112.39	10.47	10.97	0.71	19.76	25.62	4.38	20.71	33.72
NGC 4278	53.47	0.09	9.45	156.47	9.40	10.50	0.40	20.57	43.32	4.89	19.90	26.21
NGC 4314	178.77	0.12	9.75	152.44	9.70	9.28	1.62	18.30	27.07	4.33	20.55	59.58
NGC 4321	79.18	0.16	8.71	261.30	8.67	7.90	2.26	17.92	43.85	2.58	21.08	114.94
NGC 4335	120.07	0.22	11.37	83.81	11.27	12.24	0.46	21.20	28.02	5.32	20.75	17.63
NGC 4429	178.12	0.56	8.96	231.68	8.93	9.61	0.73	19.09	46.89	4.25	20.20	57.68
NGC 4450	93.86	0.43	9.17	218.24	9.13	9.46	0.94	18.99	42.69	4.08	20.74	58.04
NGC 4477	19.31	0.14	9.61	142.18	9.58	10.09	0.70	19.25	29.25	4.39	20.52	34.81
NGC 4526	159.75	0.70	8.54	337.08	8.50	9.68	0.51	19.86	78.53	5.23	19.75	45.57
NGC 4548	123.32	0.20	9.28	217.25	9.20	9.73	0.71	20.27	57.13	3.82	21.52	80.08
NGC 4552	142.26	0.13	9.07	202.90	9.02	9.92	0.49	20.36	52.64	5.37	20.07	34.11
NGC 4579	177.58	0.25	8.68	251.94	8.61	9.72	0.43	20.82	76.34	4.23	20.76	77.27
NGC 4636	144.03	0.20	8.68	264.19	8.63	9.00	0.81	19.59	58.31	4.43	20.94	72.16
NGC 4698	111.10	0.11	9.89	134.68	9.84	10.34	0.69	19.63	30.42	4.46	20.31	35.10
NGC 4800	71.94	0.07	10.73	75.44	10.70	11.43	0.54	19.40	16.23	3.63	19.81	20.53
NGC 5005	32.04	0.53	8.81	207.82	8.79	9.59	0.63	18.73	39.29	3.98	19.73	51.96
NGC 5127	25.55	0.29	11.58	82.72	11.46	12.28	0.54	21.11	27.70	4.63	21.41	23.31
NGC 5248	138.61	0.16	9.61	165.17	9.56	9.18	1.58	18.30	29.13	3.58	20.72	66.22
NGC 5252	83.50	0.45	12.04	68.31	11.93	13.09	0.46	21.22	22.65	4.64	20.83	17.93
NGC 5347	165.10	0.07	11.97	59.64	11.91	11.64	1.36	18.96	12.01	3.46	21.34	30.66
NGC 5490	92.15	0.22	11.23	84.70	11.14	12.00	0.53	20.68	24.66	5.50	20.67	16.69
NGC 5695	151.27	0.26	12.00	57.14	11.95	12.66	0.60	19.95	13.34	4.07	20.48	14.98
NGC 5879	122.79	0.61	10.67	125.47	10.62	11.47	0.64	19.74	28.91	4.08	20.36	26.91
UGC 7115	96.41	0.28	12.28	66.21	12.04	13.03	0.47	22.32	33.78	6.33	21.95	17.77

Table 4.5 – Continued

Galaxy	PA (°)	ϵ	$m_{24.5}$ (mag)	$R_{24.5}$ ($''$)	$m_{\rm tot}$ (mag)	$m_{\rm disk}$ (mag)	D/T	μ_0 (mag arcsec^{-2})	h ($''$)	C_{28}	$\mu_{\rm e}$ (mag arcsec^{-2})	$r_{\rm e}$ ($''$)
$M_\bullet$ from sample 2												
Abell 1836	107.86	0.22	12.17	63.47	12.03	12.90	0.59	21.24	21.05	4.80	21.57	17.61
NGC 1068	5.51	0.30	8.17	329.45	8.12	8.89	0.59	19.98	78.65	5.63	19.67	44.48
NGC 2778	13.21	0.19	11.77	53.45	11.74	12.23	0.71	19.11	10.50	4.57	20.19	12.02
NGC 3227	106.11	0.47	9.91	162.41	9.84	10.84	0.51	20.45	45.84	3.30	20.77	59.08
NGC 3245	78.83	0.38	10.05	127.02	9.97	11.53	0.29	21.33	46.20	5.15	19.95	26.68
NGC 3377	2.80	0.11	9.51	201.63	9.34	10.28	0.47	21.77	83.93	5.00	21.23	59.52
NGC 3379	4.39	0.11	8.54	246.37	8.49	9.24	0.54	20.03	60.67	5.26	20.00	56.99
NGC 3384	28.09	0.56	8.88	227.66	8.85	9.09	1.10	18.16	39.26	5.74	20.14	37.69
NGC 3607	136.66	0.10	9.24	183.12	9.18	9.94	0.54	20.12	45.72	4.79	20.22	36.42
NGC 3608	15.55	0.14	10.19	123.25	10.13	10.73	0.63	19.93	29.73	4.87	20.48	28.42
NGC 3998	129.80	0.19	9.73	128.72	9.68	11.15	0.29	20.94	40.17	5.47	19.67	20.40
NGC 4026	90.02	0.63	9.70	138.74	9.69	9.15	2.35	16.42	18.63	5.50	18.88	21.11
NGC 4261	99.42	0.32	9.36	236.04	9.15	10.31	0.40	22.35	123.59	5.78	21.38	56.63
NGC 4342	102.67	0.26	11.34	57.41	11.26	13.16	0.20	21.86	25.55	5.91	18.06	7.59
NGC 4374	175.20	0.06	8.42	258.44	8.37	8.95	0.66	19.73	59.18	4.89	20.38	53.79
NGC 4459	176.05	0.25	9.34	200.03	9.23	10.43	0.40	21.49	75.17	5.25	20.66	40.99
NGC 4473	178.13	0.35	9.33	192.69	9.27	10.23	0.50	20.23	49.31	5.49	20.00	34.79
NGC 4486A	170.01	0.34	11.04	111.52	11.20	12.51	0.36	19.33	11.32	4.44	18.32	5.82
NGC 4486	139.27	0.16	8.06	301.69	8.03	8.52	0.70	19.29	62.00	4.46	20.20	68.38
NGC 4564	41.86	0.41	10.18	113.23	10.15	11.18	0.49	19.66	25.82	5.14	19.45	22.41
NGC 4596	161.17	0.24	9.61	164.73	9.56	9.81	0.92	19.16	34.01	4.50	20.73	56.20
NGC 4649	167.95	0.21	8.01	322.54	7.96	8.63	0.62	19.66	71.96	4.79	20.14	67.47
NGC 4697	119.54	0.25	8.57	253.13	8.53	9.09	0.69	19.53	56.18	4.36	20.23	59.72
NGC 5576	6.18	0.46	9.76	202.00	9.52	10.75	0.41	22.37	113.89	6.82	21.43	49.36
NGC 5845	140.39	0.22	11.48	50.59	11.45	13.23	0.24	20.47	12.69	4.91	17.68	4.34
Upper limits on $M_\bullet$ from sample 2												
NGC 3310	78.70	0.04	10.56	107.72	10.48	11.73	0.33	21.60	38.35	4.16	19.66	16.30
NGC 4041	29.69	0.13	10.64	101.39	10.57	11.48	0.47	20.55	27.94	3.95	20.48	21.36
NGC 4435	80.27	0.26	9.92	120.79	9.88	10.65	0.57	19.44	26.45	4.81	19.58	25.19

NOTES. —
Col.(1): Galaxy name. Col.(2): Position angle of the isohotes. Col.(3): Ellipticity of the isophotes. Col.(4): Integrated light within the isophote at a surface-brigthness level of 24.5 mag arcsec^{-2} corrected for Galactic extinction, K-correction, and internal extinction following (Shao et al. 2007). Col.(5): Radius of isophote at a surface brightness level of 24.5 of mag arcsec^{-2}. Col.(6): Total extrapolated magnitude of galaxy. Col.(7): Total magnitude of the fitted disk. Col.(8): Disk-to-total light ratio. Col.(9): Disk central surface brightness. Col.(10): Disk scale length. Col.(11): Concentration index $C_{28} = 5\log(r_{80}/r_{20})$ where r_{80} and r_{20} are the radii that enclose 80% and 20% of total light, respectively. Col.(12): Effective surface brightness. Col.(13): Effective radius.

Table 4.6 Structural parameters of the galaxies from SDSS g-band images

Galaxy	PA	ϵ	$m_{24.5}$	$R_{24.5}$	$m_{\rm tot}$	$m_{\rm disk}$	D/T	μ_0	h	C_{28}	$\mu_{\rm e}$	$r_{\rm e}$
	(°)		(mag)	($''$)	(mag)	(mag)		(mag arcsec^{-2})	($''$)		(mag arcsec^{-2})	($''$)
(1)	(2)	(3)	(4)	(5)	(6)	(7)	(8)	(9)	(10)	(11)	(12)	(13)
Upper limits from sample 1												
NGC 1052	141.62	0.19	11.14	101.64	10.80	12.03	0.39	22.18	47.41	4.69	21.23	30.92
NGC 2685	3.71	0.52	11.88	109.31	11.15	12.34	0.60	21.37	36.92	5.04	21.50	32.71
NGC 2903	54.50	0.46	9.43	257.87	8.92	9.37	1.01	19.44	55.74	1.85	21.39	102.00
NGC 2911	129.46	0.35	12.32	95.07	11.73	12.35	0.81	21.89	40.11	4.42	23.43	48.98
NGC 2964	162.05	0.48	11.75	87.08	11.29	11.82	0.91	19.52	19.20	2.61	20.87	31.67
NGC 3021	142.43	0.37	12.54	48.35	12.18	13.51	0.39	20.88	15.01	2.77	20.69	20.42
NGC 3351	64.60	0.10	10.29	171.46	10.06	10.00	1.23	19.86	39.32	3.71	22.05	69.85
NGC 3368	104.57	0.19	9.80	205.03	9.54	9.71	1.03	19.75	45.02	4.06	21.17	62.99
NGC 3627	93.08	0.52	9.35	279.45	8.76	9.82	0.61	20.53	79.53	3.35	21.29	84.95
NGC 3642	107.72	0.12	12.09	69.72	11.73	12.63	0.49	22.71	44.15	4.54	22.51	33.47
NGC 3675	79.91	0.39	10.52	171.09	10.06	11.11	0.52	21.69	66.47	3.53	21.77	76.47
NGC 3801	144.11	0.39	12.67	78.91	12.04	12.87	0.69	21.98	33.85	4.01	22.76	38.68
NGC 3862	121.80	0.33	13.01	59.99	12.17	13.08	0.61	23.49	59.24	5.90	24.13	49.20
NGC 3953	69.23	0.52	10.71	179.66	10.15	10.18	1.57	19.12	35.30	3.39	22.25	70.38
NGC 3982	89.38	0.13	11.92	55.53	11.75	12.31	0.67	19.73	13.01	2.26	20.72	18.55
NGC 3992	17.60	0.51	10.39	216.79	9.83	10.03	1.33	19.55	46.11	2.25	22.43	109.62
NGC 4036	4.46	0.51	11.27	107.43	10.74	12.07	0.46	20.80	31.88	4.29	20.60	30.59
NGC 4088	34.26	0.64	10.83	168.10	10.14	8.64	7.39	16.23	22.02	2.19	21.57	75.74
NGC 4143	121.10	0.32	11.62	68.63	11.33	12.06	0.65	19.62	15.70	4.76	20.40	17.25
NGC 4150	123.60	0.33	12.19	61.67	11.85	12.58	0.67	20.06	15.28	4.49	21.11	18.03
NGC 4203	82.54	0.09	11.01	100.91	10.93	11.07	0.97	19.80	23.33	4.74	21.73	31.26
NGC 4212	13.46	0.34	11.57	88.05	11.19	10.86	1.86	18.38	15.67	2.46	21.32	40.42
NGC 4245	97.00	0.20	11.84	87.24	11.55	12.09	0.74	20.86	25.40	4.30	21.89	34.41
NGC 4278	53.47	0.09	10.79	111.28	10.52	11.64	0.41	21.89	46.97	4.90	21.32	28.95
NGC 4314	178.77	0.11	11.04	129.53	10.81	10.48	1.56	19.55	27.61	4.32	21.75	60.20
NGC 4321	79.18	0.16	9.79	237.96	9.53	8.93	2.11	19.00	45.17	2.37	22.03	117.59
NGC 4335	120.07	0.22	12.75	57.80	12.32	13.31	0.50	22.54	31.60	5.19	22.26	20.67
NGC 4429	178.12	0.55	10.57	183.75	9.95	10.85	0.74	20.38	48.30	4.14	21.45	62.59
NGC 4450	93.86	0.43	10.61	171.30	10.13	10.61	0.95	20.13	42.59	3.94	21.90	59.80
NGC 4477	19.31	0.14	11.01	106.82	10.73	11.30	0.72	20.47	29.41	4.35	21.80	35.38
NGC 4526	159.75	0.70	10.27	245.19	9.46	10.90	0.52	21.10	79.70	5.20	21.05	47.27
NGC 4548	123.32	0.20	10.69	165.39	10.32	10.37	1.22	20.26	42.44	3.51	22.67	80.57
NGC 4552	142.26	0.13	10.48	143.91	10.15	11.11	0.51	21.59	53.50	5.50	21.43	35.67
NGC 4579	177.58	0.25	10.09	183.27	9.64	10.94	0.41	22.23	83.48	3.96	21.98	80.60
NGC 4636	144.03	0.20	10.05	204.10	9.73	10.16	0.83	20.77	59.15	4.33	22.21	75.51
NGC 4698	111.10	0.11	11.19	105.63	10.94	11.54	0.67	20.97	32.56	4.54	21.57	36.03
NGC 4800	71.94	0.07	11.85	58.07	11.68	12.65	0.46	20.75	17.30	3.41	20.84	21.26
NGC 5005	32.04	0.53	10.25	168.83	9.74	10.86	0.55	20.25	44.17	3.77	21.04	57.11
NGC 5127	25.55	0.29	13.05	55.16	12.56	13.52	0.54	22.37	28.01	4.53	22.64	23.56
NGC 5248	138.61	0.16	10.77	132.36	10.51	10.23	1.53	19.44	30.30	3.15	21.74	70.55
NGC 5252	83.50	0.44	13.60	46.15	12.83	14.13	0.50	22.68	27.46	4.80	22.40	21.28
NGC 5347	165.10	0.06	13.09	49.58	12.87	12.35	1.81	19.47	10.95	3.06	22.42	32.48
NGC 5490	92.15	0.22	12.71	57.24	12.27	13.25	0.53	22.05	26.05	5.47	22.07	17.67
NGC 5695	151.27	0.26	13.32	40.14	12.99	13.63	0.70	20.54	11.18	3.54	21.41	15.02
NGC 5879	122.79	0.61	11.92	114.01	11.30	12.08	0.82	20.27	27.87	3.84	21.69	31.63
UGC 7115	96.41	0.28	13.84	35.78	13.15	14.24	0.50	23.40	31.97	6.15	23.26	18.49

Table 4.6 – Continued

Galaxy	PA	ϵ	$m_{24.5}$	$R_{24.5}$	$m_{\rm tot}$	$m_{\rm disk}$	D/T	μ_0	h	C_{28}	$\mu_{\rm e}$	$r_{\rm e}$
	(°)		(mag)	($''$)	(mag)	(mag)		(mag arcsec^{-2})	($''$)		(mag arcsec^{-2})	($''$)
(1)	(2)	(3)	(4)	(5)	(6)	(7)	(8)	(9)	(10)	(11)	(12)	(13)
$M_\bullet$ from sample 2												
Abell 1836	107.86	0.22	13.53	36.96	13.24	14.23	0.66	22.15	17.29	4.62	22.85	16.33
NGC 1068	5.51	0.30	9.09	257.79	8.97	9.90	0.57	21.11	83.06	5.77	20.64	45.26
NGC 2778	13.21	0.19	12.94	39.78	12.85	13.45	0.69	20.39	10.79	4.39	21.41	12.38
NGC 3227	106.11	0.47	10.88	131.51	10.78	11.49	0.78	20.52	35.19	3.37	21.86	59.40
NGC 3245	78.83	0.38	11.15	92.22	11.03	12.27	0.44	21.39	33.77	4.98	21.13	26.85
NGC 3377	2.80	0.11	10.60	146.17	10.24	11.35	0.43	23.45	111.28	5.41	22.62	67.97
NGC 3379	4.39	0.11	9.80	174.64	9.67	10.56	0.51	21.40	62.23	5.29	21.23	55.91
NGC 3384	28.09	0.56	9.86	188.81	9.79	10.35	1.00	19.53	41.34	5.88	21.30	38.60
NGC 3607	136.66	0.10	10.45	135.26	10.32	11.02	0.60	21.10	43.56	4.54	21.52	38.83
NGC 3608	15.55	0.14	11.35	94.06	11.23	11.88	0.64	21.05	29.37	4.80	21.65	28.76
NGC 3998	129.80	0.19	10.95	90.66	10.81	12.36	0.29	22.42	45.63	5.52	21.03	22.03
NGC 4026	90.02	0.63	10.70	115.68	10.65	10.72	1.65	18.22	20.66	5.64	20.09	20.95
NGC 4261	99.42	0.32	10.64	147.86	10.18	11.39	0.43	24.01	162.06	6.18	23.03	71.42
NGC 4342	102.67	0.26	12.55	35.92	12.51	13.17	0.68	19.22	7.53	5.32	19.00	6.30
NGC 4374	175.20	0.06	9.68	191.38	9.56	10.20	0.66	20.91	56.99	4.77	21.62	53.83
NGC 4459	176.05	0.25	10.63	122.46	10.45	11.62	0.46	21.90	52.61	4.81	21.70	36.49
NGC 4473	178.13	0.35	10.47	141.40	10.34	11.26	0.59	21.05	44.77	5.43	21.22	35.16
NGC 4486A	139.27	0.16	9.31	227.85	9.21	9.86	0.65	20.79	66.51	4.44	21.54	70.98
NGC 4486	170.01	0.34	12.16	49.13	11.11	11.91	0.64	24.65	172.90	10.12	25.53	144.59
NGC 4564	41.86	0.41	11.29	86.69	11.21	12.06	0.67	20.24	22.47	5.00	20.71	23.11
NGC 4596	161.17	0.24	10.76	132.66	10.63	11.08	0.83	20.66	37.78	4.43	22.01	60.02
NGC 4649	167.95	0.21	9.30	229.89	9.18	9.93	0.62	20.86	68.95	4.70	21.44	67.80
NGC 4697	119.54	0.25	9.76	196.62	9.64	10.40	0.63	20.98	60.02	4.29	21.50	61.47
NGC 5576	6.18	0.46	10.83	135.61	10.61	11.85	0.48	22.28	65.92	6.20	22.08	36.29
NGC 5845	140.39	0.22	12.67	29.55	12.64	13.95	0.41	19.88	6.92	4.42	18.78	4.04
upper limits from sample 2												
NGC 3310	78.70	0.04	11.02	78.24	10.83	12.32	0.28	22.11	36.94	3.67	19.53	14.58
NGC 4041	29.69	0.13	11.66	75.59	11.43	12.29	0.52	21.14	25.23	3.78	21.63	24.14
NGC 4435	80.27	0.26	11.29	97.35	10.96	11.85	0.57	20.75	27.95	4.76	20.86	26.40

NOTES. — Col.(1): Galaxy name. Col.(2): Position angle of the isohotes. Col.(3): Ellipticity of the isophotes. Col.(4): Integrated light within the isophote at a surface-brigthness level of 24.5 mag arcsec^{-2} corrected for Galactic extinction, K-correction, and internal extinction following (Shao et al. 2007). Col.(5): Radius of isophote at a surface brightness level of 24.5 of mag arcsec^{-2}. Col.(6): Total extrapolated magnitude of galaxy. Col.(7): Total magnitude of the fitted disk. Col.(8): Disk-to-total light ratio. Col.(9): Disk central surface brightness. Col.(10): Disk scale length. Col.(11): Concentration index $C_{28} = 5\log(r_{80}/r_{20})$ where r_{80} and r_{20} are the radii that enclose 80% and 20% of total light, respectively. Col.(12): Effective surface brightness. Col.(13): Effective radius.

Table 4.7 Fitting parameters for the different relations

Relation	Sample	Normalization	Slope	Scatter
$M_\bullet - \sigma_\mathrm{e}$	1	8.62 ± 0.05	3.93 ± 0.25	0.41
	2	8.18 ± 0.06	4.04 ± 0.37	0.42
	joint	8.60 ± 0.07	3.94 ± 0.53	0.36
$M_\bullet - L_{i,\mathrm{bulge}}$	1	8.81 ± 0.14	1.10 ± 0.15	0.58
	2	8.94 ± 0.17	1.32 ± 0.24	0.61
	joint	8.97 ± 0.11	1.01 ± 0.13	0.58
$M_\bullet - M_{\mathrm{vir,bulge}}$	1	8.70 ± 0.11	0.94 ± 0.11	0.54
	2	8.41 ± 0.14	1.05 ± 0.15	0.55
	joint	8.59 ± 0.08	0.94 ± 0.09	0.55
$M_\bullet - n$	1	6.87 ± 0.28	2.53 ± 0.44	0.69
	2	7.66 ± 0.48	1.20 ± 0.70	0.68
	joint	7.03 ± 0.23	2.25 ± 0.39	0.71
$M_\bullet - L_{i,\mathrm{gal}}$	1	8.87 ± 0.14	1.64 ± 0.21	0.63
	2	8.98 ± 0.13	1.67 ± 0.21	0.57
	joint	8.92 ± 0.10	1.71 ± 0.16	0.63
$M_\bullet - M_{\star,\mathrm{gal}}$	1	8.18 ± 0.08	1.50 ± 0.19	0.59
	2	8.24 ± 0.12	1.63 ± 0.18	0.56
	joint	8.20 ± 0.07	1.56 ± 0.14	0.59
$M_\bullet - V_\mathrm{c}$	1	1.97 ± 1.22	2.57 ± 0.42	0.67
	2	3.18 ± 2.27	2.12 ± 0.95	0.83
	joint	2.23 ± 1.11	2.48 ± 0.48	0.74
$M_{\mathrm{vir,gal}}$	1	8.29 ± 0.07	1.39 ± 0.12	0.46
	2	8.04 ± 0.11	1.39 ± 0.18	0.52
	joint	8.19 ± 0.06	1.36 ± 0.09	0.49
$M_{\mathrm{dyn,gal}}$	1	7.74 ± 0.14	1.10 ± 0.13	0.67
	2	7.37 ± 0.39	0.93 ± 0.13	0.77
	joint	7.64 ± 0.12	1.08 ± 0.10	0.66

NOTES. — For the variable x a correlation of the form $\log(M_\bullet) = \alpha + \beta \log(x)$ is assumed, where the normalization is α and β is the logarithmic slope. The normalization gives $\log(M_\bullet/\mathrm{M}_\odot)$ for $\sigma_\mathrm{e} = 200$ km s^{-1}, $L_{i,\mathrm{bulge}} = 10^{11}$ L$_\odot$, $M_{\mathrm{vir,bulge}} = 10^{11}$ M$_\odot$, $L_{i,\mathrm{gal}} = 10^{11}$ L$_\odot$, $M_{\star,\mathrm{gal}} = 10^{11}$ M$_\odot$, $M_{\mathrm{vir,gal}} = 10^{11}$ M$_\odot$, $M_{\mathrm{dyn,gal}} = 10^{11}$ M$_\odot$.

Table 4.8 Fitting Parameters for the linear combinations

Relation	Sample	Normalization	Slope	Scatter
$M_\bullet - \sigma_{\rm e}^{\alpha} r_{\rm e,bulge}^{\beta}$	1	8.69	3.25, 0.28	0.46
	2	8.32	3.94, 0.33	0.35
	joint	8.54	3.03, 0.28	0.44
$M_\bullet - L_{i,\rm bulge}^{\alpha} r_{\rm e,bulge}^{\beta}$	1	8.98	1.34, -0.69	0.55
	2	8.85	1.62, -0.83	0.37
	joint	8.72	0.80, -0.20	0.57
$M_\bullet - \sigma_{\rm e}^{\alpha} L_{i,\rm bulge}^{\beta}$	1	8.78	2.95, 0.30	0.45
	2	8.40	3.55, 0.35	0.37
	joint	8.60	2.69, 0.26	0.46
$M_\bullet - {M_{\rm vir,bulge}}^{\alpha} r_{\rm e,bulge}^{\beta}$	1	8.46	1.63, -1.34	0.46
	2	8.04	1.97, -1.64	0.35
	joint	8.32	1.51, -1.23	0.46
$M_\bullet - \sigma_{\rm e}^{\alpha} {M_{\rm vir,bulge}}^{\beta}$	1	8.65	2.69, 0.28	0.46
	2	8.27	3.27, 0.33	0.35
	joint	8.49	2.45, 0.28	0.46
$M_\bullet - \sigma_{\rm e}^{\alpha} r_{\rm e,gal}^{\beta}$	1	8.59	3.19, 0.51	0.43
	2	8.26	4.14, 0.24	0.37
	joint	8.47	3.00, 0.54	0.45
$M_\bullet - \sigma_{\rm e}^{\alpha} L_{i,\rm gal}^{\beta}$	1	8.69	2.79, 0.43	0.43
	2	8.30	3.94, 0.22	0.37
	joint	8.57	2.54, 0.49	0.44
$M_\bullet - L_{i,\rm gal}^{\alpha} r_{\rm e,gal}^{\beta}$	1	8.79	1.80, -1.20	0.56
	2	8.82	1.73, -0.86	0.48
	joint	8.75	1.69, -0.89	0.56
$M_\bullet - \sigma_{\rm e}^{\alpha} M_{\star,\rm gal}^{\beta}$	1	8.48	2.59, 0.45	0.42
	2	8.20	3.81, 0.26	0.37
	joint	8.31	2.36, 0.48	0.44
$M_\bullet - M_{\star,gal}^{\alpha} r_{\rm e,gal}^{\beta}$	1	8.04	1.74, -1.33	0.51
	2	8.01	1.77, -0.97	0.45
	joint	8.03	1.60, -0.94	0.52

NOTES. — For the variables (x, y) a correlation of the form $\log(M_\bullet) = \alpha \log(x) + \beta \log(y) + \gamma$ is assumed, where the normalization is γ, and α and β are the logarithmic slopes. The normalization gives $\log(M_\bullet/{\rm M}_\odot)$ for $\sigma_{\rm e} = 200$ km s^{-1}, $L_{\rm bulge}$= 10^{11} L$_\odot$, $M_{\rm vir,bulge}$= 10^{11} M$_\odot$, $L_{i,\rm gal}$= 10^{11} L$_\odot$, $M_{\star,\rm gal}$= 10^{11} M$_\odot$, $r_{\rm e,bulge}$=5 kpc, $r_{\rm e,gal}$=5 kpc. .

5

Seeking the most massive black holes: the case of NGC 1265-3C 83.1B

Based on Beifiori A., Sarzi M., Davies R. L. , Cappellari M., & Houghton R. C. W., MNRAS, in preparation

We present the K-band adaptive optics-assisted spectroscopic observations of the central region of the archetype head-tail radio galaxy NGC 1265 − 3C 83.1. The near-infrared (NIR) data taken with the Altair-NIRI on the Gemini North have a spatial resolution of FWHM = 0.″11 (39 pc). We adopted the Jeans anisotropic models to fit the stellar kinematics and surface distribution to determine the best fitting value for anisotropy and supermassive black hole mass ($M_\bullet$). We assumed the orbital anisotropy in the range $\beta = 0 - 0.2$ and the K-band mass-to-light ratio in the range $(M/L)_K = 0.5 - 2.5(\mathrm{M}_\odot/\mathrm{L}_\odot)$ because our measurements do not allow us to fit them. The upper limit for the $M_\bullet$ ranges between 1×10^9 $\mathrm{M}_\odot$ and 3.45×10^9 $\mathrm{M}_\odot$ depending on the assumed values of β and $(M/L)_K$, respectively. This range of masses is consistent with the $M_\bullet - L_{K,\mathrm{bulge}}$ relation by Marconi & Hunt (2003).

5.1 Introduction

It is now commonly accepted that supermassive black holes (SMBHs) are found in the centers of galaxies and that their mass accretion history is connected to the formation and evolution of their hosts. The most striking evidence for this link is the discovery of the relations between the mass of the supermassive black holes, $M_\bullet$, and many properties of the hosting galaxies, as

the tightest correlations with the bulge stellar velocity dispersion σ (Ferrarese & Merritt 2000; Gebhardt et al. 2000a; Tremaine et al. 2002; Ferrarese & Ford 2005; Lauer et al. 2007a; Gültekin et al. 2009b) or with its luminosity $L_{\rm bulge}$ (Kormendy & Richstone 1995; Marconi & Hunt 2003; Gültekin et al. 2009b), for example.

Several authors (Merloni et al. 2003; Falcke et al. 2004; Merloni et al. 2006; Körding et al. 2006; Wang et al. 2006) found that the observed correlations between the luminosities of radio and X-ray emission in radio galaxy cores may be part of a fundamental plane, linking the radio core luminosity at 5 GHz, L_R in $\mathrm{erg\,s^{-1}}$, and the X-ray luminosities at the energy of 2-10 keV, $L_{\rm X}$ in $\mathrm{erg\,s^{-1}}$, with $M_\bullet$ in terms of $\mathrm{M_\odot}$, in both SMBHs and stellar black holes. Gültekin et al. (2009a) by using the sample of galaxies that have directly measured black hole mass from Gültekin et al. (2009b) were able to investigate this correlation, finding that it is not as tight as the $M_\bullet - \sigma$ relation, although using only a subsample of low activity AGNs the scatter could be reduced.

The tightness of the relations linking quantities on vastly different scales, bulge and SMBH scales, is indicative of a formation and evolutionary history in which SMBHs and galaxies are connected. The coevolution of SMBHs and galaxies implies that the galaxy evolution affects the SMBH growth with the inflow of gas in the center that forms or refuels the SMBH, and on the other end SMBHs affect the galaxy properties, driving the chemical galaxy evolution, and quenching the star formation. The understanding of these relation provides a powerful constraint on models of galaxy formation(e.g., Haehnelt & Kauffmann 2000).

In the past, measurements of $M_\bullet$ for which the sphere of influence was resolved were performed thanks to the *Hubble Space Telescope* (*HST*) mainly in early-type galaxies with σ in the range of $120-250$ $\mathrm{km\,s^{-1}}$. More determinations are needed in particular for high (as in Houghton et al. 2006; Gebhardt et al. 2007; Dalla Bontà et al. 2009; Gebhardt & Thomas 2009) and small values of σ (as in Nowak et al. 2007; Barth et al. 2009) to understand better the nature and the well debated parameters of the scaling relations, and the trend of the $M_\bullet$ for different kind of galaxies (e.g., in terms of bar presence see the different results by Graham 2008; Beifiori et al. 2009, , and Chapter 3).

At present, the ambiguities on the trend of the scaling relations at high σ, are fundamental for determine the parameterization of the scaling relation (see Gültekin et al. 2009b) and for characterizing the SMBH mass function above 10^9 $\mathrm{M_\odot}$ (Lauer et al. 2007a). Recent results on the $M_\bullet$ for M87 (Gebhardt & Thomas 2009), suggested that the dark matter is a fundamental component that must be taken into account in the dynamical models of $M_\bullet$ in galaxies with steeper light profiles. Therefore, the $M_\bullet$ measured in the high-σ range may be

affected by the fact that up to now all the dynamical models did not take into account for this contribution.

In the last years, the 8-m class telescopes with adaptive-optics (AO) facilities associated to near infrared (NIR) data allowed to resolve the sphere of influence of the SMBH in galaxies that could not have been studied in the same way with *HST* (Häring-Neumayer et al. 2006; Davies et al. 2006; Houghton et al. 2006; Neumayer et al. 2007; Nowak et al. 2007, 2008, 2009; Cappellari et al. 2009; Krajnović et al. 2009).

5.1.1 NGC 1265-3C 83.1B

NGC 1265 is the second brightest galaxy in the Perseus cluster, at 27″ northwest of the cluster center, that is moving through the cluster potential at high speed with a radial velocity higher then of Perseus cD galaxy indicating a large infall. For NGC 1265 we assumed the Perseus cluster distance equal to 73 Mpc obtained from the recessional velocity, $V = 5366$ km s^{-1}, from Struble & Rood (1999), by using $H_0 = 73$ km s^{-1} Mpc^{-1}, $\Omega_m = 0.27$, and $\Omega_\Lambda = 0.73$.

NGC 1265 contains a powerful active galactic nucleus (AGN) displaying a strong radio emission (O'Dea & Owen 1986, 1987; Xu et al. 1999), it is the typical archetype of the narrow-angle head tail radio galaxies, i.e. the type I Fanaroff-Riley (FRI) radio galaxy (Fanaroff & Riley 1974). The radio morphology is complicated, with two narrow east-west jets that emerge from the nucleus forming two tails, that merge far away from the nucleus. The shape of the head-tail radio galaxies can be explained as due to its movement at a high velocity through a static intra-cluster gas. The radio emitting beams are decelerated by the ram pressure of the intra-cluster gas and form a trail behind the galaxy. The high velocity of the galaxy is a result of the gravitational potential of the cluster.

From the first optical studies of this galaxy (Bertola & Perola 1973) many other have been undertaken in the past although, none have been made spectroscopically with the spatial resolution available with AO system.

The galaxy has been studied in the NIR by several authors by using Near-Infrared Camera and Multiobject Spectrograph (NICMOS) onboard the *HST* in the H-band (i.e., Madrid et al. 2006) and combining these images with the TNG ground-based K'-band images (Marchesini et al. 2005; Donzelli et al. 2007; Tremblay et al. 2007). Donzelli et al. (2007) tabulated a total absolute H-band magnitude of $M_H = -26.63$ and the effective radius of the galaxy $r_{\rm e}$= 12.01 kpc, at the galaxy distance they used of 108 Mpc.

Wide Field and Planetary Camera 2 (WFPC2) images of NGC 1265 are present in the *HST* archive, with the filter F702W and F673N, revealing a nor-

mal elliptical structure, with a dust lane of $1''$ almost perpendicular to the jet direction and aligned with the galaxy major axis. The presence of this dust lane could indicate that the gas is moving with a well-behaved kinematics (Ho et al. 2002). Chiaberge et al. (1999) found the evidence of a non-thermal nuclear sources in NGC 1265 (and in general in a sample of FR I radio galaxies) by using these WFPC2 broad-band images. This compact emission might be associated with the AGN and it is strongly connected with the radio core emission. They suggest that this source originates from the optical synchrotron radiation produced in the inner regions of a relativistic jet as it is done for the radio core emission. This was confirmed by Capetti et al. (2005), that studying *HST* narrow band images and spectra of a sample of low luminosity radio-galaxies, found a strong correlation between line and optical continuum nuclear emission, which suggests that the optical cores, most likely of non-thermal origin, can be directly associated to the source of ionizing photons, i.e. the jet-ionized narrow line region.

NGC 1265 has also a weak X-ray emission from three inner radio knots in the jets, with indications of interaction between the jets and the X-ray corona. The narrow jets carry great amounts of energy out of the central AGN and release the energy outside the corona. The cooling of the X-ray corona potentially provides fuel to the central SMBH. Sun et al. (2005) comparing the $0.5 - 1.5$ keV Chandra emission and the WFPC2 F702W image found an asymmetric distribution of the X-ray light compared to the optical light. Balmaverde et al. (2006) by studying the Chandra observations of a 3C/FR I sample of low luminosity radio-galaxies confirmed that the origin of the X-ray cores seems to suggest a common origin for the radio, optical, and X-ray cores, most likely associated to the base of a relativistic jet. The luminosity in the three bands are in fact correlated. With the same sample of galaxies Balmaverde et al. (2008) measured the jet power from the nuclear radio-luminosity, finding that the accretion power correlates linearly with the jet power. These results indicate that hot gas accretion is the dominant process in FR I radio galaxies across their full range of radio-luminosity. Furthermore, the fact that AGN activity is related to the SMBH growth, via accretion, implies that the accretion process in AGN has a powerful influence on galaxy evolution (Balmaverde et al. 2008).

Observations of NGC 1265 were planned as part of a campaign aimed at measuring $M_\bullet$ using ground-based telescopes and adaptive optics facilities. The galaxy was selected between all of the system with a bright reference star close to the nucleus that can be seen in *HST* images, and between the galaxies without a triaxial structure (see also Houghton et al. 2006). In fact, a bright reference star, not aligned with the major axis of NGC 1265, is present at $3''$ south-west from the galaxy center, and a fainter stars is found roughly half way

between the AO-star and the nucleus (see Figure 5.1). The choice of galaxies without triaxial structure is dictated from the models we will be using, that make use of the assumption that galaxies are axisymmetric oblate spheroids. For triaxial galaxies the final $M_\bullet$ mass calculate with axisymmetric models will led a biased values of the $M_\bullet$ (e.g., in van den Bosch et al. 2009).

The stellar velocity dispersion of NGC 1265 is unknown. We used the absolute H-band magnitude from Donzelli et al. (2007), to estimate the expected $M_\bullet$ from Marconi & Hunt (2003), by first converting H-band magnitude in K-band magnitude assuming $(H-K)=0.21$, and rescaling it to the distance we used, obtaining $L_K = 3.9 \times 10^{11} \mathrm{L}_\odot$. The resulting $M_\bullet = 9.8^{+1.2}_{-5.0} \times 10^8$ $\mathrm{M}_\odot$ (adopting the 0.31 dex scatter), would place the SMBH of NGC 1265 in the upper side of the $M_\bullet - L_{K,\mathrm{bulge}}$ relation.

The structure of this chapter is as follows. The observations and the data reduction are discussed in Section 5.2; the imaging and kinematics analysis are presented in Section 5.3; the dynamical modeling is presented in Section 5.4; the discussion is contained in Section 5.5; the conclusions are presented in the Section 5.6.

5.2 Observations and data reduction

5.2.1 Observations

Our AO-assisted K-band observations of NGC 1265 consist both of spectra and images, which were taken between November 2004 and January 2006 using the Near InfraRed Imager and Spectrograph (NIRI, Hodapp et al. 2003) and the Altair adaptive optics system (Herriot et al. 2000) on the Gemini North telescope. The long-slit observations were alternated to short images in order to measure the quality of the AO correction, by monitoring its performance on the reference star, and to obtain a high-resolution K-band image of the galaxy itself that could be used for the dynamical modeling. In principle, the quality of the AO performance could be monitored during the spectroscopic observations by keeping the reference star in the slit (like in Houghton et al. 2006), but in the case of NGC 1265 this would have been obtained by taking nearly minor-axis observations, which are not optimal for modeling the nuclear kinematics.

NIRI uses a InSb ALLADIN 1024×1024 pixels CCD sensitive from 1 to 5 μm. The spectroscopic observations were obtained with the grism f/32 K-band with a coverage of $1.96 - 2.41 \mu$m and a resolving power of $\lambda/\Delta\lambda = 775$ at 2.20 μm corresponding to an instrumental broadening of $\sigma_{\mathrm{inst}} = 165$ km s^{-1}, by using the slit with a $0\farcs144$ width and a $22''$ length. The images were obtained with the broad-band K(short) filter (G0205) with a central wavelength of 2.15 μm, coverage of $1.99 - 2.30$ μm, and a field of view of $22\farcs4 \times 22\farcs4$. The spatial

Table 5.1 NGC 1265 spectroscopic observations.

Obs. Date	$t_{\rm exp}$ (m)	Airmass
(1)	(2)	(3)
2005 Oct 13	5 × 10	1.090
2005 Oct 31	6 × 10	1.598
2005 Nov 13	5 × 10	1.085
2005 Nov 16,1	4 × 10	1.179
2005 Nov 16,2	6 × 10	1.096
2005 Nov 16,3	6 × 10	1.336
2005 Nov 19	4 × 10	1.237
2005 Dec 25	6 × 10	1.173
2005 Dec 31	3 × 10	1.089
2006 Jan 02	6 × 10	1.117
2006 Jan 15	6 × 10	1.505

NOTES. — Col. (1): Observation date. Three observations of the object were obtained during the night of 2005 November 16. Col. (2): Total exposure time. Here, we show only the sequences we used for the final spectrum (see Section 5.2.2 for details). Col. (3): Airmass of the observations.

scale of the observations was $0\farcs0218$ pixel^{-1}.

To take into account for the sky-background variations we used a typical NIR ABBA technique, consisting in six sequences of exposures of 10 minutes for a total of 60 minutes. This allows to correct the NIR sky variability. Dithered offsets in the vertical position were also used to help in the bad pixels removing, for improving the pixel sampling and the flatfield correction because each image of the object is placed on slightly different positions on the array. All the details of the observations are summarized in Table 5.1.

The AO correction was monitored every 60 minutes with a short sequence of 4 images before and 4 after the spectra with a single exposure time of 5 seconds. All the images were dithered for removing the bad pixels.

To compensate for the atmospheric absorption in the galaxy spectra, telluric standard stars were observed with the same ABBA technique, with an exposure time for each observation of 15 seconds (see Table 5.2 for details). Telluric standards are bright stars, usually O or B stars, of known spectral type for which the intrinsic stellar features are either negligible or easily separated from features introduced by the Earth's atmosphere. They should be observed with the same airmass of the target because the strength of the telluric features depend on it.

For the kinematics studies we observed three kinematical templates just after the observations to match the airmass of the telluric stars and scientific

Table 5.2 Telluric standards observations.

Name	Obs. Date	t_{exp} (s)	Sp. Type	V (mag)	H (mag)	Airmass
(1)	(2)	(3)	(4)	(5)	(6)	(7)
HD 66665	2005 Oct 13	15	B1V	7.8	8.6	1.112
HD 21856	2005 Oct 31	15	B1V	5.9	6.1	1.835
HD 21856	2005 Nov 13	15	B1V	5.9	6.1	1.049
HD 21856	2005 Nov 16,1	15	B1V	5.9	6.1	1.063
HIP 12151	2005 Nov 16,2(*)	15	B8V	6.8	6.9	1.110
HD 21856	2005 Nov 16,2	15	B1V	5.9	6.1	1.093
HD 21856	2005 Nov 16,3	15	B1V	5.9	6.1	1.457
HD 21856	2005 Nov 19	15	B1V	5.9	6.1	1.336
HD 21856	2005 Dec 25	15	B1V	5.9	6.1	1.073
HD 21856	2005 Dec 31	15	B1V	5.9	6.1	1.087
HD 21856	2006 Jan 02	15	B1V	5.9	6.1	1.250
HD 21856	2006 Jan 15	15	B1V	5.9	6.1	1.696

NOTES. — Col. (1): Telluric standard name. Col. (2): Observation date. Three observations of NGC 1265 were repeated during the night of 2005 November 16. The same is true for the telluric standard. All the telluric standards were observed after NGC 1265. Only (*) was observed before. We did not use this star for the telluric correction. Col. (3): Total exposure time. Col. (4): Spectral type from SIMBAD. Col. (5): V-band magnitude from SIMBAD. Col. (6): H-band magnitude from SIMBAD. Col. (7): Airmass of the observations.

object, following the same ABBA technique with an exposure time of each observation of 2 seconds. All the observations are summarized in Table 5.3.

To achieve the same spectral resolution of the scientific observations the stellar light of both telluric and kinematical templates was made to fill the slit in order to mimic an extended source. This was done by degrading the high-order AO correction until the FWHM of the star was equal to the slit width.

5.2.2 Data reduction

The spectra were reduced using IRAF[1]. The sky emission was removed using the typical ABBA technique. Before reducing the data we correct the spectra and the images affected by noise patterns. The spectra were then flat-fielded, wavelength calibrated, telluric features corrected and combined all together.

[1]IRAF is distributed by NOAO, which is operated by AURA Inc., under contract with the National Science Foundation

Table 5.3 Spectroscopic template observations.

Name	Obs. Date	$t_{\rm exp}$ (s)	Sp. Type	V (mag)	H (mag)	Airmass
(1)	(2)	(3)	(4)	(5)	(6)	(7)
HD 76010	2005 Oct 13	0.2	MOIII	7.0	3.3	1.144
HD 31098(*)	2005 Dec 31	0.2	K2III	9.1	4.2	1.087
64 Ari	2006 Jan 02	0.2	K4III	5.5	2.9	1.37

NOTES. — Col. (1): Spectroscopic standard name. (*) Not suitable for the analysis. Col. (2): Observation date. Col. (3): Total exposure time. Col. (4): Spectral type from SIMBAD. Col. (5): V-band magnitude from SIMBAD. Col. (6): H-band magnitude from SIMBAD. Col. (7): Airmass of the observations.

Spectroscopic reduction

The first step in the data reduction was to update the raw data headers with the NPREPARE task in the GEMINI package in IRAF. The task creates also the variance and data quality files, adding some keywords in the header as the gain (e^-/ADU), the read noise (e^-), the saturation level (ADU), the level at which the data start to be non-linear (ADU), and the array bias voltage. NPREPARE modifies the header keyword EXPTIME to be the total exposure (the original exposure time multiplied by the number of coadds). NPREPARE adds also a keyword COADDEXP that contains the original exposure time for each individual frame.

The spectra of the scientific object and stars were then reduced with the standard NIR technique. The sky emission was removed by subtracting the corresponding image in each nodding pair and then flat-fielded. The cosmic ray events were removed using the task LACOS_SPEC by van Dokkum (2001). The wavelength calibration and the geometric distortion correction were applied along the dispersion and the spatial axes by using the Argon arc frame and the stellar spectra described above, respectively. To perform the telluric correction we extracted the galaxy spectrum and the stellar spectrum over a large aperture, to maximize the S/N, and an aperture as large as the FWHM of the stellar profile, respectively.

We first removed the stellar continuum from one dimensional spectrum of the telluric standard, by dividing it by a black body function of the appropriate temperature of the star. The black body function was obtained by fitting the telluric stellar spectrum with the task NFIT1d in IRAF to obtain the parameters used to construct the function with the FUNCTION task. We continuum normalized the telluric spectrum using the CONTINUUM task, dividing by a

polynomial fit to regions where the atmospheric transmission seems to be 100%.

The telluric absorption varies with airmass, and the strength of the sharp prominent absorption features in the normalized telluric spectrum should match those in the object spectrum of similar airmass. To have the best telluric correction we wanted the average value of the airmass of the target, the telluric stars, and the kinematics stars, to be maximum within $0.1 - 0.2$ of difference (this was not always respected in our data, see Table 5.2).

To remove spectral features that were imprinted into the scientific spectrum we used the task TELLURIC which uses the Beer's law to approximate the extinction due to telluric lines, and divided the object by the telluric spectrum, applying small shifts in the wavelength direction to compensate the differences in the zero-point and rescale to match the telluric spectrum.

We first minimized the residuals around the strong telluric features and then the last adjustments were made to remove features in the CO(2.3 μm) region. The telluric templates have lines that are stronger than the scientific spectrum, creating false features on the resulting spectrum due to overcorrection, that should be reminded.

Finally, we aligned the individual 2-dimensional telluric corrected spectra from each night along the spatial direction to median combine them together with a 3-sigma rejection that allows us to have a good removing of the bad pixels, thanks to the large number of spectra.

Removal of the noise patterns

Many of our spectra and images were affected by an electronic pattern noise that consists of variations in the intensity between the columns of the array, as vertical stripes with a period of eight columns, that we call odd-even column effect, because it affects the odd and the even column alternatively. This noise depends on the quadrant of the CCD, in the sense that it is usually different in each quadrant, and it might not be present in all quadrants, and in the cleaning they were treated separately. Moreover, it is a function of the flux in the array and it changes with time, but it does not scale linearly with the flux.

To remove this noise we used the IDL[2] script NIRINOISE.PRO kindly provided to us by the Gemini Support which subtracts the median intensity of every 8th row and 8th column in every quadrant, to smooth the variations in the intensity.

Nevertheless, part of these pattern-affected spectra were too noisy at the end of the correction, and they could not be used for the following analysis.

[2]Interactive Data Language is distributed by Research System Inc.

We do not think this is due to the correction, because we discarded some noisy spectra even among the exposures not affected by the pattern.

Some spectra presented the typical circle features produced by the InSb devices, that occur randomly in the data. These patterns appear after large detector temperature changes in the detectors, as the cool-down. Unlikely, these features strongly affected some of our spectra and we discarded them.

Some data, in particular with very short exposures as the telluric and kinematics stars, presented also arched intensity variation patterns, that could not be removed. See in Table 5.3 one example of kinamtical star discarded for this effect.

Out of the 28 hours initially allocated to this program, a total of 12 hours were eventually collected by the end of the observations, 1 hour was dedicated to imaging and 11 hours to spectroscopy. The data quality was variable between the nights that the data were recorded, and exposures in which the spectra quality was lower than average were discarded. From the initial 11 hours of data we obtained a final spectrum of 9 hours and 40 minutes.

There were not spectrophotometric standards to perform the flux calibration, therefore we rescaled our spectrum to the maximum flux (see Figure 5.6).

Imaging reduction

Because the variations in the AO affects our kinematic measurements, they should be known in order to be accounted in the model. We monitored the quality of the AO correction in different nights by measuring the point spread function (PSF) from the images of the reference star that were observed alternatively to the spectroscopy.

The imaging data were first corrected for the noise patterns by using the IDL procedure described above, then flat-fielded to take into account the disuniformities in the CCD response. The sky flats are not part of the baseline calibration set, but they can be derived using the sky images. We median combine all the dithered images of each night, treating the images in two groups: the images taken before the spectroscopic observations separately from the images taken afterwards. This is because the sky background changes before and after the spectroscopic observations. In most of the cases the combination of these 4 images allowed to remove the bad pixel. Then we applied LACOS_IM software of van Dokkum (2001) to remove cosmic rays events. For each night, the flat-field was then obtained from the sky image by normalizing it in both the directions, spatial and spectral, by using the RESPONSE task in IRAF. All the single images were finally divided by the flat-field. The sky level was subtracted from the single flat-fielded images of each run separately by using the

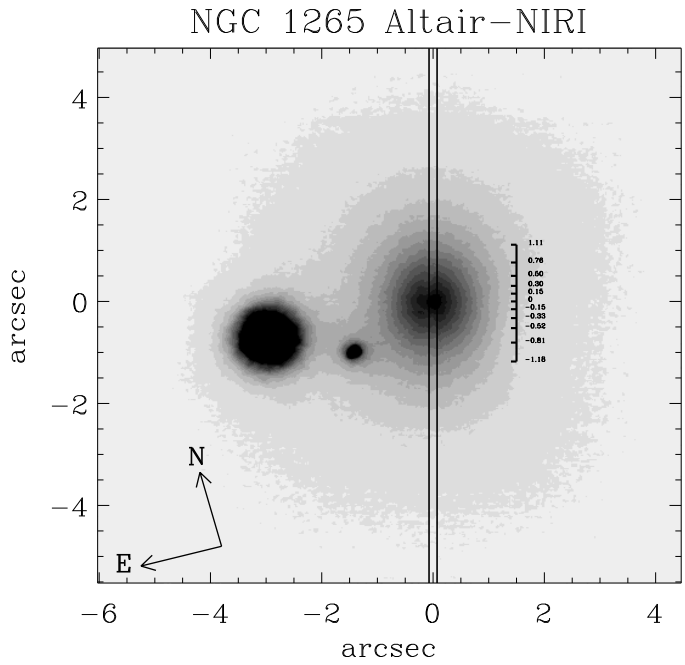

Figure 5.1 *K*s-band image of NGC 1265 within the central 10″×10″. The slit alignment is shown in the figure. The AO reference star is approximately 3″ south-west from the galaxy, and another small star, is present closer to the galaxy. The PA=165° of the galaxy is shown. We show also the region within which we could measure the kinematics in the galaxy. This image is zoomed within the central 6″ of the original image.

night sky image we created for every night. We decided to apply this procedure to the single images because the sky changes during the different observations.

Finally we combined all the 70 sky-subtracted-reduced dithered exposures, obtaining the final 350 s image shown in Figure 5.1. By combining this large amount of images we could remove all the bad pixels. This image was used to constrain the stellar light distribution in the very inner regions of NGC 1265.

5.2.3 PSF monitoring and spatial resolution

To asses the AO correction we measured the full width at half maximum (FWHM) of the radial profile of the star and the encircled energy (EE), i.e. the radial energy distribution of the image, in each group of 4 images before

and after the spectroscopic observations for each run.

The FWHM was measured using the task IMEXAM in IRAF. Ideally it should be at least equal to the width of the slit to match the spectral resolution of the galaxy and stellar observations.

The EE was measured with the IRAF task RADPROF, that first calculates the total energy of the PSF then determines the centroid of the PSF. Circles of increasing radius are then created in this centroid and the PSF energy within each circle is calculated and divided by the total energy. As the circle increases with the radius more of the PSF energy is enclosed, until the circle is sufficiently large to completely contain all the PSF energy. The final EE curve ranges from 0 to 1. It shows what portion of the energy is contained within a circle of given radius, centered at the intensity peak of the diffraction pattern. Therefore, it gives a detailed picture of intensity distribution of an optical system.

Figure 5.2 shows the FWHM of the natural-guide star monitored, as well as the radius containing 90% of the flux, along the different nights. During the different nights, the seeing conditions were good and stable with a FWHM $\sim$ $0\farcs1$, and the radius at which the 90% of the energy is encircled ranged from $0\farcs3 - 0\farcs35$, with small differences between the groups of images before and after the spectroscopic observations.

For the photometric analysis that will be adopted in our modeling we need also to measure the PSF in the combined Altair image, using the natural guide star. We performed the profile of the star by first masking the galaxy from the original image, by using the task IMREPLACE in IRAF. We described the normalized PSF by a sum of two Gaussian components: one narrow component describing the PSF core (i.e., the diffraction limited component) and one broader component (i.e., the seeing halo).

$$\mathrm{PSF} = \frac{\mathrm{F_1}}{2\pi\sigma_1^2} * \mathrm{e}^{-(\mathrm{r}-\mathrm{r_1})^2/2\sigma_1^2} + \frac{\mathrm{F_2}}{2\pi\sigma_2^2} * \mathrm{e}^{-(\mathrm{r}-\mathrm{r_2})^2/2\sigma_2^2} \tag{5.1}$$

where F_1 is the ratio between the peak flux of the narrow component and the total peak flux of the PSF that we previously normalized at 1, whereas $F_2 = 1 - F_1$ represents the peak flux of the second component.

From our fit the narrow component has a $\mathrm{FWHM}_1 = 0\farcs11$ and a peak intensity of $F_1 = 0.827$, while the second component has $\mathrm{FWHM}_2 = 0\farcs63$ and a $F_2 = 1 - F_1 = 0.173$ (see Figure 5.3). Conventionally, the diffraction-limited level is set at the Strehl ratio of 0.80. This is another confirmation of the goodness of our data.

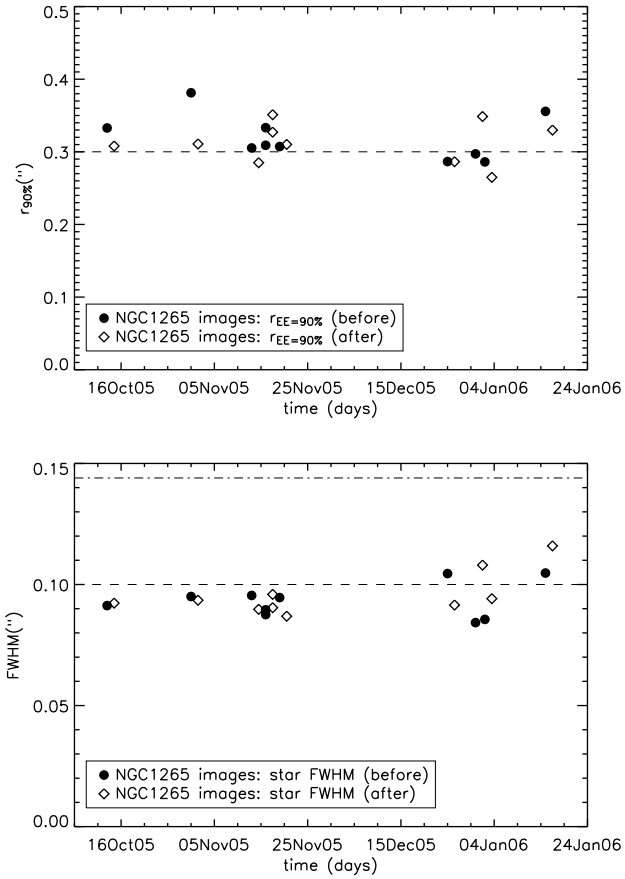

Figure 5.2 *Top Panel*: The radius containing 90% of the flux. *Bottom Panel*: FWHM of the natural-guide star measured in these images. Filled and open circles show the quality of the AO correction before and after our spectroscopic observations, respectively. The dashed and the dotted-dashed lines indicate the average FWHM during the nights and slit width, respectively.

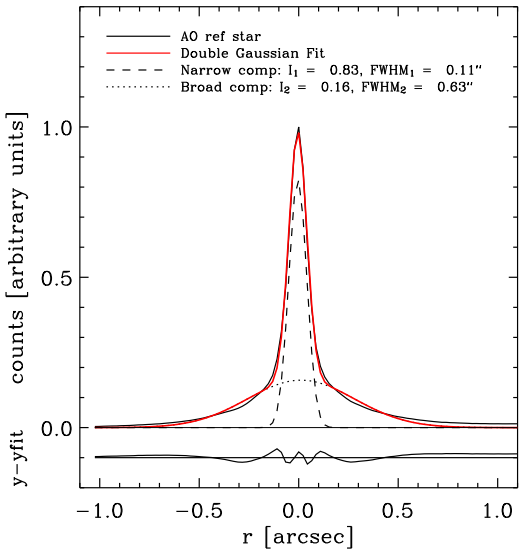

Figure 5.3 Double Gaussian fit of the K-band Altair-NIRI PSF. The FWHM of the narrow component is $0''.11$ and the FWHM of the larger component is $0''.63$. The residuals from this fit are shown.

5.3 Data Analysis

5.3.1 Photometry: the multi-Gaussian expansion

To obtain the parameterization of the stellar surface density we used the multi-Gaussian expansion (MGE) technique proposed by Monnet et al. (1992) and Emsellem et al. (1994), which describes the observed surface brightness as a sum of Gaussians. We used the MGE code described by Cappellari (2002) [3].

Our NIRI high-resolution Ks-band image is not enough extended to cover the outer parts of the galaxy. Therefore, we combined it with the K'-band image by Marchesini et al. (2005) obtained at the Telescopio Nazionale Galileo (TNG). It was kindly provided to us by these authors. Marchesini et al. (2005) obtained this image as part of a campaign of observations of 3CR galaxies. The one of NGC 1265 was obtained with the NICS (Near Infrared Camera Spectrometer) in the small-field of view mode with a pixel size of $0''.13$, a field of view of $2'.2\times2'.2$, in the K'-band filter with a central wavelength of 2.12 μm and a FWHM of 0.35 μm. The NICS individual integration time was set to 1

[3] It is available at http://www-astro.physics.ox.ac.uk/~mxc/idl/

minute, with a total integration time of 20 minutes for each source. The seeing of the observations had a FWHM = $1\farcs76 \pm 0\farcs04$ and the the zero point for the calibration was 21.858 mag obtained by observing the spectrophotometric standards in the field. All the details relative to the data reduction are in Marchesini et al. (2005).

To have a good sampling of our data we first rescaled the TNG image to the same level and pixel scale of the NIRI. Then we extracted logarithmically-sampled photometric profiles on the combined image, along sectors, after masking the AO bright star and the small one close to the galaxy. We checked the sky level subtraction of the TNG image by requiring the final profile to tend asymptotically to a power-law at large radii. To control that we performed a correct sky subtraction also in the NIRI image we applied the same technique to the NIRI image alone.

We determined the adequate scaling ratio between the two images by matching the two luminosity profiles, avoiding the intermediate regions of the two profiles, i.e. NIRI was used within the $4\farcs8$, whereas the TNG image from $4\farcs8$ to $46''$. This allowed us to avoid the inner regions of the TNG profiles (where seeing effects are important) and neglect the most of the outer regions of the NIRI image (where the S/N drops). The best match was chosen looking at the errors in this region and then trying to reduce the χ^2 of the fit (the final best fitting χ^2 is 2.653). While combining the two profiles we assumed that the Ks and K' color gradient is null. Our resulting fit comprising of 8 Gaussians is shown in Figures 5.4 and 5.5.

Our MGE model shows a central Gaussian that parameterizes the non-thermal nucleus which was identified also in the previous studies of NGC 1265. This Gaussian is unresolved because the FWHM of the NIRI image is $\sim 0\farcs11$. This nucleus will dominate the light at small radii (within the $0\farcs11$) and it should not be taken into account when we will parameterize the stellar light in our dynamical models. Furthermore, it should also be taken into account to extract a correct central kinematics, because the stellar absorptions are diluted by the active galactic nucleus, resulting in a decrease in the observed line-strength (see Section 5.3.2).

Finally, we converted our MGE parameters (i.e., counts, σ and flattening of each Gaussians) to the TNG flux and pixel scale to be used for the photometric calibration. They were converted in physical units and then deprojected. The counts of each Gaussians were first converted into the corresponding peak of surface brightness in counts pixels^{-1}, then into the surface brightness in mag arcsec^{-2} by using the TNG nightly calibrated photometric zero-point, and finally into surface density in $L_\odot pc^{-2}$ assuming a K-band absolute magnitude for the Sun of $M_{K,\odot} = 3.39$ (Table 2.1 of Binney & Merrifield 1998). The

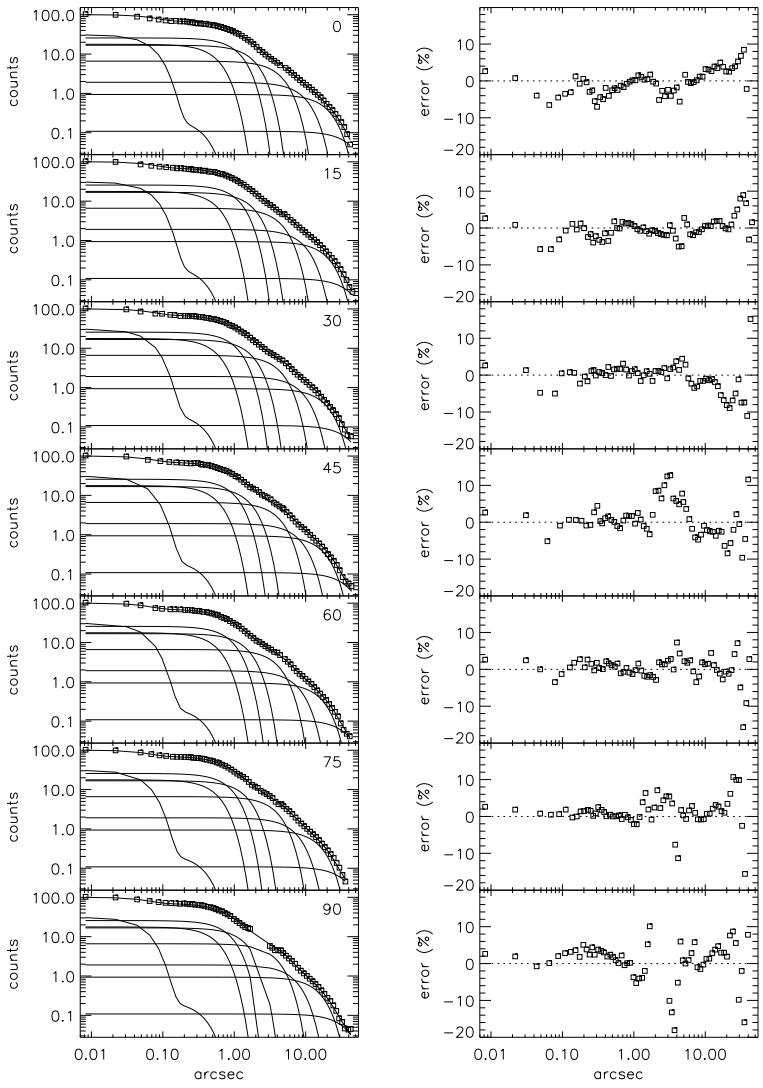

Figure 5.4 *Left Panels*: From the top to the bottom are shown the model fit convolved with the PSF measured along different sectors from the major to the minor axis. *Right panels*: Percentage errors along the profile for different sectors.

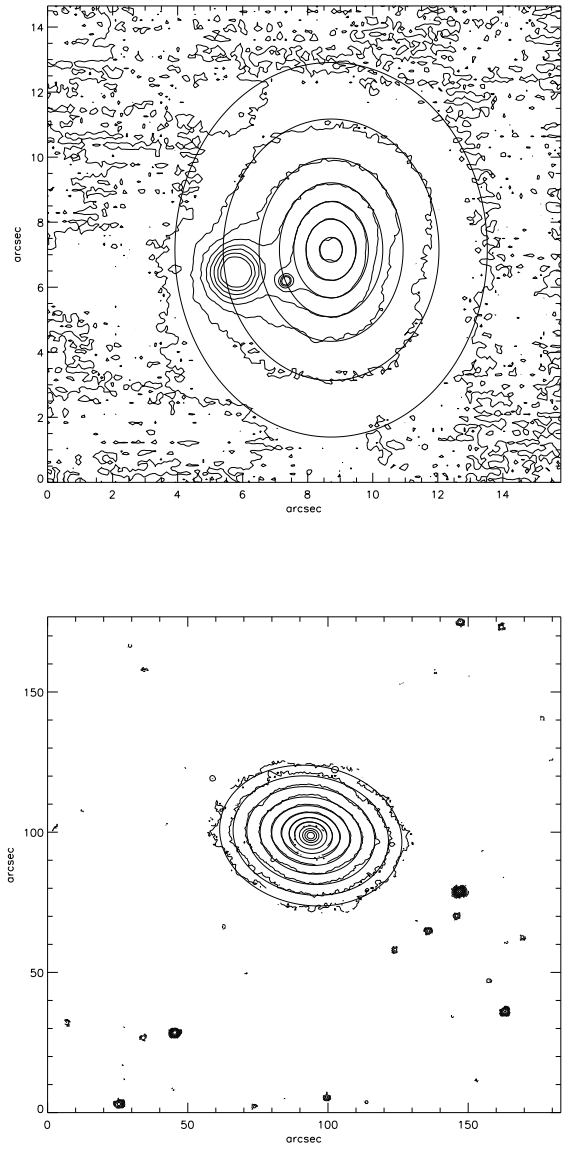

Figure 5.5 Contour plots of the central 4.″8 × 4.″8 NIRI image,and of the 46″ × 46″ TNG image. Superimposed on the two plots are the logarithmically-spaced contours of the intrinsic MGE surface brightness, convolved with the PSF.

Table 5.4 Parameters of the surface brightness of NGC 1265 obtained from the multi-Gaussian expansion.

i	I_i ($L_\odot pc^{-2}$)	σ_i ($''$)	σ_i (pc)	q_i	L_i ($L_{\odot,K}$)
1	105371.75	0.034	11.97	0.874	8.30×10^7
2	20951.40	0.414	146.41	1.000	2.82×10^9
3	29274.20	0.851	301.24	0.749	1.25×10^{10}
4	18811.05	1.375	486.63	0.761	2.13×10^{10}
5	7357.09	3.331	1178.99	0.855	5.50×10^{10}
6	2130.62	7.026	2486.56	0.743	6.15×10^{10}
7	1042.38	15.033	5320.55	0.749	1.39×10^{11}
8	120.69	32.583	11531.71	0.839	8.46×10^{10}

luminosity of each Gaussians was measured as $L = 2\pi I_0 \sigma_{\rm obs}^2 q_{\rm obs}$.

To deproject the parameters we adopted $i = 90^\circ$ as obtained from the orientation of the dust lane in the WFPC2 image. The fact that this galaxy is seen edge-on allows to have a unique deprojection of the surface brightness (Rybicki 1987), with a final luminosity of each Gaussians , σ, and also flattening ($q_{\rm intr} = q_{\rm obs}$) that does not change with the deprojection.

The Table 5.4 summarizes all the parameters we obtained from the photometric analysis. The first, second and fourth columns, $I(L_\odot {\rm pc}^{-2})$, the σ ($''$), the observed flattening $q_{\rm obs}$, will be used in the dynamical model of the galaxy.

We derived the total K-band luminosity of the galaxy, L_K, by summing the single Gaussian luminosity obtaining $L_K = (3.77 \pm 0.6) \times 10^{11}$ $L_\odot$, consistent with the previous studies of Marchesini et al. (2005) (see Section 5.1.1 where we derived their L_K from the H-band magnitude by taking into account for the different distance we used and the color between H and K-band. The assumed uncertainty for the luminosity was estimated from the different values of L_K we obtained by using different minimum level in the MGE fit.

From the mean intrinsic flattening, $q_{\rm intr}$, we obtained the mean ellipticity of the galaxy, $\epsilon_{\rm intr}$, as $\epsilon_{\rm intr} = 1 - q_{\rm intr} = 0.18$. It will be used in the dynamical model.

5.3.2 Kinematics

Measuring the stellar kinematics with the purpose of $M_\bullet$ determinations requires high-S/N spectra.

To achieve the highest S/N we first binned the central 7 rows of the spectrum, that means extracting a central squared aperture of $0\farcs14 \times 0\farcs144$ and

reaching a $S/N\sim47$. At larger radii we binned a number of rows necessary to maintain a S/N of the same order of magnitude. At the farthest row ($R = 1\farcs2$) the S/N is about 34.

The near-infrared kinematics is dominated by strong stellar absorptions, namely the $(2-0)^{12}$CO(2.29μm) band-head, NaI (2.21 μm), and CaI (2.26μm) features. Origlia et al. (1993) demonstrated that the NIR features (CO in particular) are a good set of indicators for constraining the average spectral type and luminosity class of cool stars and evolved giant stars. This is shown by the relation between the equivalent width (EW) of the first CO features and stellar type (Kleinmann & Hall 1986; Origlia et al. 1993), that is translated in a relation with the effective temperature and surface gravity of the star, in the sense that decreasing the effective temperature (or increasing the stellar radius) increases the CO equivalent width. The M and K giant stars are the best to represent the early-type galaxies in the IR because they give the major contribution to the integrated light of the galaxy (e.g., Cesetti et al. 2009). In particular, the CO band-head, is the strongest absorption feature of evolved stars in the wavelength range of our interest. Therefore, to have a good kinematical measurement it is important to use a set of templates with different CO equivalent widths and in particular giant stars (Silge & Gebhardt 2003).

We extracted the stellar kinematics by using the penalized pixel fitting method (pPXF) [4] described by Cappellari & Emsellem (2004). We fitted the logaritmically rebinned spectra of our galaxy with the stellar templates, convolved with a line-of-sight velocity distribution (losvd) described by the Gauss-Hermite expansions (van der Marel & Franx 1993; Gerhard 1993). We fitted V, σ, h_3, h_4, to detect the deviations of the losvd from the Gaussian shape (van der Marel & Franx 1993; Bender et al. 1994). In our Jeans modeling we then use only the V, σ.

We first used the kinematical template stars we observed. They are the two giants HD 76010(MOIII) and 64 Ari (K4III) (see Table 5.3 for details). The data of the third kinematical standard (HD 31098) were not suitable for the analysis. We first obtained the optimal combination of these two templates by fitting them to the galaxy spectrum by binning the central 30 rows to have high S/N ($\sim$88). This best template was then applied to all bins of our measurements, thus implicitly assuming that stellar population gradients are negligible. Alternatively, we tried also to fit in each bin with the the two stars separately. We fitted the region between 2.26$-$2.41 μm, by rejecting the deviant pixels from the spectra. In addition to the stellar templates, we used an additive Legendre polynomial of degree two to help the continuum fit. The

[4] It is available at http://www-astro.physics.ox.ac.uk/$\sim$mxc/idl/

resulting rms of the fit was high because with only two giant stars we could not reproduce the NaI(2.21μm) feature for which we would have had dwarfs stars in our kinematical sample.

To be able to fit also the NaI line we used the GNIRS library of 29 NIR-kinematical standards by Winge et al. (2009). This set of late spectral type stars (dwarfs and giants, with luminosity class from II-V, see Table 5.5) were observed with GNIRS instrument at the Gemini North telescope[5]. The instrument was configured as IFU in the K-band and the observation were carried out with a resolving power of $R = 5900$ corresponding to a instrumental dispersion of $\sigma_{\rm inst} = 26$ km s^{-1} in two spectral ranges, one bluer (2.15−2.33μm) and one redder (2.24−2.43μm). In our analysis we used the combined spectra for 23 stars, in the range of 2.15−2.43μm. The library contains one dimensional spectra in which the continuum shape was removed by fitting a low order polynomial, and were normalized to 1. The spectra are not corrected to the rest wavelength. Therefore, we brought them to a common velocity before combining them as optimal template. Table 5.5 contains the list of the stellar templates with their heliocentric radial velocity, magnitude from SIMBAD, spectral type, effective temperature, and surface gravity (Cayrel de Strobel et al. 1997).

We first determine the best combination of templates of the library, by fitting our spectrum in the central coadded 30 rows in order to have an high S/N (~ 88). This best template was then applied to all bins of our measurements, thus implicitly assuming that stellar population gradients are negligible. The fit was performed using also a multiplicative Legendre polynomial of the second degree to render the shape of the continuum of the templates. We fitted the region between $2.26 - 2.41$ μm to avoid the noisiest part of the galaxy spectrum and because the GNIRS templates have a shorter wavelength range than the galaxy spectrum. Then, we excluded some pixels from the fit, where the telluric feature correction was not satisfactory (see for example the region between the two CO band-head in the bin at $R = 0\farcs52$ in Figure 5.7).

In Table 5.5 we show the weight of the 3 templates selected by pPXF for building the optimal template. Even with a large library of spectral types, the best template is formed by 3 stars, two giants, that well reproduce the CO(2.3μm) band-heads, and one dwarf, that well reproduce the NaI(2.21μm). The optimal template obtained by the GNIRS library reproduces well the galaxy spectrum in the selected spectral region of $2.26 - 2.41$ μm, with smaller residual in the fit than our own template stars (see Figure 5.6). Moreover, we see that the two giants provide a good fit of the spectrum by them self, and the dwarf is required mainly to reproduce the depth of the NaI feature and reduce the

[5]It is available at http://www.gemini.edu/sciops/instruments/nir/spectemp/index.html

Table 5.5 Parameters of the GNIRS stellar templates.

Name	V (mag)	v_r (km s^{-1})	Sp.Type	T_{eff} (K)	logg	Weight
(1)	(2)	(3)	(4)	(5)	(6)	(7)
HD 113538(b)	9.02	37.8	K8V			114.49201
HD 173764	4.23	-21.5	G4IIa	4700	0.94	0
HD 1737	5.17	20.6	G5III	4790	3.05	0
HD 20038	8.91	27	F7III	5196	2.62	0
HD 206067	5.11	-34.7	K0III	4740	2.73	0
HD 212320	5.92	-14.2	G6III	4790	2.87	0
HD 218594	3.66	21.1	K1III	4430	2.34	0
HD 224533	4.89	-0.2	G9III	4960	3.19	0
HD 2490	5.43	32.3	M0III	3652	4.0	190.26115
HD 26965	4.41	-42.2	K1V(a)	5091	4.31	0
HD 32440(b)	5.47	25.8	K6III			0
HD 34642	4.83	21.1	K0IV	4730	3.39	0
HD 35369	4.14	-18.2	G8III	4880	2.76	0
HD 36079	2.84	-13.6	G5II	5170	2.27	0
HD 38392	6.15	-10.1	K2V	4990	4.50	0
HD 39425	3.12	88.9	K2III	4582	2.80	0
HD 4188	4.78	0.6	K0III	4755	2.90	0
HD 4730	5.61	3.5	K3III	4220	2.10	0
HD 63425B(b)	7.71	-	K7III			31.896540
HD 64606	7.44	93.4	G8V	5040	4.0	0
HD 6461	7.65	1	G3V	5110	2.30	0
HD 720	5.42	-5.7	K5III	4160	2.02	0
HD 9138	4.84	34.0	K4III	4040	1.91	0

NOTES. — Col. (1): Name. Col. (2): V-band magnitude from SIMBAD. Col. (3): Radial velocity from SIMBAD. Col. (4): Spectral type from Cayrel de Strobel et al. (1997). Col. (5): Effective temperature from Cayrel de Strobel et al. (1997). Col. (6): Surface gravity from Cayrel de Strobel et al. (1997). Col. (7): Weights for the different templates obtained with pPXF for the final optimal template. (a) Spectral type from SIMBAD; (b) Not in Cayrel de Strobel et al. (1997) list, all information are from SIMBAD.

residuals in the fit.

In the photometric analysis we noticed that at $R < 0\farcs1$ a non-thermal source dominates the emission from the stars. This emission affects our central (within $0\farcs14$) kinematical measurement because the stellar absorptions are diluted by the AGN, resulting in a decrease in the observed line-strength and σ (see also van der Marel & Franx 1993).

Over this central region, the power-low continuum can be approximated as a constant. Therefore we applied a correction for the AGN contribution by subtracting the non-thermal source before the pPXF fit, and then we performed the fit with the same technique we used for the other rows, similarly to Cappellari et al. (2009) for Centaurus A. We derived this constant by integrating the light

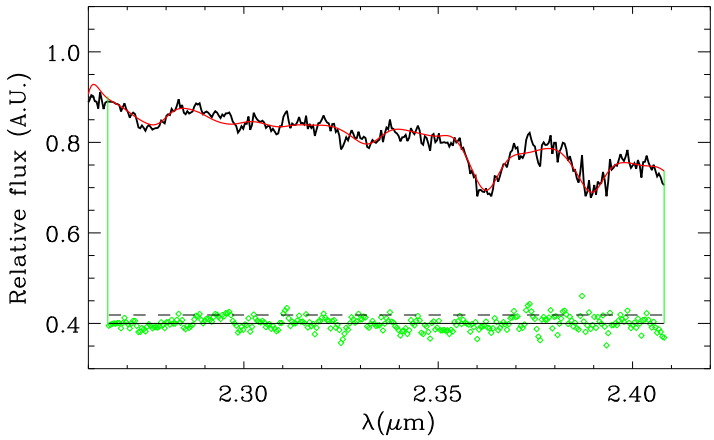

Figure 5.6 Spectrum of NGC 1265 obtained by binning the 30 central rows (S/N $\sim$ 88) and the optimal template fit (in red). The fit residuals are shown in green in the region were the fit was applied. They were vertically shifted by an arbitrary amount for better visibility. The central continuous line represents the average of the residual. The dashed line is the rms of the scatter.

coming from the first Gaussian in the MGE model within 0.″1, by assuming no color terms between Ks filter of our images and the standard K filter used for spectroscopic observation. The final contribution is small of the order of 10% of the total flux.

Figure 5.8 shows the nuclear kinematics of NGC 1265. The galaxy appears not to be rotating within 1.″2, and the σ profile appears to be quite flat. The third panel shows the residual in the fit.

We estimated the uncertainties from a set of 100 Monte Carlo simulations, in which each spectrum has an added perturbation consistent with the random noise, obtained from by the robust standard deviation of the difference between the best fit and the original spectrum. The typical errors are 15 km s^{-1} and 20 km s^{-1}, for V and σ, respectively.

With our measurements we could only study the central 1.″2 of the galaxy, this will affect both the dynamical modeling we use and our constrain on the $(M/L)_K$.

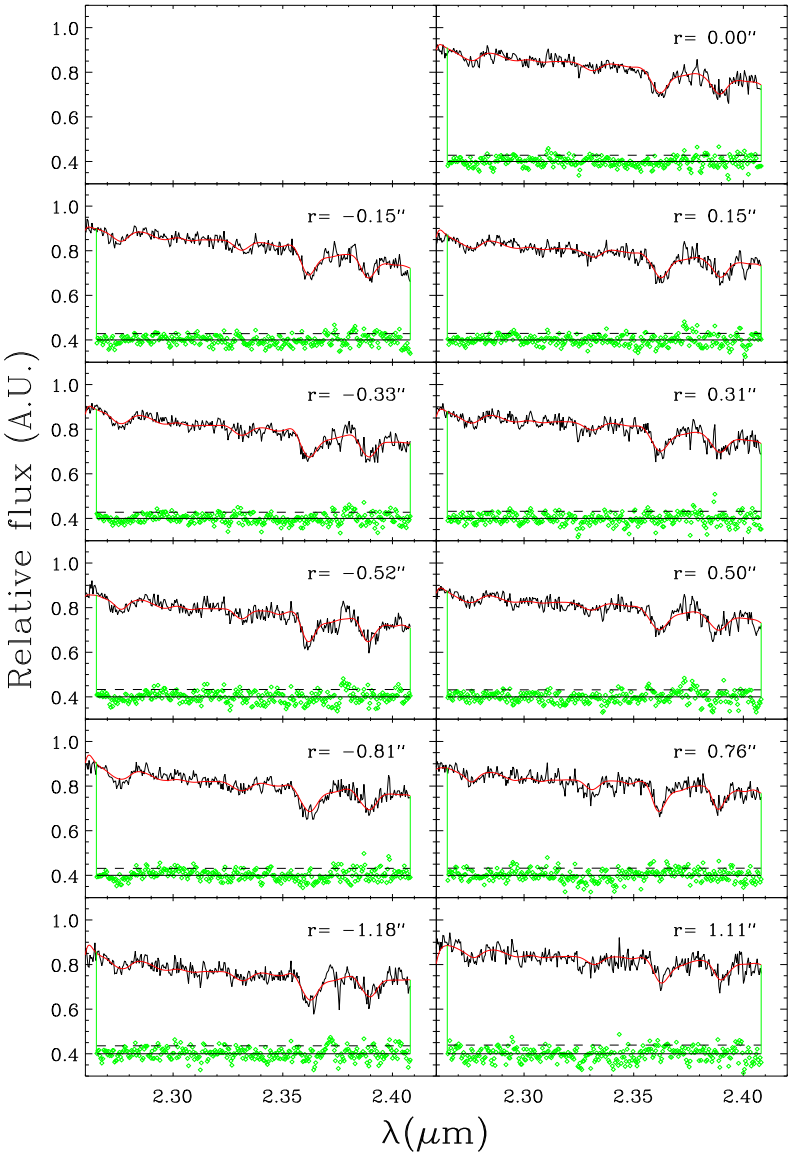

Figure 5.7 The spectra of NGC 1265 with the optimal template fit obtained at different radii as indicated in the figure. The fit residuals are shown in green in the region were the fit was applied. They were vertically shifted by an arbitrary amount for better visibility. The central continuous line represents the average of the residual and the dashed line the rms of the scatter.

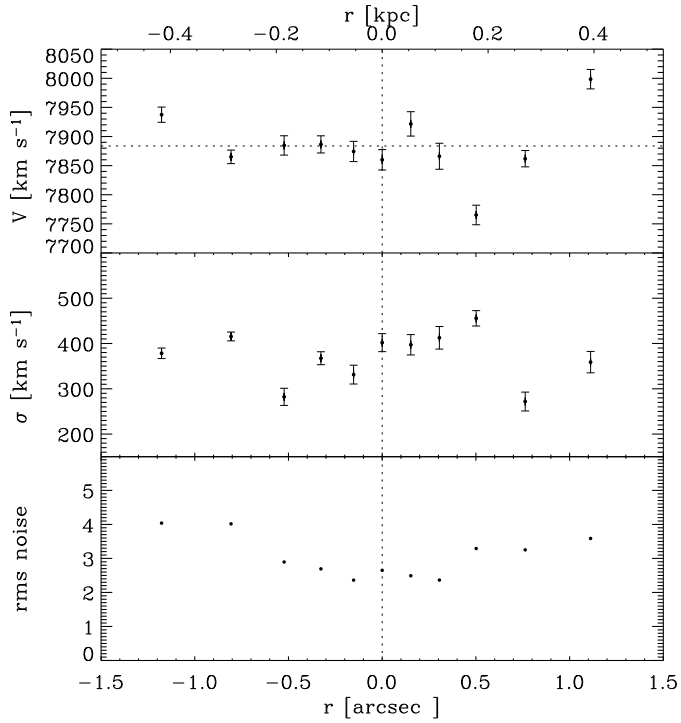

Figure 5.8 The kinematics in the central 1.″2 (428 pc) of NGC 1265. The three panels show the velocity V, velocity dispersion σ, and rms of the residuals between the fit and the model, respectively.

5.4 Jeans Anisotropic Models

To measure the $M_\bullet$ we used the Jeans Anisotropic MGE package (JAM) described by Cappellari (2008). This code calculates the prediction of the second velocity moments $V_{\rm rms} = (V^2 + \sigma^2)^{0.5}$, projected onto the sky plane, for a axisymmetric galaxy model with variable anisotropy profile $\beta = 1 - (\sigma_z/\sigma_R)$ in the meridional plane, dynamical mass-to-light ratio $(M/L)_K$ and $M_\bullet$.

The code needs a MGE parameterization of the surface brightness of the galaxy, a value for the anisotropy parameter in the meridional plane β, a value for the $(M/L)_K$ to rescale the surface brightness parameters to the galaxy surface density, the inclination of the galaxy, a value for the central $M_\bullet$, the distance of the galaxy, the region along the galaxy major axis where the stellar

kinematics is measured, the PSF of the instrument, and the central aperture used to compute the kernel for the seeing and aperture convolution.

To estimate the β parameter, that with our data is assumed constant we used the relation proposed by Cappellari et al. (2007) between the anisotropy in the meridional plane and the average intrinsic ellipticity $\epsilon_{\rm int}$ of the galaxy. From our derived $\epsilon_{\rm int}$, $\beta = (0.6 \pm 0.1)\epsilon_{\rm int} = 0.11 \pm 0.02$. In principle, the mass-to-light ratio should be determined from the observations, with the luminosity density derived by the observed luminosity profile. This allows to compute the mass density, by simply multiplying the luminosity density by the mass-to-light ratio.

Because our kinematical data are extended as far as $\sim 1\farcs2$, we could perform only a central model of the $V_{\rm rms}$ of the galaxy, not sufficient to constrain the $(M/L)_K$ and the orbital structure of the galaxy. Therefore, our final result will be an upper limits on the $M_\bullet$ because we do not know the correct factor we should use to convert the luminosity into mass density profile. We first used a range of $(M/L)_K$=0.5 − 1.5 ($\rm M_\odot/L_\odot$), following the typical NIR value presented in Williams et al. (2009). They performed dynamical measurement of the $(M/L)_K$ for a sample of 28 edge-on spirals and lenticulars. They have the largest sample for which the $(M/L)_K$ was measured so far in the K-band, by using dynamical models and therefore independent on the populations models. They obtained a median K-band $(M/L)_K$=1.09 ($\rm M_\odot/L_\odot$) with a rms scatter of 0.31 ($\rm M_\odot/L_\odot$). Williams et al. (2009) for first found such as high value of $(M/L)_K$ since in the previous dynamical measurements it was $(M/L)_K \sim$ 0.6 − 0.7 ($\rm M_\odot/L_\odot$). We assumed a constant $(M/L)_K$ ratio for the central region of NGC 1265, where the dark matter is expected to contribute only a small fraction of the mass as it is observed from the dynamics of early type galaxies in Cappellari et al. (2006) and Thomas et al. (2007). An inclination of $i = 90^\circ$ was adopted as estimated from the dust lane in the WFPC2 image. We used a range of different $M_\bullet$ ranging $0 - 3.6 \times 10^9$ $\rm M_\odot$.

With this set of conditions we fitted our kinematical data with the model $V_{\rm rms}$ obtained from the photometric data by excluding the first Gaussian coming from a non-thermal component.

Figure 5.9 shows the contour plot of the χ^2 for all the range of $M_\bullet$, $(M/L)_K$, and $\beta = 0.1$. By using this range of $(M/L)_K$ we can rule out the absence of a black hole. None of our models without the SMBH can fit the observed kinematics, but the best $M_\bullet$ is indicating a larger $(M/L)_K$. The upper limit on the $M_\bullet$ is $3.45 \times 10^9 \rm M_\odot$.

Then, we varied the values of the anisotropy to see how our results depends on our initial constrain. We used a wider range of $\beta = 0 - 0.2$ following the Figure 7 of Cappellari et al. (2007).We adopted also a larger range of $(M/L)_K$

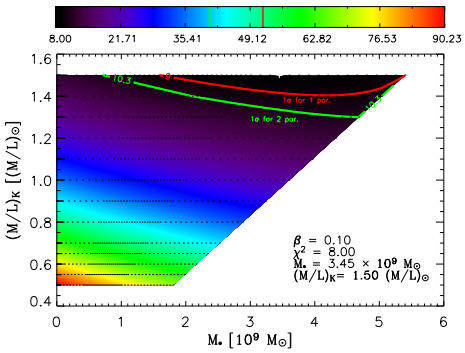

Figure 5.9 Contours of the χ^2 as a function of the $M_\bullet$ and $(M/L)_K$ by adopting $\beta = 0.1$ and $(M/L)_K$= 1.5($M_\odot/L_\odot$).

=0.5 − 2.5 ($M_\odot/L_\odot$), obtaining a best-fit upper limit on the black hole mass, ranging from $M_\bullet$= 0 to $M_\bullet$= 1×10^9 $M_\odot$ in the case of $(M/L)_K = 2$ ($M_\odot/L_\odot$), and $\beta = 0$ (see Figure 5.10).

The $V_{\rm rms}$ data-model comparison for our best-fitting model with the smallest χ^2 for the isotropic model are shown in Figure 5.11. All the significant features of the data are reproduced by the model.

5.5 Discussion

With our estimation of $M_\bullet$ and the central σ we calculated the radius of the the sphere of influence of NGC 1265, $r_{\rm infl}$ (i.e., the region where the SMBH dominates the gravitational potential before the stars take over; in this region the rotation is Keplerian). Usually one would need the stellar velocity dispersion within the effective radius, $\sigma_{\rm e}$, but being σ a luminosity weighted value we could use our central measurement where the contribution from the central luminosity is higher to perform this simple estimate. Following Eq. 2.2 we obtained $r_{\rm infl}$ ∼0.″27. The high spatial resolution we obtained with our Altair-NIRI data (FWHM diffraction limited core ∼0.″11) allow us to solve the sphere of influence of NGC 1265.

The best-fit upper limit on the black hole mass derived through dynamical modeling ranges from $M_\bullet = 1 \times 10^9 - 3.45 \times 10^9 M_\odot$ within 1 σ error, depending on our assumption. We first assumed $(M/L)_K$, following a plausible value from the literature carefully obtained with dynamical models (for which we found

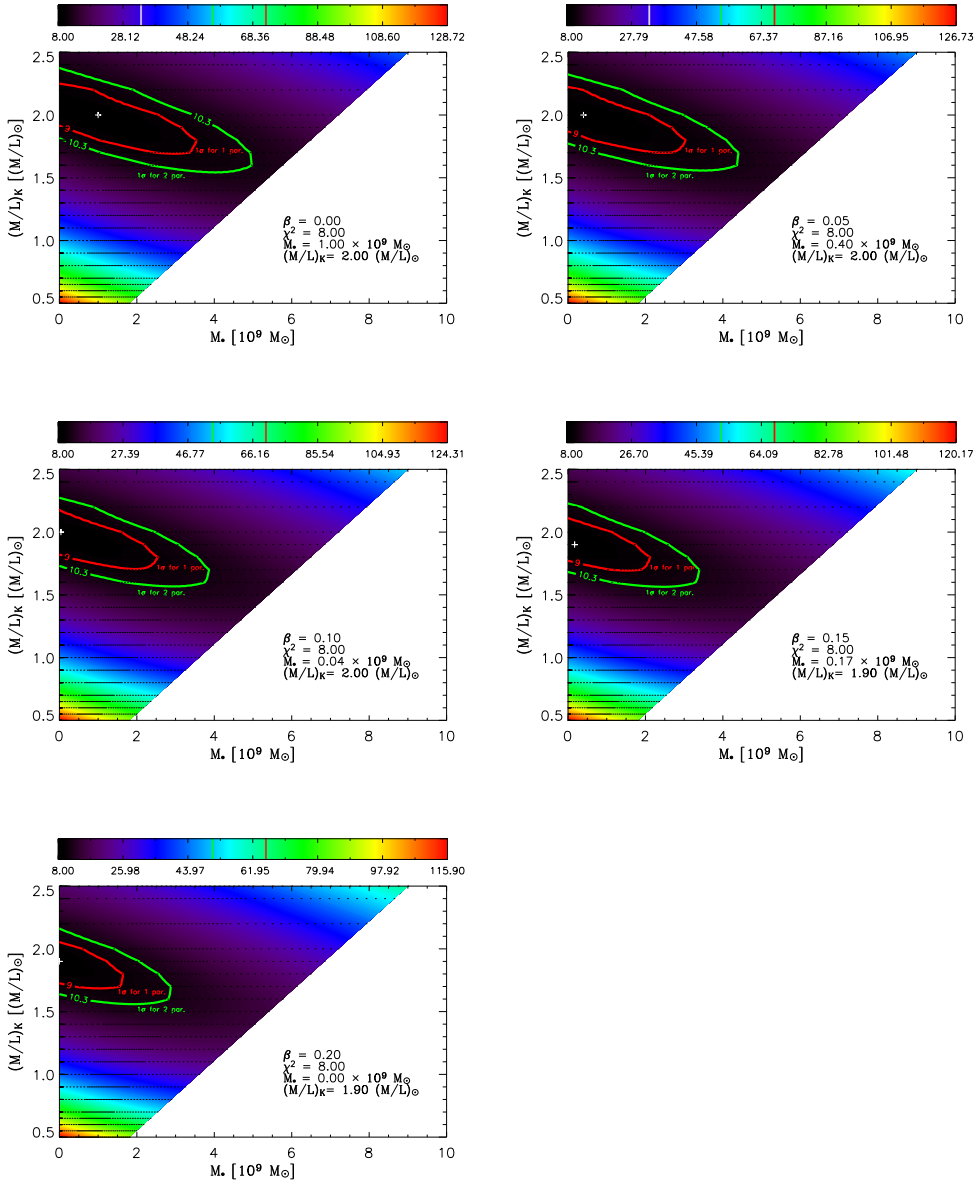

Figure 5.10 Contours of the χ^2 as a function of the $M_\bullet$ and $(M/L)_K$ for different values of $\beta = 0 - 0.2$.

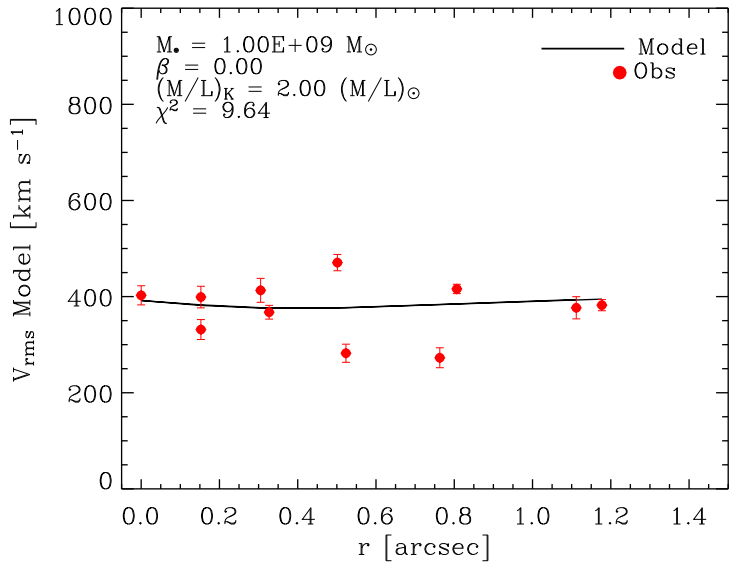

Figure 5.11 The best fitting dynamical model predictions (continuous line) compared with the kinematical data we measured (red filled dots).

largest masses of the SMBH but without a true minimum in the χ^2 distribution) or then the value suggested by our data where we found a $(M/L)_K$= 2. In this case we obtained also an high degeneration with the increasing of β, with $\beta = 0.2$ giving $M_\bullet = 0$ M$_\odot$. Therefore with this last assumptions we cannot exclude the absence of a SMBH for this value of the anisotropy.

However, we should keep in mind that the systematic uncertainties on such measurement of $M_\bullet$ are likely larger than what we have estimated with our Jeans modeling. The use of a full orbit-based code or a triaxial code, would likely accommodate a much large upper-limit. However, at this stage, with such a kind of data it is not worth the effort of that level of modeling since the kinematic data do not have much spatial leverage on the SMBH.

We compare our upper limit on $M_\bullet$ with the predictions of the near-IR $M_\bullet - L_{K,\mathrm{bulge}}$ relation by Marconi & Hunt (2003). We derived the K-band luminosity from the MGE parameterization, $L_K = (3.77 \pm 0.6) \times 10^{11}$ L$_\odot$. This corresponds to $M_\bullet = 9.6^{+1.4}_{-4.9} \times 10^8$ M$_\odot$ for a 0.31 dex scatter. In Figure 5.12 we show the agreement of our $M_\bullet$ with the relation by Marconi & Hunt (2003).

Being NGC 1265 an emitter in both X and radio wavelengths we can test

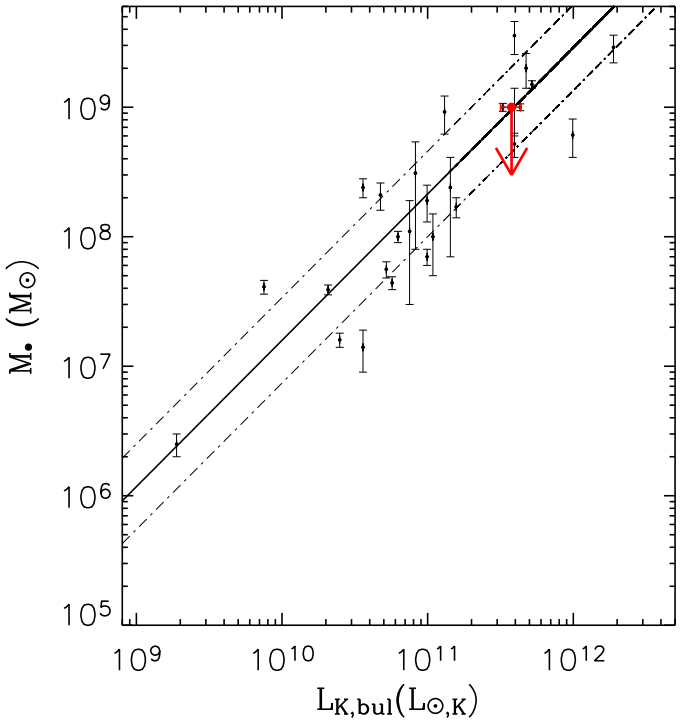

Figure 5.12 Location of the upper limit on $M_\bullet$ of NGC 1265 (red arrow) in the case of $\beta = 0$ and $(M/L)_K = 2$ with respect the near-IR $M_\bullet - L_{K,\rm bulge}$ relation by Marconi & Hunt (2003, continuous line). We plot with the black dots the SMBH masses for which the K-band luminosity of the host spheroid is available in Marconi & Hunt (2003).

the prediction of the fundamental plane of accretion onto SMBHs in the last version of Gültekin et al. (2009a). In fact, if we assume that the radio and X−luminosities are associated with the jet and accretion powers, respectively, we conclude that there must be a connection between the accretion and jet production and $M_\bullet$.

The available values of the radio core luminosity at 5 GHz, $\log L_R$=39.10 erg s^{-1}, and X−ray luminosity at the energy of 2-10 keV, $\log L_{\rm X}$ =40.95 erg s^{-1} (Balmaverde & Capetti 2006) give us a $M_\bullet$=$6.3^{+30.7}_{-5.2} \times 10^8 M_\odot$, adopting 0.77 dex scatter, according to the relation of Gültekin et al. (2009a). Our estimate of $M_\bullet$ is consistent with the values expected by this relation.

The correlation between L_R, $L_{\rm X}$, and $M_\bullet$, can be explained in the following two scenarios. First, the radio and X−ray emissions could be attributed to synchrotron emission from a relativistic jet in the jet-dominated state of an AGN. As both components, the radio emissions and the X−rays, originate from the same source, one can expect a tight correlation of both observables. One would expect the correlation to break down once a source leaves the radiatively inefficient accretion flow state and is no longer jet-dominated (Falcke et al. 2004). On the other hand, Merloni et al. (2003) suggested that the X-ray emission originates from the accretion flow, while the radio emission is still attributed to the relativistic jet. Both, the flow and the jet are presumed to be strongly coupled so that the radio and X-ray emissions are correlated. In the recent past, the statistics and slopes of the $L_R - L_{\rm X} - M_\bullet$ correlation have been used to argue for and against the synchrotron/jet models (Merloni et al. 2003; Heinz 2004). The addition of new measurements, as is done in our case, will help in the further understanding of these mechanisms.

5.6 Conclusions

This chapter presents the K-band AO spectroscopic observations of the central region of NGC 1265, taken with the Altair-NIRI on the Gemini North telescope with a spatial resolution of FWHM = $0\farcs11$. To account for the stellar contribution we performed a multi-Gaussian expansion by using the combination of the NIRI high-resolution Ks-band image and a TNG K'-band image to cover the outer parts of the galaxy. The stellar kinematics was extracted from the CO absorption bands at 2.3 μm. We applied the Jeans anisotropic models to the data to determine the best fitting values for the supermassive black hole mass $M_\bullet$. The limited quality of our spectroscopic data did not allow us to measure a very extended kinematics. Therefore, we assumed the values of $(M/L)_K$ and anisotropy β of the galaxy by following Cappellari et al. (2006, 2007), respectively. This allowed us to find an upper limit on the range of $M_\bullet = 1 \times 10^9 - 3.45 \times 10^9$ $\mathrm{M}_\odot$ depending on the assumed values of β and $(M/L)_K$, respectively.

With the addition of new kinematical data mapping the outer region of NGC 1265 we will be able to constrain better the $(M/L)_K$ and to obtain a more confident value for the $M_\bullet$. These new observations have been recently obtained on the 17 and 18 October 2009 with the Oxford SWIFT IFU spectrograph on the Hale 200-inch telescope at the Palomar Observatory.

6

The High-Mass End of the Black Hole Mass Function: Mass Estimates in Brightest Cluster Galaxies [1]

Based on Dalla Bontà, E., Ferrarese L., Corsini E. M., Miralda-Escudé, J., Coccato L., Sarzi M., Pizzella A., & Beifiori A., ApJ, 690, 537

We present *Hubble Space Telescope* imaging and spectroscopic observations of three brightest cluster galaxies, Abell 1836-BCG, Abell 2052-BCG, and Abell 3565-BCG, obtained with the Wide Field and Planetary Camera 2, the Advanced Camera for Surveys and the Space Telescope Imaging Spectrograph. The data provide detailed information on the structure and mass profile of the stellar component, the dust optical depth, and the spatial distribution and kinematics of the ionized gas within the innermost region of each galaxy. Dynamical models, which account for the observed stellar mass profile and include the contribution of a central supermassive black hole (SMBH), are constructed to reproduce the kinematics derived from the Hα and [N II] $\lambda\lambda$6548, 6583 emission lines. Secure SMBH detection with $M_\bullet = 3.61^{+0.41}_{-0.50} \times 10^9$ $M_\odot$ and $M_\bullet = 1.34^{+0.21}_{-0.19} \times 10^9$ $M_\odot$, respectively, are obtained for Abell 1836-BCG and Abell 3565-BCG, which show regular rotation curves and strong central velocity gradients. In the case of Abell 2052-BCG, the lack of an orderly rotational motion prevents a secure determination, although an upper limit of $M_\bullet \lesssim 4.60 \times 10^9$ $M_\odot$ can be placed on the mass of the central SMBH.

[1] Based on observations made with ESO telescopes at the La Silla Paranal Observatory under programme ID 279.B-5004(A).

These measurements represent an important step forward in the characterization of the high-mass end of the SMBH mass function.

6.1 Introduction

Within the past decade, the focus in supermassive black holes (SMBHs) studies has moved from the dynamical measurement of SMBH masses, $M_\bullet$, in nearby galaxies (see review by Ferrarese & Ford 2005), to the characterization of scaling relations connecting $M_\bullet$ to the large scale properties of their hosts (Kormendy & Richstone 1995; Ferrarese & Merritt 2000; Gebhardt et al. 2000a; Graham et al. 2001; Ferrarese 2002; Marconi & Hunt 2003). Such relations, combined with the knowledge of the galaxy luminosity or velocity dispersion functions, lead to a direct determination of the local SMBH mass function and, by comparison with the energetics of high redshift AGNs, accretion history (e.g. Marconi et al. 2004; Shankar et al. 2004; Benson et al. 2007; Tundo et al. 2007; Graham et al. 2007; Lauer et al. 2007b). Furthermore, the tightness of the relations linking galactic properties to $M_\bullet$ is indicative of a formation/evolutionary history in which SMBHs and galaxies are causally connected. Indeed, feedback from AGN activity is believed to play an important, perhaps even fundamental rôle in the evolution of galaxies (e.g. Binney & Tabor 1995; Suchkov et al. 1996; Ciotti & Ostriker 2001; Springel et al. 2005; Schawinski et al. 2006; Hopkins et al. 2007b; Di Matteo et al. 2008).

In this context, brightest cluster galaxies (BCGs) are of particular interest. Their privileged location at the center of a massive cluster implies that they have undergone a particularly extensive merging history (Khochfar & Silk 2006) and are likely to host the most massive SMBHs in the local Universe (Yoo et al. 2007). The latter conclusion is also supported by all scaling relations which are known to be obeyed by local SMBHs, that predict the most massive SMBHs to reside in most massive galaxies. As such, BCGs constitute an excellent laboratory to search for the local relics of the most powerful high-redshift quasars (Willott et al. 2003; Vestergaard 2004), and to investigate the rôle of mergers in the black hole mass function.

Unfortunately, direct dynamical measurements of SMBHs masses in BCGs are exceedingly difficult - with only two such measurements made to-date (in M87 and NGC 1399, Harms et al. 1994; Macchetto et al. 1997; Houghton et al. 2006). The reason for this is simple: SMBH mass measurements based on resolved kinematic tracers (gas or stars) need to be carried out within the SMBH "sphere of influence", i.e. the region of space within which the SMBH dominates the overall gravitational potential. For a 10^9 $M_\odot$ SMBH, the sphere of influence becomes unresolved for optical measurements with the *Hubble Space Telescope* (*HST*) at distances beyond $\sim$ 100 Mpc (see Figure 44 of Ferrarese

& Ford 2005). Few BCGs are located within this limit. To compound the problem, bright ellipticals are characterized by shallow stellar density profiles and faint central surface brightnesses (e.g., Ferrarese et al. 1994; Lauer et al. 1995; Rest et al. 2001; Ferrarese et al. 2006) making the detection of stellar absorption lines with *HST* prohibitively expensive. The latter difficulty can be overcome with the use of gas dynamics. Emission lines (mainly Hα and [N II]) from the gas are bright and easily measured. If the gas is confined in a disk, there is little ambiguity in the velocity distribution (Ho et al. 2002), and since the method was first used (Harms et al. 1994; Ferrarese et al. 1996; Ferrarese & Ford 1999) an increasing amount of attention has been devoted to the theoretical aspects of the dynamical modeling (Maciejewski & Binney 2001; Barth et al. 2001; Cappellari et al. 2002; Coccato et al. 2006).

The lack of a secure characterization of the SMBH mass function above the 10^9 $M_\odot$ mark is troublesome. Lauer et al. (2007a) suggest that the relations between $M_\bullet$ and host bulge luminosity, $L_{\rm bulge}$ (Kormendy & Richstone 1995), and velocity dispersion (Ferrarese & Merritt 2000; Gebhardt et al. 2000a) would predict significantly different $M_\bullet$ if extrapolated above 10^9 $M_\odot$. In particular, the $M_\bullet - \sigma$ relation would predict less massive SMBHs in BCGs than the $M_\bullet - L_{\rm bulge}$ relation, due to the slower increase of σ with galaxy luminosity observed for BCGs compared to the bulk of the early-type galaxy population (Bernardi et al. 2007). The difference in the predicted mass is such to significantly affect (by an order of magnitude) the high-mass end of the local SMBH mass function. von der Linden et al. (2007) argue that the shallower dependence of σ on L applies to BCG but not to comparably massive non-BCG galaxies, which instead follow the canonical Faber-Jackson relation defined by less massive systems. This implies that BCGs and non-BCG galaxies of comparable mass must occupy a different locus in either, or both, the $M_\bullet - \sigma$ and $M_\bullet - L_{\rm bulge}$. This result is in contrast with the findings of Batcheldor et al. (2007), who argue that SMBHs masses predicted from NIR luminosities (Marconi & Hunt 2003) are consistent with those predicted from σ. They attributed the discrepancy noted by Lauer et al. (2007b) (who used $V-$band luminosities) to a bias introduced by the inclusion, when computing $L_{\rm bulge}$, of extended blue envelopes around BCGs. At present these ambiguities prevent us from testing any theoretical prediction on the high-mass end of the black hole mass function based on the observed quasar abundances and merger histories.

In this chapter, we analyze the kinematics of the ionized gas in the nuclear region of three BCGs – Abell 1836-BCG, Abell 2052-BCG, and Abell 3565-BCG – in order to constrain the mass of the central SMBHs. The data were obtained using the Space Telescope Imaging Spectrograph (STIS) on board the *HST*, supplemented with imaging data from the Advanced Camera for Surveys

(ACS) and the Wide Field and Planetary Camera 2 (WFPC2). Furthermore, the central stellar velocity dispersion of Abell 1836-BCG was obtained from ground based spectroscopy. The chapter is organized as follows. The criteria of galaxy selection are presented in Section 6.2. ACS and STIS observations are described and analyzed in Sections 6.3 and 6.4, respectively. Ground based spectroscopic observations of Abell 1836-BCG are described and analyzed in Section 6.5.

The SMBH masses of Abell 1836-BCG and Abell 3565-BCG, and an upper limit for the SMBH mass of Abell 2052-BCG are derived in Section 6.6. In Section 6.7 results are compared to the predictions of the SMBHs scaling laws and conclusions are given.

6.2 Galaxy sample

Naturally, the place to search for the most massive black holes in the universe is in the most nearby and most massive BCGs, where the problems of angular resolution to measure black hole masses are minimized. The galaxies discussed in this contribution were selected from the BCG sample observed by Laine et al. (2003) with the *HST* Wide Field and Planetary Camera 2 (WFPC2). Dynamical studies in giant ellipticals are performed more effectively by modeling gas, rather than stellar kinematics (see discussion in Ferrarese & Ford 2005), both because of the low stellar surface brightness that characterizes the core regions of such systems (e.g. Ferrarese et al. 2006) and because when applied to slowly-rotating, pressure supported galaxies, stellar dynamical models depend heavily on the knowledge of the anisotropy in the stellar velocity dispersion, a difficult quantity to constrain observationally (e.g., van der Marel & van den Bosch 1998).

Eleven of the 81 galaxies in the Laine et al. (2003) sample appear to contain well defined nuclear dust structures, which can trace regular gas kinematics (Ho et al. 2002). After selecting the most regular nuclear dust structures among those eleven objects and after excluding galaxies for which existing ground based spectra showed no evidence of nuclear Hα and [N II] $\lambda\lambda 6548, 6583$ in emission, we selected the four BCGs predicted to host the most massive SMBHs (based on the correlations between $M_\bullet$ and the host bulge stellar velocity dispersion, σ, and/or B-band luminosity, L_B) and for which the SMBH sphere of influence could be well resolved using the $0''.1$ wide slit of *HST*'s STIS.

One galaxy (Abell 2593-BCG) was not observed due to the premature failure of STIS. The sample discussed in this chapter therefore includes three BCGs, namely Abell 1836-BCG (PGC 49940), Abell 2052-BCG (UGC 9799) and Abell 3565-BCG (IC 4296). The main properties of these galaxies are

Table 6.1 Basic parameters of the sample galaxies

Galaxy	Other name	Type (RC3)	cz ($\mathrm{km\,s^{-1}}$)	D (Mpc)	σ_c ($\mathrm{km\,s^{-1}}$)
(1)	(2)	(3)	(4)	(5)	(6)
Abell 1836-BCG	PGC 49940	SA0$^-$:	11036	147.2	288 ± 9^a
Abell 2052-BCG	UGC 9799	E	10575	141.0	233 ± 11^b
Abell 3565-BCG	IC 4296	E	3834	50.8	322 ± 12^c

NOTES. — Col. (1): Galaxy name from Abell (1958) and Abell et al. (1989). Col. (2): Alternative identification. Col. (3): Morphological classification from RC3. Col (4): Systemic velocities in the frame of the Cosmic Microwave Background, from Laine et al. (2003) Col. (5): Distances from systemic velocity and $H_0 = 75$ km s^{-1} Mpc^{-1}, except for Abell 3565-BCG (Jensen et al. 2003). Col. (6): Stellar velocity dispersion (a: this chapter; b: Smith et al. 2000, c: Tonry 1985) corrected to a circular aperture of size $1/8 r_e$.

Table 6.1 – Continued

Galaxy	D_{25} (arcmin)	r_e (arcsec)	m_B (mag)	m_K (mag)
(1)	(2)	(3)	(4)	(5)
Abell 1836-BCG	1.4	13.10^a	14.56 ± 0.14^a	9.99 ± 0.04
Abell 2052-BCG	1.8	55.98^b	14.4 ± 0.03^b	9.55 ± 0.06
Abell 3565-BCG	3.4	41.41^a	11.61 ± 0.05^c	7.50 ± 0.02

NOTES. — Col. (1): Galaxy name from Abell (1958) and Abell et al. (1989). Col. (2): Apparent major isophotal diameter measured at the surface brightness level $\mu_B = 25$ mag arcsec^{-2} from RC3. Col. (3): Effective radius (a: from RC3, b: from Hudson et al. 2001). Col. (4): Total apparent $B-$band magnitude (a, c: from RC3, b: from Postman & Lauer 1995). Col. (5): Total apparent $K-$band magnitude from 2MASS.

summarized in Tables 6.1.

6.3 Observations, data reduction, and analysis: imaging

6.3.1 Observations and data reduction

The luminosity density and ionized gas distribution of the target galaxies, both of which are required for the dynamical modeling described in Section 6.6, have been constrained using *HST* ACS and WFPC2 images. Basic information about the data can be found in Table 6.2.

The ACS images were obtained with the High Resolution Channel (HRC) as part of program GO-9838 (P.I. L. Ferrarese). The HRC detector is a 1024×1024 SITe CCD with a plate scale of $0\farcs028 \times 0\farcs025$ pixel^{-1}. Because of the large, but

Table 6.2 Log of the ACS and WFPC2 observations.

Galaxy	Filter	Pivot λ (Å)	Width (Å)	Exp. Time (s)	Obs. Date
(1)	(2)	(3)	(4)	(5)	(6)
		ACS			
Abell 1836-BCG	F435W	4311	310	2×895	2004 Feb 20
	FR656N	6803	136	2×1382.5	2004 Feb 20
Abell 2052-BCG	F435W	4311	310	2×900	2003 Sep 3
	FR656N	6788	136	2×1380	2003 Sep 3
Abell 3565-BCG	F435W	4317	293	2×900	2004 Aug 7
	FR656N	6645	133	2×1388	2004 Aug 7
		WFPC2			
Abell 1836-BCG	F814W	8012	1539	2×500	2001 Apr 11
Abell 2052-BCG	F814W	8012	1539	2×500	2001 Apr 17
Abell 3565-BCG	F814W	8012	1539	$1 \times 900 + 5 \times 1100 + 4 \times 1300$	1996 Jan 19-20

NOTES. — Col. (1): Galaxy name. Col. (2): Filter name. Col. (3): Pivot wavelength (ACS: Sirianni et al. 2005, WFPC2: Heyer et al. 2004). Col. (4): Filter width (ACS: Sirianni et al. 2005, WFPC2:Heyer et al. 2004). Col. (5): Total exposure time. Col. (6): Observation date.

well characterized, geometric distortion affecting the ACS, the $29'' \times 26''$ HRC field of view projects on the plane of the sky as a rhomboid with x and y axes forming a $84^{\circ}.2$ angle. Each galaxy was observed with two filters: F435W (which approximates the Johnson B-band) and the narrow-band ramp filter FR656N, tuned to cover a 130 Å wide spectral region centered on the redshifted Hα and [N II] $\lambda\lambda 6548, 6583$ emission expected at the nuclear location. To help in identifying and correcting cosmic ray events, two back-to-back exposures were taken with each filter.

The WFPC2 images, all employing the F814W filter (similar to the Kron-Cousin I band), belong to programs GO-5910 (P.I. T. Lauer) and GO-8683 (P.I. R.P. van der Marel) and were downloaded from the public *HST* archive. Two images with a total exposure time of 1000 s are available for each Abell 1836-BCG and Abell 2052-BCG, while ten images are available for Abell 3565-BCG, for a total 11,600 s exposure. In all cases, the galaxies are centered on the higher resolution Planetary Camera (PC), which consists of an 800×800 pixels Loral CCD with a plate scale of $0''.0455$ pixel^{-1}, yielding a nominal field of view of $36'' \times 36''$. For both ACS and WFPC2 images, the telescope was guiding in fine lock, giving a typical rms tracking error per exposure of $0''.005$.

All images were calibrated using the standard reduction pipelines maintained by the Space Telescope Science Institute (CalACS for the ACS images and CalWFPC for the WFPC2 images). Reduction steps include bias subtraction, dark current subtraction and flat-fielding, as described in detail in the

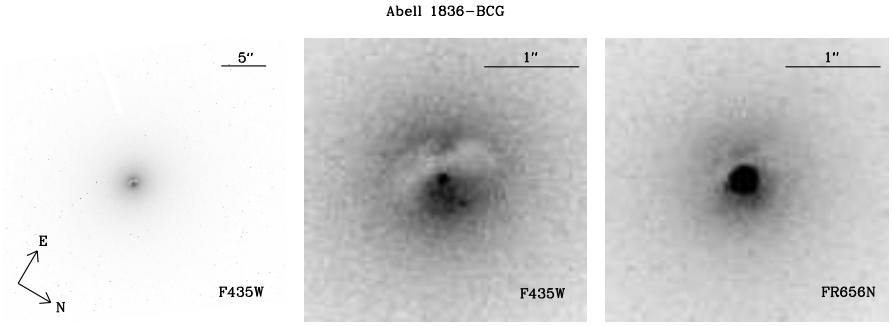

Figure 6.1 ACS/HRC images of Abell 1836-BCG. The panels show the F435W full frame (*left*) and a zoom toward the center (*center*). The same central section is shown in the *right panel* for the FR656N image. The grey-scale used for the left panel (full frame) is kept the same in Figures 6.1-6.3, while the gray-scale for the other panels changes from filter to filter in order to highlight the distribution of the nuclear dust. All images have been background subtracted.

ACS and WFPC2 instrument and data handbooks (Baggett et al. 2002; Heyer et al. 2004; Pavlovsky et al. 2004a,b).

Subsequent analysis was performed using standard tasks in IRAF [2]. For each galaxy, the alignment of images obtained with the same instrument and filter was checked by comparing the centroids of stars in the field of view; in all cases but one, the alignment was found to be better than a few hundredths of a pixel and the images were combined without further processing using IMCOMBINE. The exception are the WFPC2 images of Abell 3565-BCG, which were dithered by $\approx 1''$ relative to one another. These images were aligned using IMSHIFT prior to being combined.

In combining the images, pixels deviating by more than three times the local sigma – calculated from the combined effect of Poisson and read-out noise – were flagged as cosmic rays and rejected. Finally, the resulting ACS images were corrected for geometric distortion using PYDRIZZLE.

The final, calibrated ACS and WFPC2 images of each galaxy are shown in Figures 6.1−6.3 and 6.4, respectively.

[2]IRAF is distributed by the National Optical Astronomy Observatories which are operated by the Association of Universities for Research in Astronomy (AURA) under cooperative agreement with the National Science Foundation.

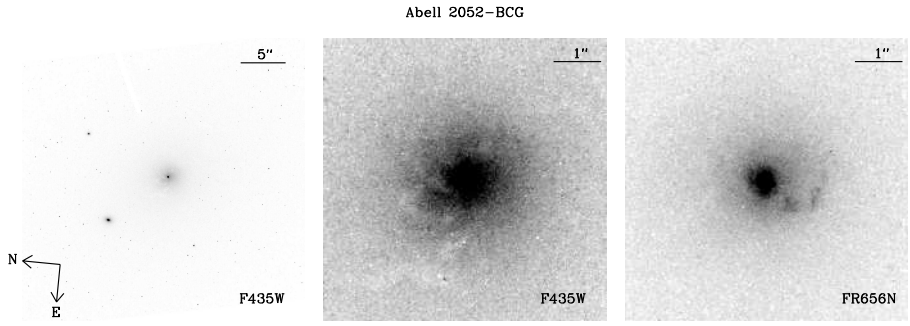

Figure 6.2 ACS/HRC images of Abell 2052-BCG. See Figure 6.1 for details.

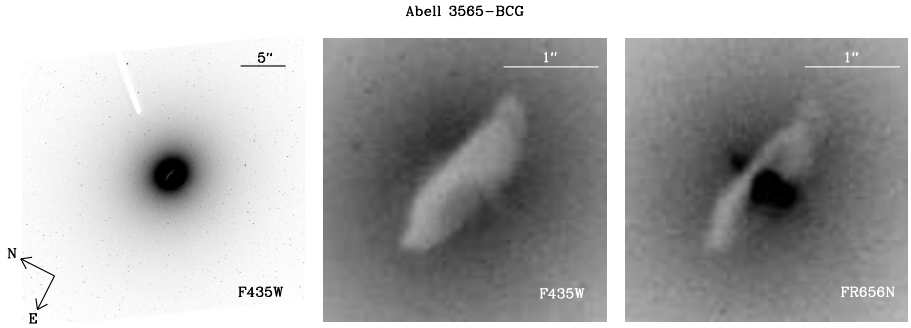

Figure 6.3 ACS/HRC images of Abell 3565-BCG. See Figure 6.1 for details.

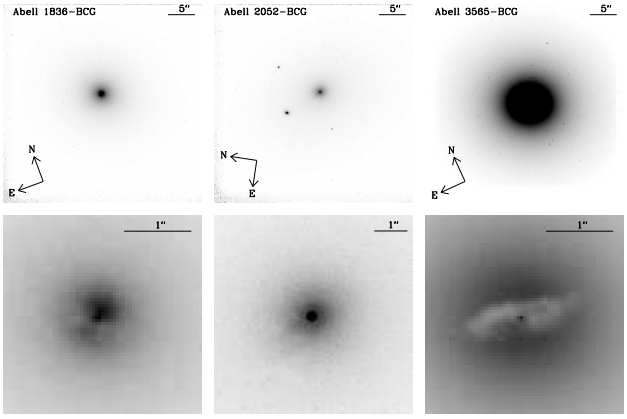

Figure 6.4 WFPC2/F814W images of Abell 1836-BCG (*left panels*), Abell 2052-BCG (*middle panels*), and Abell 3565-BCG (*right panels*). The *top panels* show the full frame, while the *bottom panels* show a zoom toward the center. The grey-scale used for the top (full frame) images is kept the same for all the three galaxies, while the gray-scale for the central sections changes from galaxy to galaxy to highlight the distribution of the nuclear dust. All images have been background subtracted.

6.3.2 Isophotal analysis

Isophotal parameters (coordinates X, Y of the isophotal center; surface brightness profile $I(\phi)$; ellipticity ϵ; major axis position angle θ; and deviations of the isophotes from pure ellipses) were measured using the IRAF task ELLIPSE (Jedrzejewski 1987). For each semi-major axis length, the best fitting set of parameters X, Y, ϵ and θ are those that minimize the sum of the squares of the residuals between the data and the first two moments of the Fourier series expansion of the azimuthally-sampled intensity

$$I(\phi) = I_0 + \sum_k [A_k \sin(k\phi) + B_k \cos(k\phi)] \tag{6.1}$$

The third and fourth order moments (A_3, B_3, A_4 and B_4) describe three and four-fold deviations of the isophotes from pure ellipses, respectively. The B_4 term in particular describes the shape by distinguishing boxy ($B_4 < 0$) from disky ($B_4 > 0$) galaxies.

The isophotal semi-major axis was increased logarithmically, with each isophote being fitted at a semi-major axis 10% longer than that of the isophote

preceding it. The dust structure in Abell 2052-BCG is localized enough not to affect significantly the recovery of the underlying stellar distribution, so all parameters were allowed to vary freely while fitting the isophotes. For the other galaxies, a fully unconstrained isophotal solution could be found only in the regions unaffected by dust ($r > 0''.6$ and $r > 0''.9$ for Abell 1836-BCG and Abell 3565-BCG, respectively). In the areas affected by dust, the isophotes were fitted by fixing both ellipticity and position angle to the average values obtained in the dust-unaffected region ($0''.6 < r < 10''$ and $0''.9 < r < 10''$ for Abell 1836-BCG and Abell 3565-BCG, respectively). In all cases, pixels deviating by more than three times the standard deviation of the mean intensity along each trial isophote were excluded from the fit, thereby avoiding contamination by foreground stars, companion galaxies (as in the case of Abell 2052-BCG), globular clusters, and bad pixels. All isophotal parameters are plotted in Figures 6.5–6.7 as a function of the "geometric mean" radius $r_{\rm geo}$, defined as $a[1-\epsilon(a)]^{1/2}$, a being the semi-major axis length.

Conversion of $I(\phi)$ (which is given in counts per seconds) to surface brightness in the AB magnitudes system was performed following (Holtzman et al. 1995a) for the WFPC2 images, and (Sirianni et al. 2005) for the ACS images:

$$\mu_{F814W} = -2.5 \log I_s(\phi)_{\rm F814W} + 14.998, \tag{6.2}$$

$$\mu_{\rm F435W} = -2.5 \log I_s(\phi)_{\rm F435W} + 16.150, \tag{6.3}$$

where $I_s(\phi)_{\rm F814W}$ and $I_s(\phi)_{\rm F435W}$ represent the azimuthally averaged, background subtracted intensity (in counts per second per pixel) in F814W and F435W respectively. Because the galaxies completely fill the field of view of the ACS/HRC and WFPC2/PC detectors, a nominal sky background, as listed in the ACS (Pavlovsky et al. 2004a) or WFPC2 (Heyer et al. 2004) Instrument Handbooks, was adopted.

6.3.3 Dust obscuration and optical depth map

Correction for dust obscuration is necessary to recover the intrinsic stellar luminosity density and the spatial distribution of the ionized gas within each galaxy. We adopted the procedure described in Ferrarese et al. (2006), which works under the assumption that the F435W-F814W intrinsic color of the galaxy in the regions obscured by dust can be estimated by linearly interpolating across the dust area (or extrapolating, if the dust affects the center) the azimuthally-averaged color measured in the regions unaffected by dust. The dust absorption

[2]Extinction in all relevant passbands are related to A(V) as $A_{\rm F435W}/A_{\rm V} = 1.362$, $A_{\rm F814W}/A_{\rm V} = 0.597$, $A_{\rm FR656N}/A_{\rm V} = 0.781, 0.783$, and 0.805 for Abell 1836-BCG, Abell 2052-BCG, and Abell 3565-BCG, respectively (Cardelli et al. 1989; Schlegel et al. 1998).

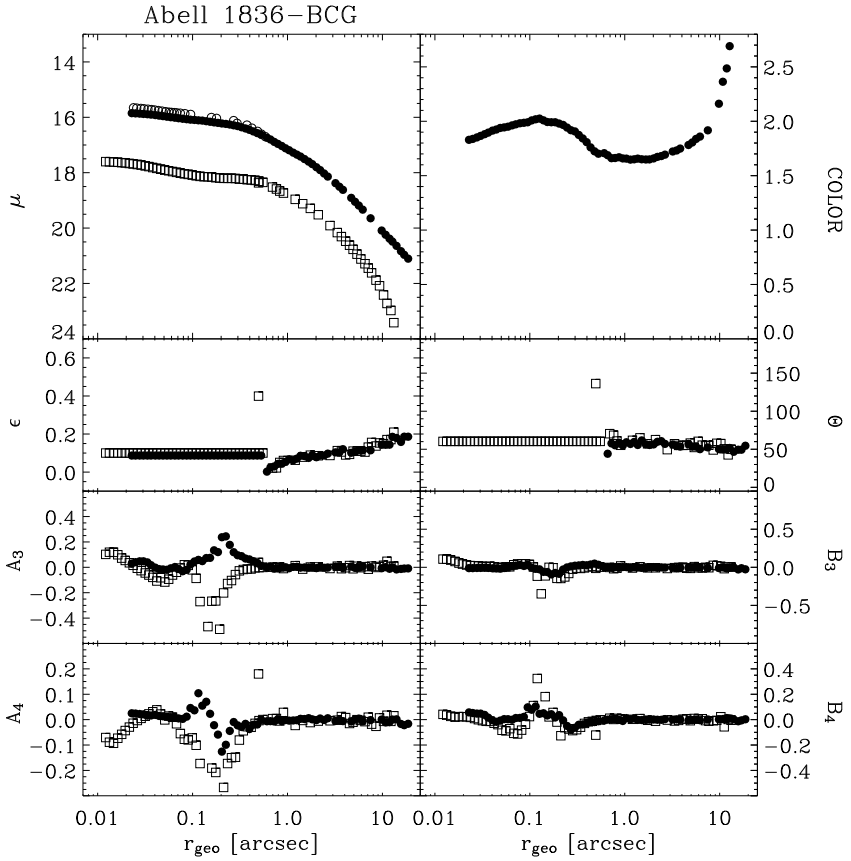

Figure 6.5 Isophotal parameters for Abell 1836-BCG plotted against the "geometric mean" radius $r_{\rm geo} = a(1-\epsilon)^{1/2}$, with a measured along the semimajor axis of the galaxy. The panels show the radial profiles of: surface brightness μ (in mag arcsec^{-2}) in ACS/F435W (squares) and WFPC2/F814W (filled circles) bands, F435W−F814W (filled circles) color, ellipticity ϵ, position angle θ (in degrees, measured from north to east), and parameters A_3, A_4, B_3, and B_4, measuring deviations of the isophotes from pure ellipses (see text for details). Open circles show the inner radial profile of μ measured on the WFPC2/F814W image corrected for dust obscuration (as described in the text) with the addition of the Galactic extinction correction by Schlegel et al. (1998).

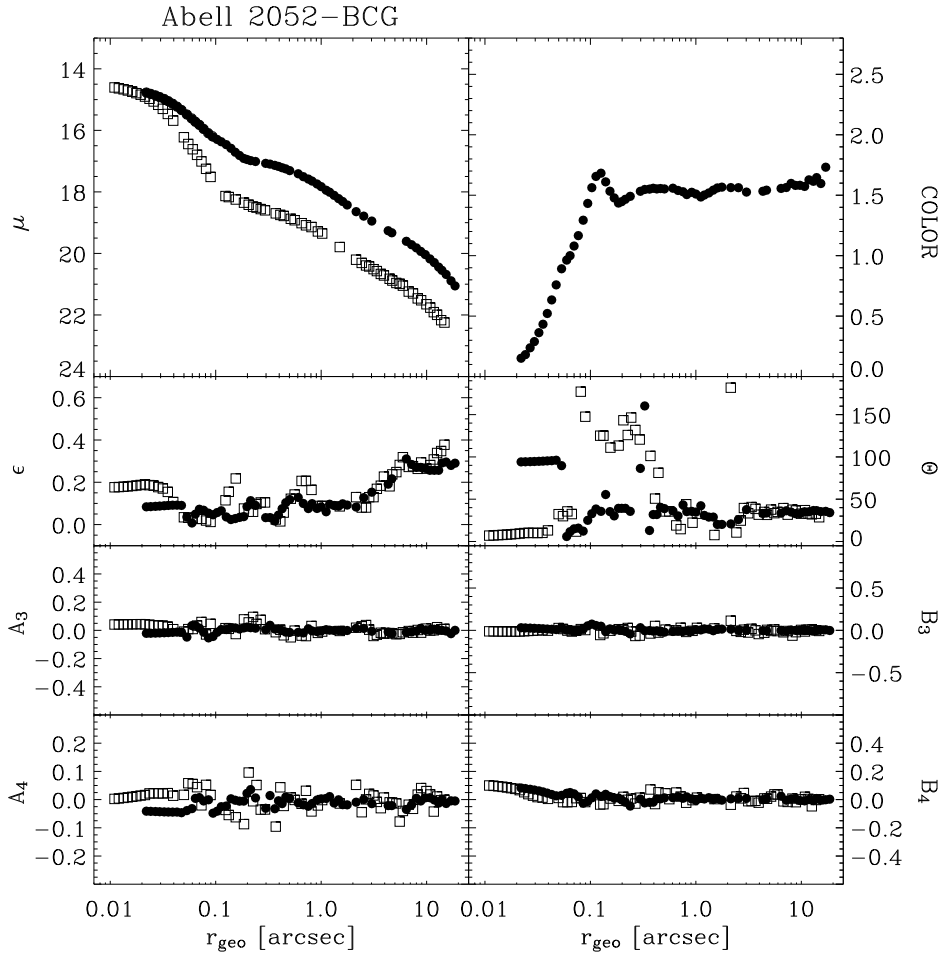

Figure 6.6 The same as for Figure 6.5, but for Abell 2052-BCG.

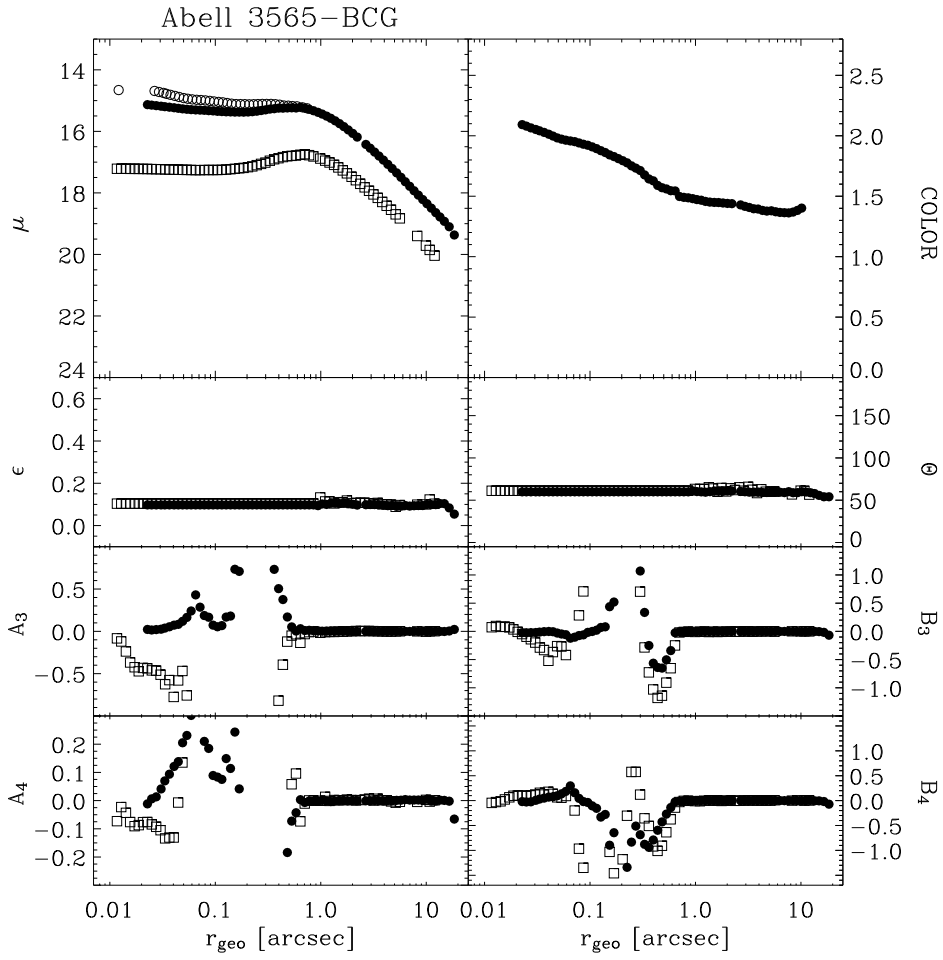

Figure 6.7 The same as for Figure 6.5, but for Abell 3565-BCG.

at each pixel then follows by comparing the intrinsic and observed (extincted) color maps, once the ratio of the absorption in F435W and F814W is known (see equation (2) of Ferrarese et al. 2006). The latter, $A_{\rm F435W}/A_{\rm F814W} = 2.2814$ (where A_λ is given in magnitudes), has been derived using the extinction law of Cardelli et al. (1989), integrated over the filter passbands, and assuming a ratio of total-to-selective absorption $R_V = 3.1$ (see also Schlegel et al. 1998). It is further assumed that the dust lies in the galaxy foreground (the "screen" approximation); the values quoted below for the dust absorption therefore represent firm lower limits to the true absorption. Once the absorption in a specific passband is known, the intrinsic fluxes are easily recovered simply by correcting the measured fluxes for the derived magnitude loss due to dust obscuration.

In producing the F435W-F814W color maps, the ACS images were rotated (using the information about the position angle of the telescope axis contained in the header) and resampled using PYDRIZZLE in order to match the orientation and scale of the lower-resolution WFPC2 images.

Dust absorption maps are shown in the left panel of Figures 6.8–6.10. In Abell 1836-BCG, the average extinction (corrected to the $V-$band[3]) within the regular nuclear dust disk is $\langle A(V)\rangle = 0.27$ mag, with values as high as $A(V)_{max} = 0.85$ mag (in the screen approximation). The nuclear dust disk in Abell 3565-BCG is quite similar, with $A(V)_{max} = 1.1$ mag and $\langle A(V)\rangle = 0.21$ mag. Recovering a dust extinction map for Abell 2052-BCG, in which the dust is distributed in an irregular filamentary pattern and the amount of extinction is more modest, was more challenging. Within the inner $\approx 1''$, we find $A(V)_{max} = 0.35$ mag and $\langle A(V)\rangle = 0.14$ mag. At larger radii, dust patches with lower levels of dust obscuration, although visible in the color maps, could not be properly modeled. These areas, which affect less than 50% of pixels along any given isophote, were simply masked when deriving the galaxy's surface brightness profile.

The extinction corrected F814W surface brightness profiles of the sample galaxies are shown in Figures 6.5–6.7.

6.3.4 Deprojected stellar density models

The deprojected luminosity density, $\Gamma(x, y, z)$, needed to constrain the stellar gravitational potential, was recovered from the redder (and thereby less affected by dust obscuration), extinction corrected, WFPC2/F814W images, using the multi-Gaussian expansion (MGE) method (Monnet et al. 1992; Emsellem et al.

[3]Extinction in all relevant passbands are related to A(V) as $A_{\rm F435W}/A_{\rm V} = 1.362$, $A_{\rm F814W}/A_{\rm V} = 0.597$, $A_{\rm FR656N}/A_{\rm V} = 0.781, 0.783$, and 0.805 for Abell 1836-BCG, Abell 2052-BCG, and Abell 3565-BCG, respectively (Cardelli et al. 1989; Schlegel et al. 1998).

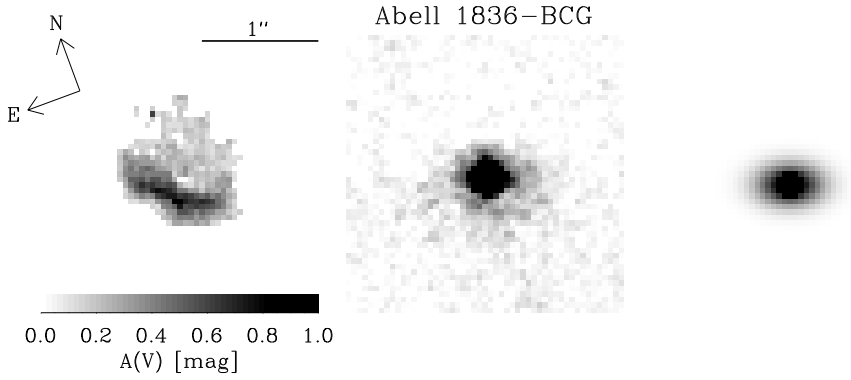

Figure 6.8 Optical depth map of Abell 1836-BCG (*left panel*), and continuum-subtracted emission-line images in the ACS/FR656N band pass before (*central panel*) and after deconvolution (*right panel*). The field of view is $6''.9 \times 6''.9$. Orientation and scale are given in the left panel and they are kept the same for all the panels.

1994), as implemented by (Cappellari 2002, see also Section 5.3.1) [4].

Briefly, the MGE procedure starts by determining the galaxy's average ellipticity, position angle, and coordinates of the luminosity-weighted center. The galaxy image is then divided in quadrants, and a number of photometric profiles is measured along sectors uniformly spaced in angle from the major axis to the minor axis. Surface brightness profiles from sectors in the four quadrants are averaged together (an acceptable simplification for our galaxies since position angle and isophotal center do not show a significant radial dependency), and each is then fitted as the sum of Gaussian components. The best-fitting MGE model surface brightness is then determined iteratively by comparison with the observed surface brightness, after having been convolved with the instrumental PSF (generated, in our case, using the TINY TIM package, Krist & Hook 1999, and parameterized as the sum of circular Gaussians). The Gaussian width coefficients of the MGE model were constrained to be a set of logarithmically-spaced values, thus simplifying the fitting algorithm into a general non-negative least-squares problem for the corresponding Gaussian amplitudes. During the entire procedure, pixels for which correction for dust obscuration did not perform correctly (as in the case of Abell 2052-BCG) were masked.

The best-fitting MGE model (prior to PSF convolution) is then deprojected to a luminosity density $\Gamma(r)$ under the assumption that the galaxy is spherically

[4] It is available at http://www-astro.physics.ox.ac.uk/∼mxc/idl/

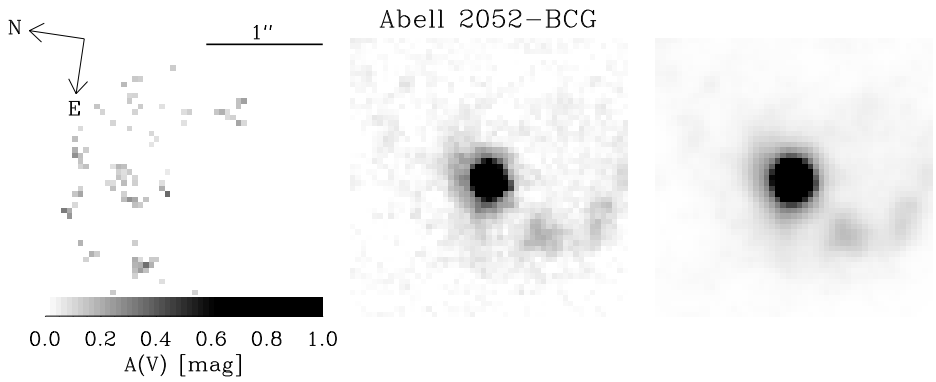

Figure 6.9 As in Figure 6.8, but for Abell 2052-BCG.

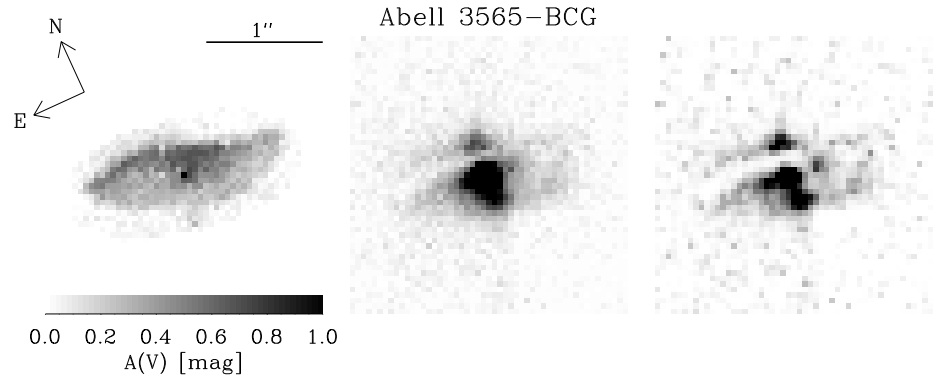

Figure 6.10 As in Figure 6.8, but for Abell 3565-BCG.

symmetric – a justifiable simplification since the isophotes are nearly circular throughout the main body of our galaxies, including the radial range where the ionized-gas kinematics probes the galaxy potential (where however uncertainties are larger due to the presence of dust residuals, see Figures 6.5–6.7). For a radially-independent mass-to-light ratio, $(M/L)_\star$, the stellar mass density $\rho(r)$ is then simply expressed as $\rho(r) = (M/L)_\star \Gamma(r)$, and the stellar gravitational potential can be expressed in terms of error functions. The best-fitting, PSF-convolved MGE models to the observed surface-brightness profiles are shown in Figures 6.11–6.13, along with the deprojected luminosity density profiles (prior to PSF-convolution), and the corresponding circular velocity curves (for $(M/L)_\star = 1$).

6.3.5 Ionized-gas distribution

Continuum-free emission-line images for the sample galaxies were obtained by subtracting the WFPC2/F814W images from the ACS/FR656N images which isolate the spectral region characterized by the redshifted Hα and [N II] $\lambda\lambda$6548, 6583 emission lines. All images were previously extinction corrected as described in Section 6.3.3, after having been resampled and rotated in order to match the pixel scale and orientation of the lower-resolution WFPC2/F814W images. Before subtraction, the FR656N images were multiplied by a factor equal to the mean ratio between the F814W and resampled FR656N images, calculated in emission-free regions. The resulting emission line maps are shown in the central panels of Figures 6.8–6.10. The intrinsic (prior to PSF broadening) surface-brightness distribution of the ionized gas, a key input to our modeling, was obtained independently using both the iterative method based on the Lucy-Richardson algorithm (Richardson 1972; Lucy 1974) and the MGE method already described in Section 6.3.4. According to van den Bosch & Emsellem (1998) the two methods give consistent results, however, one might be preferable to the other depending on the specifics of the images (e.g., signal-to-noise ratio S/N, presence of asymmetric features, etc..). Both methods employed the PSF generated using TINY TIM for the WFPC2/F814W images. The Lucy-Richardson algorithm, as implemented in the IRAF task LUCY, was found to give satisfactory results in the case of Abell 2052-BCG and Abell 3565-BCG, for which the method converged after only five and six iterations, respectively. In the case of Abell 1836-BCG, for which the emission-line images have lower S/N, LUCY produced unacceptable noise amplification before convergence could be reached, and the intrinsic emission-line distribution was therefore recovered using the MGE method. We note that the latter failed to produce acceptable results for Abell 2052-BCG and Abell 3565-BCG, for which the distribution of

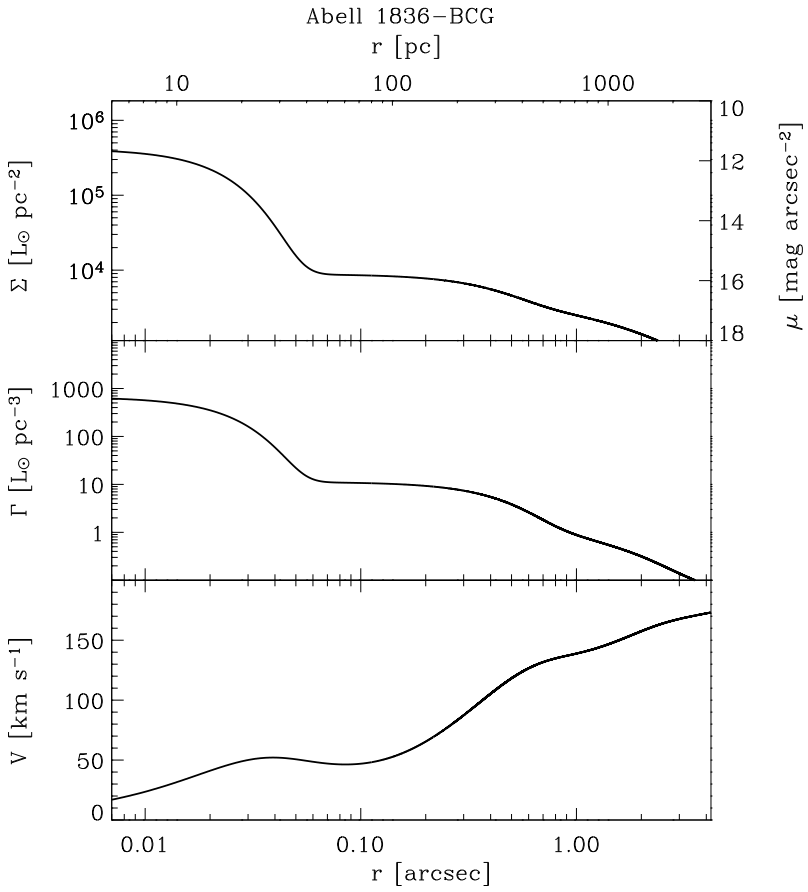

Figure 6.11 Deprojection steps for the stellar mass profile of Abell 1836-BCG. *Top panel:* Multi-Gaussian fit to the PSF-deconvolved surface brightness profile derived from the extinction-corrected WFPC2/F814W image. *Middle panel:* Deprojected stellar luminosity density profile. *Bottom panel:* Circular velocity curve assuming $(M/L)_\star = 1$.

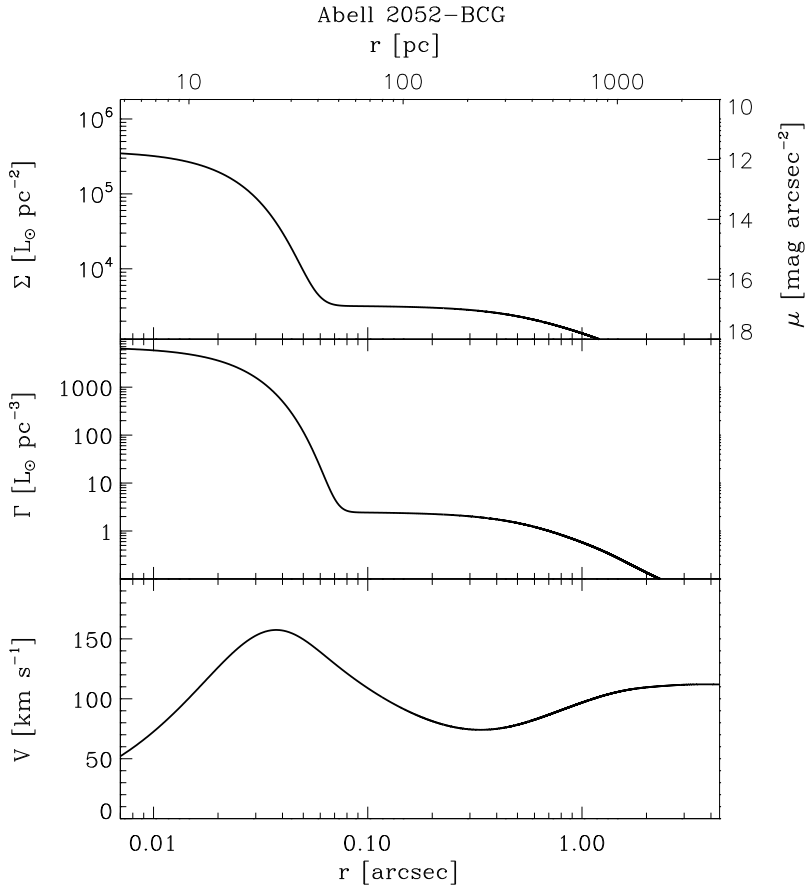

Figure 6.12 As in Figure 6.11, but for Abell 2052-BCG.

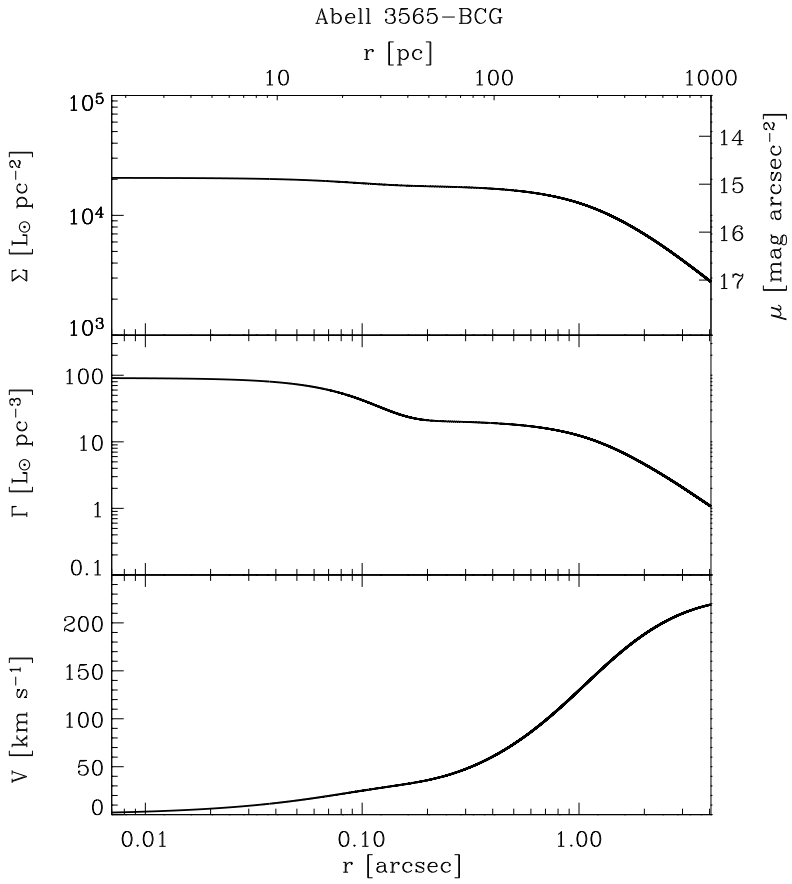

Figure 6.13 As in Figure 6.11, but for Abell 3565-BCG.

the ionized gas is less symmetric, violating the four-fold symmetry required by the MGE algorithm. The deconvolved surface-brightness distributions of the emission line gas are shown in the right panels of Figures 6.8–6.10.

6.4 Observations, data reduction and analysis: STIS spectroscopy

The spectroscopic observations of the sample galaxies were carried out with STIS between 2003 August 16 and 2004 February 21 as part of program GO-9838. The G750M grating was used at the prime tilt in combination with the $0\farcs1\times52''$ slit for Abell 1836-BCG and Abell 2052-BCG, and the $0\farcs2\times52''$ slit for Abell 3565-BCG. The slit width was selected to ensure that the sphere of influence of the SMBH estimated to reside in each galaxy (based on the $M_\bullet - \sigma$ and $M_\bullet - M_B$ relations) could be comfortably resolved, while at the same time allowing for reasonable throughput. The G750M grating covers the wavelength range from 6480 Å to 7050 Å, which includes the Hα, [N II] $\lambda\lambda6548, 6583$, and [S II] $\lambda\lambda6716, 6731$ emission lines. The dispersion is 0.56 Å pixel^{-1}, and the instrumental resolution is 0.83 Å (FWHM, corresponding to $\sigma_{\rm instr} \simeq 16.0$ km s^{-1} at [N II] $\lambda6583$) for the $0\farcs1\times52''$ slit, and 1.5 Å ($\sigma_{\rm instr} \simeq 30.5$ km s^{-1}) for the $0\farcs2\times52''$ slit (see also Section 2.3). The spatial scale of the 1024×1024 SITe CCD is $0\farcs05$ pixel^{-1}.

For each target galaxy, spectra were taken at three different slit positions, the first crossing the nucleus of the galaxy, and two additional ones displaced by one slit width ($0\farcs1$ for Abell 1836-BCG and Abell 2052-BCG, and $0\farcs2$ for Abell 3565-BCG) on either side, perpendicularly to the slit axis. All slits were oriented along the photometric major axis. In the case of Abell 3565-BCG, for which the wider slit allowed for shorter exposure times, one spectrum was taken at each slit position. For Abell 1836-BCG and Abell 2052-BCG two spectra were taken at each location, the second shifted along the slit axis by four pixels to facilitate removal of bad pixels and other CCD defects. A 90 s tungsten lamp flat exposure was taken after each galaxy spectrum, to correct for the fringing affecting the STIS CCD at wavelengths longer than ≈ 7000 Å. A log of the STIS observations can be found in Table 6.3.

The spectra were reduced using the CALSTIS reduction pipeline maintained by STScI. The basic reduction steps included overscan subtraction, bias subtraction, dark subtraction, flatfield correction, wavelength calibration as well as correction for geometric distortion. Correction for fringing was performed with the DEFRINGE task. In the case of Abell3565-BCG, for which only one spectrum is available at each slit location, cosmic ray events and hot pixels were removed using the task LACOS_SPEC (van Dokkum 2001). For the other two

Table 6.3 Log of the STIS observations.

Galaxy	Offset ($''$)	PA ($^\circ$)	Exp. Time (s)	Obs. Date
(1)	(2)	(3)	(4)	(5)
	0.0	−127.9	2040 + 2800	2004 Feb 21
Abell 1836-BCG	−0.1	−127.9	2 × 2800	2004 Feb 21
	+0.1	−127.9	2 × 2800	2004 Feb 21
	0.0	51.0	2030 + 2800	2003 Sept 2
Abell 2052-BCG	−0.1	51.0	2 × 2800	2003 Sept 2
	+0.1	51.0	2 × 2800	2003 Sept 2
	0.0	75.4	2010	2003 Aug 16
Abell 3565-BCG	−0.2	75.4	2735	2003 Aug 16
	+0.2	75.4	2735	2003 Aug 16

NOTES. — Col. (1): Galaxy name. Col. (2): Measured offset of the slit center with respect to the galaxy nucleus. Col. (3): Position angle of the slit, measured from north to east. Col. (4): Total exposure time. Col. (5): Observation date.

galaxies, the two spectra obtained at the same slit position were aligned with IMSHIFT using the center of the stellar-continuum radial profile as a reference, and then combined using IMCOMBINE. Cosmic ray rejection was performed with the CRREJECT option in IMCOMBINE, additionally, pixels flagged by running LACOS_SPEC separately on each spectrum were also removed. The sky background was determined from the combined, calibrated spectra between $15''$ and $30''$ from the nucleus and then subtracted. Finally, individual spectra were extracted every $0''.05$ (corresponding to 1 pixel) up to $\approx 0''.2$, $0''.3$, and $0''.7$ from the center for Abell 1836-BCG, Abell 2052-BCG, and Abell 3565-BCG, respectively. At larger radii, the decreasing intensity of the emission lines required binning in the spatial direction (see Table 6.4 and Figures 6.14–6.16 for details) to obtain a S/N of at least 10 at the peak of the [N II] λ6583 emission line in the combined spectrum, a condition deemed necessary for an accurate measurement of the line kinematics (Section 4.1). The final spectra along the major and offset axes of the sample galaxies are plotted in Figures 6.14(b)–6.16(b).

The location of the slit relative to the galaxy center was checked using STIS images taken after acquisition of the target galaxies. A series of "synthetic" slits were extracted from the acquisition images by averaging four adjacent columns for Abell 1836-BCG and Abell 2052-BCG (corresponding to a $0''.1$-wide slit), and eight adjacent columns for Abell 3565-BCG (corresponding to a $0''.2$-wide slit) at the nominal slit orientation. The radial brightness profiles in each synthetic slit were then compared to the profiles obtained by collapsing the spectrum at the nuclear location along the wavelength direction. The best

match was determined by minimizing the χ^2 of the difference between the light profile of the spectrum and the light profile extracted from the acquisition image. In all cases, the slits were found to be all positioned at the nominal locations.

6.4.1 Measurement of the emission lines

The ionized-gas kinematics were measured from the narrow [N II] λ6583 line, the brightest of the lines detected in our spectra. This line is preferred to Hα since the latter is more severely blended, and could be significantly affected by emission from circumnuclear star-forming regions (e.g., Verdoes Kleijn et al. 2000; Coccato et al. 2006).

The emission lines central wavelengths, FWHMs, and intensities were measured following Beifiori et al. (2009) (see also Sections 2.3.3 and 3.2.2). The best-fitting Gaussian parameters were derived using a non-linear least-squares minimization based on the robust Levenberg-Marquardt method (e.g., Press et al. 1992) implemented by Moré et al. (1980). The actual computation was done using the MPFIT algorithm[5] implemented by C. B. Markwardt under the IDL[6] environment.

Because the line profiles are assumed to be Gaussian, it was often necessary to include two components in order to reproduce the extended wings observed for several of the emission lines (most notably Hα but, in some cases, also [N II] $\lambda\lambda$6548, 6583 and [S II] $\lambda\lambda$6716, 6731). Lines in the same doublet ([N II] and [S II]) were assumed to have the same velocity and velocity width. A flux ratio of 1:2.967 was assumed for the two [N II] lines, as dictated by atomic physics (e.g., Osterbrock 1989). The stellar continuum was approximated with a low-order polynomial.

The major axis spectrum of Abell 1836-BCG displays both a narrow and a broad Hα line within the inner $0''.25$. The broad-line emission appears to be spatially extended, with FWHM of $0''.17$, compared to the typical FWHM of the STIS PSF ($\sim 0''.075$). Only the $-0''.1$ offset spectrum shows a broad Hα component within the inner $0''.1$ (two rows), which possibly originates in the same nebular complex that gives rise to the broad-line emission observed along the central slit.

Only the major axis spectrum of Abell 3565-BCG displays broad-line emissions. Within the inner $0''.15$ the spectrum shows an Hα component while from $0''.15$ to $0''.41$ it shows broad components in Hα, [N II] $\lambda\lambda$6548, 6583, and [S II] $\lambda\lambda$6716, 6731. The broad Hα emission is spatially extended, with a FWHM

[5]The code is available on http://cow.physics.wisc.edu/∼craigm/idl/idl.html
[6]Interactive Data Language is distributed by Research System Inc.

Table 6.4: [N II] λ6583 kinematics.

r [″] (1)	V (km s^{-1}) (2)	σ km s^{-1}) (3)	r (″) (4)	V (km s^{-1}) (5)	σ (km s^{-1}) (6)	r (″) (7)	V (km s^{-1}) (8)	σ (km s^{-1}) (9)
				Abell 1836-BCG				
	+0″.1 offset			major axis			−0″.1 offset	
−0.23	11382 ± 25	80 ± 28	−0.23	11500 ± 28	165 ± 27	−0.23	11418 ± 24	133 ± 24
−0.18	11398 ± 51	256 ± 52	−0.18	11422 ± 31	289 ± 31	−0.18	11361 ± 17	137 ± 18
−0.13	11402 ± 53	369 ± 51	−0.13	11455 ± 18	266 ± 22	−0.13	11341 ± 18	200 ± 18
−0.08	11288 ± 26	306 ± 27	−0.08	11413 ± 11	294 ± 13	−0.08	11283 ± 18	275 ± 19
−0.03	11307 ± 19	286 ± 20	−0.03	11369 ± 11	370 ± 13	−0.03	11237 ± 30	396 ± 38
0.02	11199 ± 17	228 ± 17	0.02	11118 ± 13	362 ± 17	0.02	11094 ± 35	260 ± 31
0.07	11202 ± 43	346 ± 45	0.07	11001 ± 13	208 ± 17	0.07	11082 ± 30	301 ± 43
0.12	11094 ± 21	132 ± 22	0.12	10993 ± 11	114 ± 12	0.12	11024 ± 60	241 ± 64
0.17	11091 ± 28	164 ± 29	0.17	10978 ± 20	123 ± 21			
0.22	11014 ± 14	51 ± 19	0.22	10982 ± 21	92 ± 23			
				Abell 2052-BCG				
	+0″.1 offset			major axis			−0″.1 offset	
−0.25	10189 ± 27	103 ± 28	−0.30	10172 ± 56	209 ± 56	−0.30	10100 ± 17	83 ± 18
−0.20	10220 ± 39	229 ± 37	−0.25	10156 ± 34	179 ± 31	−0.25	10011 ± 33	213 ± 30
−0.15	10247 ± 17	158 ± 16	−0.20	10130 ± 17	183 ± 17	−0.20	9979 ± 13	193 ± 13
−0.10	10318 ± 16	169 ± 16	−0.15	10160 ± 15	176 ± 23	−0.15	9912 ± 11	102 ± 15
−0.05	10330 ± 8	132 ± 9	−0.10	10154 ± 10	171 ± 16	−0.10	9908 ± 7	186 ± 9
0.00	10329 ± 11	169 ± 12	−0.05	10220 ± 9	150 ± 13	−0.05	9930 ± 7	199 ± 9
0.0	10348 ± 15	211 ± 15	0.00	10436 ± 18	294 ± 20	0.00	10075 ± 12	168 ± 16
0.10	10312 ± 23	236 ± 22	0.05	10494 ± 23	190 ± 28	0.05	10186 ± 25	215 ± 29
0.15	10311 ± 16	176 ± 15	0.10	10364 ± 19	187 ± 21	0.10	10242 ± 26	162 ± 35
0.20	10311 ± 22	132 ± 22	0.15	10251 ± 23	199 ± 21	0.15	10236 ± 16	147 ± 16
0.25	10313 ± 21	97 ± 21	0.20	10251 ± 16	133 ± 16	0.20	10242 ± 21	191 ± 21
0.30	10328 ± 29	194 ± 29	0.25	10263 ± 12	83 ± 13	0.25	10296 ± 15	73 ± 16
0.36	10268 ± 22	97 ± 23	0.30	10301 ± 30	138 ± 30			
0.41	10459 ± 35	109 ± 36	0.36	10293 ± 88	159 ± 89			
0.46	10312 ± 14	38 ± 19	0.46	10293 ± 32	113 ± 33			
				Abell 3565-BCG				
	+0″.1 offset			major axis			−0″.1 offset	
−0.76	4018 ± 20	86 ± 23	−0.81	4011 ± 13	62 ± 16	−0.71	4015 ± 26	135 ± 27
−0.71	4010 ± 11	80 ± 12	−0.71	4045 ± 24	133 ± 25	−0.61	4054 ± 18	86 ± 21
−0.66	4020 ± 11	97 ± 12	−0.66	4073 ± 16	113 ± 17	−0.56	3999 ± 11	69 ± 13
−0.61	4046 ± 12	115 ± 13	−0.61	4057 ± 14	88 ± 16	−0.51	4006 ± 16	112 ± 17
−0.56	4032 ± 9	107 ± 9	−0.56	4064 ± 13	100 ± 14	−0.46	4017 ± 15	113 ± 16
−0.51	4057 ± 10	132 ± 11	−0.51	4102 ± 16	119 ± 17	−0.41	3987 ± 15	120 ± 16
−0.46	4077 ± 12	154 ± 12	−0.46	4101 ± 15	117 ± 16	−0.36	3976 ± 13	110 ± 14
−0.41	4073 ± 11	142 ± 12	−0.41	4085 ± 14	111 ± 15	−0.30	3970 ± 12	97 ± 13
−0.36	4054 ± 13	177 ± 12	−0.36	4099 ± 13	143 ± 14	−0.25	3954 ± 8	82 ± 10
−0.30	4028 ± 12	181 ± 12	−0.30	4116 ± 16	193 ± 16	−0.20	3939 ± 8	107 ± 9
−0.25	4032 ± 13	213 ± 14	−0.25	4125 ± 12	206 ± 12	−0.15	3898 ± 9	147 ± 10
−0.20	4016 ± 10	224 ± 10	−0.20	4077 ± 9	204 ± 10	−0.10	3866 ± 6	115 ± 7
−0.15	3970 ± 8	227 ± 9	−0.15	4068 ± 19	226 ± 14	−0.05	3833 ± 5	112 ± 6
−0.15	3971 ± 8	234 ± 8	−0.10	4116 ± 15	251 ± 15	0.00	3824 ± 4	109 ± 4
−0.10	3926 ± 5	206 ± 5	−0.05	4084 ± 17	399 ± 18	0.05	3815 ± 4	97 ± 4
−0.05	3874 ± 4	191 ± 4	0.00	3830 ± 13	451 ± 16	0.10	3804 ± 4	99 ± 5
0.00	3818 ± 3	155 ± 3	0.05	3673 ± 6	254 ± 8	0.15	3746 ± 15	195 ± 15
0.05	3791 ± 3	138 ± 3	0.10	3607 ± 6	203 ± 8	0.20	3725 ± 12	167 ± 12
0.10	3762 ± 5	164 ± 5	0.15	3590 ± 8	171 ± 10	0.25	3681 ± 16	176 ± 17
0.15	3729 ± 8	201 ± 8	0.20	3572 ± 14	149 ± 15	0.30	3685 ± 16	134 ± 16
0.20	3686 ± 9	204 ± 9	0.25	3599 ± 8	181 ± 8	0.36	3669 ± 17	155 ± 17
0.25	3655 ± 11	165 ± 11	0.30	3551 ± 11	166 ± 11	0.41	3629 ± 22	163 ± 23
0.30	3652 ± 10	150 ± 10	0.36	3551 ± 14	179 ± 14	0.46	3670 ± 19	168 ± 20
0.36	3648 ± 9	130 ± 9	0.41	3583 ± 23	260 ± 23	0.51	3650 ± 19	130 ± 20
0.41	3636 ± 8	96 ± 9	0.46	3566 ± 22	195 ± 23	0.56	3685 ± 11	81 ± 12
0.46	3621 ± 10	120 ± 11	0.51	3523 ± 37	195 ± 37	0.61	3659 ± 13	99 ± 15
0.51	3588 ± 14	140 ± 15	0.56	3583 ± 40	216 ± 41	0.66	3672 ± 21	150 ± 22
0.56	3582 ± 13	149 ± 14	0.61	3495 ± 22	119 ± 23	0.71	3629 ± 17	85 ± 19
0.61	3595 ± 11	109 ± 12	0.66	3481 ± 26	94 ± 29	0.76	3671 ± 16	68 ± 20
0.66	3622 ± 13	101 ± 14	0.76	3552 ± 29	119 ± 31			
0.71	3624 ± 18	94 ± 20						

NOTES. — Col. (1)-(3): Galactocentric distance, line-of-sight heliocentric velocity (uncorrected for inclination), and line-of-sight velocity dispersion (uncorrected for instrumental velocity dispersion) measured from the [N II] λ6583 line in the +0″.1 offset spectrum. Col. (4)-(6): As in Col. (1)-(3) but for the major-axis spectrum. Col. (7)-(9): As in Col. (1)-(3) but for the −0″.1 offset spectrum.

of 0″.13.

The major-axis and the −0″.1 offset spectra of Abell 2052-BCG show both narrow and broad components in Hα, [N II] $\lambda\lambda$6548, 6583, and [S II] $\lambda\lambda$6716, 6731 within the inner 0″.30. The 0″.1 offset spectrum shows all the broad components in the inner 0″.1. The broad lines have a FWHM of 0″.10 for Hα, 0″.12 for the [N II] doublet, 0″.18 for [S II] λ6716, and 0″.08 for [S II] λ6731 ([S II] broad lines have the same radial extension). They appear to be less extended than for the other two galaxies, although still marginally resolved.

Figures 6.17–6.19 show the results of the multi-Gaussian fitting for the spectra extracted at the nuclear location, and at a location displaced, along the major axis, by $\approx$ 70 parsec (0″.15, 0″.10, and 0″.25 for Abell 1836-BCG, Abell 2053-BCG, and Abell 3565-BCG respectively).

Line-of-sight heliocentric velocities, velocity dispersions and line intensities measured from the [N II] λ6583 line along the major and offset axes of the nuclear dust disks are plotted in Figures 6.14(c)–6.16(c) and listed in Table 6.4.

6.4.2 Ionized-gas kinematics and dust morphology

In the remainder of this Section, we will comment briefly on the kinematics of each individual galaxy. Before doing so, we note that both Abell 1836-BCG and Abell 3565-BCG display regular and symmetric velocity fields, as suggested by the smoothness and regularity of the ionized-gas disks. In contrast, Abell 2052-BCG, which is characterized by a more irregular emission-line morphology, shows irregular kinematics.

Abell 1836-BCG. The rotation curve, velocity dispersion profile, and flux profile along the major axis are relatively regular (Figure 6.14c), which makes this object appealing for dynamical modeling. The rotation velocity increases rapidly within the inner 0″.1, reaching approximately 200 km s^{-1}, and flattening at larger distances. The velocity dispersion peaks at about 370 km s^{-1} at the nuclear location, and declines on either side, although not symmetrically. The off-axis kinematics show a similar pattern.

Abell 2052-BCG. The dust distribution in this galaxy is somewhat irregular, with several filaments distributed in a spiral-like pattern (Figure 6.2). This lack of symmetry is reflected in the flux distribution of the ionized gas, which is also not symmetric with respect to the center (lower panels of Figure 6.15c), and in the [N II] λ6583 kinematics, which could be measured out to about 0″.3 from the center along each slit positions (Figure 6.15c). At the nuclear location, the maximum rotation velocity (200 km s^{-1}) is reached at 0″.05, with the velocity decreasing on either side, while the velocity dispersion curve is more symmetric, reaching $\approx$ 500 km s^{-1}at the nuclear location. The spectra flanking the nuclear

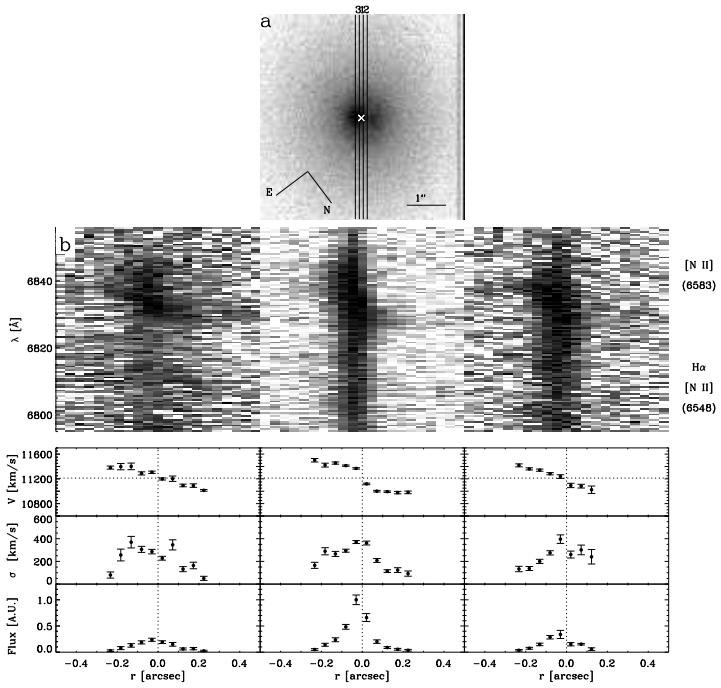

Figure 6.14 *a) HST* STIS/F28X50LP acquisition image of Abell 1836-BCG. The image has been rotated to the STIS instrumental frame. Orientation and scale are given. The white cross is the position of the nucleus from STIS acquisition procedure. The rectangles overplotted on the image show the actual locations of the slit during the spectroscopic observations. *b)* Portions of the bidimensional STIS spectra obtained in position 1 (major axis of the dust disk, *central panel*), 2 ($-0''.1$ offset, *left panel*) and 3 ($+0''.1$ offset, *right panel*). The spectral region centered on the Hα emission line is shown after wavelength calibration, flux calibration and geometrical rectification. The spatial axis is horizontal and ranges between $-0''.5$ and $+0''.5$, while the wavelength axis is vertical and ranges from 6795 to 6856 Å. Individual emission lines ([N II] λ6548, Hα, and [N II] λ6583) are identified on the right side of the figure. *c)* [N II] λ6583 kinematics from the spectra obtained in position 1 (*central panels*), 2 (*right panels*) and 3 (*left panels*). For each slit position the line-of-sight velocity curve (*top panel*), the radial profile of the line-of-sight velocity dispersion (uncorrected for instrumental velocity dispersion, *middle panel*), and the radial profile of line flux in arbitrary units (*bottom panel*) are given. Heliocentric velocities and velocity dispersions are not corrected for inclination and instrumental velocity dispersion, respectively.

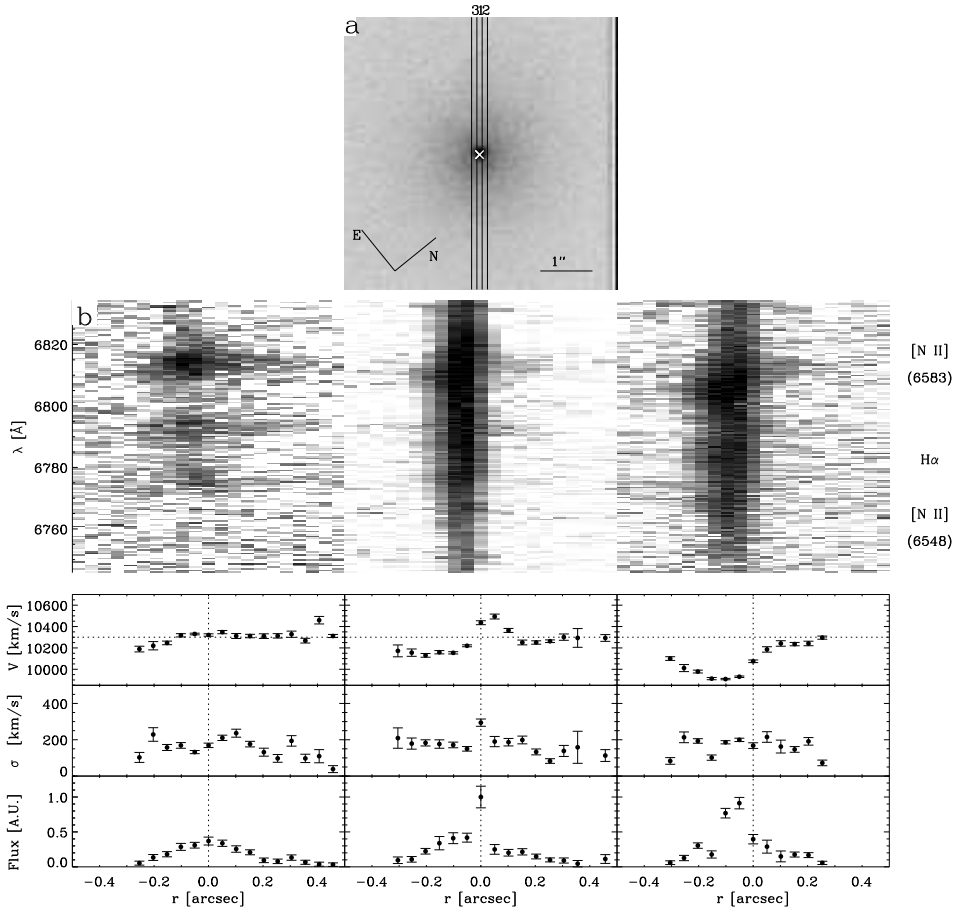

Figure 6.15 As in Figure 6.14, but for Abell 2052-BCG. In *b)* the spatial axis is horizontal and ranges between $-0''.5$ and $+0''.5$, while the wavelength axis ranges from 6746 to 6834 Å.

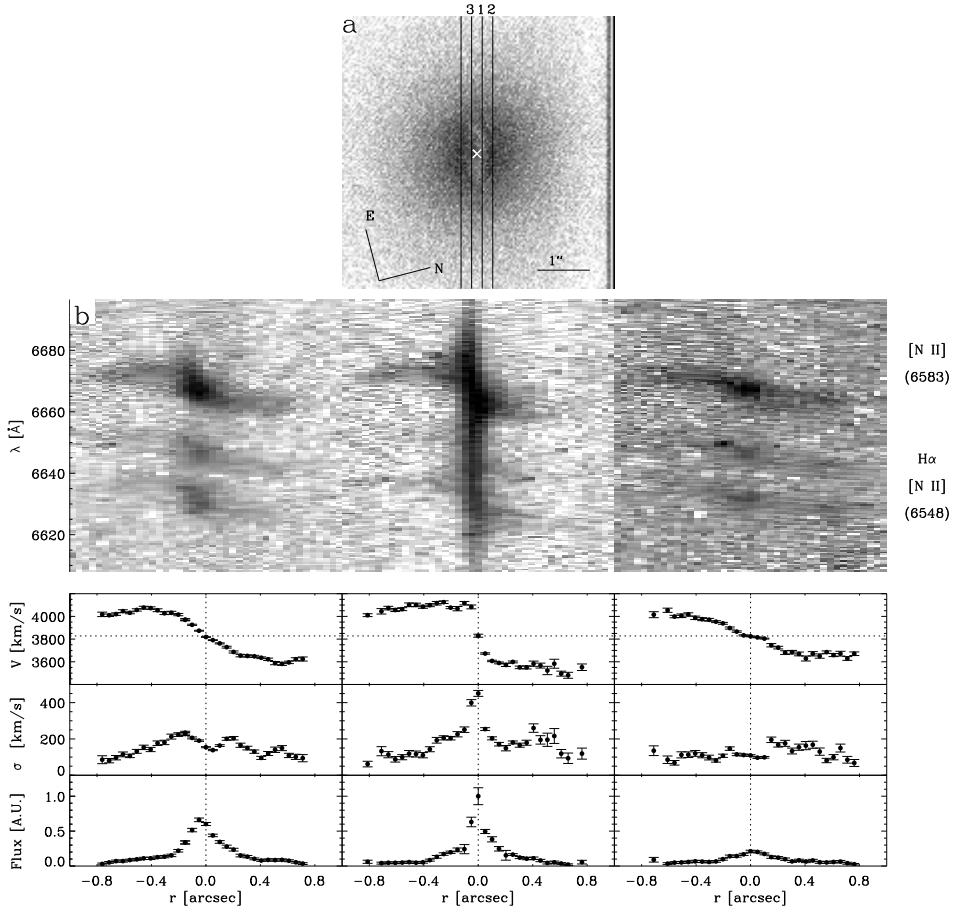

Figure 6.16 As in Figure 6.14, but for Abell 3565-BCG. In *b)* the spatial axis is horizontal and ranges between $-1''.0$ and $+1''.0$, while the wavelength axis ranges from 6608 to 6697 Å. Positions 2 and 3 correspond to a slit-position offset of $-0''.2$ and $+0''.2$, respectively.

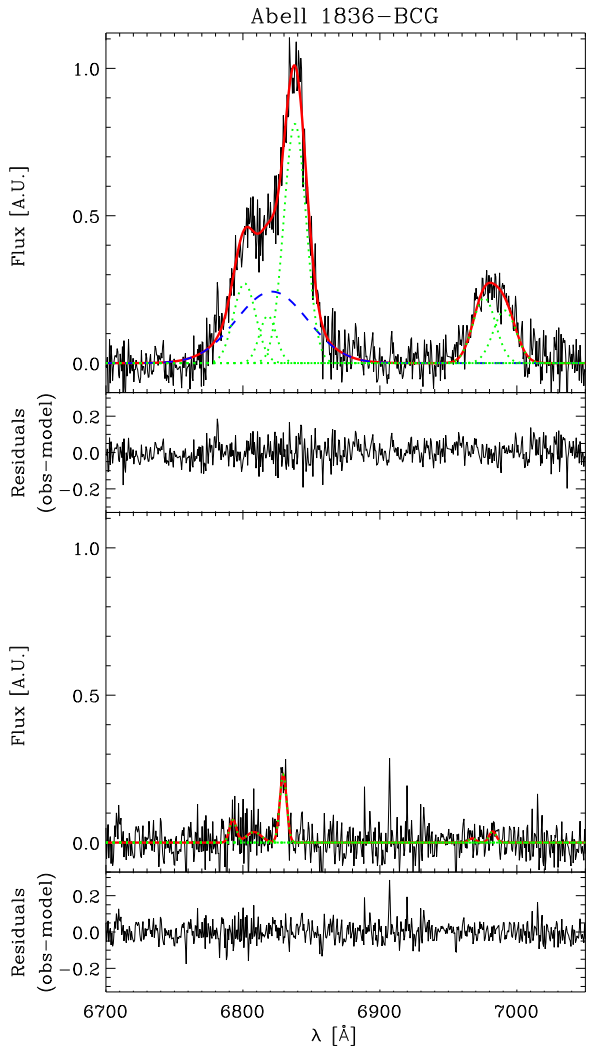

Figure 6.17 Nuclear spectrum (*upper panel*) and spectrum extracted at $r = +0''.15$ (*lower panel*), along the major axis of the dust disk of Abell 1836-BCG. Each spectrum is plotted with the Gaussian-model narrow (dotted lines) and broad (dashed lines) components, reconstructed blend, and residuals.

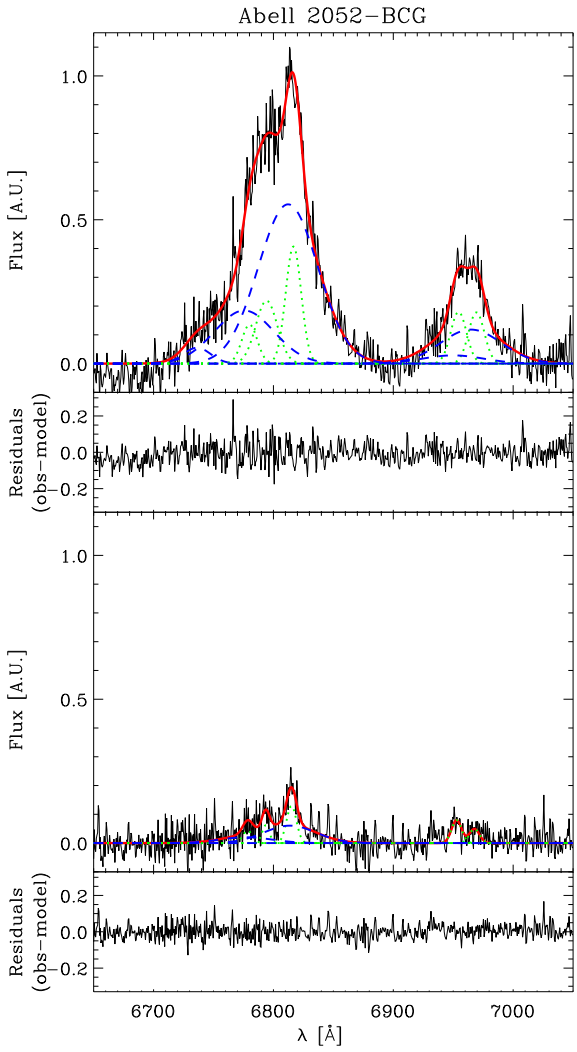

Figure 6.18 As in Figure 6.17, but for Abell 2052-BCG. The outer spectrum was extracted at $r = +0''.10$.

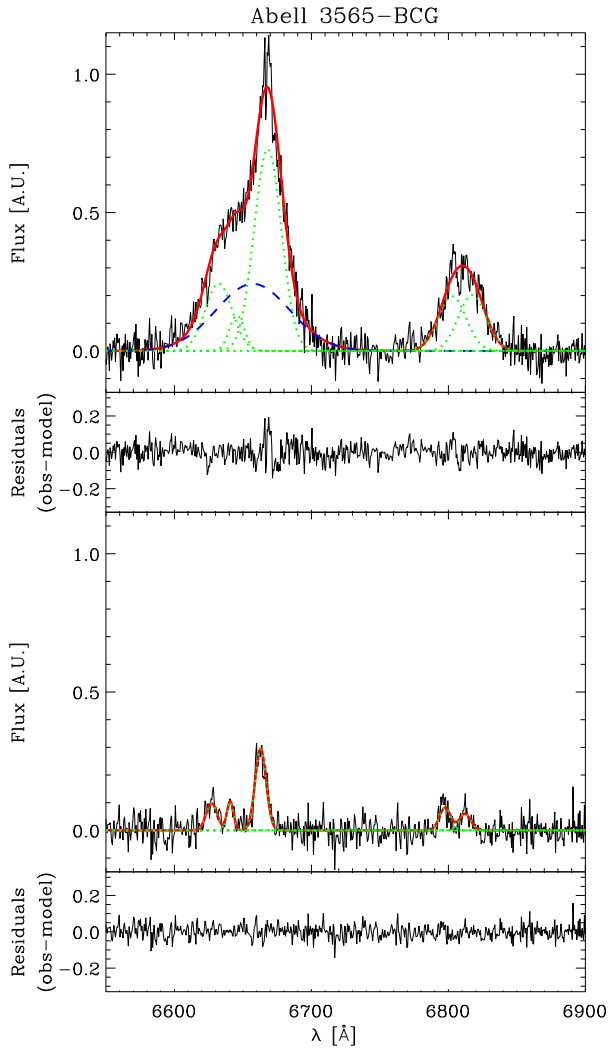

Figure 6.19 As in Figure 6.17, but for Abell 3565-BCG. The outer spectrum was extracted at $r = +0''.25$.

spectra are characterized by similar velocity dispersion profiles, but very different rotation curves; in particular, almost no rotation is observed along the slit displaced by 0″.1 to the South-East. Because of this lack of regularity in the gas kinematics, we are only able to place an upper limit on the SMBH mass of Abell 2052-BCG (Section 6.6.3).
Abell 3565-BCG. The [N II] λ6583 kinematics are measured within 0″.8 from the center along all three slit locations (Figure 6.16c). Although the smooth and well defined dust disk in Abell 3565-BCG starts to tilt slightly at large radii from the center (Figure 6.3), such a warp is clearly visible, and presumably kinematically important, only beyond the region where the ionized-gas kinematics is measured. The major-axis rotation velocity has a steep gradient, increasing to approximately 250 km s^{-1} within 0″.1. It remains approximately constant out to the last observed point along the approaching side, while it decreases to about 100 km s^{-1} for radii larger than 0″.5 along the receding side. The velocity dispersion profile is fairly symmetric and strongly peaked, reaching $\approx$ 450 km s^{-1} at the center. The offset axes show rather similar kinematics, although the line fluxes are rather different. The rotation velocity increases almost linearly with radius, up to $\approx$ 200 km s^{-1} at $\approx$ 0″.3 from the center, while the velocity dispersion remains fairly constant at 120 km s^{-1}. Like Abell 1836-BCG, Abell 3565-BCG is a promising candidate for dynamical modeling.

6.5 Observations, data reduction and analysis: ground-based spectroscopy

Although not used in the dynamical analysis, large scale stellar kinematics are necessary to place measured SMBH masses on the $M_\bullet - \sigma_c$ relation. Velocity dispersions measurements exist in the literature for Abell 2052-BCG and Abell 3565-BCG, but not for Abell 1836-BCG. Ground-based spectroscopic observations of Abell 1836-BCG were therefore carried out in service mode with the 3.5-m New Technology Telescope (NTT) at the European Southern Observatory (ESO) in La Silla (Chile) on 2007 May 20 and July 10 [DDT programme ID 279.B-5004(A), P.I. E. Dalla Bontà]. The NTT mounted the ESO Multi-Mode Instrument (EMMI) in red medium-dispersion spectroscopic (REMD) mode, using the grating No. 7 with 600 grooves mm^{-1} in first order with a 1″.0 $\times$ 5′.5 slit. The detector was the No. 62 MIT/LL CCD with 2048 $\times$ 4096 pixels of 15 $\times$ 15 μm^2. After a 2 $\times$ 2 on-chip pixel binning it yielded a wavelength coverage between about 4546 Å and 6096 Å with a reciprocal dispersion of 0.83 Å pixel^{-1}. The instrumental resolution was 2.5 Å (FWHM) corresponding to $\sigma_{\rm inst} \approx$ 55 km s^{-1} at 5900 Å. The spatial scale was 0.332 arcsec pixel^{-1}. We took three spectra of 2400 s along the major axis of the galaxy (PA= 54°).

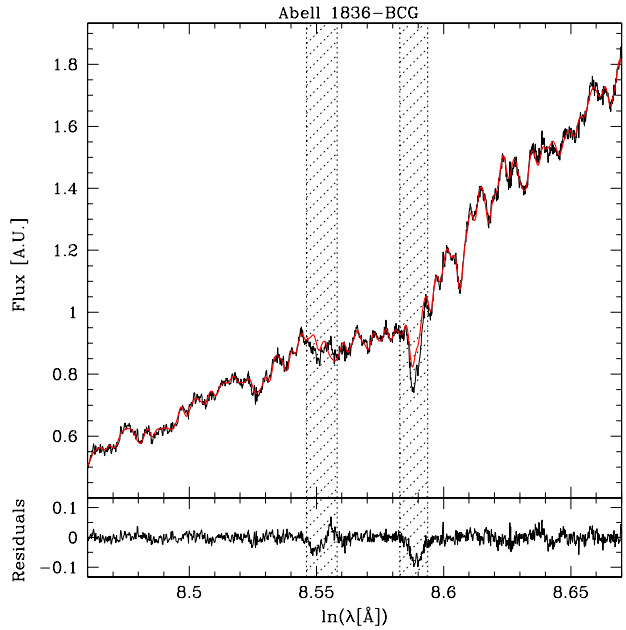

Figure 6.20 Best fit of the broadened spectrum of the template star (thick red line) to the spectrum of Abell 1836-BCG (thin black line) used to measure the galaxy velocity dispersion. The hatched regions mark the spectral ranges excluded from the fit to minimize the mismatch of the abundance ratios. The difference between the galaxy spectrum and broadened template spectrum is shown in the bottom panel.

The integration time was split into three exposures to deal with cosmic rays. Spectra of six giant stars with spectral type ranging from G7III to K5III were obtained, to use as templates. Arc lamp spectra were taken before and after every exposure to allow an accurate wavelength calibration. The average seeing FWHM during the observing runs was 1.0 arcsec in May 20 and 1.1 arcsec in July 10, as measured by the ESO Differential Image Motion Monitor.

All spectra were bias subtracted, flatfield corrected, cleaned of cosmic rays, corrected for bad pixels and columns, and wavelength calibrated using standard IRAF routines. It was checked that the wavelength rebinning was done properly by measuring the difference between the measured and predicted wavelengths (Osterbrock et al. 1996) for the brightest night-sky emission lines in the observed spectral ranges.The spectra were co-added using the center of the stellar continuum as reference. The contribution of the sky was determined from the

outermost $\sim 30''$ and $\sim 60''$ at the two edges of the resulting spectrum, respectively, and then subtracted. A one-dimensional sky-subtracted spectrum was obtained for each kinematical template star. Flux calibration was not performed.

The stellar velocity dispersion was measured from the galaxy absorption features present in the wavelength range including the Mg line triplet ($\lambda\lambda\, 5164, 5173$, 5184 Å) using the Fourier Correlation Quotient method (Bender 1990) as done in Corsini et al. (2008). HR7429 (K3III) was adopted as the kinematical template. The stellar velocity dispersion was measured within an aperture of $1/8 r_{\rm e}$. It was then applied the correction of Jørgensen et al. (1995) to derive the velocity dispersion within a circular aperture of radius $1/8 r_{\rm e}$. The correction was negligible, because the stellar velocity dispersion profile shows constant values, within the errors, toward the center. The stellar velocity dispersion of Abell 1836-BCG within a circular aperture of size $1/8 r_{\rm e}$ (Table 6.1) resulted to be $\sigma_{\rm c} = 309 \pm 11$ km s^{-1}. A consistent value ($\sigma_{\rm c} = 308 \pm 10$ km s^{-1}) was obtained by measuring the velocity dispersion with the Penalized Pixel-Fitting Method (Cappellari & Emsellem 2004) as done in Méndez-Abreu et al. (2008b) (see also Section 5.3.2). The measurement of the velocity dispersion from spectra obtained in the Mg triplet region can be problematic for massive ellipticals, due to possible mismatch of the abundance ratios with those of the adopted stellar templates (e.g., Barth et al. 2003). To address this issue, the Mg region was masked out (Figure 6.20). A lower value of $\sigma_{\rm c} = 288 \pm 9$ km s^{-1} was found after applying the aperture correction, and this was adopted for Abell 1836-BCG.

6.6 Dynamical modeling

Modeling of gas dynamics from *HST* data has steadily improved since the first successful applications of the method (Harms et al. 1994; Ferrarese et al. 1996; Barth et al. 2001; Sarzi et al. 2001; Marconi et al. 2003). For this study, we will use the procedure described in Coccato et al. (2006), where a detailed description of the method can be found. Briefly, a synthetic velocity field is generated assuming that the ionized gas is moving in circular orbits under the combined gravitational potential of stars and SMBH. The gas is assumed to be confined in an infinitesimally thin disk centered at the photometric center of the galaxy. The model is projected onto the plane of the sky for a given inclination of the gaseous disk, and then degraded to simulate the actual setup of the spectroscopic observations. The latter step includes accounting for the width and location (namely position angle and offset with respect to the center) of each slit, instrumental PSF and charge bleeding between adjacent pixels. The free parameters of the model are the mass $M_\bullet$ of the SMBH, the mass-to-light

ratio $(M/L)_\star$ of the stellar component (which we give in the $I-$band), and the inclination i of the gaseous disk; both $(M/L)_\star$ and i are assumed to be radially invariant. Although i can be estimated from the minor-to-major axial ratio of the disk, which is easily measured from the images, previous studies (Ferrarese et al. 1996; Ferrarese & Ford 1999; Sarzi et al. 2001; Shapiro et al. 2006) have shown that slight warps are common. When the ionized-gas emission arises predominantly from the innermost region of the dust disk, it is therefore best to treat i as a free parameter. The location of the slits, as well as the surface brightness distribution of the ionized gas (derived as described in Section 6.3.5) are treated as input. $M_\bullet$, $(M/L)_\star$, and i are determined by finding the model parameters which produce the best match to the observed velocity curve, obtained by minimizing $\chi^2 = \sum(v - v_{mod})^2/\delta^2(v)$ where $v \pm \delta(v)$ and v_{mod} are the observed and model velocity along the different slit positions, respectively.

It has been noted in a number of studies of the kinematics of gas disks (Ferrarese et al. 1996; Ferrarese & Ford 1999; van der Marel & van den Bosch 1998; Verdoes Kleijn et al. 2000, 2002, 2006) that the measured velocity dispersion of the emission lines greatly exceeds what is expected from instrumental broadening and radial variations in rotational velocity of the gas within a single slit element, and requires an intrinsic component of random motion. In our model, this is assumed to be described by a radial function of the form $\sigma(r) = \sigma_0 + \sigma_1 e^{-r/r_\sigma}$. In principle, the exact characterization of $\sigma(r)$ affects the recovered velocity field, and therefore σ_0, σ_1, and r_σ should be treated as free parameters in the model, along with $M_\bullet$, i, and $(M/L)_\star$. In practice, however, previous studies (Verdoes Kleijn et al. 2000; Barth et al. 2001; Coccato et al. 2006) have found that σ_0, σ_1, and r_σ are fairly insensitive to the values of $M_\bullet$, i, and $(M/L)_\star$. We have run a set of preliminary models in order to find the shape of the intrinsic velocity dispersion profile that is required to match our data, within the typical range of our key model parameters. Specifically, we explored a reasonable grid of values for black hole mass, inclination, and stellar $I-$band mass-to-light ratio, finding for each combination of these parameters the values of σ_0, σ_1, and r_σ that minimized $\chi^2 = \sum(v-v_{mod})^2/\delta^2(v)+\sum(\sigma-\sigma_{mod})^2/\delta^2(\sigma)$ where $\sigma \pm \delta(\sigma)$ and σ_{mod} are the observed and the model velocity dispersion along the major axis. In our final modeling procedure we have then fixed σ_0, σ_1, and r_σ to the values that were found for the best of such preliminary models (see next Sections).

In the following, the results for each galaxy will be discussed separately.

6.6.1 Abell 1836-BCG

We explored a three-dimensional grid of models with $0 \leq M_\bullet \leq 3.6{\times}10^{10}$ $M_\odot$ in $2.4{\times}10^8$ $M_\odot$ steps, $0^\circ \leq i \leq 90^\circ$ in 1° steps, and $0 \leq (M/L)_\star \leq 33$ ($M_\odot/L_\odot$) in 0.4 ($M_\odot/L_\odot$) steps. Within this range, the intrinsic velocity dispersion of the gas best able to reproduce the observables is $\sigma(r) = 12 + 204\, e^{-r/0.1\ \mathrm{kpc}}$ km s^{-1}. The model adopts three parameters to fit 28 data points (the values of the rotational velocity), for a total of 25 degrees of freedom. The best model fitting the observed rotation curve (given the intrinsic velocity dispersion profile given above) requires $M_\bullet = 3.61^{+0.41}_{-0.50} \times 10^9$ $M_\odot$, $i = 69.0^\circ{}^{+1.7^\circ}_{-1.9^\circ}$, and $(M/L)_\star = 5.0^{+1.8}_{-0.9}$ ($M_\odot/L_\odot$)(in the $I-$band), where the errors on $M_\bullet$, i, and $(M/L)_\star$, are quoted at the 1σ confidence level. The model, which has $\chi^2 = 85.3$ and a reduced $\chi^2_r = 3.4$, is compared to the observed spectrum and kinematics in Figure 6.21 and Figure 6.22, respectively.

The small-scale asymmetries present in the model rotation curve (most evident at the central position) are a direct consequence of using in the models the intrinsic, PSF-deconvolved Hα+[N II] intensity map (bottom panel of Figure 6.22). The observed rotation curves are well reproduced in general; the slight mismatch observed at $r \sim 0''.1$ for the slit located on the North-West side (-$0''.1$) of the nucleus (Figure 6.22) might be due to the presence of a slight warp in the outer part of the gas disk, which is not reproducible within the model's framework.

The inclination angle derived from modeling the ionized kinematic data ($i = 69.0^\circ{}^{+1.7^\circ}_{-1.9^\circ}$), which extend only as far as $r \lesssim 0''.2$, is significantly different from the inclination angle suggested by the axial ratio of the outer edge ($r \approx 0''.5$) of the disk, $i = 46^\circ \pm 5^\circ$. This suggests the presence of a warped structure, although such a tilting does not need to extend to the innermost regions where the kinematics was measured, and effectively our images can not constrain the gas geometry.

Figures 6.23–6.25 show the 1σ, 2σ and 3σ confidence levels (following the $\Delta\chi^2$ variations expected for two free parameters, i.e., 2.30, 6.17 and 11.8 Press et al. 1992) in the two-dimensional space of two of the fitted parameters, where the third parameter is held fixed at the best fitted value listed above. Finally, Figure 6.26 shows 1σ, 2σ, and 3σ confidence levels individually on $M_\bullet$, i, and $(M/L)_\star$, according to the $\Delta\chi^2$ variations expected for one parameter (i.e., 1, 4, and 9, Press et al. 1992), marginalizing over all other parameters.

6.6.2 Abell 3565-BCG

The rotation curves along the three slit positions, for a total of 90 velocity data-points, were fitted for a grid of model parameters defined by $0 \leq M_\bullet \leq$

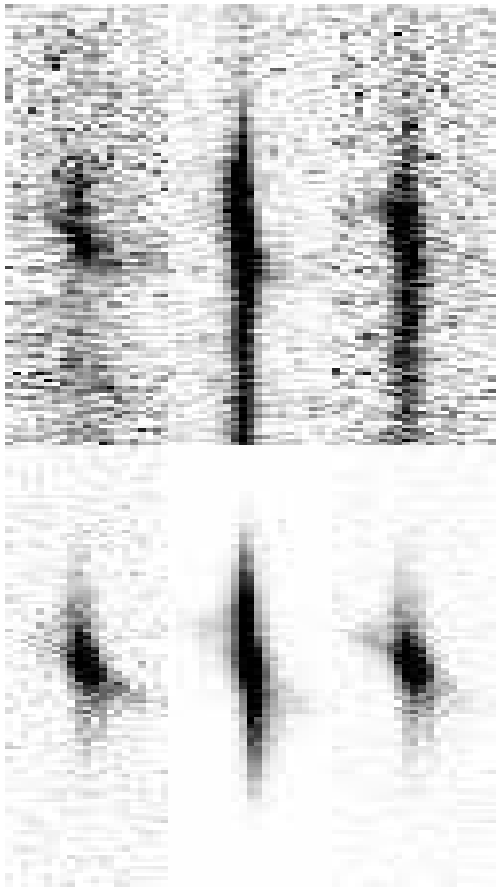

Figure 6.21 Comparison between the bidimensional observed (*upper panels*) and synthetic spectra (*lower panels*) for the best-fitting model of Abell 1836-BCG. Spectra obtained in position 1 (*central panels*), 2 (*right panels*), and 3 (*left panels*) are shown. In the models we added a random noise to mimic the actual S/N of the observed spectra.

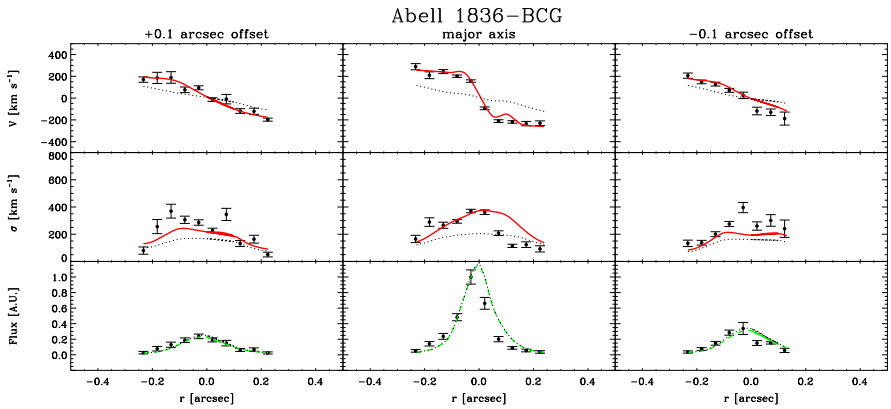

Figure 6.22 Observed [N II] λ6583 kinematics (*filled circles*) along with the best-fitting model (*solid lines*) for the SMBH mass of Abell 1836-BCG. The observed and modeled velocity curve (*top panels*), velocity dispersion radial profile (*central panels*), and flux profile (*bottom panels*) are shown for the slit along the $+0\farcs1$ offset position (*left panels*), the major axis (*central panels*), and the $-0\farcs1$ offset position (*right panels*) of the gas disk. The dotted lines correspond to a model obtained with $M_\bullet = 0$ $M_\odot$, $i = 69.0°$, and $(M/L)_\star$= 5.0 ($M_\odot/L_\odot$)(in the $I-$band).

6.4×10^9 $M_\odot$ in $2.6{\times}10^7$ $M_\odot$ steps, $0° \leq i \leq 90°$ in $1°$ steps, and $0 \leq (M/L)_\star \leq 12$ ($M_\odot/L_\odot$) in 0.3 ($M_\odot/L_\odot$) steps. Within this range, the intrinsic velocity dispersion of the gas best able to reproduce the observables is $\sigma(r) = 122 + 98\,e^{-r/0.01\ \mathrm{kpc}}$ km s^{-1}. The best model, which has $\chi^2 = 1518$ and a reduced $\chi^2_r = 17.5$ (for 87 degrees of freedoms), requires $M_\bullet = 1.34^{+0.21}_{-0.19} \times 10^9$ $M_\odot$, $i = 66.0°^{+3.5°}_{-3.4°}$ and $(M/L)_\star$= $6.3^{+1.1}_{-1.0}$ ($M_\odot/L_\odot$), where all errors are given at the 1σ confidence level. Such formal uncertainties were conservatively estimated after scaling up our errors on the velocity measurement until $\chi^2_r = 1$ (following Sarzi et al. 2001), acknowledging that our thin-disk model fails to reproduce some of the velocity structure observed in particular at the central and South-Eastern slit positions. Contrary to the case of Abell 1836-BCG, the dynamical inclination angle of the disk is much closer to the morphological inclination angle, $i = 71° \pm 1°$, derived from the axial ratio of the outer edge of the disk ($r \approx 1\farcs4$). Although our kinematic data extend almost to this radius ($r \lesssim 0\farcs8$) in practice the luminosity weighting assigns more leverage to the data from the innermost region. The model is compared to the observed spectrum and kinematics in Figure 6.27 and Figure 6.28, respectively.

Figures 6.29–6.31 show the 1σ, 2σ, and 3σ confidence levels in the two-

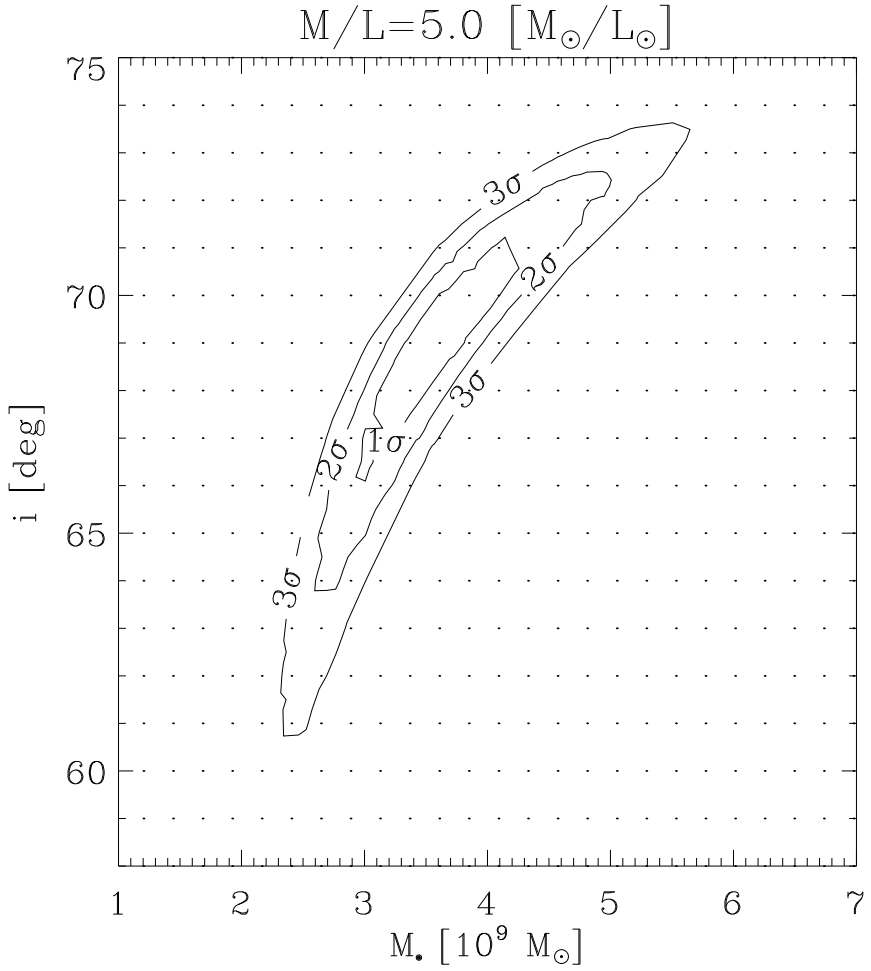

Figure 6.23 Locus of points of equal χ^2 values around the minimum χ^2_m value for the model of Abell 1836-BCG. The 1σ, 2σ, and 3σ confidence levels expected for two free parameters are shown in the $M_\bullet$-i plane, with $(M/L)_\star$= 5.0 ($M_\odot/L_\odot$) corresponding to the χ^2_m value. The grid of models explored is shown by the dots.

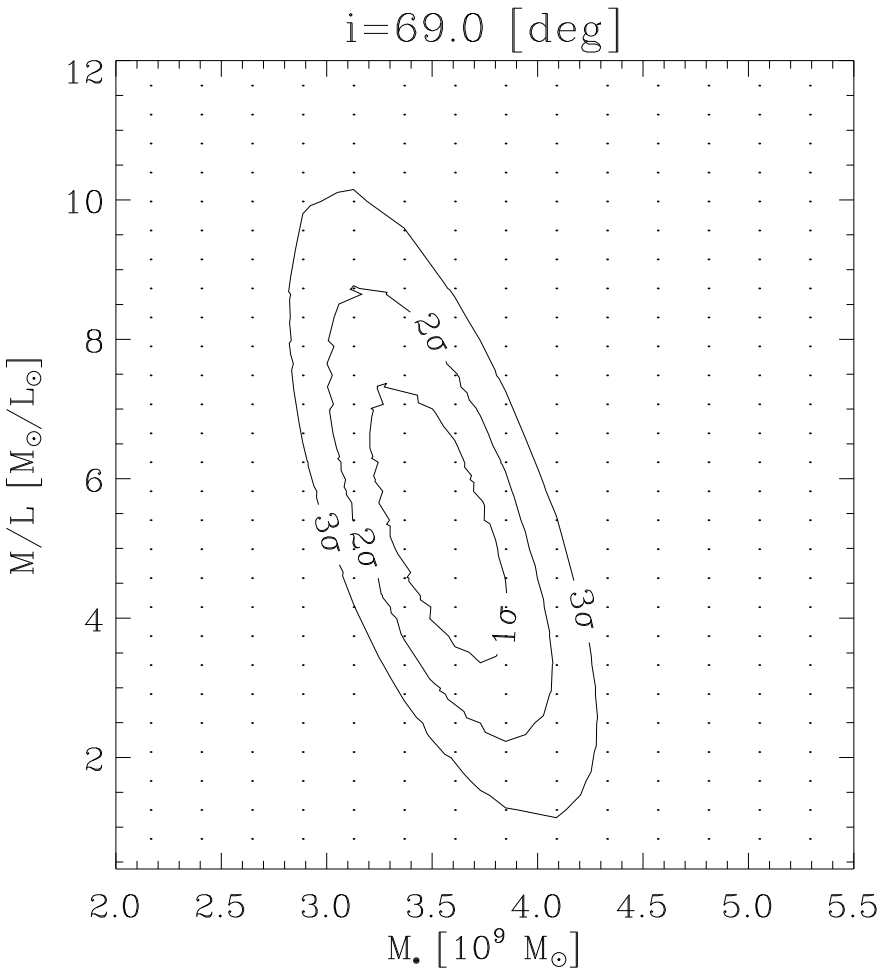

Figure 6.24 As in Figure 6.23, but for the 1σ, 2σ, and 3σ confidence levels expected for two free parameters shown in the $M_\bullet$-$(M/L)_\star$ plane with $i = 69°$ corresponding to the χ^2_m value.

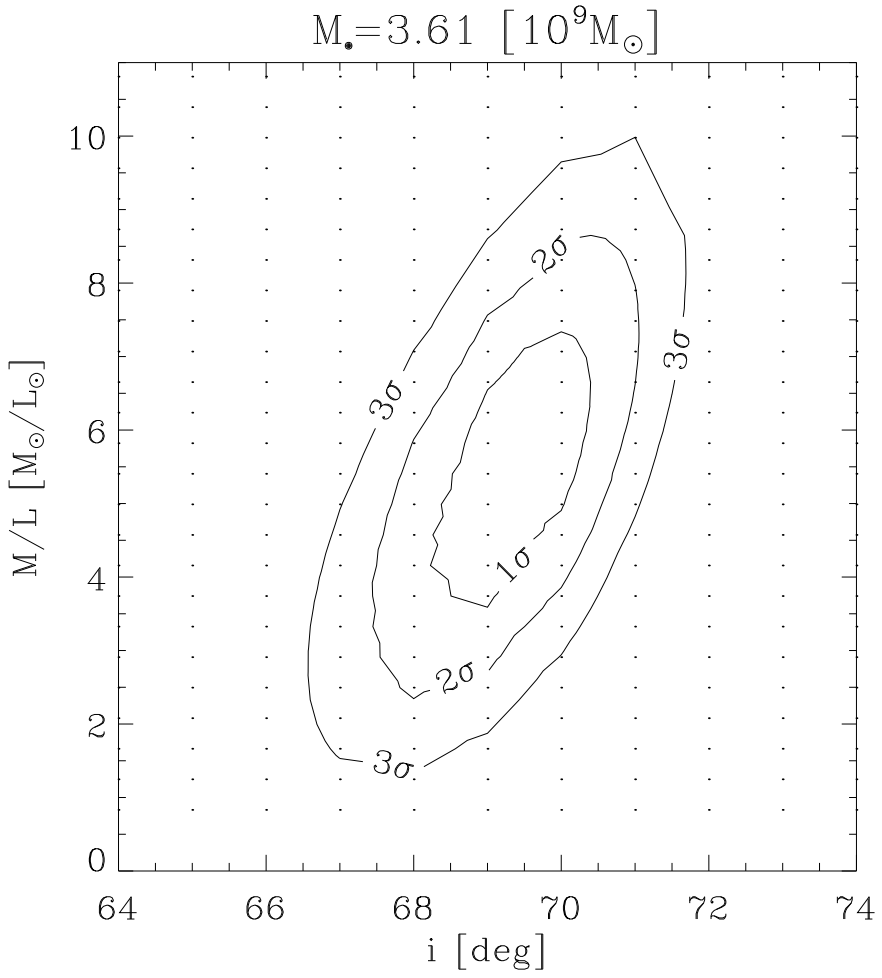

Figure 6.25 As in Figure 6.23, but for the 1σ, 2σ, and 3σ confidence levels expected for two free parameters shown in the i-$(M/L)_\star$ plane with $M_\bullet = 3.61 \cdot 10^9$ $M_\odot$ corresponding to the χ^2_m value.

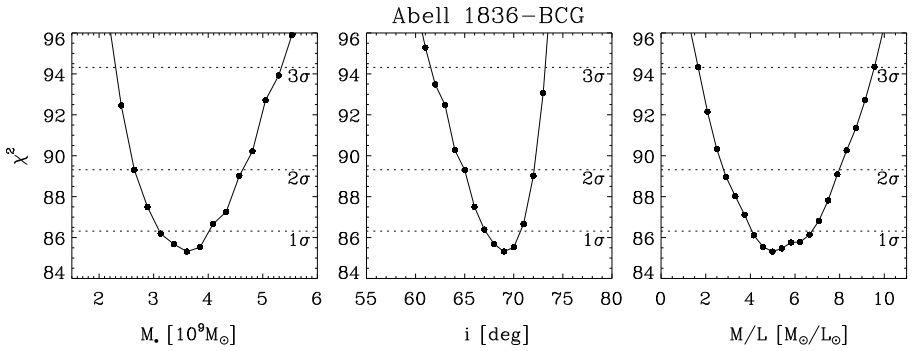

Figure 6.26 χ^2 distribution for Abell 1836-BCG as a function of $M_\bullet$ (*left*), inclination (*center*), and $(M/L)_\star$ (*right*). The dotted horizontal lines indicate the confidence levels on the best fitting values, marginalizing over all other parameters.

dimensional space of two of the fitted parameters, where the third parameter is held fixed at the best fitted value listed above. Figure 6.32 shows 1σ, 2σ, and 3σ confidence levels on $M_\bullet$, i, and $(M/L)_\star$ alone, marginalizing over all other parameters. It is worth noticing that mass-to-light ratios derived by the models refer to the nucleus of the galaxy, and might differ from the stellar population characterizing the galaxy on larger scale.

6.6.3 Abell 2052-BCG

In the case of Abell 2052-BCG, the asymmetric nature of the gas kinematics (Section 4.2) prevents the application of the method described above to pinpoint $M_\bullet$. An upper limit on the SMBH mass can however still be obtained as described in Sarzi et al. (2002) (see also Section 3.2.3). In brief, an upper limit can be derived under the assumption that the central [N II] λ6583 emission-line width, σ, is produced by gas moving on circular orbits in a coplanar, randomly oriented disk in the Keplerian potential of the central black hole. If the line broadening is caused in part by non-gravitational forces, the derived upper-limit would well exceed the actual SMBH mass.

The model was implemented under the assumption that the intrinsic radial flux profile of the gas can be described by a Gaussian:

$$F(r) = F_0 + F_1 \exp[-(r - r_0)^2/2\sigma^2_{\rm flux}], \tag{6.4}$$

where the parameters F_0, F_1, r_0, and $\sigma_{\rm flux}$ are derived by matching $F(r)$, after convolution with the STIS PSF, to the observed emission flux profile along the

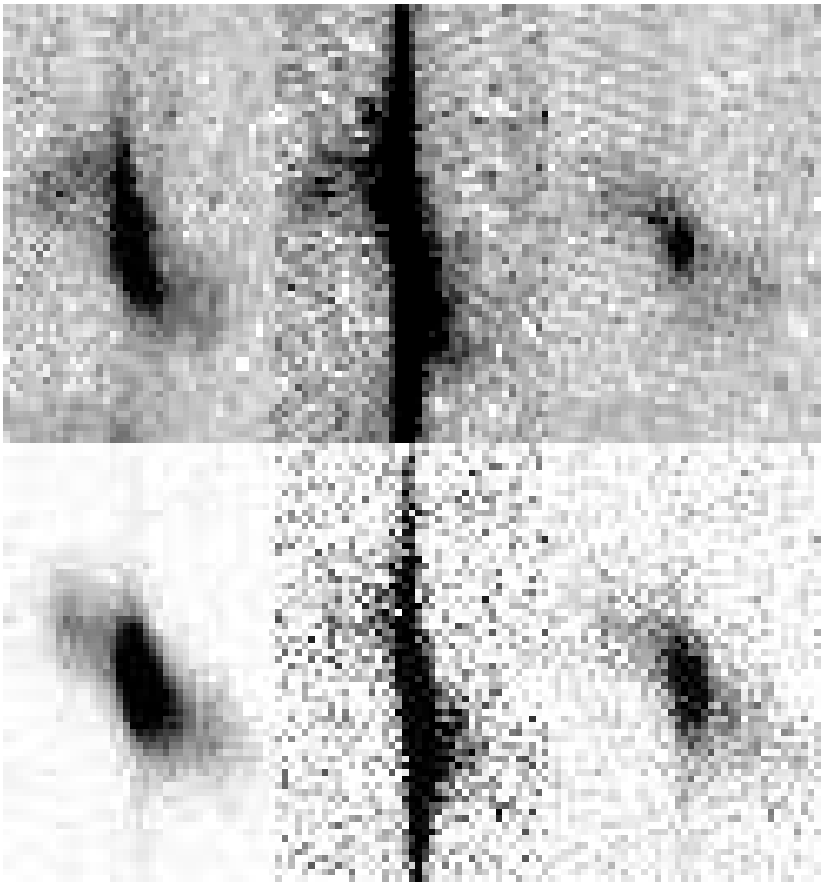

Figure 6.27 As in Figure 6.21, but for Abell 3565-BCG.

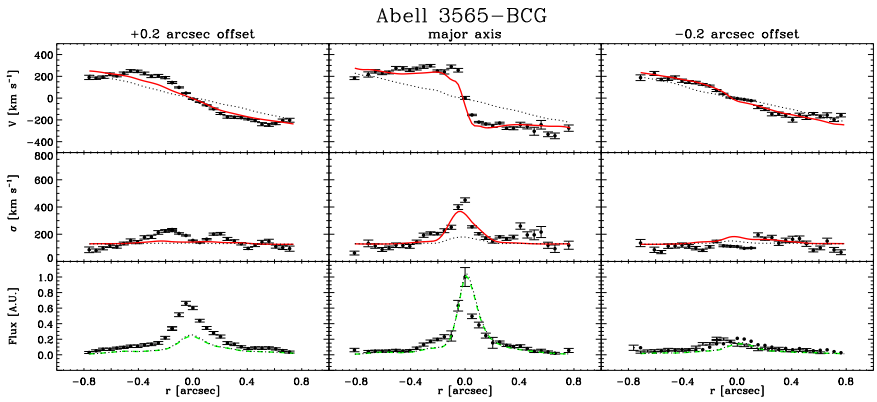

Figure 6.28 Observed [N II] λ6583 kinematics (*filled circles*) along with the best-fitting model (*solid lines*) for the SMBH mass of Abell 3565-BCG. The observed and modeled velocity curve (*top panels*), velocity dispersion radial profile (*central panels*), and flux profile (*bottom panels*) are shown for the slit along the $+0''.1$ offset position (*left panels*), the major axis (*central panels*), and the $-0''.1$ offset position (*right panels*) of the gas disk. The dotted lines correspond to a model obtained with $M_\bullet = 0$ $M_\odot$, $i = 66.0°$, and $(M/L)_\star = 6.3$ $(M_\odot/L_\odot)$(in the $I-$band).

slit. For a given black-hole mass, and under the previous assumptions regarding the gas geometry and kinematics, the model produces two-dimensional projected maps for the moments of the line-of-sight velocity distribution (LOSVD) at any position (x, y) on the sky:

$$\overline{\Sigma v^k}(x,y) = \int \mathrm{LOSVD}(x,y,v_z) v_z^k \mathrm{d}v_z \ (k = 0, 1, 2). \tag{6.5}$$

$\overline{\Sigma v^k}$ is then convolved with the STIS PSF; finally, the velocity dispersion, σ, which corresponds to $(\overline{\Sigma v^2}/\overline{\Sigma v^0} - (\overline{\Sigma v^1}/\overline{\Sigma v^0})^2)^{1/2}$, is extracted within a $0.05'' \times 0.1''$ aperture for comparison to the observables.

There is no information on the orientation of the gaseous disk within the central aperture, nor is it possible to estimate it by analyzing the dust morphology, which is irregular and does not show a disk-like structure. In principle, a lower-limit on the SMBH mass can be estimated assuming an edge configuration, whereas a model with a perfectly face-on disk would allow for an infinite SMBH mass. Fortunately such extreme configurations are statistically rare, and considering that randomly oriented disks have uniformly distributed $\cos i$ we can estimate 1σ upper and lower limits on $M_\bullet$ by using models with $i = 33°$ and $i = 81°$, corresponding to $\cos i = 0.84$ and 0.16, respectively. For each i, the

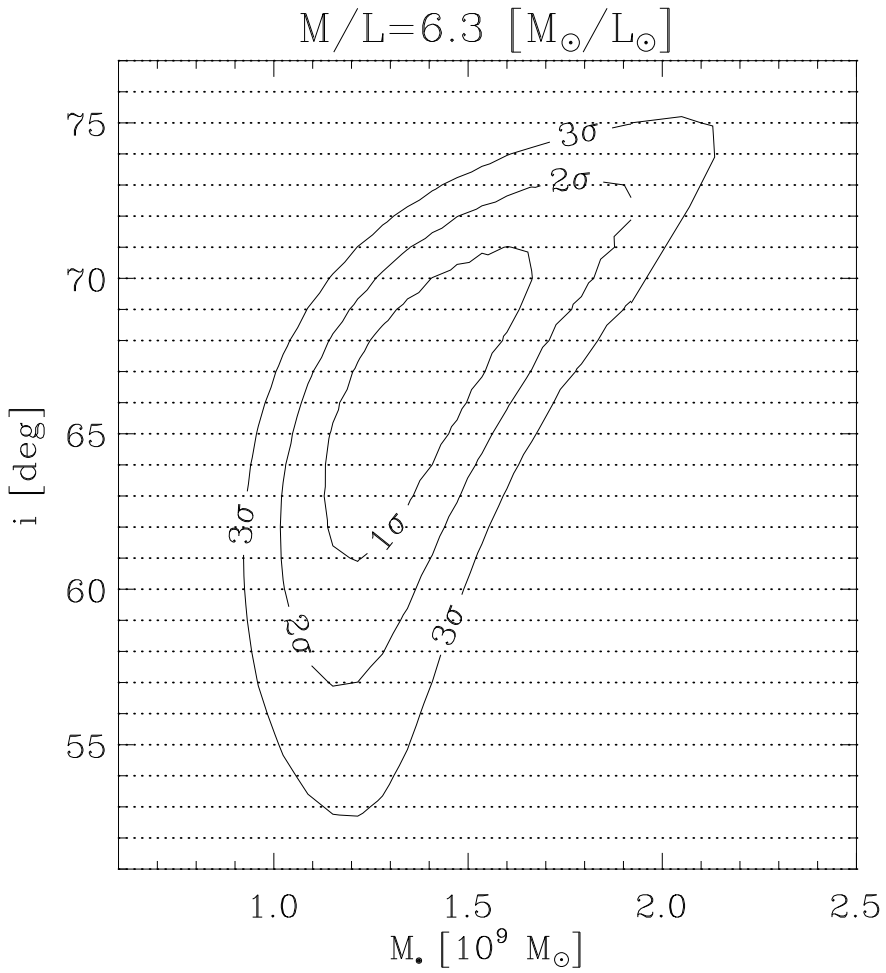

Figure 6.29 Locus of points of equal χ^2 values around the minimum χ^2_m value for the modeling of Abell 3565-BCG. The 1σ, 2σ, and 3σ confidence levels expected for two free parameters are shown in the $M_\bullet$-i plane, with $(M/L)_\star$= 6.3 ($M_\odot/L_\odot$) corresponding to the χ^2_m value.

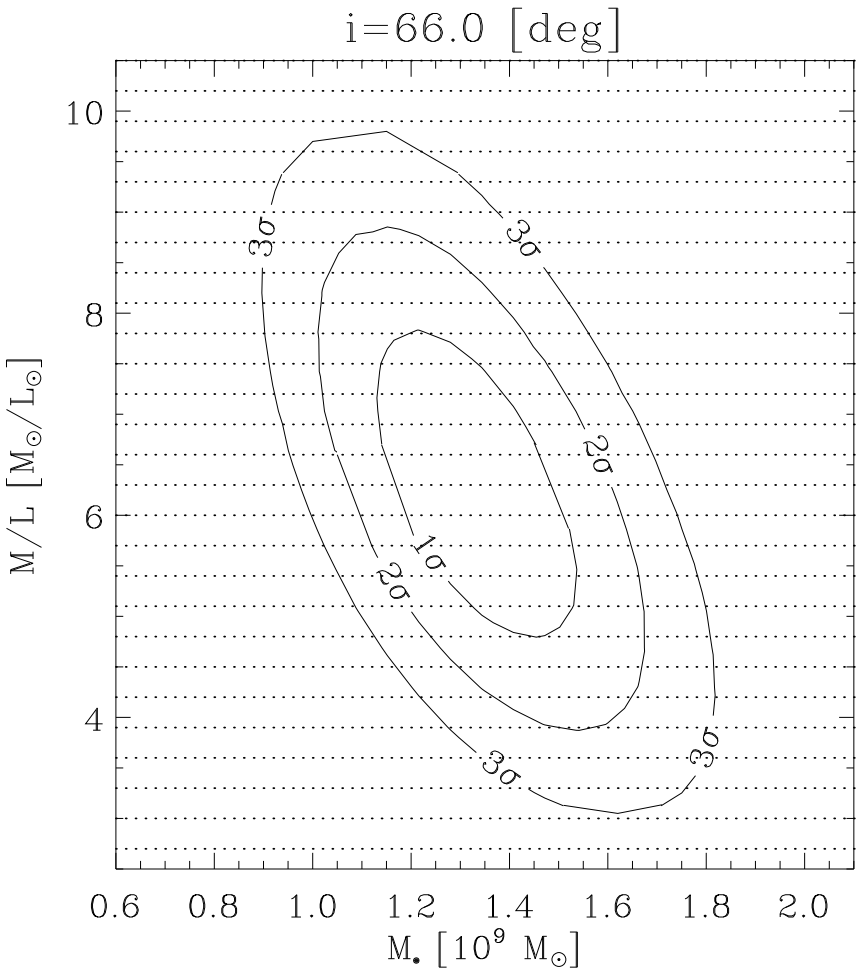

Figure 6.30 As in Figure 6.29, but for the 1σ, 2σ, and 3σ confidence levels expected for two free parameters shown in the $M_\bullet$-$(M/L)_\star$ plane with $i = 66°$ corresponding to the χ^2_m value.

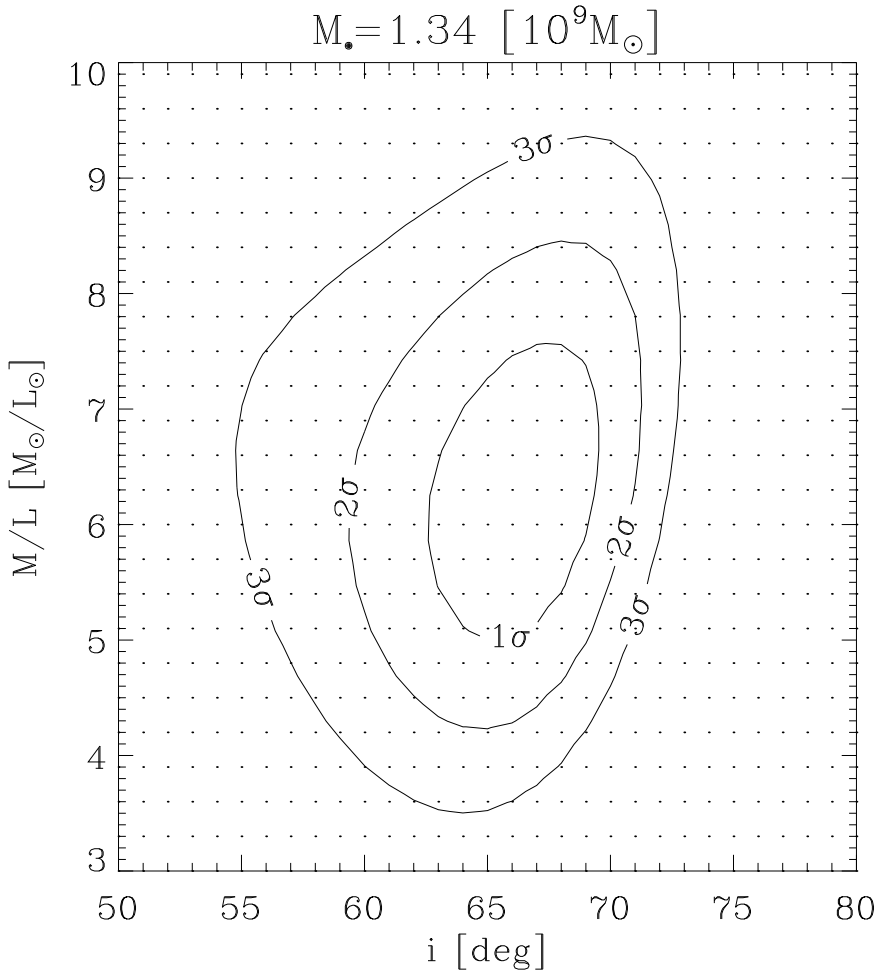

Figure 6.31 As in Figure 6.29, but for the 1σ, 2σ, and 3σ confidence levels expected for two free parameters shown in the i-$(M/L)_\star$ plane with $M_\bullet = 1.34{\cdot}10^9$ $M_\odot$ corresponding to the χ^2_m value.

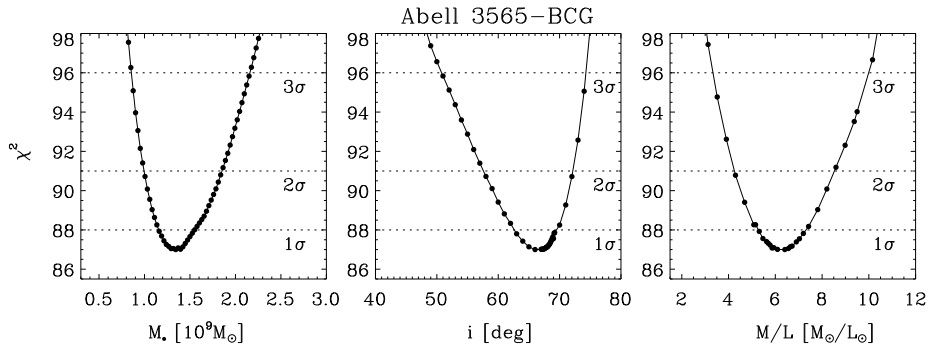

Figure 6.32 Same of Figure 6.26, but for Abell 3565-BCG.

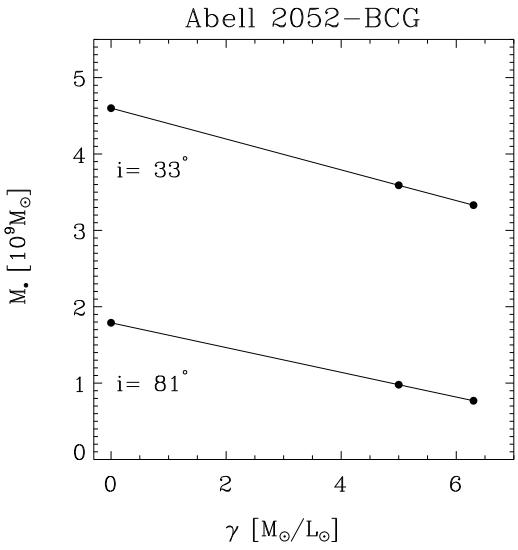

Figure 6.33 Upper limit of SMBH mass of Abell 2052-BCG as function of the $(M/L)_\star$ assumed, for an inclination of the gas-disk $i = 33°$ and $i = 81°$.

SMBH mass was varied in 0.1×10^6 $M_\odot$ steps between $6\times10^6 \leq M_\bullet \leq 11.0\times10^9$ $M_\odot$ until the observed gas velocity dispersion was matched. The models were run for three values of mass-to-light ratio: $(M/L)_\star$=0, 5.0 ($M_\odot/L_\odot$) (derived for Abell 1836-BCG), and 6.3 (as in the case of Abell 3565-BCG) ($M_\odot/L_\odot$). The most conservative upper limit is obtained by neglecting altogether the stellar contribution to the gravitational potential, $(M/L)_\star$=0, giving $M_\bullet \leq 4.6 \times 10^9$ $M_\odot$ and $M_\bullet \leq 1.8 \times 10^9$ $M_\odot$ for $i = 33°$ and $i = 81°$ respectively. Consistent with Sarzi et al. (2002), adopting $(M/L)_\star$=5.0 or 6.3 ($M_\odot/L_\odot$), has very little effect: $M_\bullet$ decreases slightly to 3.6×10^9 $M_\odot$ and 3.3×10^9 $M_\odot$ respectively for $i = 33°$ and 9.8×10^8 $M_\odot$ and 7.7×10^8 $M_\odot$ respectively for $i = 81°$. Figure 6.33 shows the dependence of $M_\bullet$ on the assumed $(M/L)_\star$ for $i = 33°$ and $i = 81°$.

6.7 Discussion and conclusions

We have presented a dynamical analysis aimed at constraining the masses of the SMBHs in three brightest cluster galaxies: Abell 1836-BCG, at a distance of 147.2 Mpc, Abell 2052-BCG, at a distance of 141.0 Mpc, and Abell 3565-BCG, at a distance of 50.8 Mpc. The models are based on data obtained with the *HST*. Broad-band WFPC2 and broad and narrow-band ACS images were used to constrain the luminosity profile and the distribution of the ionized gas, as traced by the Hα+[N II] emission, while STIS was employed to measure the rotation velocity and velocity dispersion profiles, from the [N II] λ6583 emission, along three parallel slits positions, the first aligned along the photometric major axis, and the others adjacent to the first on either side of the nucleus.

In the case of Abell 1836-BCG and Abell 3565-BCG, the regular morphology and kinematics observed for the ionized gas led to secure black hole mass detections of $M_\bullet = 3.61^{+0.41}_{-0.50}\times10^9$ $M_\odot$ and $1.34^{+0.21}_{-0.19}\times10^9$ $M_\odot$ (where the uncertainties represent 1σ errors[7]), respectively. For Abell-2052-BCG, which displays irregular kinematics, an upper limit of $M_\bullet \leq 4.60 \times 10^9$ $M_\odot$ was derived under the conservative assumption of a negligible stellar contribution to the gravitational potential, and an inclination angle for the gas disk of 33°. At face value, the black hole in Abell 1836-BCG is the most massive to have been dynamically measured to-date.

In our modeling we have neglected the potential impact on our SMBH mass determination of assigning a dynamical origin to the additional kinematic broadening that we have used in our models to match the observed profile for the gas velocity dispersion. Although it has been argued that this additional turbulence does not affect the bulk motion of the gas (e.g. van der Marel &

[7]Barth et al. (2001) show that the total error budget for gas-dynamical modeling is likely to be twice as large as such formal error estimates.

van den Bosch 1998), it is important to notice that ignoring the possibility that the gas might be supported by dynamical pressure will lead to *under*-estimate the SMBH mass. For instance, Barth et al. (2001) have shown that including a classical asymmetric drift correction led to an 12% increase of their best $M_\bullet$ value. Unfortunately, we could not repeat this analysis in our models since the observed line-broadening exceeds by far the circular velocity, breaking down the epicyclic approximation on which the asymmetric drift correction is based. Nonetheless, our best SMBH mass measurements are still likely to be underestimations of the real SMBH mass.

Figure 6.34 shows the location of Abell 1836-BCG, Abell 2052-BCG, and Abell 3565-BCG in the $M_\bullet - \sigma$ (Tremaine et al. 2002; Ferrarese & Ford 2005) and K-band $M_\bullet - L_{K,\mathrm{bulge}}$ (Marconi & Hunt 2003; Graham 2007) planes. K-band Two-Micron All-Sky Survey (2MASS) magnitudes were retrieved from the NASA/IPAC Infrared Science Archive, and corrected for Galactic extinction following Schlegel et al. (1998). Stellar velocity dispersions are from this chapter (see Section 6.5) for Abell 1836-BCG, from Smith et al. (2000) in the case of Abell 3565-BCG (we adopt his high S/N measurement, $\sigma = 335 \pm 12$ km s^{-1}), and Tonry (1985) for Abell 2052-BCG. We note that published estimates of σ for Abell 2052-BCG range between 250 km s^{-1} and 370 km s^{-1}; the high end of this spread is probably due to contamination from a companion galaxy located only 8″ away in the North-East direction. The contribution from this galaxy was explicitly accounted for by Tonry (1985), whose value, $\sigma = 253 \pm 12$ km s^{-1}, we have adopted. Correcting the adopted values of σ to a circular aperture of size $1/8 r_\mathrm{e}$ (Table 6.1), following Jorgensen1995, we find $\sigma_\mathrm{c} = 288 \pm 9$ km s^{-1}, $\sigma_\mathrm{c} = 233 \pm 11$ km s^{-1}, and $\sigma_\mathrm{c} = 322 \pm 12$ km s^{-1} for Abell 1836-BCG, Abell 2052-BCG and Abell 3565-BCG, respectively.

The SMBH mass detected in Abell 3565-BCG, $M_\bullet = 1.34^{+0.21}_{-0.19} \times 10^9$ M$_\odot$, is consistent both with the $M_\bullet - \sigma_\mathrm{c}$ (Ferrarese & Ford 2005) and the $M_\bullet - L_{K,\mathrm{bulge}}$ (Graham 2007) relations, which predict $M_\bullet = 1.7^{+2.0}_{-0.9} \times 10^9$ M$_\odot$ (the error is computed adopting a 0.34 dex scatter in $M_\bullet$) and $M_\bullet = 1.1^{+1.1}_{-0.6} \times 10^9$ M$_\odot$ (adopting a 0.30 dex scatter), respectively.

For Abell 2052-BCG, although the conservative upper limit on the black hole mass obtained for reasonable assumptions for $(M/L)_\star$ and i (Section 5.3), is consistent with both the $M_\bullet - \sigma_\mathrm{c}$ (Ferrarese & Ford 2005) and the K-band $M_\bullet - L_{K,\mathrm{bulge}}$ (Graham 2007) relations, these predict significantly different masses, $3.5^{+4.1}_{-1.9} \times 10^8$ M$_\odot$ (adopting a 0.34 dex scatter) and $1.3^{+1.3}_{-0.6} \times 10^9$ M$_\odot$ (adopting a 0.30 dex scatter) respectively (but note the above caveat regarding the measurement of σ for this galaxy). Although the sense of the discrepancy is consistent with the one argued for by Lauer et al. (2007a), the lack of a precise

determination of the SMBH mass in this galaxy prevents us from establishing which, if either, of the two relations better predicts $M_\bullet$ in this case. The only two BCGs in the literature with a dynamically measured SMBH mass are M87 (Macchetto et al. 1997) and NGC 1399 (Houghton et al. 2006). M87 appears to have a more massive black hole than expected based on its $K-$band luminosity while it obeys the $M_\bullet - \sigma_c$ relation. NGC 1399 is consistent with both the relations within their scatter.

Abell 1836-BCG appears to be an outlier in all SMBH scaling relations. The dynamically measured SMBH mass reported in this chapter, $M_\bullet = 3.61^{+0.41}_{-0.50} \times 10^9$ M$_\odot$, is larger, at the 3σ level, than the value of $M_\bullet = 9.6^{+9.5}_{-4.8} \times 10^8$ M$_\odot$ (adopting a 0.30 dex scatter), predicted by the $M_\bullet - L_{K,\rm bulge}$ relation (Graham 2007). It is also larger, at the 3σ level, than the value of $M_\bullet = 9.77^{+11.6}_{-5.30} \times 10^8$ M$_\odot$ (adopting a 0.34 dex scatter), predicted by the $M_\bullet - \sigma_c$ relation of Ferrarese & Ford (2005). Finally, the SMBH mass of Abell 1836-BCG is not consistent with the value of $M_\bullet = 6.3^{+11.5}_{-4.1} \times 10^8$ M$_\odot$ predicted by the fundamental plane relation for SMBHs by Hopkins et al. (2007b), adopting an effective radius $r_e = 13''.1 = 9.3$ kpc with a scatter of 0.45 dex in $M_\bullet$.

The existence of extremely massive SMBHs as outliers to the empirical $M_\bullet - \sigma$ relation would not be surprising. As shown by Lauer et al. (2007a), the $M_\bullet - L_{\rm bulge}$ relation predicts a greater abundance of the most massive SMBHs, given the luminosities of the BCGs and the lack of galaxies with velocity dispersions larger than ~ 350 km s^{-1}. At the same time, the observed luminosity function of AGN implies the presence of SMBHs as massive as $\sim 5 \times 10^9$ M$_\odot$ within the distance of the clusters we have observed, and SMBHs mergers can increase the highest SMBH masses in these massive clusters up to $\sim 10^{10}$ M$_\odot$ (Yoo et al. 2007). A larger sample of SMBH masses measured in massive clusters would be required to test models of the effect of mergers in increasing the largest SMBH masses in the universe.

In conclusion, both the $M_\bullet - \sigma$ and $M_\bullet - L_{\rm bulge}$ relations appear at their high-$M_\bullet$ end to be consistent with the SMBH mass measured for one BCG, Abell 3565-BCG, but inconsistent with another one, Abell 1836-BCG. For the remaining target, Abell 2052-BCG, although the ionized-gas kinematics allowed us only to set an upper-limit on $M_\bullet$ it seems unlikely that this galaxy could obey both relations simultaneously. The fact that Abell 1836-BCG is an outliers in both the $M_\bullet - \sigma$ and $M_\bullet - L_{\rm bulge}$ relations would appear to weaken the claim of Lauer et al. (2007b) that $L_{\rm bulge}$ is more reliable predictor of $M_\bullet$ for BCGs. Overall, our results might indicate that the scatter of SMBH scaling relations increases at the high end, although additional data are necessary to test this claim.

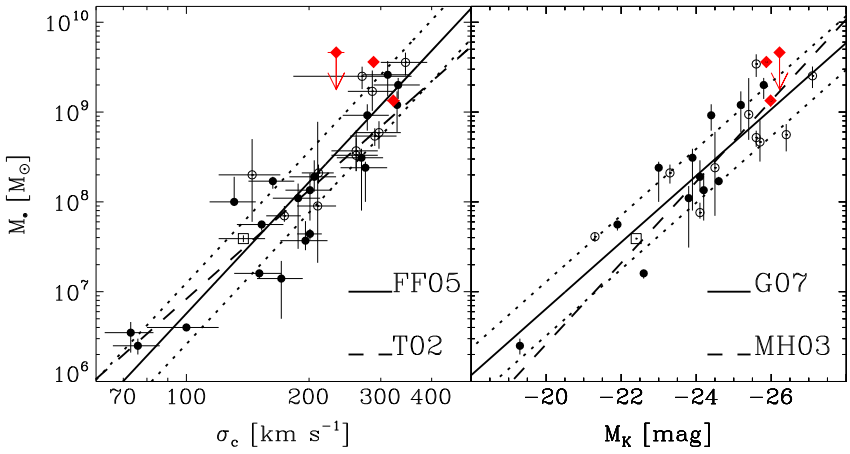

Figure 6.34 *Left panel*: Location of the SMBHs masses of our BCG sample galaxies (diamonds) with respect to the $M_\bullet - \sigma_c$ relation by Ferrarese & Ford (2005). We plot the SMBH masses based on resolved dynamical studies of ionized gas (open circles), water masers (open squares), and stars (filled circles) from Table 2 of Ferrarese & Ford (2005). The dashed line represents the Tremaine et al. (2002) relation. *Right panel*: Location of our BCG sample galaxies with respect to the near-infrared $M_\bullet - L_{K,\mathrm{bulge}}$ relation by Graham (2007). Data are taken from Table 2 of Graham (2007) and symbols are as in the left panel. Masses and magnitudes of NGC 5252, NGC 6251 and Cygnus A were adjusted to a distance obtained with $H_0 = 75$ km s^{-1} Mpc^{-1}. The dashed line represents the Marconi & Hunt (2003) relation. In both panels, we added the data relative to NGC 1399 Houghton et al. (2006) and the dotted lines represent the 1σ scatter in $M_\bullet$.

7

The ultraviolet flare at the center of the elliptical galaxy NGC 4278

Based on Cardullo, A., Corsini, E. M., Beifiori, A., Buson, L. M. , Dalla Bontà E., Morelli L., Pizzella A., & Bertola F., 2009, A&A, 508, 641

A large fraction of otherwise normal galaxies shows a weak nuclear activity. One of the signatures of the low-luminosity active galactic nuclei (LLAGNs) is ultraviolet variability which was serendipitously discovered in the center of some low-ionization nuclear emission-line region (LINER) galaxies. There is a pressing need to acquire better statistics about UV flaring and variability in galaxy nuclei, both in terms of the number and monitoring of targets. The Science Data Archive of the *Hubble Space Telescope* was queried to find all the elliptical galaxies with UV images obtained in different epochs with the Wide Field Planetary Camera 2 (WFPC2) and possibly with nuclear spectra obtained with the Space Telescope Imaging Spectrograph (STIS) in the region of the Hα emission line. These data were found only for the elliptical radio galaxy NGC 4278. The UV flux of the nuclear source of NGC 4278 was measured by means of aperture photometry on the WFPC2/F218W images obtained between June 1994 and January 1995. The mass of the central supermassive black hole (SMBH) was estimated by measuring the broad components of the emission lines observed in the STIS/G750M spectrum and assuming that the gas is uniformly distributed in a sphere. The nucleus of NGC 4278 hosts a barely resolved but strongly variable UV source. Its UV luminosity increased by a factor of 1.6 in a period of 6 months. The amplitude and scale time of the UV flare in NGC 4278 are remarkably similar to those of the brightest UV nuclear transients which were found earlier in other LLAGNs.

The mass of the SMBH was found to be in the range between 7×10^7 and 2×10^9 $M_\odot$. This is in agreement with previous findings based on different assumptions about the gas distribution and with the predictions based on the galaxy velocity dispersion. All the LINER nuclei with available multi-epoch UV observations and a detected radio core are characterized by a UV variable source. This supports the idea that the UV variability is a relatively common phenomenon in galaxy centers, perhaps providing the missing link between LINERs and true AGN activity.

7.1 Introduction

A large fraction of otherwise normal galaxies shows weak nuclear activity. These low-luminosity active galactic nuclei (LLAGNs) occupy the faintest end of the luminosity function of the AGNs and have very low accretion rates or radiative efficiencies onto the central supermassive black hole (SMBH, see Ho 2008 for a review).

One of the signatures of LLAGNs is ultraviolet (UV) variability as observed with *Hubble Space Telescope* (*HST*) in the nuclei of some low-ionization nuclear emission-line region (LINER) galaxies. There have been a number of reports after the serendipitous discovery of a UV flare in the center of the elliptical galaxy NGC 4552 (Renzini et al. 1995; Cappellari et al. 1999). The images of its nucleus obtained in a five year period with the Faint Object Camera (FOC) showed an increase of the UV luminosity by a factor of 4.5 followed by a dimming of a factor of 2. O'Connell et al. (2005) unveiled a similar phenomenon in the giant elliptical NGC 1399 using the Space Telescope Imaging Spectrograph (STIS), while a rapidly fading UV source was detected in the Virgo cluster spiral NGC 4579 (Maoz et al. 1995; Barth et al. 1996). This kind of research took on a more systematic approach by Maoz et al. (2005), who monitored the UV variability of a sample of 17 LINER galaxies with compact nuclear UV sources by means of the *HST* Advanced Camera for Surveys (ACS). They detected a significant UV variability in almost all the sample galaxies, which were mostly spirals, with amplitudes ranging from a few to 50 percent.

This suggests that the UV variability is a relatively common phenomenon in galaxy centers. Given this, there is a need to acquire better statistics, both in terms of the number of targets and monitoring the UV-variable nuclei. Maoz et al. (1995) already queried the *HST* Science Data Archive for ACS data and observed mostly spiral galaxies. We searched the Wide Field Planetary Camera 2 (WFPC2) archive for all the RC3 (de Vaucouleurs et al. 1991) elliptical galaxies having UV images obtained with the same filter in different epochs before 2008. We found 37 objects (12 LINERs, 2 Seyferts, 1 transition and 1 H II nucleus, 17 quiescent galaxies, and 4 objects with unknown nuclear activity; Ho et al. 1997a, and NASA/IPAC Extragalactic Database) with at least one F218W or F300W image. NGC 4278 was the only galaxy with multi-epoch

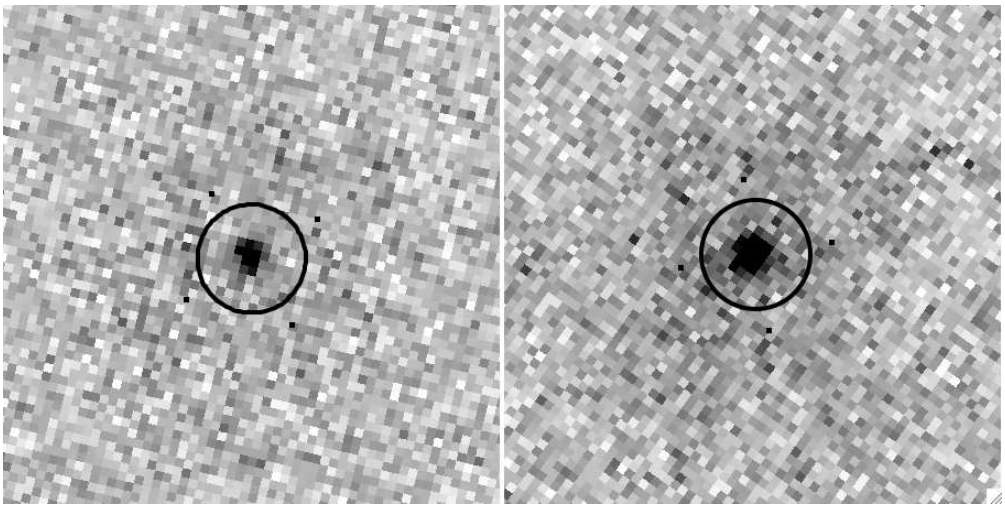

Figure 7.1 WFPC2/F218W images of the NGC 4278 nucleus of 2 June 1994 (*left*) and 14 January 1995 (*right*), displayed with the same grayscale. Each panel is 2.″5 on a side, north is up and east at the left. The UV flux was measured within the aperture marked by the circle ($r = 0.''28$).

WFPC2/F218W images, which was not studied before. A nuclear spectrum obtained within a subarcsecond aperture by STIS in the Hα region was also available in the *HST* Science Data Archive (see Figure 2.2). In this chapter, we present and discuss the results about the UV variability of its nucleus including an estimate of the mass of its SMBH based on STIS spectroscopy.

7.2 NGC 4278

NGC 4278 is a large ($4.'1 \times 3.'8$, RC3) and bright ($B_T = 11.09$, RC3) elliptical galaxy. It is classified E1–2 and hosts a LINER nucleus (L1.9, Ho et al. 1997a). Its total absolute magnitude is $M^0_{B_T} = -20.03$ (RC3), adopting a distance of 16.1 Mpc (Tonry et al. 2001). NGC 4278 is member of the Coma I cloud (Forbes 1996). It was one of the first elliptical galaxies in which neutral hydrogen was detected (Gallagher et al. 1977) and used to infer the dark mater content at large radii (Bertola et al. 1993). It is distributed in an inclined outer ring (Raimond et al. 1981), which is possibly associated with the inner disk of ionized gas (Goudfrooij et al. 1994; Sarzi et al. 2006). The northwest side of the galaxy is heavily obscured by large-scale dust patches and filaments which seem to spiral down into the nucleus (Carollo et al. 1997).

The optical and radio properties of the nucleus have been investigated in

detail (see Giroletti et al. 2005, and references therein). The radio data reveal two symmetric steep-spectrum jets on a sub parsec scale. They emerge from a flat-spectrum core and are responsible for the bulk of the emission at radio to optical frequencies in a similar way to that seen in more powerful radio loud AGNs. However, the total radio luminosity of NGC 4278 is at least 2 orders of magnitude less than those objects (Condon et al. 1998). This makes NGC 4278 an LLAGN (Giroletti et al. 2005).

7.3 Observations, data reduction, and analysis

7.3.1 Nuclear ultraviolet variability

The multi-epoch images obtained with the WFPC2 and the F218W filter were retrieved from the *HST* Science Data Archive. A 1800 s exposure was taken on 2 June 1994 (Prog. Id. 5380, P.I. A. Koratkar). Two exposures of 2200 s and 2300 s were obtained on 14 January 1995 (Prog. Id. 5381, P.I. A. Koratkar). The exposures were taken with the telescope guiding in fine lock mode, which typically gave an rms tracking error of $0\farcs003$. We focused our attention on the Planetary Camera (PC) chip where the nucleus of the galaxy was centered. This consists of 800×800 pixels of $0\farcs0455 \times 0\farcs0455$ each, yielding a field of view of about $36'' \times 36''$.

The images were calibrated using the standard WFPC2 reduction pipeline maintained by the Space Telescope Science Institute (STScI). Reduction steps including bias subtraction, dark current subtraction, and flat-fielding are described in detail in the WFPC2 instrument and data handbooks (Holtzman et al. 1995a; Baggett et al. 2002; Mc Master & Biretta 2008). Subsequent reduction was completed using standard tasks in the STSDAS package of IRAF[1]. The bad pixels were corrected by means of a linear one-dimensional interpolation using the data quality files and the WFIXUP task. The two 1995 images were aligned and combined using IMSHIFT and knowledge of the offset shifts. Cosmic ray events and residual hot pixels were removed using the LACOS_IMA procedure (van Dokkum 2001). The cosmic ray removal and bad pixel correction were checked by inspection of the residual image between the cleaned and the original frame to ensure that the nuclear region was not affected by light loss. The residual cosmic rays and bad pixels in the PC were corrected by manually editing the resulting image with IMEDIT. The sky level (~ 1 count pixel^{-1}) was determined from apparently empty regions in the Wide Field chips and subtracted from the PC frame after appropriate scaling.

[1]Imaging Reduction and Analysis Facilities is distributed by National Optical Astronomy Observatories (NOAO).

The flux calibration was performed by adopting the Vega magnitude system (Whitmore 1995) and by taking into account the time dependence of the UV response (Mc Master & Whitmore 2002). The presence of contaminants within WFPC2 causes a gradual build-up of material on the cold CCD faceplate of the camera, resulting in a decrease in the UV throughput. The contaminants are evaporated by periodically heating the camera to restore the instrumental throughput to its nominal value. The contamination rate is remarkably constant during each decontamination cycle, and can be accurately modeled by a simple linear decline following the decontaminations. The observed fluxes were corrected by assuming a decline in the F218W/PC normalized count rate of $(4.78 \pm 0.28) \times 10^{-3}$ per day since decontamination. This was derived during the decontamination cycles performed between April 1994 and June 1995 (Mc Master & Whitmore 2002), which bracket the observations of NGC 4278.

Evidence of the presence of a nuclear source was found in the two final images of NGC 4278. It is barely resolved (FWHM = 0.″07) when compared to the WFPC2/F218W point spread function (PSF, FWHM = 0.″06) derived with the TINY TIM package (Krist & Hook 1999). The total flux of the nuclear source was estimated as the flux in the circular aperture of radius of 0.″28 (Figure 7.1). The background level was determined as the median of the flux within the annulus of 0.″37–0.″51 centered on the source. The correction for the finite aperture radius has been performed by multiplying counts by 1.18 ± 0.01, based on the encircled-energy value of a point source tabulated in Holtzman et al. (1995b). The errors were calculated taking in account the Poisson and CCD readout noises, charge transfer efficiency, correction for contamination, and correction for finite aperture. The UV flux of the central source of NGC 4278 in the WFPC2/F218W passband increased from $(6.94 \pm 0.46) \times 10^{-16}$ to $(10.83 \pm 0.25) \times 10^{-16}$ erg cm^{-2} s^{-1} Å^{-1} from 2 June 1994 to 14 January 1995 (Figure 7.2).

7.3.2 Estimate of the mass of the central black hole

The long-slit spectrum of the nucleus of NGC 4278 obtained with STIS in the region of the [N II] $\lambda\lambda 6548, 6583$, H$\alpha$, and [S II] $\lambda\lambda 6716, 6731$ emission lines (Prog. Id. 7403, P.I. A. Filippenko) was retrieved from the *HST* Science Data Archive. The G750M grating was used at the secondary tilt $\lambda_c = 6581$ Å covering the wavelength range 6295–6867 Å. The spectrum was taken with the $0.''2 \times 52''$ slit placed across the galaxy nucleus with a position angle of 87.°9. The total exposure time was 3128 s (see Table 2.3). The dispersion is 0.55 Å pixel^{-1}. The instrumental resolution is 1.6 Å (FWHM) corresponding to $\sigma_{\rm inst} \approx 32$ km s^{-1} at Hα (see Section 2.3). The spatial scale of the 1024×1024

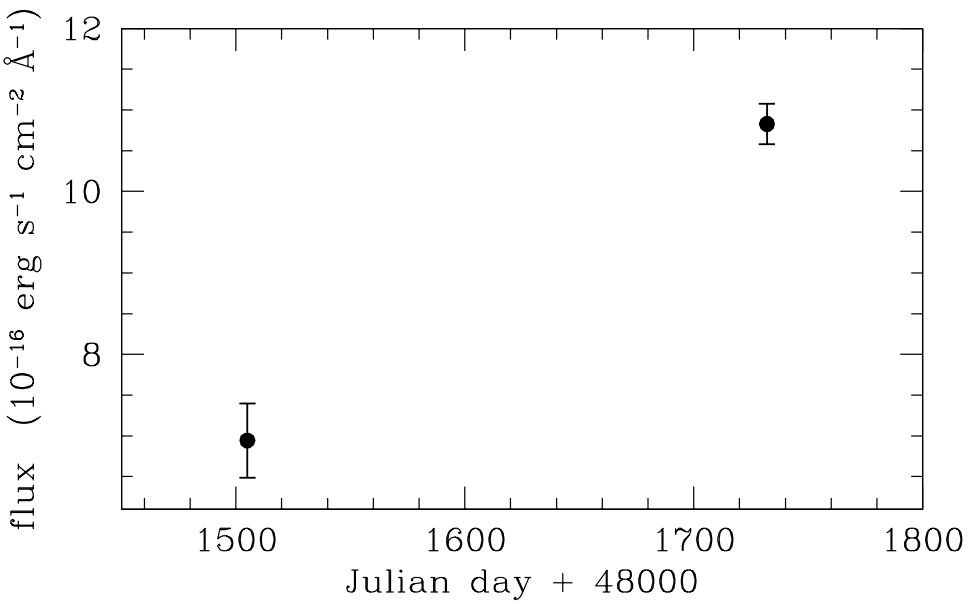

Figure 7.2 UV light curve in WFPC2/F218W band for the nucleus of NGC 4278. Points correspond to fluxes measured on 2 June 1994 and 14 January 1995, respectively.

SITe CCD is $0\farcs05$ pixel^{-1}.

The spectrum was reduced using IRAF and the STIS reduction pipeline maintained by the STScI. The basic reduction steps including overscan subtraction, bias subtraction, dark subtraction, and flatfield correction are described in detail in the STIS instrument and data handbooks (Kim Quijano et al. 2007; Dressel et al. 2007). The cosmic ray events and hot pixels were removed using the task LACOS_SPEC by van Dokkum (2001). The residual bad pixels were corrected by means of a linear one-dimensional interpolation using the data quality files. The wavelength and flux calibration as well as geometric correction for two-dimensional distortion were performed following the standard STIS reduction pipeline and applying the X2D task. This task corrected the wavelength scale to the heliocentric frame as well (see Section 2.3.1).

The central wavelengths, FWHMs, and intensities of the all the observed emission lines were measured following Beifiori et al. (2009) (see Sections 2.3.3 and 3.2.2). The broad and narrow components of the emission lines were fitted with multiple Gaussians, while describing the stellar continuum with a low-order polynomial. A flux ratio of 1:2.96 was assumed for the [N II] doublet, as dictated by atomic physics (e.g., Osterbrock 1989) and both the [N II] and

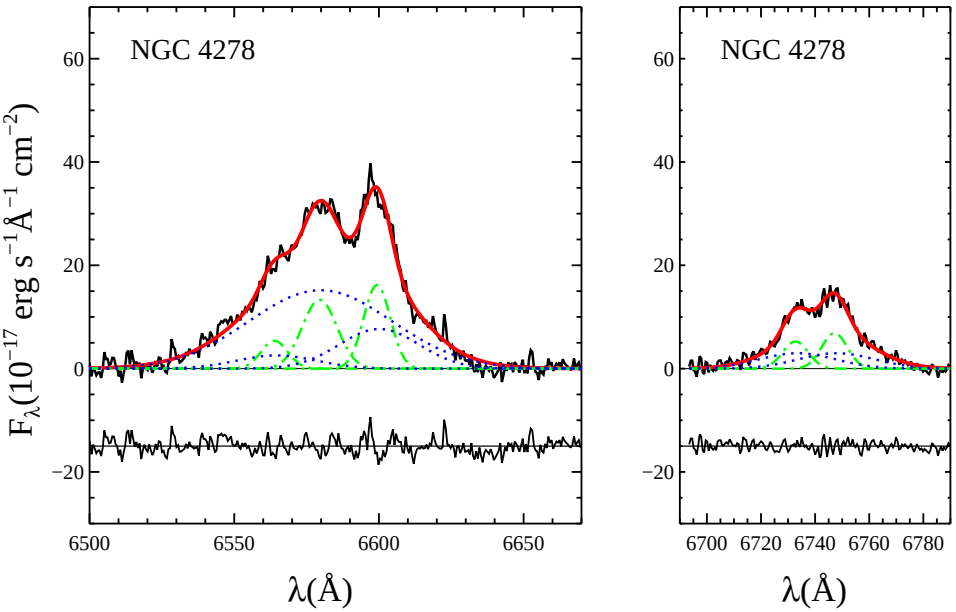

Figure 7.3 Continuum-subtracted central spectrum of NGC 4278 in the Hα+[N II] (*left panel*) and [S II] (*right panel*) regions. In each panel, the red solid line shows the overall line blend, whereas the green dashed-dotted lines and blue dotted lines show the adopted narrow and broad Gaussian components, respectively. Also are shown the fit residuals offset for better visibility.

[S II] doublets were assumed to share a common line centroid and width. A broad component was needed to describe the Hα emission out to 0.″20 from the center. The forbidden [N II] and [S II] lines required a broad component from −0.″05 to +0.″1. Figure 7.3 shows the continuum-subtracted nuclear spectrum of NGC 4278 with the fitted emission lines. It was extracted from the three central rows of the Hα STIS/G750M spectrum centered on the continuum peak. It thus consists of the central emission convolved with the STIS spatial PSF and sampled over a nearly square aperture of 0.″15 × 0.″2 (corresponding to 12 × 16 pc^2).

The mass $M_\bullet$ of the central SMBH can be estimated from the virial theorem by assuming that the gas is uniformly distributed within a sphere of radius R and moves around the SMBH with a mean velocity measured from the width of the broad component of the Hα line.

The lower limit on the size of the broad-line emitting region is given by the upper limit to the gas density as set by the forbidden lines and Hα luminosity.

Following Osterbrock (1989)

$$R_{\rm min} = \left(\frac{3 L_{\rm H\alpha}}{4\pi f n_{\rm e}^2 \alpha_{\rm H\alpha}^{\rm eff} h \nu_{\rm H\alpha}} \right)^{\frac{1}{3}} \tag{7.1}$$

where $L_{\rm H\alpha}$ is the total luminosity of the Hα broad component, f is the volume filling factor, $n_{\rm e}$ is the electron density of the gas, $\alpha_{\rm H\alpha}^{\rm eff}$ is the recombination coefficient for Hα, h is the Planck constant, and $\nu_{\rm H\alpha}$ is the frequency of the Hα line. The ratio of the [S II] lines sets $n_{\rm e} \approx 10^5$ cm^{-3}, whereas the spherical and uniform distribution of the gas gives a filling factor equal to 1. It is $L_{\rm H\alpha} = 4.13 \times 10^{38}$ erg s^{-1} from the measured flux $(1.34 \pm 0.10) \times 10^{-14}$ erg s^{-1} cm^{-2} and assumed distance. We then find $R_{\rm min} = 0.1$ pc. In this region $\sigma_V = 1224 \pm 40$ km s^{-1}, which corresponds to a lower limit on the SMBH mass of $M_\bullet \geq R_{\rm min}\sigma_V^2/G \simeq 7 \times 10^7$ M$_\odot$.

The upper limit on the size of the broad-line emitting region $R_{\rm max}$ can be estimated from the intrinsic emissivity distribution of the gaseous sphere. An intrinsically Gaussian flux profile centered on the stellar nucleus was assumed. It has a FWHM $= 0\farcs19$ (15 pc) when accounting for the STIS PSF (FWHM $= 0\farcs09$). The choice of a Gaussian parameterization is also conservative, since cuspier functions would have led us to estimate smaller $M_\bullet$. We find $R_{\rm max} = 5.9$ pc and $\sigma_V = 1127 \pm 30$ km s^{-1} which translates into an upper limit on the SMBH mass of $M_\bullet \leq R_{\rm max}\sigma_V^2/G \simeq 2 \times 10^9$ M$_\odot$.

7.4 Conclusions

UV variability with amplitudes ranging from a few to 50 percent over a timescale of a decade was detected in most of the LINER nuclei observed more than once (Maoz et al. 2005) suggesting a possible link between UV flares and SMBH-related activity in LLAGNs. To acquire better statistics, both in terms of the number of targets and their monitoring, we queried the *HST* Science Archive for all the elliptical galaxies with available UV images obtained with the WFPC2 in different epochs.

Multi-epoch images were found only for NGC 4278, a nearby radio galaxy known to host a LLAGN (Giroletti et al. 2005). It is characterized by a barely resolved nuclear source, which increased its UV luminosity by a factor of 1.6 in a period of 6 months. The amplitude and scale time of the variation are similar to those of the UV-brightest nuclear transients, which were earlier discovered in NGC 4552 (Renzini et al. 1995; Cappellari et al. 1999), NGC 4579 (Maoz et al. 1995; Barth et al. 1996), and NGC 1399 (O'Connell et al. 2005).

These serendipitous findings support the idea that the UV variability is a common event at the center of galaxies where SMBHs reside. Some alternatives

to the AGN interpretation were explored to explain the UV variability. Maoz et al. (2005) pointed out that individual supergiants in galactic nuclei are not plausible candidates to produce the observed UV flux variations. On the other hand, the even brighter Wolf-Rayet and luminous blue variable stars could only explain the variations measured in the nuclei of lower UV luminosity. The fallback of debris onto the SMBH, and collisions between precessing debris orbits (Rees 1988; Kim et al. 1999) are expected to produce bright UV/X-rays flares (Ulmer 1999). But given their rarity ($\approx 10^{-4}$ yr^{-1} per galaxy, Magorrian & Tremaine 1999; Wang & Merritt 2004), the stellar tidal disruptions can emerge only in all-sky deep X-ray (Donley et al. 2002; Esquej et al. 2007) and UV surveys (Gezari et al. 2006, 2008, 2009) and cannot account all the observed variable nuclei. This is particularly true for the galaxies with repeated episodes of UV variability, like NGC 4552 (Renzini et al. 1995; Cappellari et al. 1999; Maoz et al. 2005).

It was possible to estimate the mass of the SMBH at the center of NGC 4278. The central width and radial extension of the broad components of the emission lines were measured over a subarcsecond aperture in the available STIS spectrum of the nucleus. If the gas is uniformly distributed within a sphere then it is $7 \times 10^7 \leq M_\bullet \leq 2 \times 10^9$ M$_\odot$. This is consistent with the predictions of the $M_\bullet - \sigma$ relations by Ferrarese & Ford (2005) and Lauer et al. (2007a) when adopting a central velocity dispersion $\sigma_c = 333 \pm 8$ km s^{-1} (Beifiori et al. 2009, see Tables 2.2 and 3.1). There is also a good agreement with the upper limits on $M_\bullet$ given by Beifiori et al. (2009) (see Table 3.2). They measured the nuclear width of the narrow component of the [N II] λ6583 emission line and modelled it as due to the Keplerian motion of a thin disk of ionized gas around the putative SMBH. They found $M_\bullet \leq 5 \times 10^7$ for a nearly edge-on disk and $M_\bullet \leq 2 \times 10^8$ M$_\odot$ for a nearly face-on disk.

According to Giroletti et al. (2005) this SMBH is active and able to produce the relativistic jet, responsible for most of the emission at optical and radio frequencies of this LLAGN. It is the same process as the ordinary radio loud AGNs despite a much lower power. The AGN interpretation is a promising way to explain the UV variability. In fact, all the LINER nuclei with multi-epoch observations and a detected radio core are characterized by UV variable sources (Maoz et al. 2005). This is the case of NGC 4278, too, suggesting that UV variability could provide the missing link between LINERS and true AGN activity (Cardullo et al. 2009). Unfortunately, it is the only elliptical galaxy observed by *HST* at different epochs in the UV and which was not studied before. This fact does not allow us to derive any firm statistical conclusion about the frequency of UV flares at the center of elliptical galaxies. Nevertheless, out of 37 galaxies, the only object with multi-epoch UV observations turned out to

be variable. This is a further suggestion that this phenomenon may be quite common. Additional imaging with the Wide Field Camera 3 recently installed on *HST* to monitor the UV variablity in a statistically significant sample of quiescent and active nuclei and STIS spectra to measure their SMBHs are highly desirable to gain insights into this subject in the near future.

8

Conclusions

The aim of this thesis was to understand the rôle of supermassive black holes (SMBHs) in the evolution of galaxies. This was done by studying the fundamental correlations between the SMBH mass $M_\bullet$, and the properties of the hosting galaxy.

Yet, the existing samples still comprise mainly of early-type galaxies with few $M_\bullet$ determinations in galaxies with high and small stellar velocity dispersion σ, or in spiral galaxies where nuclear clusters often appear as a prominent central component. In fact, the uncertainties in the actual slope and scatter of all the scaling relations are still under debate. A better statistics in term of number of targets, morphological type subdivision, and methods of measurement would be helpful in the understanding the coevolution between SMBHs and their host. Throughout this thesis, we have presented a series of new results to increase such a statistics from the lower to the upper end of the local SMBH population to understand whether $M_\bullet$ relates more closely to the bulge or to the host galaxy as a whole, including the dark matter halo.

The main conclusions of this thesis can be summarized as follows. 1) We could map the $M_\bullet - \sigma$ relation from the lower to the upper end of the local SMBH population by using simple estimates of $M_\bullet$ but for the largest and most various sample of host galaxies. These $M_\bullet$ estimates are consistent with the known $M_\bullet - \sigma$ relation, with no dependence on galaxy distance, morphological type or bar presence. They can be adopted to study the trend and scatter of the other $M_\bullet$ scaling relations. 2) Following the results of this work we focused on the interpretation of the demography of SMBHs, specifically in trying to understand whether the $M_\bullet$ relates more closely to the mass of the bulge or to the total mass of the host galaxy, included dark matter. We confirmed that

$M_\bullet$ is fundamentally driven by σ for all Hubble types. The same is true for the fundamental plane of SMBHs. 3) We explored the high-mass end of the SMBH mass function to understand the link between the evolution of SMBHs and the hierarchical build-up of galaxies, by analyzing adaptive-optics stellar observations of the central regions of massive elliptical galaxies such us NGC 1265 and estimating $M_\bullet$ in three brightest cluster galaxies by measuring the gaseous kinematics with *Hubble Space Telescope* (*HST*). The first results indicates a steepening of the trend of the $M_\bullet - \sigma$ relation in the high-σ range, that suggests either a higher scatter or the necessity of a different law, which predicts a faster grow of the SMBH with respect to σ.

8.1 Summary of the main results

8.1.1 Atlas of *HST*/STIS Spectra and Images of 177 nearby galaxies (*Chapter 2*)

We present the data compilation of all nearby galaxies ($D < 100$ Mpc), with long-slit spectra available in the *HST* archive and taken with the Space Telescope Imaging Spectrograph (STIS) mounting the G750M grating. The spectra cover the region of the Hα line and of [N II] $\lambda\lambda 6548, 6583$ and [S II] $\lambda\lambda 6716, 6731$ emission-line doublets. This atlas comprises 177 galaxies observed in the central $0\farcs10 - 0\farcs3$. We measured the ionized-gas velocity dispersion from the width of the [N II] $\lambda 6583$ line by fitting Gaussians to the narrow and broad components of the [N II] and [S II] doublets, while the Hα line and broad components of the doublets were fitted with additional Gaussians with different width and velocity. This lead to the most comprehensive spectral atlas of low-luminosity AGNs. The gaseous kinematics could be measured in 122 galaxies. 111 had the stellar velocity dispersion available in the literature. These measurements are necessary to estimate upper limits on $M_\bullet$ for a large and various sample of galaxies. The STIS acquisition images were used to identify the presence of nuclear star clusters in these galaxies (see Chapter 3). We performed also two-dimensional bulge-to-disk decomposition of the 2MASS and UKIDSS images of 65 sample galaxies in order to measure the K-band spheroidal luminosity $L_{K,\mathrm{bulge}}$ and determine the effective radius r_e to correct the central velocity dispersion of the stellar component.

8.1.2 Upper limits on the masses of 105 supermassive black holes from *HST*/STIS archival data (*Chapter 3*)

To expand and homogenize the existing sample of $M_\bullet$ we undertook a project aimed at measuring upper limits on the mass of SMBHs in 105 nearby galaxies

(<100 Mpc), for which nuclear spectra were obtained with STIS/G750M including the region of the Hα line and the [N II] $\lambda\lambda$6548, 6583 and [S II] $\lambda\lambda$6716, 6731 doublets. These $M_\bullet$ upper limits were derived by modeling the widths of the observed emission lines in terms of gas motions in a thin disk of unknown orientation but known spatial extent. This sample spans a wide range of Hubble types (E−Sc) and includes objects with published values for their central σ (58−419 km s^{-1}).

The upper limits that we derived are consistent with both the $M_\bullet - \sigma$ relation of Ferrarese & Ford (2005) and Lauer et al. (2007a) and with the secure $M_\bullet$ determinations. Most important, independent of the galaxy distance, morphological type or bar presence, our $M_\bullet$ upper limits run parallel and above the previous two versions of $M_\bullet - \sigma$ relations. This suggests that, although strictly speaking we cannot rule out the rôle of non-gravitational forces, our line-width measurements actually trace well the nuclear regions dominated by the central SMBH, which in practice allows us to estimate $M_\bullet$.

Yet, at small σ some $M_\bullet$ upper limits systematically exceed the expected $M_\bullet$, as the line-width measurements for such low-σ outliers are most likely affected by the stellar contribution to the gravitational potential due to the presence of conspicuous nuclear clusters. At high σ values, the comparison of our upper limits with Ferrarese & Ford (2005) suggests a flattening of the $M_\bullet$ distribution, which contrasts with the steepening of the $M_\bullet - \sigma$ relation found in Wyithe (2006) and in Dalla Bontà et al. (2009, see Section 8.1.5) and suggested by the local velocity dispersion function studies Sheth et al. (2003).

8.1.3 On the relationships between supermassive black holes, spheroids, and dark matter halos (*Chapter 4*)

We coupled the large sample of upper limits from Chapter 3 and the most up to date compilation of $M_\bullet$ from Gültekin et al. (2009b) with libraries of galaxy velocity dispersions, maximum rotational velocities, and galaxy photometric parameters extracted from SDSS i-band images to establish correlations between $M_\bullet$ and the properties of bulge and the host galaxy, including the dark matter halo. We tested correlations between $M_\bullet$ and stellar velocity dispersion, i-band bulge luminosity, bulge virial mass, bulge Sérsic index, total i-band luminosity of the galaxy, galaxy stellar mass, maximum circular velocity, and galaxy dynamical and virial masses. While we confirmed the tightness of the $M_\bullet - \sigma$ relation, we found that galaxies do not follow a $M_\bullet - V_\mathrm{c}$ relation. Moreover, the total galaxy potential plays less rôle in setting $M_\bullet$. We searched for dependences between the residuals of the known relations and galaxy parameters to understand whether the relations we found are a sufficient description

of our data or if there is the evidence of an additional dependence on more We confirmed that the $M_\bullet$ is fundamentally driven by σ for all Hubble types. The fundamental plane of SMBHs is mainly driven by σ, with a small fraction of the tilt due to the effective radius.

8.1.4 Seeking the most massive black holes: the case of NGC 1265-3C 83.1B (*Chapter 5*)

The advent of the adaptive-optics (AO) facilities in the 8-m class telescope allowed to measure $M_\bullet$ in galaxies as giant ellipticals, and the dusty nuclei of spirals that could not have been studied in the past with *HST* (e.g., Houghton et al. 2006; Nowak et al. 2008). An interesting object is NGC 1265-3C 83.1B, the second brightest galaxy in the Perseus cluster. NGC 1265 is a well known powerful active galactic nucleus displaying a strong radio emission. For NGC 1265, we modelled the K-band AO assisted spectroscopic observations with the aim of constraining the mass of the SMBH. The near-infrared data taken with the AltairNIRI on the Gemini North have a spatial resolution of FWHM $= 0\farcs11$ (39 pc). To account for the stellar contribution, we performed a multi-Gaussian expansion (Cappellari 2002) by using a combination of our NIRI high-resolution K-band image and a TNG K'-band image (Marchesini et al. 2005) to cover the outer parts of the galaxy. We extracted the stellar kinematics by using the penalized pixel fitting method (Cappellari & Emsellem 2004) from the CO absorption bands at 2.29 μm. Jeans anisotropic models (Cappellari 2008) were adopted to fit the stellar kinematics and surface distribution to determine the best fitting value for anisotropy and $M_\bullet$. The limited quality of our kinematical data did not allow us to measure a very extended kinematics, hence we made just a preliminary estimation of the $M_\bullet$. We resorted to assuming fixed values for both the $(M/L)_K$ and anisotropy β, using the results by Cappellari et al. (2006, 2007). The derived upper limit on $M_\bullet$ ranges between 1×10^9 $M_\odot$ and 3.4×10^9 $M_\odot$ depending on the values of β and $(M/L)_K$, respectively. This mass estimate is in agreement with the $M_\bullet - L_{K,\mathrm{bulge}}$ relation by Marconi & Hunt (2003). The addition of the new observations, recently obtained with the Oxford SWIFT spectrograph on the Hale 5-m telescope at Palomar Observatory will be useful to constrain $(M/L)_K$ and to obtain a higher confidence value for $M_\bullet$.

8.1.5 The high-mass end of the supermassive black hole mass function: mass estimates in brightest cluster galaxies (*Chapter 6*)

The study of the high mass end of the local SMBH mass function is a useful tool to understand the link between the evolution of SMBHs and the hierarchical

build-up of galaxies.

To this aim were measured the $M_\bullet$ of three galaxies brightest cluster galaxies (BCGs) by using observations made with STIS, the Wide Field and Planetary Camera 2 (WFPC2) and the Advanced Camera for Surveys (ACS) on *HST*. The data provided detailed information on the structure and mass profile of the stellar component, dust optical depth, and spatial distribution and kinematics of the ionized gas within the innermost region of each galaxy. Dynamical models, which account for the observed stellar mass profile and include the contribution of a central SMBH were constructed to reproduce the kinematics derived from the [N II] λ6583 emission line. Secure SMBH detection with $M_\bullet = 3.61^{+0.41}_{-0.50} \times 10^9$ $M_\odot$ and $1.34^{+0.21}_{-0.19} \times 10^9$ $M_\odot$, respectively, were obtained for Abell 1836-BCG and Abell 3565-BCG, which show regular rotation curves and strong central velocity gradients. In the case of Abell 2052-BCG, the lack of an orderly rotational motion prevented a secure determination, although an upper limit of $M_\bullet < 4.60 \times 10^9$ $M_\odot$ could be placed on the mass of the central black hole. These measurements are an important step forward in characterizing the high-mass end of the SMBH mass function. The results suggest a steepening of the trend of the $M_\bullet - \sigma$ relation in the high-σ range, that suggest either a higher scatter or the necessity of a different law, which predicts a faster grow of the SMBH with respect to the σ.

8.1.6 The ultraviolet flare at the center of the elliptical galaxy NGC 4278 (*Chapter 7*)

A large fraction of otherwise normal galaxies shows a weak nuclear activity. One of the signatures of the low-luminosity active galactic nuclei (LLAGNs) is ultraviolet variability which was serendipitously discovered in the center of some low-ionization nuclear emission-line region (LINER) galaxies. There is a pressing need to acquire better statistics about UV flaring and variability in galaxy nuclei, both in terms of the number and monitoring of targets. The Science Data Archive of the *HST* was queried to find all the elliptical galaxies with UV images obtained in different epochs with WFPC2 and possibly with nuclear spectra obtained with STIS in the region of the Hα emission line. These data were found only for the elliptical radio galaxy NGC 4278, a galaxy for which we already studied the kinematics of the narrow component of [N II] λ6583 and measured an upper limit on $M_\bullet$.

The UV flux of the nuclear source of NGC 4278 was measured by means of aperture photometry on the WFPC2/F218W images obtained between June 1994 and January 1995. We estimated an upper and lower limit on the mass of the central SMBH by using the broad emission-line measurements we made in

the STIS/G750M spectrum and assuming that the gas is uniformly distributed in a sphere of radius R. The $M_\bullet$ is found to be in the range between 7×10^7 and 2×10^9 $M_\odot$ depending on the radius we obtained from estimations of the dimensions of the broad line region. This $M_\bullet$ was compared with the upper limits we derived in Chapter 3 finding a good agreement. The nucleus of NGC 4278 hosts a barely resolved but strongly variable UV source. Its UV luminosity increased by a factor of 1.6 in a period of 6 months. The amplitude and scale time of the UV flare in NGC 4278 are remarkably similar to those of the brightest UV nuclear transients which were found earlier in other LLAGNs.

8.2 Future work

The results presented here have led to a series of new projects which were not ready to be included in this thesis.

8.2.1 Supermassive black hole masses and K-band luminosity of galaxies

In establishing the connection between SMBHs and the properties of their host galaxies, there is another often overlook source of uncertainty, the bulge properties with which the $M_\bullet$ is compared. Considering the most widely adopted bulge property, σ, in general this is not consistently and accurately measured, and is also an ill-defined property to derive in the case of the bulges in spirals due to the dynamical presence of the disk. An alternative way to investigate the $M_\bullet$ budget across the entire Hubble sequence is to consider the K-band bulge luminosity ($L_{K,\mathrm{bulge}}$). It traces the stellar mass and can be disentangled from the disk luminosity by means of accurate photometric decompositions.

The $L_{K,\mathrm{bulge}}$ was found to correlate with the $M_\bullet$ by Marconi & Hunt (2003) although on the basis of a limited sample. In order to further test the $M_\bullet - L_{K,\mathrm{bulge}}$ relation for all kind of galaxies we are planning to obtain new deep photometric observations for the upper limits on the $M_\bullet$ described in Chapter 3. Deep images are indeed necessary to constrain the disk properties and properly isolate the contribution of the bulge to the total luminosity of the galaxy. As shown in Chapter 2, archival 2MASS images often do not fulfill these requirements. Measuring $L_{K,\mathrm{bulge}}$ from such shallow images in disk galaxies is further complicated by the presence of additional structures like bars and spiral arms.

In Chapter 2 we also demonstrated that the high-resolution UKIDSS images are deep enough to obtain accurate structural parameters for our galaxies. We will search in the latest UKIDSS data release for new images and seek the Visible and Infrared Survey Telescope for Astronomy (VISTA, Dalton et al.

2004) archive for all the galaxies in the Southern hemisphere. The remaining galaxies will be sampled with the infrared spectrograph and imaging camera (SofI) on the New Technology Telescope (NTT) at La Silla Observatory in Chile, and with the Near Infrared Camera Spectrometer (NICS) at the Telescopio Nazionale Galileo (TNG) at La Palma. The use of new version of the GASP2D code (Méndez-Abreu 2008) will allow us to correctly decompose the light distribution of barred galaxies.

8.2.2 Searching for a supermassive black hole in the nuclear cluster of NGC 278

Over the last few year a series of imaging and spectroscopic surveys carried out with the *HST* have revealed that the nuclear regions of late-type spirals and of small early-type galaxies very often host a compact, photometrically distinct stellar cluster (Böker et al. 2002; Côté et al. 2006). Most intriguingly, the mass of such nuclear clusters (NCs) appears to correlate with the mass of their host galaxies like SMBHs do (Rossa et al. 2006; Ferrarese et al. 2006). NCs tend to be approximately ten times more massive than SMBHs for a given bulge mass. These findings have lead to suggest that SMBHs may find it more difficult or may not even not form at all in the center of the less massive galaxies, where NCs may instead replace SMBHs as the principal nuclear component. Although signs of black-hole accretion have been detected in a few objects with NCs, the presence and mass of a SMBH in a galaxy with a NC has yet to be directly established, with a few exceptions (Shields et al. 2008; Barth et al. 2009).

In this respect, the case of NGC 278 provides a golden opportunity. This galaxy hosts a NC which was observed with the STIS spectrograph with both the G430L and G750M gratings to study its stellar populations and emission-line properties, respectively (Sarzi et al. 2005). In the course of our analysis of archival STIS/G750M data we established that the nucleus of NGC 278 is mostly devoid of emission (see the spectrum of this galaxy in Figure 2.2). We found that the stellar kinematics of its NC could be measured with the Hα and Ca+Fe λ6495 Å absorption lines, while using as a template the G750M spectrum of a star that was accidentally acquired during the same observations. This star turned out to have an A-star spectral type, which fits well with the young age of the NC. The stellar velocity dispersion of NGC 278, estimated by Ho et al. (2009) from the Ca+Fe feature at 6495 Å is $\sigma = 47.6 \pm 8.9$ km s^{-1} and makes NGC 278 an excellent probe of the low$-M_\bullet$ end of the $M_\bullet - \sigma$ relation.

We will model the stellar kinematics of the NC of NGC 278 using the same tools that we used for the NGC 1265, in order to constrain the mass of the central SMBHs also in this galaxy and establish whether SMBHs and NCs can

indeed coexist. No extra observations will be needed in the case of NGC 278, as the stellar mass-to-light ratio of its NC will be tightly constrained by determining the stellar population content using the G430L spectra (e.g., Sarzi et al. 2005; Rossa et al. 2006).

8.2.3 New measurements of the stellar velocity dispersion for galaxies with a measured upper limits on the black hole mass

To complete the sample of upper limits on the $M_\bullet$ measured from the *HST*/STIS emission lines described in Chapter 2, we still miss 11 galaxies without σ in the literature. They are mainly late-type spirals. We are planning long-slit observations of their stellar component from both the Southern and Northern hemisphere. A high instrumental resolution is required to measure the central velocity dispersion which is expected to be $\sigma < 100$ km s^{-1}. The σ will be derived by simultaneously fitting the emission and absorption lines in the spectra by using the GANDALF software (Sarzi et al. 2006), coupled with a stellar library developed for stellar population synthesis modeling (e.g., Sánchez-Blázquez et al. 2006). This will allow us to complete the analysis of all nearby galaxies with STIS/G750M Hα spectra in the *HST* archive.

8.2.4 Study of the emission-line kinematics in the nuclear regions of nearby galaxies

The study of the emission-line kinematics in low-luminosity AGNs (LLAGNs) with high-resolution *HST*/STIS data helps in the understanding of the behavior of the gas in the central region of the galaxies. By using *HST*/STIS Walsh et al. (2008) studied the central $50 - 100$ pc of a sample of LLAGNs finding that the [N II] $\lambda\lambda 6548, 6583$ emission peaks within the SMBH sphere of influence allowing the study of the kinematics dominated by the SMBH. At larger aperture the width of the [N II] lines decreases, approaching the stellar velocity dispersion, indicating a relation to the bulge properties. This results has a possible implication for the fueling of the central SMBH and for the connection between the stellar σ and formation of the SMBH (Ho 2009). The emission-line gas can be either a source of fuel or a tracer of the fuel for any nuclear activity. The existence of the $M_\bullet - \sigma$ relation suggests that there is a mechanism that mediates the black hole growth as a function of the stellar σ in the sense that the stellar σ drives up the gas σ and prevents the gas from settling and falling into the black hole (Noel-Storr et al. 2007). The *HST*/STIS data allowed also to find the presence of chaotic motions in the narrow line region (Ho et al. 2002; Atkinson et al. 2005; Noel-Storr et al. 2003, 2007; Verdoes Kleijn et al. 2006) that are thought to be connected with the Eddington ratio (Boroson

2005; Greene & Ho 2005a; Ho 2009), and therefore to the AGN feedback and effects on host-galaxy properties.

In order to properly interpret SMBH mass models and models of fueling mechanisms, it is essential to understand the dynamics of the gas disks themselves in a systematic manner by using galaxies with different nuclear activity and Hubble types in respect to the previous studies. By using all the parameters obtained to measure the upper limits on the $M_\bullet$ of for the sample of 118 nearby galaxies described in Chapter 2 we can study the dynamical state of the gas for a large and variegate sample of galaxies, searching for possible motions that might be related to AGN fueling. All the data collected from the STIS spectra will allow us to study the emission-line ratios to analyze the ionization mechanisms at work in the nuclear regions of this large and various sample of galaxies. Previous studies (e.g., Noel-Storr et al. 2003) found line ratios compatible with typical values due to the photoionization and shock models (see Dopita et al. 1997) but for a smaller sample of radio galaxies. By studying a sample of early-type galaxies, Sarzi et al. (2009) recently found that the diffuse and old stellar sources are the the main contributors of the ionizing photons. This study will be done by comparing the trend of the [N II] flux as a function of the flux of the narrow component of Hα. We will also derive the ratio [S II] λ6716/[S II] λ6731 as a function of the radial distance to estimate the electron density (see Osterbrock 1989).

8.2.5 Analysis of the central region of galaxies with a measured upper limit on the black hole mass

The *HST* archive offer us a large compendium of images that we can use to study the central region of galaxies for which we derived the upper limits on $M_\bullet$. A large part of our sample have ACS and WFPC2 images in the *HST* archive that can be used to study the structure of the inner region. This was not always possible with the acquisition images that are too small to properly perform a decomposition of the central components (e.g., nuclear disks, nuclear bars, nuclear spirals). A better study of the central regions will allow us to better understand the distribution of our upper limits on $M_\bullet$ against σ in terms of central structure and bar presence. In fact, while we did not find difference in the distribution between barred and non-barred galaxies some authors suggest the contrary (Hu 2008; Graham 2008; Graham & Li 2009).

The ACS and WFPC2 images will be also useful to obtain the parameterization of the stellar surface density for our galaxy sample applying multi-Gaussian expansion (MGE, Cappellari 2002) This will allow us to account properly of the stellar component in the estimation of $M_\bullet$. The addition of Near-Infrared Cam-

era and Multi Object Spectrometer (NICMOS) archival images we will allow us to produce color maps of the dust features and the studying of the morphologies, extending the work of Carollo et al. (1998), Martini & Pogge (1999), Laine et al. (2001), Hughes et al. (2003), to a larger sample of galaxies.

8.2.6 Supermassive black hole mass in the high-end of the SMBH population

The sample of upper limits on $M_\bullet$ described in Chapter 2 is useful to select galaxies for which we can further measure precise $M_\bullet$. To increase the number of measurements of $M_\bullet$ in massive galaxies we are planning to observe a sample of 5 galaxies characterized by high values of σ ($\geq$ 300km s^{-1}). With the archival data we cannot perform an appropriate modeling for these galaxies, so that we think that the stellar kinematics would be a better instrument to determine the $M_\bullet$. There are few measurements of $M_\bullet$ for the most massive galaxies characterized by such a high values of σ (i.e., the highest and rare allowed value of σ according to the velocity dispersion function of Sheth et al. 2003). A measurement of the $M_\bullet$ hosted by such galaxies would represent an important step forward in the characterization of the SMBH-bulge relationship, exploring the actual extreme of the σ range. We will derive precise measurements of $M_\bullet$, by modeling the kinematics of the CO absorption bands at 2.3 μm. To this purpose we are planning observations with the NIR SINFONI integral-field spectrograph installed on the Very Large Telescope coupled with the AO module.

Bibliography

Abazajian, K. N., et al. 2009, ApJS, 182, 543

Abell, G. O. 1958, ApJS, 3, 211

Abell, G. O., Corwin, Jr., H. G., & Olowin, R. P. 1989, ApJS, 70, 1

Adams, F. C., Graff, D. S., Mbonye, M., & Richstone, D. O. 2003, ApJ, 591, 125

Adams, F. C., Graff, D. S., & Richstone, D. O. 2001, ApJ, 551, L31

Aguerri, J. A. L., Iglesias-Páramo, J., Vílchez, J. M., Muñoz-Tuñón, C., & Sánchez-Janssen, R. 2005, AJ, 130, 475

Aller, M. C. & Richstone, D. O. 2007, ApJ, 665, 120

Anderson, J. & van der Marel, R. P. 2009, ArXiv e-prints

Andredakis, Y. C. & Sanders, R. H. 1994, MNRAS, 267, 283

Arribas, S., Mediavilla, E., Garcia-Lorenzo, B., & del Burgo, C. 1997, ApJ, 490, 227

Atkinson, J. W., et al. 2005, MNRAS, 359, 504

Baes, M., Buyle, P., Hau, G. K. T., & Dejonghe, H. 2003, MNRAS, 341, L44

Baggett, S., et al. 2002, HST WFPC2 Data Handbook v. 4.0 (ed. B. Mobasher, Baltimore, STScI)

Baggett, W. E., Baggett, S. M., & Anderson, K. S. J. 1998, AJ, 116, 1626

Balcells, M., Morganti, R., Oosterloo, T., Perez-Fournon, I., & Gonzalez-Serrano, J. I. 1995, A&A, 302, 665

Balmaverde, B., Baldi, R. D., & Capetti, A. 2008, A&A, 486, 119

Balmaverde, B. & Capetti, A. 2006, A&A, 447, 97

Balmaverde, B., Capetti, A., & Grandi, P. 2006, A&A, 451, 35

Bandara, K., Crampton, D., & Simard, L. 2009, ApJ, 704, 1135

Barth, A. J., Greene, J. E., & Ho, L. C. 2005, ApJ, 619, L151

Barth, A. J., Ho, L. C., Rutledge, R. E., & Sargent, W. L. W. 2004, ApJ, 607, 90

Barth, A. J., Ho, L. C., & Sargent, W. L. W. 2002, AJ, 124, 2607

—. 2003, ApJ, 583, 134

Barth, A. J., et al. 1996, AJ, 112, 1829

Barth, A. J., et al. 2001, ApJ, 555, 685

Barth, A. J., Strigari, L. E., Bentz, M. C., Greene, J. E., & Ho, L. C. 2009, ApJ, 690, 1031

Barway, S. & Kembhavi, A. 2007, ApJ, 662, L67

Batcheldor, D., et al. 2005, ApJS, 160, 76

Batcheldor, D. & Koekemoer, A. M. 2009, PASP, 121, 1245

Batcheldor, D., Marconi, A., Merritt, D., & Axon, D. J. 2007, ApJ, 663, L85

Beifiori, A., et al. 2009, ApJ, 692, 856

Bell, E. F., McIntosh, D. H., Katz, N., & Weinberg, M. D. 2003, ApJS, 149, 289

Bender, R. 1990, A&A, 229, 441

Bender, R., et al. 2005, ApJ, 631, 280

Bender, R., Saglia, R. P., & Gerhard, O. E. 1994, MNRAS, 269, 785

Benson, A. J., Džanović, D., Frenk, C. S., & Sharples, R. 2007, MNRAS, 379, 841

Bernardi, M., et al. 2002, AJ, 123, 2990

Bernardi, M., et al. 2003, AJ, 125, 1866

Bernardi, M., Sheth, R. K., Tundo, E., & Hyde, J. B. 2007, ApJ, 660, 267

Bertola, F., et al. 1998, ApJ, 509, L93

Bertola, F. & Perola, G. C. 1973, Astrophys. Lett., 14, 7

Bertola, F., Pizzella, A., Persic, M., & Salucci, P. 1993, ApJ, 416, L45+

Bettoni, D. & Galletta, G. 1997, A&AS, 124, 61

Binney, J. & Merrifield, M. 1998, Galactic astronomy (Princeton University Press, Princeton series in astrophysics)

Binney, J. & Tabor, G. 1995, MNRAS, 276, 663

Bogdanović, T., Smith, B. D., Sigurdsson, S., & Eracleous, M. 2008, ApJS, 174, 455

Böker, T., et al. 2002, AJ, 123, 1389

Böker, T., et al. 2004, AJ, 127, 105

Bonfanti, P., Rampazzo, R., Combes, F., Prugniel, P., & Sulentic, J. W. 1995, A&A, 297, 28

Booth, C. M. & Schaye, J. 2009, ArXiv e-prints

Boroson, T. 2005, AJ, 130, 381

Bottinelli, L., Gouguenheim, L., Paturel, G., & de Vaucouleurs, G. 1983, A&A, 118, 4

Bower, G. A., et al. 1998, ApJ, 492, L111+

Braatz, J. A., Wilson, A. S., & Henkel, C. 1994, ApJ, 437, L99

Bruzual, G. & Charlot, S. 2003, MNRAS, 344, 1000

Byun, Y. I. & Freeman, K. C. 1995, ApJ, 448, 563

Caon, N., Capaccioli, M., & D'Onofrio, M. 1993, MNRAS, 265, 1013

Capetti, A., Verdoes Kleijn, G., & Chiaberge, M. 2005, A&A, 439, 935

Cappellari, M. 2002, MNRAS, 333, 400

—. 2008, MNRAS, 390, 71

Cappellari, M., et al. 2006, MNRAS, 366, 1126

Cappellari, M. & Emsellem, E. 2004, PASP, 116, 138

Cappellari, M., et al. 2007, MNRAS, 379, 418

Cappellari, M. & McDermid, R. M. 2005, Classical and Quantum Gravity, 22, 347

Cappellari, M., et al. 2010, ArXiv e-prints

Cappellari, M., et al. 2009, MNRAS, 394, 660

Cappellari, M., et al. 1999, ApJ, 519, 117

Cappellari, M., et al. 2002, ApJ, 578, 787

Cardelli, J. A., Clayton, G. C., & Mathis, J. S. 1989, ApJ, 345, 245

Cardullo, A., et al. 2009, A&A, 508, 641

Carollo, C. M., Danziger, I. J., & Buson, L. 1993, MNRAS, 265, 553

Carollo, C. M., Franx, M., Illingworth, G. D., & Forbes, D. A. 1997, ApJ, 481, 710

Carollo, C. M., Stiavelli, M., & Mack, J. 1998, AJ, 116, 68

Casali, M., et al. 2007, A&A, 467, 777

Cattaneo, A. 2001, MNRAS, 324, 128

Cavaliere, A. & Menci, N. 2007, ApJ, 664, 47

Cavaliere, A. & Padovani, P. 1989, ApJ, 340, L5

Cayrel de Strobel, G., Soubiran, C., Friel, E. D., Ralite, N., & Francois, P. 1997, A&AS, 124, 299

Cesetti, M., et al. 2009, A&A, 497, 41

Chiaberge, M., Capetti, A., & Celotti, A. 1999, A&A, 349, 77

Chokshi, A. & Turner, E. L. 1992, MNRAS, 259, 421

Ciotti, L. & Ostriker, J. P. 2001, ApJ, 551, 131

Coccato, L., et al. 2009, MNRAS, 394, 1249

Coccato, L., et al. 2006, MNRAS, 366, 1050

Condon, J. J., et al. 1998, AJ, 115, 1693

Corbett, E. A., et al. 2003, MNRAS, 343, 705

Corsini, E. M., et al. 1999, A&A, 342, 671

Corsini, E. M., et al. 2008, ApJS, 175, 462

Côté, P., et al. 2006, ApJS, 165, 57

Courteau, S., McDonald, M., Widrow, L. M., & Holtzman, J. 2007, ApJ, 655, L21

Cox, T. J., et al. 2006, ApJ, 650, 791

Cretton, N. & van den Bosch, F. C. 1999, ApJ, 514, 704

Croton, D. J. 2009, MNRAS, 394, 1109

Croton, D. J., et al. 2006, MNRAS, 365, 11

Dalla Bontà, E., et al. 2009, ApJ, 690, 537

Dalton, G. B., et al. 2004, in Presented at the Society of Photo-Optical Instrumentation Engineers (SPIE) Conference, Vol. 5492, Society of Photo-Optical Instrumentation Engineers (SPIE) Conference Series, ed. A. F. M. Moorwood & M. Iye, 988–997

Davies, R. I., et al. 2006, ApJ, 646, 754

Davies, R. L., et al. 1987, ApJS, 64, 581

de Francesco, G., Capetti, A., & Marconi, A. 2006, A&A, 460, 439

—. 2008, A&A, 479, 355

de Lorenzi, F., Debattista, V. P., Gerhard, O., & Sambhus, N. 2007, MNRAS, 376, 71

De Lucia, G., Springel, V., White, S. D. M., Croton, D., & Kauffmann, G. 2006, MNRAS, 366, 499

de Souza, R. E., Gadotti, D. A., & dos Anjos, S. 2004, ApJS, 153, 411

de Vaucouleurs, G., et al. 1991, Third Reference Catalogue of Bright Galaxies (Volume 1-3, XII, 2069 pp. 7 figs.. Springer-Verlag Berlin Heidelberg New York)

Debattista, V. P., Corsini, E. M., & Aguerri, J. A. L. 2002, MNRAS, 332, 65

Decarli, R., et al. 2010, MNRAS, 27

Devereux, N., Ford, H., Tsvetanov, Z., & Jacoby, G. 2003, AJ, 125, 1226

Di Matteo, T., Colberg, J., Springel, V., Hernquist, L., & Sijacki, D. 2008, ApJ, 676, 33

Di Matteo, T., Springel, V., & Hernquist, L. 2005, Nature, 433, 604

di Nella, H., Garcia, A. M., Garnier, R., & Paturel, G. 1995, A&AS, 113, 151

Djorgovski, S. & Davis, M. 1987, ApJ, 313, 59

Doi, M., Fukugita, M., & Okamura, S. 1993, MNRAS, 264, 832

Donley, J. L., Brandt, W. N., Eracleous, M., & Boller, T. 2002, AJ, 124, 1308

Donzelli, C. J., et al. 2007, ApJ, 667, 780

Dopita, M. A., et al. 1997, ApJ, 490, 202

Douglas, N. G., et al. 2007, ApJ, 664, 257

Dressel, L., et al. 2007, STIS Data Handbook, Version 5.0 (Baltimore:STScI)

Dressler, A., et al. 1987, ApJ, 313, 42

Dumas, G., Mundell, C. G., Emsellem, E., & Nagar, N. M. 2007, MNRAS, 379, 1249

Emsellem, E., et al. 2007, MNRAS, 379, 401

Emsellem, E., Monnet, G., & Bacon, R. 1994, A&A, 285, 723

Eracleous, M. & Halpern, J. P. 2003, ApJ, 599, 886

Erwin, P., Graham, A. W., & Caon, N. 2004, in Coevolution of Black Holes and Galaxies, ed. L. C. Ho

Esquej, P., et al. 2007, A&A, 462, L49

Falcke, H., Körding, E., & Markoff, S. 2004, A&A, 414, 895

Falcón-Barroso, J., et al. 2006, MNRAS, 369, 529

Falcón-Barroso, J., Peletier, R. F., & Balcells, M. 2002, MNRAS, 335, 741

Fanaroff, B. L. & Riley, J. M. 1974, MNRAS, 167, 31P

Feoli, A. & Mancini, L. 2009, ApJ, 703, 1502

Ferrarese, L. 2002, ApJ, 578, 90

Ferrarese, L., et al. 2006, ApJ, 644, L21

Ferrarese, L. & Ford, H. 2005, Space Science Reviews, 116, 523

Ferrarese, L. & Ford, H. C. 1999, ApJ, 515, 583

Ferrarese, L., Ford, H. C., & Jaffe, W. 1996, ApJ, 470, 444

Ferrarese, L. & Merritt, D. 2000, ApJ, 539, L9

Ferrarese, L., van den Bosch, F. C., Ford, H. C., Jaffe, W., & O'Connell, R. W. 1994, AJ, 108, 1598

Filippenko, A. V. & Halpern, J. P. 1984, ApJ, 285, 458

Filippenko, A. V. & Ho, L. C. 2003, ApJ, 588, L13

Filippenko, A. V. & Sargent, W. L. W. 1988, ApJ, 324, 134

Fisher, D. 1997, AJ, 113, 950

Fisher, D., Franx, M., & Illingworth, G. 1995, ApJ, 448, 119

Forbes, D. A. 1996, AJ, 112, 1409

Freedman, W. L., et al. 2001, ApJ, 553, 47

Freeman, K. C. 1966, MNRAS, 133, 47

—. 1970, ApJ, 160, 811

Gadotti, D. A. 2009, MNRAS, 393, 1531

Gadotti, D. A., Baes, M., & Falony, S. 2010, ArXiv e-prints

Gadotti, D. A. & Kauffmann, G. 2009, MNRAS, 399, 621

Gallagher, J. S., Knapp, G. R., Faber, S. M., & Balick, B. 1977, ApJ, 215, 463

Ganda, K., et al. 2006, MNRAS, 367, 46

Garcia-Rissmann, A., et al. 2005, MNRAS, 359, 765

Gaskell, C. M. 2009, ArXiv e-prints

Gebhardt, K., et al. 2000a, ApJ, 539, L13

Gebhardt, K., et al. 2000b, ApJ, 543, L5

Gebhardt, K., et al. 2001, AJ, 122, 2469

Gebhardt, K., et al. 2007, ApJ, 671, 1321

Gebhardt, K., Rich, R. M., & Ho, L. C. 2002, ApJ, 578, L41

Gebhardt, K., et al. 2003, ApJ, 583, 92

Gebhardt, K. & Thomas, J. 2009, ApJ, 700, 1690

Gerhard, O., Kronawitter, A., Saglia, R. P., & Bender, R. 2001, AJ, 121, 1936

Gerhard, O. E. 1993, MNRAS, 265, 213

Gezari, S., et al. 2008, ApJ, 676, 944

Gezari, S., et al. 2009, ApJ, 698, 1367

Gezari, S., et al. 2006, ApJ, 653, L25

Ghez, A. M., et al. 2003, ApJ, 586, L127

Ghez, A. M., et al. 2005, ApJ, 620, 744

Ghez, A. M., et al. 2008, ApJ, 689, 1044

Gillessen, S., et al. 2009, ApJ, 692, 1075

Giroletti, M., Taylor, G. B., & Giovannini, G. 2005, ApJ, 622, 178

Goudfrooij, P., Hansen, L., Jorgensen, H. E., & Norgaard-Nielsen, H. U. 1994, A&AS, 105, 341

Graham, A. W. 2007, MNRAS, 379, 711

—. 2008, ApJ, 680, 143

Graham, A. W. & Driver, S. P. 2005, Publications of the Astronomical Society of Australia, 22, 118

—. 2007, ApJ, 655, 77

Graham, A. W., Driver, S. P., Allen, P. D., & Liske, J. 2007, MNRAS, 378, 198

Graham, A. W., Erwin, P., Caon, N., & Trujillo, I. 2001, ApJ, 563, L11

Graham, A. W., Erwin, P., Caon, N., & Trujillo, I. 2003, in Revista Mexicana de Astronomia y Astrofisica Conference Series, Vol. 17, Revista Mexicana de Astronomia y Astrofisica Conference Series, ed. V. Avila-Reese, C. Firmani, C. S. Frenk, & C. Allen, 196–197

Graham, A. W. & Li, I. 2009, ApJ, 698, 812

Granato, G. L., De Zotti, G., Silva, L., Bressan, A., & Danese, L. 2004, ApJ, 600, 580

Greene, J. E. & Ho, L. C. 2005a, ApJ, 627, 721

—. 2005b, ApJ, 630, 122

—. 2006, ApJ, 641, L21

Greene, J. E., Ho, L. C., & Barth, A. J. 2008, ApJ, 688, 159

Greenhill, L. J., et al. 2003, ApJ, 582, L11

Gu, Q., et al. 2006, MNRAS, 366, 480

Gültekin, K., et al. 2009a, ApJ, 706, 404

Gültekin, K., et al. 2009b, ApJ, 698, 198

Haehnelt, M. G. & Kauffmann, G. 2000, MNRAS, 318, L35

Haehnelt, M. G., Natarajan, P., & Rees, M. J. 1998, MNRAS, 300, 817

Hambly, N. C., et al. 2008, MNRAS, 384, 637

Häring, N. & Rix, H. 2004, ApJ, 604, L89

Häring-Neumayer, N., et al. 2006, ApJ, 643, 226

Harms, R. J., et al. 1994, ApJ, 435, L35

Haynes, M. P. & Giovanelli, R. 1984, AJ, 89, 758

Heckman, T. M. 1980, A&A, 87, 142

Heckman, T. M., Miley, G. K., & Green, R. F. 1984, ApJ, 281, 525

Heckman, T. M., Miley, G. K., van Breugel, W. J. M., & Butcher, H. R. 1981, ApJ, 247, 403

Heinz, S. 2004, MNRAS, 355, 835

Héraudeau, P. & Simien, F. 1998, A&AS, 133, 317

Héraudeau, P., Simien, F., Maubon, G., & Prugniel, P. 1999, A&AS, 136, 509

Herriot, G., et al. 2000, in Society of Photo-Optical Instrumentation Engineers (SPIE) Conference Series, Vol. 4007, Society of Photo-Optical Instrumentation Engineers (SPIE) Conference Series, ed. P. L. Wizinowich, 115–125

Herrnstein, J. R., Moran, J. M., Greenhill, L. J., & Trotter, A. S. 2005, ApJ, 629, 719

Hewett, P. C., Warren, S. J., Leggett, S. K., & Hodgkin, S. T. 2006, MNRAS, 367, 454

Heyer, I., et al. 2004, WFPC2 Instrument Handbook, Version 9.0 (ed. I. Heyer, J. Biretta, Baltimore: STScI)

Hinz, J. L. & Rieke, G. H. 2006, ApJ, 646, 872

Ho, L. C. 2007, ApJ, 668, 94

—. 2008, ARA&A, 46, 475

—. 2009, ApJ, 699, 638

Ho, L. C., Darling, J., & Greene, J. E. 2008a, ApJS, 177, 103

—. 2008b, ApJ, 681, 128

Ho, L. C., Filippenko, A. V., & Sargent, W. L. W. 1997a, ApJS, 112, 315

Ho, L. C., Filippenko, A. V., Sargent, W. L. W., & Peng, C. Y. 1997b, ApJS, 112, 391

Ho, L. C., Greene, J. E., Filippenko, A. V., & Sargent, W. L. W. 2009, ApJS, 183, 1

Ho, L. C., et al. 2000, ApJ, 541, 120

Ho, L. C., et al. 2002, PASP, 114, 137

Hodapp, K. W., et al. 2003, PASP, 115, 1388

Holtzman, J. A., et al. 1995a, PASP, 107, 1065

Holtzman, J. A., et al. 1995b, PASP, 107, 156

Hopkins, P. F., et al. 2005a, ApJ, 630, 705

Hopkins, P. F., et al. 2005b, ApJ, 630, 716

—. 2006, ApJS, 163, 1

Hopkins, P. F., Hernquist, L., Cox, T. J., Robertson, B., & Krause, E. 2007a, ApJ, 669, 45

—. 2007b, ApJ, 669, 67

Hopkins, P. F., Murray, N., & Thompson, T. A. 2009, MNRAS, 398, 303

Houghton, R. C. W., et al. 2006, MNRAS, 367, 2

Hu, J. 2008, MNRAS, 386, 2242

—. 2009, ArXiv e-prints

Hudson, M. J., Lucey, J. R., Smith, R. J., Schlegel, D. J., & Davies, R. L. 2001, MNRAS, 327, 265

Hughes, M. A., et al. 2003, AJ, 126, 742

Jahnke, K., et al. 2009, ApJ, 706, L215

Jarrett, T. H., et al. 2000, AJ, 119, 2498

Jarvis, B. J., Dubath, P., Martinet, L., & Bacon, R. 1988, A&AS, 74, 513

Jedrzejewski, R. I. 1987, MNRAS, 226, 747

Jensen, J. B., et al. 2003, ApJ, 583, 712

Jørgensen, I., Franx, M., & Kjaergaard, P. 1995, MNRAS, 276, 1341

Johansson, P. H., Burkert, A., & Naab, T. 2009, ApJ, 707, L184

Jore, K. P., Broeils, A. H., & Haynes, M. P. 1996, AJ, 112, 438

Jørgensen, I., et al. 2007, ApJ, 654, L179

Jørgensen, I., Franx, M., & Kjaergaard, P. 1996, MNRAS, 280, 167

Kaspi, S., et al. 2005, ApJ, 629, 61

Kaspi, S., et al. 2000, ApJ, 533, 631

Kassin, S. A., de Jong, R. S., & Pogge, R. W. 2006, ApJS, 162, 80

Kent, S. M. 1985, ApJS, 59, 115

Khochfar, S. & Silk, J. 2006, ApJ, 648, L21

Kim, S. S., Park, M., & Lee, H. M. 1999, ApJ, 519, 647

Kim Quijano, J., et al. 2007, STIS Instrument Handbook, Version 8.0 (Baltimore:STScI)

Kleinmann, S. G. & Hall, D. N. B. 1986, ApJS, 62, 501

Kodaira, K., Okamura, S., & Ichikawa, S. 1990, Photometric atlas of northern bright galaxies (Tokyo: University of Tokyo Press, 1990, edited by Kodaira, Keiichi; Okamura, Sadanori; Ichikawa, Shin-ichi)

Koprolin, W. & Zeilinger, W. W. 2000, A&AS, 145, 71

Körding, E., Falcke, H., & Corbel, S. 2006, A&A, 456, 439

Kormendy, J. 1977, ApJ, 217, 406

—. 1988, ApJ, 335, 40

Kormendy, J. 2001, in ASP Conf. Ser. 230: Galaxy Disks and Disk Galaxies, ed. J. G. Funes & E. M. Corsini, 247–256

Kormendy, J. 2004, in Coevolution of Black Holes and Galaxies, ed. L. C. Ho, 1

Kormendy, J. & Bender, R. 2009, ApJ, 691, L142

Kormendy, J., Fisher, D. B., Cornell, M. E., & Bender, R. 2009, ApJS, 182, 216

Kormendy, J. & Gebhardt, K. 2001, in AIP Conf. Proc. 586: 20th Texas Symposium on relativistic astrophysics, ed. J. C. Wheeler & H. Martel, 363–+

Kormendy, J. & Kennicutt, Jr., R. C. 2004, ARA&A, 42, 603

Kormendy, J. & Richstone, D. 1995, ARA&A, 33, 581

Krajnović, D., Cappellari, M., Emsellem, E., McDermid, R. M., & de Zeeuw, P. T. 2005, MNRAS, 357, 1113

Krajnović, D., McDermid, R. M., Cappellari, M., & Davies, R. L. 2009, MNRAS, 1306

Krist, J. & Hook, R. 1999, Tiny Tim User's Guide (Baltimore:STScI)

Kronawitter, A., Saglia, R. P., Gerhard, O., & Bender, R. 2000, A&AS, 144, 53

Laine, S., Knapen, J. H., Pérez-Ramírez, D., Englmaier, P., & Matthias, M. 2001, MNRAS, 324, 891

Laine, S., et al. 2003, AJ, 125, 478

Lake, G. & Dressler, A. 1986, ApJ, 310, 605

Lauer, T. R., et al. 1995, AJ, 110, 2622

Lauer, T. R., et al. 2007a, ApJ, 662, 808

Lauer, T. R., Tremaine, S., Richstone, D., & Faber, S. M. 2007b, ApJ, 670, 249

Laurikainen, E., Salo, H., & Buta, R. 2005, MNRAS, 362, 1319

Laurikainen, E., Salo, H., Buta, R., & Vasylyev, S. 2004, MNRAS, 355, 1251

Lawrence, A., et al. 2007, MNRAS, 379, 1599

Lucy, L. B. 1974, AJ, 79, 745

MacArthur, L. A., Courteau, S., Bell, E., & Holtzman, J. A. 2004, ApJS, 152, 175

Macchetto, F., et al. 1997, ApJ, 489, 579

Maciejewski, W. & Binney, J. 2001, MNRAS, 323, 831

Madrid, J. P., et al. 2006, ApJS, 164, 307

Magorrian, J. & Ballantyne, D. 2001, MNRAS, 322, 702

Magorrian, J. & Tremaine, S. 1999, MNRAS, 309, 447

Magorrian, J., et al. 1998, AJ, 115, 2285

Maoz, D., et al. 1995, ApJ, 440, 91

Maoz, D., Nagar, N. M., Falcke, H., & Wilson, A. S. 2005, ApJ, 625, 699

Marchesini, D., Capetti, A., & Celotti, A. 2005, A&A, 433, 841

Marconi, A., et al. 2003, ApJ, 586, 868

Marconi, A. & Hunt, L. K. 2003, ApJ, 589, L21

Marconi, A., et al. 2006, A&A, 448, 921

Marconi, A., et al. 2004, MNRAS, 351, 169

Martini, P. & Pogge, R. W. 1999, AJ, 118, 2646

Marulli, F., Bonoli, S., Branchini, E., Moscardini, L., & Springel, V. 2008, MNRAS, 385, 1846

Mc Master, M., et al. 2008, WFPC2 Instrument Handbook, Version 10.0 (STScI, Baltimore)

Mc Master, M. & Whitmore, B. 2002, WFPC2 Instruments Science Report, 02-07 (STScI, Baltimore)

McDonald, M., Courteau, S., & Tully, R. B. 2009, MNRAS, 394, 2022

McLure, R. J. & Dunlop, J. S. 2002, MNRAS, 331, 795

—. 2004, MNRAS, 352, 1390

McLure, R. J., Jarvis, M. J., Targett, T. A., Dunlop, J. S., & Best, P. N. 2006, MNRAS, 368, 1395

Méndez-Abreu, J. 2008, PhD thesis, Universitá Degli Studi di Padova, Universidad de la Laguna, 2008

Méndez-Abreu, J., Aguerri, J. A. L., Corsini, E. M., & Simonneau, E. 2008a, A&A, 478, 353

Méndez-Abreu, J., et al. 2008b, ApJ, 679, L73

Merloni, A., Heinz, S., & di Matteo, T. 2003, MNRAS, 345, 1057

Merloni, A., et al. 2006, New Astronomy, 11, 567

Miyoshi, M., et al. 1995, Nature, 373, 127

Moiseev, A. V., Valdés, J. R., & Chavushyan, V. H. 2004, A&A, 421, 433

Möllenhoff, C., et al. 1999, A&A, 352, L5

Möllenhoff, C. & Heidt, J. 2001, A&A, 368, 16

Monaco, P., Fontanot, F., & Taffoni, G. 2007, MNRAS, 375, 1189

Monnet, G., Bacon, R., & Emsellem, E. 1992, A&A, 253, 366

Moré, J. J., Garbow, B. S., & Hillstrom, K. E. 1980, User guide for MINPACK-1 (Technical Report ANL-80-74, Argonne National Laboratory, Argonne,IL)

Napolitano, N. R., et al. 2009, MNRAS, 393, 329

Nelson, C. H. & Whittle, M. 1995, ApJS, 99, 67

Neumayer, N., et al. 2007, ApJ, 671, 1329

Noel-Storr, J., Baum, S. A., & O'Dea, C. P. 2007, ApJ, 663, 71

Noel-Storr, J., et al. 2003, ApJS, 148, 419

Novak, G. S., Faber, S. M., & Dekel, A. 2006, ApJ, 637, 96

Nowak, N., et al. 2008, MNRAS, 391, 1629

Nowak, N., et al. 2007, MNRAS, 379, 909

Nowak, N., et al. 2009, ArXiv e-prints

Noyola, E., Gebhardt, K., & Bergmann, M. 2008, ApJ, 676, 1008

O'Connell, R. W., et al. 2005, ApJ, 635, 305

O'Dea, C. P. & Owen, F. N. 1986, ApJ, 301, 841

—. 1987, ApJ, 316, 95

Oemler, Jr., A. 1976, ApJ, 209, 693

Oliva, E., Origlia, L., Kotilainen, J. K., & Moorwood, A. F. M. 1995, A&A, 301, 55

Origlia, L., Moorwood, A. F. M., & Oliva, E. 1993, A&A, 280, 536

Osterbrock, D. E. 1989, Astrophysics of Gaseous Nebulae and Active Galactic Nuclei (Sausalito, California, University Science Books)

Osterbrock, D. E., Fulbright, J. P., Martel, A. R., Keane, M. J., Trager, S. C., & Basri, G. 1996, PASP, 108, 277

Pahre, M. A., Djorgovski, S. G., & de Carvalho, R. R. 1998, AJ, 116, 1591

Pastorini, G., et al. 2007, A&A, 469, 405

Paturel, G., et al. 1997, A&AS, 124, 109

Paturel, G., et al. 2003a, A&A, 412, 45

Paturel, G., et al. 2003b, A&A, 412, 57

Pavlovsky, C., et al. 2004a, ACS Instrument Handbook, Version 5.0 (Baltimore:STScI)

Pavlovsky, C., Koekemoer, A., & Mack, J. 2004b, ACS Data Handbook, Version 3.0 (Baltimore:STScI)

Peterson, B. M. & Bentz, M. C. 2006, New Astronomy Review, 50, 796

Pierce, M., et al. 2006, MNRAS, 366, 1253

Pizzella, A., et al. 2005, ApJ, 631, 785

Postman, M. & Lauer, T. R. 1995, ApJ, 440, 28

Press, W. H., Teukolsky, S. A., Vetterling, W. T., & Flannery, B. P. 1992, Numerical recipes in FORTRAN. The art of scientific computing (Cambridge: University Press, —c1992, 2nd ed.)

—. 1996, Numerical Recipes in Fortran 77: The Art of Scientific Computing (Cambridge: Cambridge University Press)

Prieto, M., Aguerri, J. A. L., Varela, A. M., & Muñoz-Tuñón, C. 2001, A&A, 367, 405

Proctor, R. N. & Sansom, A. E. 2002, MNRAS, 333, 517

Raimond, E., Faber, S. M., Gallagher, III, J. S., & Knapp, G. R. 1981, ApJ, 246, 708

Rees, M. J. 1984, ARA&A, 22, 471

—. 1988, Nature, 333, 523

Renzini, A., et al. 1995, Nature, 378, 39

Rest, A., et al. 2001, AJ, 121, 2431

Rice, M. S., et al. 2006, ApJ, 636, 654

Richardson, W. H. 1972, Journal of the Optical Society of America (1917-1983), 62, 55

Robertson, B., et al. 2006a, ApJ, 641, 21

Robertson, B., et al. 2006b, ApJ, 641, 90

Rossa, J., et al. 2006, AJ, 132, 1074

Rybicki, G. B. 1987, in IAU Symposium, Vol. 127, Structure and Dynamics of Elliptical Galaxies, ed. P. T. de Zeeuw, 397–+

Saglia, R. P., et al. 1993, ApJ, 403, 567

Saglia, R. P., Kronawitter, A., Gerhard, O., & Bender, R. 2000, AJ, 119, 153

Sánchez-Blázquez, P., et al. 2006, MNRAS, 371, 703

Sarzi, M. 2004, in Coevolution of Black Holes and Galaxies, ed. L. C. Ho

Sarzi, M., et al. 2006, MNRAS, 366, 1151

Sarzi, M., et al. 2005, ApJ, 628, 169

Sarzi, M., et al. 2001, ApJ, 550, 65

Sarzi, M., et al. 2002, ApJ, 567, 237

Sarzi, M., et al. 2009, ArXiv e-prints

Scarlata, C., et al. 2004, AJ, 128, 1124

Schawinski, K., et al. 2006, Nature, 442, 888

Schechter, P. L. 1983, ApJS, 52, 425

Schlegel, D. J., Finkbeiner, D. P., & Davis, M. 1998, ApJ, 500, 525

Schmidt, M. 1963, Nature, 197, 1040

Schödel, R., et al. 2003, ApJ, 596, 1015

Schödel, R., et al. 2002, Nature, 419, 694

Schwarzschild, M. 1979, ApJ, 232, 236

Sersic, J. L. 1968, Atlas de galaxias australes (Cordoba, Argentina: Observatorio Astronomico, 1968)

Seth, A., Agüeros, M., Lee, D., & Basu-Zych, A. 2008, ApJ, 678, 116

Shankar, F. 2009, New Astronomy Review, 53, 57

Shankar, F., Salucci, P., Granato, G. L., De Zotti, G., & Danese, L. 2004, MNRAS, 354, 1020

Shao, Z., et al. 2007, ApJ, 659, 1159

Shapiro, K. L., et al. 2006, MNRAS, 370, 559

Sheth, R. K., et al. 2003, ApJ, 594, 225

Shields, G. A., et al. 2003, ApJ, 583, 124

Shields, G. A., Menezes, K. L., Massart, C. A., & Vanden Bout, P. 2006, ApJ, 641, 683

Shields, J. C., et al. 2007, ApJ, 654, 125

Shields, J. C., et al. 2008, ApJ, 682, 104

Shier, L. M., Rieke, M. J., & Rieke, G. H. 1996, ApJ, 470, 222

Silge, J. D. & Gebhardt, K. 2003, AJ, 125, 2809

Silge, J. D., Gebhardt, K., Bergmann, M., & Richstone, D. 2005, AJ, 130, 406

Silk, J. & Rees, M. J. 1998, A&A, 331, L1

Simien, F. & Prugniel, P. 1997a, A&AS, 122, 521

—. 1997b, A&AS, 126, 15

—. 1997c, A&AS, 126, 519

—. 1998, A&AS, 131, 287

—. 2002, A&A, 384, 371

Siopis, C., et al. 2009, ApJ, 693, 946

Sirianni, M., et al. 2005, PASP, 117, 1049

Skrutskie, M. F., et al 2006, AJ, 131, 1163

Smith, R. J., Lucey, J. R., Hudson, M. J., Schlegel, D. J., & Davies, R. L. 2000, MNRAS, 313, 469

Sofue, Y., Tomita, A., Tutui, Y., Honma, M., & Takeda, Y. 1998, PASJ, 50, 427

Soltan, A. 1982, MNRAS, 200, 115

Somerville, R. S. 2009, MNRAS, 399, 1988

Springel, V., Di Matteo, T., & Hernquist, L. 2005, MNRAS, 361, 776

Standord, S. A. & Balcells, M. 1990, ApJ, 355, 59

Struble, M. F. & Rood, H. J. 1999, ApJS, 125, 35

Suchkov, A. A., Berman, V. G., Heckman, T. M., & Balsara, D. S. 1996, ApJ, 463, 528

Sun, M., Jerius, D., & Jones, C. 2005, ApJ, 633, 165

Terlevich, E., Diaz, A. I., & Terlevich, R. 1990, MNRAS, 242, 271

Thomas, J., et al. 2007, MNRAS, 382, 657

Tonry, J. L. 1985, AJ, 90, 2431

Tonry, J. L., Blakeslee, J. P., Ajhar, E. A., & Dressler, A. 2000, ApJ, 530, 625

Tonry, J. L. & Davis, M. 1981, ApJ, 246, 666

Tonry, J. L., et al. 2001, ApJ, 546, 681

Tremaine, S., et al. 2002, ApJ, 574, 740

Tremblay, G. R., et al. 2007, ApJ, 666, 109

Treu, T., Malkan, M. A., & Blandford, R. D. 2004, ApJ, 615, L97

Treu, T., Woo, J., Malkan, M. A., & Blandford, R. D. 2007, ApJ, 667, 117

Trujillo, I., Aguerri, J. A. L., Cepa, J., & Gutiérrez, C. M. 2001, MNRAS, 328, 977

Trujillo, I., Erwin, P., Asensio Ramos, A., & Graham, A. W. 2004, AJ, 127, 1917

Tully, R. B. 1988, Nearby Galaxies Catalog (Cambridge: Cambridge University Press)

Tundo, E., Bernardi, M., Hyde, J. B., Sheth, R. K., & Pizzella, A. 2007, ApJ, 663, 53

Ulmer, A. 1999, ApJ, 514, 180

Ulvestad, J. S., Greene, J. E., & Ho, L. C. 2007, ApJ, 661, L151

Valluri, M., Ferrarese, L., Merritt, D., & Joseph, C. L. 2005, ApJ, 628, 137

Valluri, M., Merritt, D., & Emsellem, E. 2004, ApJ, 602, 66

van den Bosch, F. C. & Emsellem, E. 1998, MNRAS, 298, 267

van den Bosch, F. C. & van der Marel, R. P. 1995, MNRAS, 274, 884

van den Bosch, R. C. E., de Zeeuw, P. T., (, &). 2009, MNRAS, ArXiv 0910.0844

van den Bosch, R. C. E., van de Ven, G., Verolme, E. K., Cappellari, M., & de Zeeuw, P. T. 2008, MNRAS, 385, 647

van der Marel, R. P., Cretton, N., de Zeeuw, P. T., & Rix, H. 1998, ApJ, 493, 613

van der Marel, R. P. & Franx, M. 1993, ApJ, 407, 525

van der Marel, R. P. & van den Bosch, F. C. 1998, AJ, 116, 2220

van Dokkum, P. G. 2001, PASP, 113, 1420

Vega Beltrán, J. C., et al. 2001, A&A, 374, 394

Verdoes Kleijn, G. A., van der Marel, R. P., Carollo, C. M., & de Zeeuw, P. T. 2000, AJ, 120, 1221

Verdoes Kleijn, G. A., van der Marel, R. P., de Zeeuw, P. T., Noel-Storr, J., & Baum, S. A. 2002, AJ, 124, 2524

Verdoes Kleijn, G. A., van der Marel, R. P., & Noel-Storr, J. 2006, AJ, 131, 1961

Verheijen, M. A. W. & Sancisi, R. 2001, A&A, 370, 765

Verolme, E. K., et al. 2002, MNRAS, 335, 517

Vestergaard, M. 2002, ApJ, 571, 733

—. 2004, ApJ, 601, 676

Vestergaard, M. & Peterson, B. M. 2006, ApJ, 641, 689

Vittorini, V., Shankar, F., & Cavaliere, A. 2005, MNRAS, 363, 1376

Volonteri, M. 2007, ApJ, 663, L5

Volonteri, M., Haardt, F., & Madau, P. 2003, ApJ, 582, 559

Volonteri, M. & Natarajan, P. 2009, MNRAS, 400, 1911

von der Linden, A., Best, P. N., Kauffmann, G., & White, S. D. M. 2007, MNRAS, 379, 867

Wagner, S. J. & Appenzeller, I. 1988, A&A, 197, 75

Walsh, J. L., et al. 2008, AJ, 136, 1677

Wandel, A., Peterson, B. M., & Malkan, M. A. 1999, ApJ, 526, 579

Wang, J., et al. 2009, ApJ, 705, L76

Wang, J. & Merritt, D. 2004, ApJ, 600, 149

Wang, R., Wu, X., & Kong, M. 2006, ApJ, 645, 890

Warren, S. J., et al. 2007, MNRAS, 375, 213

Wegner, G., et al. 2003, AJ, 126, 2268

Whitmore, B. 1995, Calibrating Hubble Space Telescope: Post Servicing Mission (eds. A. Koratkar, C. Leitherer, Baltimore, STScI)

Whitmore, B. C. & Kirshner, R. P. 1981, ApJ, 250, 43

Whitmore, B. C., Schechter, P. L., & Kirshner, R. P. 1979, ApJ, 234, 68

Whittle, M. 1985a, MNRAS, 213, 1

—. 1985b, MNRAS, 213, 33

Williams, M. J., Bureau, M., & Cappellari, M. 2009, MNRAS, ArXiv 0909.0680

Willott, C. J., McLure, R. J., & Jarvis, M. J. 2003, ApJ, 587, L15

Winge, C., Riffel, R. A., & Storchi-Bergmann, T. 2009, ArXiv e-prints

Wold, M., Lacy, M., Käufl, H. U., & Siebenmorgen, R. 2006, A&A, 460, 449

Wolf, J., et al. 2009, ArXiv e-prints

Woo, J., Treu, T., Malkan, M. A., & Blandford, R. D. 2006, ApJ, 645, 900

—. 2008, ApJ, 681, 925

Wyithe, J. S. B. 2006, MNRAS, 365, 1082

Wyithe, J. S. B. & Loeb, A. 2002, ApJ, 581, 886

—. 2003, ApJ, 595, 614

Xanthopoulos, E. 1996, MNRAS, 280, 6

Xu, C., O'Dea, C. P., & Biretta, J. A. 1999, AJ, 117, 2626

Yoo, J., Miralda-Escudé, J., Weinberg, D. H., Zheng, Z., & Morgan, C. W. 2007, ApJ, 667, 813

York, D. G., et al. 2000, AJ, 120, 1579

Younger, J. D., Hopkins, P. F., Cox, T. J., & Hernquist, L. 2008, ApJ, 686, 815

Yu, Q. & Tremaine, S. 2002, MNRAS, 335, 965

Zasov, A. V., Petrochenko, L. N., & Cherepashchuk, A. M. 2005, Astronomy Reports, 49, 362

Zeilinger, W. W., et al. 2001, Ap&SS, 276, 643